PROBING THE ELECTROCHEMICAL DYNAMICS OF SOLUBLE REDOX ACTIVE POLYMERS

BY

MARK BURGESS

DISSERTATION

Submitted in partial fulfillment of the requirements
for the degree of Doctor of Philosophy in Chemistry
in the Graduate College of the
University of Illinois at Urbana-Champaign, 2017

Urbana, Illinois

Doctoral Committee:

Assistant Professor Joaquín Rodríguez-López, Chair, Director of Research
Professor Jonathan Sweedler
Professor Jeffrey S. Moore
Assistant Professor David W. Flaherty

Abstract

It is an exciting time for exploring the synergism between the chemical and dimensional properties of redox nanomaterials for addressing the manifold performance demands faced by energy storage technologies. Our groups are interested in the development and implementation of a new strategy for non-aqueous flow batteries (NRFBs) for grid energy storage. Our motivation is to solve major challenges in NRFBs, such as the lack of membranes that simultaneously allow fast ion transport while minimizing redox active species crossover between anolyte (negative electrolyte) and catholyte (positive electrolyte) compartments. This pervasive crossover leads to deleterious capacity fade and materials underutilization.

Redox active polymers (RAPs) are highlighted as soluble nanoscopic energy storing units that enable the simple but powerful size-exclusion concept for NRFBs. Crossover of the redox component is suppressed by matching high molecular weight RAPs with simple and inexpensive nanoporous commercial separators. In contrast to the vast literature on the redox chemistry of electrode-confined polymer films, studies on the electrochemistry of solubilized RAPs are incipient. Here, viologen-, ferrocene- and nitrostyrene-based polymers in various formats exhibit properties that make amenable their electrochemical exploration as solution-phase redox couples.

A main finding is that RAP solutions store energy efficiently and reversibly while offering chemical modularity and size versatility. Beyond the practicality toward their use in NRFBs, the fundamental electrochemistry exhibited by RAPs is fascinating, showing clear distinctions in behavior from that of small molecules. Whereas RAPs conveniently translate the redox properties of small molecules into a nanostructure, they give rise to charge transfer mechanisms and electrolyte interactions that elicit distinct electrochemical responses. To understand how the electrochemical characteristics of RAPs depend on molecular features, including redox moiety,

macromolecular size, and backbone structure, a range of techniques has been employed by our groups, including voltammetry at macro- and microelectrodes, rotating disk electrode (RDE) voltammetry, bulk electrolysis, and scanning electrochemical microscopy (SECM).

Herein, we characterize the charge transfer mechanisms, identify the impact of backbone tether length and structure, demonstrate the role of the composition of the supporting electrolyte, and explore how electrostatic interactions and polyelectrolyte dynamics all affect the reactivity of soluble RAPs. Finally, new tools to study the energy storage capabilities of bulk RAP solutions and the possibility to interrogate single entities using SECM methods are highlighted as promising technologies to advance the electrochemical characterization of nanostructured macromolecular redox architectures.

Acknowledgements

This work is dedicated to my parents and Martine, who have never stopped believing in me. They are always pushing me to pursue my desires, wherever they may take me. I want to thank my family, friends, and lab mates for their enduring support and camaraderie during my graduate studies. Without their help, encouragement, and companionship I would not have been successful in my efforts.

I want to recognize my graduate research advisor, Dr. Joaquín Rodríguez-López, for allowing me to join his research laboratory when it was in its infancy and be able to contribute to the legacy of the group. Joaquín has been an excellent mentor from whom I have learned so much. He pushes me to be a better experimentalist, writer, and person. With Joaquín's guidance and teaching, I have grown as an individual and strengthened my abilities as a scientist beyond what I thought was possible. I will take my experiences working in the Rodríguez-López group far in life, and I would not trade any opportunities I have had in this laboratory for anything else.

I want to express gratitude to the rest of my doctoral supervisory committee comprised of Dr. Jeffrey S. Moore, Dr. Jonathan Sweedler, and Dr. David W. Flaherty for their time and efforts in evaluating my progress over the course of my graduate studies. Their words of criticism and encouragement have been exceptionally helpful in shaping my scholarship and thought process. Beyond their time, discussions with students in their laboratories, and at times some of their experimental resources, have been remarkably helpful in my research efforts.

My research has been greatly assisted by amazing collaborators and partners whom I want to recognize. Dr. Kenneth Hernandez-Burgos, Dr. Etienne Chenard, Dr. Nagarjuna Gavvalappali, Elena Montoto, Burton H. Simspon, Zachary J. Barton, Zachary Gossage, Jingshu Hui, Jonathon

K. Schuh, Randy H. Ewoldt, Rajeev S. Assary, Kevin J. Cheng, and Lily A. Robertson have all offered assistance, guidance, or prepared samples that were used in my studies. Without the help from these individuals my research not have been as successful.

I extend appreciation to some important funding sources which have paid for the research I have performed while in graduate school. Without these generous funding resources none of the research I have performed would be possible. I have been supported by a National Science Foundation Graduate Research Fellowship, funding from the Joint Center for Energy Storage Research (JCESR) an Energy Innovation Hub sponsored by the Department of Energy Office of Science Basic Energy Sciences, startup funding from the University of Illinois, and additional fellowship funds from the University of Illinois Department of Chemistry.

I recognize and appreciate the supportive staff in the Materials Research Laboratory at the University of Illinois for training me on experimental techniques and assisting with data analysis.

Finally, I want to thank the helpful and kind secretarial staff in the University of Illinois Department of Chemistry for assisting me in every process of my professional graduate studies. Julie Sides, Becky Duffield, and Gayle Adkission were always available to help set up meetings, assist in filing paperwork, provided a never ending bowl of candy, and were always willing to hear out our daily grievances. Their assistance is instrumental to us graduate students, and cannot be recognized enough.

Table of Contents

Chapter 1: Redox Active Polymers as Soluble Nanomaterials for Energy Storage

Notes and Acknowledgements

This chapter contains material from a review article that was published in the journal *Accounts of Chemical Research* with authors Burgess, M.; Moore, J. S.; Rodríguez-López, J. "Redox Active Polymers as Soluble Nanomaterials for Energy Storage". **2016,** 49, 2649–2657. The cited text and figures are reprinted with the permission of the publisher and is available from http://www.pubs.acs.org and using DOI: 10.1021/acs.accounts.6b00341. M.B. helped write the manuscript and aided in making figures. This work was supported as part of the Joint Center for Energy Storage Research, an Energy Innovation Hub funded by the U.S. Department of Energy, Office of Science, Basic Energy Sciences. M.B. acknowledges support by the National Science Foundation Graduate Research Fellowship Program under grant No. DGE-1144245.

Abstract

It is an exciting time for exploring the synergism between the chemical and dimensional properties of redox nanomaterials for addressing the manifold performance demands faced by energy storage technologies. The call for widespread adoption of alternative energy sources requires the combination of emerging chemical concepts with redesigned battery formats. Our groups are interested in the development and implementation of a new strategy for non-aqueous flow batteries (NRFBs) for grid energy storage. Our motivation is to solve major challenges in NRFBs, such as the lack of membranes that simultaneously allow fast ion transport while minimizing redox active species crossover between anolyte (negative electrolyte) and catholyte (positive electrolyte) compartments. This pervasive crossover leads to deleterious capacity fade and materials underutilization.

In this chapter, redox active polymers (RAPs) are highlighted as soluble nanoscopic energy storing units that enable the simple but powerful size-exclusion concept for NRFBs. Crossover of the redox component is suppressed by matching high molecular weight RAPs with simple and inexpensive nanoporous commercial separators. In contrast to the vast literature on the redox chemistry of electrode-confined polymer films, studies on the electrochemistry of solubilized RAPs are incipient. This is due in part to challenges in finding suitable solvents that enable systematic studies on high polymers. Here, viologen-, ferrocene- and nitrostyrene-based polymers in various formats exhibit properties that make amenable their electrochemical exploration as solution-phase redox couples.

A main finding is that RAP solutions store energy efficiently and reversibly while offering chemical modularity and size versatility. Beyond the practicality toward their use in NRFBs, the fundamental electrochemistry exhibited by RAPs is fascinating, showing clear distinctions in behavior from that of small molecules. Whereas RAPs conveniently translate the redox properties of small molecules into a nanostructure, they give rise to charge transfer mechanisms and electrolyte interactions that elicit distinct electrochemical responses. To understand how the electrochemical characteristics of RAPs depend on molecular features, including redox moiety, macromolecular size, and backbone structure, a range of techniques has been employed by our groups, including voltammetry at macro- and microelectrodes, rotating disk electrode voltammetry, bulk electrolysis, and scanning electrochemical microscopy.

Introduction

The widespread adoption of alternative energy sources calls for the fusion of versatile chemical concepts with redesigned battery formats to address manifold performance demands.[1] Redox flow batteries (RFBs) are emerging as promising solutions to grid-level energy storage due

to their scalability and ability to level the inherently intermittent nature of solar and wind inputs. With wider electrochemical stability windows from organic solvents, exploring non-aqueous flow batteries (NRFBs) is an attractive direction of research.[2] However, the development of NRFBs has been slowed by the lack of suitable membranes that simultaneously allow fast ion transport while minimizing redox active species crossover between anolyte (negative electrolyte) and catholyte (positive electrolyte) compartments.

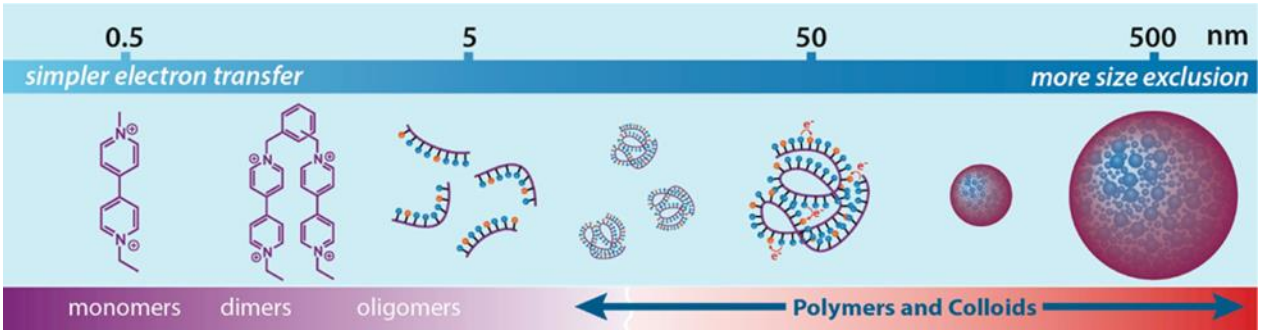

Figure 1.1. Redox active organic molecules integrated into polymers of different size exhibit distinct electrochemical properties and physical interactions.

Highly soluble redox active polymers (RAPs) are promising candidates as electrochemical storage media in a fluid format for the new concept of size-exclusion NRFBs. As schematized in Figure 1.1, RAPs dramatically extend the size range of redox polymers and related materials such as dendrimers,[3] micelles,[4] and nanoparticles.[5] Size exclusion increases with molecular weight.[6] Therefore, matching larger RAPs to existing nanoporous separators offers an attractive strategy for NRFBs. This scheme opens a rich space to explore distinct RAP properties that are not found in small molecule species, such as long-range charge transport.[7-9] Work from our groups introduces the first characterization of RAPs as soluble nanoscopic charge storage media for size-exclusion NRFBs,[6] characterizes their charge transfer mechanisms,[10] explores the impact of specific

interactions brought by the supporting electrolyte,[11, 12] and demonstrates the nano-characterization of individual RAPs.[13]

Concepts of Electron Transfer in RAPs

In the 1940s, the dynamics of polymer solutions were presented in pioneering publications from Flory and Huggins, among others.[14, 15] These theories would become the foundation for an entire subset of macromolecular chemistries. However, despite these polymer dynamic models being fairly comprehensive in their scope, they are not yet robust enough to describe more complex scenarios involving macromolecular redox chemistry. Original work from Bard and Anson presented for the first time the voltammetry of low molecular weight (<16 kDa) poly(vinylferrocene) in solution and found that this system behaved much like its constituent monomer.[16] This RAP exhibited a single oxidation wave with an intensity proportional to a system of *n* ferrocene centers. A single redox process was observed because the ferrocene units were linked by an electronically insulating backbone. Each pendant behaved as an independent ferrocene molecule. In contrast, conjugated systems display electronic interactions that modify their redox potentials.[17] These original studies opened the way to RAPs, but prior to 2012, a detailed understanding of the role of polymer molecular weight and electrolyte dependencies on the electrochemical responses of soluble RAPs was largely unknown.

Charge transport within RAPs and at the electrode/electrolyte interface is affected by polymer dynamics that do not arise in solutions of monomers or are less relevant in small polymers. Some of the most prevalent high polymer characteristics pertaining to RAPs are depicted in Figure 1.2. Small redox shuttles such as ferrocene undergo facile outer sphere electron transfer reactions at an electrode via electron tunneling. However, with larger RAPs, this mode is replaced by electron transfer at the polymer/electrode interface followed by intraparticle charge transport.

When using an insulating backbone, charge propagates pendant-to-pendant through a charge diffusion process mediated by self-exchange reactions, i.e., the hopping of charge between neighboring redox species.[18-21]

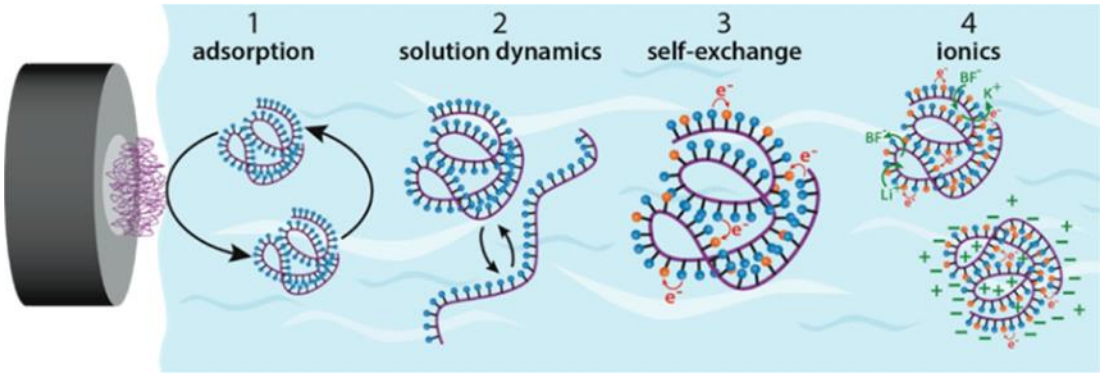

Figure 1.2. Possible contributions of polymer dynamics to RAP electrochemical response. During all electrochemical measurements, there is an adsorbed polymer layer (1) that will mediate charge transfer to solution phase RAPs. Polyelectrolyte solution dynamics (2) of RAPs can change the conformation and orientation of the coil depending on the state of charge. Self-exchange of charges (3) and ionic interactions (4) modulate electrolysis rates of the particles.

Despite their high solubility, polymers tend to adsorb as surface films due to electrostatic effects and to minimize their energy.[22] The film is pervasive and mediates charge transfer. Furthermore, ionics that typically play a much subtler role in small molecules dramatically impact reactivity of RAPs. As RAP coils are a molecularly large and ionic interface, the electrolyte ions readily establish a Debye layer around it, which affects the coil size and shape depending on the supporting electrolyte characteristics and concentration.[23] Understanding all of these effects is imperative to model the electrochemical behavior of RAPs.

As emphasized in Figure 1.2, charge transport through self-exchange becomes very relevant for larger RAP structures. A highly recurred model for describing charge diffusion, D_E, in a system of mixed redox centers is the Dahms–Ruff formalism[24] shown in equation 1.1. Here, the diffusion of charges inside a RAP is related to the rate constant for self-exchange, k_{EX}, and a

distance parameter, δ, describing the separation between redox centers. This equation has been particularly successful for describing the rates of electron hopping in small molecule dimer systems and in redox active polymer films.[18, 25]

(1.1) $$D_E = \frac{k_{EX}\delta^2}{6}$$

However, when more degrees of structural freedom are added, as is the case for large RAPs, it is not certain whether this simple mathematical relation is sufficient to accurately describe charge hopping. It is known that polymer size is suitably well described by the radius of gyration, but the distance between any two redox centers varies widely depending on which chain segments are chosen. Thus, an assignment of the pendant separation distance parameter δ is ambiguous. Furthermore, after undergoing charge transfer reactions, polymer segments necessitate the migration of supporting electrolyte ions to compensate for the local charge.[26] It is known that polymer coils in a non-theta solvent will have excluded volume effects, and thus, accessibility of the supporting electrolyte ions could be hindered in these crowded structures. This is a characteristic not faced in small molecule systems.[22]

A complete theory for charge transport inside RAPs is still developing, but studies on a diverse set of systems have revealed that the backbone structure and molecular size are essential elements to be understood. Synthetic control and systematic studies on RAPs are helping to fill this knowledge gap in the cutoff boundary that distinguishes small and large redox systems. This is relevant as it is not always the case that the redox properties of monomers scale linearly in polymer form. An example of this is the redox mediator N,N,N′,N′-tetramethyl-p-phenylenediamine (TMPD), which is highly inaccessible to charge transfer in polymer form.[8] As the majority of published research on RAPs has centered on characterizing polymer films, new

insights are gained by examining the electrochemistry of soluble RAPs. To probe the solution phase electrochemical properties of RAPs, more rigorous measurements such as bulk electrolysis, steady-state voltammetry, and even single-particle electrochemistry are needed.

Characterizing RAPs for Size-Exclusion NRFBs

Redox flow batteries (RFBs) operate by exchanging electrons via electrode terminals at the anode (negative electrode) and cathode (positive electrode) and passing through an external load. However, unlike solid-state systems, RFBs do not store their charge in a stationary electrode or at the surface. RFBs store charge by electrolysis, i.e., changing oxidation state, of a redox active electrolyte in solution. Separate containers for catholyte and an anolyte are electrolyzed when flowed through high surface area working electrodes. For high Coulombic efficiencies to be maintained in RFBs, the anolyte and catholyte charge storage media must not cross through the separator and mix, as they will spontaneously discharge. To date, the best performing and most common RFB utilizes small molecule vanadium complexes in aqueous media for charge storage and a Nafion ion exchange membrane that electrostatically excludes vanadium from the membrane pores. However, in non-aqueous media, the solubility of vanadium complexes is poor, and the ionic conductivity of a Nafion membrane suffers by orders of magnitude, making this system unattractive.[27] Despite the complexity illustrated in Figure 1.2, RAPs are efficient charge storage nanomaterials that enable a new concept in size-exclusion NRFBs.

Our groups introduced the size-exclusion concept for a new type of RFB, Figure 1.3A.[6] As predicted from polymer static partition coefficients, so long as the polymer particles have sizes on the same order as the pore size, they can be effectively rejected from crossing over a porous membrane with near quantitative exclusion for $r_{particle}/r_{pore} \approx 0.6$.[28] In our system, small molecule redox components were replaced by nano-dimensioned viologen RAPs (Figure 1.3B) with

molecular weights between approximately 20 and 300 kDa, corresponding to a size range of 4–8 nm in radius. These RAPs were successfully excluded with over 90% rejection from crossing through a commercial separator, Celgard 2325 (~12 nm pore radius). Higher rejection values should be attainable by means of a separator with smaller pore size or larger particle size, but the observed decreased crossover of active species already enables the operation of a RAP flow battery. Our first generation of viologen RAPs exhibited a facile modular synthesis following a simple substitution of a polymer backbone, poly(vinylbenzyl chloride), with a ethyl-viologen derivative. Viologen species are known to be reversible redox couples and are soluble in an assortment of non-aqueous solvents.

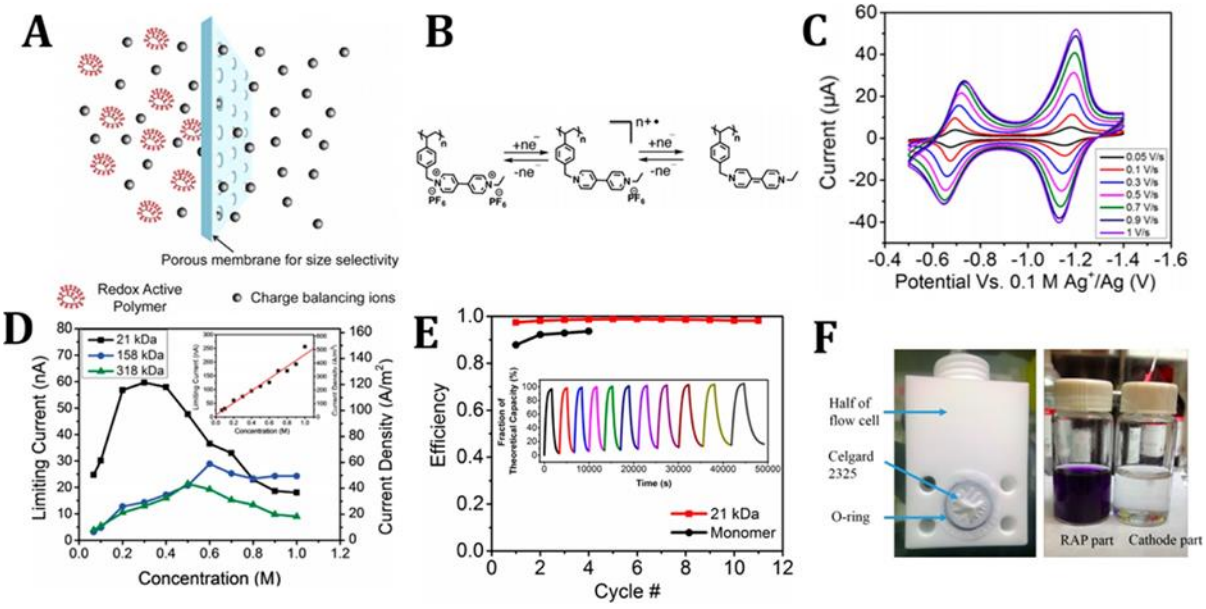

Figure 1.3. (A) A schematic for the size exclusion principle for redox flow batteries. (B) Chemical structures and electrochemical pathways for viologen RAPs (592 g/mol of equivalent weight). (C) Cyclic voltammetry of an adsorbed sample of a 21 kDa viologen polymer in a blank supporting electrolyte solution. (D) Ultramicroelectrode steady-state current obtained with a series of viologen RAPs at different concentrations. The inset shows the viscosity-corrected limiting currents via Walden's rule for the 21 kDa RAP. (E) Charge storage properties of a 21 kDaA viologen RAP demonstrated by 11 cycles of bulk electrolysis. Inset shows the fraction of theoretical capacity (5.78 C) utilized. (F) The flow cell used for battery testing of the size selective approach. The porous separator was able to effectively reject the redox active polymer from crossing over. All experiments were performed in acetonitrile as solvent. Figures are adapted with permission from reference 6. Copyright (2014) American Chemical Society.

Viologen RAPs form a redox active layer (Figure 1.3C) that shuttles charge from the electrode to the solution. Despite this layer, and similar to the earlier work by Bard and Anson, the voltammetry of the viologen RAPs strongly resembles that of viologen monomer with two reversible reductions at the known thermodynamic potentials. Of special interest for charge storage energy density, viologen RAPs are highly soluble in acetonitrile and other solvents. Concentrated solutions of up to 1 M RAPs are electrochemically active as evaluated by microelectrode voltammetry (Figure 1.3D). As the polymer concentration increases, so does the viscosity of the solution. This causes a decrease in the diffusion coefficient of the RAP and hence its current at an electrode. However, by correcting for viscosity effects via Walden's rule, the projected current increases linearly with concentration. This is encouraging for applications in NRFBs given the complexity of the system. Further probing of RAPs via bulk electrolysis, and monitoring via ultramicroelectrode voltammetry, showed that polymers with molecular weights between 20 and 300 kDa were quantitatively and reversibly converted between oxidation states with over 99% Coulombic efficiency over several charge cycles (Figure 1.3E), highlighting RAP electrochemical stability. Stability studies of the reduced viologen radicals indicate that they were stable over the course of days, allowing for charge to be stored in solution phase without immediately needing to be utilized.

A demonstration that size-exclusion of macromolecular electrolytes is a viable approach to minimize crossover was accomplished by pairing the viologen RAPs with a commercial $LiNi_{0.33}Mn_{0.33}Co_{0.33}O_2$ (NMC) cathode in a stirred cell design (Figure 1.3F). The cell performed well over several cycles under constant current control with smooth voltage transitions that were consistent with the solution transformation of redox states of the viologen RAPs. Monitoring of the crossover via UV–vis spectroscopy showed very little contamination of the cathode

compartment with viologen species, proving that the size-exclusion approach is effective at rejecting RAPs from crossing over and maximizes supporting electrolyte migration. The tested setup had an effective concentration of monomers of 10 mM, which is more than an order of magnitude lower than state of the art flow batteries, but these early tests in the dilute polymer regime where the dynamics are easier to predict demonstrate that the size-selective approach is viable using RAPs. Recently, other groups have adopted this size-exclusion approach and provided evidence that this strategy is also effective for aqueous redox flow batteries using water-soluble RAPs.[29] In this case, a dialysis membrane was used as a separator, and also used a viologen RAP as anolyte, but used a TEMPO-based RAP as catholyte. This cell performed with high Coulombic efficiencies over the course of more than 10,000 cycles, demonstrating the longevity of these platforms for reversible and cost-effective energy storage.

As the feasibility of the size-exclusion approach has been demonstrated on a technical level, future efforts to improve these systems will necessitate new chemistries that lead to highly soluble, energy dense, and chemically stable redox couples. However, a fundamental exploration of RAPs requires knowledge regarding their charge transfer mechanisms and whether these are different than those of the parent redox motifs and between different RAP chemistries. To that end, subsequent chapters address specific questions pertaining to the intricate chemical and electrochemical processes involved in RAP reactivity. The following chapters help to shed light on the interplay of macromolecular material properties and the associated electrochemical dynamics in RAPs.

Chapter 2 focuses on first approaches to characterize the charge transfer mechanisms of ferrocene and viologen RAPs by use of specialized electrochemical techniques. Specifically, scanning electrochemical microscopy (SECM) approach curves and rotating disk electrode (RDE)

studies are employed to test the molecular weight dependence on the rate of charge transfer, k^0, in RAPs. Additionally, finite element simulation analysis of SECM approach curves provides crucial clarity into the details of the electrochemical reaction pathway. Here, it is determined that the reactivity of RAPs is considerably more complex than their monomer counterparts and is described by a "CE" mechanism with several concurrent chemical equilibria preceding electron transfer.

Chapter 3 centers on a fundamental hypothesis of how to improve the rate limiting steps of electron transfer to RAPs that bear viologen redox active pendants, as it was found that RAP redox kinetics suffered by orders of magnitude compared to monomers. This section encompasses a comprehensive bottom up study inspired by conclusions from the Marcus-Hush theory for electron transfer. Here, it is expected that improvements in the rates of self-exchange (k_{EX}) of charges should result in a proportional improvement in redox kinetics. This hypothesis was tested in a series of viologen dimers and polymers which had different tether lengths and backbone structures which systematically alters the inter-pendant distance of redox units. In order to characterize the structure dependent redox kinetics, kinetics of self-exchange, and quantify the inter-pendant distances, SECM approach curves, RDE measurements, computational analysis via density functional theory, spectroelectrochemical measurements, and temperature dependent UV-vis studies were all performed. Overall, this broad study highlights remaining challenges in predicting charge transfer processes in soluble macromolecular redox active structures and the limitations of chemical models to describe RAPs that were derived from small molecule systems.

Chapter 4 covers studies of a different RAP, poly(para-nitrostyrene) (PNS), probing specific electrostatic interactions with supporting electrolyte ions. PNS is an attractive species for use as an analyte in flow batteries because of its low reduction potential and light equivalent weight of monomer. Upon reduction, nitro groups in PNS form a radical anion which can complex with

cations that are present in the background supporting electrolyte. These electrolyte interactions were probed with PNS present as an adsorbed film or as a solution species in K^+, Li^+, and tetrabutyl ammonium salt solutions via voltammetry, the surface interrogation mode of SECM, and alkali metal stripping voltammetry at Hg capped SECM tips. Supporting electrolyte identity studies with PNS demonstrate that ionic accessibility into RAPs is a critical component to understand and significant improvements in material performance are possible via tuning of the supporting electrolyte composition.

Chapter 5 probes the role of supporting electrolyte concentration on the reactivity of RAPs. The monomeric structures of the viologen and ferrocene RAPs contain quaternary amines which give them an overall cationic nature and higher solubility in targeted non-aqueous solvents such as acetonitrile and dimethylformamide. Upon polymerization, the viologen and ferrocene monomers form RAPs that fall into another subset of polymers known as polyelectrolytes, which are polymers that are also ionic. There exists extensive historical precedent to describe the dynamics of non-redox active polyelectrolyte coils in which the conformation, formation of adsorbed layers, and electrostatic interactions of polyelectrolytes are all strongly correlated to the concentration of any added salt to the solution. These polyelectrolyte dynamics were investigated in conjunction with electrochemical measurements in viologen, ferrocene, and PNS RAPs. This study effectively demonstrates that when using polyelectrolyte RAPs as soluble media in electrochemical measurements there are clear conditions of optimum ionic strength which will give rise to maximum reactivity as an adsorbed film or diffusing species. This is in contrast to PNS, a polymer which is neutral in its oxidized state, which does not show any dependencies on the supporting electrolyte concentration in its electrochemical performance. Understanding the dynamic nature of redox active polyelectrolyte coils as a function of supporting electrolyte

concentration is imperative to identify best operating conditions for flow battery applications and for performing quantitative electroanalytical measurements which require facile mass transfer limited reactivity.

Chapter 6 presents an alternative method to measure the electrochemical kinetics of ferrocene, viologen and PNS RAPs by use of the substrate generation / tip collection (SG/TC) mode of SECM. SG/TC SECM identifies electrochemical kinetics via modeling of microelectrode voltammetry signatures that were measured in solutions containing multiple oxidation states of a redox couple. This simple setup allows for probing the oxidation state dependency of RAP redox kinetics, a query not previously investigated. This first report of SG/TC SECM being applied to macromolecule systems highlights this methodology as a convenient experimental platform that can explore the bulk chemical reversibility of RAP systems in small volume conditions and minimize input sample required. Altogether, this method could provide higher throughput analysis of the energy storage capabilities of polymeric materials that are targeted for use in flow battery applications.

Finally, Chapter 7 provides a brief commentary on future and ongoing electrochemical studies of RAP systems and gives an outlook for the still developing field.

References

1. Darling, R. M.; Gallagher, K. G.; Kowalski, J. A.; Ha, S.; Brushett, F. R. *Energy Environ. Sci*., **2014,** 7, 3459−3477.
2. Dunn, B.; Kamath, H.; Tarascon, J. M. *Science*, **2011,** 334, 928−935.
3. Amatore, C.; Bouret, Y.; Maisonhaute, E.; Goldsmith, J. I.; Abruna, H. D. *Chem. Euro. J*., **2001,** 7, 2206−2226.
4. Zu, X. L.; Rusling, J. F. *Langmuir*, **1997,** 13, 3693−3699.
5. Song, Z. P.; Zhou, H. S. *Energy Environ. Sci*., **2013,** 6, 2280−2301.

6. Nagarjuna, G.; Hui, J.; Cheng, K.; Lichtenstein, T.; Shen, M.; Moore, J. S.; Rodriguez-Lopez, J. *J. Am. Chem. Soc*., **2014,** 136, 16309−16316.

7. Gellett, W.; Kesmez, M.; Schumacher, J.; Akers, N.; Minteer, S. D. *Electroanalysis*, **2010,** 22, 727−731.

8. Conte, S.; Rodriguez-Calero, G. G.; Burkhardt, S. E.; Lowe, M. A.; Abruna, H. D. *RSC Adv*., **2013,** 3, 1957−1964.

9. Arico, A.S.; Bruce, P.; Scrosati, B.; Tarascon, J.M.; Van Schalkwijk, W. *Nat. Mater*., **2005,** 4, 366−377.

10. Burgess, M.; Hernańdez-Burgos, K.; Simpson, B. H.; Lichtenstein, T.; Avetian, S.; Nagarjuna, G.; Cheng, K. J.; Moore, J. S.; Rodríguez-Lopẻz, J. *J. Electrochem. Soc*., **2016,** 163, H3006−H3013.

11. Burgess, M.; Hernandez-Burgos, K.; Cheng, K. J.; Moore, J. S.; Rodriguez-Lopez, J. *Analyst*, **2016,** 141, 3842−3850.

12. Sevov, C.S.; Brooner, R. E. M.; Cheńard, E.; Assary, R. S.; Moore, J. S.; Rodríguez-Lopẻz, J.; Sanford, M. S. *J. Am. Chem. Soc*., **2015,** 137, 14465−14472.

13. Montoto, E. C.; Nagarjuna, G.; Hui, J.; Burgess, M.; Sekerak, N. M.; Hernandez-Burgos, K.; Wei, T.-S.; Kneer, M.; Grolman, J. M.; Cheng, K. J.; Lewis, J. A.; Moore, J. S.; Rodriguez-Lopez, J. *J. Am. Chem. Soc*., **2016,** 138, 13230–13237

14. Flory, P. J. *J. Chem. Phys*., **1941,** 9, 660−661.

15. Huggins, M. L. *J. Chem. Phys*., **1941,** 9, 440−440.

16. Flanagan, J. B.; Margel, S.; Bard, A. J.; Anson, F. C. *J. Am. Chem. Soc*., **1978,** 100, 4248−4253.

17. Levanda, C.; Bechgaard, K.; Cowan, D. O.; Rausch, M. D. *J. Am. Chem. Soc*., **1977,** 99, 2964−2968.

18. Buttry, D. A.; Anson, F. C. *J. Electroanal. Chem. Interfacial Electrochem*., **1981,** 130, 333−338.

19. Murray, R. W. *Chem. Rev*., **2008,** 108, 2688−2720.

20. Brennan, J. L.; Branham, M. R.; Hicks, J. F.; Osisek, A. J.; Donkers, R. L.; Georganopoulou, D. G.; Murray, R. W. *Anal. Chem*., **2004,** 76, 5611−5619.

21. Bard, A. J. *Annu. Rev. Anal. Chem*., **2014,** 7, 1−21.

22. Dobrynin, A. V.; Rubinstein, M. *Prog. Polym. Sci*., **2005,** 30, 1049−1118.

23. Kewalramani, S.; Guerrero-Garcia, G. I.; Moreau, L. M.; Zwanikken, J. W.; Mirkin, C. A.; de la Cruz, M. O.; Bedzyk, M. J. *ACS Cent. Sci*., **2016,** 2, 219−224.

24. Dahms, H. *J. Phys. Chem*., **1968,** 72, 362−364.

25. Buttry, D. A.; Saveant, J. M.; Anson, F. C. *J. Phys. Chem*., **1984,** 88, 3086−3091.

26. Rivnay, J.; Inal, S.; Collins, B. A.; Sessolo, M.; Stavrinidou, E.; Strakosas, X.; Tassone, C.; Delongchamp, D. M.; Malliaras, G. G. *Nat. Commun*., **2016,** 7, 11287.

27. Su, L.; Darling, R. M.; Gallagher, K. G.; Xie, W.; Thelen, J. L.; Badel, A. F.; Barton, J. L.; Cheng, K. J.; Balsara, N. P.; Moore, J. S.; Brushett, F. R. *J. Electrochem. Soc*., **2016,** 163, A5253−A5262.

28. Casassa, E. F. *J. Polym. Sci., Part B: Polym. Lett*., **1967,** 5, 773−778.

29. Janoschka, T.; Martin, N.; Martin, U.; Friebe, C.; Morgenstern, S.; Hiller, H.; Hager, M. D.; Schubert, U. S. *Nature*, **2015,** 527, 78−81.

Chapter 2: Scanning Electrochemical Microscopy and Hydrodynamic Voltammetry Investigation of Charge Transfer Mechanisms on Redox Active Polymers

Notes and Acknowledgements

This chapter appeared in its entirety in the *Journal of The Electrochemical Society* with authors Burgess, M.; Hernández-Burgos, K.; Simpson, B. H.; Lichtenstein, T.; Avetian, S.; Nagarjuna, G.; Cheng, K. J.; Moore, J. S.; Rodríguez-López, J. "Scanning Electrochemical Microscopy and Hydrodynamic Voltammetry Investigation of Charge Transfer Mechanisms on Redox Active Polymers". **2016**, 163, H3006-H3013. This article is reprinted with the permission of the publisher and is available with the accompanying Supporting Information file from http://www.jes.ecsdl.org and using DOI: 10.1149/2.0021604jes. M.B. performed all of the SECM analysis, helped write the manuscript, made figures, and helped perform the RDE studies. This work was supported as part of the Joint Center for Energy Storage Research, an Energy Innovation Hub funded by the U.S. Department of Energy, Office of Science, Basic Energy Sciences. Jingshu Hui assisted in performing AFM analysis of the RAP film thickness. M.B. acknowledges support by the National Science Foundation Graduate Research Fellowship Program under grant No. DGE-1144245.

Abstract

We recently showed that viologen-based redox active polymers (RAPs) with molecular weights between 21 and 318 kDa are attractive charge storage materials as anolytes for size-selective non-aqueous redox flow batteries. Here, we characterize the electron transfer mechanisms of these RAPs, as well as a ferrocene based catholyte RAP, in acetonitrile/Li^+ electrolyte. We utilized scanning electrochemical microscopy (SECM) and rotating disk electrode (RDE) voltammetry to measure the rate of electron transfer and the rate of charge hopping between

neighboring pendants along the insulating backbone of RAPs. The electron transfer kinetics of a 271 kDa ferrocene RAP mimic the facile kinetics of its monomer repeating unit. In contrast, viologen RAPs displayed RDE and SECM signatures that suggest a preceding chemical step to electron transfer. Viologen RAPs adsorb strongly to the electrode surface and create a redox active film that controls the rate of electron transfer via self-exchange. In addition, finite element simulations including a preceding chemical step demonstrated that a purely mass-transfer limited model is insufficient to recreate the viologen RAP feedback SECM response. The mechanistic insight obtained by combining SECM and RDE provided a powerful toolset for understanding and enhancing RAP reactivity for size-selective flow battery applications.

Introduction

Non-aqueous redox flow batteries (NRFBs) are emerging technologies for electrical energy storage, and are an attractive alternative to their aqueous counterparts.[1–6] The choice of organic solvents with voltage windows larger than that required for the electrolysis of water enables the use of a larger variety of redox molecules and electrolyte systems, where the combination of high solubility and higher reaction potentials leads to increased energy density. A major challenge in NRFBs is to increase the conductivity of the electrolyte through the commonly used ion exchange membrane. In response to this challenge, our groups recently reported on a new size-selective concept in flow batteries where a porous separator replaces poorly performing ion exchange membranes.[7–9] These porous separators are coupled to high energy density redox active polymers (RAPs) that replaced small molecules as charge storage media. RAPs consist of an unconjugated polymer backbone densely decorated with redox active pendants. We previously reported on the electrochemical characterization of viologen-based RAPs with molecular weight between 21 and 318 kDa, which displayed hydrodynamic radii between 4 and 7 nm. Increasing the size of RAPs

decreased transport through Celgard which was used as a porous separator. However, we are also interested in understanding the impact of size on the rate and mechanisms of charge transfer and transport on RAPs to determine their ultimate performance limit.[10]

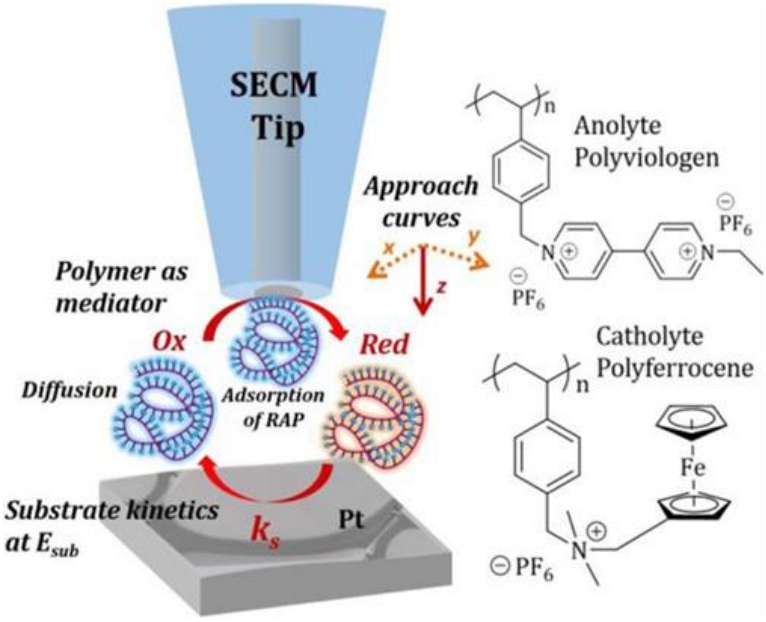

Figure 2.1. General schematic showing RAPs being used as mediators in SECM studies to measure the kinetics of electron transfer. Inset shows the structural motifs for the viologen based anolyte RAPs and ferrocene based catholyte RAP studied in this work.

RAPs displayed attractive electrochemical properties such as similar standard reduction potentials than those of the parent monomer, efficient bulk electrolysis with up to +98% of redox groups reversibly accessible, and high solubility of up to 2.8 M with quantitative electrode reactivity even when at 1.0 M. Despite these promising features, little is known about electron transfer mechanisms and the scaling of electron transfer kinetics for soluble macromolecules consisting of hundreds to thousands of redox active centers. Previous experimental emphasis has been placed on studying surface-confined films which readily form on electrode surfaces or on oligomeric redox active species.[11,12] While earlier work demonstrated some of the fundamental

processes that occur on redox active macromolecules,[13–15,44,45] they do not account for solution phase dynamics such as those introduced by hydrodynamic transport, as well as considerations of residence time on the electrode. In this manuscript, we expand on our previous work and characterize for the first time both catholyte and anolyte RAPs for flow cell applications, focusing on their fundamental mechanisms of charge transfer and transport.

Here, we characterize the mechanistic and kinetic properties of RAPs using a hydrodynamic technique, rotating disk electrode (RDE) voltammetry, and a steady state diffusion-based technique, scanning electrochemical microscopy (SECM). To the best of our knowledge, this study is the first to employ large sized polymers (>20 kDa) as solution based redox mediators in either SECM or RDE analysis. A general schematic of SECM approach curve experiments and the structural motifs of the RAPs used in this study are shown in Figure 2.1. Together, SECM and RDE analyses provide a view of the impact of adsorption/desorption equilibria and solution-phase dynamics on the redox kinetics and charge transport mechanisms within RAPs. Using these techniques, we measured the electron transfer rate constants, polymer diffusion coefficients, and the intra-particle self-exchange constant which describes the rate of diffusion of charges down the RAP. These are critical parameters for flow applications, as the electrode current will be limited by both the mass transfer of the species to the electrode and by the hopping of charges within the constantly changing three-dimensional conformation that RAPs have in solution.[16–18]

Experimental

Chemicals

Poly(vinylbenzyl ethyl) viologen of five different molecular weights (M_n = 21, 104, 158, 233, and 318 kDa) were synthesized following a previously reported methodology.10 A model

ferrocene derivative, 12 poly(vinylbenzyl aminomethyl) ferrocene was synthesized with molecular weight of M_n = 271 kDa. Details of the synthesis and characterization of the ferrocene RAP are shown in Apendix A. Briefly, a solution of (dimethylaminomethyl)ferrocene was added to a solution of poly(vinylbenzyl) chloride for a day under stirring conditions to allow nucleophilic substitution of the ferrocene monomer onto the polymer backbone. Substituted ferrocene polymer was collected by precipitation and rinsing with acetone/water/and methanol. Lithium tetrafluorborate (Aldrich 98%), anhydrous acetonitrile (Aldrich 99.8%), and ethyl viologen diperchlorate (Aldrich 98%) were used as received with no further purification.

Electrodes

A 25 μm diameter platinum (99.9%) wire from Goodfellow (Devon, PA) was used to prepare the SECM tips. The platinum wire was sealed in a glass capillary (World Precision Instruments, Sarasota, FL) by using a previously reported methodology.[19] The tip was sharpened using silicon carbide paper and polished using 1 and 0.3 μm alumina slurry on a polishing cloth. After polishing, the tip was rinsed with water then sonicated in acetone for five minutes. The SECM electrode had a radius of 12.5 μm and an average $\underline{R_g}$ of 2. The R_g is the ratio of total electrode radius including the glass divided by the metal electrode radius. A 1.15 mm diameter platinum disk was used as a substrate electrode (CH Instruments, Austin TX) and was polished in the same manner as the SECM tip. A platinum wire (Goodfellow, Devon PA 99.9%) was used as the counter electrode and a non-aqueous Ag/Ag+ reference electrode (CHI112, 0.1 M AgNO3) was used. All potentials reported are with respect to 0.1 M Ag/Ag^+ unless otherwise stated.

Rotating Disk Electrode Voltammetry

All the RDE experiments were done using a CHI 601E (CH Instruments, Austin TX) potentiostat. The RDE voltammetry was done using a Pine rotator model ASR. A three-electrode electrochemical cell was used with a 3 mm glassy carbon working electrode, a Ag/Ag^+ reference electrode, and Pt wire as the counter electrode. The working electrode was cleaned by polishing with 1 μm alumina slurry on a polishing cloth, followed by rinsing with water and acetone prior to use. To prevent any water or oxygen contamination, all the experiments were performed in a dry argon atmosphere glove box (MBraun Stratham, NH). For these experiments, 0.1 M electrolyte solutions of $LiBF_4$ in acetonitrile were prepared.

Scanning Electrochemical Microscopy

All solutions were prepared in an argon atmosphere glove box (MBraun Stratham, NH) with stringent control of oxygen and water to be less than 0.1 ppm. Electrochemical control of the cell and of the positioning of the electrodes inside of the glove box was achieved using a CHI920D SECM station (CH Instruments, Austin, TX). A four-electrode configuration was used for all SECM measurements. Leveling of the substrate, initial distance from substrate, and R_g value of the tip was evaluated using a 10 mM solution of ethyl viologen diperchlorate with 0.1 M $LiBF_4$ as supporting electrolyte in acetonitrile. Approach curves to the substrate were performed at 1 μm/s. After approaching and leveling, the cell and SECM tip were thoroughly rinsed and the cell was refilled with the solution of 0.1 M supporting electrolyte and 10 mM of the RAP in solution. Approach curves were plotted by recording the tip current, i_{tip}, as a function of the inter-electrode distance, d. Distance and preliminary kinetic information was obtained by fitting the approach curves to theoretical curves based on equations developed by Lefrou and Cornut.[20] Numerical simulations of approach curves were performed using version 4.4 of COMSOL Multiphysics. The

transport of dilute species, and deformed mesh physics modules were employed to simulate diffusive transport in solution and a moving tip electrode, respectively. The surface reactions physics module was included to model a three-step tip process of adsorption, electron transfer to the adsorbed species, and desorption. A thorough description of the model is included in Appendix A. Within this model, experimentally relevant values were input for known parameters (a, D, C^0, k_f, etc.), while adsorption and desorption kinetics were evaluated.

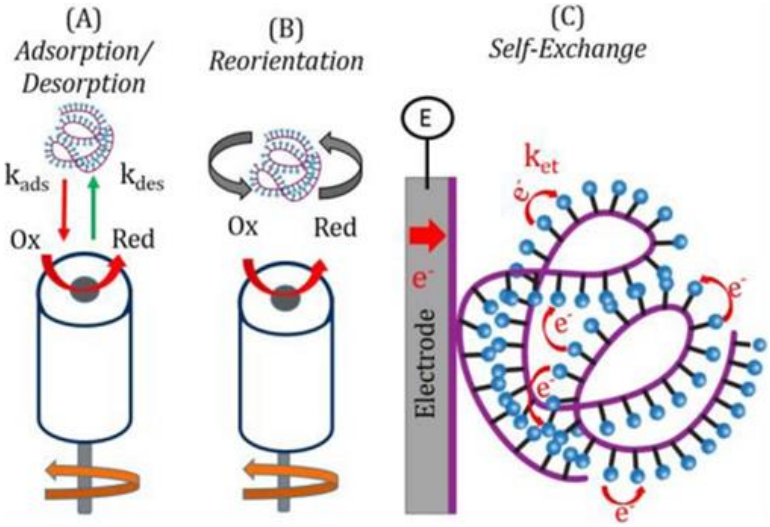

Figure 2.2. Generalized schematic explaining the three possible chemical steps that precede electron transfer for a RAP. (A) Adosrption/desorption of RAP onto the electrode surface (B) Solution space reorientation of RAPs in three dimensions (C) Self-exchange limitations through a RAP film on the electrode (shown in purple), or within individual RAPs, will dictate the rate at which solvated RAPs can release or take up any new charges from the electrode.

Results and Discussion

Rotating Disk Electrode Voltammetry

RDE uses hydrodynamic transport via electrode rotation to bring reactants toward the electrode surface,[21] making it a suitable technique for assessing reaction mechanisms of RAPs in a flow configuration. Additional advantages of this technique include the measurement of steady

state transport, which mitigates the contribution of transient voltammetric and double-layer charging effects on the measured current. RDE is useful for calculating the diffusion coefficients (D), electron transfer rate constants (k_f) and standard rate constants ($k^{0'}$) via Levich and Koutecky-Levich equations which are shown in Appendix A Figure A.21.[22,23]

Previously, we have reported that viologen-based RAPs display adsorption at metal electrodes. Charge hopping via self-exchange reactions likely take place between the RAP film on the electrode and solution RAPs.[24] as well as within individual RAPs. In parallel, adsorption/desorption equilibria are plausible, as are molecular and polymer dynamics that substantially modify RAP-electrode interactions. These include rotational dynamics,[25] deformation upon impact with the electrode,[14] and the co-existence of multiple configurations in solution. Different configurations are predicted by the "bead and rod" model[17,16] in the absence and presence of flow strain. A concise depiction of these processes is presented in Figure 2.2. We approached the analysis of the impact of these factors through various RDE strategies.[26]

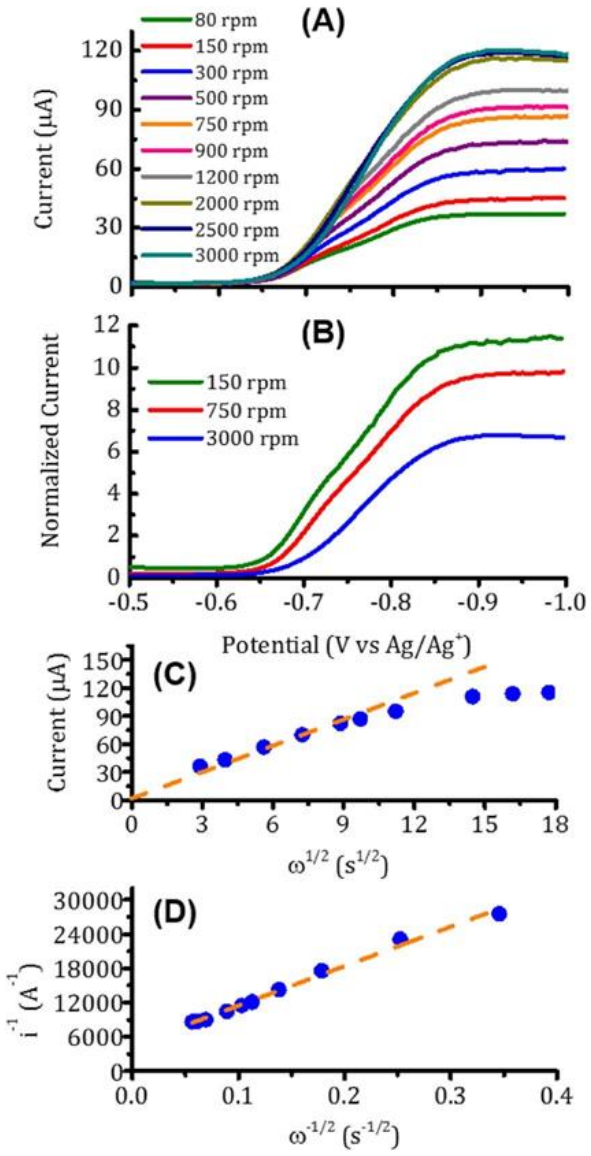

Figure 2.3. (A) LSVs at different rotation rates for the 158 kDa Viologen-RAP, (B) Normalized (by $\omega^{1/2}$) LSVs. (C) Levich plot (i vs $\omega^{1/2}$) and (D) Koutecky- Levich plot (i^{-1} vs $\omega^{-1/2}$). Solution concentration of RAP was 5 mM in 0.1 M $LiBF_4$ electrolyte. Area of the electrode was 0.0765 cm2.

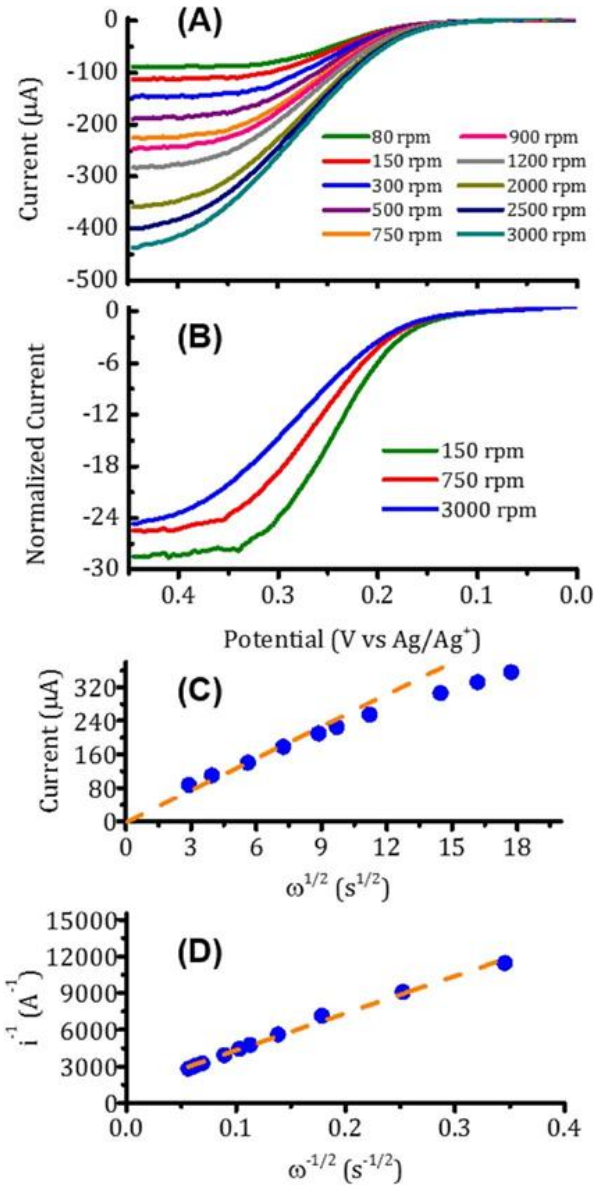

Figure 2.4. (A) LSVs at different rotation rates for the 271 kDa ferrocene RAP, (B) Normalized (by ω1/2) LSVs. (C) Levich plot (i vs $\omega^{1/2}$) and (D) Koutecky- Levich plot (i^{-1} vs $\omega^{-1/2}$). Solution concentration of RAP was 5 mM in 0.1 M $LiBF_4$ electrolyte. Area of the electrode was 0.0765 cm^2.

First, we focus on the characterization of the electrochemical and transport parameters via steady state voltammetry of RAPs versus rotation rate. We obtained the linear sweep voltammograms (LSV) of all viologen-based RAPs (21 kDa to 318 kDa series). For simplicity of discussion, we show in Figure 2.3 the corresponding plots for the 158 kDa viologen RAP and in

Figure 2.4 the corresponding plots for the 271 kDa ferrocene RAP (refer to Appendix A to see the LSVs for the rest of the RAPs). We calculated the electron transfer rate constant (k_f) using Koutecky-Levich analysis (Figures 2.3C, 2.3D, 2.4C, and 2.4D). In these studies, we defined the k_f at specified potentials and the standard rate constant ($k^{0'}$) from the difference between $E^{o'}$ and the specified E as shown in Equation 2.6. In these calculations, the transfer coefficient (α) was assumed to be 0.5. The values for k_f and $k^{0'}$ are presented in Table 2.1, and the calculated diffusion coefficients are shown in Table 2.2.

Table 2.1 Calculated k_f and $k^{0'}$ using RDE

Molecular Weight Of Species	**k_f (cm/s) from RDE**	**$k^{0'}$ (cm/s) from RDE**
	Viologen RAPs	
21 kDa	6.2×10^{-3} (-0.71 V)	1.0×10^{-3}
104 kDa	6.4×10^{-3} (-0.79 V)	4.0×10^{-3}
158 kDa	6.5×10^{-3} (-0.87 V)	8.1×10^{-4}
233 kDa	9.0×10^{-3} (-0.79 V)	4.0×10^{-3}
318 kDa	1.4×10^{-2} (-0.78 V)	3.0×10^{-3}
	Ferrocene RAP	
271 kDa	2.2×10^{-2} (-0.71 V)	0.32

In order to probe the charge transfer mechanism of RAPs, LSV plots were normalized with respect to the square root of the rotation rate, as shown in Figures 2.3B and 2.4B. We note a significant deviation from the expected Levich behavior at the higher rotation rates, suggesting mechanistic complications under conditions where mass transfer should be limiting. The normalized LSVs display a large decrease of the rotationally normalized steady state currents

consistent with a CE type mechanism.[27] This observation supports our hypothesis that either preceding or concurrent chemical processes are operational upon electrochemical activation of RAPs. Changes in the polymer conformation due to the hydrodynamic transport of RAPs might impact the effectiveness of charge transfer and of charge transport within the solution phase polymer. If the rotation rate of the electrode is increased, it allows less time for a RAP to undergo conformational changes before being swept off the electrode surface. A similar situation is foreseen for self-exchange between the polymer pendants, where a shorter residence time possibly leads to partial electrolysis of the RAP. The effects of adsorption/desorption will affect RAP reactivity, but these are better studied using a technique involving ultramicroelectrodes, for which as we will show in the following section, scanning electrochemical microscopy was very sensitive to this parameter.

Table 2.2 Calculated Diffusion Coefficients (D_0) Using Different Electrochemical Techniques

Molecular Weight Of Species	***D_0* (cm^2/s) from Steady State Voltammetry**	***D_0* (cm^2/s) from RDE**
	Viologen RAPs	
21 kDa	1.22×10^{-6}	1.7×10^{-6}
104 kDa	9.5×10^{-7}	5.4×10^{-6}
158 kDa	6.7×10^{-7}	1.4×10^{-6}
233 kDa	7.3×10^{-7}	9.0×10^{-6}
318 kDa	6.6×10^{-7}	1.2×10^{-5}
	Ferrocene RAP	
271 kDa	5.4×10^{-6}	6.3×10^{-6}

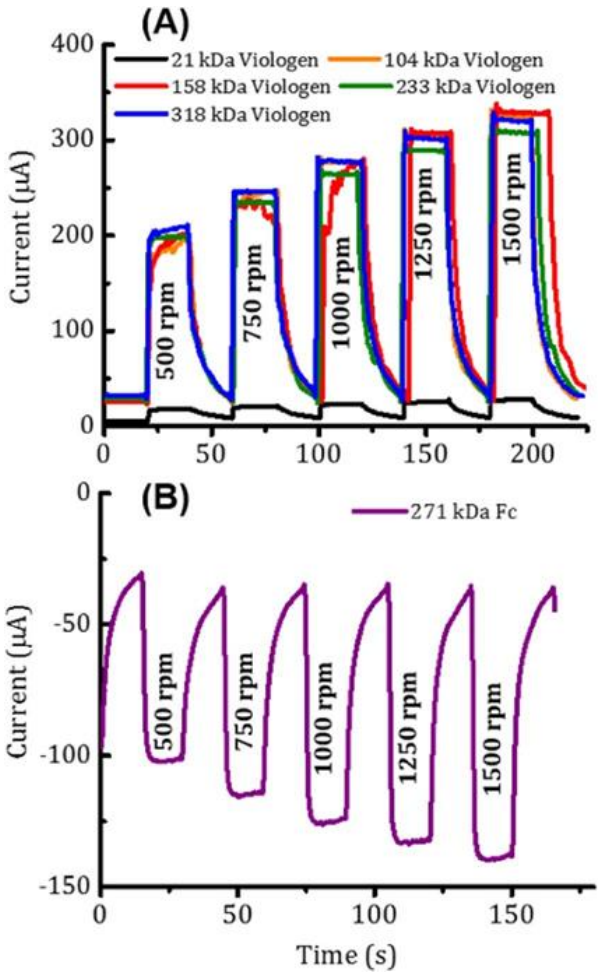

Figure 2.5. Chronoamperogram used to calculate the homogeneous electron exchange constant for all the RAPs (A) Viologen-RAPs and (B) Fc-RAP. Higher currents indicates when the rotation is on. Solution concentration of monomer was 5 mM in 0.1 M $LiBF_4$ electrolyte. Area of the electrode was 0.0765 cm^2.

It is challenging to separate rotational dynamics from other charge transport effects. However, provided the RAPs are immobile on the surface, as in the RAP film that forms on the electrode upon exposure to a solution containing them,[10] it is possible to estimate their charge hopping dynamics. For this purpose, we followed the method previously reported by Murray *et al.*[26] (Appendix A Figure A.21). Briefly, the RDE surface was covered with a RAP film by drop casting a small amount RAP solution onto the surface and letting the solvent evaporate. Verification of the presence of the film was done by cyclic voltammetry in electrolyte solution in

which a voltammogram characteristic of surface-confined redox species was observed (Appendix A Figure A.18). Chronoamperograms of the RAP-filmed RDE in the presence of the RAP monomer in solution as the rotation is turned on and off were performed. The analysis based on the on/off currents yields the rate of self-exchange on the polymer film. The RDE results for this technique are shown in Figure 2.5.

The current obtained by using this analysis is given by Equation 2.1:

(2.1) $$\frac{1}{i_{LIM}} = \frac{1}{i_A} + \frac{1}{i_E}$$

where i_A is given by the Levich equation (refer to SI) and the electron hopping current is given by Equation 2.2:

(2.2) $$i_E = \frac{nFAD_EC}{d}$$

where n is the number of electrons, F is the Faraday constant, D_E is the electron diffusion through the film, C is the electrolyte concentration in solution (0.1 M) because the forward sweep wave shape of the RAP film voltammetry appears to be diffusive[46] (shown in Appendix A Figure A.18), and d is the thickness (obtained via AFM to be on average 15 nm thick, shown in the Appendix A in Figure A.22). To calculate the self-exchange rate constant (k_{EX}) we used the Dahms-Ruff equation,[28] Equation 2.3:

(2.3) $$D_E = \frac{k_{EX}\delta^2}{6}$$

The factor δ was estimated using universal force fields as implemented in Avogadro software,[29] and shown in Appendix A Figure A.23. The δ term refers to the distance between two nuclei (in our case the distance between redox active pendants), approximately 9.5 Å. By using this analysis, we learned that the there is no trend on the values of k_{EX} as a function of polymer

molecular weight in the studied interval. This result highlights the reactivity of RAPs as an intrinsic property of the pendant to pendant interactions leading to charge hopping and not the weight of the polymer chain. The electron diffusion was calculated to be $7.9 \times 10^{-11} \pm 3.1 \times 10^{-11}$ cm^2/s and 5.6×10^{-12} cm^2/s for the viologen RAPs and ferrocene RAP respectively. By using this calculated values of D_E the k_{EX} was calculated to be $5.3 \times 10^4 \pm 2.1 \times 10^4$ s^{-1} and 4.2×10^3 s^{-1} for the viologen RAPs and ferrocene RAP respectively. Previously reported values for the k_{EX} for a viologen based RAP was shown to be 3.6×10^5 s^{-1} showing consistency with our viologen RAP.[24]

SECM Feedback Analysis with Catholyte Ferrocene Based RAP

Evaluation of RAPs using scanning electrochemical microscopy (SECM), operated in the feedback mode, was used with the intention of comparing the kinetics measured from RDE and provide further insight into the processes outlined in Figure 2.2. SECM is a powerful tool for evaluating the electron transfer kinetics of redox species in solution.[30–34] SECM uses a tip electrode, here an ultramicroelectrode (a = 12.5 μm), and a conductive substrate electrode (Pt) of much larger size, here 1.15 mm. The potential at the ultramicroelectrode is set at a sufficient overpotential such that the solution-phase redox species reacts at the tip under mass transfer limited steady state conditions. When the SECM tip is within close proximity of a surface the tip current is additionally a function of both the distance between the tip and substrate electrode, and the rate of electron transfer to the solution species at the substrate. This happens at distances less than 10 L, where $L = d/a$ is the normalized distance, and d being the absolute distance between tip and substrate. Electron transfer kinetics can be determined by fitting approach curves to theory via a plot of the normalized tip current I_T versus L. The normalized tip current, I_T, is related to the steady-state current, i_∞, at effective infinite distance from a substrate ($I_T = i_{tip}/i_\infty$). The approach curve shape is dictated by a normalized rate constant given by Equation 2.4:[35]

(2.4) $$\kappa = \frac{ka}{D_{RAP}}$$

Where in our case D_{RAP} is the diffusion coefficient of the mediator, a is the radius of the SECM tip, and k is the rate of electron transfer at the substrate, often termed k_b and k_f respectively for oxidation or reduction of solution species at the substrate electrode.

Table 2.3 Kinetic Parameters of Different Sized Ferrocene Species Assuming Butler-Volmer Kinetics

Molecular Weight Of Ferrocene Species	**Fitted κ**	**Fitted k_f (cm/s)**	**Calculated $k^{0'}$(cm/s)**
Monomer (0.186 kDa)	24.89	0.179	1.86
271 kDa	7.53	0.0325	0.339

The values for the dimensionless rate constant (κ) will vary from approximately 1×10^{-4} and 50, with larger values indicating higher rates of electron transfer, but also bound by mass-transfer limitations where the approach curves become experimentally indistinguishable from each other. The upper bound of the curve represents a condition termed positive feedback, while the lower bound represents negative feedback, where reactivity is low and geometrical constraints make the tip current decrease.

The measured SECM approach curves for ferrocene RAPs show a behavior consistent with positive feedback, as shown in Figure 2.6. The value for the fitted κ can be accounted for from a combination of a large electrochemical rate constant, or from relatively slow diffusion of the RAPs. The approach curves for the ferrocene based RAP show no apparent complications in feedback and fit very well to existing theory. We estimate that the 271 kDa ferrocene exhibits one order of magnitude slower kinetics than the monomer, as shown in Table 2.3. The apparent

diffusion coefficients of the RAPs were calculated from steady state voltammetry at the microdisk assuming a single electron transfer is contributing to the redox event at any given time[36] using Equation 2.5:

(2.5) $$i_{steady-state} = 4nFaD_{RAP}C^*_{RAP}$$

Where *n* is assumed to be 1 electron, *F* is Faraday's constant, *a* is the SECM tip electrode radius, and C_{RAP} is the bulk concentration of RAP calculated with respect to the molecular weight of the redox repeat unit.

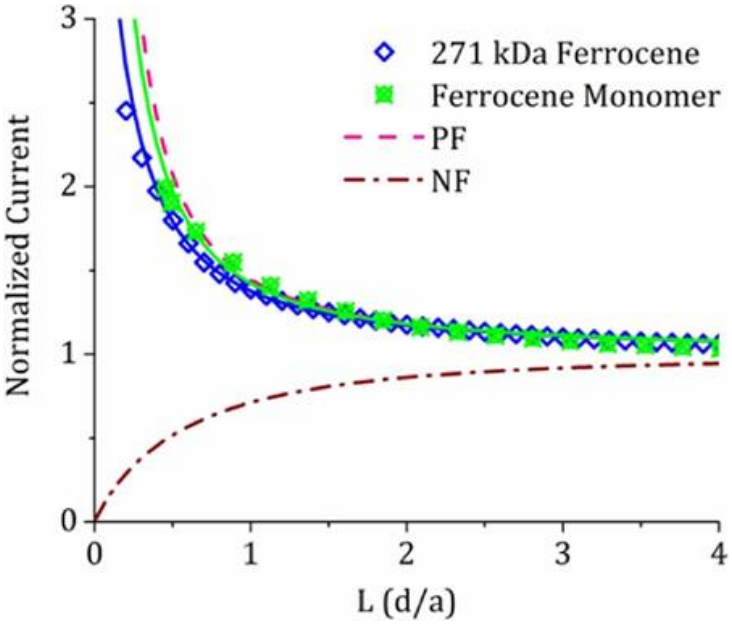

Figure 2.6. SECM approach curves of Ferrocene species to a 1.15 mm Pt disk. Tip potential was 0.5 V vs Ag/Ag^+ and substrate potential was 0.1 V vs. Ag/Ag^+ (120 mV overpotential from $E^{0\prime}$). The approach speed was 0.5 μm/second. The solid lines indicate the fitted curve and the open symbols indicate the experimental data points used to construct the fitted approach curve. PF and NF designate theoretical mass transfer limited approach curves for perfect positive and perfect negative feedback respectively.

The standard rate constant parameter, $k^{0\prime}$, was calculated using the Butler-Volmer relation described in Equation 2.6:[36]

(2.6) $$k_f = k^{0\prime} e^{-(\alpha f\left(E-E^{0\prime}\right))}$$

where α is assumed to be equal to 0.5, f is 38.94 V^{-1}, and E-$E^{0\prime}$ is the overpotential at the substrate. Although RAPs are much larger than their monomeric counterparts, it can be safely stated that the excellent monomer reactivity is maintained after polymerization. This is consistent with previously studied ferrocene oligomers,[12] making larger RAPs good candidates for size-selective NRFBs.

SECM Feedback Analysis with Anolyte Viologen Based RAPs

In contrast to ferrocene based RAPs, viologen based RAPs gave SECM approach curves that displayed mechanistic deviations from simple substrate-controlled electron transfer. We unsuccessfully attempted to fit them to reported models that add kinetic contributions to the shape of the approach curve in studies concerning electron transport on redox active monolayers, but found this model cannot fit approach curves having any negative feedback influences.[37] Similarly, while at first glance the shape of our approach curves appear much like the ones reported by Bard et al. for an ECE/DISP mechanism,[38] the chemistry of that system is inconsistent with ours. Figure 2.7 shows theoretical approach curves fitted for viologen RAPs, as well as a selected area of experimental points in which conventional SECM electron transfer theory seems to apply. The shape of these approach curves appears to respond mainly to negative feedback until small values of L are attained ($L < 2$), when the normalized current for most of the species finally starts to rise again. Based on the selected area fits shown in Figure 2.7, rate constants obtained through the model proposed by Cornut and Lefrou are shown in Table 2.4.[20] Contrary to how this model typically operates, we defined the normalized current with respect to the current observed at L = 2. While the accuracy of this method is questionable, it does allow us to roughly approximate the

rate of electron transfer for comparison to RDE experiments. When the k_f values calculated using RDE are compared with the ones calculated using SECM (Tables 2.3 and 2.4) a good agreement was obtained, especially with the lower molecular weight polymers.

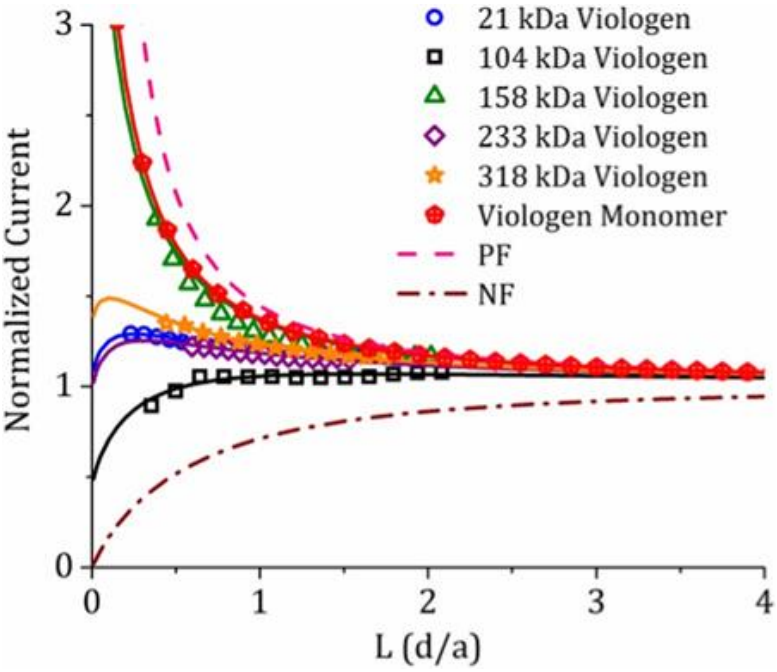

Figure 2.7. SECM approach curves with different molecular weight viologen RAPs approached to a 1.15 mm Pt disk. The tip was biased at −0.9 V vs Ag/Ag+ in order to fully activate the first reduction of the viologen RAPs. The substrate was biased at −0.6 V vs. Ag/Ag+ (~120 mV overptoential *from* E^{0r}) in order to measure the approach curves under kinetic control. The motor speed was 0.5 micrometers/second. The solid lines indicate the fitted curve and the open symbols indicate the experimental data points used to construct the fitted approach curve. Curves were fit to an R_g of 2. Only a small portion of the experimental points from L = 2 and less were used to construct this plot in order to ensure fitting to a diffusion only based model as an approximation of electron transfer kinetics. PF and NF designate theoretical mass transfer limited approach curves for perfect positive and perfect negative feedback respectively.

The extrapolated forward electron transfer kinetics for all of the species fall very close to each other and all are within one order of magnitude, independent of size. Likewise, the apparent diffusion coefficients of all the viologen RAPs are all within one order of magnitude of each other as shown in our previous work.[10] However, the low diffusion coefficients measured imply that the transit time of the polymers from the tip to the substrate electrode needs to be taken into account

for accurately measuring the approach curves. Accounting for SECM feedback happening over a maximum distance of 10 L for a 12.5 micrometer radius microdisk, the SECM tip should not be moved toward the surface any faster than a rate dictated by a characteristic diffusion time, as predicted by Equation 2.7:[36]

$$t = \frac{d^2}{2D} \tag{2.7}$$

As an example, the 233 kDa viologen RAP would take approximately 117 seconds to make the round trip between the tip and substrate at L = 10 distance, and thus the tip should be moved toward the surface at no faster than 10 L worth of distance in 117 seconds, which equates to approximately 1 micrometer per second. This analysis applies for all the RAPs presented in this study. Feedback approach curves with viologen RAPs when the tip was moved too fast toward the surface relative to the diffusion rate of the polymer are shown in Appendix A (Figure A.5), which appear as almost pure negative feedback, thus complicating kinetic measurements. Interestingly, the shape of the approach curves was insensitive to the overpotential applied on the substrate electrode. This can be understood by considering that the adsorbed film of RAPs controls electron transfer to solution species, as depicted in Figure 2.2. Once the RAP film is fully activated via equilibrium with the electrode, it is primarily the chemical self-exchange between adsorbed and solution phase RAP-RAP interactions that controls the rate of electron transfer. As this interaction was calculated to be similar in all viologen RAP samples, regardless of size, this would explain why the heterogeneous rate constants in Table 2.4 are similar. Viologen species are known to be fast electrochemical mediators in SECM,[39,40] yet the observation that self-exchange controls electron transfer does not fully explain why the approach curves deviate from diffusion-controlled feedback behavior. Therefore, finite element simulations were used to further investigate the

impact of plausible reaction mechanisms accompanying electron transfer in the evaluation of SECM approach curves.

Table 2.4 Found Kinetic Parameters of Different Sized Viologen Species Assuming Butler-Volmer Kinetics

Molecular Weight Of Viologen Species	**Fitted κ**	**Fitted k_f (cm/s)**	**Calculated $k^{0'}$(cm/s)**
Monomer (0.413 kDa)	7.28	0.121	1.20
21 kDa	1.25	1.22×10^{-3}	1.27×10^{-2}
104 kDa	0.554	4.21×10^{-4}	4.38×10^{-3}
158 kDa	4.25	2.28×10^{-3}	2.37×10^{-2}
233 kDa	1.20	7.03×10^{-4}	7.32×10^{-3}
318 kDa	1.85	9.77×10^{-4}	1.01×10^{-2}

SECM Feedback Simulations Incorporating Adsorption

Per the discussion of Figure 2.2 it is reasonable to suspect that adsorption/desorption processes at an SECM tip could complicate the approach curve response. We performed digital simulations, as described in the Appendix A (Section 3.0) which incorporate an adsorption step with constant k_{ads} preceding electron transfer, and a desorption step with constant k_{des} preceding RAP diffusion from the tip to the substrate. Currently, our experimental resources are not sufficient to distinguish between the three mechanisms shown in Figure 2.2, but this adsorption/desorption equilibrium effectively describes reactivity at the tip as a "black-box" in which all three mechanisms could be operational, and can be viewed as a "pre-equilibrium" step that matches our findings with RDE voltammetry. Our simulations indicated that as long as the tip and substrate

heterogeneous rate constants were fast ($k_{electron\ transfer} > 1\ s^{-1}$), desorption kinetics had a very pronounced effect on the shape of the approach curve, and matched qualitatively with our experimental observations. As shown in Figure 2.8A, when desorption is fast ($k_{des} \geq 1\ s^{-1}$), approach curves fit well to the numerical approximations for uncomplicated positive feedback.[20] However, slower desorption kinetics produce approach curves with significant deviations from these approximations. In Figure 2.8A, the $k_{des} = 0.001\ s^{-1}$ curve shows that if this process is slow enough, positive feedback is so strongly obscured that a severely distorted negative feedback approach would be obtained even for a substrate with extremely fast electron transfer kinetics. As seen in Figure 2.8B, the simulated approaches for very fast desorption match well to the shape of approaches with ferrocene RAPs, while simulations with slow desorption kinetics match what was observed for viologen RAPs. This suggests that while desorption kinetics might limit the electron transfer kinetics of viologen RAPs, ferrocene RAPs interact much less strongly with the electrode. This differential interaction is consistent with the RAP-electrode interaction, as the potential of zero charge of Pt in a lithium electrolyte in acetonitrile has been reported as −0.48 V vs. Ag/Ag^+.[41] This value suggests a larger likelihood of attractive interactions to the $2^+/1^+$ viologen redox pair used as anolyte than to the $0/1^+$ ferrocene redox pair used as catholyte.

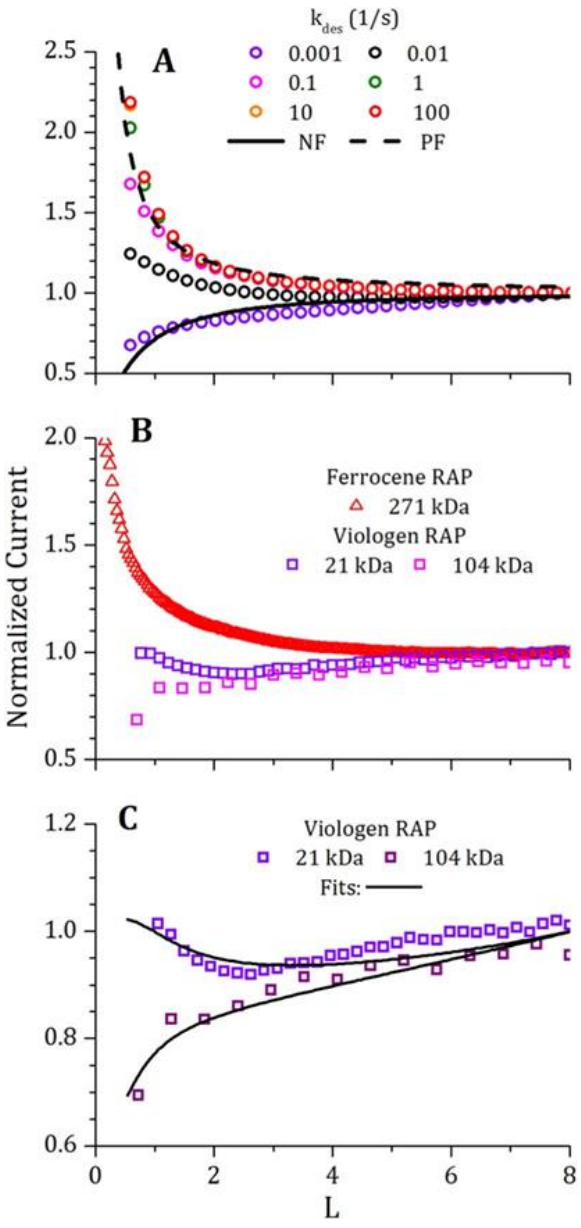

Figure 2.8. (A) Simulated approach curves for different values of desorption kinetics. When desorption kinetics are extremely fast and negligible compared to the rate of electron transfer, the curves look identical to curves predicted by the model of Cornut and Lefrou for positive feedback.[20] Slow desorption kinetics manifest as negative feedback independent of electrochemical kinetics on the tip or substrate. (B) Complete experimentally measured approach curves for 271 kDa ferrocene RAP and 20 and 104 kDa viologen RAPs. (C) Fits for desorption kinetics from complete SECM approach curves for the 20 and 104 kDa viologen RAPs.

Mechanistically, these simulations suggest something akin to a CE mechanism[36] in which the RAP must undergo a "chemical" equilibrium step on the tip electrode to adsorb/desorb and

also potentially change conformation preceding an electron transfer. These equilibrium steps that precede electron transfer are rate limiting in the tip current response, and complicate SECM feedback. To the best of our knowledge, this work would be the first time that chemical steps occurring at the tip prior to electron transfer have been approximated via SECM. Previously, work has been done on characterizing chemical steps that happen on a substrate concerning the dissolution of ionic crystals occurring before SECM feedback,[42,43] but these experiments do not include any chemical steps on the tip electrode itself preceding electron transfer.

In addition to providing a reasonable explanation for the deviations from theory, it is instructive to follow the implications of this simple model as it allows for an estimation of the desorption kinetics, a proxy for residence time. Figure 2.8C shows approach curves using 21 and 104 kDa viologen RAPs alongside simulated curves of best fit, (others shown in Appendix A). Desorption rate constants obtained from these fits, as well as the residence times obtained through the reciprocal of k_{des} are summarized in Table 2.5. RAPs with longer residence times show the most deviation from diffusion based SECM approach curve theory, but also from uncomplicated Levich behavior as evaluated in RDE experiments. This confirms a strong parallelism between the chemical steps postulated for these two techniques. Regarding the goodness of the fit for SECM approach curves, we observed that as the molecular weight of the polymer increased, it became more difficult to properly recreate the shape of the approach curve. Larger numbers of redox centers on RAPs possibly make charge transport through the polymer more important as molecular weight increases. The ferrocene based RAP had extremely fast desorption kinetics. The residence time on the electrodes was calculated to be less than 1 second. Using this residence time and a reformulation of Equation 2.7, as well as $D_E = 5.6 \times 10^{-12}$ cm^2/s for the ferrocene based RAP, the

extent of the charge-hopping diffusion layer is nearly 33 nm, sufficiently large for charge-hopping likely not to be rate-limiting on RAPs of this size.

Table 2.5 Table of Desorption Standard Rate Constants from Fitting Experimental Approaches to Simulations

Molecular Weight Of Viologen Species	k_{des} **(s^{-1})**	**Approximate Residence Time on Electrode (s)**
21 kDa	5×10^{-3}	200
104 kDa	1.26×10^{-3}	794
158 kDa	7.94×10^{-3}	126
233 kDa	3.98×10^{-3}	251
318 kDa	6.31×10^{-3}	158

Conclusions

Soluble viologen based RAPs of molecular weight between 21 and 318 kDa and a ferrocene RAP of 271 kDa were characterized for their electrochemical performance by SECM approach curve analysis and RDE voltammetry for the first time using these techniques. The information garnered from these different studies employing both macrodisk and ultramicroelectrode measurements are congruent amongst each other, offering many approaches to reliably study the kinetics of RAPs. While the ferrocene based RAP essentially exhibited mass-transport limited responses in both SECM and RDE studies, the charge transfer mechanisms on the viologen based RAPs suggested preceding chemical steps that significantly impacted their voltammetric and SECM behavior. Estimations of the charge transfer kinetics on the viologen systems strongly suggested independence from molecular weight in the range measured, as well as kinetic control

by the electrode surface RAP film. Moreover, the diffusion of electrons through RAPs was measured and it was similarly found to be an intrinsic property of the RAP.

Possible contributions to the preceding chemical steps observed in RDE and SECM included adsorption/desorption, solution phase reorganization and charge hopping through pendant self-exchange. The observation that the rate of self-exchange among ferrocene and viologen RAPs is similar, suggests that this effect is not rate-controlling on this molecular weight interval. Instead, solution phase dynamics and adsorption/desorption equilibria seem to be more dominating, as evaluated via simulations of SECM approach curves. Characterizing the competition between desorption, charge transport, and charge transfer into a comprehensive theory to fit approach curves is beyond the scope of this paper, but development of methods to collect this information are ongoing. Our group is actively pursuing strategies to control adsorption and increase k_{EX} and D_E based on molecular, electrode and polymer design. We see the present study as a first step to evaluate rate determining processes on the electrochemical activity of RAPs. Understanding how to balance the rates of these events will be essential to developing RAPs capable of providing high power density in flow battery applications.

References

1. Brushett, F. R.; Vaughey, J. T.; Jansen, A. N., *Adv. Energy Mat.,* **2012,** *2*, 1390-1396.
2. Shin, S. H.; Yun, S. H.; Moon, S. H., *RSC Adv.*, **2013,** *3*, 9095-9116.
3. Alotto, P.; Guarnieri, M.; Moro, F., Renew. *Sust. Energy Rev.*, **2014,** 29, 325-330.
4. Darling, R. M.; Gallagher, K. G.; Kowalski, J. A.; Ha, S.; Brushett, F. R., *Energy Environ. Sci*., **2014,** *29*, 325-335.
5. Wang, Y. R.; He, P.; Zhou, H. S., *Adv. Energy Mat*., **2012,** *2*, 770-779.
6. Wang, X. J.; Hou, Y. Y.; Zhu, Y. S.; Wu, Y. P.; Holze, R., *Sci. Rep*., **2013,** *3*, *16-22*.
7. Yamamoto, K.; Higuchi, M.; Uchida, K.; Kojima, Y., Macromol. *Rapid Comm.*, **2001,** *22*, 266-270.

8. Yamamoto, K.; Higuchi, M.; Uchida, K.; Kojima, Y., *Macromolecules*, **2002,** *35*, 5782-5788.

9. Darling, R.; Gallagher, K.; Xie, W.; Su, L.; Brushett, F. R., *J. Electrochem. Soc*., **2016,** *163*, A5029-A5040.

10. Nagarjuna, G.; Hui, J.; Cheng, K.; Lichtenstein, T.; Shen, M.; Moore, J. S.; Rodriguez-Lopez, J., *J. Am. Chem. Soc*., **2014,** *136*, 16309-16316.

11. Kokkinidis, G.; Papoutsis, A.; Poulios, I., *J. Electroanal. Chem*., **1994,** *379*, 379-387.

12. Flanagan, J. B.; Margel, S.; Bard, A. J.; Anson, F. C., *J. Am. Chem. Soc.*, **1978,** *100*, 4248-4253.

13. Amatore, C.; Bouret, Y.; Maisonhaute, E.; Goldsmith, J. I.; Abruna, H. D., *Chem. Euro. J*., **2001,** *7*, 2206-2226.

14. Amatore, C.; Bouret, Y.; Maisonhaute, E.; Goldsmith, J. I.; Abruna, H. D., *Chemphyschem*, **2001,** *2*, 130-137.

15. Amatore, C.; Oleinick, A. I.; Svir, I., *Chemphyschem*, **2010** 11, 159-165.

16. Bird, R. B., *Chem. Eng. Comm*, **2010,** *11*, 159-174.

17. Doyle, P. S.; Shaqfeh, E. S. G., *J. Non-Newtonian Fluids*, **2000,** *92*, 275-278.

18. Tothova, J.; Lisy, V., *Acta Phys. Slov*, **2015,** *65*, 1-U65.

19. Rodriguez-Lopez, J.; Shen, M.; Nepomnyashchii, A. B.; Bard, A. J., *J. Am. Chem. Soc.*, **2012,** *134*, 9240-9250

20. Lefrou, C.; Cornut, R, *Chemphyschem*, **2010,** *11*, 547-556

21. Macpherson, J. V., *Electroanalysis*, **2000,** *12*, 1001-1011.

22. Leddy, J.; Bard, A. J., *J. Electroanal. Chem*, **1983,** *153*, 223-242.

23. Leddy, J. A.; Bard, A. J.; Maloy, J. T.; Saveant, J. M., *J. Electroanal. Chem*., **1985,** *187*, 205-227.

24. Dalton, E. F.; Murray, R. W., *J. Phys. Chem*., **1991,** *95*, 6383-6389.

25. Mann, J. A.; Rodríguez-López, J.; Abruña, H. D.; Dichtel, W. R., *J. Am. Chem. Soc*., **2011,** *133*, 17614-17617.

26. Lee, D.; Donkers, R. L.; DeSimone, J. S.; Murray, R. W., *J. Am. Chem. Soc*., **2003,** *125*, 1182-1183.

27. Compton, R. G.; Harland, R. G., *J. Chem. Soc., Faraday Trans. 1 Phys. Chem. Condensed Phases*, **1989,** *85*, 761-771.

28. Blauch, D. N.; Saveant, J. M., *J. Am. Chem. Soc*., **1992,** *114*, 3323-3332.

29. Hanwell, M. D.; Curtis, D. E.; Lonie, D. C.; Vandermeersch, T.; Zurek, E.; Hutchison, G. R., *J. Cheminfo.,* **2012**, 6, *4-12*.

30. Mirkin, M. V., *Mikrochim. Acta*, **1999**, *130*, 127-153**.**

31. Mirkin, M. V.; Horrocks, B. R., *Anal. Chim. Acta*, **2000,** *406*, 119-146.

32. Amemiya, S.; Bard, A. J.; Fan, F. R. F.; Mirkin, M. V.; Unwin, P. R., *Ann. Rev. Anal. Chem.,* **2008,** *1*, 95-131.

33. Bard, A. J.; Mirkin, M. V.; Unwin, P. R.; Wipf, D. O., *J. Phys. Chem.,* **1992,** *96*, 1861-1868.

34. Kwak, J.; Bard, A. J., *Anal. Chem*., **1989,** *61*, 1221-1227.

35. Borgwart, K.; Heinze, J., *Scanning Electrochemical Microsocopy*. Marcel Dekker: **2001**.

36. Bard, A. J.; Faulkner, L. R., *Electrochemical Methods: Fundamentals and Applications. 2nd Edition* Wiley: **2000**.

37. Peterson, R. R.; Cliffel, D. E., *Langmuir,* **2006,** *22*, 10307-10314.

38. Demaille, C.; Unwin, P. R.; Bard, A. J., *J. Phys. Chem*., **1996,** *100*, 14137-14143.

39. Ritzert, N. L.; Rodriguez-Lopez, J.; Tan, C.; Abruna, H. D., *Langmuir*, **2013,** *29*, 1683-1694.

40. Rodriguez-Lopez, J.; Minguzzi, A.; Bard, A. J., *J. Phys. Chem. C*, **2010,** *114*, 18645-18655.

41. Petrii, O. A.; Khomchenko, I. G., *J. Electroanal. Chem*., **1980,** *106*, 277-286.

42. Macpherson, J. V.; Unwin, P. R., *J. Phys. Chem.,* **1994,** *98*, 1704-1713.

43. Macpherson, J. V.; Unwin, P. R., *J. Phys. Chem*., **1996,** *100*, 19475-19483.

44. Andrieux, C. P.; Saveant, J. M., *J. Electroanal. Chem. Interfacial Electrochem.,* **1978,** 93, 163-170.

45. Andrieux, C. P.; Saveant, J. M., *J. Electroanal. Chem. Interfacial Electrochem.,* **1980,** 111, 377-382.

46. Abruna, H.D., "*Electrode Modification with Polymeric Reagents", Chapter 3 in Electroresponsive Molecular and Polymeric Systems*, Volume 1, T. A. Skotheim, Ed., Marcel Dekker, New York, **1988**.

Chapter 3: Impact of Backbone Tether Length and Structure on the Electrochemical Performance of Viologen Redox Active Polymers

Notes and Acknowledgements

This chapter appeared in its entirety in the journal *Chemistry of Materials* with authors Burgess, M.; Chenard, E.; Hernández-Burgos, K.; Nagarjuna, G.; Assary, R.S.; Hui, J.; Moore, J. S.; Rodríguez-López, J. "Impact of Backbone Tether Length and Structure on the Electrochemical Performance of Viologen Redox Active Polymers". **2016,** 28, 7362–7374. This article is reprinted with the permission of the publisher and is available with the accompanying Supporting Information file from http://www.pubs.acs.org and using DOI: 10.1021/acs.chemmater.6b02825. M.B., E.C., and K.H.B. all contributed equally to this work. M.B performed all the SECM analysis, helped in voltammetry experiments, helped in spectroelectrochemical measurements, helped in temperature dependent UV-vis studies, did all bulk electrolysis measurements, helped write the manuscript, helped in data analysis, and made figures. This work was supported as part of the Joint Center for Energy Storage Research, an Energy Innovation Hub funded by the U.S. Department of Energy, Office of Science, Basic Energy Sciences. M. B. acknowledges support by the National Science Foundation Graduate Research Fellowship Program under grant No. DGE-1144245. Materials characterization was carried out in part in the Frederick Seitz Materials Research Laboratory Central Research Facilities at the University of Illinois at Urbana–Champaign. K.H.B. gratefully acknowledges the Beckman Institute Postdoctoral Fellowship at the University of Illinois at Urbana−Champaign, with funding provided by the Arnold and Mabel Beckman Foundation. J.R.L. acknowledges additional support from a Sloan Research Fellowship. The authors thank Prof. Catherine J. Murphy for allowing us to use the near IR UV–vis spectrometer in her laboratory.

Abstract

The design of chemically stable and electrochemically reversible redox active polymers (RAPs) is of great interest for energy storage technologies. Particularly, RAPs are new players for flow batteries relying on a size-exclusion based mechanism of electrolyte separation, but few studies have provided detailed molecular understanding of redox polymers in solution. Here, we use a systematic molecular design approach to investigate the impact of linker and redox-pendant electronic interactions on the performance of viologen RAPs. We used scanning electrochemical microscopy, cyclic voltammetry, bulk electrolysis, temperature-dependent absorbance, and spectroelectrochemistry to study the redox properties, charge transfer kinetics, and self-exchange of electrons through redox active dimers and their equivalent polymers. Stark contrast was observed between the electrochemical properties of viologen dimers and their corresponding polymers. Electron self-exchange kinetics in redox active dimers that only differ by their tether length and rigidity influences their charge transfer properties. Predictions from the Marcus–Hush theory were consistent with observations in redox active dimers, but they failed to fully capture the behavior of macromolecular systems. For example, polymer bound viologen pendants, if too close in proximity, do not retain chemical reversibility. In contrast to polymer films, small modifications to the backbone structure decisively impact the bulk electrolysis of polymer solutions. This first comprehensive study highlights the careful balance between electronic interactions and backbone rigidity required to design RAPs with superior electrochemical performance.

Introduction

With the impetus of sustainable energy technologies such as wind and solar, there is a demand for efficient electrical energy storage devices that couple to these intermittent sources.

Non-aqueous flow batteries (NRFBs) are attractive candidates for grid energy storage that address issues related to energy density and load leveling.[1,2] These devices store charge in solution by utilizing high energy density redox couples, that is, an anolyte and a catholyte, which are retained in separate compartments and flown through an electrode assembly.[3,4] Redox active polymers (RAPs) based on organic moieties offer exceptional chemical and structural versatility as redox couples for NRFBs.[5-8,62,63] Recently, our groups reported on the use of a highly soluble viologen polymer **1** (Figure 3.1) as a charge storage medium for use in a new type of size exclusion NRFB.[9] This strategy solves issues with the lack of high-performance membranes for nonaqueous electrolytes and minimizes species crossover between compartments.

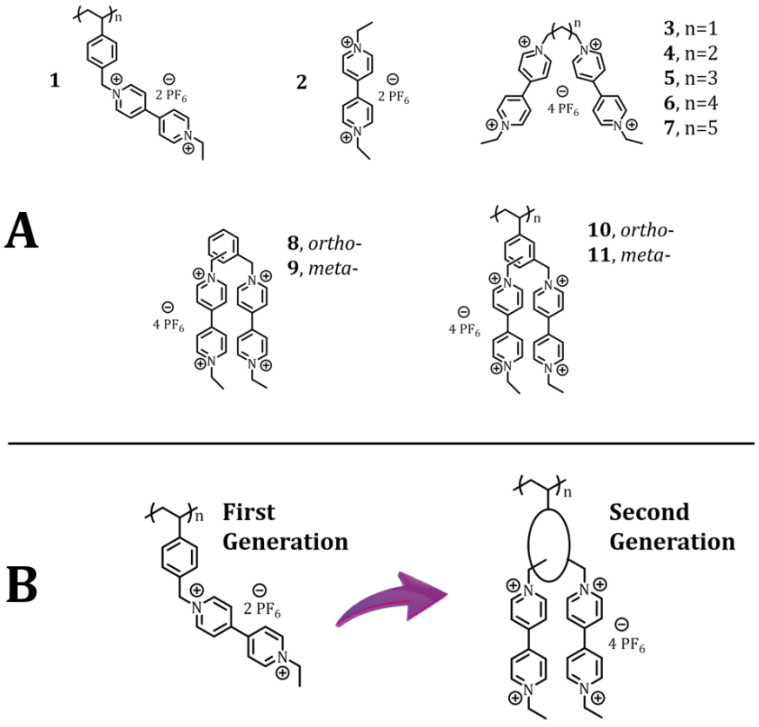

Figure 3.1. (A) Chemical structures of all the species studied in this work. (B) Second generation of viologen RAPs have two redox active pendants per repeat unit that are closer together to encourage intramolecular interactions.

While the size-exclusion approach effectively opens a viable pathway for the deployment of NRFBs, long-distance charge transfer and high current density demands on RAPs are conceivably limiting factors in their performance. Increasing the size of RAPs enhances size-exclusion effects, but it also increases the time for particle electrolysis due to three-dimensional charge transport within RAP films and particles. A kinetic study of RAP **1** suggested that steps associated with adsorption and intraparticle charge transfer introduce a preceding chemical step that sets an upper boundary to charge transfer kinetics.[10] Regardless of size, it is desirable to understand the intrinsic factors that determine rate performance in RAPs. Here, we explore the impact of electronic and structural modulations on the redox kinetics, intrinsic charge transport, and bulk reversibility of RAPs and their solutions.

Scheme 3.1 Preparation of Viologen Dimers[a]

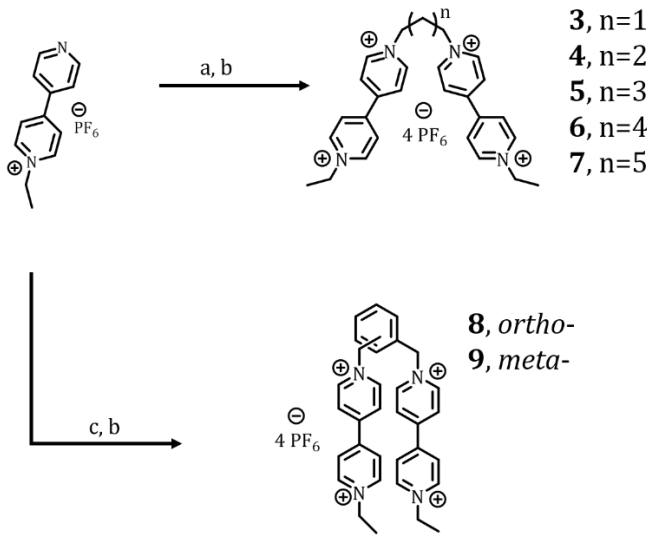

[a](a) Dibromoalkanes, DMF, 60 °C, 2-3 days; (b) $TBAPF_6$, MeCN, H_2O, 24 h (**3** = 12%, **4** = 67%, **5** = 66%, **6** = 71%, **7** = 32%, **8** = 65%, **9** =27%, yields over 2 steps); (c) *ortho bis*(bromomethyl)benzene or *meta-bis*(bromomethyl)benzene, DMF, 60 °C, 2-3 d.

Despite numerous studies on polymer films,[10-12] there are far fewer scientific reports that have studied the characteristics of RAPs in solution. Investigating the impact of electronic interactions between neighboring pendants via a synthetic bottom-up approach enables us to explore the applicability of modular design principles on solution phase RAPs. Seminal studies on isonicotinate dimers demonstrated that the structure of the tether has an effect on their electronic structure as evaluated spectroscopically.[13-17] However, these dimer studies did not extend to their polymer counterparts, nor did they address their electrochemical properties. On the other hand, viologen dimers and similar analogues have been synthesized and studied before in photochemical and electrochemical investigations.[18-22] To expand on the convenient properties of viologen systems as electrochemical and spectroscopic probes, here, we explore how bottom-up molecular design aimed at enhancing interpendant electron transfer, impacts the electrochemistry of a RAP. New insight was achieved through the comparative analysis of RAP **1** and its viologen monomer **2**, alkyl spacer dimers (**3**–**7**), rigid xylyl spacer dimers (**9** and **10**), and their polymers (**10** and **11**). Schemes 3.1 and 3.2 depict a workflow of their synthesis.

A chemical property that has the potential to be strongly modulated by pendant–pendant interactions is charge diffusion (D_E). Because RAPs and their films require three-dimensional charge transfer to attain full electrolysis, enhancing this parameter may influence the electrode response of polymer solutions. A recurrent model in charge diffusion in polymeric films is one originally proposed by Dahms and Ruff (Equation 3.1), which considers the impact of electron self-exchange, k_{EX}, and interpendant distance, δ:

(3.1) $$D_E = \frac{k_{EX}\delta^2}{6}$$

Scheme 3.2 Synthetic Steps for the Preparation of the Second Generation of Viologen Polymers (Poly *ortho*-benzene **10** and Poly *meta*-benzene **11**[a]

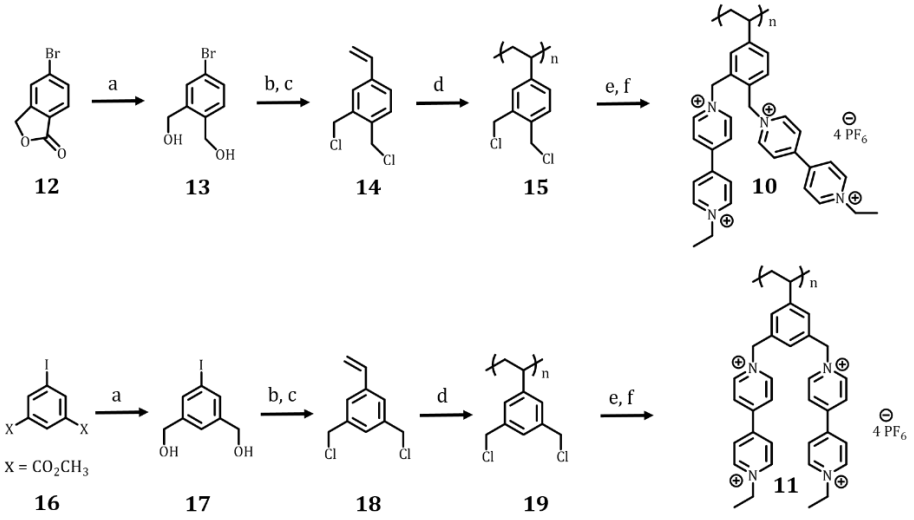

[a](a) LiBH , MeOH, THF, 24 h (**13** = 95%, **17** = 72%); (b) PdCl, PPh3, potassium vinyltrifluoroborate, THF, H2O, 24 h; (c) NCS, PPh3, THF, 24 h (**14** = 72%, **18** = 59%, yields over 2 steps); (d) AIBN, ethyl 2-(phenylcarbonothioylthio)-2-phenylacetate, DMF (**15** = 58%, *Mn* 80 kDa, PDI 1.9 and **19** = 55%, *Mn* 53 kDa, PDI 1.4); (e) *N*-ethyl bipyridinium hexafluorophosphate, DMF, 60 °C, 5 days; (f) $TBAPF_6$, MeCN, H2O, 24 h (**10** = 80%, **11** = 64%, yields over 2 steps).

In our studies, the parameter δ was estimated by density functional theory (DFT) calculations (Appendix B). Equation 3.1 suggests that, given similar concentrations of the redox active pendant in a polymer film or particle, it is possible to modulate the rate of charge diffusion by enhancing k_{EX}. In the Marcus–Hush theory, the rate of electron transfer between species is also related with the self-exchange of charges.[23-27] Self-exchange is the sharing of electrons between neighboring redox groups that only differ in their oxidation state, a process well-known to occur effectively in viologens undergoing charge transfer.[28, 29] Using UV–vis spectroscopy in combination with the Marcus and Hush theory provided us an understanding of the effect of tether

length on k_{EX}. Furthermore, increasing this quantity should have an impact on the heterogeneous rate for electron transfer, k^0, as understood from Equation 3.2:[30]

(3.2) $$k^0 \propto \sqrt{k_{EX}}$$

We present, for the first time, a bottom-up approach for evaluating the impact of structural and electronic effects on the electrochemistry of a solution-phase RAP. We further explore how the electrochemical reactivity of the monomer propagates to the polymer form.

Materials and Methods

All chemicals were used as received unless otherwise stated. 5-Bromophtalide was purchased from Alfa Aesar. Halide alkyl, 1,2-bis(bromomethyl)benzene, 1,3-bis(bromomethyl)benzene, PPh_3, $PdCl_2$, and ethyl 2-(phenylcarbonothioylthio)-2-phenylacetate (CIA) were purchased from Aldrich. Potassium vinyltrifluoroborate and Cs_2CO_3 were purchased from AK Scientific. AIBN was recrystallized. Dimethylformamide (DMF) and dry dichloromethane were obtained from an in house solvent dispensing system. A thorough description of all the synthetic procedures and yields for the synthesis of the monomer, dimer species, polymer weight characterization for poly *o*-benzene dimer **10** (432 kDa), and poly *m*-benzene dimer **11** (286 kDa) are shown in Appendix B. Dynamic light scattering measurements of poly *o*-benzene dimer **10** and poly *m*-benzene dimer **11** found that these species had solvated radii of 5.6 and 7.1 nm, respectively (Appendix B Figure B.38), making them comparable in size with respect to the family of viologen RAPs previously reported by our groups.[9]

General Protocol for the Preparation of Viologen Dimers (Scheme 3.1)

Dihalide linker (1 equiv) was added to a solution of N-ethyl-4,4′-bipyridinium hexafluorophsphate (2.1 equiv) in DMF ([bipyridinium] = 3 M). The solution was then allowed to

reach 60 °C and stirred at this temperature for 3 days. As the reaction progressed, an orange solid precipitated. Et_2O was added to the mixture, and the solid was filtered and rinsed with a solution of CH_2Cl_2/Et_2O (1:1, v/v). The solid was then dissolved in a minimal amount of $MeCN/H_2O$ (1:4, v/v) and NH_4PF_6 (10 equiv) with H_2O added in small portions. The resulting mixture was stirred for 24 h. MeCN was removed in vacuo with a rotary evaporator, and H_2O was added to the mixture to further precipitate out the solid. The solid was filtered out and rinsed with H_2O, MeOH, and then Et_2O. The solid was dried under vacuum for 24 h to yield tethered viologen as a solid.

General Protocol for the Preparation of the Second Generation of Viologen Polymers (Scheme 3.2)

RAPs **10** and **11** were synthesized using similar protocol sequences. The sequence for the preparation of polymer **10** begins with the reduction of lactone **12** to give the known diol **13** in good yield, with full conversion within the first 30 min.[31] The intermediate from the Pd-catalyzed coupling reaction between diol **13** and potassium vinyltrifluoroborate was chlorinated to provide product **14**. Polymerization of **14** proceeded smoothly to give polymer **15** with a *Mn* = 80 kDa, PDI = 1.9. Subsequent functionalization of polymer **15** with N-ethyl bipyridinium hexafluorophosphate followed by ion exchange provided polymer **10**. For the preparation of polymer **11**, we started the sequence with the reduction of diester **16**. The reaction sequence for the preparation of **11** followed the same synthetic steps as the preparation of **15**. Polymerization of **18** gave polymer **19** with a *Mn* = 53 kDa and PDI = 1.4.

Electrochemistry

DMF (anhydrous 99.8%), acetonitrile (anhydrous 99.8%), tetrabutlyl ammonium hexafluorophosphate (>99%), lithium tetrafluoroborate (anhydrous powder 99.99% trace metal

analysis), ferrocene (98%), and tris(4-bromophenyl)ammoniumyl hexachloroantimonate (98%) were all purchased from Sigma-Aldrich and used as received in electrochemical experiments.

Materials Characterization

Characterization of the synthesized species was done when applicable by a set of methods including Fourier transform-infrared spectroscopy (FT-IR), ^{1}H, ^{13}C, ^{31}P, and ^{19}F NMR, high resolution mass analysis by electrospray and electron impact ionization (ESI and EI) mass spectrometry, CHN analysis, size exclusion chromatography (SEC), and melting point. All of the instruments used and data obtained from these characterization tools are reported in Appendix B.

Electrochemical Experiments

All electroanalytical measurements were performed using either a CH Instruments 760E bipotentiostat or a CH Instruments 920D scanning electrochemical microscope (SECM). Spectroelectrochemistry experiments were performed using a SEC 2000-spectrometer from ALS Co. (Japan) in absorbance mode. Temperature-dependent UV–vis experiments used a Varian-Cary Bio 50 spectrometer equipped with a single cell Peltier heating accessory. Capped UV–vis cells (Starna Cells) were used to keep the sample free from ambient moisture and oxygen. All solutions were prepared and all electrochemical experiments were carried out in an inert atmosphere glovebox (MBRAUN, Stratham, NJ) with strict monitoring of the environmental conditions to have an oxygen and water content to be less than 0.1 ppm. W-cells were purchased from Adams and Chittenden for use as a bulk electrolysis cell. The W-cells had ultrafine pore fritted glass separators between the chambers, which ensured that the working, counter, and reference electrode compartments minimized any analyte crossover.

Electrodes

The 1.5 mm radius platinum disk electrodes for use in voltammetry were purchased from CH Instruments (Austin, TX). Ultramicroelectrodes (UMEs) with a radius of 12.5 μm were custom-made using a previously reported procedure.[32] UMEs used in scanning electrochemical microscopy experiments had an R_g of 2, where R_g is the radius of the electrode including the glass sheath, divided by the radius of the Pt microdisk. A Wollaston wire nano-SECM tip was fabricated as described elsewhere using a 300 nm radius Pt wire from Goodfellow.[33] A Pt wire was used as the counter electrode in all voltammetric experiments, and a carbon rod was used in bulk electrolysis measurements. A large piece of carbon felt (GFA 6) was used as the working electrode in bulk electrolysis (SGL Group). All electrochemical experiments are listed versus a 0.1 M Ag/Ag^+ reference electrode.

Scanning Electrochemical Microscopy Approach Curves

SECM approach curve analysis was used to measure the standard heterogeneous rate constant of redox species over a Pt macrodisk. Fitted approach curves were expressed in terms of the overall dimensionless constant K that relates the diffusion coefficient (D) of the species, heterogeneous rate constant (k_f), and radius (a) of the electrode as shown in equation 3.3:[34]

$$K = \frac{k_f a}{D} \tag{3.3}$$

Transformation of k_f to the standard rate constant (k^0) was done by using the Butler–Volmer equation after accounting for the overpotential between the tip and substrate electrode.[23] Calibration of the tip separation distance when at the approached position (d_0) was done using ferrocene under pure positive feedback conditions (Appendix B Figure B.4).

Results and Discussion

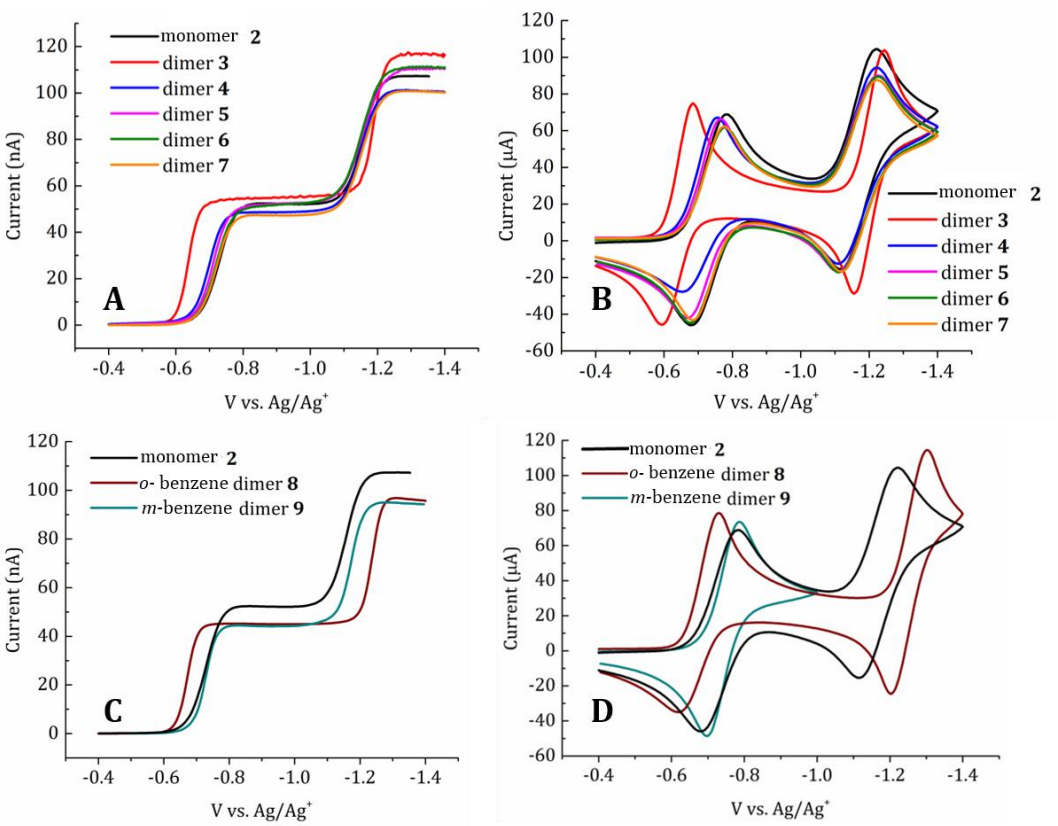

Figure 3.2. All voltammetry was done in a solution of 5 mM of the dimers (10 mM viologen) with 0.1 M $LiBF_4$ supporting electrolyte in acetonitrile. (A) Linear sweep voltammograms of all the alkyl based dimers at 50 mV/s with a 12.5 µm radius Pt UME. (B) Macrodisk cyclic voltammetry of all the alkyl based dimers using a 1.5 mm radius Pt disk electrode at 75 mV/s. (C) Linear sweep voltammograms of the benzene dimers at 50 mV/s with a 12.5 µm radius Pt UME. (D) Macrodisk cyclic voltammetry of the benzene based dimers using a 1.5 mm radius Pt disk electrode at 75 mV/s. Only the first reduction of the *m*-benzene dimer **9** is shown for the larger disk electrode because the second electron was highly unstable upon access. Macrodisk voltammetry with the second electron is shown in Appendix B Figure B.1.

Electrochemical Characterization of Dimers

The electrochemical characterization of the synthesized viologen dimers **3** to **7** was done by steady state voltammetry at a microelectrode (MECV) and macrodisk cyclic voltammetry (CV) with 5 mM of the dimer, that is, 10 mM effective viologen concentration. CV and MECV of the dimers were compared to measurements with ethyl viologen **2** at 10 mM concentration. The results

of these studies are shown in Figure 3.2, panels A and B. Voltammetry shows that all species have similar diffusion coefficients. These were calculated from the MECV following a chronoamperometric step at the first reduction wave. The steady-state current at a UME is expressed by, $i_{steady\ state} = 4nFaDC^*$, where n is the number of electrons transferred per redox active species (2), F is Faraday's constant (96,485 C/mol), a is the electrode radius (12.5 μm), and C^* is the bulk concentration of analyte (5 mM). Bulk electrolysis (BE) under potential control[23, 9] of the dimers **3**–**7** informed that the first reduction event corresponded to the transfer of two electrons (Appendix B Figures B.9–B.12). The CV waves correspond to the reduction processes DV^{4+}/DV^{2+} (∼−0.7 V) and DV^{2+}/DV (∼−1.2 V), where DV stands for viologen dimer. Only two reductions were observed for all species, further confirming the concurrent transfer of two charge equivalents per redox event. Table 3.1 summarizes the observed trends.

CV and MECV experiments evidenced the large impact of tether-length on the energies of electron transfer. Potential shifts as a function of structure have been seen before in other viologen systems,[22, 35] but we are unaware of systematic studies of tether length. As the tether length was decreased toward a three carbon linker in dimer **3**, the first reduction potential shifted 80 mV more positive relative to that of the viologen monomer **2** (Figure 3.2). The other members of the dimer series also exhibited a positive shift, which decreased with longer linker length. This shift suggests a thermodynamically more favorable reduction process with respect to monomer **2**. In contrast to the first reduction wave, the second wave was shifted to more negative potentials. This suggests additional driving force requirements, possibly to overcome interactions created during the first reduction. A molecular structure that fosters viologen–viologen interactions in a more direct fashion was also evaluated. Benzene spacers allow rigidity since there are fewer possible conformers compared to alkane chains, thus "locking" the dimers and affording them less

rotational degrees of freedom. Furthermore, these benzene-based dimers closely resemble the repeating unit structure of viologen polymers that our groups has previously studied (RAP **1**).[9] CV and MECV of the *ortho*- (dimer **8**) and *meta*- (dimer **9**) substituted benzene dimers are shown in Figure 3.2, panels C and D. A similarly altered reactivity with respect to monomer **2** was observed. The *o*-benzene dimer **8** had electrochemical signatures much closer to dimer **3** than to dimer **4**. The *m*-benzene dimer **9** with an additional carbon displayed characteristics similar to dimers **4** and **5**. Because all dimer species are composed of viologen units, an intuitive expectation is that the dimers display similar electrochemistry to the monomer, although with two charge equivalents. At the other extreme, if the interpendant interactions caused a strong coupling of the viologen units, it would be expected to see up to four single electron CV waves with potentials defined by Born-sphere electrostatic effects.[23, 36] Instead, single two-electron waves with overall potential shifts were observed, which suggested intermediately strong interactions. DFT simulations recreated the shifts in reduction potential of all the dimer species as a function of tether length and structure, as shown in the Appendix B, Figure B.35. These calculations predict that π-staking of the dimers takes place upon reduction, with the conformation limits imposed by the length and structure of the alkyl/xylyl linkers. In general, the best agreement between experiment and theory was observed when alkyl-linker dimers **3**–**7** changed from an initially linear conformation to a bent one upon reduction. Dimers **8** and **9** were predicted to only slightly decrease the distance between viologen units due to their rigidity (Appendix B Figure B.36 and Table B.2). Nonetheless, significant differences in the reduction potentials between dimers **8** and **9** were observed. CV studies strongly suggested differential interviologen interactions as a function of linker structure.

Table 3.1 Derived Electrochemical Parameters

Species	***D* (cm^2/s)**	E_1^0 **(V)**	E_2^0 **(V)**	k^0 **(cm/s)**	k_{EX} **(s^{-1})**
monomer **2**	2.0 x 10^{-5}	-0.72	-1.16	7.5 ± 0.01	N/A
dimer **3**	2.1 x 10^{-5}	-0.64	-1.19	1.9 ± 0.01	2.3 x 10^{11}
dimer **4**	2.4 x 10^{-5}	-0.70	-1.16	0.75 ± 0.01	1.9 x 10^{8}
dimer **5**	2.2 x 10^{-5}	-0.71	-1.16	0.61 ± 0.03	9.2 x 10^{6}
dimer **6**	2.3 x 10^{-5}	-0.715	-1.16	0.51 ± 0.20	N/A
dimer **7**	1.7 x 10^{-5}	-0.72	-1.16	0.56 ± 0.04	N/A
o-benzene dimer **8**	1.9 x 10^{-5}	-0.67	-1.23	1.01 ± 0.02	1.4 x 10^{10}
m-benzene dimer **9**	1.9 x 10^{-5}	-0.72	-1.16	0.59 ± 0.01	2.4 x 10^{8}
poly *o*-benzene dimer **10**	3.2 x 10^{-7}	-0.64	-1.20	0.0011 ± 5 x 10^{-4}	6.7 x 10^{8}
poly *m*-benzene dimer **11**	4.1 x 10^{-7}	-0.68	-1.20	0.0017 ± 5 x 10^{-4}	6.0 x 10^{7}
poly benzene monoviologen **1**	6.6 x 10^{-7}	-0.69	-1.16	0.01 ± 5 x 10^{-4}	8.1 x 10^{6}

The kinetics of electron transfer is also affected by dimer structure. Accurately measuring electrochemical kinetics for facile systems requires the use of more specialized electroanalytical techniques[37-39] such as scanning electrochemical microscopy (SECM) approach curve analysis.[40]

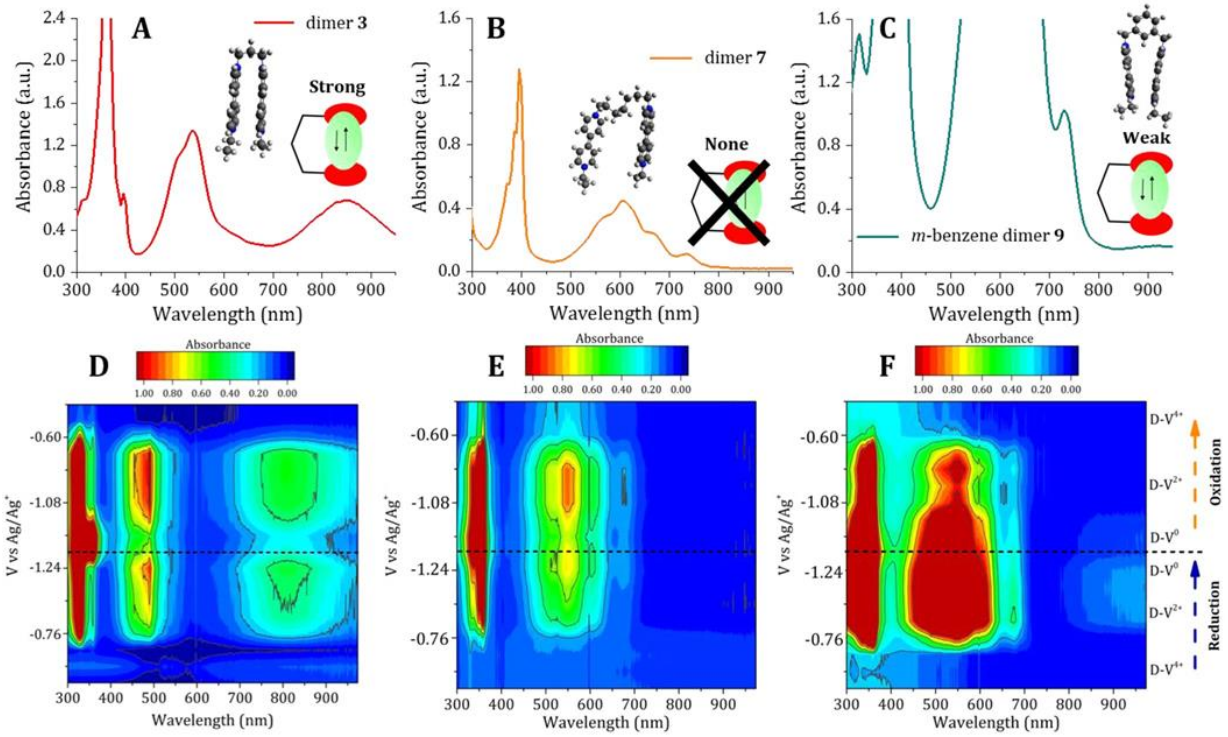

Figure 3.3. UV−vis spectra for (A) dimer **3** at a concentration of 0.06 mM; inset shows a schematic representation of the self-exchange process occurring at ~850 nm, (B) dimer **7** at a concentration of 0.06 mM with no observed self-exchange reactions, and (C) *m*-benzene dimer **9** at a concentration of 0.3 mM with weak self-exchange reactions. Chemical structures shown in insets are the optimized structures of the dimers from DFT calculations (Appendix B Figure B.36). Contour plot of the in situ UV−vis spectroelectrochemistry for (D) dimer **3** (0.5 mM), (E) dimer **7** (0.5 mM), and (F) *m*-benzene dimer **9** (2.0 mM).

The approach curves for all of the viologen dimers are shown in Appendix B Figure B.2. Approach curves in the feedback mode were measured by poising the Pt UME at −0.9 V so that the first reduction (DV^{4+}/DV^{2+}) of the viologen dimers would occur at mass transfer limited conditions. The tip was then moved toward the substrate electrode, a Pt disk, which was biased at 120 mV positive of the E^0, that is, at constant overpotential, so that the substrate could regenerate the viologen species back to its original oxidation state (DV^{2+}/DV^{4+}). To probe the kinetics of dimer **3** and monomer **2** more accurately, approach curves were performed with a nano-SECM tip (Appendix B Figures B.5–B.7). Table 3.1 summarizes the obtained kinetic data.

As the alkyl tether length is increased, the level of positive feedback decreases. This strongly suggests that the proximity of redox pendants in the viologen dimers is directly related to the charge transfer kinetics, k^0.[41] As the tether length for the alkyl dimers increases from dimer **3** to dimer **7**, k^0 decreases by a factor of 4, despite the fact that the redox pendants in these species are identical. In contrast, dimers **8** and **9** show higher k^0 than their alkyl counterparts despite them having the same number of carbon spacers between them (Figure 3.3B and Table 3.1). Because the identity of the redox active species is identical between the dimers, other factors must govern the rate of electron transfer. The extrapolated values of k^o for all of the viologen dimers in this study are consistent with the order of magnitude found with other facile redox systems.[42] To verify that the fast redox kinetics for the dimers found from SECM was on the right order of magnitude, additional experiments and simulations of nano-electrode voltammetry were made with some of the dimers and monomer. As can be seen in Appendix B Figures B.39 and B.40, fast electrochemical kinetics is able to be differentiated via voltammetry with a 300 nm radius Pt electrode by following the wave shape and position. Fitting of experimental cyclic voltammetry curves measured of monomer **2** and dimers **6** and **7** using DigiElch (Gamry instruments) finds that the order of magnitude and values of kinetics agree very well.

Equation 3.2 links k^o to the rate constant for self-exchange, k_{EX}. Thus, we hypothesized that voltammetric and kinetic differences observed in dimers **3**–**9** had an origin in different degrees of k_{EX} modulated by the linker structure. Because increased electron mobility would aid in increasing the redox kinetics of dimers and polymers, we now turn to evaluate the extent and impact of k_{EX} on their electrochemical response.

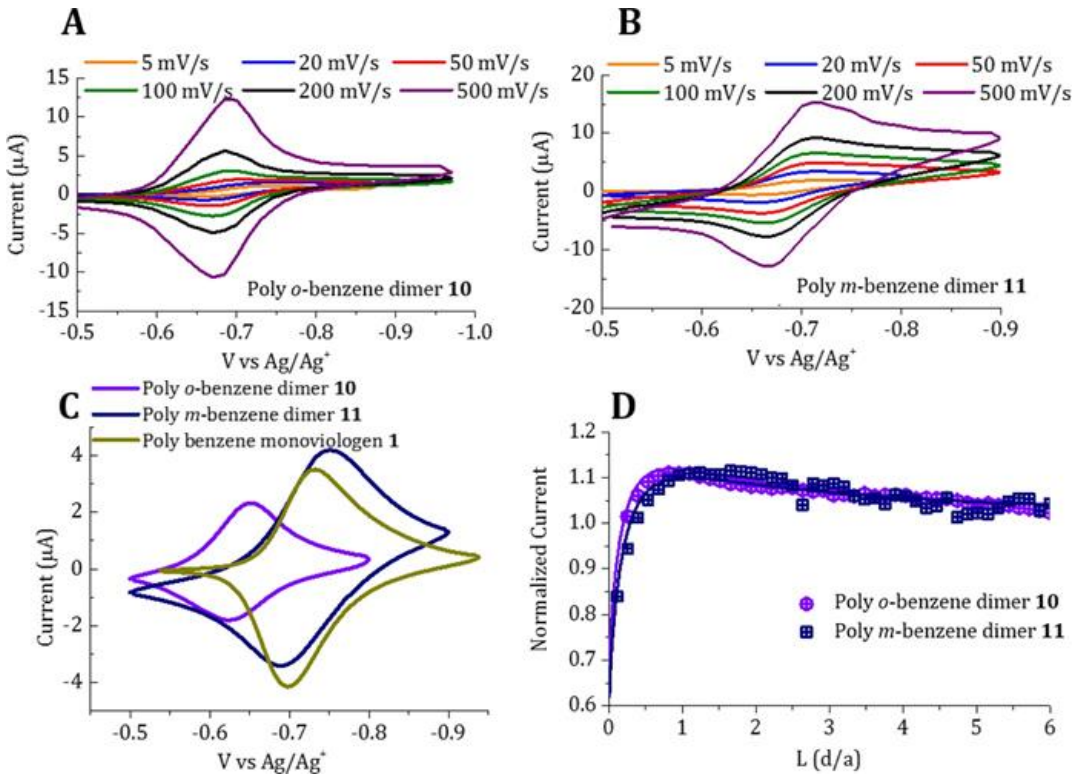

Figure 3.4. Scan rate dependent voltammograms at a concentration of 1 mM for (A) poly *o*-benzene dimer **10**, (B) *m*-benzene dimer **9**. (C) Cyclic voltammograms at 10 mV/s for the polymer film in a solution only containing 0.1 M supporting electrolyte (refer to Appendix B for deposition CVs) and (D) SECM approach curves for poly *o*-benzene dimer **10** and poly *m*-benzene dimer **11**.

Spectroelectrochemistry of Dimers

Intervalence compounds are materials that can delocalize electrons and that exhibit large constants for self-exchange, k_{EX}.[24, 43, 44] There are three classes of intervalence compounds (IC).[43, 44] Class I compounds have complete charge localization; therefore, the intramolecular electron transfer (ET) between their redox active groups will not occur.[44, 43] Class II, to which our viologen dimers correspond, have a detectable interaction arising from a partial mix of the electronic states of its redox units. Finally, class III compounds present full delocalization of charges.[43, 44]

UV–vis absorbance methods were used to conveniently extract k_{EX}.[45-50] Hush proposed that for class II intervalence compounds, the band maximum ($\tilde{\upsilon}_{max}$) of the Gaussian shaped peak in an absorption spectra correlates with the intervalence interactions between two redox centers with different oxidation states and is equal to the Marcus reorganization energy (λ).[43, 44] By knowing the reorganization energy, the electronic coupling element, *H*, is calculated using equations 3.4 and 3.5:

(3.4) $$H = \frac{0.0206(\tilde{\upsilon}_{max}\Delta\tilde{\upsilon}_{1/2}\varepsilon_{max})^{1/2}}{r}$$

(3.5) $$\Delta\tilde{\upsilon}_{1/2} = 48.06(\tilde{\upsilon}_{max})^{1/2}$$

where ε_{max} is the extinction coefficient of the intervalence peak, *r* is the distance in Å between the two redox centers (calculated using DFT methods, refer to Appendix B Figure B.36 and Table B.2), and $\Delta\tilde{\upsilon}_{1/2}$ is the peak width at half-maximum derived from equation 3.5.[43] Once the reorganization energy and the electronic coupling element are known, the Marcus theory predicts for mixed valence systems that the free energy of activation for electron transfer ($\Delta G^{\ddagger}$) can be calculated using equation 3.6. With knowledge of $\Delta G^{\ddagger}$, the intramolecular self-exchange constant (k_{EX}) can be calculated by using the Marcus and Hush formalism shown in equation 3.7:[44]

(3.6) $$\Delta G^{\ddagger} = \frac{(\lambda - 2H)^2}{4\lambda}$$

(3.7) $$k_{EX} = k\upsilon_n e^{-\Delta G^2/RT}$$

where κ can be approximated as 1 for strongly coupled adiabatic centers, υ_n is the vibration frequency associated with electron transfer (reported to be 10^{12} s^{-1} for mixed valence phenylene bridge radical cations),[44] *R* is the gas constant (8.314 J/mol K), and *T* is the temperature in Kelvin.

In addition to electrochemical methods, viologen species offer a unique spectroscopic opportunity to use an intervalence band as a molecular gauge for measuring the rate of pendant-to-pendant self-exchange. For the UV–vis experiments, we studied the reduced forms of all the viologen dimers by following two procedures to reach the desired oxidation state. First, we used Zn dust to chemically reduce the dimers (DV^{4+}/DV^{2+}),[51] and second, we used spectroelectrochemical methods within a thin-layer cell. Figure 3.3, panels A–C show the UV–vis spectra for the selected chemically reduced dimer **3**, dimer **7**, and *m*-benzene dimer **9** (see Appendix B for other UV–vis spectra, Figures B.20–B.27). We consistently observed the reported radical cation peak at 350–400 nm and the resulting peak of intramolecular radical interactions at 500–600 nm.[23, 44, 51-55] Dimers **3** and **9** showed the distinctive peak that corresponds to the formation of an intervalence state, at 850 and 895 nm, respectively. This peak was not present or was very weak for the longer linker species, such as dimers **5**–**7**. The k_{EX} was calculated from these spectra.[43, 44] No other peaks were observed in the near-infrared (up to 2500 nm, Appendix B Figure B.34).

Spectroelectrochemical studies showed similar trends to the chemical reduction using Zn. The resulting UV–vis data are shown in Figure 3.3, panels D–F, with the rest of the species shown in Appendix B (Figures B.20–B.30). The contour plots in Figure 3.3, panels D–F show the potential dependence of the UV–vis signal. We observed that the characteristic intervalence peak of the DV^{2+} state became weaker as the DV species formed. Once more, dimer **7** did not show any intervalence peak. On the other hand, the *m*-benzene dimer **9** showed the intervalence band from 800–980 nm.

The highest k_{EX} value was obtained for dimer **3** (Table 3.1), which also had the smallest interviologen *r* value. For a similar interpendant distance, alkyl spacers (dimers **4** and **5**) displayed

a k_{EX} that was approximately two orders of magnitude smaller compared to the rigid spacer (dimers **8** and **9**). When benzene was used as the linker, the π–π interactions between viologens were facilitated. When k_{EX} was obtained via chemical reduction, it showed the same trend (Appendix B Table B.1).

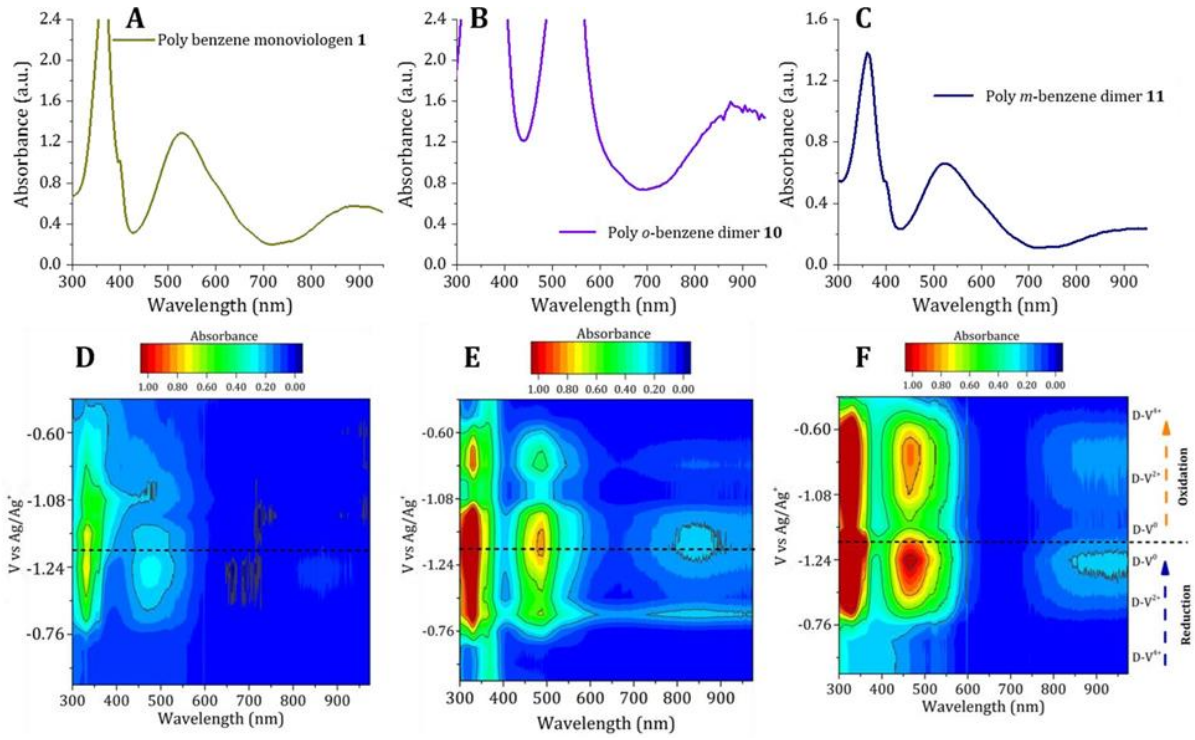

Figure 3.5. UV−vis spectra for (A) poly benzene monoviologen **1** at a concentration of 0.3 mM, (B) poly *o*-benzene dimer **10** at a concentration of 0.06 mM, and (C) poly *m*-benzene dimer **11** at a concentration of 0.06 mM. Contour plot of the in situ UV−vis spectroelectrochemistry for (D) poly benzene monoviologen **1**, (E) poly *o*-benzene dimer **10**, and (F) poly *m*-benzene dimer **11** at a concentration of 0.05 mM. For polymer structures, refer to Figure 3.1.

An increase in k_{EX} in dimers **3**–**9** is associated with increased kinetics. The Marcus theory predicts that an increase in k_{EX} should increase the k^0 of a system in a square root relationship. In Figure 3.7A, we show that the trend predicted by the Marcus relation applies well for dimers **3**–**9**. However, an experimental slope of 4 on a log–log plot was observed. This is higher than the theoretical slope of 1. We attribute these differences to experimental and model uncertainties.[56]

Bulk electrolysis of the viologen dimers gave further insight into the effects of pendant proximity on chemical stability. We performed the electrolysis of a few of the small molecule dimers **3** and **7**, and *o*-benzene dimer **8**, at 10 mM of dimer concentration (Appendix B Figures B.8–B.13). These experiments demonstrated that the dimers are completely electrochemically reversible upon charge cycling with over 90% of the theoretical charge accessed. Armed with the insight provided by the dimeric systems, we now evaluate the persistence of these characteristics on polymer systems using a bottom-up approach.

Voltammetry with Polymers

Following on our first reported viologen RAP,[9] we studied the electrochemical behavior of the "second generation" viologen polymers **10** and **11**, as shown in Figure 3.4, panels A and B. Polymers **10** and **11** are constitutional isomers, but as observed for dimers **8** and **9**, differences in their reactivity are expected. The *o*-benzene polymer **10** showed a positive E^0 shift when compared to the *m*-benzene polymer **11**, which had almost a zero potential shift indicating that the reactivity is similar to the first generation polymer **1**. However, these differences are much smaller than for the dimer/monomer comparisons. For the *o*-benzene polymer **10** at high scan rates (≥100 mV/s) the shape of the voltammogram and peak splitting of the solution phase polymer is controlled by an adsorbed polymer film on the electrode, as seen in Figure 3.4, panel A. In contrast, *m*-benzene polymer **11** (Figure 3.4B) shows a more diffusive-like profile. By incorporating measured parameters for these polymers, such as the diffusion coefficient and the standard rate constant, we simulated the cyclic voltammetry behavior of these polymers using DigiElch (Appendix B Figure B.17). From these digital simulations, we learned that the adsorption equilibrium constant is approximately 20-times higher for the *o*-benzene polymer **10** and therefore favors the surface

confined CV behavior at high scan rates. The formation of an adsorbed layer, however, requires closer examination.

It is important to note that even though the second generation of RAPs has double the viologen units per repeat unit, that the high solubility of the polymer is maintained. Both polymers **10** and **11** were soluble with respect to the repeat unit to at least 1.2 mol/kg in acetonitrile, which is 2.4 mol/kg of viologen active units. This is consistent with the solubility of polymer **1**, which was previously reported in the molar range in acetonitrile.[11] The reversible reactivity of poly *m*-benzene dimer **11** was verified in highly concentrated solutions of up to 472 mM via UME voltammetry (Appendix B Figure B.41), as UMEs allow the measuring of electrochemistry without complications from *i*-*R* drops from the solution.

To test the electrochemical behavior of an electroactive film for both of these polymers, we electrodeposited a polymer film onto the electrode surface by cycling 10 times to −1.4 V, a procedure that yielded controllable and reproducible layers (Appendix B Figure B.18). The electroactive polymer layers were characterized via voltammetry in a solution that only contained supporting electrolyte (Figure 3.4C). Although the RAP layer was confined to the electrode surface, its redox signatures were consistent with charge diffusion. We used ex-situ AFM analysis to estimate the thickness of the resulting polymer layers, such that the charge diffusion coefficient, D_E, on the film could be estimated from a chronoamperometric analysis (Appendix B Figure B.37). The D_E for RAP **10** was calculated as 4.1×10^{-11} cm^2/s, while that for RAP **11** was only 2.5×10^{-11} cm^2/s. D_E for the first generation RAP **1** was calculated as 7.9×10^{-11} cm^2/s. We will return to an evaluation of the significance of these film metrics in the following section. Interestingly, approach curves fit to feedback theory showed that the k^0 for both of these systems (1×10^{-3} cm/s) is within experimental error to be identical (Table 3.1). Therefore, we performed

spectroelectrochemical measurements to determine the degree of self-exchange kinetics for these polymers.

Spectroelectrochemistry with Polymers

We explored the translation of the electronic properties of dimer constituents onto the polymer form. We performed the spectroelectrochemical experiments previously described using Zn as a chemical reducing agent as well as spectroelectrochemistry in a thin layer cell. All polymers showed bands in the range of 300–400 nm and 500–600 nm that strongly resemble the ones seen for the dimeric species. Interestingly, the intervalence peak at 890 nm was not only present in RAPs **10** and **11**, but also in the first generation polymer **1**. This observation demonstrated that redox pendants within the polymer exhibit a certain degree of interaction due to close proximity, thus highlighting the role of the backbone.

Spectroelectrochemical inspection showed a potential dependence on the intensity of the intervalence peak. The resulting UV–vis data are shown in Figure 3.5, panels D–F and additional data in Appendix B. The appearance of the intervalence peak for *o*-benzene polymer **10** and *m*-benzene polymer **11** is consistent with their dimers and appears when the polymers oxidation state is DV^{2+}. However, the intervalence peak appears weaker or disappears for the dimers during the second reduction process. For polymer **1**, the intervalence peak first appears during this second reduction. Furthermore, the contour plot for the *o*-benzene polymer **10** showed three distinctive regions associated with the electrode potential. In the first region, the intervalence band appears after the first reduction and quickly disappears. In the second region, the intervalence band appears again at the second reduction, similarly to polymer **1**. Finally, the third region shows the reappearance of the intervalence peak once the oxidation state of the polymer returns to DV^{2+}. These observations suggest that some disproportionation of DV into DV^{2+} is possible and that time

delays are associated with charge transfer within the sample. This delay is evident in polymers **10** and **1**. In contrast, the *m*-benzene polymer **11** behaves more closely like the dimer **9**, in which the charge propagation in the polymer chain is instantaneous and reversible.

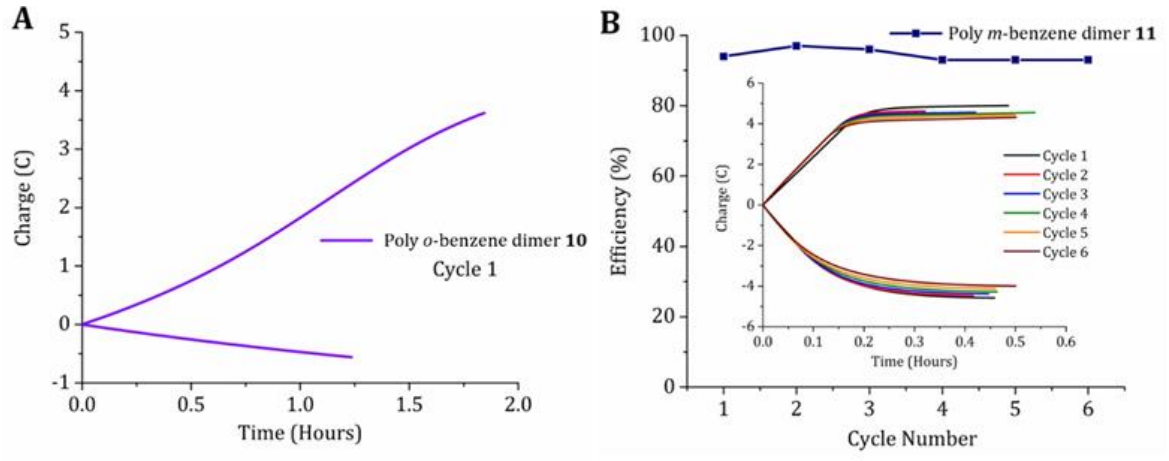

Figure 3.6. Charge storage properties of the (A) poly *o*-benzene dimer **10** and (B) poly *m*-benzene dimer **11**. The working electrode was a Pt mesh for the *o*-benzene polymer **10** and a carbon felt mesh for the *m*-benzene polymer **11**. The bulk electrolysis cells contained 5 mM of the RAP (10 mM viologen) and 0.1 M $LiBF_4$ supporting electrolyte in acetonitrile. The working electrodes were held at −0.9 V for the bulk electrolysis charging (DV^{4+}/DV^{2+}) and −0.35 V for the discharge (DV^{2+}/DV^{4+}). Outset to panel B shows the charge cycling efficiency of the subsequent bulk electrolysis cycles. The efficiency was calculated as the ratio of the charge collected from bulk electrolysis oxidation to the reduction for each cycle.

This analysis highlights how k_{EX} affects the chemical reversibility. The resulting k_{EX} value (6.7×10^8 s^{-1}) for the *o*-benzene polymer **10** is much higher than the first generation viologen polymer 1 (8.1×10^6 s^{-1}). For the *m*-benzene polymer **11**, the k_{EX} value (6.0×10^7 s^{-1}) is one order of magnitude smaller than for the *o*-benzene polymer **10**, but still one order of magnitude higher than polymer **1**. This demonstrates that it is possible to build self-exchange interactions within RAPs from a bottom-up approach, albeit displaying reduced values for k_{EX} within the polymer framework compared to the dimers. Since dimer **8** behaved well during bulk electrolysis (Appendix B Figure B.13–B.14), that is, was chemically reversible and had high Coulombic efficiency, all while displaying large values for k_{EX} and k^0, we were hopeful that these properties

would translate into polymers **10** and **11**. However, the performance of the polymers did not scale accordingly. An example of the bulk electrolysis results with *o*-benzene polymer **10** is shown in Figure 3.6, panel A. This polymer charged relatively slowly and struggled to reach the full theoretical charge (4.82 C) during the first reduction. More importantly, the bulk electrolysis was completely irreversible, and no appreciable amount of charge was able to be extracted from the system upon re-oxidation. This irreversibility was independent of electrode overpotential.

Bulk electrolysis with this RAP was attempted in several conditions using different ionic strengths (0.1, 0.2, and 0.5 M), different electrolytes ($LiBF_4$ and $TBAPF_6$), different electrode materials (carbon, platinum, and mercury), and even in mixed solvents (50:50 acetonitrile and dimethylformamide), yet similar results were observed in all cases. The data in Figure 3.6, panel A with a Pt mesh electrode are representative of the irreversible electrochemical performance. Additional experiments were performed to chemically cycle the redox states of the *o*-benzene polymer **10** by reducing it with Zn dust and oxidizing it with the strong agent tris(4-bromophenyl)ammoniumyl hexachloroantimonate ("magic blue"). These experiments showed that the bulk of the polymer solution is not chemically decomposed upon reduction. However, only the use of large excess of strong chemical oxidant or the prolonged exposure to air or oxidant (e.g., few minutes) could reverse what we hypothesize is a strong radical pairing. This result was unexpected, as we envisioned that the high levels of self-exchange for this RAP would enhance the reactivity of the system by facilitating efficient charge hopping along the polymer backbone through the viologen pendants.

Given the irreversibility observed with RAP **10**, we turned to evaluating the *m*-benzene RAP **11**. In this species, the longer distance between viologen units may prevent the strong stabilization arising from π-interactions. Bulk electrolysis experiments with the *m*-benzene

polymer **11** are shown in Figure 3.6, panel B, and the results are in stark contrast to the *o*-benzene RAP **10** despite their structural similarities. Bulk electrolysis with RAP **11** performed excellently, with over six cycles with Coulombic efficiencies above 90%. The half cycles are very symmetric in shape indicating that there are no electrochemical limitations in accessing each oxidation state. The *m*-benzene polymer **11** is highly substituted with viologen units by achieving a charge upon reduction of 4.9 C, which is 92% of the theoretical charge for this RAP solution assuming 100% functionalization. Steady state UME voltammograms before and after the bulk electrolysis cycles (Appendix B Figure B.14) show that the *m*-benzene polymer **11** quantitatively changes redox states. Although the calculated level of self-exchange for the *m*-benzene polymer **11** was lower than the *o*-benzene polymer **10** by about an order of magnitude, its energy storage capabilities are greatly enhanced.

To the best of our knowledge, this work would be the first to effectively demonstrate the implications of redox pendant proximity on the electrochemical reversibility of RAP systems. Additionally, the *m*-benzene polymer **11** demonstrates that the second generation of RAPs is stable and has doubled the number of accessible redox groups per repeat unit compared to the first generation of poly benzene monoviologen **1**.

Marcus Relationship and Kinetic Evaluation of Second Generation RAPs

Figure 3.7 shows the correlation between k^0 and k_{EX} for dimers and polymers. The k_{EX} for the *o*-benzene RAP **10** was more than one order of magnitude larger than that for the *m*-benzene RAP **11**. Equation 3.2 suggests that the charge transfer rate constant for RAP **10** should be superior to those of RAP **11**. This relation for the polymers is shown in Figure 3.7, panel B. Furthermore, both polymers should exhibit faster electron transfer characteristics compared to the first generation RAP **1**, which exhibited $k^0 \approx 10^{-2}$ cm/s.[32]

However, as shown in Table 3.1, the k^0 values for the second generation viologen polymers were found to be within experimental error equal to 10^{-3} cm/s. Therefore, either the Marcus theory is not sufficiently suited to describe electron transfer to more complex macromolecular architectures or the ability for us to measure the k^0 for the RAPs is limited.

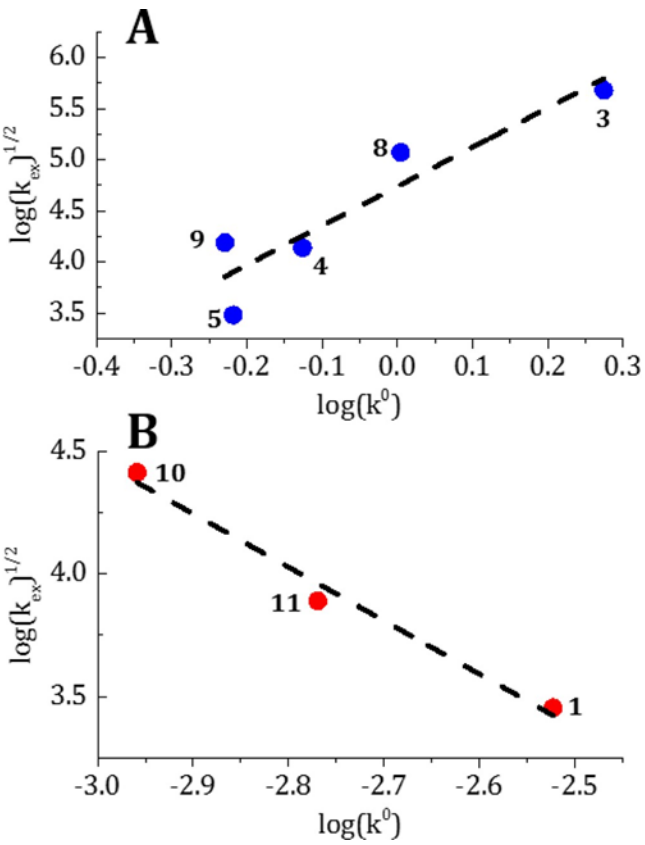

Figure 3.7. (A) Marcus relation for the viologen based dimer species. (B) Marcus relation for the polymeric forms of these dimers for which we do not observe the expected trend.

On the first point, it is known in the Marcus theory that the observed electrochemical kinetics depends on the collisional frequency of the species to the electrode surface.[56, 57]There is a large difference in the diffusion coefficients and collisional frequencies of the RAPs compared to the dimers, where the RAP has an areal impingement rate one order of magnitude lower than that of the dimers. We applied a simple argument based on a polymer hydrodynamic radius (calculated

based on electrochemical diffusion coefficients) of 12 nm versus that of the dimer of 0.2 nm to estimate the collisional frequencies (Appendix B).

Although it is theorized that the maximum electrochemical rate constants for facile systems should be $\geq 10^3$ cm/s,[42, 58] the fastest electrochemical rate constant ever measured is on the order of 10 cm/s.[59] If we assume a kinetic roof of 1.9 cm/s for dimer **3**, then it is likely that a maximum measurable k^0 for the polymer is one order of magnitude lower, that is, 10^{-1} cm/s. We note however that both RAPs **10** and **11** displayed slower kinetics than this from SECM approach curves values and at rotating disk electrode experiments (Appendix B Figure B.19), suggesting that the second generation of RAPs do not show any significant mechanistic improvement over the first generation RAP **1**.[32]

On the second point, so far we have neglected the participation of the pervasive polymer film that forms on the electrode upon exposure to RAP solutions. This film is responsible for mediating electron transfer from the electrode to solution species similarly to an inner sphere mechanism. Because RAP **10** displays a larger value for k_{EX}, it is expected per equation 3.1 that it would also display a larger D_E. This expectation was fulfilled in part per the results shown in Appendix B Table B.3. Any observable improvement, however, seems to be overwhelmed by the loss in reversibility obtained upon bulk electrolysis.

In considering additional structural factors that might impact D_E, we note that ion mobility within RAP films have been shown to affect their response.[11] An unintended consequence of enhancing the interaction between pendants by increasing their proximity is to increase the steric constraints on counter ion insertion into the film. Nonetheless, we note that the overall effect of one small structural perturbation on the RAP structure, that is, a carbon–carbon bond's length difference between pendants, is unexpectedly high. Thus, understanding the conformational

reversibility of RAPs in solution might elucidate pathways to unleash rate enhancements attainable through modulation of k_{EX}.

Temperature Dependent UV–vis Studies

The stability of the self-exchange interactions is dependent upon the linker length and structure. To probe these effects, we performed a temperature dependent UV–vis study on the polymers and dimers in the reduced DV^{2+} form. An Eyring analysis was applied according to equation 3.8:[60, 61]

(3.8) $$ln\frac{k_{EX}}{T} = \frac{-\Delta H^{\ddagger}}{RT} + ln\frac{k_B}{h} + \frac{\Delta S^{\ddagger}}{R}$$

Where T is the temperature in Kelvin, $\Delta H^{\ddagger}$ is the change in enthalpy of the transition state (kJ/mol K), R is the gas constant (8.314 J/mol K), k_B is the Boltzmann constant (1.38×10^{-23} J/K), h is the Planck constant (6.626×10^{-34} J/s), and $\Delta S^{\ddagger}$ is the change in entropy of the transition state (J/K).

The temperature dependent UV–vis spectra and the resulting Eyring plots are shown in Figure 3.8. Linear regression to obtain $\Delta H^{\ddagger}$ and $\Delta S^{\ddagger}$ is shown in Table 3.2. In general, as the temperature increases, the peak intensity associated with self-exchange decreases. Figure 3.8 shows that samples with low k_{EX}, such as dimer **7**, show a very small temperature dependence. Dimers with alkyl spacers are more susceptible to having the self-exchange interaction interrupted than ones with benzene spacers, as shown by the more negative values of $\Delta H^{\ddagger}$. In this case, the motional degrees of freedom for the alkyl spacers are higher than for the rigid benzene ones. This stability of the self-exchange interactions based upon structure is further demonstrated in the macromolecular systems, in which the polymer backbone holds all the repeat units within close

proximity to each other. In doing so, the self-exchange process between pendants is more stabilized.

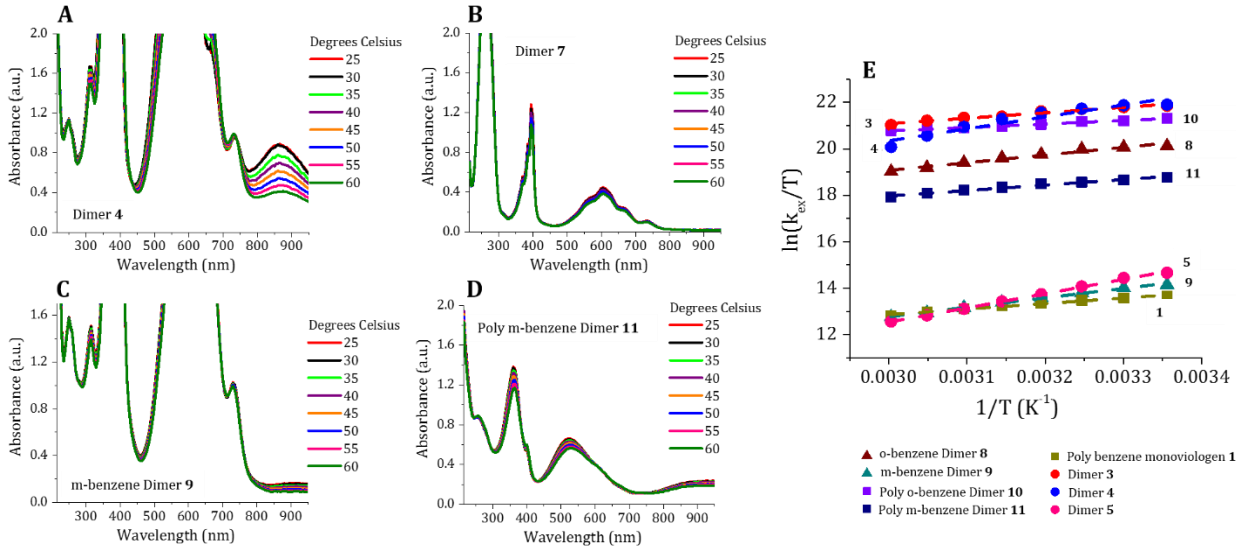

Figure 3.8. Temperature dependent UV−vis data for (A) dimer **4** at a concentration of 0.06 mM, (B) dimer **7** at a concentration of 0.06 mM, (C) *m*-benzene dimer **9** at a concentration of 0.3 mM, (D) poly *m*-benzene dimer **11** at a concentration of 0.05 mM, and (E) Eyring relation for all the systems. From this plot, the entropy and enthalpy of activation can be calculated from the intercept and slope, respectively.

The calculated values for $\Delta S^{\ddagger}$ are intuitive to understand. When the viologen systems are in their oxidized state, the molecules move freely. However, when reduced, the viologen units interact with each other through radical-pairing forces, which drive local viologens to orient themselves "face to face".[51] The increased ordering of the viologen dimers and polymers will necessarily mean a decrease in the systems entropy. However, systems that were already somewhat ordered in their oxidized state, such as polymers and benzene based dimers, will have to undergo less structural reorientation to facilitate self-exchange. This is demonstrated most clearly by comparing the values of $\Delta S^{\ddagger}$ between the *o*-benzene polymer **10** and the dimer **5**. Overall, an Eyring analysis revealed the effects of rigidity and proximity of redox pendants on the polymer backbone.

These solution-phase methods may help in the near future to tailor balanced interactions that lead to reversible behavior while retaining facile charge transport characteristics.

Table 3.2 Calculated Eyring Parameters

Species	**$\Delta H^{\ddagger}$(kJ/mol*K)**	**$\Delta S^{\ddagger}$(J/K)**
dimer **3**	-19.6	-81.2
dimer **4**	-42.8	-156.8
dimer **5**	-51.1	-246.5
o-benzene dimer **8**	-27.4	-121.2
m-benzene dimer **9**	-33.8	-192.8
poly *o*-benzene dimer **10**	-12.6	-62.5
poly *m*-benzene dimer **11**	-19.7	-107.3
poly benzene monoviologen **1**	-19.9	-150.2

Conclusions

In this study, we systematically studied the effect of molecular structure on the electrochemical characteristics of model viologen dimers and polymers. Such models included dimers with an alkyl spacer that varied from three to seven carbons (dimer **3**–**7**) and dimers with a more rigid benzene linker (dimers **8** and **9**), together with their polymers. Despite all these systems having the same redox active constituents, that is, viologen, the tether length and structure have a pronounced role on their reactivity. Viologen dimers with a shorter or more rigid tether have positive shifts in the reduction potential, exhibit enhanced levels of electrochemical kinetics and self-exchange, and can store charge reversibly. Computational analysis by DFT indicated that the

dimers undergo conformational changes upon reduction to that reduces the interpendant distance to facilitate self-exchange interactions. The *ortho*- and *meta*-substituted benzene based dimers were incorporated into a pair of second generation RAPs, and their electrochemical properties were compared with their dimeric complements and the first generation of RAP (polymer **1**).

Consistent with the characteristics of the model dimers, the individual monomeric units of these new RAPs represented an enhancement from the previous generation as the number of redox pendants per unit are doubled. However, the *o*-benzene polymer **10** exhibited irreversible redox chemistry, suggestive of extensive radical-ion pairing, which makes this polymer not attractive for energy storage applications. Yet, the *m*-benzene polymer **11** cycled efficiently during bulk electrolysis experiments and had faster k_{EX} than polymer **1**. There appears to be a practical limit on how large the k_{EX} parameter should be to have good electrochemical performance in these macromolecular systems. The level of electrochemical kinetics correlates well with the measured self-exchange of charges in the small dimeric systems that is consistent with predictions from the Marcus theory for electron transfer. However, there were challenges in applying the Marcus model to more complex polymeric systems, which has not previously been attempted. Lastly, we demonstrated that our optimized dimer and RAP systems have more stability for intermolecular interactions as demonstrated by temperature dependent spectroscopic studies.

The use of different linker decisively impacts the bulk electrolysis of polymer solutions but is less evident in the polymer films. This first comprehensive study highlights the careful balance between electronic interactions and linker rigidity required to design RAPs with superior reactivity.

References

1. Mai, T.; Hand, M. M.; Baldwin, S. F.; Wiser, R.H.; Brinkman, G.L.; Denholm, P.; Arent, D. J.; Porro, G.; Sandor, D.; Hostick, D. J.; Milligan, M.; DeMeo, E. A.; Bazilian, M.. *IEEE Trans. Sust. Energy*, **2014,** 5, 372−378.

2. Rugolo, J.; Aziz, M. J. *Energy Environ. Sci*., **2012,** 5, 7151−7160.

3. Darling, R.M.; Gallagher, K. G.; Kowalski, J.A.; Ha, S.; Brushett, F. R. *Energy Environ. Sci*., **2014,** 7, 3459−3477.

4. Darling, R.; Gallagher, K.; Xie, W.; Su, L.; Brushett, F. *J. Electrochem. Soc.,* **2016,** 163, A5029−A5040.

5. Frischmann, P. D.; Gerber, L.C.H.; Doris, S. E.; Tsai, E. Y.; Fan, F. Y.; Qu, X.; Jain, A.; Persson, K. A.; Chiang, Y.-M.; Helms, B. A. *Chem. Mater*., **2015,** 27, 6765−6770.

6. Janoschka, T.; Martin, N.; Martin, U.; Friebe, C.; Morgenstern, S.; Hiller, H.; Hager, M. D.; Schubert, U. S. *Nature*, **2015,** 527, 78−81.

7. Schmidt, D.; Haupler, B.; Friebe, C.; Hager, M. D.; Schubert, U.S. *Polymer*, **2015,** 68, 321−327.

8. Duan, W.; Vemuri, R. S.; Milshtein, J. D.; Laramie, S.; Dmello, R.D.; Huang, J.; Zhang, L.; Hu, D.; Vijayakumar, M.; Wang, W.; Liu, J.; Darling, R. M.; Thompson, L.; Smith, K.; Moore, J. S.; Brushett, F. R.; Wei, X. *J. Mater. Chem. A*, **2016**, 4, 5448−5456.

9. Nagarjuna, G.; Hui, J.; Cheng, K.; Lichtenstein, T.; Shen, M.; Moore, J. S.; Rodriguez-Lopez, J. *J. Am. Chem. Soc*., **2014**, 136, 16309−16316.

10. Flanagan, J.B.; Margel, S.; Bard, A.J.; Anson, F. C. *J. Am. Chem. Soc*., **1978**, 100, 4248−4253.

11. Dalton, E. F.; Murray, R. W. *J. Phys. Chem*., **1991**, 95, 6383−6389.

12. Ghimire, G.; Yi, Y.; Derylo, M. A.; Baker, L. A.; Ito, T. *Langmuir*, **2015**, 31, 12307−12314.

13. Mohammad, M.; Khan, A. Y.; Iqbal, M.; Iqbal, R.; Razzaq, M. *J. Am. Chem. Soc*., **1978**, 100, 7658−7660.

14. Itoh, M.; Kosower, E.M. *J. Am. Chem. Soc*., **1968**, 90, 1843−1849.

15. Hermolin, J.; Kosower, E.M. *J. Am. Chem. Soc*., **1981**, 103, 4813−4816.

16. Hermolin, J.; Talmor, D.; Kirowa-Eisner, E. *J. Electroanal. Chem*., **2000**, 491, 148−153.

17. Kosower, E. M.; Teuerstein, A. *J. Am. Chem. Soc*., **1976**, 98, 1586− 1587.

18. Furue, M.; Nozakura, S. I. *Chem. Lett*., **1980**, 9, 821−824.

19. Furue, M.; Nozakura, S. I. *Bull. Chem. Soc. Jpn*., **1982**, 55, 513−516.

20. Heinen, S.; Walder, L. *Angew. Chem., Int. Ed.*, **2000**, 39, 806−809.

21. Buck, A. T.; Paletta, J. T.; Khindurangala, S. A.; Beck, C. L.; Winter, A. H. *J. Am. Chem. Soc*., **2013**, 135, 10594−10597.

22. Imabayashi, S.-I.; Kitamura, N.; Tazuke, S.; Tokuda, K. *J. Electroanal. Chem. Interfacial Electrochem.*, **1988**, 243, 143−160.

23. Bard, A.J.; Faulkner, L.R. *Electrochemical Methods: Fundamentals and Applications*, 2nd ed.; Wiley: New York, **2000**.

24. Marcus, R.A. *Rev. Mod. Phys*., **1993**, 65, 599−610.

25. Marcus, R.A. *Annu. Rev. Phys. Chem.*, **1964**, 15, 155−196.

26. Hush, N. S. *J. Electroanal. Chem*., **1999**, 460, 5−29.

27. Reimers, J. R.; Hush, N. S. *Adv. Chem. Ser*., **1989**, 226, 27−63.

28. Tokue, H.; Oyaizu, K.; Sukegawa, T.; Nishide, H. *ACS Appl. Mater. Interfaces*, **2014**, 6, 4043−4049.

29. Grampp, G.; Mladenova, B. Y.; Kattnig, D. R.; Landgraf, S. *Appl. Magn. Reson*., **2006**, 30, 145−164.

30. Marcus, R.A. *J. Chem. Phys.*, **1956**, 24, 966−978.

31. Moni, L.; Banfi, L.; Basso, A.; Galatini, A.; Spallarossa, M.; Riva, R. *J. Org. Chem*., **2014**, 79, 339−351.

32. Burgess, M.; Hernańdez-Burgos, K.; Simpson, B.H.; Lichtenstein, T.; Avetian, S.; Nagarjuna, G.; Cheng, K. J.; Moore, J. S.; Rodríguez-Lopéz, J. *J. Electrochem. Soc*., **2016**, 163, H3006−H3013.

33. Hui, J.; Burgess, M.; Zhang, J.; Rodríguez-Lopéz, J. *ACS Nano*, **2016**, 10, 4248−4257.

34. Borgwart, K.; Heinze, J. *Scanning Electrochemical Microsocopy*; Marcel Dekker, **2001**.

35. Wang, Y.; Frasconi, M.; Liu, W.G.; Sun, J.; Wu, Y.; Nassar, M. S.; Botros, Y.Y.; Goddard, W. A.; Wasielewski, M. R.; Stoddart, J. F. *ACS Cent. Sci*., **2016**, 2, 89−98.

36. Shen, M.; Rodríguez-Lopéz, J.; Huang, J.; Liu, Q.; Zhu, X.-H.; Bard, A. J. . *J. Am. Chem. Soc*., **2010**, 132, 13453−13461.

37. Bard, A. J.; Mirkin, M. V.; Unwin, P.R.; Wipf, D. O. *J. Phys. Chem*., **1992**, 96, 1861−1868.

38. Zoski, C.G. *J. Electrochem. Soc*., **2016**, 163, H3088−H3100.

39. Kim, J.; Bard, A. J. *Anal. Chem*., **2016**, 88, 1742−1747.

40. Ritzert, N. L.; Rodriguez-Lopez, J.; Tan, C.; Abruna, H.D. *Langmuir*, **2013**, 29, 1683−1694.

41. Lefrou, C.; Cornut, R. *ChemPhysChem*, **2010**, 11, 547−556.

42. Sun, P.; Mirkin, M. V. *Anal. Chem*., **2006**, 78, 6526−6534.

43. Nelsen, S.F. *Chem. Euro. J*., **2000**, 6, 581−588.

44 Barnes, J. C.; Fahrenbach, A. C.; Dyar, S. M.; Frasconi, M.; Giesener, M. A.; Zhu, Z. X.; Liu, Z. C.; Hartlieb, K. J.; Carmieli, R.; Wasielewski, M.R.; Stoddart, J. F. *Proc. Natl. Acad. Sci. U. S. A*., **2012**, 109, 11546−11551.

45. Neta, P.; Richoux, M.C.; Harriman, A. *J. Chem. Soc., Faraday Trans*. 2, **1985**, 81, 1427−1443.

46. Sun, D.L.L.; Rosokha, S. V.; Lindeman, S. V.; Kochi, J. K. *J. Am. Chem. Soc*., **2003**, 125, 15950−15963.

47. Brunschwig, B. S.; Sutin, N. *Chem. Rev*., **1999**, 187, 233−254.

48. Norman, S. *Progress in Inorganic Chemistry: An Appreciation of Henry Taube*; Wiley, **2007**; Vol. 30, pp 441−498.

49. Sun, D.; Rosokha, S. V.; Kochi, J. K. *J. Am. Chem. Soc*., **2004**, 126, 1388−1401.

50. Lindeman, S. V.; Rosokha, S. V.; Sun, D.; Kochi, J. K. *J. Am. Chem. Soc*., **2002**, 124, 843−855.

51. Wang, Y.; Frasconi, M.; Liu, W.-G.; Sun, J.; Wu, Y.; Nassar, M.S.; Botros, Y. Y.; Goddard, W. A.; Wasielewski, M. R.; Stoddart, J. F. *ACS Cent. Sci*., **2016**, 2, 89−98.

52. Wang, Y.; Frasconi, M.; Liu, W.-G.; Liu, Z.; Sarjeant, A. A.; Nassar, M. S.; Botros, Y. Y.; Goddard, W. A.; Stoddart, J. F. *J. Am. Chem. Soc*., **2015**, 137, 876−885.

53. Gadgil, B.; Dmitrieva, E.; Damlin, P.; Aaritalo, T.; Kvarnstrom, C. *J. Solid State Electrochem*., **2015**, 19, 77−83.

54. Randles, J. E. B. *Trans. Faraday Soc*., **1948**, 44, 327−338.

55. Ševcík, A. *Czech. Chem. Commun*., **1948**, 13, 349−377.

56. Marcus, R. A. *Electrochim. Acta*, **1968**, 13, 995−1004.

57. Hupp, J. T.; Weaver, M. J. *J. Electroanal. Chem. Interfacial Electrochem*., **1983**, 152, 1−14.

58. Sun, P.; Mirkin, M. V. *J. Am. Chem. Soc*., **2008**, 130, 8241−8250.

59. Zhou, M.; Yu, Y.; Hu, K. K.; Mirkin, M. V. *J. Am. Chem. Soc*., **2015**, 137, 6517−6523.

60. Eyring, H.; Boyce, R. P.; Spikes, J. D. *Comparative Biochemistry*, **1960**, 15−73.

61. Johnson, F. H.; Eyring, H. *Ann. N. Y. Acad. Sci*., **1948**, 49, 376−396.

62. Schmidt, D.; Haupler, B.; Hager, M.D.; Schubert, U. S. *J. Polym. Sci., Part A: Polym. Chem*., **2016**, 54, 1998−2003.

63. Muench, S.; Wild, A.; Friebe, C.; Haüpler, B.; Janoschka, T.; Schubert, U. S. *Chem. Rev*., **2016**, 116, 9438−9484.

Chapter 4: Impact of Electrolyte Composition on the Reactivity of a Redox Active Polymer Studied Through Surface Interrogation and Ion-Sensitive Scanning Electrochemical Microscopy

Notes and Acknowledgements

This chapter appeared in its entirety in the journal *The Analyst* with authors Burgess, M.; Hernández-Burgos, K.; Cheng, K..; Moore, J. S.; Rodríguez-López, J. "Impact of Electrolyte Composition on the Reactivity of a Redox Active Polymer Studied Through Surface Interrogation and Ion-Sensitive Scanning Electrochemical Microscopy". **2016**, 141, 3842-3850. This article is reprinted with the permission of the publisher and is available with the accompanying Supporting Information file from http://www.pubs.rsc.org and using DOI: 10.1039/C6AN00203J. M.B. performed all of the SECM analysis, helped in voltammetry experiments, helped write the manuscript, helped with data analysis, and made figures. This work was supported as part of the Joint Center for Energy Storage Research, an Energy Innovation Hub funded by the U.S. Department of Energy, Office of Science, Basic Energy Sciences. M. B. acknowledges support by the National Science Foundation Graduate Research Fellowship Program under grant No. DGE-1144245.

Abstract

Elucidating the impact of interactions between the electrolyte and electroactive species in redox active polymers is key to designing better-performing electrodes for electrochemical energy storage and conversion. Here, we present on the improvement of the electrochemical activity of poly(para-nitrostyrene) (PNS) in solution and as a film by exploiting the ionic interactions between reduced PNS and K^+, which showed increased reactivity when compared to tetrabutylammonium (TBA^+)- and Li^+-containing electrolytes. While cyclic voltammetry enabled the study of the effects of cations on the electrochemical reversibility and the reduction potential of PNS, scanning

electrochemical microscopy (SECM) provided new tools to probe the ionic and redox reactivity of this system. Using an ion-sensitive Hg SECM tip allowed to probe the ingress of ions into PNS redox active films, while surface interrogation SECM (SI-SECM) measured the specific kinetics of PNS and a solution phase mediator in the presence of the tested electrolytes. SI-SECM measurements illustrated that the interrogation kinetics of PNS in the presence of K^+ compared to TBA^+ and Li^+ are greatly enhanced under the same surface concentration of adsorbed radical anion, exhibiting up to a 40-fold change in redox kinetics. We foresee using this new application of SECM methods for elucidating optimal interactions that enhance polymer reactivity for applications in redox flow batteries.

Introduction

As the implementation of renewable energy production schemas such as wind and solar technologies become more pervasive in their use, low cost and effective means for grid level energy storage are needed to compliment these intermittent sources to provide power in times of night or little sunshine. Our group is interested in studying the electrochemical mechanisms and implementation of redox active polymers (RAPs) for use in size selective non-aqueous redox flow batteries.[1,2] It has been identified that in order for non-aqueous redox flow batteries to be an economically attractive technology for grid level energy storage, the charge storage media must have low equivalent weights and function well in the presence of lightweight supporting electrolytes such as $LiBF_4$, as the cost of these systems scales with mass.[3] However, many organic based anolytes have been found to be irreversible in the presence of Li^+ because of strong coupling between reduced products and the alkali metal ions.[4] Electrochemical compatibility of supporting electrolytes with redox couples has been studied since at least 1963, when quinones were found to be irreversible in the presence of alkali metals, especially with Li^+.[5]

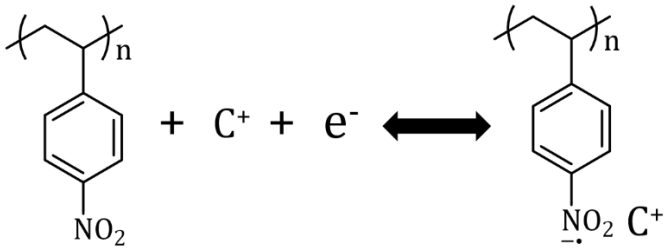

Figure 4.1. Chemical structure of the synthesized PNS. When PNS is reduced, the repeating nitro based pendants can be reduced to form a radical anion. This radical anion necessitates that a supporting electrolyte cation, C^+, migrate to each pendant and compensate for the charge.

In this work, we explore the reactivity of a nitrostyrene based RAP that we envision could be used as an anolyte. When the monomeric units of poly(para-nitrostyrene) (PNS) are reduced, the nitro groups become charged with a radical anion. The synthesized structure and redox products of this species are shown in Figure 4.1. While PNS has been studied electrochemically since at least the 1970s,[6,7] not much work has gone into testing these systems thoroughly in various electrolytes. We explored the reactivity of PNS in the presence of tetrabutylammonium (TBA^+), lithium (Li^+), and potassium (K^+) electrolytes to see the effects on electrochemical reversibility and the reduction potential. It is known that carbonyl based organic molecules in the presence of metal based electrolytes can have strong ionic interactions and shift the reduction potentials more positive.[8,9] Here, consistent with previous reports, we observe that PNS electrochemistry is reversible in the presence of TBA^+, and completely irreversible in the presence of Li^+ due to strong ionic coordination. However, surprising results were found with a K^+-containing electrolyte in which there was an improvement in the overall level of current for both the oxidation and reduction of PNS by almost an order of magnitude.

Understanding the impact of ion intake into a polymer film on its reactivity requires new tools. Here, we explored the altered reactivity of PNS in these electrolytes using scanning

electrochemical microscopy (SECM). Using ion-sensitive Hg-probe based measurements, we observed the differential intake of alkali metals K^+ and Li^+ into a modified microelectrode with a redox active film of PNS. Hg capped SECM tips have previously been employed for the selective and spatially resolved detection of metals in other studies.[10–12] Here, SECM studies with Hg capped microelectrodes reveal that PNS films specifically pull in K^+ and Li^+ ions as a function of applied potential. Lastly, the surface interrogation mode of SECM (SI-SECM) was employed to measure specific kinetic effects for the reactivity of PNS in the presence of the tested electrolytes. SI-SECM has been previously used to quantify adsorbed reactive species on microelectrodes and extended semiconducting surfaces via micro- and nano-redox titrations.[13–15] Here, the first SI-SECM measurements of an adsorbed redox active polymer film are performed via redox titrations of the radical anions formed in the PNS film upon reduction. SI-SECM measurements illustrate that the interrogation kinetics of PNS in the presence of K^+ compared to TBA^+ and Li^+ were greatly enhanced under the same surface concentration of adsorbed radical anion. Thus, this work introduces the novel use of SECM-based methods for elucidating the interaction of ions with polymer films with the intention of understanding reaction mechanisms that potentially enhance the performance of these materials for applications in energy storage.

Experimental

Chemicals

All reagents were used as received from commercial sources without any further purification or modification unless otherwise stated. Poly(para-nitrostyrene) (PNS) with a molecular weight, M_n, of 270 kDa was synthesized following a procedure previously reported.[16] A flask was charged with 4-nitrotoluene (100 mL) and polystyrene (5.0 g). Then nitric acid (80 mL) was added to the flask and stirred vigorously while cooled to 0 °C in an ice bath. Sulfuric acid

(20 mL) was added slowly to the flask under vigorous stirring. The mixture was allowed to return to room temperature and stirred for 16 hours. The resultant emulsion product was precipitated into isopropanol and then re-dissolved into dimethylformamide. The precipitation was repeated three times and placed under high vacuum for 24 hours. Functionalization of the polystyrene with 4-nitrotoluene was found to be 78% by UV-Vis spectroscopy. Full characterization of the synthesized PNS is shown in Appendix C.

Electrolytes used in the electrochemical studies of PNS were tetrabutylammonium hexafluorphosphate ($TBAPF_6$) (electrochemical grade ≥99%), potassium tetrafluoroborate (KBF_4) (96%), and lithium hexafluorphosphate ($LiPF_6$) (battery grade ≥99.99%) all received from Sigma. N,N,N′,N′-Tetramethyl-p-phenylenediamine (TMPD) ≥97% from Sigma was used as the redox mediator for SECM studies.

Electrodes

25 μm diameter platinum (99.9%) wires from Goodfellow (Devon, PA) were used to prepare all SECM tips. The platinum wire was sealed in a glass capillary (World Precision Instruments, Sarasota, FL) by using a previously reported methodology.[17] Tip sharpening was done using silicon carbide paper and polishing used 1 μm and 0.3 μm alumina slurries on a polishing cloth. After polishing, the tip was rinsed with water then sonicated in acetone for five minutes. SECM tips were fabricated to have an R_g of 2 or less, which has been identified as a prerequisite to properly co-align two ultramicroelectrodes.[15] The R_g is the ratio of total electrode radius including the glass divided by the metal electrode radius. A 1.15 mm radius platinum disk (CH Instruments, Austin TX) was used as a macrodisk electrode for voltammetric characterization of PNS in solution and as a film. The Pt macrodisk was polished in the same manner as the SECM

tips. A platinum wire (Goodfellow, Devon PA 99.9%) was used as the counter electrode. All potentials reported are with respect to 0.1 M Ag/Ag^+ unless otherwise stated.

Mercury capped microelectrodes were fabricated by electrodeposition of Hg from a solution of 10 mM $Hg(NO_3)_2$ in water with a tetramethylammonium nitrate electrolyte, and 0.1% by volume nitric acid.[10] The SECM tip was poised at a potential to reduce mercury onto the tip (−0.4 V vs. W QRE) for 400 seconds to deposit a charge of approximately 50 μC (Appendix C Figure C.6). When accounting for the size of the tip electrode, the mercury capped electrode has an *h* value of 1, where *h* is the ratio of the height of the mercury droplet divided by the radius of the electrode. An *h* value of 1 makes fitting SECM approach curves with a mercury capped electrode consistent with a fitting protocol previously reported.[18]

Scanning Electrochemical Microscopy and Stationary Voltammetry

All solutions were prepared and tested in an argon atmosphere glovebox (MBraun Stratham, NH) with rigorous control of the levels of oxygen and water to be less than 0.1 ppm at all times. The DMF solvent was anhydrous and of 99.8% purity (Sigma). Control of all the electrochemical cells and the positioning of the SECM tip electrodes when necessary was done using a CHI920D SECM platform (CH Instruments, Austin, TX). A custom Teflon SECM cell was used which would hold a microelectrode as the substrate. A four-electrode configuration was used for all SECM measurements in which both working electrodes were SECM tips. The tips were aligned using probe scan curves in the *x* and *y* directions using either the feedback or collection modes of SECM.[17] In either of these modes, one of the SECM tips is performing the first oxidation of TMPD and the other is reducing any local amount of oxidized TMPD. Once the probes were aligned in both the *x* and *y* directions, the probes were approached to one another. Approach curves were plotted by recording the tip current, i_{tip}, as a function of the inter-electrode

distance, *d*. Distance was obtained by fitting the approach curves to theoretical curves based on equations developed by Lefrou and Cornut,[19] or Denuault *et al*. for mercury capped electrodes.[18]

Results and Discussion

Electrochemical Characterization of PNS

Initial electrochemical characterization of the synthesized PNS product was performed in the presence of a non-interacting electrolyte (TBA^+) via cyclic voltammetry with a Pt macrodisk electrode; these studies are shown in Figure 4.2. The results from this voltammetry indicate that the polymer is functionalized with redox accessible nitro groups with a reduction potential of −1.6 V, which agrees well with previous literature studying other nitrostyrene redox active polymers.[7] PNS redox chemistry operates without any major kinetic complications as evidenced by a peak separation in the macrodisk voltammetry of ∼150 mV and the near unity of the peak cathodic current divided by the peak anodic current. The Randles–Sevcik analysis in Figure 4.2B suggests a diffusion limited process[20] as the peak current is increasing linearly as a function of the square root of the scan rate. Additionally, the nearly identical magnitude for the slopes, ∼9 μA $((V\ s^{-1})^{1/2})^{-1}$, in the Randles–Sevcik analysis for both the cathodic and anodic branches indicates the reversibility of the redox couple.

Seeing that the PNS RAP exhibited chemically reversible behavior in TBA^+ electrolyte, we then explored the reactivity of this system in other electrolytes to test their compatibility with the radical anion that is generated upon reduction of PNS (Figure 4.1). In these studies, 5 mM of PNS was dissolved in 0.1 M TBA^+ electrolyte and the reduction potential and current were measured by cyclic voltammetry. Then, solutions of either K^+ or Li^+ containing electrolyte were spiked into the cell, which also contained PNS so as to maintain a constant concentration of PNS

in the cell. The voltammograms under all of these electrolyte conditions are plotted in Figure 4.3. When K^+ containing electrolyte was added (17 mM in the PNS solution), the reduction potential shifted approximately 100 mV more positive, indicating a more favorable reduction process.[20] The phenomenon of reduction potential shifts has been observed before in other electrochemical systems that contain nitro or quinone groups that have ionic interactions with their reduced products.[8,9,21–23] Beyond the reduction potential shift of PNS in the presence of K^+ containing electrolyte, some interesting features about the reactivity were observed. First, the facile kinetics for the reduction of PNS appear to be conserved in the presence of K^+, as seen from the similar peak separation potentials compared to TBA^+. Additionally, the magnitudes of the cathodic and anodic peaks were still nearly identical. However, the use of K^+ increased the measured currents by about 75%. This increased current suggests a larger fraction of PNS electrochemically accessed per unit of time.

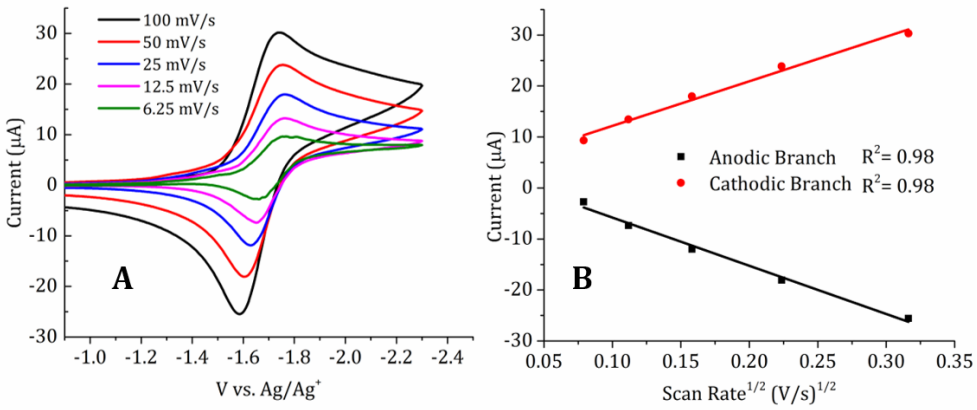

Figure 4.2. (A) Cyclic voltammetry with 33 mM (repeat unit) of PNS in 0.1 M $TBAPF_6$ at various scan rates using a 1.15 mm radius Pt disk (0.04 cm^2) working electrode. (B) Randles–Sevcik analysis.

The reduced PNS interaction with K^+ is also seen on PNS filmed electrode as shown in Figure 4.3B, where adsorption of a thin electroactive film of 36.7 µC/cm^2 (average thickness <1 nm as described in Appendix C)[27] allowed measurement of ion interactions in the absence of mass

transfer complications. Under surface confined voltammetry conditions, the interaction with the alkali metal electrolyte is even more significant, shifting the reduction potential more positive than the solution phase voltammetry, but the enhanced reactivity is still present. We hypothesize that the increased reactivity of PNS with K^+ is due to the enhanced movement of this ion throughout the polymer film to coordinate with the reduced nitro groups more efficiently than the bulky TBA^+ cations. A quick estimation of the free-energy of the K^+/reduced PNS system using Gibb's equation and its comparison to TBA^+ showed a formation energy of 9.6 kJ mol^{-1} for the K^+ system. When the polymer is being reduced, electroneutrality requirements necessitate that the supporting electrolyte cations migrate throughout the polymer network at the same rate as the injection of charges from the electrode. If the cations cannot move throughout the polymer efficiently, their migration will be rate limiting in the current process and fewer redox pendants in the PNS can be reduced per unit of time.

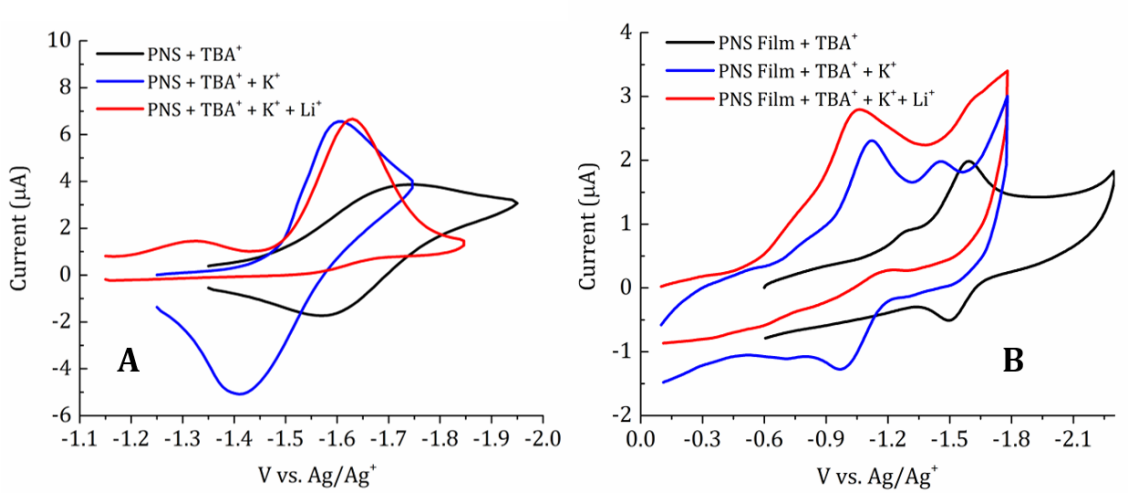

Figure 4.3. (A) Cyclic voltammetry experiments performed with 5 mM PNS in solution scanned at 20 mV/s. All experiments contained 0.1 M $TBAPF_6$ electrolyte, and spikes of K^+ or Li^+ containing electrolyte were added to make a final concentration of 17 mM. (B) PNS film voltammetry at 100 mV/s. The PNS film was generated by cycling a 1.15 radius mm Pt disk electrode in a solution of 33 mM PNS for 30 cycles between −1 V and −2 V at 50 mV/s. The electrode was then rinsed and placed in a neat solution of 0.1 M $TBAPF_6$ before measuring any additional voltammetry. 17 mM of K^+ and 17 mM Li^+ electrolyte were added when appropriate.

When PNS was put in the presence of Li^+ containing electrolyte, a positive potential shift was also observed but the chemical reversibility of the system suffered. An ill-defined anodic process was observed and prevents us from estimating the formation energy of the Li^+/reduced PNS system with confidence. As shown in Appendix C Figure C.4, continuous cycling on the potential range where the cathodic PNS wave was observed led to a diminishing current, which was only recovered upon excursion to a potential of 2 V more positive than that for TBA^+. We suspect that the Li^+-radical anion coordination from the PNS is too strong to be easily reversed and thus no anodic wave is seen in the potential window in Figure 4.3. These interesting observations about altered PNS reactivity in the presence of alkali electrolytes prompted us to explore this phenomenon further by use of another electroanalytical technique, scanning electrochemical microcopy.

SECM Characterization of Alkali Metal Adsorption into PNS Films

In order to probe the alkali electrolyte interactions with PNS further, SECM experiments were carried out to measure the intake of metal ions into a polymer film. To make a typical Pt based SECM tip ionically sensitive, Hg was deposited on the Pt probe. The electrodeposition of Hg onto the UME is shown in the Appendix C Figure C.6. Incorporating stripping voltammetry into SECM experiments has been described in recent years and enables SECM to now probe ionics.[10–12,24,25] Here, stripping voltammetry at a mercury capped SECM tip was utilized for the (simultaneous) detection of K^+ and Li^+ in DMF above a PNS-filmed UME of the same size nominal size as the working tip electrode. Experimental setups have been borrowed from surface interrogation-SECM (SI-SECM) measurements which typically utilize two co-aligned UMEs to probe the amount of adsorbed intermediates on electrode surfaces.[13,15,26] To the best of our

knowledge, this work would be the first time SECM and stripping voltammetry have ever been used to measure the intake of alkali metals into a redox active polymer film.

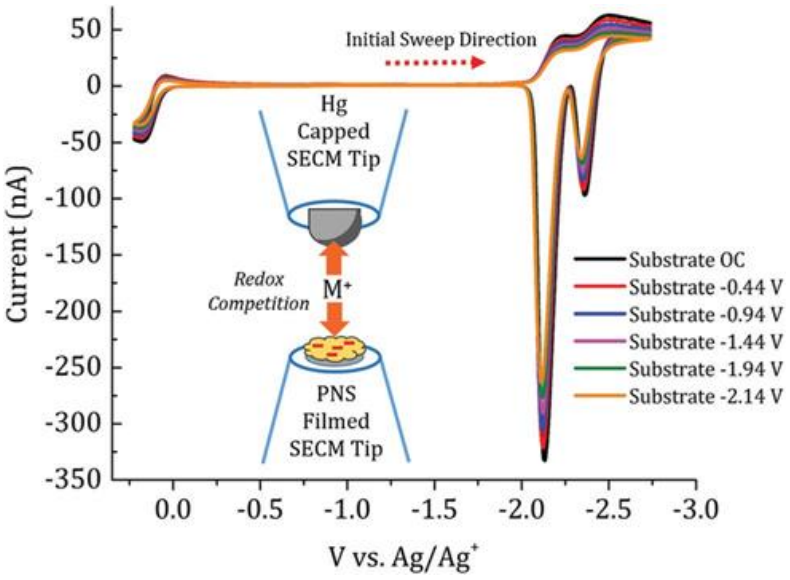

Figure 4.4. Cyclic voltammograms measured at the Hg capped tip UME with an initial sweep direction towards negative potentials at 0.5 V/s in the presence of 10 mM TMPD, 17 mM KBF_4, 17 mM $LiPF_6$, and 0.1 M $TBAPF_6$. Subsequent voltammograms were collected at increasingly negative potentials on the substrate. Inset shows a schematic representation of how the two UME electrodes were oriented in space and depicts how each electrode are operating. The Hg capped SECM tip is performing stripping voltammetry with metal ions, M^+, while the substrate UME is reducing PNS to form radical anions denoted as red "–" symbols.

The Pt UME used as the substrate electrode for these experiments was filmed with PNS by poising the electrode at −2 V for 500 seconds in a 33 mM PNS solution with a total charge passed of ~3.5 μC (Appendix C Figure C.9). Afterwards, the electrode was rinsed and put into a TBA^+ electrolyte solution in DMF, and then a CV was measured to see how much of the PNS film remained on the electrode. The filmed UME CV for the reduction of PNS was integrated to find how many nitro groups were on the electrode surface (Appendix C Figure C.10). This calculation yielded 2.85×10^{11} nitro groups on the substrate UME surface. Using the integrated charge from the film voltammogram and a method reported by Bard *et al*. to calculate polymer film thickness,[27]

assuming a polymer density of 1.05 g/cm^3 (the density of the precursor polystyrene before functionalization with 4-nitrotoluene) we find the polymer film was approximately 130 nm thick.

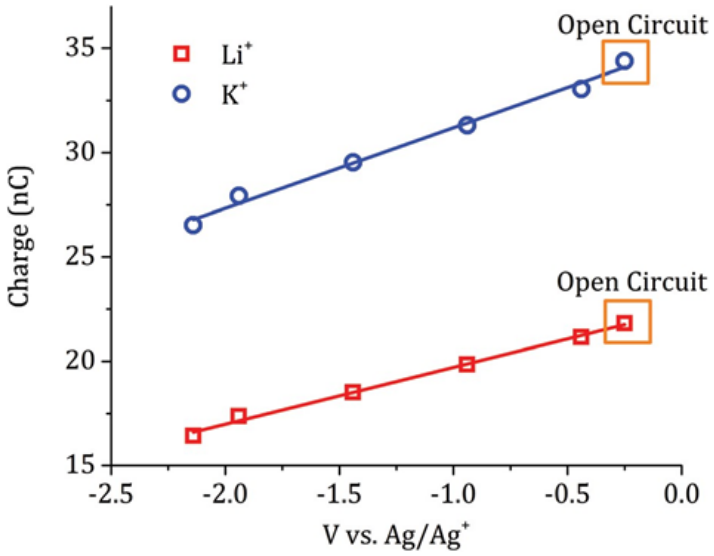

Figure 4.5. Integrated stripping charges for both K^+ and Li^+ as a function of potential applied to the substrate UME. Open circuit substrate measurements are denoted by an orange square at a false potential location in order to show trend between points.

After verification of the PNS film on the UME in the presence of TBA^+ electrolyte, alkali based salts were added in 17 mM concentration. TMPD was also added to the solution as an oxidative redox mediator for the purpose of aligning the UMEs through the feedback mode. Once the tips were aligned in both the *x* and *y* dimensions (Appendix C Figure C.7), the mercury capped SECM tip was approached to the substrate UME. The approach curve manifests as negative feedback which is expected under the studied conditions as the substrate is at open circuit and the Pt UME is not large enough to facilitate open circuit positive feedback.[17] The presence of the relatively thick polymer film in Li^+ containing electrolyte made approaching the Hg capped tip UME to the substrate UME complicated using positive feedback, but negative feedback sufficed in placing the Hg capped UME accurately over the substrate. Fitting of the approach curve

consistent with mercury capped approach curve theory[18] finds that the tips were separated by a distance of approximately 5 microns when accounting for the size of mercury drop to have a height equivalent to the radius of the electrode, 12.5 microns (Appendix C Figure C.8). Verification of probe alignment when at the approached position is seen from collection voltammograms shown in Appendix C Figure C.7.

The voltammograms of the mercury capped SECM tip at the approached position are shown in Figure 4.4, in which both the first oxidation of TMPD (0.1 V) and the formation of amalgams for potassium (−2.13 V) and lithium (−2.37 V) and their subsequent stripping at the same potentials can readily be identified. The system appears to be clean without any apparent oxygen or water contamination in the cell as evident from the distinct lack of any other redox events observed in the voltammetry. To the best of our knowledge, this work would be the first to demonstrate stripping voltammetry at a micro-dimensioned mercury drop electrode in the presence of a redox mediator. These voltammograms demonstrate the utility of such an SECM probe as we were able to probe both redox active and ionic species with a single easily fabricated probe.

The voltammetry shown in Figure 4.4 demonstrates that both the TMPD feedback and stripping signals are decreasing with increasingly negative potentials held at the substrate relative to the open circuit condition. The integrated K^+ and Li^+ stripping charges decrease linearly with increasing substrate potential on the surface as shown in Figure 4.5. The decrease in the measured stripping charges is indicative of a decrease in the local concentration of K^+ and Li^+ in solution between the two UMEs, as the stripping signal is proportional to local concentration of those ions.[10] The detected decrease in the local alkali metal concentration at the tip electrode could not be accounted for from loss of Hg at the tip UME. Voltammetry was performed before SECM experiments and afterwards when the tips were retracted from one another, and it showed that the

Hg drop did not change in size as the measured current for both the TMPD signal and stripping signals was nearly identical (Appendix C Figure C.11). We observed a linear change in concentration of K^+ and Li^+ as a function of substrate potential. Although we expected sharp changes in the local ion current indicative of the discrete reduction of PNS units, it must be noted that this reduction process actually takes place over a broad potential region (Figure 4.3B), likely leading to the linear trend within the potential resolution used in our measurements. The difference in stripping charge between open circuit and −2.14 V substrate conditions for K^+ and Li^+ were 7.87 nC and 5.38 nC, respectively. This charge differential indicates that the PNS film is taking in more K^+ than Li^+. One possibility for this observation relies on the mobility effects for these species, as the ionic mobility of K^+ is known to be nearly double that of Li^+.[28] Regarding the decrease in the feedback signal from TMPD, it is possible that film swelling could trap some local TMPD molecules within it. The adsorption of TMPD into other redox active films has been previously reported,[29,30] and the trapping of TMPD molecules in the PNS film could lead to a decreased oxidation signal at the tip.

Surface Interrogation SECM of PNS Films

Given that we had seen evidence through voltammetry that PNS has altered reactivity in the presence of alkali metals, we explored this system further utilizing the surface interrogation mode of SECM (SI-SECM). The surface interrogation mode of SECM was developed in 2008 and provided a new *in-situ* means of quantifying the reactivity and amount of reactive adsorbed species on an electrode surface through micro-redox titrations.[31–33] These measurements utilize two co-aligned UMEs, one which generates some adsorbed analyte, and the other which generates a titrant to consume that surface confined reactive species. Here, this method is utilized for the first time to perform measurements on an adsorbed redox active polymer.

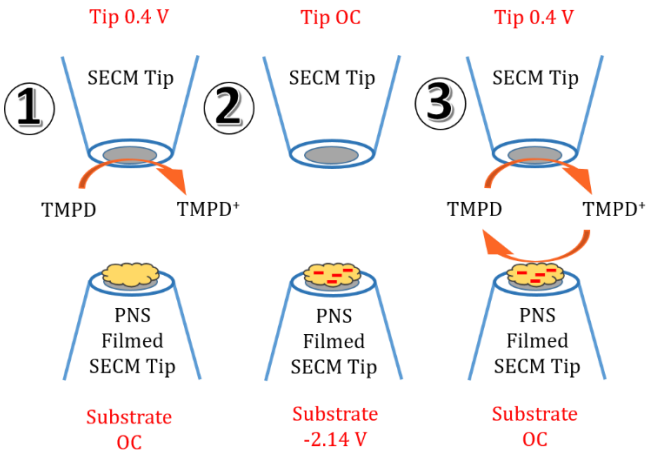

Figure 4.6. A generalized schematic showing the orientation of the two UMEs used in the SI-SECM studies and how the micro-titration studies are performed. The first step involves cleaning the substrate of any reactive adsorbed species by generating $TMPD^+$ at the tip UME while the substrate UME is at open circuit. In the next step the substrate UME is poised at −2 V for 60 seconds to reduce adsorbed PNS and form radical anion groups shown as red "–" symbols, while the tip UME is at open circuit. Immediately afterwards, the substrate UME goes back to open circuit and the tip UME is pulsed to 0.4 V for 100 seconds and a transient signal for the oxidation of TMPD is measured.

Our SI-SECM measurements were carried out using a substrate UME filmed with PNS. The PNS film in these studies was created from a solution of 50 μM of PNS in TBA+ electrolyte by cycling the electrode 20 times between −0.9 V and −2.3 V. As will be shown below through SI-SECM measurements, this procedure led to a lower surface coverage of PNS film, 1700 $\mu C/cm^2$ (average thickness of 24 nm as described in Appendix C)[27] that did not present any detectable issues with trapping TMPD inside of it, as positive feedback with TMPD was achievable under any of the negative substrate potentials used in this study. How SI-SECM experiments were implemented in this work is illustrated schematically in Figure 4.6. Briefly, two UMEs were co-aligned through the use of probe scan curves using the collection mode of SECM[34,35] (Appendix C Figure C.12 and C.13). Once aligned, the tips were approached together using the feedback mode to be separated by a distance of less than 6 μm, found from fitting the approach curves to theory developed by Cornut and Lefrou,[19] which is shown in Appendix C Figure C.14–C.17. At

the approached position, the tip UME was set to generate $TMPD^+$ at the mass transfer limited rate for 100 seconds while the substrate UME remained at open circuit. Under these conditions, negative feedback was observed as the substrate UME was not able to recycle the redox mediator. This step was done to ensure that the substrate was depleted of any reactive adsorbed species. Next, the substrate UME was poised at −2.0 V for 60 seconds to generate a reactive adsorbed species, in the case of this study the radical anion formed from the reduction of the PNS film adsorbed on the substrate UME surface. During this process, the tip UME remained at open circuit. Immediately afterwards, with no delay time, the substrate UME was placed at open circuit and the tip UME was stepped to 0.4 V for 100 seconds to begin generating $TMPD^+$. $TMPD^+$ can then react with any available radical anions on the PNS units and be reduced back to neutral TMPD. The resulting positive feedback proceeded until the reactive adsorbed species were consumed, after which negative feedback at the tip UME was observed. After each experiment, the tip UME was retracted and the solution removed from the SECM cell. The entire cell was rinsed with 0.1 M $TBAPF_6$ in DMF six times to ensure that nothing would carry over between experiments. Afterwards, the cell was filled up again with a solution of 1 mM TMPD dissolved in 0.1 M TBA^+ that also contained K^+ or Li^+ containing electrolytes when appropriate. The tips were then realigned and approached together. The results of these measurements are shown in Figure 4.7.

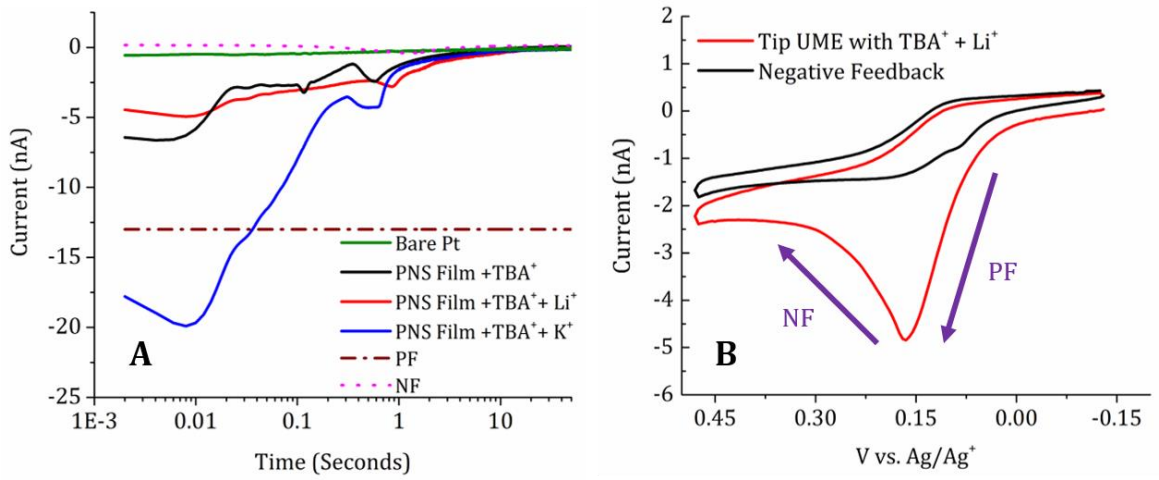

Figure 4.7. (A) SI-SECM measurements. Tip UME poised at 0.4 V in the presence of 1 mM TMPD, following a 60 second pulse at −2 V at the substrate UME with a PNS film or with a bare Pt UME substrate. All experiments were performed in 0.1 M $TBAPF_6$ and 17 mM KBF_4 or 17 mM $LiPF_6$ when appropriate. PF and NF designate the maximum positive feedback and negative feedback measured in an experimental setup with a bare Pt substrate UME separated from the tip UME by approximately 5 µm. (B) Titrating the adsorbed reactive species on a PNS filmed substrate UME after a 60 second potential step at −2 V via the production of $TMPD^+$ from the tip UME in cyclic voltammetry scanned at 0.1 V/s. Experiments were done in 1 mM TMPD with 0.1 M $TBAPF_6$ and 17 mM $LiPF_6$ as electrolyte.

As can be seen from Figure 4.7A, the SI-SECM transients were able to detect the titration of the radical anion produced from the reduction of the PNS film. This positive feedback signal was not observed when a bare Pt UME substrate was used. SI-SECM measurements unambiguously showed that the level of transient positive feedback was greatly influenced by the selection of electrolyte in the cell. The trends in the magnitude of the early positive feedback from the interrogation transients qualitatively agree with the trends in reactivity seen in stationary voltammetry with PNS. We observed that the K^+ based electrolyte had much more positive feedback signal compared to the experiments that contained TBA^+ or Li^+ salts. This increased positive feedback in the presence of K^+ would indicate that there is a larger bimolecular rate constant,[14,36] k_{SI} (m^3/ mol·s), for the reaction of $TMPD^+$ with adsorbed reduced PNS groups in the presence of K^+ than with TBA^+ or Li^+. The complex SI-SECM transients shown in Figure 4.7A make simulation analysis challenging. A preliminary analysis based on the initial rates of reaction,

obtained in the early SI-SECM transients, allowed us to compare the feedback signal to an equivalent heterogeneous rate of electron transfer at the substrate using conventional SECM feedback expressions. Provided all experiments were performed under similar conditions (e.g. tip separation, ion concentration, film thickness), this analysis indicated that the substrate kinetics for the K^+ containing electrolyte were mass-transfer limited, while TBA^+ and Li^+ exhibited substrate kinetics, 0.01 cm/s and 0.006 cm/s respectively, at least 40-fold lower than K^+. Since the reduction potential of PNS in the presence of the different electrolytes follows the order $Li^+ > K^+ > TBA^+$ it would be expected that the reactivity with respect to TMPD also followed this order, as dictated by an increasing overpotential when going from Li^+ to TBA^+. Clearly, the K^+ system stands out as an outlier.

Finally, integration of the SI-SECM transients showed that the amount of adsorbed radical anion from the PNS groups between experiments was very similar. The calculated surface coverage was found to be 17 ± 5 nmol/cm^2 as an average for all three experiments. This is a reassuring result as it would indicate the stability of the PNS film on the electrode surface was maintained between experiments. To verify the SI-SECM transients were indicative of an actual titration on the surface, another methodology of SI-SECM was employed which is shown in Figure 4.7B. Here, the PNS filmed substrate UME was still pulsed for 60 seconds at −2 V while the tip UME remained at open circuit. Afterwards, the substrate UME was placed at open circuit and the tip UME initiated a cyclic voltammogram in which the oxidation of TMPD was activated. As can be seen in the voltammogram, the generation of $TMPD^+$ by voltammetry at the tip UME is able to titrate the surface and be sensed as positive feedback until about 0.15 V producing a current of nearly 5 nA, which agrees well with the level of positive feedback measured in the transient in the presence of Li+. More positive than 0.15 V, the voltammogram immediately starts to decay into

negative feedback (~2 nA) because the reduced PNS on the surface has been titrated and TMPD can no longer be recycled. The time for this titration to occur can be estimated by knowing that $TMPD^+$ is being generated at the tip UME between 0 and 0.15 V for 3 seconds, after accounting for the scan rate of 0.1 V/s. This amount of time agrees well with the SI-SECM transients in which we see the titration using a potential step at the tip UME takes a little more than a second. The voltammetry method of titration is slightly slower because most of the voltammogram is in the kinetically dominated region for the oxidation of TMPD, whereas the potential step method at the tip UME with a potential of 0.4 V is operating under mass transfer conditions.[20]

Conclusions

This work demonstrates the use of scanning electrochemical microscopy combined with conventional voltammetric methods for understanding the interaction of electrolyte ions with redox active polymer films. A redox active polymer, PNS, displayed an increased reactivity in the presence of K^+ containing electrolytes in contrast to Li^+ or TBA^+ containing ones. The choice of electrolytes with the PNS redox system is shown to be a critical factor in its redox kinetics and chemical reversibility. We explored the interaction of alkali metals and reduced PNS further by use of novel analytical methods that have not previously been applied to study redox active polymers, via SECM with Hg capped microelectrodes, and the surface interrogation mode of SECM. The results of the employed SECM studies are in strong agreement with the trends observed through voltammetry of the PNS system, but enable powerful capabilities for obtaining information regarding the preferential intake of ions into reacting PNS films and regarding its reactivity towards solution phase redox mediators. Enhanced SI-SECM kinetics are indicative of improved electrochemical kinetics. Our group will continue to study the interaction of different electrolytes with soluble polymers and polymer films for applications in energy storage and

catalysis. Furthermore, the combination of ion- and redox-sensitive SECM studies demonstrated in this work set a precedent for the study of a wide variety of polymer film properties such as their structural/functional heterogeneity, charge trapping and charge transport amongst others.

References

1. Burgess, M.; Hernández-Burgos, K.; Simpson, B. H.; Lichtenstein, T.; Avetian, S.; Nagarjuna, G.; Cheng, K. J.; Moore, J. S.; Rodríguez-López, *J. Electrochem. Soc*., **2016,** *163*, H3006-H3013.
2. Nagarjuna, G.; Hui, J.; Cheng, K.; Lichtenstein, T.; Shen, M.; Moore, J. S.; Rodriguez-Lopez, J., *J. Am. Chem. Soc*., **2014,** *136*, 16309-16316.
3. Sevov, C. S.; Brooner, R. E. M.; Chénard, E.; Assary, R. S.; Moore, J. S.; Rodríguez-López, J.; Sanford, M. S., *J. Am. Chem. Soc*., **2015,** *137*, 14465-14472.
4. Wei, X. L.; Xu, W.; Huang, J. H.; Zhang, L.; Walter, E.; Lawrence, C.; Vijayakumar, M.; Henderson, W. A.; Liu, T. B.; Cosimbescu, L.; Li, B.; Sprenkle, V.; Wang, W., *Angew. Chem., Int. Ed.,* **2015,** *54*, 8684-8687.
5. Peover, M. E.; Davies, J. D., *J. Electroanal Chem*., **1963,** *6*, 46-53.
6. Kerr, J. B.; Miller, L. L.; Vandemark, M. R., *J. Am. Chem. Soc.,* **1980,** 102, 3383-3390.
7. Vandemark, M. R.; Miller, L. L, *J. Am. Chem. Soc*., **1978,** *100*, 3223-3225.
8. DeBlase, C. R.; Hernandez-Burgos, K.; Rotter, J. M.; Fortman, D. J.; Abreu, D. D.; Timm, R. A.; Diogenes, I. C. N.; Kubota, L. T.; Abruna, H. D.; Dichtel, W. R., *Angew. Chem., Int. Ed*., **2015,** *54*, 13225-13229.
9. Hernandez-Burgos, K.; Rodriguez-Calero, G. G.; Zhou, W. D.; Burkhardt, S. E.; Abruna, H. D., *J. Am. Chem. Soc*., **2013,** *135*, 14532-14535.
10. Barton, Z. J.; Rodriguez-Lopez, J., *Anal. Chem*., **2014,** *86*, 10660-10667.
11. Alpuche-Aviles, M. A.; Baur, J. E.; Wipf, D. O., *Anal. Chem*., **2008,** *80*, 3612-3621.
12. Diaz-Ballote, L.; Alpuche-Aviles, M.; Wipf, D. O., *J. Electroanal. Chem*., **2007,** *604*, 17-25.
13. Ahn, H. S.; Bard, A. J., *J. Am. Chem. Soc*., **2015,** *137*, 612-615.
14. Simpson, B. H.; Rodriguez-Lopez, J., *J. Am. Chem. Soc*., **2015,** *137*, 14865-14868.
15. Rodriguez-Lopez, J., *Electroanalytical Chemistry: a Series of Advances*, **2012,** *24*, 287-351.
16. Philippides, A.; Budd, P. M.; Price, C.; Cuncliffe, A. V., *Polymer*, **1993,** *34*, 3509-3513.
17. Borgwart, K.; Heinze, J., *Scanning Electrochemical Microscopy*, Marcel Dekker, 2001.

18. Lindsey, G.; Abercrombie, S.; Denuault, G.; Daniele, S.; De Faveri, E., *Anal. Chem.*, **2007,** 79, 2952-2956.

19. Lefrou, C.; Cornut, R., *ChemPhysChem*, **2010,** *11*, 547-556.

20. Faulkner, L.R.; Bard, A.J., *Electrochemical Methods: Fundamentals and Applications, 2nd edn*, Wiley, **2000**.

21. Carter, M. T.; Rodriguez, M.; Bard, A. J., *J. Am. Chem. Soc.*, **1989,** *111*, 8901-8911.

22. Squella, J. A.; Bollo, S.; Nunez-Vergara, L. J., *Curr. Org. Chem.*, **2005,** *9*, 565-581.

23. Catalan, M.; Alvarez-Lueje, A.; Bollo, S., *Bioelectrochemistry*, **2010,** *79*, 162-167.

24. Souto, R. M.; Gonzalez-Garcia, Y.; Battistel, D.; Daniele, S., *Chem. Euro. J.*, **2012,** *18*, 230-236.

25. Daniele, S.; Ciani, I.; Baldo, M. A.; Bragato, C., *Electroanalysis*, **2007,** *19*, 2067-2076.

26. Rodriguez-Lopez, J.; Bard, A. J., *J. Am. Chem. Soc.*, **2010,** *132*, 5121-5129.

27. Merz, A.; Bard, A. J., *J. Am. Chem. Soc.*, **1978,** *100*, 3222-3223.

28. Barry, P. H.; Lynch, J. W., *J. Membr. Biol.*, **1991,** *121*, 101-117.

29. Kudo, K.; Nagaoka, M.; Kuniyoshi, S.; Tanaka, K, *Synth. Met.*, **1995,** *71*, 2059-2060.

30. Kuniyoshi, S.; Nagaoka, M.; Kudo, K.; Terashita, S.; Ozaki, Y.; Iriyama, K.; Tanaka, K., *IEICE T. Electron*, **1994,** *E77C*, 657-661.

31. Rodríguez-López, J.; Alpuche-Avilés, M. A.; Bard, A. J., *J. Am. Chem. Soc.*, **2008,** *130*, 16985-16995.

32. Wang, Q.; Rodríguez-López, J.; Bard, A. J., *J. Am. Chem. Soc.*, **2009,** *131*, 17046-17047.

33. Zoski, C. G., *J. Electrochem. Soc.*, **2016,** *163*, H3088-H3100.

34. Jamali, S. S.; Moulton, S. E.; Tallman, D. E.; Forsyth, M.; Weber, J.; Wallace, G. G., *Electrochim. Acta*, **2015,** *152*, 294-301.

35. Cao, F. H.; Kim, J.; Bard, A. J., *J. Am. Chem. Soc.*, **2014,** *136*, 18163-18169.

36 Simpson, B. H.; Rodriguez-Lopez, J., *Electrochim. Acta*, **2015,** *179*, 74-83.

Chapter 5: Impact of Polyelectrolyte Dynamics on the Reactivity of Solubilized Redox Active Polymers

Notes and Acknowledgements

This chapter contains data that is in preparation for a manuscript for publication with authors Burgess, M.; Hernández-Burgos, K.; Schuh, J.K.; Davila, J.; Montoto, E.C.; Ewoldt, R.H.; Moore, J.S.; and Rodríguez-López, J. M.B. and K.H.B. contributed equally to this work. M.B. performed all DLS and ellipsometry experiments, helped do voltammetry measurements, helped do data analysis, helped write the manuscript, made figures, and helped make samples. The authors acknowledge the Joint Center for Energy Storage Research (JCESR), an Energy Innovation Hub funded by the Department of Energy, Office of Science, Basic Energy Sciences for funding. M.B. acknowledges additional support from the National Science Foundation Graduate Research Fellowship Program under Grant No. DGE-114425. Materials characterization was carried out in part in the Frederick Seitz Materials Research Laboratory Central Research Facilities at the University of Illinois at Urbana-Champaign. K.H.B. gratefully acknowledges the Beckman Institute Postdoctoral Fellowship at the University of Illinois at Urbana-Champaign, with funding provided by the Arnold and Mabel Beckman Foundation. J.R.L acknowledges additional support from a Sloan Research Fellowship.

Abstract

Studying solubilized redox active polymers (RAPs) has become an important topic in the search for new materials for non-aqueous energy storage applications. Importantly, understanding the roles of polymer dynamics and charge transfer mechanisms is crucial for the development of better performing materials for their desired applications. Herein we study soluble RAPs that are polyelectrolytes that bear viologen or ferrocene redox active pendants in different ionic strength

solutions. We compare these results with ones from a nitrobenzene based RAP which does not have polyelectrolyte characteristics. These studies are divided in three stages consisting of probing effects of polyelectrolyte dynamics on electrochemical measurements, heterogeneous charge transfer and film properties, and viscometric analysis of polyelectrolyte properties. To study the RAP dynamics at different concentrations of the polymer and supporting electrolyte we performed a suite of electrochemical experiments consisting of ultramicroelectrode (UME) voltammetry, rotating disk electrode (RDE) voltammetry, and macrodisk / modified electrode measurements. These studies show that the ionic strength strongly modulates the reactivity of solution species and modifies the thermodynamics of adsorbed RAP films. We characterized the hydrodynamic radii of the RAPs in solution via dynamic light scattering (DLS) and viscometric analysis and compared how these results agreed with the ones extracted from the electrochemical measurements. This study highlights the importance of the charge mediation process through the polymer electrode interphase that controls the reactivity and the charge transfer kinetics of the species in solution. Viscometric experiments allowed us to study and understand the electrochemical results by highlighting different regions in which the RAPs are either dilute enough to have clear and expected mass transfer limited electrochemical results or in a high enough concentration that the RAPs are entangled and therefore present complications in their electrochemical response. Finally, we show that RAPs behave much differently than their monomer constituents and special considerations need to be taken into account in electrochemical measurements of RAPs that balances solution conductivity with electrostatic effects in order to unleash the full potential and performance of soluble RAP materials.

Introduction

Understanding the role of enhanced electrostatics within nano-confined geometries has received considerable interest within the electrochemical community in nano-particle screening,[1,2] redox cycling,[3,4] and scanning electrochemical microscopy,[5,6,7] to only name a few. Here, electrified interfaces can be separated by distances small enough that it is possible to have overlapping electrical double layers whose thickness is described by a Debye length, κ^{-1}. Modulating this double layer thickness within these nano-dimensioned cells via changing the supporting electrolyte concentration can have pronounced effects on the electrochemical reactivity and particle transport.

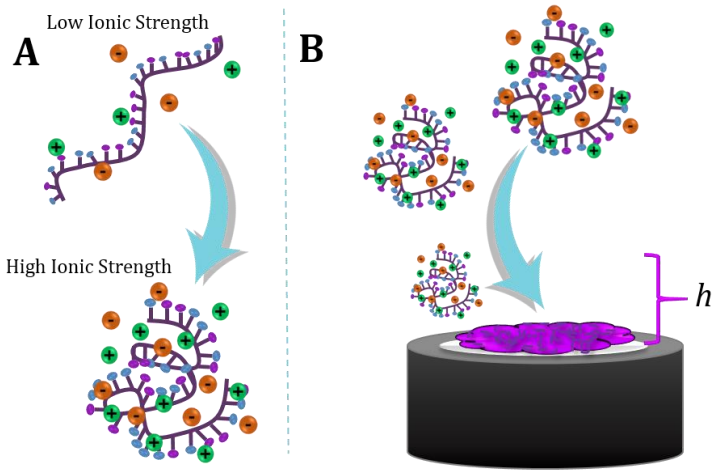

Figure 5.1. (A) Depiction of an arbitrary polyelectrolyte coil whose hydrodynamic radii (r_H) is related to the ionic strength of the solution. With excess added salts to the solution the polyelectrolyte will contract in size as the electrostatics of the ionic pendants have been screened out (B) Polyelectrolyte coils adsorb to surfaces at a rate determined by the solution and surface electrostatics. These adsorbed polyelectrolytes will form heterogeneous films with a nominal thickness (h) which will depend on the experimental conditions.

On another front, since the 1950's there have been massive efforts to pin down the behavior and solution dynamics of polyelectrolytes.[8,9,10] Polyelectrolytes, by their nature are ionic polymers and their behavior is strongly influenced by the electrostatics of the solution. Just like in nano-

electrochemical cells, the electrostatic interactions between charged repeat units in polyelectrolytes can be tuned by modifying the structure of the polyelectrolyte chain,[11] or by altering the amount of dissolved salts in the solution. In low added salt regimes, when Debye lengths are their longest, the pendants of polyelectrolytes are electrostatically repelled by one another which influences the expansion of the polymer coil to minimize their electrostatic repulsions. Conversely, in high salt solutions, polyelectrolytes tend to shrink in size as their electrostatics are screened by the supporting electrolyte.[12] This occurs because large excesses of salt effectively neutralize the net charge on the polymer backbone and attractive interactions arising from Van der Waals forces from the organic backbone dominate. Finally, the amount of salt in solution has strong influences on the amount of adsorption that polyelectrolytes have on surfaces.[13,14] The origin for this comes from the well-understood "salting out" effect,[15] which can influence charged objects in solution to eventually crash out if sufficient salt is added. These polyelectrolyte behaviors are schematically depicted in Figure 5.1.

Redox active polymers (RAPs) present themselves as candidates to bridge these seemingly unlinked disciplines. Our groups have been studying RAPs for targeted use as highly soluble charge storage media in non-aqueous redox flow batteries,[16,17,18] but along the way have characterized fundamental properties of these systems including their charge transfer mechanisms,[19] identified unique interactions with supporting electrolyte ions,[20] and designed ways to enhance intramolecular interactions.[11] Yet, up to now we have overlooked the role of polyelectrolyte solution dynamics on the electrochemical performance of RAPs. Although RAPs have been studied since at least the 1960's,[21] the bulk of this work has centered on studying them in the form of polymer modified electrode surfaces. Highly soluble RAPs, i.e. polyelectrolytes,

present a model system in which polyelectrolyte dynamics and nano-scale electrochemical properties can be studied hand-in-hand.

Scheme 5.1 RAP Chemical Structures and Properties[a]

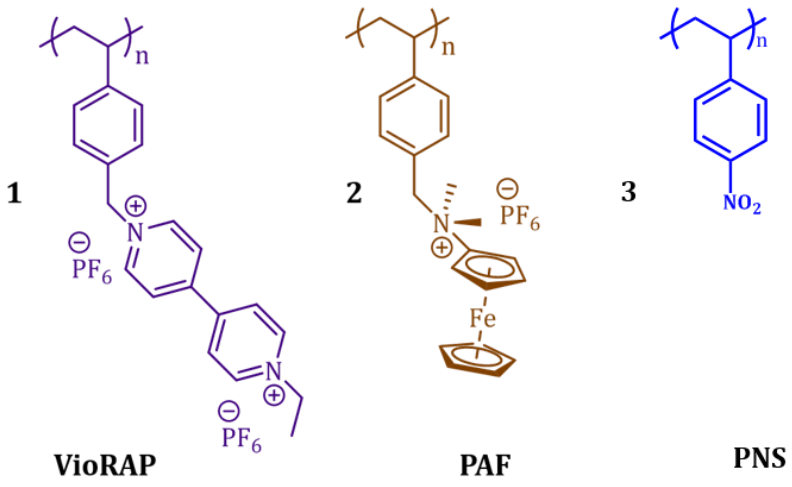

[a] **1** = poly (benzene ethyl viologen) (**VioRAP**) with a M_n of 318 kDa. **VioRAP** can undergo two reversible electrochemical reductions which changes the oxidation state of each pendant from $2^+/1^+$ and $1^+/0$, respectively. **2** = poly (amino ferrocene) (**PAF**) with a M_n of 271 kDa. **PAF** can be reversibly electrochemically oxidized at the iron center to change the oxidation state of each pendant from $1^+/2^+$. **3** = poly (para-nitrostyrene) (**PNS**) with a M_n of 50 kDa. **PNS** can be reversibly electrochemically reduced to change the oxidation state of each pendant from $0/1^-$.

Like nano-electrochemical cells, RAPs have charged interfaces (redox pendants) that can undergo electrochemical reactions. These redox active pendants have separation distances that can be comparable to the Debye length of the solution. In this study, we explore the role of electrostatics and polyelectrolyte dynamics via modulating the supporting electrolyte concentration on the electrochemical performance for three soluble RAPs, poly (amino ferrocene) (**PAF**), poly (benzene ethyl viologen) (**VioRAP**), and poly (para-nitrostyrene) (**PNS**). The structures for these RAPs are shown in Scheme 5.1.

Here, we show that not only are the dynamics of soluble RAPs similar to their non-redox active counterparts, but these polyelectrolyte dynamics have major implications on the reactivity. Studying RAP electrochemistry at different concentrations of RAP and ionic strengths via ultramicroelectrode (UME) voltammetry, rotating disk electrode (RDE) voltammetry, and macrodisk voltammetry measurements displays that the ionic strength strongly modulates the reactivity and modifies the thermodynamics of adsorbed RAP films. These ionic strength dependencies are not seen for their ferrocene and viologen monomer counterparts. Furthermore, we show the evolution of reactivity of RAPs in dilute, semi-dilute, and concentrated polymer solutions to reveal how the interactions of polyelectrolyte coils with themselves gives rise to altered electrochemical responses. RAP hydrodynamic radii were characterized via dynamic light scattering (DLS) and viscometric analysis to demonstrate that modified electrochemical signals at different ionic strengths are related to the changing hydrodynamic radii, r_H, of the polymer coils. Additionally, the charge accessibility and thickness of adsorbed RAP layers decisively impacts the electrochemical responses of solubilized RAPs reacting at polymer film / electrode interface.

This first study into the role of polyelectrolyte dynamics on solubilized RAP electrochemistry reveals that the choice in solution ionic strength is crucial for electroanalytical measurements and performance, a detail frequently overlooked as trivial. Here, we show that RAPs behave much differently than their monomer constituents and special considerations need to be taken into account that balances solution conductivity with electrostatic effects in order to unleash the full potential and performance of soluble RAP materials.

Experimental

Chemicals

All reagents were used as received without any further purification. Acetonitrile (99.8% anhydrous), dimethylformamide (99.8% anhydrous), propylene carbonate (99.7% anhydrous), tetrabutylammonium hexafluorophosphate (99% electrochemical grade), lithium tetrafluoroborate (anhydrous powder 99.99% trace metal analysis), ethyl viologen diperchlorate (98%), ferrocene (98%) were all purchased from Sigma-Aldrich (St. Louis, MO). Unsubstituted polymer backbone, Poly(vinylbenzyl chloride) (82 kDa), was purchased from Polymer source.

Electrochemical Measurements

All electrochemical measurements were performed with a CH Instruments (Austin, TX) 760E bipotentiostat inside of a glovebox from VTI Technologies (Gloucester, MA). The glovebox maintained a consistent inert atmosphere to have less than 0.1 ppm water and oxygen content. All rotating disk electrode voltammetry experiments were done with a Pine rotator. All voltammetry was measured versus a 0.1 M Ag/Ag^+ reference electrode (CH instruments) and utilized a Pt wire counter electrode. Macrodisk working electrodes for voltammetry were a 1.5 mm radius Pt disk electrode from CH Instruments. Gold coated Si substrates for measuring electrochemistry of polymer films and to produce samples to be analyzed by spectroscopic ellipsometry were fabricated via electron beam evaporation. Electron beam evaporator (Temescal Systems) was used to deposit 46 nm thick gold layer on Si wafer (Monsanto) with 5 nm Ti as adhesion layer. Thickness of both the gold and titanium layers was verified via spectroscopic ellipsometry. Pt ultramicroelectrodes (UME) with a radius of 12.5 μm were fabricated via a previously reported procedure.[19]

RAP Characterization

For a detailed description of the synthetic details of the ferrocene (271 kDa) and viologen RAPs (318 kDa) see Appendix D. Hydrodynamic radii of the RAPs in acetonitrile at a series of supporting electrolyte concentrations was evaluated spectroscopically via dynamic light scattering (DLS) using a Malvern Zetasizer Nano. Determined hydrodynamic radii are presented as *Z*-averages arising from fits of the cumulants of the autocorrelation function. All samples were measured in quartz capped cuvettes (Starna cells) to prevent evaporation or contamination with dust. Samples were passed through a 0.2 μm syringe filter (Cole Parmer) prior to measuring via DLS to remove dust contaminants and aggregates. Further characterization of solution phase RAP coil sizes in acetonitrile utilized intrinsic viscosity measurements using an m-VROC internal flow viscometer (RheoSense Inc.) that tested the RAP solutions at different shear rates (3-30 kHz). RAP film thickness on electrode surfaces was characterized *ex-situ* via spectroscopic ellipsometry using a Woolam VASE ellipsometer and a commercial software package (J.A. Woolam Co.). UV-vis measurements of reduced **VioRAPs** were taken in quartz cuvettes using a SEC2000 spectrometer from ALS Co (Japan).

Results and Discussion

Investigating Electrostatic Effects via UME voltammetry

In order to explore both the transient and steady state effects of ionic strength on the reactivity of RAPs, cyclic voltammetry (CV) and chronoamperomtric steps with a UME are utilized. The use of UMEs allows the probing of solution reactivity in the limit of no added salt in the solution because the *i-R* drop with a UME is sufficiently small.[22] As a first control experiment, UME voltammetry (Figure 5.2A) and chronoamperometric steps (Appendix D Figure D.16) of

viologen monomer are presented. As can be seen in Figure 5.2A, all the voltammetric wave shapes of viologen monomer in a series of solutions varying in ionic strength are consistent with facile electron transfer and readily attain a steady state current. Although there appears to be optimal conditions for reactivity at 100 mM salt because of a maximum in the steady state current, these differences in current are relatively small. Solutions of low ionic strength (0 mM, 10 mM) have slightly lower current relative to 100 mM due to electrical migration influences, and excess salt solutions (500 mM, 1000 mM) are lower primarily due to heightened viscosity. This facile reactivity and low dependence on the solution ionic strength is starkly contrasted by the same experiment with a **VioRAP** sample, Figure 5.2B.

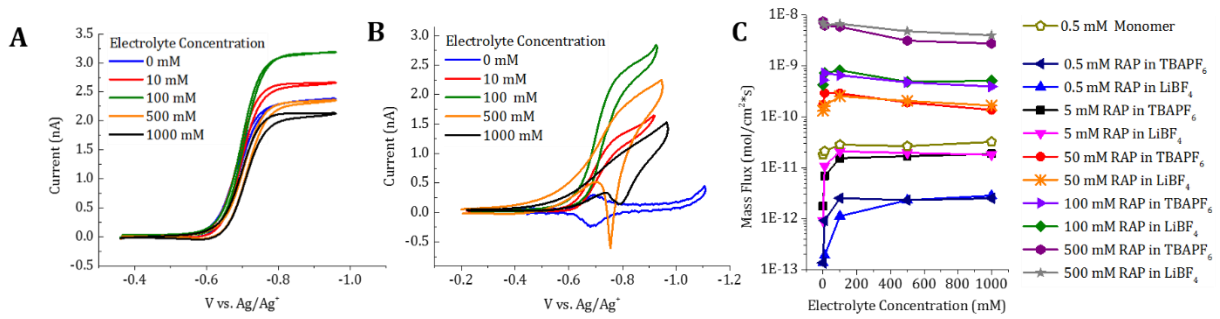

Figure 5.2. (A) UME cyclic voltammetry at 20 mV/s of 0.5 mM viologen monomer in acetonitrile at different ionic strengths. (B) UME cyclic voltammetry at 20 mV/s of 5 mM 318 kDa **VioRAP** in acetonitrile at different ionic strengths. (C) Effective mass flux as a function of electrolyte concentration ($LiBF_4$ or $TBAPF_6$) in acetonitrile for different concentrations of 318 kDa **VioRAP**. Data points come from the viscosity corrected limiting currents following a chronoamperometric step at -0.9 V vs. Ag/Ag^+.

Here, the reactivity of the viologen RAP is strongly modulated by the salt concentration in the solution. Under conditions of no added salt to the solution, the voltammetric wave shape of the **VioRAP** solution is completely dominated by a surface confined species as indicated by peaks with no splitting and a non-steady state current. Clearly, in the absence of supporting electrolyte the **VioRAP** samples have a strong proclivity for adsorption onto the electrode surface, which we believe is due to electrostatic attraction of a cationic polymer and a negatively poised electrode

surface during reduction, and decreased solubility of the RAP in polar acetonitrile upon reduction of the viologen redox units ($2^+/1^+$). In the absence of excess salt, electrostatic effects will dominate the behavior of polyelectrolytes because the Debye length, κ^{-1}, of the solution is quite large (> 3nm). It is important to note that this effect is not exclusive to **VioRAP** samples (Appendix D Figures D.1-D.12), as shown in Appendix D Figures D.18-D.21, the UME voltammetry of a **PAF** species is also completely surface confined in the absence of added supporting electrolyte. Although the condition of zero excess salt presents itself as an interesting case relative to the viologen monomer, electrochemical measurements without excess supporting electrolyte are rarely performed. However, and unexpectedly, surprising results are still seen even when supporting electrolyte is added to the solution. Under conditions of added, but moderate concentrations of supporting electrolyte (10 mM, 100 mM), the UME voltammetry of the **VioRAP** begins to resemble regular sigmoidal wave shapes that were seen with the viologen monomer. Yet, when additional salt is added (500 mM, 1000 mM) there is again strong deviations away from simple diffusive reactivity. Although there is a steady state current achieved in the forward sweep, upon reversing a large stripping peak is present. Clearly, the presence of too much supporting electrolyte again influences the adsorption of RAPs onto the electrode surface. Although a general rule of thumb for electroanalytical experiments is to have *at least* a 10:1 ratio of supporting electrolyte to active species in order to observe reactivity under diffusion controlled conditions,[22] it is clear that this rule is not sufficient enough to describe RAPs.

Having too little *or* too much supporting electrolyte in the solution leads to deleterious reactivity for RAPs, a limitation that is not observed for monomer species. Chonoamperometry with the **VioRAP**, unlike the viologen monomer, shows that the steady state currents vary by

orders of magnitude simply by changing the supporting electrolyte concentration (Appendix D Figures D.1-D.12).

These simple, but powerful, UME experiments with voltammetry and chronoamperometric steps in different ionic strength environments were rigorously tested by changing the concentration of the **VioRAP** over four orders of magnitude, and even tested the identity of the salt by probing in both in $LiBF_4$ and $TBAPF_6$ electrolytes. Both the voltammetry and the chronoamperometry for all of these studies are shown in Appendix D, but their results are summarized in Figure 5.2C. Here, the steady state currents under all of the different RAP and supporting electrolyte concentration conditions are divided by *nFa*, where *n* is the number of electrons (1 for viologen), *F* is Faraday's constant (96,485 C/mol), and *a* is the electrode radius (12.5 μm) to display the current in terms of an effective mass flux in mol/(cm^2·s). The mass flux data points have been corrected for viscosity, Appendix D Table D.1, via use of Walden's Rule.[16] An equivalent plot for **PAF** is shown in Appendix D, Figure D.23.

As seen in Figure 5.2C, when the **VioRAP** solutions are relatively dilute (< 50 mM) there are strong dependencies of the mass flux on the ionic strength that are not seen with the viologen monomer. Independent of the identity of the supporting electrolyte, the effective mass flux changes by almost 2 orders of magnitude, even though the solution contains the same amount of viologen active species. Above 50 mM concentration of **VioRAP**, the dependency of the mass flux on the ionic strength is smaller, but they are still larger than the monomer. We believe this transition of behavior is due to a changeover in the regimes of polymer dynamics. Above a critical concentration, termed the overlap concentration, polymer coils can no longer be considered independent and they will interact with one another. These effects are described in more detail in a subsequent section. Although subtle on a logarithmic plot, even after correction for viscosity,

there is almost always an optimum in the reactivity at 100 mM of supporting electrolyte. This is a surprising finding given that in the highly concentrated solutions of **VioRAP** this amount of supporting electrolyte is less than the amount of active species, or barely in excess, which runs contrary to expected mass transfer limited behavior.

These electrostatic driven effects are in part manifested in a sensitivity plot in which the viscosity corrected steady state currents are plotted versus the concentration of **VioRAP** at all of the electrolyte concentrations (Appendix D Figure D.24). Although under all of the electrolyte conditions the curves are expectedly linear, as the steady state current should increase linearly with concentration of active species with a slope of 1,[22] our evaluated slopes and uncertainty thereof are not equal. Only under the conditions of 100 mM electrolyte is the slope of this sensitivity plot closest the correct value of 1 with the least amount of regression uncertainty. Clearly, a diffusion only based model is not sufficient to capture the adsorption influenced reactivity seen for RAPs in low and high ionic strength solutions. We conclude that electrochemical sensors that are based on RAPs, or devices that are used for determining the concentration or diffusion coefficients of RAPs could be strongly dependent on the concentration of supporting electrolyte used, a concern not typically taken into account.

Macrodisk Voltammetry and RDE Studies

To demonstrate that these electrostatic effects are not confined to the realm of UMEs, the same conditions are evaluated using macrodisk and rotating disk electrodes. The use of macroelectrodes allows us to reliably study the redox properties of RAPs in different states, such as, the electrochemical reactivity in solution or as an adsorbed film. Figure 5.3A shows a representative example of macroelectrode cyclic voltammetry at 0.5 mM concentration of **VioRAP** at a series of supporting electrolyte concentrations.

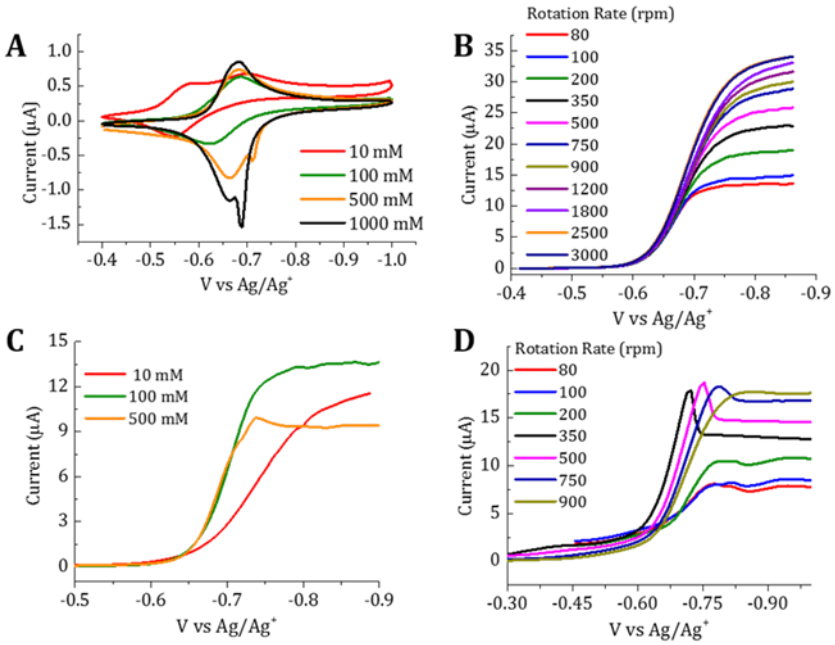

Figure 5.3. (A) Cyclic Voltammograms at 10 mV/s for 318 kDa **VioRAP** (0.5 mM) as a function of electrolyte concentration ($TBAPF_6$). (B) Linear sweep voltammograms of 318 kDa **VioRAP** (5 mM) in acetonitrile as a function of rotation rate at 100 mM of electrolyte concentration ($TBAPF_6$). (C) Linear sweep voltammograms as a function of electrolyte concentration at 80 rpm. (D) Linear sweep voltammograms of 318 kDa **VioRAP** (5 mM) in propylene carbonate as a function of rotation rate at 100 mM of electrolyte concentration ($TBAPF_6$).

Multiple observations can be made from this data set. First, at low electrolyte concentration (10 mM) a surface confined peak is observed approximately 100 mV more positive than a diffusive wave was obtained (~ -0.7 V vs Ag/Ag^+), which is representative of a pre-adsorption equilibrium due to repulsive electrostatic interactions between the charged polymer and the solvent. This phenomenon will be explored more via electrochemical simulations in the next section. Subsequently, at intermediate electrolyte concentration (100 mM) we obtained the expected reversible and diffusion controlled shape CV that is consistent with UME voltammetry. Finally, in concentrated supporting electrolyte concentrations (500 and 1000 mM) the reduction process was similar to the one at 100 mM, but upon reversal the oxidation process has a pre-peak approximately 30 mV before the oxidation wave peak potential. The shape and width of that band is consistent

with an adsorption/desorption process. Large excesses of supporting electrolyte promotes the adsorption of the polymer onto the electrode surface which can be electrochemically stripped off upon bias reversal. These observations are congruent with ones seen with UME voltammetry. Macrodisk volammetry with other concentrations of RAP (5, 50, 100, and 500 mM) at all of the tested ionic strengths are shown in Appendix D Figures D.1-D.21.

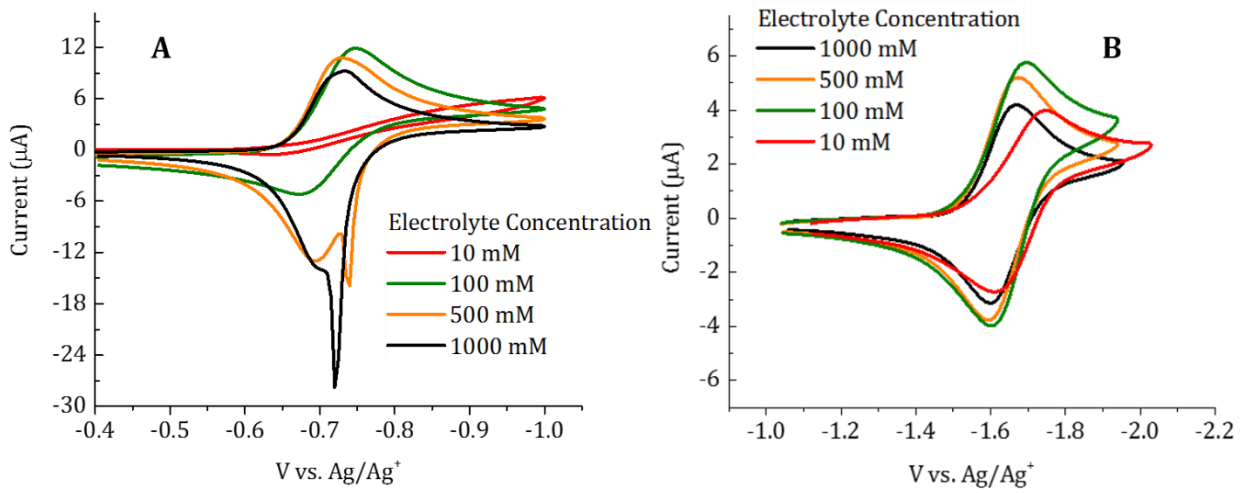

Figure 5.4. (A) Overlay of cyclic voltammograms at 50 mV/s with 5 mM of 22 kDa **VioRAP** in acetonitrile as a function of $TBAPF_6$ electrolyte concentration (B) Overlay of cyclic voltammograms at 50 mV/s with 5 mM of 50 kDa **PNS** in dimethylformamide as a function of $TBAPF_6$ electrolyte concentration.

It is evident that electrostatics strongly influence a 318 kDa **VioRAP** sample, but it is not clear where the transition point between monomer reactivity and polyelectrolyte electrochemistry occurs. To probe this query, voltammetry experiments with a 22 kDa analogue of **VioRAP** which only has 37 monomers per chain on average, are compared to the 318 kDa **VioRAP**, which has 537 monomers per chain. Macrodisk voltammetry with the 22 kDa **VioRAP** is shown in Figure 5.4A, and UME voltammetry is shown in Appendix D Figure D.62. Even though the 22 kDa **VioRAP** has fewer monomers, the same polyelectrolyte effects are observed. The 22 kDa **VioRAP** has the best reactivity at intermediate supporting electrolyte concentrations, and low or high added

salt solutions influence the adsorption of the RAP onto the electrode surface. At this moment we cannot conclude how many monomers are required for a species to exhibit polyelectrolyte effects in electrochemical measurements. However, we can confidently state that this transition occurs somewhere 2 and 37 monomers.

Moreover, we can definitively attribute these electrostatic interactions in voltammetry to ones deriving from polyelectrolyte effects and not simply because the sample is polymeric. Macrodisk voltammetry experiments with a **PNS** sample are shown in Figure 5.4B. In its oxidized state, PNS is a neutral species which forms a radical anion upon reduction. In all supporting electrolyte concentrations between 10 mM and 1 M, PNS reacts with Nernstian waves with no evidence of adsorption onto the electrode surface. Beyond changes in solution conductivity or peak magnitude from increased solution viscosity, the PNS sample has constant facile reactivity that does not depend on the ionic strength. Additional UME voltammetry experiments of PNS are shown in Appendix D Figure D.59. The results with PNS give us confidence in ascribing modulated reactivity with **VioRAP** and **PAF** when the ionic strength is modified to polyelectrolyte dynamics.

We hypothesize that the dynamic conformational effects the different ionic strengths can have on polyelectrolytes could directly affect how the polymer interacts with the electrode surface and the rate of charge injection therefrom. Rotating disk electrode voltammetry (RDE) experiments were performed to study the effects of ionic strength on the kinetics of electron transfer to RAPs. Interestingly, we could not measure any kinetic parameters for electron transfer in low supporting electrolyte concentrations (10 mM) for either **PAF** or **VioRAP** samples. This is because the RAPs strongly adsorb onto the electrode surface in a way that does not allow for efficient shuttling of charges to RAPs in solution. Under low supporting electrolyte conditions we

did not obtain a rotation rate dependence on the measured current (Appendix D Figure D.28 and D.31), which makes any evaluation of parameters from a Levich or Koutecky-Levich analysis impossible. However, for the cases in which 100 or 500 mM supporting electrolyte was used, the RDE responses did have rotation rate dependencies. The extrapolated values of k_f and k^o from a Koutecky-Levich plot[22] (Appendix D Figures D.32-D.34) did not show any strong dependence on the electrolyte concentration and the values agreed well with values for **VioRAP** and **PAF** that we have previously reported.[19] From these RDE experiments we conclude for both the 100 and 500 mM supporting electrolyte conditions that the charge transfer mechanism is the same as we have earlier described. Here, a *CE* mechanism dominates which involves a preceding adsorption equilibria of the RAPs onto the electrode surface. Although subtler in 100 mM supporting electrolyte, at 500 mM supporting electrolyte there is clear evidence for the adsorption of the **VioRAP** onto the electrode surface as evidenced by the peak before attaining steady state (Figure 5.3C).

Further examining of the kinetic information from Levich and Koutecky-Levich analyses highlights that it is not surprising that we obtained the same value of kinetics for charge transfer in different ionic strengths. As understood from the Marcus theory, the rates of self-exchange (k_{EX}) should increase in a square root relationship with the kinetics of electron transfer (k^0).[11,23] We measured the kinetics of charge hopping (k_{EX}) in acetonitrile for the radical cation in **VioRAP** by chemically reducing through the first reduction via exposure to excess Zn dust,[24] or cobaltocene in molar equivalents,[25] and measuring the resulting UV-vis spectra. We used the Marcus and Hush theory[26,27,28,29] in combination with the Dahm's-Ruff relation[30] in the same way we have previously reported to calculate the degree of k_{EX} by following the Gaussian shaped intervalence peak at ~900 nm.[11,31] From these calculations we found that there was no strong dependence on the ionic

strength for the magnitude of k_{EX} (Appendix D Figure D.46), independent of the reducing agent used. Although we have noted that there are challenges associated with applying the Marcus theory to RAPs samples, in this case there is a strong correlation between the constant magnitudes of k^o and k_{EX}. It is important to note that the same value of δ, the inter pendant separation distance, was used in all of these calculations. Our value of δ (9.5 Å) was determined via computational DFT analysis,[11] which unfortunately cannot be evaluated in the presence of large excesses of supporting electrolyte ions. Although it is possible that δ is changing when the solution ionic strength is altered, UV-vis measurements are not indicating any strong modulation of the k_{EX} peak in location or breadth, and thus we hypothesize that δ does not change dramatically.

To show that the modified reactivity of RAPs in different ionic strengths is actually due to electrostatic effects, and not simply due to the viscosity of the solution increasing when the supporting electrolyte concentration is increased, additional RDE studies were performed in dimethylformamide (DMF) and propylene carbonate (PC). The viscosity of DMF is 0.92 mPa*s and the viscosity of PC is 2.5 mPa*s which is 2.8 and 7.5 times the viscosity of acetonitrile, respectively.[32] For both DMF and PC, these more viscous solvents promote larger degrees of adsorption of the RAP, meaning that non-steady state currents are obtained under high rotation rates, Figure 5.3D and Appendix D Figures D.35-D.42. However, consistent with behavior in acetonitrile, the amount of adsorption was linked to the ionic strength of the solution and optimum conditions for mass transport dictated reactivity is seen at 100 mM supporting electrolyte. Viscosity of the solution does play a role, but it is clear that electrostatics can dominate electrochemical behavior independent of solvent. More than just viscosity, the quality of DMF and PC as a solvent for the RAPs is likely different which imparts its own effects.[33,34] We demonstrate

in a later section via viscosity analysis that acetonitrile is a great solvent choice for our RAP systems.

RAP Film Voltammetry and Simulations

In order to study the adsorbed RAP film properties we utilized a means of reproducibly creating RAP films between experiments. Here, RAP films are electrochemically deposited at different supporting electrolyte concentrations under the same experimental conditions by cycling 10 times at 50 mV/s through the second reduction of the **VioRAP**, or the oxidation of **PAF**. Using the same deposition method between films allows us to compare different experimental conditions when the ionic strength or RAP concentration is changed. Appendix D Figures D.14-D.15 shows the different deposition CVs as a function of supporting electrolyte concentration. A surface confined process is verified during electrochemical deposition by the almost zero peak splitting of the reduction and oxidation processes. Interestingly, fundamental differences in the CVs were obtained in different experimental conditions. First, the potential of the first reduction for **VioRAP** shifts positively when low amounts of supporting electrolyte were used. Additionally, the CVs of high (50 mM) versus low (0.5 mM) concentration of RAP show different behaviors in the current (amount of polymer deposited) per cycle. For example, at low RAP concentrations, the current increases with each cycle demonstrating the continuance of the deposition process. At 0.5 mM RAP concentration, we can see that the peak current magnitude for both the first and second reduction of **VioRAP** at the final cycle becomes larger with increasing ionic strength, suggesting the formation of thicker layers. However, with a larger RAP concentration (50 mM) a maximum in the current is seen after only 2 cycles, and film resistance increases which changes the CV shape. This suggests a quick saturation of the surface with RAP material.

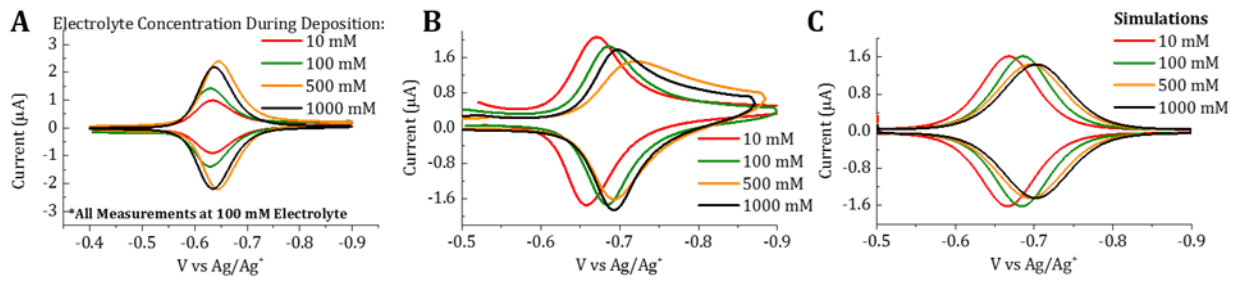

Figure 5.5. (A) Cyclic Voltammograms at 10 mV/s for 318 kDa **VioRAP** films deposited at different electrolyte concentration (as indicated in the legend), but measured at 100 mM. Film was deposited by cycling 10 times accessing the redox process (Fig. S14-S15). (B) Cyclic Voltammograms at 10 mV/s for 318 kDa **VioRAP** film deposited at a 100 mM as a function of electrolyte concentration. (C) Simulated cyclic voltammograms using the experimentally calculated data (using DigiElch Software). For these simulations the ratio absorption/desorption equilibrium was shift to simulate attractive and repulsive interaction in the polymer film, also the Frumkin parameter was shifted to increase or decrease the bandwidth.

To study the RAP film's electrochemical properties we performed two different experiments. First, we electrochemically generate a series of RAP films in solutions that have different ionic strengths. Afterwards, we rinse the filmed electrodes and place them all in a common 100 mM blank supporting electrolyte solution to test the films via voltammetry and chronoamperometry. This is done to determine the amount of adsorbed RAP material. Second, we study a RAP film that was generated in a solution containing 100 mM supporting electrolyte. This filmed electrode surface is subsequently tested in a series of blank solutions that vary in ionic strengths to test thermodynamic parameters. Figure 5.5A shows the resulting electrochemical tests of the films from the first described experimental conditions. In all of these measurements we observe well behaved surface confined species whose peak current magnitude is related to the ionic strength the film was generated in. As the supporting electrolyte was increased in concentration we can conclude that either more polymer was deposited onto the electrode surface, creating thicker layers, or we have in all cases similar films with different morphologies that lead to constrained electrochemical accessibilities. To discriminate between these two scenarios requires additional analysis.

Interestingly, when a film that was formed in 100 mM supporting electrolyte was then measured in different ionic strength solutions the film's electrochemical properties changed (Figure 5.5B). The most immediate difference is a shift in the redox potential, which shifts to more negative values with increasing ionic strength. We have confidence in the stability of our reference electrode following further calibration with an internal reference of ferrocene (Appendix D Figure D.25), and thus we attribute the observed potential shift to altered internal thermodynamic properties of the adsorbed RAP film. Changing the solution ionic strength modifies the Debye length which can alter how the film interacts with the solvent, and how the neighboring redox pendants interact with each other.

In order to model these chemical interactions a Frumkin isotherm is employed, as this model can account for attractive/repulsive interactions between adsorbed species. Physically, this model encompasses the absorption/desorption equilibrium and the attractive/repulsive interactions of the RAP with the electrode surface and the solution interphase. Using a commercial simulation software (DigiElch) we were able to simulate the potential shift and shape of the cyclic voltammogram accounting for these interactions as shown in Figure 5.5C. In our experiments, each **VioRAP** pendant carries a 2^+ charge that strongly interacts with the negatively poised electrode at reducing potentials. However, upon electrochemical reduction the solvent/electrolyte interactions become dominant. At low supporting electrolyte concentrations (10 mM) there is a positive potential shift, which can be associated (and simulated) by having an equilibrium constant that benefits the reduced state interacting with the electrode, more than the oxidized state. In terms of electrostatic repulsions between RAP pendants, having a low ionic strength solution thermodynamically promotes the polymer to decrease the redox state from 2^+ to 1^+ at lower reducing potentials in order to have a more favorable interaction with the solution interphase.

Conversely, in concentrated supporting electrolyte solutions there are sufficient counter ions in solution to screen the 2^+ charge for each viologen pendant. In this case, an equilibrium constant is present that benefits the oxidized state interacting strongly with the electrode than the reduced state, implicating that the reduced polymer film will have positive interactions with the solvent. As can be seen in Figure 5.5C and Appendix D Figure D.17, we are able to accurately simulate the changing thermodynamics of the film RAP film. We capture the attractive/repulsive interactions of the pendants in the film by changing the ratio of equilibrium constants for adsorption/desorption. The Frumkin parameter was shifted from low values (-3) to simulate repulsive interactions to high values (3) to simulate attractive interactions. The Frumkin parameter modulates the simulated voltmamogram peak width to match experimental data.

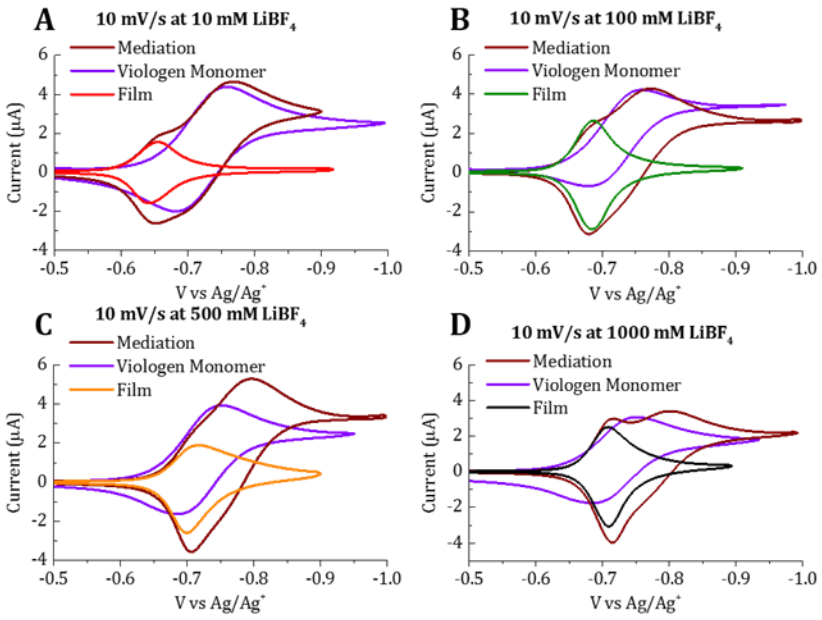

Figure 5.6. Cyclic Voltammograms at 10 mV/s for a modified 318 kDa **VioRAP** film, a 1 mM Viologen monomer solution and a modified 318 kDa **VioRAP** film in a 1 mM Viologen monomer solution at (A) 10 mM, (B) 100 mM, (C) 500 mM and (D) 1000 mM $LiBF_4$.

Interestingly, a **PAF** film generated in 100 mM supporting electrolyte shows no potential shifts or change in voltammogram shape (Appendix D Figure D.19) when placed in other ionic strength solutions. We believe this differential reactivity with **PAF** compared to **VioRAP** is due to two effects. First, as originally shown by Bard and Anson, ferrocene pendants in a RAP with an insulating backbone are largely non-interacting and thus pendants are likely neither strongly repelled nor attracted to one another.[35] Second, although both **PAF** and **VioRAP** form adsorbed films, the mechanism of formation is different. In the case of **PAF**, the electrode is poised positively in order to oxidize the ferrocene pendants. However, prior to oxidation each pendant is carrying a 1^+ charge from the quaternary amine linker which is likely electrostatically repelled from the electrode surface. This effect becomes stronger upon oxidation of ferrocene because each pendant is now carrying a 2^+ charge. We believe that we do not see potential shifts for **PAF** films because the adsorbed film during all electrochemical measurements is in a continuous state of repulsive interactions with the electrode surface.

The importance of studying RAP films in detail is that during all electrochemical measurements an adsorbed film is present. Subsequently, the RAP film will have to mediate charge through it in order to electrochemically generate any other species in solution. The rate of this mediation reaction will dictate the observed charge transfer kinetics of any solution phase species in two different ways. First, the film standard rate constant will be a limiting factor on how fast the charge transfer can occur. As observed in Figure 5.6 and Appendix D Figure D.26, when a **VioRAP** modified platinum electrode is used to measure the electrochemistry of viologen monomer probe present in solution, this process can become sluggish when the film does not mediate charge well (Figure 5.6D). Viologen monomer is known to have fast charge transfer kinetics, but when we estimate the charge transfer kinetics for this species via electrochemical

simulation when an adsorbed film of **VioRAP** is present (Appendix D Figure D.27), we find the redox kinetics to only be 0.001 cm/s. This is nearly the same value measured for the **VioRAP** via RDE.[19] A value of 10^{-3} cm/s for viologen monomer is an under estimate of its true redox kinetics by at least three orders of magnitude.[36,11,37] The second way that the film will dictate the charge transfer kinetics to solution species is due to the thermodynamics of the species on the surface. RAP films can behave similarly to conducting polymers in which there are different conducting windows depending on nature of the doping state of the polymer.[38] In order to make **VioRAP** films redox-conducting and able to facilitate the charge mediation process they need to undergo the first reduction in order to form the radical cation. When the mediation process of the **VioRAP** film and viologen monomer in solution is studied as function of solution ionic strength we observed via simulation analysis a three-fold change in redox kinetics, k^0, between the 10 mM and 1000 mM electrolyte solution (Appendix D Figure D.27). As presented in Figure 5.5, a seemingly small negative potential shift of 40 mV for the onset of reduction of adsorbed **VioRAP** can have pronounced kinetic effects for the reduction of solution species. Selecting conditions for the amount of supporting electrolyte in solution to have the adsorbed film in a conducting state relative to a solution redox probe is crucial to observe facile reactivity, and hence the ionic strength should be chosen with care.

Spectroscopic Ellipsometry Analysis of RAP Films

Thorough understanding of details pertaining to RAP films that were electrochemically determined requires additional knowledge. Chronoamperometry or voltammetry of the RAP films can give an idea of the magnitude of accessible redox groups within the film. However, reliable conversion to an effective surface concentration requires a known thickness of the adsorbed material. To characterize the thicknesses of the adsorbed RAP films that are formed during

electrochemical investigations, spectroscopic ellipsometry is utilized. Ellipsometry is one of the most widely implemented and robust methodologies for determining thicknesses of oxide layers,[39] metal deposits,[40] and polymer films.[41,42] Ellipsometry is a reflectance based technique which measures the change in polarization of an incident beam after irradiating the surface of a sample. The fundamental equation of ellipsometry, Equation 5.1, describes the interrelation of the two experimentally measured quantities.

(5.1) $$TAN\ (\Psi)e^{i\Delta} = \frac{R_p}{R_s}$$

Where Δ is the phase shift in light induced by the reflection (degrees) relative to the incident light, and Ψ is the ratio of amplitudes for the Fresnel reflection coefficients for the *p*- and *s*-components of the polarized light.

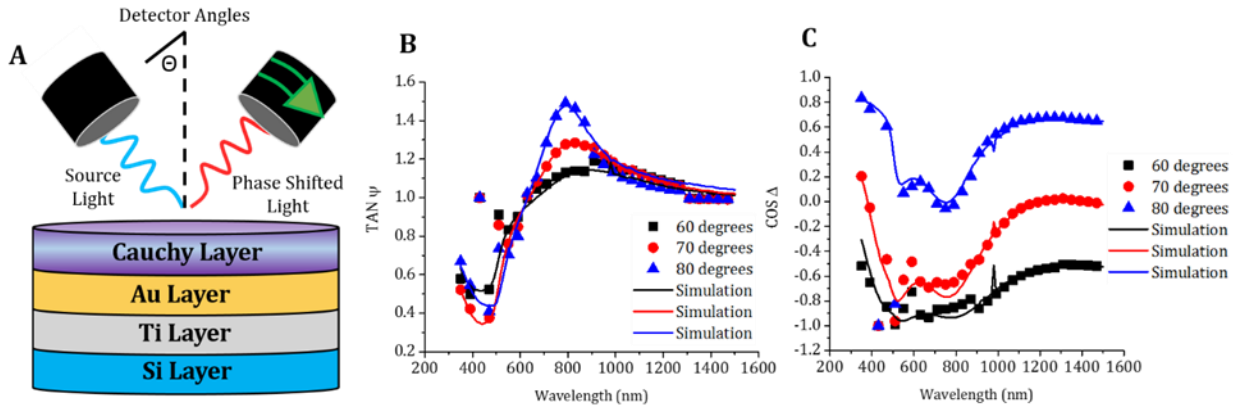

Figure 5.7. (A) Representation of the model used to fit spectroscopic ellipsometry measurements and the relative placement of the linearly polarized source light and detector following the elliptically polarized reflected light. (B) Tangent of Ψ (reflectance ratio) as a function of incident wavelength for a 318 kDa **VioRAP** film that was formed in a 100 mM supporting electrolyte solution. Data points at different detector angles are shown as symbols and the model fit shown as solid line. (C) Cosine of Δ (phase shift) as a function of incident wavelength for a 318 kDa**VioRAP** film that was formed in a 100 mM supporting electrolyte solution. Data points at different detector angles are shown as symbols and the model fit shown as solid line.

Although ellipsometric measurements are relatively easily to perform, the measured experimental parameters of Δ and Ψ do not provide any direct information about the sample of

interest without modeling of the data. Developing a reasonable virtual material model that can account for the change in optical properties of the reflected light off the real sample is imperative. The model we have used to fit our ellipsometric measurements for the purpose of determining the thickness of the RAP films is shown in Figure 5.7A. Here, a thick (>1 mm) substrate of Si accounts for the base of the Si wafer that is the electrode surface. On top of the Si wafer is a thin Ti adhesion layer (5.0 ± 0.1 nm) that binds the Au layer (46 ±1 nm) to the Si wafer. To account for an absorbed polymer, an arbitrary Cauchy layer is implemented, which is routinely used to model a transparent organic polymer layer.[43,44] The determined thicknesses of the Au and Ti layers were validated in the absence of any polymer layer to have less uncertainty (Appednix D Figure D.47). The fitted values agree well with the expected material thicknesses from electron beam evaporation fabrication protocols.

Table 5.1 Evaluated Parameters for 318 kDa **VioRAP** Films

Supporting Electrolyte Concentration (mM)	Film Thickness (nm)	Charge (mC)	Surface Coverage (mol/cm^2)	Viologen Concentration (mol/L)
10	80.6 ± 13.4	0.592	2.2 x 10^{-8}	2.72
100	164.8 ± 11.1	0.589	2.2 x 10^{-8}	1.32
500	311.9 ± 34.7	0.755	2.8 x 10^{-8}	0.90
1000	342.8 ± 48	0.749	2.8 x 10^{-8}	0.81

As can be seen in Figure 5.7B-C we are able to model the experimentally measured Ψ and Δ with high degrees of accuracy over a wavelength range of ~1400 nm for a **VioRAP** filmed electrode that was formed in the presence of 100 mM of supporting electrolyte. Spectroscopic ellipsometric measurements of both **VioRAP** and **PAF** film samples that were generated in 10,

100, 500, and 1000 mM supporting electrolyte are all shown in Appendix D Figures D.47-D.54. The ellipsometrically determined thicknesses for **VioRAP** are shown in Table 5.1 and ones for **PAF** are shown in Appendix D in Table D.2. All of the ellipsometric measurements of the RAP films are described well by the model, even for thicker films. Although there is a slight decrease in quality of fitting for measurements of Ψ as RAP films become thicker, the fitting of Δ maintains a high degree of accuracy, which is significant because the sensitivity to thickness in ellipsometry primarily comes from changes in Δ.

As can be seen in Table 5.1, the thicknesses of the **VioRAP** films are directly related to the amount of supporting electrolyte present in the solution during formation. As expected from the behavior of polyelectrolytes, the amount of adsorption of the RAPs onto the electrode surface should be larger as the ionic strength is increased.

With sufficient salt concentration in the cell (> 100 mM), electrostatic repulsive interactions between the ionic redox pendants are completely screened out and salting out effects combine with the attractive intramolecular interactions from the RAP backbones to promote surface adsorption. Although the repeat units of **PAF** carry a 1^+ charge, compared to **VioRAP** whose pendants have a 2^+ charge, the film thicknesses of both of these RAPs in the limit of high salt concentration (> 100 mM) are nearly identical (~ 300 nm). This is expected because these polymers have the exact same backbone structure and electrostatic interactions no longer dominate in large excesses of supporting electrolyte. However, when the salt concentration was low (10 mM) during film formation the different ionic character of the RAPs develops statistically different films in terms of thickness, 80 nm for **VioRAP** and 13 nm for **PAF** respectively. In acetonitrile, at 10 mM supporting electrolyte concentration the Debye length is expected to be more than 2 nm.

This Debye length is significant as this is approaching the size of a single RAP coil, and is an order of magnitude larger than the distance between neighboring pendants.

The tabulated values of surface coverage and surface concentration extracted from a Cottrell analysis for the **VioRAP** samples are shown in Table 5.1. An equivalent table for **PAF** is shown in Appendix D Table D.2 Although the **VioRAP** films were characterized *ex-situ*, their determined thicknesses and electrochemical parameters are consistent with other viologen polymer films that were electrochemically deposited and studied ellipsometrically.[45] From these results we observe that the accessed amount of charge and surface coverage for all the ionic strength conditions is similar, but the thickness and therefore the concentration changes. This leads to an unintuitive conclusion in which thicker films are found to have a lower concentration of viologen active species on the surface. We conclude that as the salt concentration in the cell is increased not only does this lead to thicker deposited RAP films, but these films are also less electrochemically addressable. We suspect this result is derived from poor ionic conductivity and electrochemical inaccessibility into thick polymer films which then critically underestimates the amount of active species in the adsorbed RAP film. To test the hypothesis that electrochemically determining the amount of charges on the surface may not be an accurate gauge, we mechanically removed the adsorbed RAP films and re-dissolved the polymer aggregates into acetonitrile and measured the resulting UV-vis spectrum for the oxidized polymer (Appendix D Figure D.45). From this experiment, we found that electrochemically we were only accessing on average 10 % of the deposited RAP film, with the lowest accessibility coming from the film deposited in 10 mM supporting electrolyte and the highest for 500 mM supporting electrolyte. Interestingly, the amount of **VioRAP** material on the electrode surface as determined by UV-vis for all the experimental conditions was nearly identical with an average of 70 ± 20 nmol. This suggests that the changes in

thickness and accessibility are due to film morphology and polymer packing. These issues will result in low reproducibility between measurements if surface concentrations are determined solely via electrochemical means. After accounting for this concentration differential, our adjusted values of surface concentration of charges in the film shown in Table 5.1 are all on the same order of magnitude and agree well with previously reported values for similar systems.[46, 39, 46, 47]

Viscometric and Spectroscopic Determination of RAP r_H

To this point we have clearly demonstrated that changing the salt concentration has dramatic effects on the electrochemical measurements of RAPs and also modulates the degree of adsorption onto electrode surfaces. A critical link between these observations is that the size in terms of hydrodynamic radii, r_H, of the RAPs is changing related to the ionic strength and this impacts the electrochemical performance. To measure r_H for the RAPs at different ionic strengths, three different techniques are utilized so that they can be compared. First, r_H is estimated via an intrinsic viscosity,$[\eta]$, analysis and subsequent transformation of $[\eta]$ to r_H via the Einstein-Simha relation.[48] Second, r_H is estimated from the viscosity corrected electrochemical diffusion coefficients measured from steady state chronoamperometry at UMEs. This electrochemically determined diffusion coefficient is transformed into r_H via the Einstein-Stokes relationship.[49] Finally, r_H is measured via dynamic light scattering (DLS) via fitting of the cumulants of an autocorrelation function. Since both an electrochemical and DLS determination of r_H requires *a priori* knowledge of the solution viscosity, it makes sense to discuss these results first.

Viscosity measurements performed via a microfluidic setup for solutions of **VioRAP** at a series of concentrations and different ionic strengths are shown in Figure 5.8A. All of the **VioRAP** samples tested behaved as Newtonian fluids within 4% at all of the shear rates tested (3-30 kHz). We have fit our viscosity measurements to an equation originally proposed by Huggins,[50] which

is shown at the top of Figure 5.8A. Here, η_s corresponds to the viscosity of acetonitrile as a blank solvent (0.334 mPa*s), $[\eta]$ is the intrinsic viscosity (L/mol), *c* is the concentration of RAP (mol/L), k_H is the Huggins parameter which describes the quality of the solvent for the polymer system, and *O* is an arbitrary variable to correspond to the coefficient for higher order cubic terms which are not used to derive any physical parameters. Solutions of **VioRAP** at 0 and 1000 mM salt were fit using only the linear terms as the viscosity did not increase enough upon increasing the RAP concentration to make fitting to second order terms appropriate. As such, we are unable to estimate k_H under these conditions. As shown in Figure 5.8A as solid lines, this equation is able to model our viscosity measurements with high degrees of accuracy under all tested conditions. Unfortunately, we were unable to do this same viscometric analysis with **PAF** as this polymer was not soluble enough at all of the tested ionic strengths on a logarithmic scale to provide significant differences in data points.

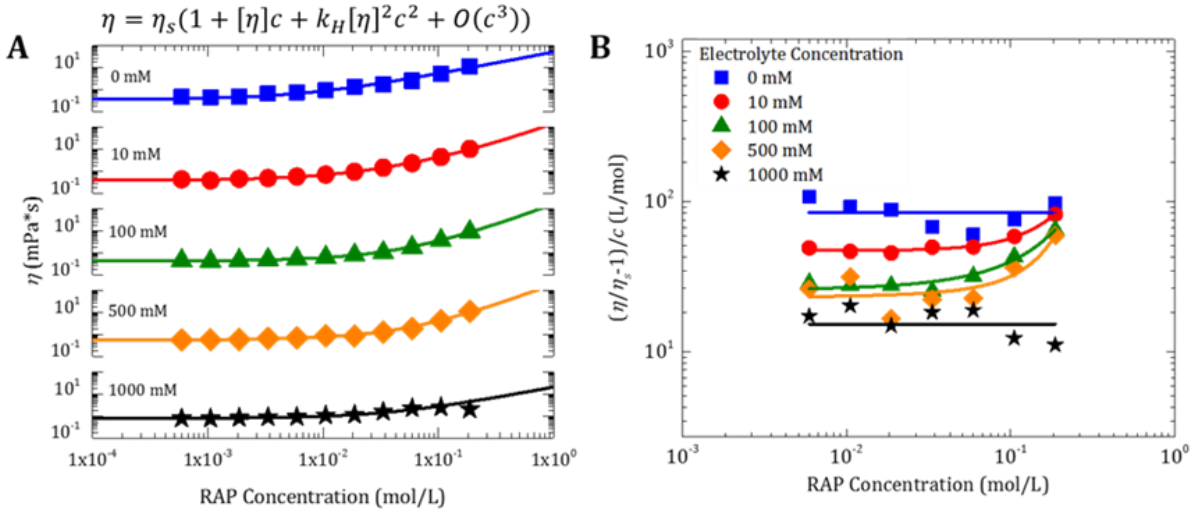

Figure 5.8. (A) Measured viscosity of 318 kDa **VioRAP** solutions at different concentrations of RAP and supporting electrolyte. Data points are shown as symbols and the model fit shown as solid line. Viscosity is modeled by the equation shown above the plot. (B) Rearrangement of the equation in (A) shows allows for the analysis of the intrinsic viscosity of 318 kDa **VioRAP** solutions at different ionic strength as the *y*-intercept in (B).

As expected, when the concentration of **VioRAP** is lowest, the viscosity trends higher as the concentration of supporting electrolyte is raised from 0 to 1000 mM. Upon addition of more RAP to the solution the viscosity raises steadily, with the lone exception of highly concentrated solutions of **VioRAP** in 1000 mM supporting electrolyte in which **VioRAP** begins to lose solubility due to salting out effects. This is consistent with the calculated values of k_H which became larger as the ionic strength was increased (Table 5.2), which shows that the quality of the solvent for our polymer system is becoming poorer with large excesses of added salt.[51] A rearrangement of the equation in Figure 5.8A provides a direct means of analyzing the intrinsic viscosities of the solution as the *y*-intercept in Figure 5.8B. The intrinsic viscosities of the **VioRAP** solutions at different ionic strengths provides a way to calculate the r_H of the **VioRAP** coils via the Einstein-Simha equation. As the intrinsic viscosity and r_H scale linearly together, higher values of the former mean lager values of the latter. The calculated values of r_H for the **VioRAP** samples at different ionic strengths are shown in Table 5.2.

Table 5.2 Evaluated Parameters for 318 kDa **VioRAP** Solutions

Supporting Electrolyte Concentration (mM)	**r_H from Electrochemistry (nm)**	**r_H from DLS (nm)**	**r_H from Viscometry (nm)**	**K_H (Huggins Parameter)**	**Overlap Concentration, C^* (mol/L)**
0	53.8	15.4	19.3	N/A	11.9×10^{-3}
10	16.8	13.4	15.4	0.06	23.1×10^{-3}
100	7.2	13.0	12.5	0.24	43.5×10^{-3}
500	5.0	12.7	11.8	0.3	51.9×10^{-3}
1000	3.2	11.6	10.9	N/A	65.5×10^{-3}

When the ionic strength of the solution is increased, the effective r_H decreases from 19.3 nm to 10.7 nm. Although it is expected that a polyelectrolyte coil should decrease in size when the ionic strength of the solution is heightened, we note that the sensitivity of this phenomenon is usually larger than ours. For many polyelectrolytes, r_H is found to decrease in a square root relationship with the ionic strength.[52] To confirm the measurements of r_H of the **VioRAP** at different ionic strengths, the viscometrically determined values were compared against ones made via dynamic light scattering (DLS). Comparing the values of r_H in Table 5.2 shows that the two techniques largely agree with each other both in magnitude and in trend. DLS measurements of the 22 kDa **VioRAP** analogue also demonstrate a similar trend in size, only changing from 3.9 nm to 2.5 nm when the salt concentration is increased from 0 mM to 1000 mM (Appendix D Figure D.64). We hypothesize that the π-π interactions between viologen groups and the potential for small amounts of reduced viologen groups to be dimerizing could make the **VioRAP** chain more rigid than expected. This would increase the value of *a* in a Mark-Houwink relation beyond that of a perfectly flexible chain[53] and provide less degrees of motional freedom to shrink when the ionic strength is increased. A possible confirmation of this hypothesis is found from DLS measurements of **PAF** at different ionic strengths in which we find that the r_H for this RAP decreases at almost the ideal rate for a flexible chain (Appendix D Figure D.57). As previously mentioned, the strength of interactions between ferrocene pendants in **PAF** are likely less than viologen ones in **VioRAP** samples. Notably, DLS measurements with **PNS** do not show any change in size when the supporting electrolyte concentration is changed, confirming this sample does not exhibit polyelectrolyte characteristics (Appendix D Figure D.60).

To check that our viscosity measurements of the **VioRAP** are consistent with previously reported scaling laws of polyelectrolytes, we analyzed the relative viscosity η/η_s versus **VioRAP**

concentration under the condition of no added salt, shown in Figure 5.9. As understood from Fuoss's Law,[8,52] the relative viscosity of a polyelectrolyte should increase in a square root relationship with increasing concentration of polyelectrolyte, provided no excess salt is added to the solution. Our **VioRAP** viscosity measurements obey this trend well as shown by the red line in Figure 5.9. We note that this trend still occurs even beyond the overlap concentration (C^*), whereby C^* (mol/L) is defined as $1/[\eta]$. For polyelectrolytes, it is known that the overlap concentration and the concentration at which polymer coils become entangled (C_e) can be different,[52] with the latter occurring at higher polymer concentration. We estimate that the critical concentration for entanglement and the beginning of reptation dynamics[54,55] for **VioRAP** to be ~100 mM. This is found via the large increase in slope in the relative viscosity plot beginning at ~100 mM of **VioRAP**. It is has been previously reported that entangled polyelectrolyte solutions will increase in their relative viscosities as a function of polyelectrolyte concentration on a log-log plot with a slope of 1.5,[52] with our experimental slope of ~1.3 being close to this value.

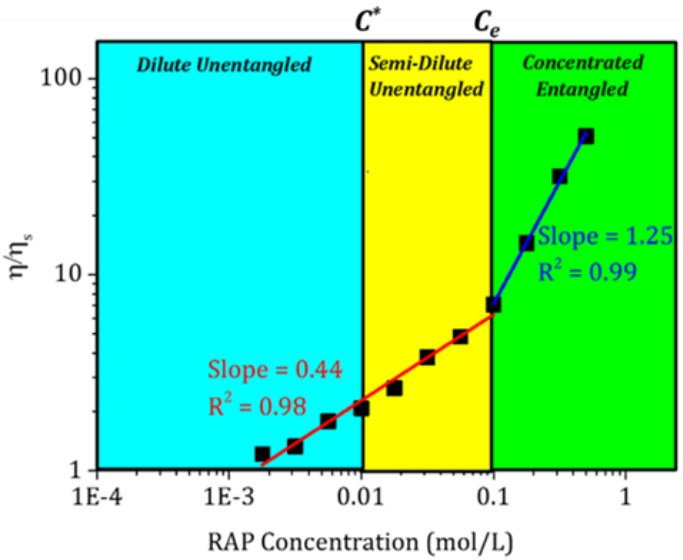

Figure 5.9. (A) Relative viscosity (η/η_s) of 318 kDa **VioRAP** solutions at different concentration of RAP in the absence of any added salt to the solution. Linear regression analysis of the two regions allows the identification of different polymer concentration regimes consistent with scaling predictions from Fuoss's Law.

Figure 5.9 helps shine light on why we see two regimes in the electrochemical behavior of Figure 5.2C. When RAP solutions are relatively dilute, there are large electrochemical dependencies on the ionic strength, but when solutions are concentrated with RAP (> 50 mM) this dependency is lessened. This makes sense from the point of view of overlapping polymer coils and the potential for polymer entanglement. In dilute RAP solutions it is possible to modulate the r_H of the RAP coils by changing the ionic strength in a way that could modify the ionic and electronic accessibility into the chains. However, above C^*, and especially when above C_e, describing RAPs with an effective r_H becomes less meaningful. In these types of solutions the polymer dynamics are more correlated and should be described in terms of polymer globules. As such, when the entire solution of polymers is entangled it is approaching the absolute limit in packing density that is possible in solution phase. Although changing the ionic strength could modify the effective size of individual RAP chains, this effect is less pronounced, and thus electrochemical measurements in entangled solutions will be dominated by behavior from the bulk, not from structural modifications to individual chains.

Finally, we point out the electrochemical methods may be able to identify the concentration region of overlapping polymers. As shown in Appendix D Figure D.57, when viscosity corrected electrochemically determined diffusion coefficients for both **PAF** and **VioRAP** are converted to r_H via the Einstein-Stokes relation, we find that the calculated r_H does decrease with increased ionic strength in an expected manner. However, for solutions of **VioRAP** (> 5 mM) the electrochemically predicted trend in r_H actually shows an *increase* in size with higher ionic strength. This can be rationalized in terms of the underlying assumptions of the Einstein-Stokes model which is calculating the effective size of an isolated and equivalent diffusing hard sphere.

When polymers are overlapping, or are entangled, they can no longer be considered isolated unique particles and thus Einstein-Stokes likely does not capture their behavior well. Deviations from Einstein-Stokes theory have been reported in concentrated polymer systems before.[56] The electrochemically determined values of r_H for **VioRAP** that are shown in Table 5.2 are for a solution containing 5 mM of RAP. The electrochemically determined values of r_H for **PAF** (Appendix D Table D.2) or **VioRAP** agree fairly well with DLS and viscometrically determined ones, assuming sufficient amount of supporting electrolyte ($\geq$ 100 mM) is present in the cell. With low amounts of supporting electrolyte (< 10 mM) we cannot eliminate possible contributions from migrational fluxes to the electrochemically determined value of r_H which then overestimates the size. Although the electrochemically determined value of r_H for **PAF** or **VioRAP** in 0 or 10 mM supporting electrolyte is quite a bit larger than ones calculated from DLS or viscosity measurements, these values are actually physically possible. An estimation of the end-to-end distance, R,[52] of a polyelectrolyte assuming 100% functionalization with ionic pendants, a monomer size of 5Å with ~600 monomers, and a Bjerrum length of 1.5 nm in acetonitrile, finds that it is possible to have an R of ~400 nm. Some reports declare that polyelectrolyte coils can extended all the way to R in solutions with no added salt,[10,52] but thus far we have not seen evidence for this occurring in our RAPs from DLS or viscosity measurements.

In summary, polyelectrolyte dynamics greatly impact the reactivity of RAPs that bear ionic pendants. From the presented electrochemical analysis and materials characterization it is clear that the concentration of both the polyelectrolyte itself and the background supporting electrolyte are significant factors to consider in order to tune the reactivity of soluble RAPs. Figure 5.10 presents a visual reference of the extreme cases for how the solubilized polyelectrolyte coils, adsorbed polymer layers, and associated electrochemical responses behave when either the

supporting electrolyte or polyelectrolyte concentration is changed. To the best of our knowledge, this work would be the first to report the generalized behavior of polyelectrolytes and their electrochemical performance in different ionic strength solutions.

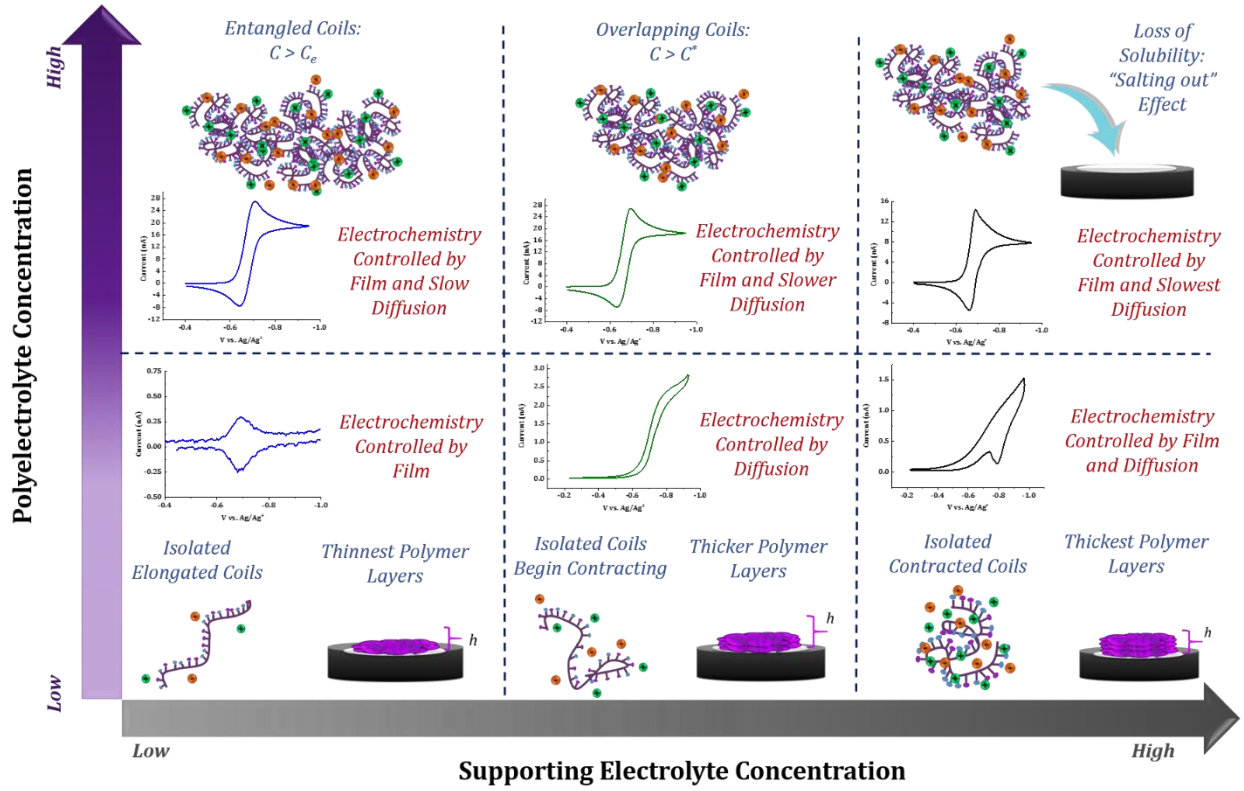

Figure 5.10. Depiction of the generalized electrochemical responses, polyelectrolyte coil conformations, and deposited film layers when either the supporting electrolyte or polyelectrolyte concentration is changed. Careful selection of polyelectrolyte and supporting electrolyte conditions are needed in order to observe different regimes of RAP reactivity.

Conclusions

This comprehensive study highlights how polyelectrolyte dynamics and charge transfer processes are strongly affected by the ionic strength of the solution. From UME voltammetry we found that by having too little *or* too much supporting electrolyte in the solution leads to deleterious RAPs reactivity, a limitation that is not observed for monomer species. In combination with UME,

macroelectrode voltammetry experiments indicate how the equilibrium of RAPs adsorption can be influenced by the electrolyte concentration by altering the electrostatic interactions between the RAP and the electrode surface.

Adsorbed RAP film reactivity was characterized by cyclic voltammetry and simulation analysis, showing that the thermodynamics of the RAP film can be tuned by the ionic strength. Simulations bring to light two important conclusions. First, a Frumkin isotherm model can explain reduction potential shifts as consequence of repulsive/attractive interaction of the polymer with itself and the electrode surface. Second, simulation of electrochemical experiments showed how importance of the onset potential for the charge mediation to species in solution through the polymer electrode interphase can have a direct impact on the observed charge transfer kinetics for the species in solution.

Spectroscopic ellipsometry measurements lead us to conclude that as the salt concentration in the cell is increased not only does this result in thicker deposited RAP films, but these films are also less electrochemically addressable. We suspect this result is derived from poor ionic conductivity and electrochemical accessibility into thick polymer films which then critically underestimates the amount of active units in the adsorbed RAP film. This observation was tested via UV/Vis experiments which suggested that we have low electrochemical addressability of RAP films which leads to over estimation of D_E and low reproducibility between measurements assuming surface concentrations are only determined via electrochemical means.

In addition, we also characterized hydrodynamic radii of the RAPs in solution via dynamic light scattering (DLS) and viscometric analysis and compared how the trends for these results agreed with the ones extracted from the electrochemical measurements. Interestingly, when the ionic strength of the solution was increased, the effective r_H decreases for the **VioRAP** from 19.3

nm to 10.7 nm, but it did not follow an expected decrease in size in relationship to the square root of the ionic strength. On the other hand, we found from DLS measurements of **PAF** at different ionic strengths that the r_H decreased at almost the ideal rate for a flexible chain. Viscosity measurements performed via a microfluidic setup for solutions of **VioRAP** at a series of concentrations and different ionic strengths behaved as Newtonian. Viscometric experiments allowed us to study and understand the electrochemical results by highlighting different regions in which the RAPs are either dilute enough to have clear and expected results or in a high enough concentration that the RAPs are entangled and therefore present complications in their electrochemical responses.

Finally, this work shows that RAPs behave much differently than their monomer constituents and special considerations need to be taken into account that balances solution conductivity with electrostatic effects in order to unleash the full potential and performance of soluble RAP materials.

References

1. Chen, Q. J.; McKelvey, K.; Edwards, M. A.; White, H. S., *J. Phys. Chem. C*, **2016,** *120*, 17251-17260.
2. Edwards, M. A.; German, S. R.; Dick, J. E.; Bard, A. J.; White, H. S., *ACS Nano*, **2015,** *9*, 12274-12282.
3. Katelhon, E.; Krause, K. J.; Singh, P. S.; Lemay, S. G.; Wolfrum, B., *J. Am. Chem. Soc.*, **2013,** *13*, 8874-8881.
4. Mampallil, D.; Mathwig, K.; Kang, S.; Lemay, S. G., *J. Phys. Chem. Lett.*, **2014,** *5*, 636-640.
5. Kim, E.; Kim, J.; Amemiya, S., *Anal. Chem.*, **2009,** *81*, 4788-4791.
6. Boika, A.; Bard, A. J., *Anal. Chem.*, **2014,** *86*, 11666-11672.
7. Zhou, M.; Yu, Y.; Hu, K. K.; Mirkin, M. V., *J. Am. Chem. Soc.*, **2015,** *137*, 6517-6523.
8. Dobrynin, A. V.; Rubinstein, M., *Prog. Polym. Sci.*, **2005,** *30*, 1049-1118.

9. Hong, L.; Granick, S., *J. Polym. Sci. Part B Polym. Phys.*, **2005,** *43*, 3497-3502.

10. Reed, W. F.; Ghosh, S.; Medjahdi, G.; Francois, J., *Macromolecules*, **1991,** *24* (23), 6189-6198.

11. Burgess, M.; Chénard, E.; Hernández-Burgos, K.; Nagarjuna, G.; Assary, R. S.; Hui, J.; Moore, J. S.; Rodríguez-López, J., *Chem. Mater.*, **2016,** *28*, 7362-7374.

12. Tanahatoe, J. J.; Kuil, M. E., *Macromolecules*, **1997,** *30*, 6102-6106.

13. Borukhov, I.; Andelman, D.; Orland, H., *Macromolecules*, **1998,** *31*, 1704-1704.

14. Andelman, D.; Joanny, J. F., *C. R. Acad. Sci. Serie Iv Phys. Astrophys.*, **2000,** *1*, 1153-1162.

15. Kewalramani, S.; Guerrero-Garcia, G. I.; Moreau, L. M.; Zwanikken, J. W.; Mirkin, C. A.; de la Cruz, M. O.; Bedzyk, M. J., *ACS Cent. Sci.*, **2016,** *2*, 219-224.

16. Nagarjuna, G.; Hui, J.; Cheng, K.; Lichtenstein, T.; Shen, M.; Moore, J. S.; Rodriguez-Lopez, J., *J. Am. Chem. Soc.*, **2014,** *136*, 16309-16316.

17. Montoto, E. C.; Nagarjuna, G.; Hui, J.; Burgess, M.; Sekerak, N. M.; Hernández-Burgos, K.; Wei, T.-S.; Kneer, M.; Grolman, J.; Cheng, K. J.; Lewis, J. A.; Moore, J. S.; Rodríguez-López, J., *J. Am. Chem. Soc.*, **2016,** *138*, 13230-13237.

18. Burgess, M.; Moore, J. S.; Rodríguez-López, J., *Acc. Chem. Res.*, **2016,** *49*, 2649-2657.

19. Burgess, M.; Hernández-Burgos, K.; Simpson, B. H.; Lichtenstein, T.; Avetian, S.; Nagarjuna, G.; Cheng, K. J.; Moore, J. S.; Rodríguez-López, J., *J. Electrochem. Soc.*, **2016,** *163*, H3006-H3013.

20. Burgess, M.; Hernandez-Burgos, K.; Cheng, K. J.; Moore, J. S.; Rodriguez-Lopez, J., *Analyst*, **2016,** *141*, 3842-3850.

21. Flanagan, J. B.; Margel, S.; Bard, A. J.; Anson, F. C., *J. Am. Chem. Soc.*, **1978,** *100*, 4248-4253.

22. Allen J. Bard, Larry. R. Faulkner., *Electrochemical Methods: Fundamentals and Applications, 2nd Edition*. Wiley: **2000**.

23. Marcus, R. A., *J. Chem. Phys.*, **1956,** *24*, 966-978.

24. Yuping, W.; Marco, F.; Wei-Guang, L.; Junling, S.; Yilei, W.; Majed, S. N.; Youssry, Y. B.; William, A. G.; Michael, R. W.; Stoddart, J. F., *ACS Cent. Sci.*, **2016,** *2*, 89-98.

25. Fernando, I. R.; Frasconi, M.; Wu, Y.; Liu, W.-G.; Wasielewski, M. R.; Goddard, W. A.; Stoddart, J. F., *J. Am. Chem. Soc.*, **2016,** *138*, 10214-10225.

26. Marcus, R. A., *Ann. Rev. Phys. Chem.*, **1964,** *15*, 155-196.

27. Marcus, R. A., *Rev. Mod. Phys.*, **1993,** *65*, 599-610.

28. Stephen, F. N., *Chem. Euro. J.*, **2000,** *6*, 581-588.

29. Reimers, J. R.; Hush, N. S., *Adv. Chem. Ser.*, **1990,** 27-63.

30. Blauch, D. N.; Saveant, J. M., *J. Am. Chem. Soc.*, **1992,** *114*, 3323-3332.

31. Barnes, J. C.; Fahrenbach, A. C.; Dyar, S. M.; Frasconi, M.; Giesener, M. A.; Zhu, Z. X.; Liu, Z. C.; Hartlieb, K. J.; Carmieli, R.; Wasielewski, M. R.; Stoddart, J. F., *Proc. Nat. Acad. Sci. U.S.A.*, **2012,** *109*, 11546-11551.

32. *CRC Handbook of Chemistry and Physics 95th edition*. CRC Press; 95 edition (June 4, 2014): **2014-2015**.

33. Huggins, M. L., *J. Am. Chem. Soc.*, **1942,** *64*, 1712-1719.

34. Huggins, M. L., *J. Chem. Phys.*, **1941,** *9*, 440-440.

35. Flanagan, J. B.; Margel, S.; Bard, A. J.; Anson, F. C., *J. Am. Chem. Soc.*, **1978,** *100*, 4248-4253.

36. Lachmanova, S.; Dupeyre, G.; Tarabek, J.; Ochsenbein, P.; Perruchot, C.; Ciofini, I.; Hromadova, M.; Pospisil, L.; Laine, P. P., *J. Am. Chem. Soc.*, **2015,** *137*, 11349-11364.

37. Rodriguez-Lopez, J.; Minguzzi, A.; Bard, A. J., *J. Phys. Chem. C*, **2010,** *114*, 18645-18655.

38. Conte, S.; Rodriguez-Calero, G. G.; Burkhardt, S. E.; Lowe, M. A.; Abruna, H. D., *RSC Adv.*, **2013,** *3*, 1957-1964.

39. Oates, T. W. H.; Wormeester, H.; Arwin, H., *Prog. Surf. Sci.*, **2011,** *86*, 328-376.

40. Carretero-Genevrier, A.; Drisko, G. L.; Grosso, D.; Boissiere, C.; Sanchez, C., *Nanoscale*, **2014,** *6*, 14025-14043.

41. Ogieglo, W.; Wormeester, H.; Eichhorn, K. J.; Wessling, M.; Benes, N. E., *Prog. Polym. Sci.*, **2015,** *42*, 42-78.

42. Van Schaftinghen, T.; Joiret, S.; Deslouis, C.; Terryn, H., *J. Phys. Chem. C*, **2007,** *111*, 14400-14409.

43. Ng, A.; Li, C. H.; Fung, M. K.; Djurisic, A. B.; Zapien, J. A.; Chan, W. K.; Cheung, K. Y.; Wong, W. Y., *J. Phys. Chem. C*, **2010,** *114*, 15094-15101.

44. Liu, P. F.; Zhang, Y.; Martin, S. T., *Environ. Sci. Tech.*, **2013,** *47*, 13594-13601.

45. Kepley, L. J.; Bard, A. J., *J. Electrochem. Soc.*, **1995,** *142*, 4129-4138.

46. Carlin, C. M.; Kepley, L. J.; Bard, A. J., *J. Electrochem. Soc.*, **1985,** *132*, 353-359.

47. Dalton, E. F.; Murray, R. W., *J. Phys. Chem.*, **1991,** *95*, 6383-6389.

48. James, J.; Ramalechume, C.; Mandal, A. B., *J. Polym. Sci. Part B Polym. Phys.*, **2007,** *45*, 2410-2420.

49. Tothova, J.; Lisy, V., *Acta Phys. Slovaca*, **2015,** *65*, 1-U65.

50. Huggins, M. L., *J. Am. Chem. Soc.*, **1942,** *64*, 2716-2718.

51. Pamies, R.; Cifre, J. G. H.; Martinez, M. D. L.; de la Torre, J. G., *Colloid Polym. Sci.*, **2008,** *286*, 1223-1231.

52. Dobrynin, A. V.; Colby, R. H.; Rubinstein, M., *Macromolecules*, **1995,** *28*, 1859-1871.

53. Wolf, B. A., *RSC Adv.*, **2016,** *6*, 38004-38011.

54. Brochard, F.; Degennes, P. G., *Europhys. Lett.*, **1986,** *1*, 221-224.

55. Degennes, P. G., *J. Phys. Lett.*, **1983,** *44*, L225-L227.

56. Maldonado-Camargo, L.; Rinaldi, C., *Nano Lett.*, **2016,** *16*, 6767-6773.

Chapter 6: Examining the Bulk Chemical and Electrochemical Reversibility of Soluble Redox Active Polymers in Confined Volumes via Scanning Electrochemical Microscopy

Notes and Acknowledgements

This chapter contains work that is in preparation for a manuscript for publication with authors Burgess, M.; Moore, J.S.; and Rodríguez-López, J. M.B. performed all of the experiments, wrote the entire document, made all figures, and did all data analysis. This work was supported as part of the Joint Center for Energy Storage Research, an Energy Innovation Hub funded by the U.S. Department of Energy, Office of Science, Basic Energy Sciences. M.B. acknowledges support by the National Science Foundation Graduate Research Fellowship Program under Grant No. DGE-1144245. J.R.L acknowledges additional support from a Sloan Foundation fellowship. We thank Elena Montoto and Dr. Yu Cao for assistance in providing samples.

Abstract

In order to increase the throughput of developing novel soluble redox active polymers (RAPs) and material screening in for use in energy storage applications, new tools are needed. Here, an alternative method to measure the electrochemical kinetics of ferrocene, viologen and nitrostyrene based RAPs using the substrate generation / tip collection (SG/TC) mode of scanning electrochemical microscopy (SECM) is presented. SG/TC SECM identifies electrochemical kinetics via modeling of microelectrode voltammetry signatures that were measured in solutions containing multiple oxidation states of a redox couple. This simple setup allows for probing the oxidation state dependency of RAP redox kinetics, a query not previously investigated. This first report of SG/TC SECM being applied to macromolecule systems highlights this methodology as a convenient experimental platform that can explore the bulk chemical reversibility of RAP systems in small volume conditions and minimize input sample required. Altogether, this method

could provide higher throughput analysis of the energy storage capabilities of polymeric materials that are targeted for use in flow battery applications.

Introduction

Shifting energy landscapes necessitate new devices that can be coupled to intermittent production schemes such as wind and solar technologies to store excess energy and assist in grid leveling.[1,2] One proposed mechanism of meeting this energy storage challenge are redox flow batteries which store energy by changing the oxidation state of soluble reactive species that differ in reduction potentials.[3,4] Our groups pioneered the approach of utilizing soluble redox active polymers (RAPs) as energy storage media in size-selective non-aqueous redox flow batteries.[5,6,7] RAPs are efficiently rejected from crossing over a simple porous separator based on size, while simultaneously allowing fast counter ion transport.[5,8] We have demonstrated that the size exclusion approach is effective as an energy storage platform,[7,6] but significant trials remain in identifying new chemistries and synthetic schemes to fabricate new RAPs with higher chemical stability and energy densities.

In the process of designing and synthesizing new RAPs, screening protocols for their performance as energy storage materials are needed. Rigorous experiments such as bulk electrolysis probe the chemical stability of RAPs by quantitatively and completely converting them between oxidation states. Facile characterization tests such as cyclic voltammetry only examine redox species within a confined diffusion layer and are typically not robust enough to predict the reversible behavior of bulk electrolysis.[6] Despite bulk electrolysis being an essential measurement to evaluate the energy storage capabilities of a material, these experiments are time intensive to perform and can require large amounts of synthesized sample. Moreover, it is not possible to investigate electrochemical kinetics during bulk electrolysis because it is a mass transfer limited

procedure.[9] It is desirable to have materials that are both chemically *and* electrochemically reversible, and being able to probe both of these characteristics in a single measurement would enhance RAP characterization protocols.

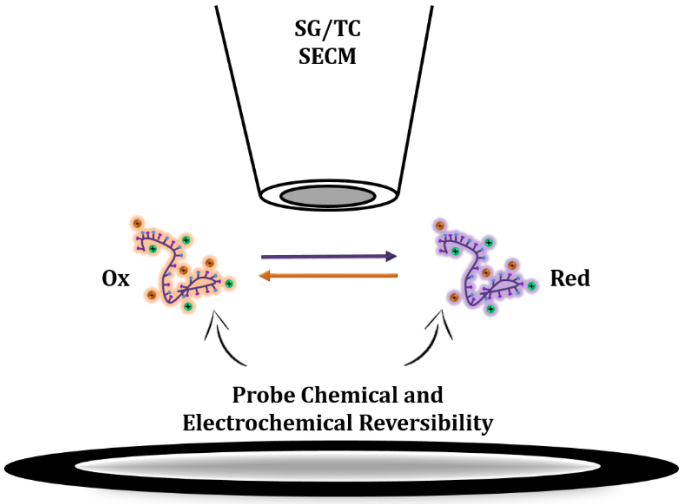

Figure 6.1. General cartoon showing RAPs being converted between different oxidation states via a Pt substrate electrode and a SECM tip in proximity collecting these products in a substrate generation / tip collection (SG/TC) experiment. Here, the substrate is able to convert the oxidation states of the RAPs underneath the SECM tip so as to probe the electrochemical and chemical reversibility of bulk material in confined volumes.

Here, an alternative method is presented which utilizes the substrate generation / tip collection mode of scanning electrochemical microscopy (SG/TC SECM) to survey the bulk chemical and electrochemical reversibility of soluble RAPs.[10,11] In SG/TC SECM, a substrate electrode generates reactive species via potential pulsing and then the products diffuse into bulk solution. The reactive species can be subsequently collected at an SECM tip placed in proximity.[12,13,14] This is schematically presented in Figure 6.1. In this way, near the substrate electrode surface it is possible to modify the local bulk ratio of oxidation states of a redox couple by pulsing at appropriate potentials relative to the formal reduction potential, as understood from the Nernst equation, Equation 6.1.[9] Within a diffusion layer above the substrate, which has a time dependent thickness, it is possible to completely convert species to any ratio of oxidation states.[10]

If a sensing SECM tip is placed within this diffusion layer, steady state voltammetric measurements can experimentally validate the conversion of redox states of a material, as the cathodic and anodic steady state currents are directly related to the concentration of each oxidation state.[9] Chemical instabilities of the probed redox couple are readily detected as the wave shape and height of microelectrode voltammograms are directly related to the diffusion coefficients and electrochemical reversibility.[9] This methodology minimizes the amount of synthesized sample required for the experiment and provides a general gauge of the bulk chemical reversibility of the dissolved RAPs in the confined volume beneath the SECM tip. Three different RAP species that we have previously investigated bearing viologen,[5] ferrocene,[15] or nitrostyrene[16] redox active units are explored here via SG/TC SECM. The structures and formal names of the RAPs used in this study are shown in Figure 6.2.

(6.1) $$E_{eq} = E^0 + \frac{RT}{nF} ln \frac{C^*_{Ox}}{C^*_{Red}}$$

Where E_{eq} is the equilibrium potential, *R* the gas constant, *T* is temperature in Kelvin, *n* is the number of electrons, *F* is the Faraday constant, C^*_{Ox} is the bulk concentration of the oxidized state, and C^*_{Red} is the bulk concentration of the reduced state.

Of further interest, it was recently reported that SG/TC SECM can be a more reliable means of measuring electrochemical kinetics than SECM approach curves.[17] Determination of redox kinetics in SG/TC SECM is facilitated via mathematical fitting of cyclic voltmamograms that were measured with a microelectrode in solutions that contain a 50/50 ratio of the oxidation states for a redox couple.[10] Although it is possible to model microelectrode cyclic voltammograms via simple numerical simulations when only one oxidation state is present, and subsequently determine redox kinetics, k^0, a required input parameter into any simulation is the reduction potential of the reaction,

E^0. Any uncertainty in the E^0 could lead to erroneously labeling electrochemical kinetics as multiple combinations of k^0 and E^0 could fit a single voltammogram.[10] However, when both the *Ox* and *Red* forms of a redox couple are present in equal proportions, there exists a zero current point in the voltammogram between cathodic and anodic reactions which exactly corresponds to the E^0 of the reaction as predicted from the Nernst equation, Equation 6.1. Species such as ferro/ferri cyanide are shelf stable as salts and making solutions containing a 50/50 ratio of oxidation states is trivial.[10] However, species such as RAPs are frequently only shelf stable in one oxidation state and thus measuring voltammetry in solutions containing a mixture of oxidation states requires the use of SG/TC SECM or bulk electrolysis on a larger scale. The equations for fitting normalized voltammograms in solutions containing a 50/50 ratio of oxidation states for a redox couple are derived and explained in more detail elsewhere by Mirkin *et.al.*, but are reprinted here in Equation 6.2.[10] Overall, SG/TC SECM provides an effective means of determining the electrochemical reversibility of RAPs at different oxidation states using a simple experimental setup. The extrapolated redox kinetic values from SG/TC SECM are then compared against ones previously measured in our labs that used SECM feedback and rotating disk electrode methods.[15]

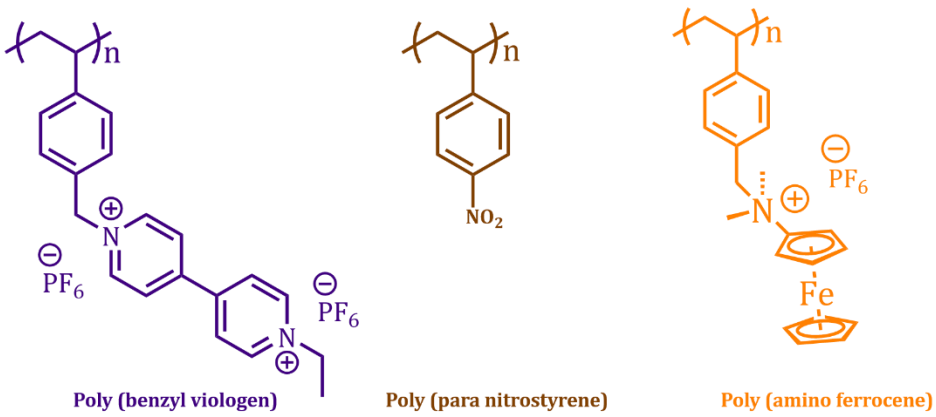

Figure 6.2. The structural motifs for the RAP materials used in this study. Poly (benzyl viologen) is noted as VioRAP, poly (para nitrostyrene) is noted as PNS, and poly (amino ferrocene) is noted as PAF throughout the document for simplicity.

(6.2) $$\frac{i}{i_{c,inf}} = \left[(\theta - 1)\frac{i_{a,inf}}{i_{c,inf}} - 1\right] / \left(\theta + \frac{\pi}{k}\frac{2\kappa\theta + 3\pi}{4\kappa\theta + 3\pi^2}\right)$$

and $$\theta = 1 + \frac{i_{c,inf}}{i_{a,inf}} exp\left[\frac{F}{RT}\left(E - E_{eq}\right)\right]$$

and $$\kappa = K\left(\frac{C^*_{Red}}{C^*_{Ox}}\right)^{\alpha} exp\left[-\alpha\frac{F}{RT}\left(E - E_{eq}\right)\right]$$

and $$K = \frac{\pi a k^0}{4D_{Ox}}$$

where $i_{c,inf}$ is the cathodic diffusion limiting current, $i_{a,inf}$ is the anodic diffusion limiting current, α is the symmetry coefficient (0.5), a is the electrode radius, and D_{Ox} is the diffusion coefficient of the oxidized species.

Experimental

Polymers

Poly (para-nitrostyrene) (PNS) with a M_n of 50 kDa was synthesized as described previously from our groups.[16] Similarly, both poly (benzyl viologen) with a M_n of 318 kDa and poly (amino ferrocene) with a M_n of 271 kDa were synthesized as detailed earlier by our groups.[15] All structures are presented in Figure 6.2.

Chemicals

All chemicals were used as received from the vendors without further purification or processing. Anhydrous acetonitrile (99.8%), anhydrous dimethylformamide (99.8%), tetrabutylammonium hexaflurophosphate (≥ 99%), ferrocene (98%), and ethyl viologen diperchlorate (98%) were all purchased from Sigma-Aldrich (St. Louis, MO).

Electrochemistry

All experiments were performed in an inert atmosphere inside of a glovebox from MBRAUN (Stratham, NH) with careful monitoring of environmental conditions to have less than 0.1 ppm of water or oxygen present. Electrochemical measurements utilized a CH Instruments (Austin, TX) 920D scanning electrochemical microscope. Counter electrodes were made of platinum wire from Goodfellow UK. All potentials are listed versus a 0.1 M Ag/Ag^+ reference electrode. Numerical simulations of electrochemical data were done using DigiElch software (Gamry Instruments). SECM tips were made following a previously reported procedure,[15,18] in which platinum wire with a radius of 12.5 µm was sealed in a glass capillary (world precision instruments) using a pipette puller from Narishige. Sealed electrodes were then exposed using sandpaper and sharpened by hand to have an R_g of 2, where the R_g is defined as the radius of the glass sheath surrounding the platinum wire including the platinum disk divided by the radius of the platinum disk.[19] Substrate electrodes used a 1.5 mm platinum disk from CH Instruments held in place by a custom made Teflon SECM cell. All electrodes were polished on a polishing pad in an alumina slurry.

Results and Discussion

In principle, it is possible to recreate experimental voltammetry signatures using simple numerical simulation protocols assuming all appropriate electrochemical parameters are known, such as the formal reduction potential (E^0), the diffusion coefficient (D), the bulk analyte concentration (C^*), the electrode radius (a), the scan rate (v), and the magnitude of redox kinetics (k^0). The experimental scan rate is an input parameter and thus it is known. Additionally, C^*, D, or a can be easily calculated when two of these three variables are known using an expression which describes the steady state diffusion limiting current (i_{ss}) at a microelectrode $i_{ss}=4nFaDC^*$,[9] where

F is the Faraday constant. Assuming the E^0 is known for the analyte of interest, the remaining parameter k^0 may be found by fitting experimental voltammograms to simulation ones holding everything else constant and screening values of redox kinetics.

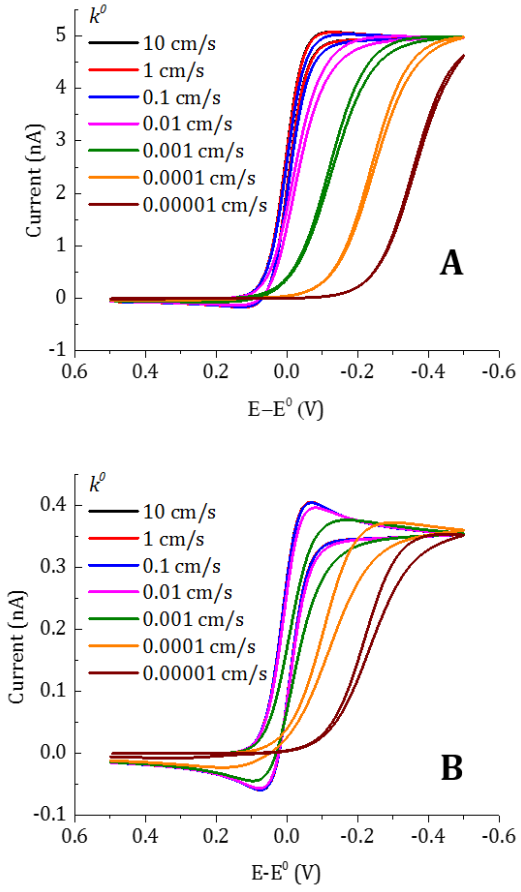

Figure 6.3. (A) Simulated voltammetry curves in DigiElch software for an arbitrary redox couple at 1 mM concentration using a 12.5 µm radius electrode with a diffusion coefficient of 1 x 10^{-5} cm^2/s at a scan rate of 20 mV/s and a series of values for redox kinetics. (B) Simulated voltammetry curves in DigiElch software for an arbitrary redox couple at 1 mM concentration using a 12.5 µm radius electrode with a diffusion coefficient of 6.5 x 10^{-7} cm^2/s at a scan rate of 20 mV/s and a series of values for redox kinetics.

However, as shown in Figure 6.3A, there are no obvious differences in simulated microelectrode voltammetric profiles from perfect Nernstian reversible waves when the redox kinetics are quicker than 0.01 cm/s, for an electrode with a radius of 12.5 µm and a diffusion coefficient of 1 x 10^{-5} cm^2/s . In turn, using simulation analysis to accurately determine redox

kinetics from microelectrode voltammetry beyond mass transfer limited conditions is confined to quasi reversible systems. This conclusion is even more pronounced when the diffusion coefficient is decreased from a level for a fast diffusing small molecule to one that is more fitting for a soluble polymeric species.[5] These simulated curves are shown in Figure 6.3B. Under slow diffusion conditions (6.5×10^{-7} cm^2/s), even less resolution is seen between curves when redox kinetics are screened. In the best case, redox kinetics for a polymeric species cannot be differentiated from Nernstian reversibility above 0.001 cm/s, an order of magnitude less resolution than for a fast diffusing species. This is due to a decreased mass transfer coefficient (m_0), where m_0 has the form $\frac{4D}{\pi a}$ for a disk microelectrode.[9] When the diffusion coefficient is decreased, m_0 also decreases, which means less redox active material per unit time reach the electrode surface challenging the redox kinetics of the system to a lesser degree.[18]

To increase the resolution between curves in Figures 6.3 the electrode radius would need to be decreased to the nanoscale. However, there are known challenges in fabricating good nano-electrodes,[20,21,22] and some species such as RAPs can quickly foul nano-electrode surfaces which makes simulating their wave shapes impractical. Yet, even using nano-electrodes does not alleviate a significant shortfall of this methodology. Specifically, although the degree of *electrochemical* reversibility can be determined via simple simulations, the bulk *chemical* reversibility is still unknown. In order to also probe the chemical reversibility more specialized measurements are needed. An electroanalytical technique that has the ability to monitor both of these criterions is SG/TC SECM.

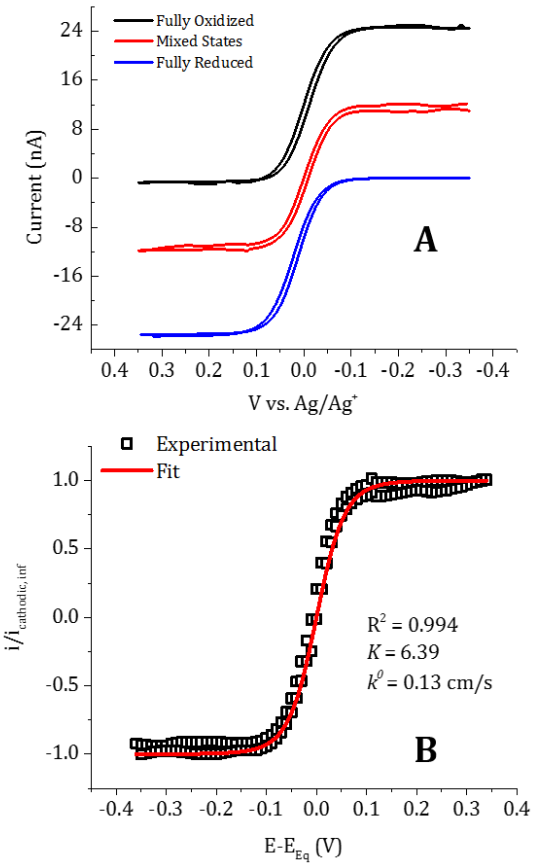

Figure 6.4. (A) Cyclic voltammetry using a 12.5 µm radius electrode with 2.2 mM ferrocene species at scan rate of 20 mV/s in 0.1 M $TBAPF_6$ in acetonitrile. The fully reduced voltammogram was taken at infinite distance from the substrate with the substrate at open circuit. The fully oxidized voltammogram was taken at ~ 40 µm distance from the substrate with the substrate held at 0.5 V. The mixed state voltammogram was taken at ~ 40 µm distance from the substrate with the substrate held at 0.05 V. (B) Normalized steady state voltammetry of the mixed states presented in (A), with respect to the limiting cathodic and anodic currents as a function of overpotential with respect to the observed equilibrium potential. Open symbols are experimental data and solid red line represents the theoretical fit to kinetic model in Equation 6.2.

A demonstration of the SG/TC mode of SECM being used to probe both the electrochemical reversibility and chemical reversibility is first shown in Figure 6.4 for a small molecule system in the form of ferrocene. First, a voltammogram for ferrocene is taken when the SECM tip is placed far away from the substrate at an effective infinite distance to measure the reactivity of bulk ferrocene in its completely reduced state. Then the tip is placed within proximity (~ 40 µm away) to the platinum substrate that is now poised at a potential to begin generating

oxidized ferrocene, ferrocenium. Foremost, the substrate potential is chosen to be one with high overpotential (0.4 V) to completely oxidize the local environment of ferrocene. After 100 seconds of quiet time, the SECM tip scans the voltage window to measure a cyclic voltammogram to collect the ferrocenium. As seen in Figure 6.4A, the bulk ferrocene concentration has been completely depleted and the microelectrode now reduces the ferrocenium back to ferrocene. It is important to note that the steady state current magnitude, ~24 nA, for both conditions of fully oxidized and fully reduced ferrocene is an indicator that both species have similar diffusion coefficients and that there is no extra current being observed from redox cycling and SECM feedback.

Comparing the curves for the completely oxidized and reduced forms of ferrocene illustrates the point of bulk chemical reversibility as the voltammetric wave shape is preserved between oxidation states. Additionally, since the half wave potentials of the voltammograms are identical for both the forward and reverse reactions, pinpointing the E^0 is now trivial. To prove this, the substrate is now held at the E^0 (~ 0V) to generate a mixture of both oxidation states of ferrocene as understood from Equation 6.1.[9] The resulting voltmamogram in Figure 6.4A shows a solution that is composed of almost exactly a half and half mixture of oxidation states of ferrocene. Under the conditions of mixed oxidation states it is now possible to compute the redox kinetics by normalizing the steady state currents for both the cathodic reaction (reducing ferrocenium) and the anodic reaction (oxidizing ferrocene) and transforming the voltage axis to be in terms of overpotential with respect to the E^0. The expressions in Equation 6.2 are able fit this normalized voltammogram with high degrees of accuracy, Figure 6.4B. The extracted kinetic value for this fitting knowing the size of the electrode and the diffusion coefficient of ferrocenium estimates the k^0 for ferrocene to be 0.13 cm/s. This value is at least two orders of magnitude slower than the reported value of 8 cm/s,[23] but 0.13 cm/s is likely more appropriately listed as mass transfer

limited. As understood from Figure 6.3A there are no discernable differences between voltammetric curves for this size of microelectrode above ~0.1 cm/s. Moreover, values of *K* greater than 4 are known to be indicative of Nerstian kinetics.[10] As the SG/TC mode of SECM has been demonstrated to effectively track both the electrochemical and chemical reversibility of a small molecule system, we now move to probing a series of RAPs.

Firstly, a viologen RAP is examined for both electrochemical and chemical reversibility. We have previously communicated that there are significant challenges in using RAPs as SECM mediators for reliably locating a probe near a surface.[15] To alleviate this, ferrocene monomer is also placed in solution for the purpose of accurately determining distance from the platinum substrate via approaching under pure positive feedback conditions and fitting of the approach curve to theory reported by Cornut and Lefrou,[24] Figure 6.5A. Results with VioRAP are very similar to ones seen with ferrocene. Examining the curves in Figure 6.5B-C shows the VioRAP species can be readily converted between oxidation states via substrate potential modulation and subsequently collected at the SECM tip without any deviation of wave shape/height or location. One major difference in applying the SG/TC method with polymers over monomers is that the probe needs to be located much closer to the surface in order to get complete conversion of species. This is because the time dependent depth of the geometric region of converted species evolving from the substrate extending into bulk solution scales exponentially with changes in diffusion coefficient.[10] In order to completely bulk electrolyze the VioRAP in the volume under the SECM tip, the probe needed to be placed 5 μm above the surface. This location is close enough that significant positive feedback is seen with the reference ferrocene mediator, Figure 6.5B, but no observable feedback is seen with the VioRAP, Figure 6.5C. This is likely due to the much slower diffusion coefficient

of the RAP compared to the monomer which does not allow for efficient redox cycling during the course of the voltammetry measurements.

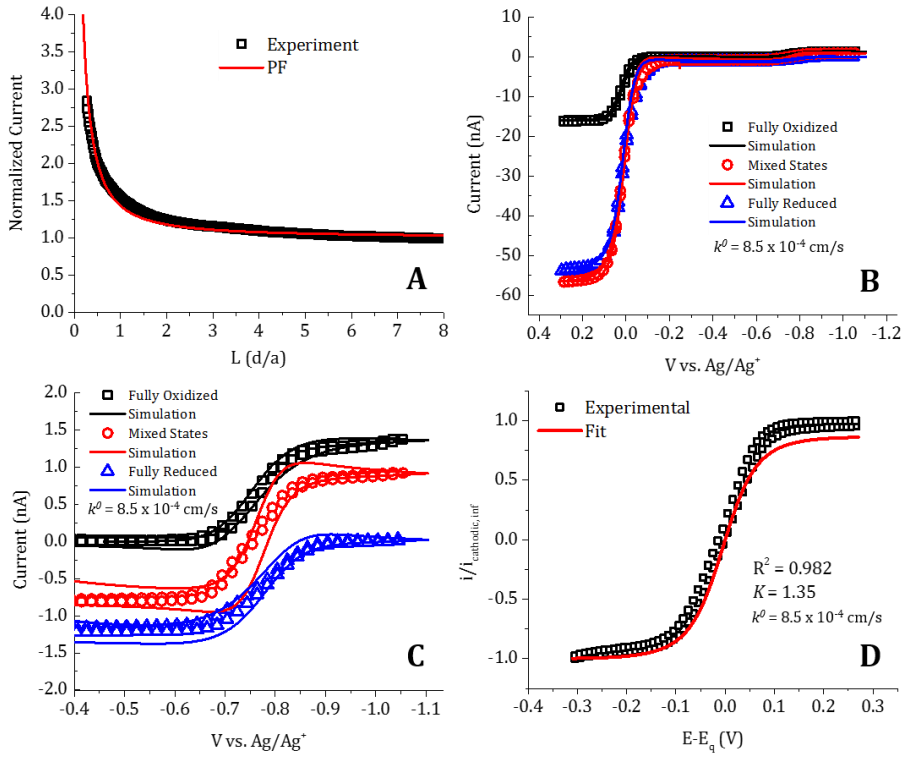

Figure 6.5. (A) SECM approach curve with a 12.5 µm tip with an R_g of 2 with 1.5 mM ferrocene monomer in 0.1 M $TBAPF_6$ in acetonitrile to a 1.5 mm platinum disk substrate. Open symbols are experimental data points and the solid red line is a fitting to pure positive feedback conditions[24] to determine distance from substrate. Substrate was held at -0.3 V and the SECM tip was held at 0.4 V. (B) Cyclic voltammetry using a 12.5 µm radius electrode with 1.5 mM ferrocene species and 5 mM VioRAP at scan rate of 20 mV/s in 0.1 M $TBAPF_6$ in acetonitrile. The fully oxidized voltammogram was taken at infinite distance from the substrate with the substrate at open circuit. The fully reduced voltammogram was taken at ~ 5 µm distance from the substrate with the substrate held at -1.1 V. The mixed state voltammogram was taken at ~ 5 µm distance from the substrate with the substrate held at -0.75 V. Open symbols are experimental data and solid lines represent the simulated model using DigiElch at the specified kinetic value. (C) Zoom in of (B). (D) Normalized steady state voltammetry of the mixed states presented in (C), with respect to the limiting cathodic and anodic currents as a function of overpotential with respect to the observed equilibrium potential. Open symbols are experimental data and solid red line represents the theoretical fit to kinetic model.

Again, the Mirkin method describes the normalized voltammogram well for VioRAP when in mixed oxidation states (Figure 6.5 D). Thhe extracted kinetic values from this analysis are shown in Table 6.1. A fitted value of 9.5 x 10^{-4} cm/s for VioRAP redox kinetics is close to the

kinetic value previously found from our lab of 3.3 x 10^{-3} cm/s using rotating disk electrode methods.[15] To further verify that the fitted value of 8.5 x 10^{-4} cm/s is a reasonable approximation of the VioRAP redox kinetics, this value was used in a DigiElch simulation recreation of the experimental data as shown in Figure 6.5B-C This simulation used the known parameters of E^0 (-0.73 V), the diffusion coefficient of the VioRAP (6.2 x 10^{-7} cm^2/s), the known electrode radius (12.5 µm), a scan rate of 20 mV/s, and the bulk concentration of active species to be 5 mM. Using a kinetic value of 8.5 x 10^{-4} cm/s in the simulation for the VioRAP fits the experimental cyclic voltammograms very well in all of the different oxidation states. The internal ferrocene reference was simulated with constant redox kinetics of 8 cm/s for internal consistency, a reported value.[23] Given the internal structural complexity of solubilized RAP coils, and the possibility for changing of coil conformation following the reduction of viologen units to form radical cations that tend to orient "face to face"[25] and facilitate self-exchange reactions,[26] it is then interesting to find that the redox kinetics for the VioRAP appear to be independent of oxidation state. This finding could possibly be explained by the redox kinetics being completely dominated by an adsorbed RAP film, an argument we have previously made.[26,15]

Table 6.1 Calculated Parameters from SG/TC SECM

Species	***K* (dimensionless)**	**k^0 (cm/s)**	**Is k^0 Dependent on Oxidation State?**
Ferrocene Monomer	6.39	0.13	No
VioRAP	1.35	9.2 x 10^{-4}	No
PNS	0.95	5.3 x 10^{-4}	No
PAF	1.23	2.5 x 10^{-4}	No

Beyond redox kinetics, these experiments also clearly demonstrate the energy storage capabilities of the VioRAP material by showing that this RAP can be reversibly bulk electrolyzed in the confined volume under the tip. Although the SG/TC SECM measurements do not allow for quantitative charge counting as is typical in traditional bulk electrolysis experiments,[6,9] to the best of our knowledge this work would be the first report of using SECM methods to screen the bulk chemical reversibility of soluble polymeric species.

SG/TC SECM experiments with PNS and PAF largely have the same conclusions as ones from VioRAP. We are effectively and efficiently able to produce all of the oxidation states for both PNS and PAF using the SG/TC mode of SECM after approaching to the surface first with a small molecule redox mediator (ethyl viologen or ferrocene) and these results are shown in Figures 6.6 and 6.7. Placing the SECM tip approximately 5 μm above the surface was also necessary to effectively electrolyze these polymeric samples. However, as was the case with VioRAP, PNS and PAF do not show any signal enhancement from feedback at this separation distance. The electrolysis results with PNS are particularly attractive as bulk electrolysis with this species via traditional methods is challenging as the radical anion that is produced upon reduction of PNS is very sensitive to any environmental oxygen and reduced PNS is highly reducing which has the possibility to degrade cell components.[16] Miniaturizing the reactor vessel to the size of an SECM cell minimizes both of these experimental challenges.

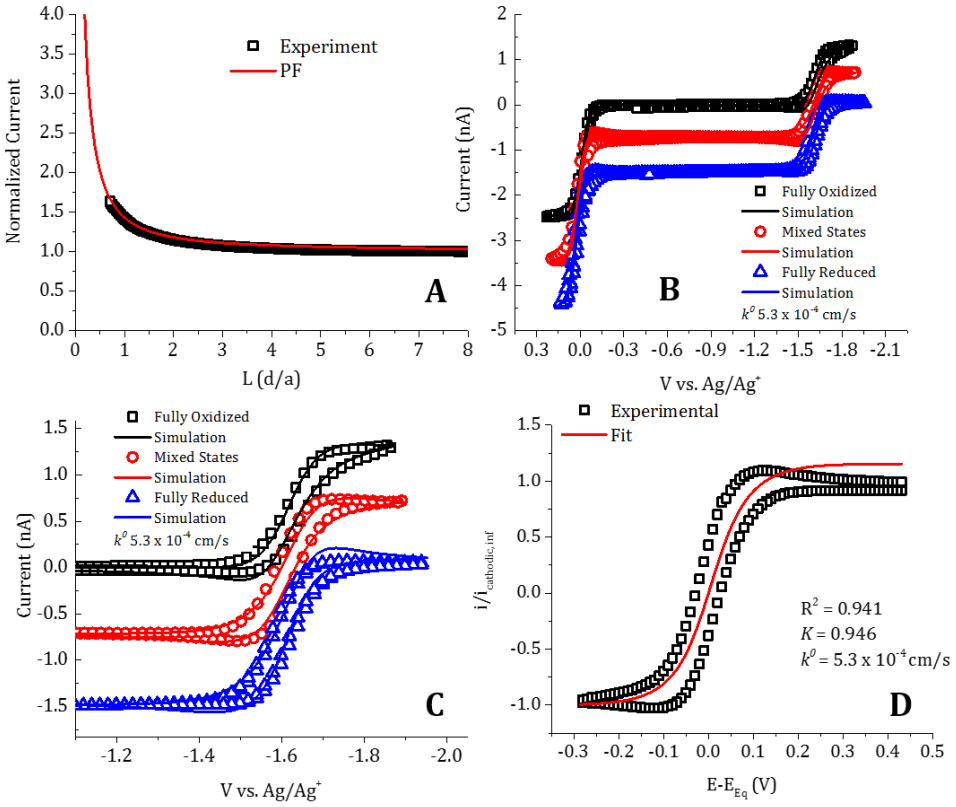

Figure 6.6. (A) SECM approach curve with a 12.5 µm tip with an R_g of 2 with 0.23 mM ferrocene monomer in 0.1 M $TBAPF_6$ in dimethylformamide to a 1.5 mm platinum disk substrate. Open symbols are experimental data points and the solid red line is a fitting to pure positive feedback conditions[24] to determine distance from substrate. Substrate was held at -0.3 V and the SECM tip was held at 0.4 V. (B) Cyclic voltammetry using a 12.5 µm radius electrode with 0.23 mM ferrocene species and 5 mM PNS at scan rate of 20 mV/s in 0.1 M $TBAPF_6$ in dimethylformamide. The fully oxidized voltammogram was taken at infinite distance from the substrate with the substrate at open circuit. The fully reduced voltammogram was taken at ~ 5 µm distance from the substrate with the substrate held at -1.9 V. The mixed state voltammogram was taken at ~ 5 µm distance from the substrate with the substrate held at -1.6 V. Open symbols are experimental data and solid lines represent the simulated model using DigiElch at the specified kinetic value. (C) Zoom in of (B). (D) Normalized steady state voltammetry of the mixed states presented in (C), with respect to the limiting cathodic and anodic currents as a function of overpotential with respect to the observed equilibrium potential. Open symbols are experimental data and solid red line represents the theoretical fit to kinetic model.

Both PNS and PAF retain electrochemical wave shape/height between oxidation states indicating that all oxidation states have similar diffusion coefficients and are chemically stable in either oxidation state (Figure 6.6 B-C and Figure 6.7 B-C). However, the diffusion coefficient of PAF is slower than PNS which gives rise to the mixed peak and steady state behavior of the voltammograms. Fitting of the normalized mixed oxidation state voltammograms for PNS and

PAF to the Mirkin method is slightly less rigorous as the wave shapes deriving from slow polymer diffusion are not perfectly described by the fitting paradigm, Figure 6.6D and Figure 6.7D. However, we can still use this method as an approximation of the redox kinetics for PNS and PAF. The extracted values for k^0 for PNS and PAF are shown in Table 6.1. In the same way as VioRAP, we can use these estimated kinetics in a numerical simulation to determine if this value of k^0 fits the experimental voltammograms well. As with VioRAP, the kinetics found from the Mirkin method describe the experimental voltammograms with high accuracy as seen in Figure 6.6B-C and Figure 6.7B-C. As with before, the internal ferrocene reference in the PNS experiments was fit to a constant k^0 value of 8 cm/s, and the ethyl viologen reference in PAF experiments was fit to a constant k^0 of 7.5 cm/s, a value previously reported.[26]

Despite the SG/TC SECM determined kinetic values effectively reproducing the experimental voltammetry data for PAF and PNS, there are some lingering concerns. The redox kinetics for PAF from the Mirkin method (2.5×10^{-4} cm/s) are slower than values previously determined from rotating disk and SECM feedback measurements by at least two orders of magnitude.[15] Similarly, the redox kinetics from the Mirkin method for PNS (5.3×10^{-4} cm/s) are at least an order of magnitude lower than ones estimated from the surface interrogation mode of SECM.[16] Clearly, the modality chosen to evaluate redox kinetics for these RAPs can have a large impact on the magnitude thereof. As previously mentioned, the Mirkin method fits the normalized voltammograms for PNS and PAF with less accuracy than ferrocene monomer and VioRAP samples, highlighting the different chemical nature of these species. It is unclear at this moment which specific value of redox kinetics for PNS and PAF is the most correct. This is because we have also previously pointed out that there are complications in determining redox kinetics for RAPs using rotating disk or SECM feedback methods because these materials strongly adsorb onto

electrode surfaces.[15] However, there are interesting conclusions that can be universally drawn from the SG/TC SECM analysis of the RAPs.

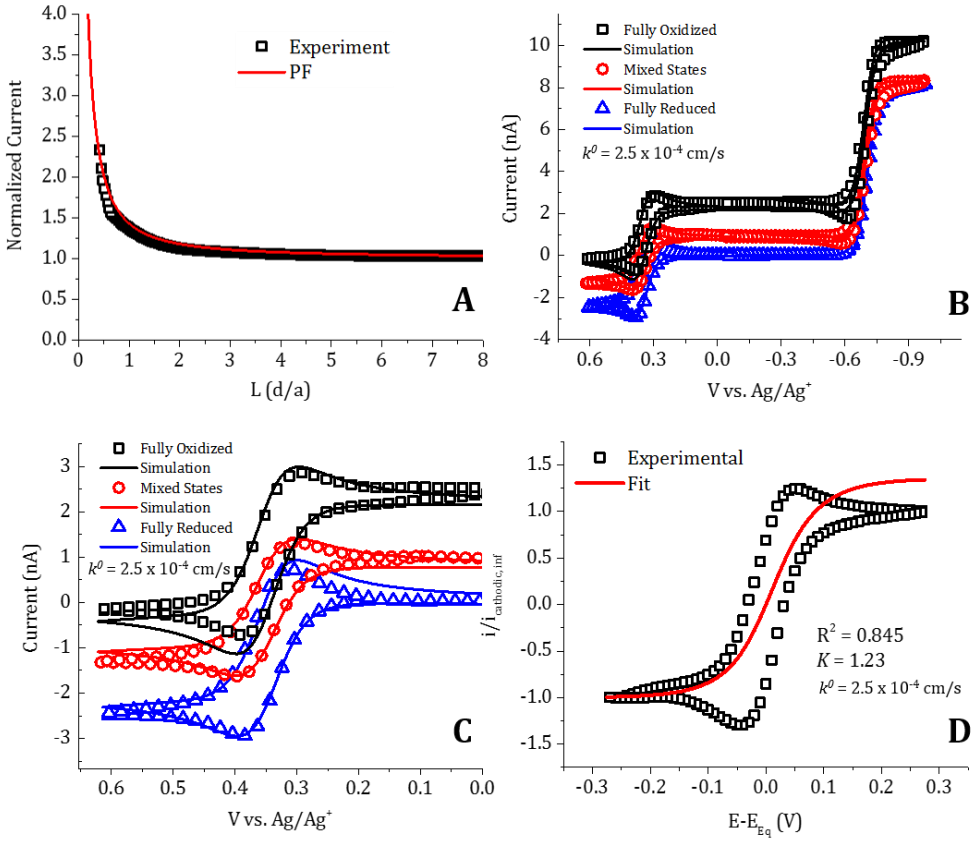

Figure 6.7. (A) SECM approach curve with a 12.5 µm tip with an R_g of 2 with 1.5 mM ethyl viologen diperchlorate in 0.1 M $TBAPF_6$ in acetonitrile to a 1.5 mm platinum disk substrate. Open symbols are experimental data points and the solid red line is a fitting to pure positive feedback conditions[24] to determine distance from substrate. Substrate was held at -0.3 V and the SECM tip was held at -1 V. (B) Cyclic voltammetry using a 12.5 µm radius electrode with ethyl viologen diperchlorate species and 20 mM PNS at scan rate of 20 mV/s in 0.1 M $TBAPF_6$ in acetonitrile. The fully reduced voltammogram was taken at infinite distance from the substrate with the substrate at open circuit. The fully oxidized voltammogram was taken at ~ 5 µm distance from the substrate with the substrate held at 0.7 V. The mixed state voltammogram was taken at ~ 5 µm distance from the substrate with the substrate held at 0.35 V. Open symbols are experimental data and solid lines represent the simulated model using DigiElch at the specified kinetic value. (C) Zoom in of (B). (D) Normalized steady state voltammetry of the mixed states presented in (C), with respect to the limiting cathodic and anodic currents as a function of overpotential with respect to the observed equilibrium potential. Open symbols are experimental data and solid red line represents the theoretical fit to kinetic model.

Upon analyzing the data in Table 6.1 and the voltammetry results in Figures 6.5-6.7 it is clear that the three tested RAP species are all chemically stable at bulk level concentrations in all

applicable oxidation states. Furthermore, the magnitude of redox kinetics does not appear to be dependent upon the oxidation state of the material, even if there are some small experimental uncertainties into the exact magnitude of the kinetics. This is an important conclusion to note, because if we assume that the value of k^0 is sufficiently rate limiting in the redox behavior of RAPs, then having the same limits in the forward and backward reactions is convenient. All of these RAPs are targeted for use in flow battery applications, in which the batteries are charge cycled via chronopotentiometric methods at constant current densities.[7] A such, having the same redox kinetics for both the charge and discharge reactions allows for consistent flow battery testing and data comparisons between cycles.

Finally, if we assume that the Mirkin method does provide a good gauge of the redox kinetics for RAPs, it is remarkable to observe that all of the tested RAPs have more or less the same value of redox kinetics on the order of ~ 10^{-4} cm/s. We have previously noted that RAP kinetics tend to suffer by orders of magnitude compared to their monomer constituents, despite them having the same redox active components because of complicated electrochemical pathways associated with a "CE" mechanism.[15] We have explored methods to improve the redox kinetics in viologen RAPs via structural tuning, but thus far have had limited success.[26] Intriguingly PNS, PAF, and VioRAP all contain redox active pendants that are known to be highly reversible redox mediators.[6] Yet, all of these RAPs appear to react at the same quasi reversible rates independent of molecular weight differences or chemical identity of the redox active groups. We are eager to postulate that this is the definitive k^0 that is possible with reversible RAPs. However, this conclusion requires more exploration before being ultimate.

In summary, developing theoretical models from the ground up that can describe the transient current functions of RAPs is imperative, as our ability to measure the redox kinetics of

RAPs with any electroanalytical method employed is presently limited. This is because all of the current electroanalytical models were empirically derived for small molecule systems, which may or may not accurately describe the reactivity of RAPs. This is an avenue our groups will be pursuing in the near future.

Conclusions

In order to increase the throughput of material screening and analysis in the development of novel soluble RAPs for use in energy storage applications, new tools are needed that minimize synthesized sample required. In this work, the substrate generation / tip collection mode of SECM was used to evaluate the bulk chemical and electrochemical reversibility of three different RAP species bearing viologen, ferrocene, and nitrostyrene redox active pendants. Although these RAPs have already been demonstrated in our laboratories as good candidates for use in flow batteries, this is the first time that they have been probed via SG/TC SECM methods to probe their degrees of chemical and electrochemical reversibility. Moreover, this work demonstrates the versatility of SG/TC SECM being extended to soluble macromolecular systems, something not previously established. SG/TC SECM kinetic analysis of RAPs largely agrees with earlier reports from our labs that utilized SECM feedback and rotating disk methods finding that redox kinetics in RAPs are quasi reversible despite their redox centers being known to have fast kinetics as monomers. This conclusion provides experimental flexibility to experimentalists evaluating RAPs, as there are several electroanalytical tools that can arrive at similar results. Finally, we explored the oxidation state dependency of redox kinetics and found that despite the structural complexity of solubilized RAP coils, in all oxidation states the redox kinetics are preserved.

References

1. Rugolo, J.; Aziz, M. J., *Energy Environ. Sci.*, **2012,** *5*, 7151-7160.

2. Mai, T.; Hand, M. M.; Baldwin, S. F.; Wiser, R. H.; Brinkman, G. L.; Denholm, P.; Arent, D. J.; Porro, G.; Sandor, D.; Hostick, D. J.; Milligan, M.; DeMeo, E. A.; Bazilian, M., *IEEE Trans. Sustain. Energy*, **2014,** *5*, 372-378.

3. Huang, Y.; Gu, S.; Yan, Y. S.; Li, S. F. Y., *Current Opinion Chem. Eng.*, **2015,** *8*, 105-113.

4. Darling, R. M.; Gallagher, K. G.; Kowalski, J. A.; Ha, S.; Brushett, F. R., *Energy Environ. Science*, **2014,** *7*, 3459-3477.

5. Nagarjuna, G.; Hui, J.; Cheng, K.; Lichtenstein, T.; Shen, M.; Moore, J. S.; Rodriguez-Lopez, J., *J. Am. Chem. Soc.*, **2014,** *136*, 16309-16316.

6. Burgess, M.; Moore, J. S.; Rodríguez-López, J., *Acc. Chem. Res.*, **2016,** *49*, 2649-2657.

7. Montoto, E. C.; Nagarjuna, G.; Hui, J.; Burgess, M.; Sekerak, N. M.; Hernández-Burgos, K.; Wei, T.-S.; Kneer, M.; Grolman, J.; Cheng, K. J.; Lewis, J. A.; Moore, J. S.; Rodríguez-López, J., *J. Am. Chem. Soc.*, **2016,** *138*, 13230-13237.

8. Janoschka, T.; Martin, N.; Martin, U.; Friebe, C.; Morgenstern, S.; Hiller, H.; Hager, M. D.; Schubert, U. S., *Nature*, **2015,** *527*, 78-81.

9. Allen J. Bard, Larry. R. Faulkner., *Electrochemical Methods: Fundamentals and Applications, 2nd Edition*. Wiley: **2000**.

10. Yu, Y.; Sun, T.; Mirkin, M. V., *Anal. Chem.*, **2016,** *88*, 11758-11766.

11. Sanchez-Sanchez, C. M.; Rodiriguez-Lopez, J.; Bard, A. J., *Anal. Chem.*, **2008,** *80*, 3254-3260.

12. Minguzzi, A.; Battistel, D.; Rodriguez-Lopez, J.; Vertova, A.; Rondinini, S.; Bard, A. J.; Daniele, S., *J. Phys. Chem. C*, **2015,** *119*, 2941-2947.

13. Cannan, S.; Cervera, J.; Steliaros, R. J.; Bitziou, E.; Whitworth, A. L.; Unwin, P. R., *Phys. Chem. Chem. Phys.*, **2011,** *13*, 5403-5412.

14. Polcari, D.; Dauphin-Ducharme, P.; Mauzeroll, J., *Chem. Rev.*, **2016,** *116*, 13234-13278.

15. Burgess, M.; Hernández-Burgos, K.; Simpson, B. H.; Lichtenstein, T.; Avetian, S.; Nagarjuna, G.; Cheng, K. J.; Moore, J. S.; Rodríguez-López, J., *J. Electrochem. Soc.*, **2016,** *163*, H3006-H3013.

16. Burgess, M.; Hernandez-Burgos, K.; Cheng, K. J.; Moore, J. S.; Rodriguez-Lopez, J., *Analyst*, **2016,** *141*, 3842-3850.

17. Lu, X.; Wang, Q.; Liu, X., *Anal. Chim. Acta*, **2007,** *601*, 10-25.

18. Kim, J.; Bard, A. J., *Anal. Chem.*, **2016,** *88*, 1742-1747.

19. Amemiya, S.; Bard, A. J.; Fan, F. R. F.; Mirkin, M. V.; Unwin, P. R., *Ann. Rev. Anal. Chem.*, **2008,** *1*, 95-131.

20. Mirkin, M. V.; Horrocks, B. R., *Anal. Chim. Acta*, **2000,** *406*, 119-146.

21. Gossage, Z. T.; Simpson, B. H.; Schorr, N. B.; Rodríguez-López, J., *Anal. Chem.*, **2016,** *88*, 9897-9901.

22. Mirkin, M. V.; Sun, T.; Yu, Y.; Zhou, M., *Acc. Chem. Res.*, **2016,** *49*, 2328-2335.

23. Sun, P.; Mirkin, M. V., *Anal. Chem.*, **2006,** *78*, 6526-6534.

24. Lefrou, C.; Cornut, R., *Chemphyschem*, **2010,** *11*, 547-556.

25. Wang, Y.; Frasconi, M.; Liu, W.-G.; Sun, J.; Wu, Y.; Nassar, M. S.; Botros, Y. Y.; Goddard, W. A.; Wasielewski, M. R.; Stoddart, J. F., *ACS Cent. Sci.*, **2016,** *2*, 89-98.

26. Burgess, M.; Chénard, E.; Hernández-Burgos, K.; Nagarjuna, G.; Assary, R. S.; Hui, J.; Moore, J. S.; Rodríguez-López, J., *Chem. Mater.*, **2016,** *28*, 7362-7374.

Chapter 7: Future Directions

Notes and Acknowledgements

This chapter contains content pertaining to in progress research and some material from a review article that was published in the journal *Accounts of Chemical Research* with authors Burgess, M.; Moore, J. S.; Rodríguez-López, J. "Redox Active Polymers as Soluble Nanomaterials for Energy Storage". **2016,** 49, 2649–2657. M.B. performed all of the experiments, helped write the document, helped do data analysis, and made figures. The cited text and figures are reprinted with the permission of the publisher and is available from http://www.pubs.acs.org and using DOI: 10.1021/acs.accounts.6b00341. This work was supported as part of the Joint Center for Energy Storage Research, an Energy Innovation Hub funded by the U.S. Department of Energy, Office of Science, Basic Energy Sciences. M.B. acknowledges support by the National Science Foundation Graduate Research Fellowship Program under Grant No. DGE-1144245. J.R.L acknowledges additional support from a Sloan Foundation fellowship. Dr. Nagarjuna Gavvallappali, Kevin J. Cheng, and Elena Montoto have synthesized some samples that are tested. Zachary Gossage and Jingshu Hui assisted in creating monolayer samples for electrochemical testing.

Abstract

Beyond exploring redox active polymers (RAPs), a new class of macromolecular architecture in the form of redox active colloids (RACs) offers new challenges in understanding long range charge transport and energy storage within cross linked spherical polymer particles. Single particle interrogations utilizing scanning electrochemical microscope (SECM) and atomic force microscope (AFM) methods can help shed light on the efficiencies of charge storage and mechanical properties of these particles. Additionally, extending the application of SECM

feedback studies to utilize RACs as solution phase redox mediators aids in the development of new models to describe redox cycling of large polymeric materials between electrodes. Moreover, SECM imaging using RACs as mediators is a promising direction to advance a novel type of electrochemical imaging of porous substrates relying on size-exclusion of RACs.

Future Direction #1: Electrochemical and Mechanical Interrogations of Individual Redox Active Colloids

While we have largely been successful in employing RAPs in operating size exclusion non-aqueous redox flow batteries,[1] characterizing their electrochemical mechanisms,[2,3] and probing their solution dynamics, it is unclear whether or not RAPs will be the first choice of energy material moving forward. Recently, our groups have reported on a second generation material in the form of redox active colloids (RACs), soluble crosslinked spherical polymer particles, as discrete energy storage carriers.[1] RACs have many advantageous characteristics compared to RAPs which make them attractive materials for use in next generation size exclusion flow batteries.

Like RAPs, RACs have similar molecular structures and can be synthesized to have the same redox active pendants. However, unlike RAPs, RACs are monodisperse in size which makes selecting porous separators for size exclusion simpler. Monodispesity can inherently lead to less crossover of active material between storage containers in a flow battery arrangement, provided an appropriate pore size is chosen.[4] Beyond the monodispersity of RACs, is their size magnitude in terms of hydrodynamic radii. RACs are synthesized via dispersion or emulsion polymerization protocols,[1] which can be tweaked to modulate the particle size in the range of tens of nanometers to several microns in diameter.[1] At the size limit of several microns, RACs are easily rejected from crossing over unassuming materials such as common laboratory filter paper. This opens up new

low cost pathways to redox flow batteries, where expensive designer membranes are not required for a battery separator.[5,6] Instead, inexpensive off the shelf common materials can fulfill this role.

One of the most remarkable features of RACs is that they can be completely bulk electrolyzed with quantitative charge access, despite their rigid cross linked structure that only allows the outer surface of the particle to ever come into contact with an electrode surface. Charge access into the core of the particles is only possible through charge diffusion mechanisms, via a pathway that is still not completely understood. Efficient charge diffusion is definitively occurring within RAC particles, but it is not known if this process follows a conduit similar to ones seen in other energy materials. For example, lithium iron phosphate particles have been labeled with several different charging mechanism models including a shrinking core, reaction migration, or domino cascade. [7,8,9] First attempts at describing charge diffusion in RACs have employed scanning electrochemical microscopy (SECM) to interrogate single RAC particles. This experiment is schematized in Figure 7.1.

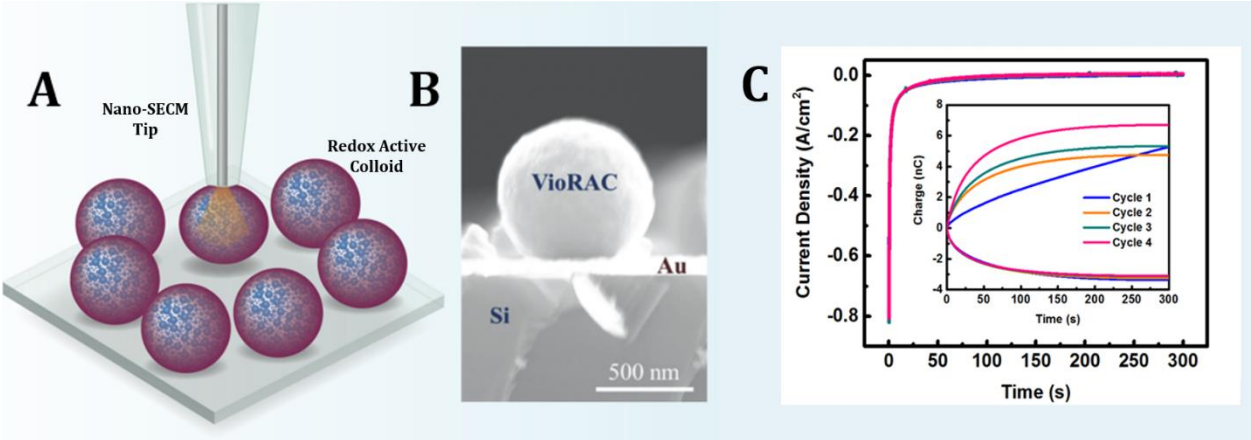

Figure 7.1. (A) Schematic representation of the electrochemical interrogation of a single ~800 nm diameter RAC by means of contact via a nano-SECM tip. (B) SEM image of an ~800 nm diameter viologen RAC (VioRAC) from the side. (C) Charging transient from nanoelectrolysis of RACs. Inset shows the charging/discharging electrolysis profiles over several cycles. Figures are adapted with permission from reference 1. Copyright (2016) American Chemical Society.

Here, a nano-SECM tip makes electrical contact via an approach curve with an 800 nm diameter viologen RAC that is resting on top of an insulating glass surface. Upon contact, the nano-SECM tip can probe the reactivity of the particle via cyclic voltammetry or chronoamperometic steps which have the possibility to completely charge/discharge the material. Chronoampermoetric steps with these single particles is a "nano-bulk electrolysis" and allows us to probe the energy storage capabilities of RACs. This experiment is shown in Figure 7.1C. The RACs via nano-electrolysis stored charge reversibly and with high Coulombic efficiency over several cycles. These measurements provide a gauge of the accessible current densities for RACs (0.8 A/cm^2) via the fully reproducible anodic steps. We believe the effective transport of charges within RACs is the result of the increased surface area and swelling of the particle, which enhances counterion diffusion within. Direct titration of RACs and their monolayers yielded redox active species concentrations in the molar range, highlighting the potential of high energy capacity in these nanomaterials.[1] Single-entity SECM experiments and corroborating fine element modeling currently ongoing in our lab will further contribute to reliably probing the effect of supporting electrolyte, molecular structure, and solvent on the charge diffusion properties within polymer particles.

The utility of SECM to probe individual redox active nanostructures is unique amongst electrochemical platforms, but there are limitations in using only this technique to underpin charge diffusion pathways or discern other material properties about RACs. Because SECM is an electrochemical modality, the ability to infer information about the studied sample is typically limited to measurements of current or voltage, which in the case of Figure 7.1, is also without spatial resolution. Moreover, a common critique of performing SECM experiments at the nanoscale is that fabricating suitable SECM tips with a high success rate is still a significant

challenge and remains more of an art than a science.[10] Another approach that can potentially discern other information for single particles during electrochemical measurements, such as mechanical properties, employs atomic force microscope (AFM) technologies.

AFM methods are expedient because it is not an experimental issue for the tip to hit the surface. With many nano-SECM tips, operating in the standard constant height mode can cause the tip to hit the surface of an unleveled substrate which easily breaks the electrode because of their extreme fragility. In contrast, many of the operational modes of AFM actually require for the tip to directly come in contact with the surface as a feedback mechanism. Additionally, most AFM tips inherently have better spatial resolution than the majority of SECM electrodes because AFM cantilevers have nano-dimensioned apexes. Moreover, pre-fabricated AFM cantilevers can be purchased from commercial sources.

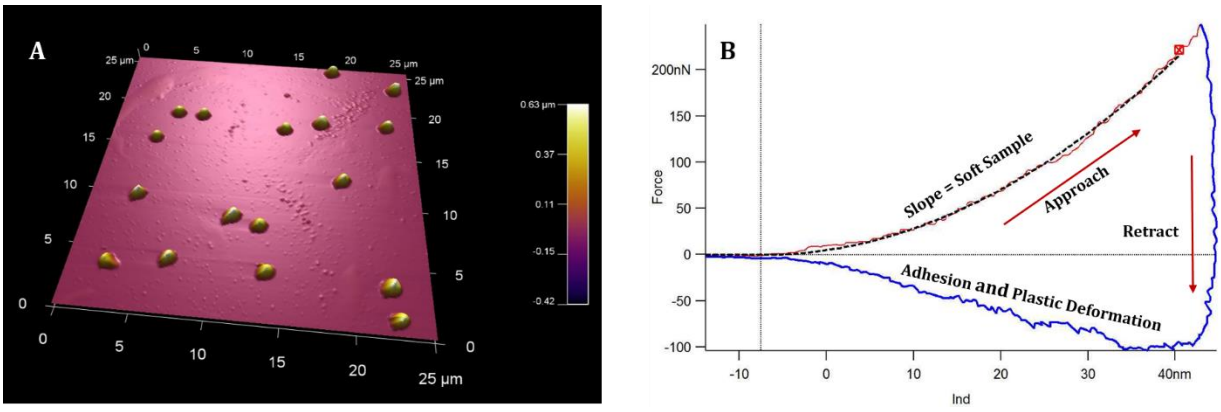

Figure 7.2. (A) AFM tapping mode image of the topography of ~800 nm diameter viologen RACs randomly distributed on a glass microscope slide surface. (B) AFM force curve to a single viologen RAC in (A). The red line is the approach curve, and blue line is the subsequent retraction. Dotted line for approach curve is a theoretical fit to a model to determine the Young's modulus of the RAC particle.

Preliminary AFM measurements of large ~800 nm diameter viologen RACs are shown in Figure 7.2. These RACs were placed on a glass substrate after drop casting a dilute (0.5 mM)

solution of RACs in acetonitrile. After evaporation, the RACs are left behind on the glass surface and without any further sample preparation these substrates can be analyzed by AFM. Figure 7.2A shows a topographic image taken in tapping mode using a standard SiN AFM cantilever of the RAC covered glass surface. As these RAC particles are fairly large, AFM imaging can easily detect them randomly distributed across the surface. Moreover, the AFM image provides a secondary confirmation that RAC particles are in fact monodisperse in size as the width and height profiles of all the particles are nearly identical and correspond well to images taken with electron microscopy methods.[1] A force curve to a single RAC particle is shown in Figure 7.2B. The shape of this force curve is indicative of a "soft" surface which can deform under the force from the cantilever. The ensuing retraction of the cantilever displays that the particle also has some adhesion qualities. Fitting of this force approach curve to existing models finds that the RAC particle in its dry state has a Young's modulus of 0.186 GPa. This Young's modulus is similar to low-density polyethylene,[11] which is not surprising given that RACs are also a polymeric material whose composition is very similar to latex.

Ensuing AFM studies of RACs will transition to being in *in-situ* solvent conditions, so that the mechanical properties of the RACs can be examined as a function of different charge states of the particles during electrochemical measurements. While there are reported examples of hybrid AFM-SECM techniques which could potentially evaluate individual RAC particles electrochemically in a similar manner as Figure 7.1, this modality is plagued by highly complex AFM-SECM tip fabrication and data analysis procedures that have limited the adoption of this method beyond highly specialized labs.[12] A conceivably simpler means of probing the Young's modulus of the RACs during electrochemical interrogations is placing the RACs on top of a conductive substrate to make electrical contact, and then performing force curves using standard

AFM tips to individual RACs during electrochemical measurements activated by the conductive substrate.

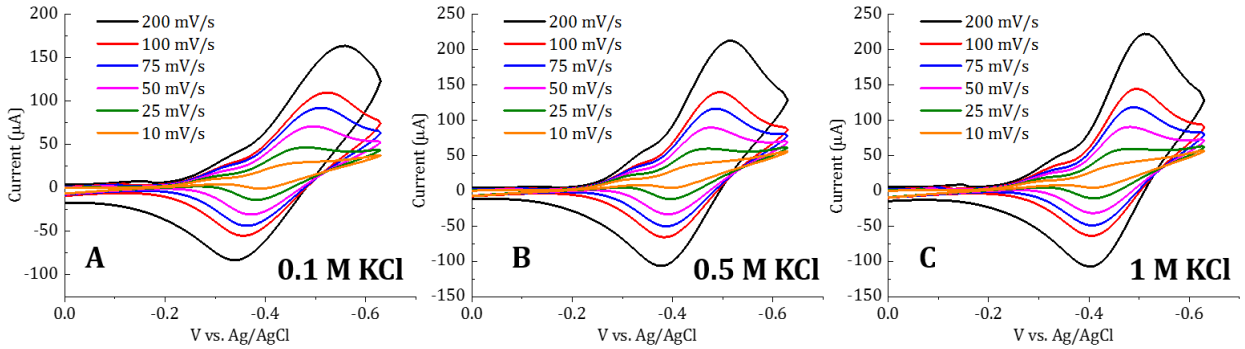

Figure 7.3. (A) Cyclic voltammetry at a series of scan rates for a gold electrode coated in a monolayer of 60 nm diameter viologen RACs in water at 100 mM concentration of KCl. (B) Cyclic voltammetry at a series of scan rates for a gold electrode coated in a monolayer of 60 nm diameter viologen RACs in water at 500 mM concentration of KCl. (C) Cyclic voltammetry at a series of scan rates for a gold electrode coated in a monolayer of 60 nm diameter viologen RACs in water at 1000 mM concentration of KCl.

To facilitate these proposed AFM studies, we employ previously demonstrated water-air methods to deposit RAC layers on top of a conductive gold surface. This technique has been shown to form close packed monolayer structures of RACs.[1] Preliminary electrochemical testing of a monolayer sample of 60 nm viologen RAC demonstrates that the RACs are electrochemically addressable in both water and non-aqueous environments. Interestingly, even though the reactivity of soluble RAPs was strongly linked to the supporting electrolyte concentration, as outlined in Chapter 5, supporting electrolyte concentration dependency studies of RAC monolayers do not have the same conclusions. As shown in Figure 7.3, besides changes in the resistivity in the cell from changing the background electrolyte concentration between 100 mM and 1 M, there are no appreciable differences in the voltammetry experiments with monolayers of RACs. This is likely because the RACs have more structural rigidity than their RAP counterparts, due to their

crosslinking, which does not allow their conformation to significantly change. However, ultimate conclusions about mechanical properties of RACs when immersed in solvent and during electrochemical measurements requires more studies. Of yet, the mechanical properties of RAC samples have not been evaluated when the sample is wetted with solvent, or as a function of state of charge of the particle. Determining these parameters, and correlating them with single particle electrolysis measurements will be the specific focus of Future Direction #1

Future Direction #2: Utilizing Redox Active Colloids as Mediators in Scanning Electrochemical Microscopy Feedback Measurements and Imaging

As outlined in Chapter 2, reliably utilizing RAPs as mediators in SECM feedback experiments is challenging, and fitting of entire SECM approach curves to any existing models was not possible.[2] To a large extent, this same conclusion is reached when trying to perform an SECM feedback approach curve using dispersed RACs as a redox mediator. After first reliably determining distance from a substrate with a ferrocene probe via uncomplicated positive feedback, an attempt at measuring an SECM approach curve to the exact same location with a 90 nm radius viologen RAC is shown in Figure 7.4. Like RAPs, an approach curve with RACs manifests as mostly negative feedback until small separation distances ($L < 1$) between substrate and tip, even after ensuring to move the SECM tip towards the substrate slow enough to allow for diffusional round trips between tip and substrate.[2] Unfortunately, this approach curve cannot be fit to any existing SECM feedback theories.

One potential explanation for the difficulty in observing straightforward positive feedback with both RAPs and RACs, beyond adsorption of the species onto the tip as discussed in Chapter 2, requires us to consider the hydrodynamic radius of these macromolecular structures. While it is the case that small molecule redox probes such as ferrocene can capably cycle between an SECM

tip and substrate because of fast diffusion and efficient redox kinetics, another factor that can make rapid redox cycling possible is the relatively small molecular size of ferrocene molecules compared to RAPs and RACs. In terms of hydrodynamic radii, RAPs are known to have sizes larger than 10 nm and RACs can be as large as microns, which are considerably larger than small redox probes such as ferrocene. Importantly, the hydrodynamic radii of individual RACs or RAPs has the possibility to be significant fractions of the size of the SECM electrode itself. This may require us to consider the hydrodynamic radii of these structures in SECM feedback loops, beyond just slower effective diffusion coefficients.

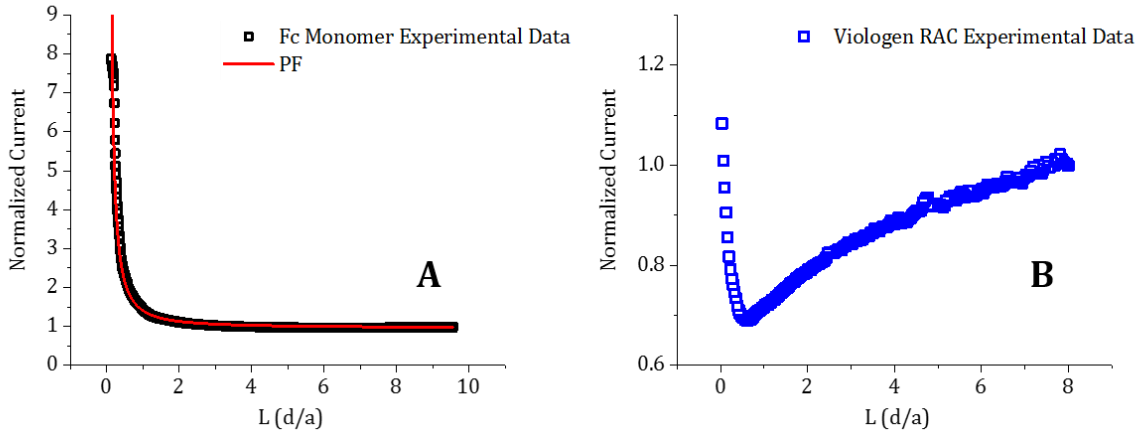

Figure 7.4. (A) SECM approach curve for the oxidation of ferrocene using a 12.5 µm radius electrode. Approach curve is measured in a solution containing 1 mM ferrocene and 5 mM of 90 nm radius viologen RAC particles in 0.1 M $TBAPF_6$ electrolyte in acetonitrile. The substrate is a 1.5 mm diameter platinum disk that is held at -0.3 V vs Ag/Ag^+. Open symbols are experimental data points and the red line is a fit to positive feedback (PF) theory from Cornut and Lefrou. (B) Subsequent SECM approach curve to the same location for the first reduction of viologen RAC using the conditions described in (A).

When trying to perform redox cycling with RAPs or RACs in the space between an SECM tip and substrate, it may be possible that RAPs or RACs actually collide with one another, akin to the self-avoiding random walk process seen in excluded volumes in polymer coils in non-theta solvents. Moreover, it may also be possible that when RAPs and RACs collide with one another

they may exchange some of their charge. If this were to happen, then the effective concentration of injected charges on any one chain or particle would be diluted. If exchange reactions between RACs are occurring, this could decrease the enhancement of the redox signal deriving from positive feedback from a particle. The envisioned SECM positive feedback loop with RAPs or RACs, with added complications such as particle collisions, is schematized in Figure 7.5. Here, RACs are proposed to elastically collide like billiards balls, whereby a RAC hitting another RAC can send it off course.

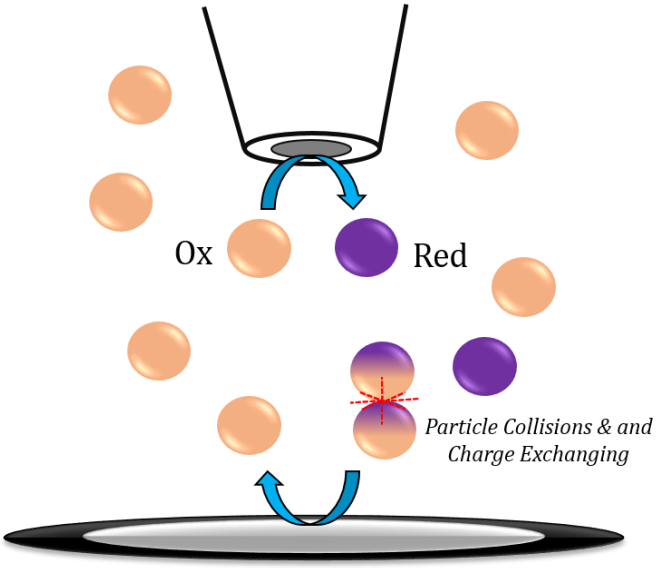

Figure 7.5. Schematized vision of an SECM feedback loop with RACs as solution phase mediators that is complicated by RAC particle effects. The positive feedback loop between *Ox* and *Red* forms of the RAC is interrupted in efficiency from collisions with other RACs in solution. Additionally, colliding RACs can exchange charges via a charge diffusion pathway in order to balance out states of charge between particles.

Although our hypothesized feedback loop with RACs requires more evidence to claim as definitive, if we assume the model in Figure 7.5 is an accurate depiction of physical reality, then there are natural conclusions that can be made. First, it is expected that decreasing the concentration of RACs within the cell would decrease the number of RAC collisions and

potentially improve the positive feedback efficiency. It may not be enough to simply operate beneath a critical bulk concentration for polymer solutions termed the overlap concentration (C^*), which can be measured from viscometric techniques as demonstrated in Chapter 5. The positive feedback process in SECM inherently gives rise to an effective higher concentration of active species under the tip via redox cycling. This redox cycling could push the local concentration of RACs to be above the overlap concentration, which could require significant optimization to avoid. Another strategy to decrease the frequency of collisions for RACs in solution between the tip and substrate is to decrease the size of the SECM tip to the nanoscale. A smaller SECM tip characteristically decreases the separation distance between tip and substrate during feedback events, because for any specified value of normalized distance (L) this distance is smaller in magnitude for a nano-electrode than a microelectrode. Both of these strategies are currently being tested in detail, but preliminary data is highlighted below.

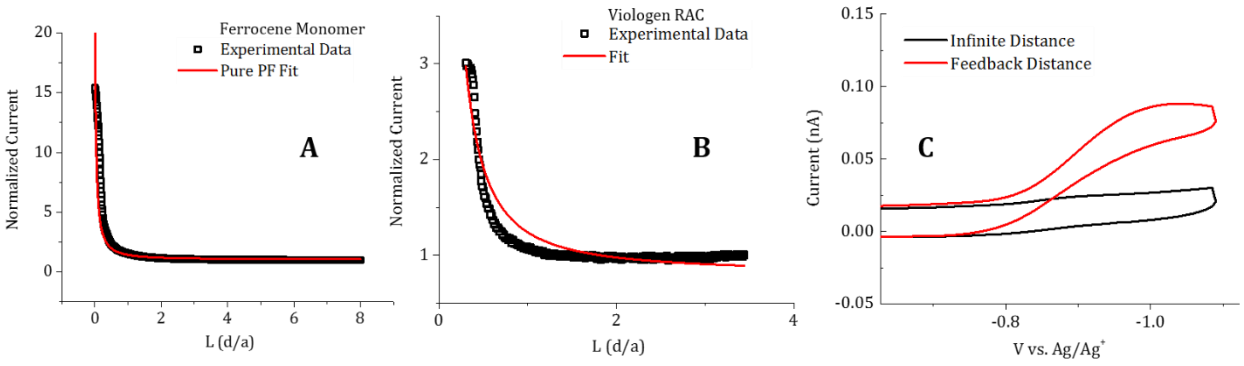

Figure 7.6. (A) SECM approach curve for the oxidation of ferrocene using a 12.5 µm radius electrode. Approach curve is measured in a solution containing 20 nM of 90 nm radius viologen RAC particles in 0.1 M $TBAPF_6$ electrolyte in acetonitrile and 1 mM ferrocene. The substrate is a 1.5 mm diameter platinum disk that is held at -0.3 V vs Ag/Ag^+. Open symbols are experimental data points and the red line is a fit to feedback theory from Cornut and Lefrou. (B) SECM approach curve for the first reduction of viologen RAC using the conditions described in (A). (C) Cyclic voltammograms taken at 20 mV/s far away from a substrate and nearby after the approach curve taken in (A).

The case of performing SECM approach curves with a traditional microelectrode (12.5 µm radius) in the presence of a highly diluted (20 nM) solution of 90 nm viologen RAC is shown in

Figure 7.6. Here, quantitative distance control between the SECM tip and substrate is again determined with a small molecule ferrocene probe. Afterwards, an approach curve is performed at a slower speed to the same location using the viologen RAC as redox mediator. Even though the approach curves in Figures 7.4B and 7.6B were performed at the same motor speed, comparing these curves shows that diluting the concentration of RAC does improve the clarity of positive feedback and the ability to fit the approach curve to standard SECM feedback theory. A concentration of 20 nM for the viologen RAC is sufficiently dilute that detecting this species via voltammetry when the SECM tip is placed far away from the substrate is nearly below the detection limit for the probe, Figure 7.6C. Yet, when close to the surface, the viologen RAC signal is now detectable because of efficient redox cycling between the tip and substrate. This signal corresponds to the known potential for the first reduction of the viologen redox couple inside of the RAC.

Intriguingly, even in very dilute solutions of RACs, we have never observed discrete events pertaining to collisions of RACs at the electrode during any electrochemical measurement, transient or steady state. Collisions of redox species at a microelectrode surface have been shown to manifest as current spikes or "blips" during transient measurements.[13] As a first approximation, we expected RACs to behave similarly to other electrochemical systems, such as emulsion droplets, that have been analyzed on the single entity level via electrode collisions. We hypothesize that slow intraparticle charge diffusion in RACs is the underlying cause for not observing current spikes from single particle collisions. However, this hypothesis requires more detailed investigation to be certain.

Further evidence that the hypothesized feedback loop in Figure 7.5 may be dominating the SECM feedback response of RACs is shown in Figure 7.7 via an SECM approach curve with a nano-electrode. Here, an approach curve was measured curve in a semi-dilute (250 μM) solution

of 90 nm viologen RAC with a Wollaston SECM tip that has a 300 nm radius Pt disk electrode. Inspecting the approach curve in Figure 7.6 shows the degree of positive feedback and the ability for the approach curve to be fit to standard feedback theory is high. It is clear that decreasing the concentration of RAC as active species and scaling the SECM electrode radius to the nanoscale both pay large dividends in improving SECM feedback measurements when using RACs as mediators.

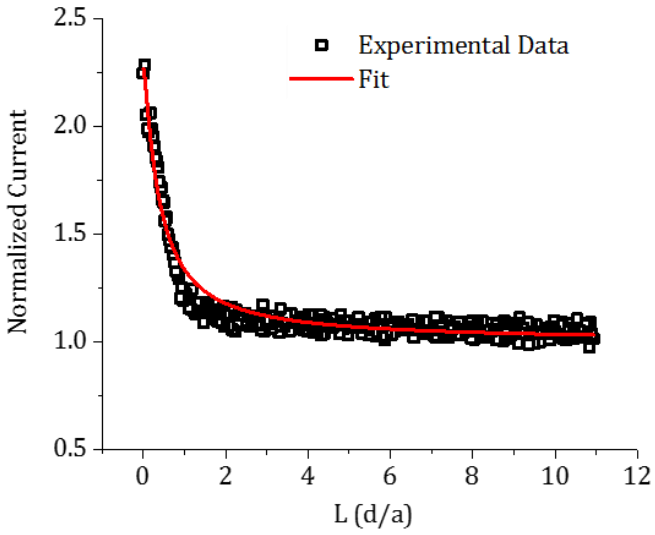

Figure 7.7. SECM approach curve for the first reduction of a viologen RAC using a Wollaston electrode with a 300 nm radius platinum disk. Approach curve is measured in a solution containing 250 µM of 90 nm radius viologen RAC particles in 0.1 M $TBAPF_6$ electrolyte in acetonitrile and 1 mM ferrocene. The substrate is a 1.5 mm diameter platinum disk that is held at -0.3 V vs Ag/Ag^+. Open symbols are experimental data points and the red line is a fit to feedback theory from Cornut and Lefrou using an R_g of 16.

As some of the basic experimental conditions have been identified for improving the efficacy of using RACs as mediators in SECM feedback studies, ongoing and future efforts will be focused on developing models and performing unique imaging experiments. Specifically, finite element modeling of SECM approach curves with redox mediators that have a defined size and shape could aid in the development of new models, or the augmentation of existing theories, to

accurately describe feedback processes with macromolecular redox structures. Of yet, no SECM theory has strictly considered the possibility for particle collisions or charge hopping between particles on the shape of an SECM approach curve. Moreover, modeling macromolecular redox mediators with a defined size in SECM studies, beyond diminished diffusion coefficients, could provide crucial insight into the behavior of redox cycling of large particles between electrodes. Having a comprehensive theory that explains the feedback modes of RACs or similar macromolecular structures is imperative to develop so that SECM imaging using RACs as mediators can be interpreted quantitatively.

We envision using RACs as SECM redox mediators in applications of imaging porous substrates with well-defined pores on the nanoscale. An example of this type of substrate sample are metallic plates that have been anodically corroded to form a surface of uniform pores.[14,15] As the feedback signal in SECM is directly related to the tip substrate separation distance, quantifiably interpreting SECM feedback data over porous substrates has proved challenging and requires special considerations.[16,17] This is because there is the possibility for traditional small molecule redox mediators to become trapped in the pores which can artificially diminish the observed feedback rate. While there are reported SECM formulations that have been developed to account for bulk porosity in a substrate, they typically offer no specific information about the actual pore size. Moreover, these methods have thus far been applied as single approach curves to a specific substrate location and have not been demonstrated on a larger scale to produce a "porosity map" over a heterogeneous surface. A porosity map could conceivably be generated using SECM protocols developed in our laboratory,[18,19] whereby an image is produced by performing an approach curve at every pixel in the image and successively fitting every approach curve for

porosity parameters. However, this method is low throughput and requires extensive *ex-situ* data analysis protocols.

A potentially simpler means of discerning comparable information from a porous substrate, with the added ability to monitor the time dependent evolution of porosity with spatial resolution, could use a similar approach we have used in size-exclusion redox flow batteries. Specifically, RACs could be rejected by size from entering the pores of a substrate when the pore size is similar to the diameter of the RACs. In this way, a standard potentiostatic SECM image of the substrate could be taken using RACs as mediators to directly discriminate between locations on a substrate that are lower in height or porous. To date, there have been no reports of using size exclusion to generate a reactivity image of a substrate via SECM. As such, this area is wide open for possibilities and ripe for experimental creativity in the development of this new mode of SECM imaging. These efforts will constitute one of the primary focuses of Future Direction #2.

Conclusions

As outlined in the preceding chapters, many of the fundamental properties and electrochemical dynamics of soluble ferrocene, viologen, and nitrostyrene based RAPs have been thoroughly investigated. This has included characterizing aspects such as their charge transfer mechanisms, exploring structure function relationships, and probing electrostatic interactions. This body of work constitutes a push towards characterizing redox active macromolecular structures beyond film modified electrode surfaces, a direction that still very much in its infancy. Overall, it is clear that designing new RAPs with improved performance or examining next generation materials such as RACs requires further measurements from a multi-faceted approach to underpin the particulars of macromolecular redox activity. Moving forward, advanced measurements and chemical modeling have the possibility to probe polymer particles on the single entity level and

will help shine light on the intricacies of electrochemical pathways for these complex materials. This information will aid in the formation of new concepts to strengthen the link between fields of research pertaining to polymer solution dynamics, and ones concerning electroanalytical examination. Likewise, the development of new measurement protocols utilizing the scanning electrochemical microscope could increase the throughput of screening of next generation RAP materials for use in redox flow batteries and provides new avenues for unique electrochemical imaging of porous substrates relying on size-exclusion of RACs.

References

1. Montoto, E. C.; Nagarjuna, G.; Hui, J.; Burgess, M.; Sekerak, N. M.; Hernández-Burgos, K.; Wei, T.-S.; Kneer, M.; Grolman, J.; Cheng, K. J.; Lewis, J. A.; Moore, J. S.; Rodríguez-López, J., *J. Am. Chem. Soc.*, **2016,** *138*, 13230-13237.

2. Burgess, M.; Hernández-Burgos, K.; Simpson, B. H.; Lichtenstein, T.; Avetian, S.; Nagarjuna, G.; Cheng, K. J.; Moore, J. S.; Rodríguez-López, J., *J. Electrochem. Soc.*, **2016,** *163*, H3006-H3013.

3. Burgess, M.; Chénard, E.; Hernández-Burgos, K.; Nagarjuna, G.; Assary, R. S.; Hui, J.; Moore, J. S.; Rodríguez-López, J., *Chem. Mater.*, **2016,** *28*, 7362-7374.

4. Casassa, E. F., *J. Polym. Sci. Part B Polym. Lett.*, **1967,** *5*, 773-778.

5. Shin, S. H.; Yun, S. H.; Moon, S. H., *RSC Adv.*, **2013,** *3*, 9095-9116.

6. Darling, R.; Gallagher, K.; Xie, W.; Su, L.; Brushett, F., *J. Electrochem. Soc.*, **2016,** *163*, A5029-A5040.

7. Delmas, C.; Maccario, M.; Croguennec, L.; Le Cras, F.; Weill, F., *Nat. Mater.*, **2008,** *7*, 665-671.

8. Laffont, L.; Delacourt, C.; Gibot, P.; Wu, M. Y.; Kooyman, P.; Masquelier, C.; Tarascon, J. M., *Chem. Mater.*, **2006,** *18*, 5520-5529.

9. Dedryvere, R.; Maccario, M.; Croguennec, L.; Le Cras, F.; Delmas, C.; Gonbeau, D., *Chem. Mater.*, **2008,** *20*, 7164-7170.

10. Gossage, Z. T.; Simpson, B. H.; Schorr, N. B.; Rodríguez-López, J., *Anal. Chem.*, **2016,** *88*, 9897-9901.

11. Ladizesky, N. H.; Ward, I. M., *J. Macromol. Sci. Phys.*, **1971,** *B 5*, 661-692.

12. O'Connell, M. A.; Wain, A. J., *Anal. Methods*, **2015,** *7*, 6983-6999.

13. Li, Y.; Deng, H. Q.; Dick, J. E.; Bard, A. J., *Anal. Chem.*, **2015,** *87*, 11013-11021.

14. Syrek, K.; Zych, M.; Zaraska, L.; Sulka, G. D., *Electrochim. Acta*, **2017,** *231*, 61-68.

15. Zaraska, L.; Syrek, K.; Hnida, K. E.; Bobruk, M.; Krzysik, A.; Lojewski, T.; Jaskula, M.; Sulka, G. D., *Electrochim. Acta*, **2016,** *205*, 273-280.

16. Kuss, C.; Payne, N. A.; Mauzeroll, J., *J. Electrochem. Soc.*, **2016,** *163*, H3066-H3071.

17. Dauphin-Ducharme, P.; Kuss, C.; Rossouw, D.; Payne, N. A.; Danis, L.; Botton, G. A.; Mauzeroll, J., *J. Electrochem. Soc.*, **2015,** *162*, C677-C683.

18. Barton, Z. J.; Rodriguez-Lopez, J., *Anal. Chem.*, **2017,** *89*, 2708-2715.

19. Barton, Z. J.; Rodriguez-Lopez, J., *Anal. Chem.*, **2017,** *89*, 2716-2723.

Appendix A: Supporting Information File for Chapter 2

Notes and Acknowledgements

This appendix appeared in its entirety in the *Journal of The Electrochemical Society* with authors Burgess, M.; Hernández-Burgos, K.; Simpson, B. H.; Lichtenstein, T.; Avetian, S.; Nagarjuna, G.; Cheng, K. J.; Moore, J. S.; Rodríguez-López, J. "Scanning Electrochemical Microscopy and Hydrodynamic Voltammetry Investigation of Charge Transfer Mechanisms on Redox Active Polymers". **2016,** 163, H3006-H3013. This Supporting Information file is reprinted with the permission of the publisher and is available from http://www.jes.ecsdl.org and using DOI: 10.1149/2.0021604jes. M.B. performed all of the SECM analysis, helped write the manuscript, made figures, and helped perform the RDE studies This work was supported as part of the Joint Center for Energy Storage Research, an Energy Innovation Hub funded by the U.S. Department of Energy, Office of Science, Basic Energy Sciences. Jingshu Hui assisted in performing AFM analysis of the RAP film thickness. M.B. acknowledges support by the National Science Foundation Graduate Research Fellowship Program under grant No. DGE-1144245.

General Information

^{1}H spectra were recorded on Varian Unity 500, and VXR 500 spectrometers. Infrared spectra (percent transmittance) were acquired on a Nicolet Nexus 670 FT-IR spectrometer with an ATR-IR attachment. UV-Vis absorption spectra were recorded on Perkin Elmer and Shimadzu instruments. Elemental analyses were performed on the following instruments: CHN analysis - Exeter Analytical CE 440 and Perkin Elmer 2440, Series II; ICP analysis - ICP-MS and ICP-OES; Halide analysis - Titration & ISE.

Unless otherwise stated, all starting materials and reagents were purchased from Sigma-Aldrich or Matrix Scientific and used without further purification. Poly(vinylbenzyl chloride) (over 90% are 4 substituted) of 82 kDa (PDI: 1.6) was purchased from Polymer Source.

Ferrocene RAP (PAF)

Dry DMF (15 mL) was added to a flask containing PVBC (1.00 g, 6.55 mmol) and (dimethylaminomethyl)ferrocene (7.5 g, 32.8 mmol) under nitrogen. Reaction mixture was stirred at RT for 1 day. Concentrated solution of ammonium hexafluoro phosphate (4 g) solution was prepared in water and added to the above reaction mixture. The resultant solution was stirred at room temperature for 1 day. The collected polymer was precipitated from acetone into H_2O twice. Then the polymer is reprecipitated once into methanol and finally into diethyl ether twice. Polymers were dried under high vacuum for 24 h. ^{1}H NMR were recorded in CD_3CN. (^{1}H NMR, ATR-IR, and elemental analyses).

Scheme A.1 Synthetic pathway for making PAF

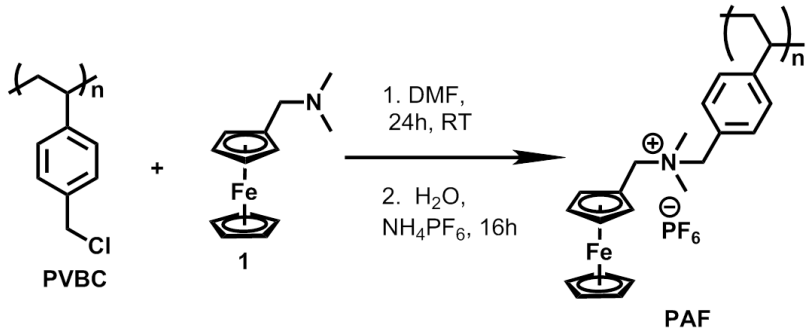

PVBC Mn (kDa)	PDI
82	1.6

PAF Mn (kDa)
271

$Dp_{PVBC} = Mn_{PVBC} / 152.62$ Da

$Mn_{PAF} = Dp_{PVBC} \times 505.27$ Da

Redox Active Polymer Characterization

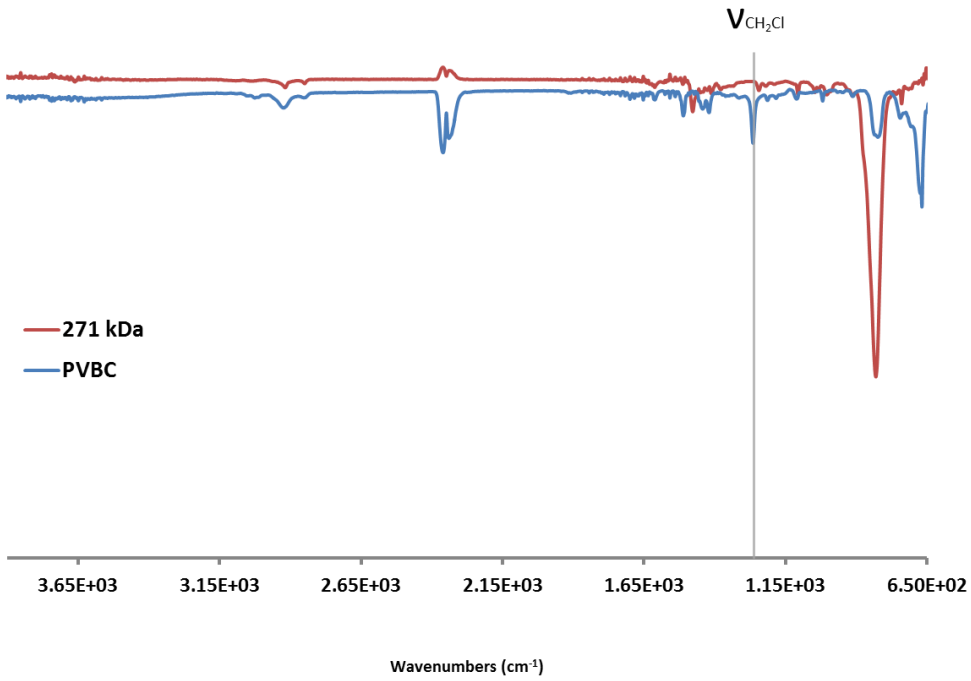

Figure A.1. ATR-IR spectra of 271 kDa ferrocene RAP in red, unfunctionalized PVBC in blue.

Table A.1 Elemental (C, H, N) analysis of 271 kDa Ferrocene RAP

	Element	**C**	**H**	**N**
271 kDa Ferrocene RAP	Theoretical (%)	52.3	5.19	2.77
	Experimental (%)	51.57	5.32	3.79
	Difference	0.73	-0.13	-1.02

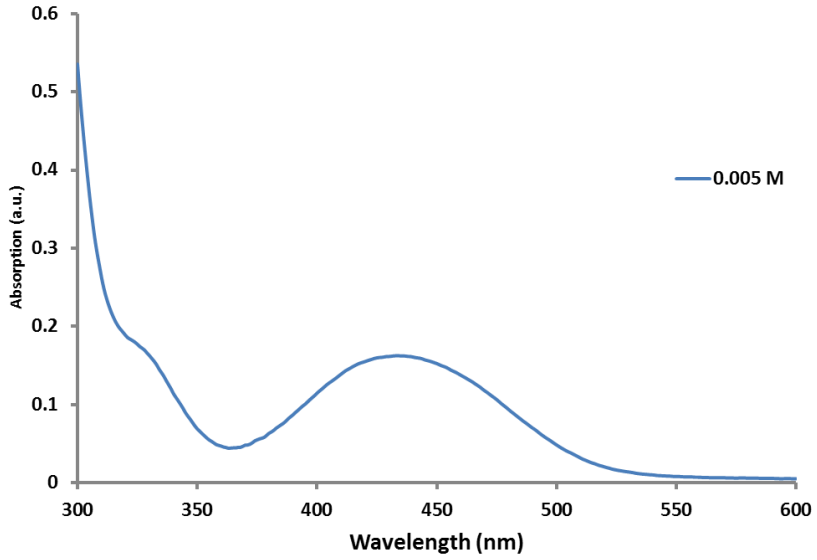

Figure A.2. Absorbance spectra of 5 mM 271 kDa ferrocene RAP M in acetonitrile.

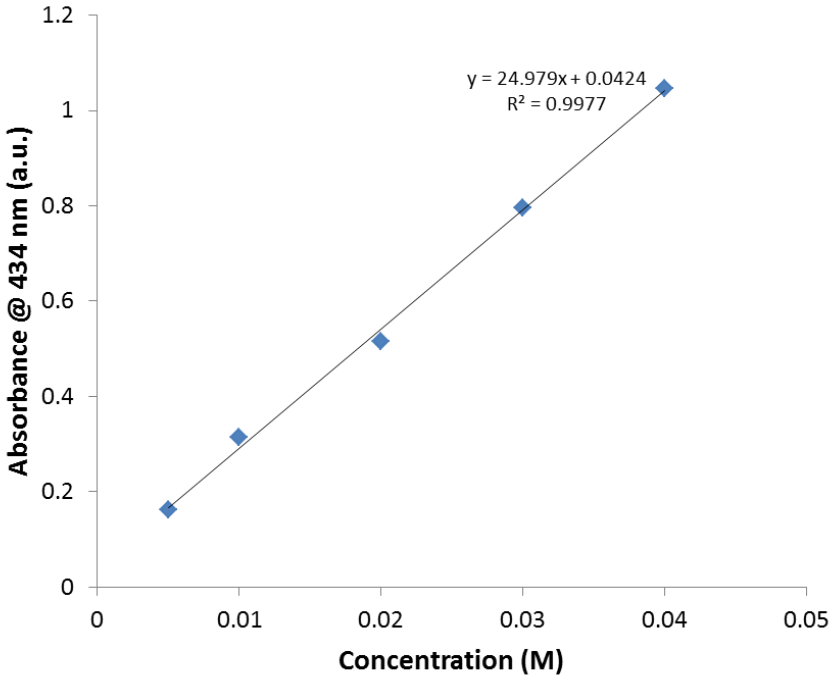

Figure A.3. Absorbance vs. concentration plots to determine molar extinction coefficient of 271 kDa ferrocene RAP.

Table A.2 Molar extinction coefficients of 271 kDa ferrocene RAP in acetonitrile

Molecular Weight (kDa)	Molar Extinction Coefficient (M^{-1} cm^{-1})
271	124.89

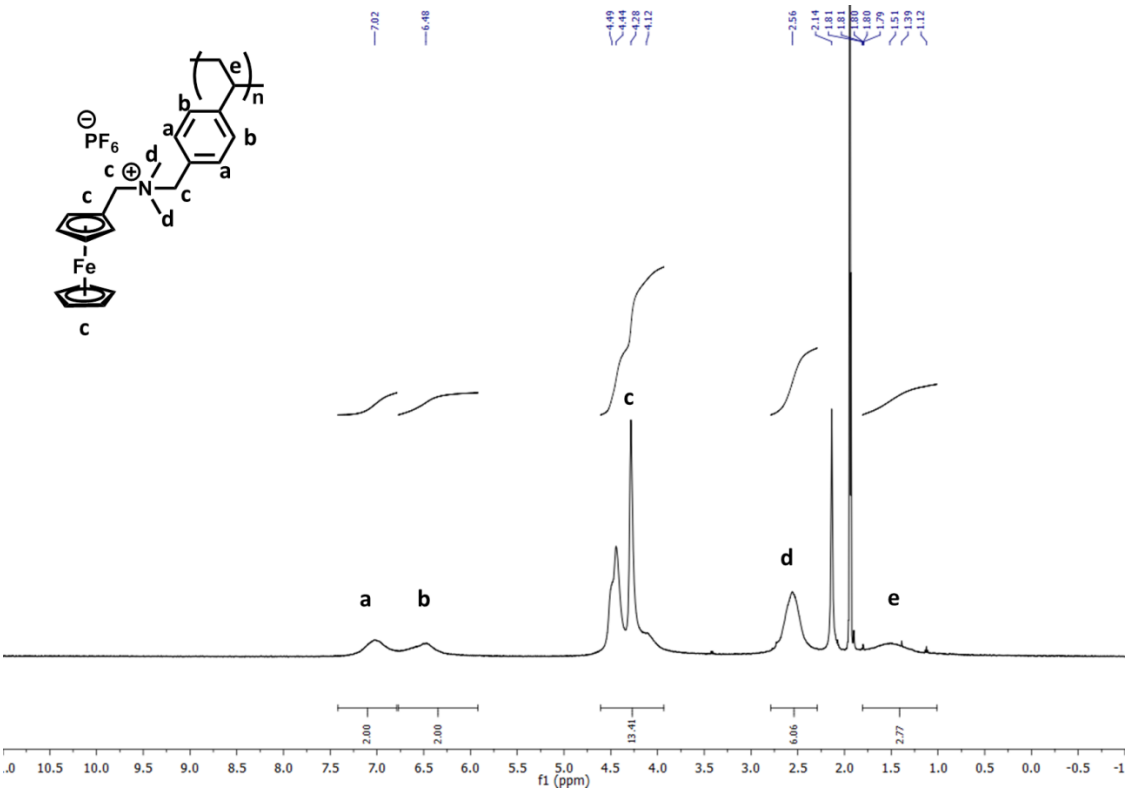

Figure A.4. ^{1}H NMR spectrum of 271 kDa ferrocene RAP in CD_3CN.

SECM Analysis of RAPs

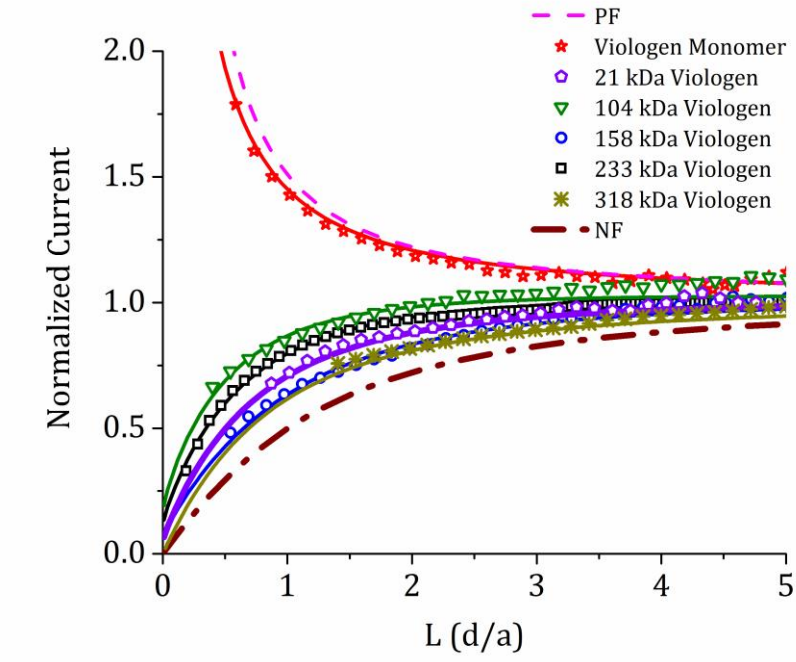

Figure A.5. SECM approach curves with 10 mM of different weight viologen RAPs approached to a 1.15 mm Pt disk at open circuit. The tip was biased at -0.9 V vs Ag/Ag^{+} in order to fully activate the first reduction of the viologen RAPs. The motor speed was 6 micrometers/second. The solid lines indicate the fitted curve and the open symbols indicate the experimental data points used to construct the fitted approach curve. Curves were fit to an *Rg* of 2. PF and NF designate theoretical mass transfer limited approach curves for perfect positive and perfect negative feedback respectively. In this experiment, the SECM tip was moved towards the surface too quickly relative to the diffusion rate of the viologen polymers, average *D* of all viologen polymers is 8.46×10^{-7} cm^2/s. When the tip is moved towards the surface faster than diffusion of the redox mediator negative feedback is observed for all species. Not properly accounting for motor movement speed in SECM approach curves can dramatically underestimate the true kinetics of the redox species being studied.

Finite Element Simulations

COMSOL v4.4 Simulation Description

The geometry shown in this figure was made of three rectangles representing the solution in the electrochemical cell and one point as shown on the top left in a 2D axis-symmetric geometry rotated around the highlighted axis of symmetry to approximate a 3D geometry. Within the rectangles, Fickian diffusion of two species (R and O) was simulated using Diffusion within the Transport of Dilute Species module (TDSM). Species R had an initial concentration, while species

O began with a concentration of 0 mol/m^3. Type 1 boundaries represent the glass sheath of the SECM tip with a No Flux boundary condition. Type 2 boundaries simulate semi-infinite bulk solution using a Concentration boundary that defines R as c^0 and O as 0. Type 3 boundaries simulate Butler-Volmer kinetics describing regeneration of R from O using a Flux condition as described in the figure. The tip mechanism shown next to the model is simulated at Type 4 edges by a Flux boundary in TDSM and a Reactions surface in the Surface Reactions module (SRM). The Flux boundary simulates adsorption of R as a negative flux with an associated rate constant while an equivalent amount is added on the surface in SRM via the Reactions surface. This is mirrored for desorption by a Reaction in SRM that decreases species B and an equivalent positive Flux of O into the solution space in TDSM. Electron transfer at the tip is modeled as part of the Reaction boundary with equal but opposite kinetic terms converting A into B. Type 5 boundaries use Constant Displacement Velocity in the Deformed Mesh module (DMM) so that these boundaries can move downward as the time moves forward in the simulation. All of the rectangles were given Free Deformation conditions to adjust meshes while Type 5 boundaries moved. The actual approach speed from experiments was used. Type 5 boundaries began at L=10 and a simulated time was chosen so that $L\approx0.5$ at the end of the simulation.

Schematic of Simulation Geometry and Boundary Conditions

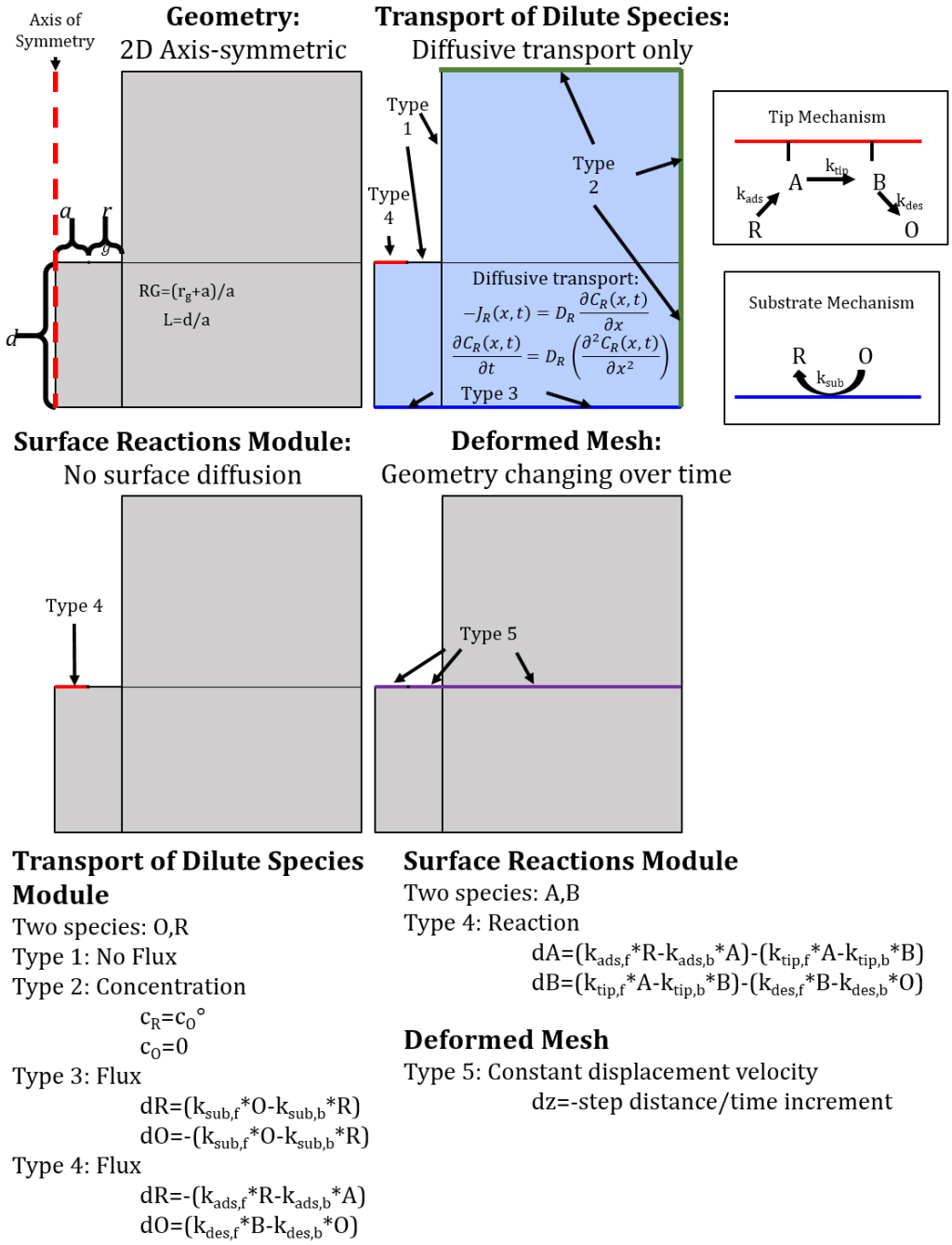

Transport of Dilute Species Module

Two species: O,R

Type 1: No Flux

Type 2: Concentration

$c_R=c_O^\circ$

$c_O=0$

Type 3: Flux

$dR=(k_{sub,f}*O-k_{sub,b}*R)$

$dO=-(k_{sub,f}*O-k_{sub,b}*R)$

Type 4: Flux

$dR=-(k_{ads,f}*R-k_{ads,b}*A)$

$dO=(k_{des,f}*B-k_{des,b}*O)$

Surface Reactions Module

Two species: A,B

Type 4: Reaction

$dA=(k_{ads,f}*R-k_{ads,b}*A)-(k_{tip,f}*A-k_{tip,b}*B)$

$dB=(k_{tip,f}*A-k_{tip,b}*B)-(k_{des,f}*B-k_{des,b}*O)$

Deformed Mesh

Type 5: Constant displacement velocity

dz=-step distance/time increment

Figure A.6. Generalized simulation scheme to model the effect of adsorption/desorption on SECM approach curves.

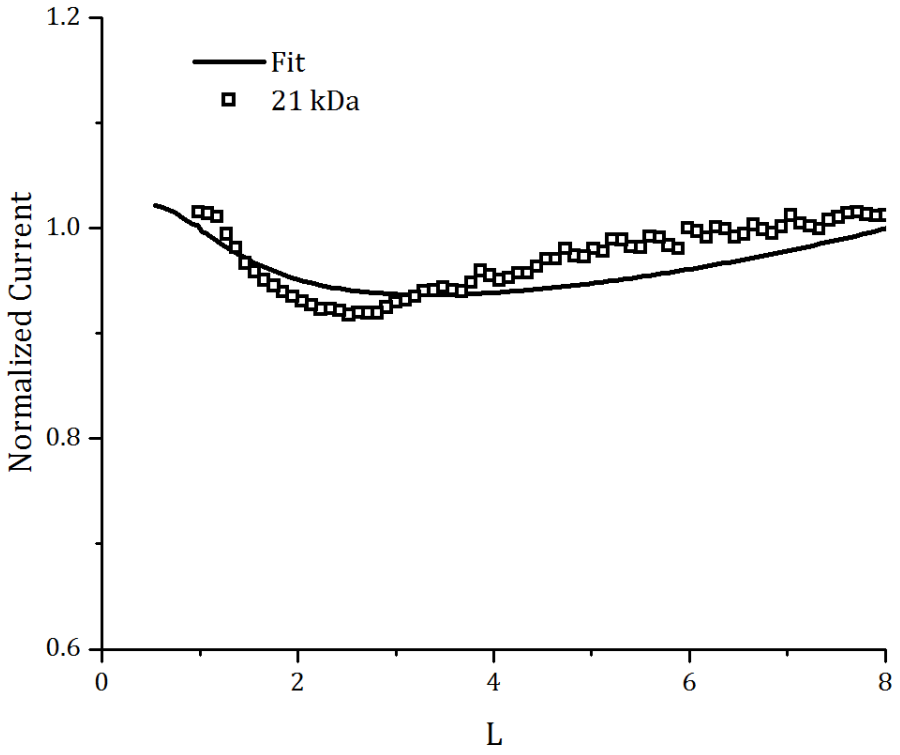

Figure A.7. Full experimental approach curve for a 10 mM solution of 21 kDa viologen polymer with the current normalized with respect to infinite distance from the substrate. Open symbols are data points and solid line is simulated fit for desorption kinetics.

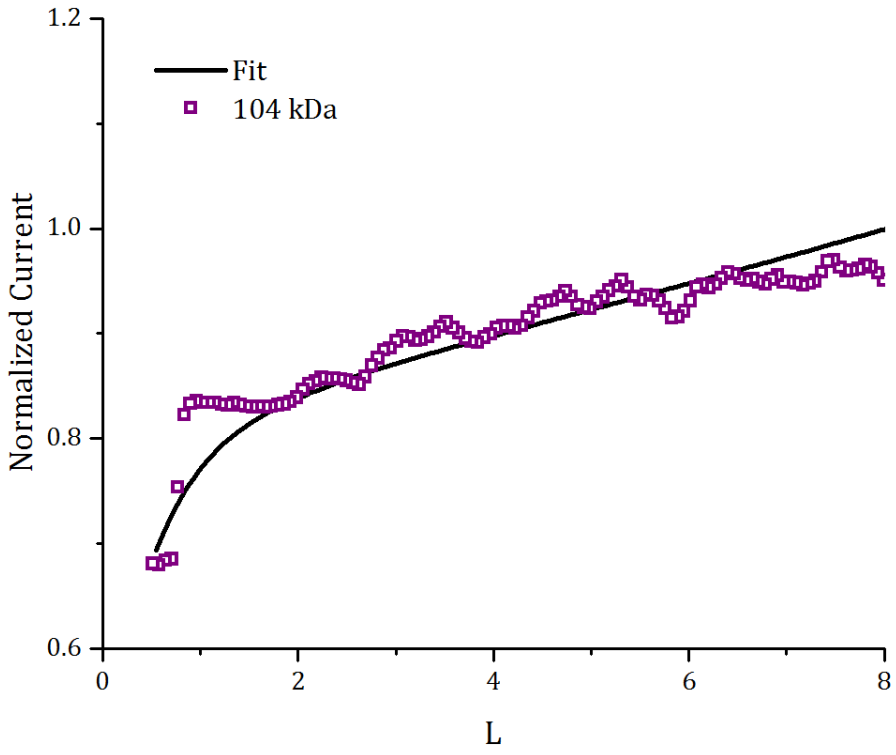

Figure A.8. Full experimental approach curve for a 10 mM solution of 104 kDa viologen polymer with the current normalized with respect to infinite distance from the substrate. Open symbols are data points and solid line is simulated fit for desorption kinetics.

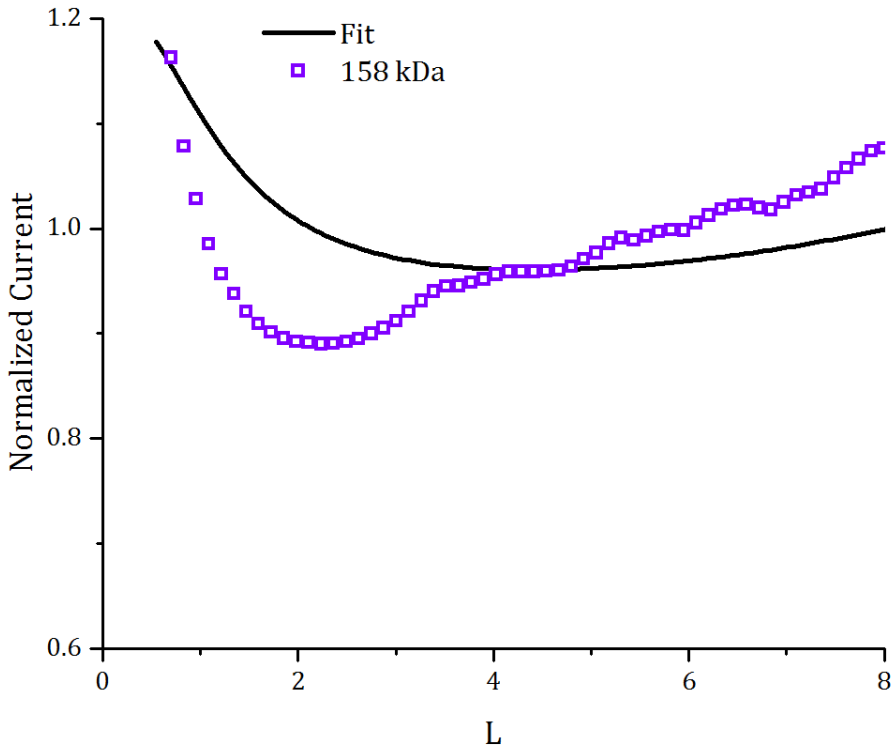

Figure A.9. Full experimental approach curve for a 10 mM solution of 158 kDa viologen polymer with the current normalized with respect to infinite distance from the substrate. Open symbols are data points and solid line is simulated fit for desorption kinetics.

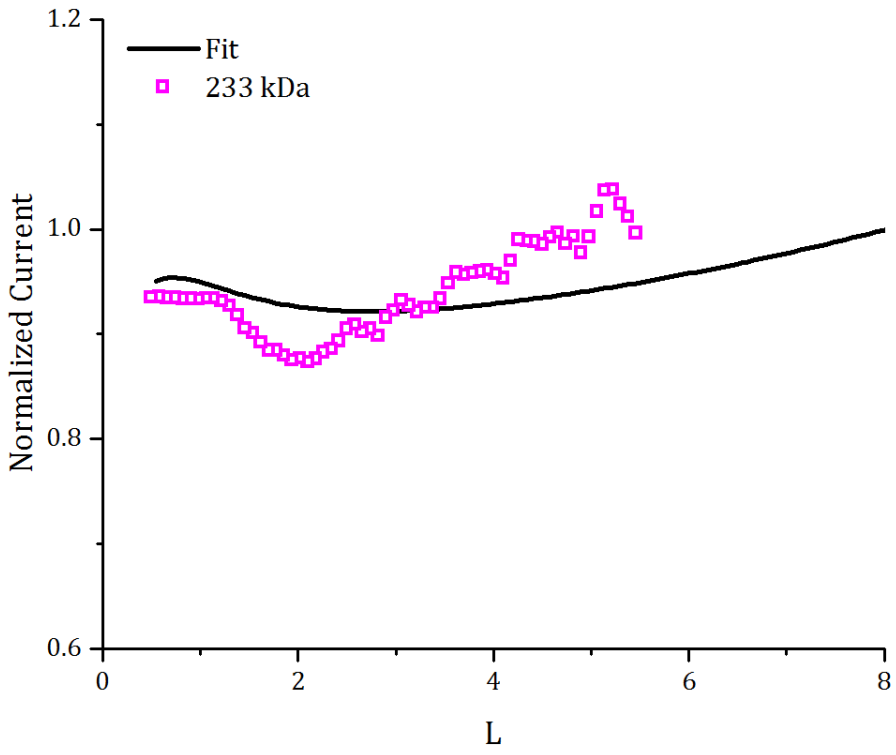

Figure A.10. Full experimental approach curve for a 10 mM solution of 233 kDa viologen polymer with the current normalized with respect to infinite distance from the substrate. Open symbols are data points and solid line is simulated fit for desorption kinetics.

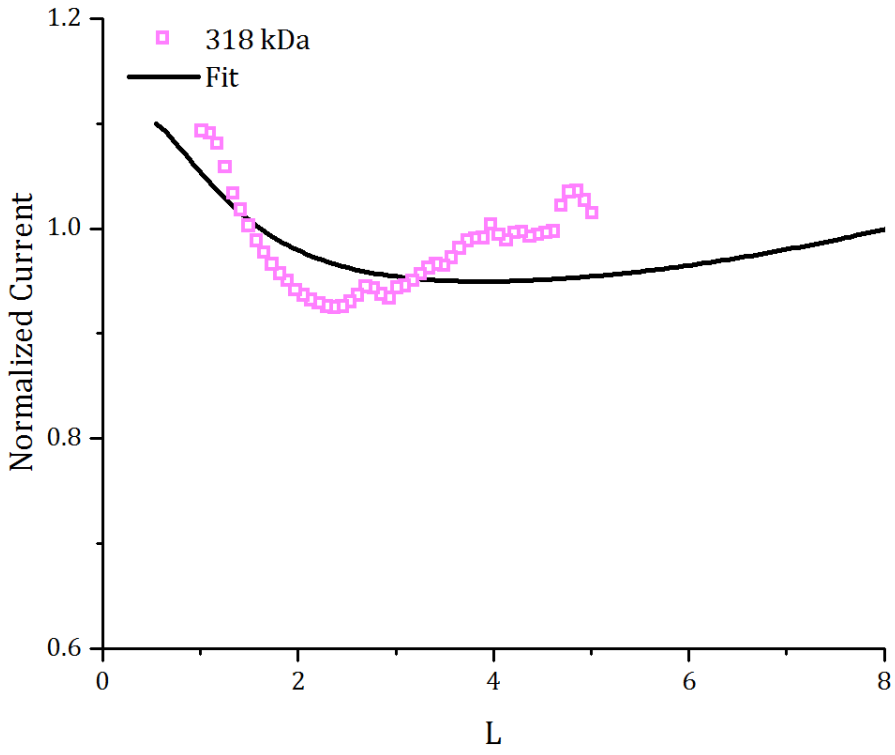

Figure A.11. Full experimental approach curve for a 10 mM solution of 318 kDa viologen polymer with the current normalized with respect to infinite distance from the substrate. Open symbols are data points and solid line is simulated fit for desorption kinetics.

Rotating Disk Electrode Voltammetry of RAPs

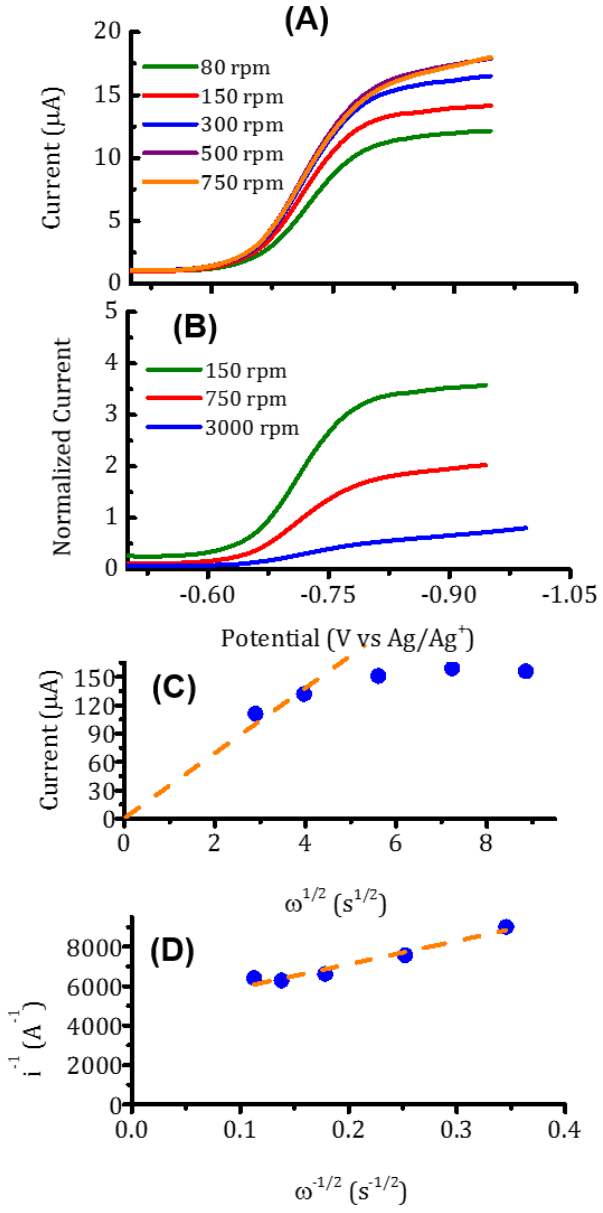

Figure A.12. (A) LSVs at different rotation rates for 5 mM 21 kDa Viologen-RAP, (B) Normalized (by $\omega^{1/2}$) LSVs. (C) Levich plot (i vs $\omega^{1/2}$) and (D) Koutecky-Levich plot (i^{-1} vs $\omega^{-1/2}$).

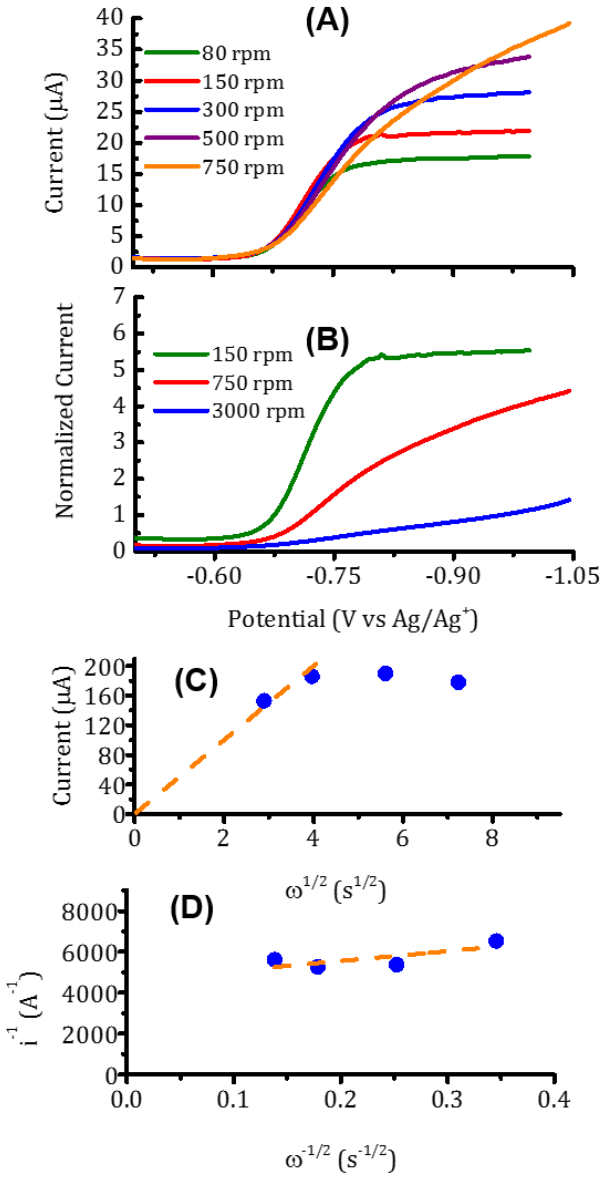

Figure A.13. (A) LSVs at different rotation rates for 5 mM 104 kDa Viologen-RAP (B) Normalized (by $\omega^{1/2}$) LSVs. (C) Levich plot (i vs $\omega^{1/2}$) and (D) Koutecky-Levich plot (i^{-1} vs $\omega^{-1/2}$).

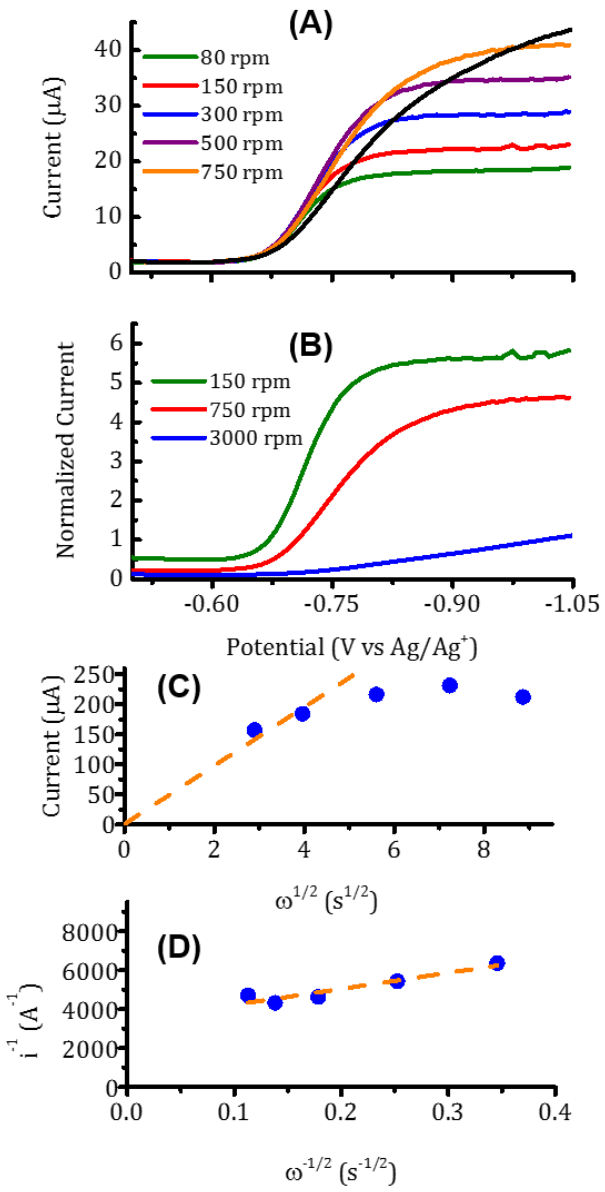

Figure A.14. (A) LSVs at different rotation rates for 5 mM 233 kDa Viologen-RAPs, (B) Normalized (by $\omega^{1/2}$) LSVs. (C) Levich plot (i vs $\omega^{1/2}$) and (D) Koutecky-Levich plot (i^{-1} vs $\omega^{-1/2}$).

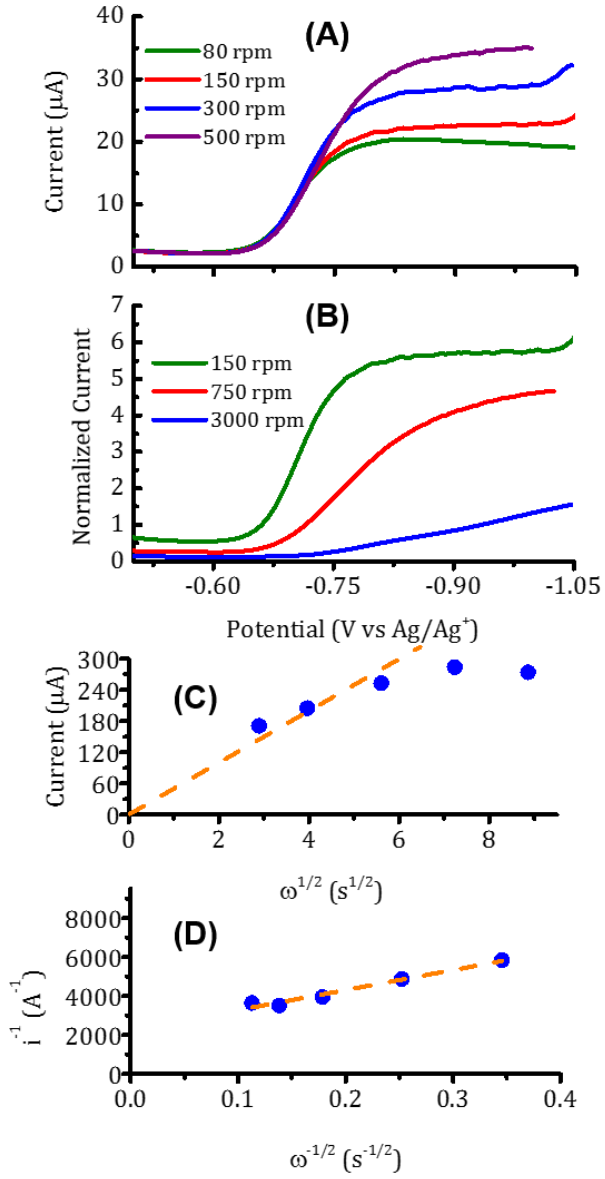

Figure A.15. (A) LSVs at different rotation rates for 5 mM 318 kDa Viologen-RAPs, (B) Normalized (by $\omega^{1/2}$) LSVs. (C) Levich plot (i vs $\omega^{1/2}$) and (D) Koutecky-Levich plot (i^{-1} vs $\omega^{-1/2}$).

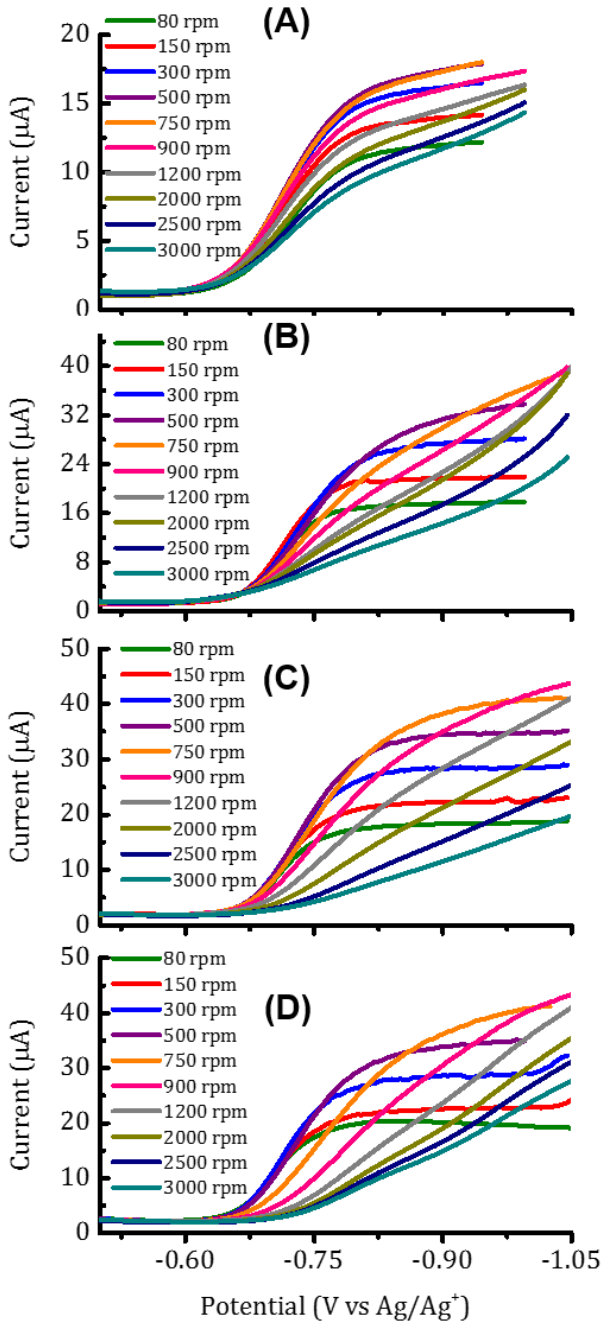

Figure A.16. LSVs at different rotation rates for 5 mM of (A) 21 kDa, (B) 104 kDa, (C) 233 kDa and (D) 318 kDa Viologen-RAPs. This strong deviation from Levich behavior at high representation is representative of the adsorption of the RAPs onto the electrode surface.

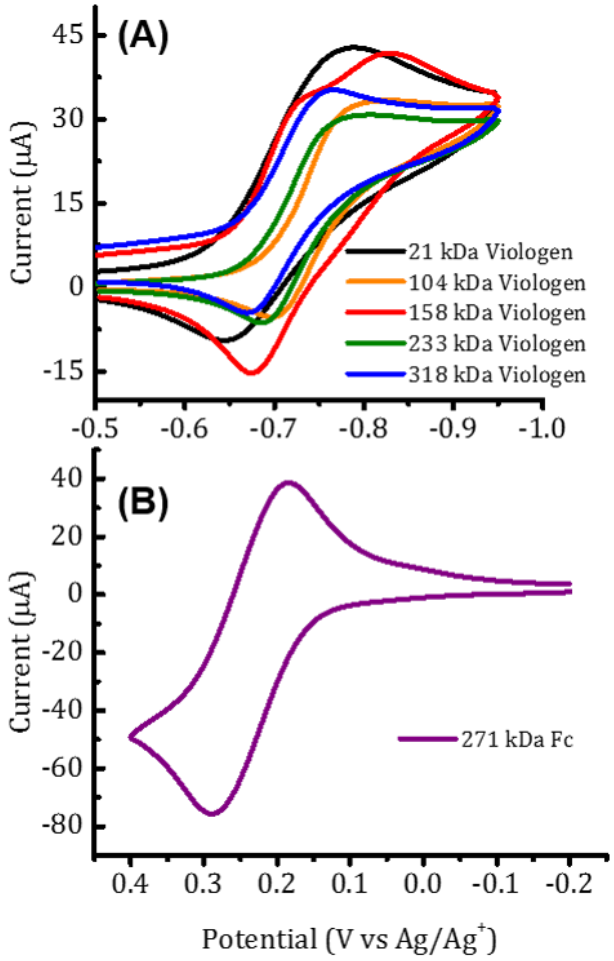

Figure A.17. Cyclic Voltammograms for the different weight 5mM (A) Viologen-RAPs and (B) Fc-RAP in a 0.1 M $LiBF_4$ in acetonitrile.

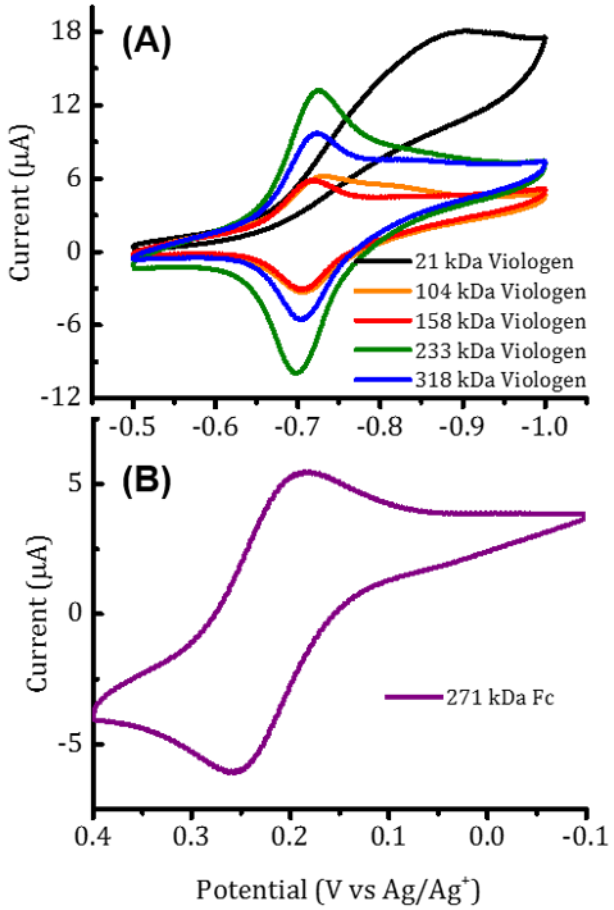

Figure A.18. Cyclic Voltammograms after dropcasting the different weight (A) Viologen-RAPs and (B) Fc-RAP on the glassy carbon electrode. Tested in a 0.1 M $LiBF_4$ in acetonitrile solution.

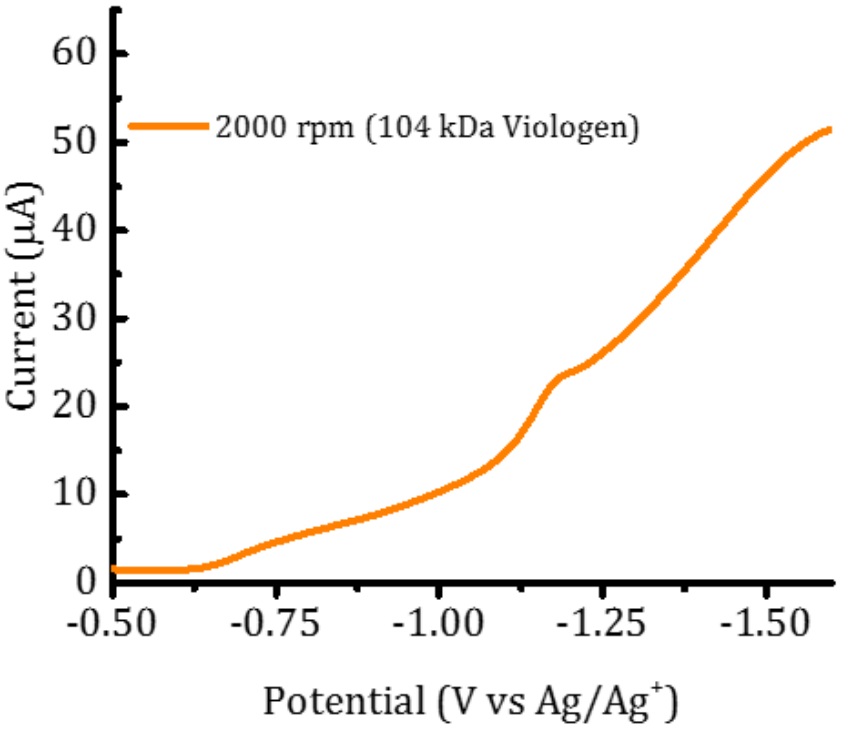

Figure A.19. LSV for the 104 kDa viologen RAP at 2000 rpm proving that the polymer is on the glassy carbon electrode and that a steady state signal cannot be obtained for this adsorbed species even with increased overpotential.

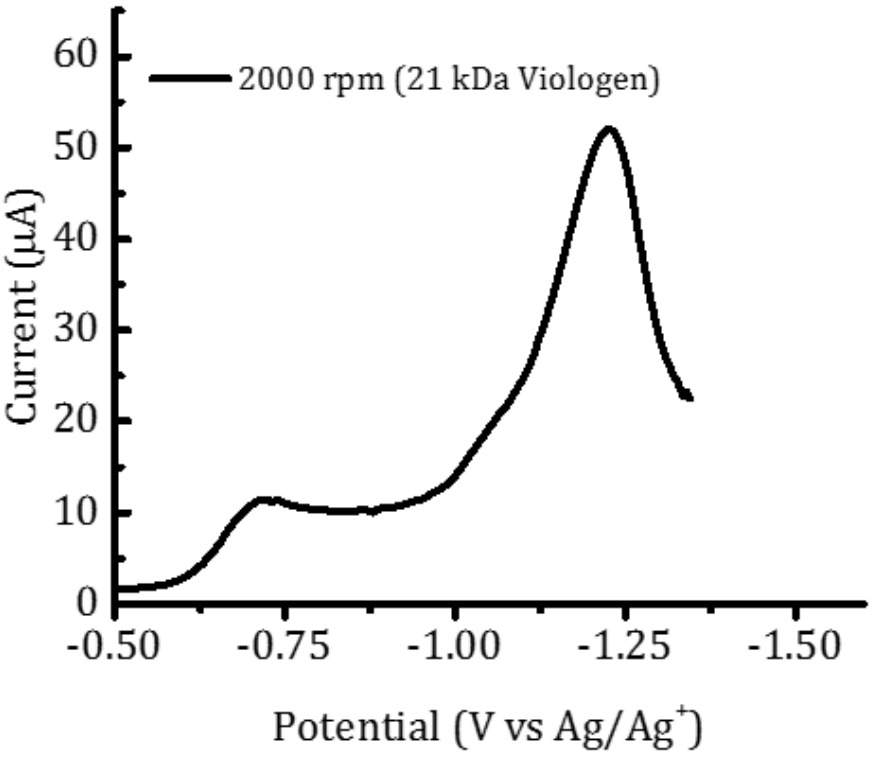

Figure A.20. LSV for the 104 kDa violoen RAP at 2000 rpm proving that the polymer adsorbs on the glassy carbon electrode surface if the second electron is attempted.

Methodology and Schematic on How to Calculate the Diffusion of Electrons from RDE

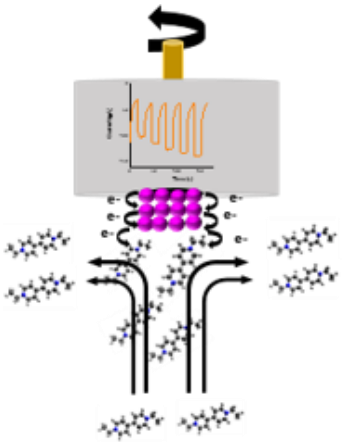

$$\frac{1}{i_{LIM}} = \frac{1}{i_A} + \frac{1}{i_E} \quad (1)$$

$$i_A = 0.62nFAC_A^0 D_A^{2/3} \nu^{-1/6} \omega^{1/2} \quad (2)$$

$$i_E = \frac{nFAD_E C_{RAP}}{d} \quad (3)$$

$$D_E = \frac{k_{ET}\delta^2}{6} \quad (4)$$

Figure A.21. (A) Schematic of the experiment to calculate the k_{ex} of the RAPs. A film of the RAP is formed on the electrode by dropcasting 100 microliters of a 5 mM solution of RAP onto the RDE electrode surface and letting it evaporate. The leftover material was tested for electrochemical activity in neat electrolyte and solvent 0.1 M $LiBF_4$ in acetonitrile. The filmed RDE was used as the working electrode in a solution containing monomer. In order for monomer to react on the RDE it must exchange electrons through the RAP film. In this sense, the rate at which the exchange of electrons happens through the RAP film is limiting the rate of reaction. (B) Equations used for the calculation of the k_{ex}. We used for all the calculations the electrolyte concentration (0.1 M) because the forward sweep wave shape of the RAP film voltammetry in Figure S18 appears diffusive. Note, the data for the 21 kDa viologen polymer was not used due to dissolution problems.

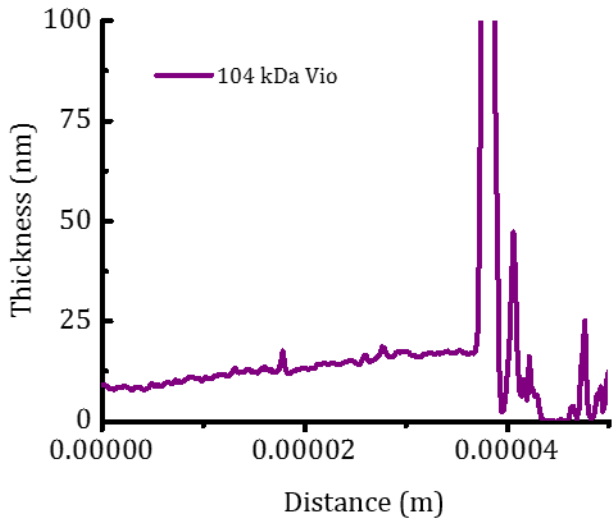

Figure A.22. AFM scan of a 104 kDa viologen RAP film used to determine the average thickness. The film was produced by drop casting 100 microliters of a 5 mM 104 kDa viologen RAP solution in acetonitrile onto a 3 mm silicon wafer and letting all the solvent evaporate. The instrument used was an Asylum Research MFP-3D AFM (California).

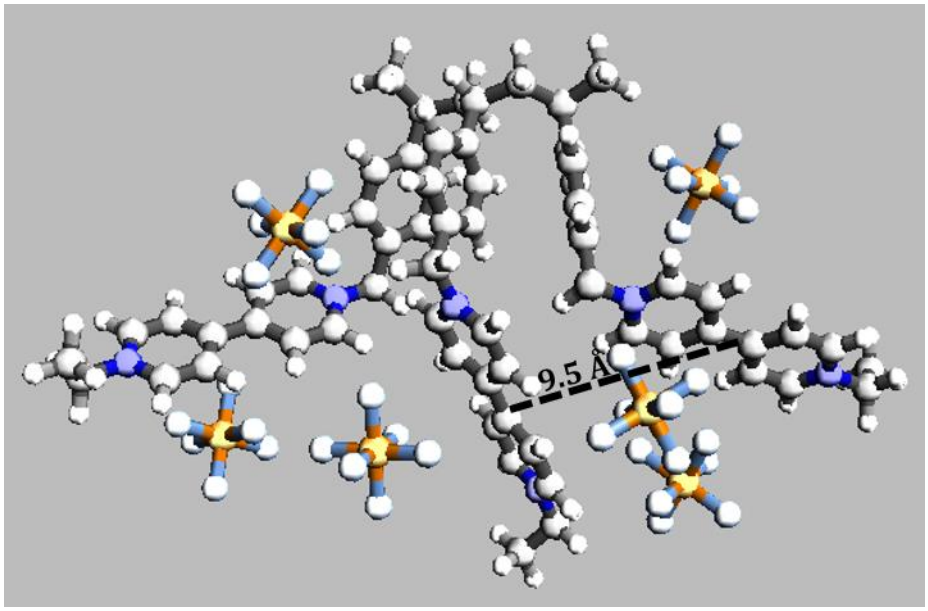

Figure A.23. Viologen RAP relaxed structure (n=3) using universal force fields in Avogadro software. To improve the accuracy of the approximation we included the respective anions (PF_6^-). The parameter δ, distance between redox units, was estimated as the distance shown in the figure as the dashed line.

Appendix B: Supporting Information File for Chapter 3

Notes and Acknowledgements

This appendix appeared in its entirety in the journal *Chemistry of Materials* with authors Burgess, M.; Chenard, E.; Hernández-Burgos, K.; Nagarjuna, G.; Assary, R.S.; Hui, J.; Moore, J. S.; Rodríguez-López, J. "Impact of Backbone Tether Length and Structure on the Electrochemical Performance of Viologen Redox Active Polymers". **2016,** 28, pp 7362–7374. This supporting information file is reprinted with the permission of the publisher and is available from http://www.pubs.acs.org and using DOI: 10.1021/acs.chemmater.6b02825. M.B., E.C., and K.H.B. all contributed equally to this work. M.B performed all the SECM analysis, helped in voltammetry experiments, helped in spectroelectrochemical measurements, helped in temperature dependent UV-vis studies, did all bulk electrolysis measurements, helped write the manuscript, helped in data analysis, and made figures. This work was supported as part of the Joint Center for Energy Storage Research, an Energy Innovation Hub funded by the U.S. Department of Energy, Office of Science, Basic Energy Sciences. M. B. acknowledges support by the National Science Foundation Graduate Research Fellowship Program under grant No. DGE-1144245. Materials characterization was carried out in part in the Frederick Seitz Materials Research Laboratory Central Research Facilities at the University of Illinois at Urbana–Champaign. K.H.B. gratefully acknowledges the Beckman Institute Postdoctoral Fellowship at the University of Illinois at Urbana−Champaign, with funding provided by the Arnold and Mabel Beckman Foundation. J.R.L. acknowledges additional support from a Sloan Research Fellowship. The authors thank Prof. Catherine J. Murphy for allowing us to use the near IR UV–vis spectrometer in her laboratory.

General Information

5-bromophtalide was purchased from Alfa Aeser. Halide alkyl, 1,2-Bis(bromomethyl)benzene , 1,3-Bis(bromomethyl)benzene, PPh_3, $PdCl_2$, and ethyl 2-(phenylcarbonothioylthio)-2-phenylacetate (CIA) were purchased from Aldrich. Potassium vinyltrifluoroborate and Cs_2CO_3 were purchased from AK Scientific. AIBN was recrystallized.

Unless otherwise noted, all manipulations were conducted under a nitrogen atmosphere in the absence of oxygen and water. Dry dichloromethane (CH_2Cl_2) and dimethylformamide (DMF) were obtained from SDS. Visualization of the TLC was performed by ultraviolet light 254 nm, by staining with potassium permanganate solution as developing agents. Flash columns chromatographies were performed using Isolera™ Prime, from Biotage®. FTIR spectra were acquired on a Nicolet Nexus 670 FT-IR spectrometer and are reported in reciprocal centimeters (cm^{-1}). Nuclear magnetic resonance spectra (^1H, ^{13}C, ^{19}F, and ^{31}P) were recorded either on a Varian Unity 400, 500, VXR 500 and Inova 400 or 600 spectrometers. Chemical shifts for ^1H NMR spectra are recorded in parts per million with the solvent resonance central peak as the internal standard ($CDCl_3$, 7.26 ppm; CD_3CN, δ 1.94 ppm).[1] Data are reported as follows: chemical shift, multiplicity (s = singlet, d = doublet, t = triplet, q = quartet, and m = multiplet), coupling constant in Hertz (Hz), integration (xH). Chemical shifts for ^{13}C NMR spectra are recorded in parts per million using the central peak of $CDCl_3$ (77.16 ppm) and CD_3CN (118.26 ppm) as the internal standard. All ^{13}C NMR spectra were obtained with complete proton decoupling. ^{31}P NMR were calibrated with a solution of 80% H_3PO_3 (δ 0.0 ppm) in water as external standard. ^{19}F NMR were recorded after calibration using a solution of $BF_3 \bullet Et_2O$ (δ −153.0 ppm) in $CDCl_3$ as external standard. High resolution mass ESI spectra were performed on a Waters Synapt G2-Si and EI spectra were performed on a Waters 70-VSE, by the Mass Spectrometry Laboratory of the School

of Chemical Science at UIUC. CHN analyses were performed by the Microanalysis Laboratory of the School of Chemical Science of UIUC, using Exeter Analytical CE 440 and Perkin Elmer 2440, Series II. Melting points (MP) are uncorrected.

Detailed Synthetic Procedures and Sample Characterization

N-Ethyl-4,4'-bipyridinium (MonoEtVPF_6)

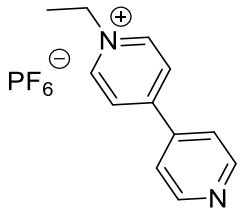

EtI (5.12 mL, 64.0, 1.00 equiv) was added to a solution of 4,4-bipyridine (10.0 g, 64.0 mmol, 1.00 equiv) in CH_2Cl_2 (50 mL). As the reaction progress, an orange solid precipitated out. The mixture was stirred for 24 h at room temperature. An orange solid was precipitated out from the solution by adding Et_2O and rinsed with a solution of CH_2Cl_2/ Et_2O (1:1, v/v). The solid was then dissolved in a minimal amount of H_2O and NH_4PF_6 (53.0 g, 325 mmol, 5.08 equiv) was added portion wise. As NH_4PF_6 was added, a beige solid precipitated out. The resulting mixture was stirred for 24 h. The solid was filtered out and rinsed with H_2O, MeOH, and then Et_2O. The resulting solid was dried under vacuum for 24 h to yield *N*-Ethyl-4,4'-bipyridinium hexafluorophosphate (6.27 g, 30%, 2 steps) as a beige solid.[2]

Diethyl viologen bis(hexafluorophosphate) **2**

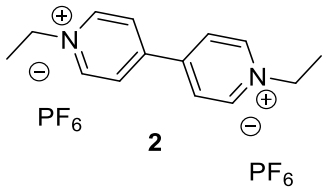

2

EtI (2.1 mL, 26. mmol, 3.7 equiv) was added to a solution of 4,4'-bipyridine (1.1 g, 7.0 mmol, 1.0 equiv) in DMF (3 mL). The solution was then allowed to reach 60 °C and stirred at this temperature for 3 days. As the reaction progress, an orange solid precipitated out. The solid was further precipitated with Et_2O, and the solid was filtered out and rinsed with a solution of CH_2Cl_2/Et_2O (1:1, v/v). The solid was then dissolved in a minimal amount of H_2O and NH_4PF_6 (7.0 g, 43. mmol, 6.7 equiv) was added portion wise. The resulting mixture was stirred for 24 h. The solid was filtered out and rinsed with H_2O, MeOH, and then Et_2O. The resulting solid was dried under vacuum for 24 h to yield diethyl viologen bis-hexafluorophosphate **2** (3.4 g, 97%) as beige solid.

M.P. 274 °C (deg.)

^{1}H NMR (499 MHz, CD_3CN) δ 8.93 (d, *J* = 6.5 Hz, 4H), 8.40 (d, *J* = 5.4 Hz, 4H), 4.68 (q, *J* = 7.3 Hz, 4H), 1.65 (t, *J* = 7.2 Hz, 6H);

^{13}C NMR (126 MHz, CD_3CN) δ 150.8, 146.4 – 145.9 (m), 128.1, 128.0, 58.6 (t, *J* = 13.6 Hz), 16.6 – 16.0 (m);

^{19}F NMR (470 MHz, CD_3CN) δ −72.9 (d, *J* = 707.3 Hz);

^{31}P NMR (202 MHz, CD_3CN) δ −143.50 (hept, *J* = 707.3 Hz);

HRMS (ESI-TOF): *m/z* for $C_{14}H_{18}N_2^{2+}$ calcd 214.1470, found 214.1469.

General Protocol for the Preparation of Tethered Viologens

Dihalide linker (1 equiv) was added to a solution of *N*-Ethyl-4,4'-bipyridinium hexafluorophsphate (2.1 equiv) in DMF or DMSO ([bipyridinium] ~ 1-3 M). The solution was then allowed to reach 60 °C and stirred at this temperature for 3 days. As the reaction progress, a solid precipitated out. The mixture was added of Et_2O, and the solid was filtered out and rinsed with a solution of Et_2O. The solid was then dissolved in a minimal amount of MeCN/H_2O (1:4, v/v) and NH_4PF_6 (10 equiv) in a minimal amount of H_2O was added portion wise. The resulting mixture was stirred for 24 h. MeCN was removed in vacuo with a rotary evaporator and H_2O was added to the mixture to further precipitate out the solid. The solid was filtered out and rinsed with H_2O, MeOH, and then Et_2O. The solid was dried under vacuum for 24 h to yield tethered viologen as a solid.

1,3-propyl bis(viologen) **3** (dimer **3**)

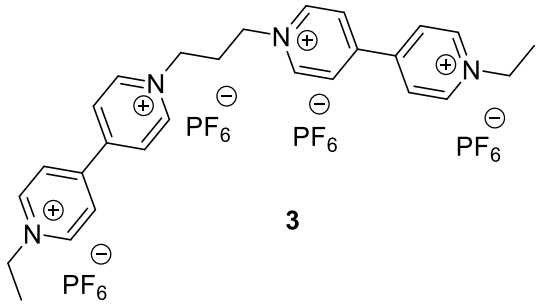

3

Following the general protocol, 1,3-dibromopropane (0. 83 g, 4.1 mmol, 1.0 equiv) was reacted with *N*-Ethyl-4,4'-bipyridinium hexafluorophosphate (3.0 g, 9.1 mmol, 2.2 equiv) in DMSO (10 mL). NH_4PF_6 (4.0 g, 25 mmol, 6.1 equiv) was used for the anionic exchange to yield the bis(viologen) **3** (0.50 g, 12%) as an off-white solid.

M.P. 259 °C (deg.)

^{1}H NMR (500 MHz, CD_3CN) δ 8.98 – 8.90 (m, 8H), 8.49 – 8.38 (m, 8H), 4.82 – 4.75 (m, 4H), 4.68 (q, *J* = 7.3 Hz, 4H), 2.81 – 2.70 (m, 2H), 1.66 (t, *J* = 7.3 Hz, 6H);

^{13}C NMR (126 MHz, CD_3CN) δ 151.5, 150.6, 146.7, 146.4 – 146.1 (m), 128.4, 128.1, 59.14, 58.6, 32.6, 16.4;

^{19}F NMR (470 MHz, CD_3CN) δ -73.0 (d, *J* = 707.2 Hz);

^{31}P NMR (202 MHz, CD_3CN) δ -143.6 (hept, *J* = 707.2 Hz);

IR (neat) 3145, 3083, 2945, 2869, 1643, 1566, 1511, 1472, 1453 1394, 1355, 1223, 1181, 826 cm^{-1};

HRMS (ESI-TOF): *m/z* for $C_{27}H_{32}N_4F_{18}P_3^+$ calcd 847.1552, found 847.1535.

1,4-butyl bis(viologen) **4** (dimer **4**)

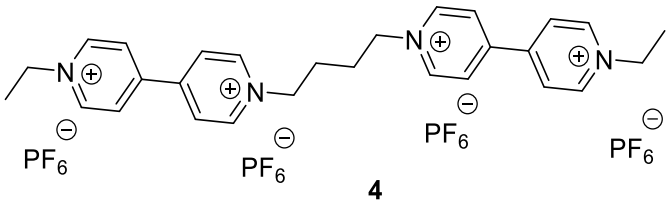

4

Following the general protocol, 1,4-diodobutane (0.19 mL, 1.4 mmol, 1.0 equiv) was reacted with *N*-Ethyl-4,4'-bipyridinium hexafluorophosphate (1.1 g, 3.3 mmol, 2.3 equiv) in DMF (1 mL). NH_4PF_6 (3.4 g, 21 mmol, 15 equiv) was used for the anionic exchange to yield the bis(viologen) **4** (0.94 g, 67%) as a beige solid.

M.P. 304 °C (deg.)

^{1}H NMR (499 MHz, CD_3CN) δ 8.93 (d, *J* = 6.7 Hz, 4H), 8.89 (d, *J* = 6.9 Hz, 4H), 8.43 – 8.36 (m, 8H), 4.71 – 4.65 (m, 8H), 2.16 – 2.10 (m, 4H), 1.65 (t, *J* = 7.3 Hz, 6H);

^{13}C NMR (126 MHz, CD_3CN) δ 151.2, 150.8, 146.51 (br s), 146.30 (br s), 128.4 – 128.0 (m), 62.0, 58.7, 28.1, 16.5 (t, *J* = 11.0 Hz);

^{19}F NMR (470 MHz, CD_3CN) δ −72.9 (d, *J* = 707.4 Hz);

^{31}P NMR (202 MHz, CD_3CN) δ −143.5 (hept, *J* = 707.4 Hz)

IR (neat) 3149, 3069, 3002, 2955, 1643, 1567, 1509, 1457, 1393, 1353, 1226, 1181, 826 cm^{-1};

HRMS (ESI-TOF): *m/z* for $C_{28}H_{34}F_{18}N_4P_3^+$ calcd 861.1709, found 861.1688.

1,5-pentyl bis(viologen) **5** (dimer **5**)

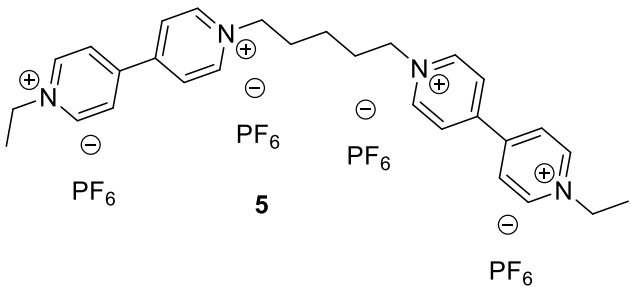

5

Following the general protocol, 1,5-diodopentane (0.21 mL, 1.4 mmol, 1.0 equiv) was reacted with *N*-Ethyl-4,4'-bipyridinium hexafluorophosphate (1.0 g, 3.0 mmol, 2.2 equiv) in DMF (1 mL). NH_4PF_6 (2.4 g, 15 mmol, 11 equiv) was used for the anionic exchange to yield the bis(viologen) **5** (0.92 g, 66%) as a light yellow solid.

M.P. 297 °C (deg.)

^{1}H NMR (499 MHz, CD_3CN) δ 8.92 (d, *J* = 6.7 Hz, 4H), 8.90 (d, *J* = 6.9 Hz, 4H), 8.43 – 8.35 (m, 8H), 4.68 (q, *J* = 7.3 Hz, 4H), 4.62 (t, *J* = 7.6 Hz, 4H), 2.13 – 2.04 (m, 4H), 1.66 (t, *J* = 7.3 Hz, 6H), 1.56 – 1.48 (m, 2H);

^{13}C NMR (126 MHz, CD_3CN) δ 150.9, 150.7, 146.5 – 145.9 (m), 128.2 – 127.8 (m), 62.43 (t, *J* = 15.4 Hz), 58.5 (t, *J* = 14.5 Hz), 30.8 (t, *J* = 12.6 Hz), 22.8 (t, *J* = 14.2 Hz), 16.5 – 15.9 (m); **^{19}F NMR** (470 MHz, CD_3CN) δ −72.8 (d, *J* = 707.9 Hz);

^{31}P NMR (202 MHz, CD_3CN) δ −143.5 (hept, *J* = 707.9 Hz);

IR (neat) 3141, 3081, 2996, 2947, 1644, 1569, 1512, 1451, 1391, 1353, 1224, 1185, 1173, 822 cm^{-1};

HRMS (ESI-TOF): *m/z* for $C_{29}H_{36}F_{18}N_4P_3^+$ calcd 875.1865, found 875.1837.

1,6-hexyl bis(viologen) **6** (dimer **6**)

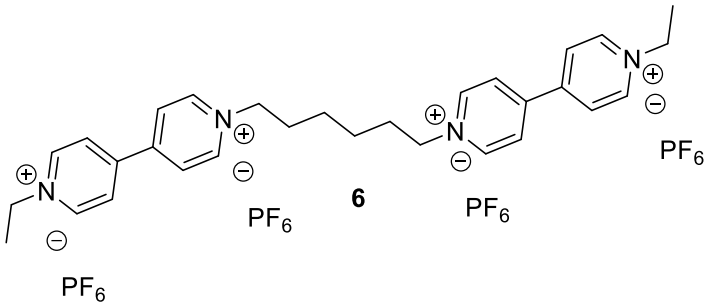

Following the general protocol, 1,6-diodohexane (0.24 mL, 1.4 mmol, 1.0 equiv) was reacted with *N*-Ethyl-4,4'-bipyridinium hexafluorophosphate (1.0 g, 3.0 mmol, 2.2 equiv) in DMF (2 mL). NH_4PF_6 (3.4 g, 21 mmol, 15 equiv) was used for the anionic exchange to yield the bis(viologen) **6** (1.0 g, 71%) as a beige solid.

M.P. 240 °C (deg.)

^{1}H NMR (499 MHz, CD_3CN) δ 9.15 – 8.73 (m, 8H), 8.39 (d, *J* = 5.9 Hz, 8H), 4.68 (q, *J* = 7.2 Hz, 4H), 4.61 (t, *J* = 7.6 Hz, 4H), 2.11 – 1.97 (m, 4H), 1.66 (t, *J* = 7.4 Hz, 6H), 1.54 – 1.42 (m, 4H);

^{13}C NMR (126 MHz, CD_3CN) δ 150.8, 150.7, 146.7 – 145.8 (m), 128.00, 127.96, 62.7, 58.5, 31.3, 25.6, 16.4;

^{19}F NMR (470 MHz, CD_3CN) δ −73.2 (d, J = 706.8 Hz);

^{31}P NMR (243 MHz, CD_3CN) δ −144.7 (hept, *J* = 706.8 Hz);

IR (neat) 3142, 3083, 2945, 2869, 1643, 1566, 1507, 1465, 1394, 1357, 1224, 1178, 826 cm^{-1};

HRMS (ESI-TOF): *m/z* for $C_{30}H_{38}F_{18}N_4P_3^+$ calcd 889.2022, found 889.1995.

1,7-heptyl bis(viologen) **7** (dimer **7**)

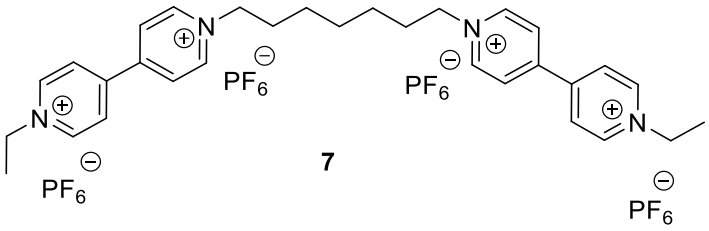

7

Following the general protocol, 1,7-dibromoheptane (2.0 g, 7.8 mmol, 1.0 equiv) was reacted with *N*-Ethyl-4,4'-bipyridinium hexafluorophosphate (6.0 g, 18 mmol, 2.3 equiv) in DMSO:DMF (1:1, 40 mL). NH_4PF_6 (6.0 g, 37 mmol, 4.7 equiv) was used for the anionic exchange to yield the bis(viologen) **7** (2.6 g, 32%) as an off-white solid.

M.P. 268 °C (deg.)

^{1}H NMR (500 MHz, CD_3CN) δ 8.94 – 8.91 (m, 4H), 8.91 – 8.87 (m, 4H), 8.39 (d, *J* = 6.2 Hz, 8H), 4.68 (q, *J* = 7.3 Hz, 4H), 4.61 (t, *J* = 7.6 Hz, 4H), 2.08 – 1.98 (m, 4H), 1.65 (t, *J* = 7.4 Hz, 6H), 1.48 – 1.36 (m, 6H);

^{13}C NMR (126 MHz, CD_3CN) δ 150.85, 150.81, 146.4, 146.3 – 146.1 (m), 128.01, 62.9, 58.6, 31.6, 28.8, 26.1, 16.4;

^{19}F NMR (470 MHz, CD_3CN) δ -73.0 (d, *J* = 707.0 Hz;

^{31}P NMR (202 MHz, CD_3CN) δ -143.5 (hept, *J* = 707.0 Hz);

IR (neat) 3143, 3080, 2945, 2867, 1642, 1566, 1508, 1465, 1395, 1356, 1221, 1177, 827 cm^{-1};

HRMS (ESI-TOF): *m/z* for $C_{31}H_{40}N_4F_{18}P_3^+$ calcd 903.2178, found 903.2156.

ortho-xylyl bis(viologen) tetra(hexafluorophoshate) **8** (*o*-benzene dimer **8**)

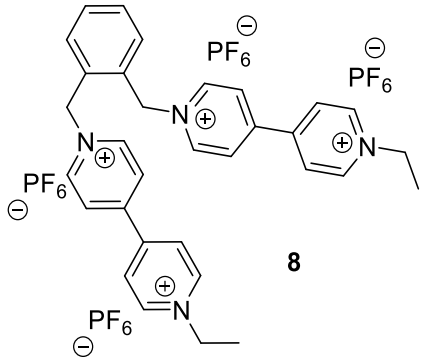

8

Following the general protocol, 1,2-di(bromomethyl)benzene (0.11 g, 0.41 mmol, 1.0 equiv) was reacted with *N*-Ethyl-4,4'-bipyridinium hexafluorophosphate (0.29 g, 0.87 mmol, 2.1 equiv) in DMF (1 mL). NH_4PF_6 (2.8 g, 11 mmol, 11 equiv) was used for the anionic exchange to yield the expected *o*-Benzene dimer **8** (0.28 g, 65%, 2 steps) as a beige solid.

M.P. 258 °C (deg.)

^{1}H NMR (400 MHz, CD_3CN) δ 8.94 (d, *J* = 6.4 Hz, 4H), 8.89 (d, *J* = 6.9 Hz, 4H), 8.47 – 8.43 (m, 4H), 8.41 (d, *J* = 6.2 Hz, 4H), 7.65 – 7.59 (m, 2H), 7.29 (dd, *J* = 5.7, 3.4 Hz, 2H), 5.94 (s, 4H), 4.69 (q, *J* = 7.3 Hz, 4H), 1.66 (t, *J* = 7.4 Hz, 6H);

^{13}C NMR (151 MHz, CD_3CN) δ 151.9, 150.6, 146.8, 146.3 (t, *J* = 8.8 Hz), 132.16, 132.15, 131.6, 128.6, 128.2, 62.1, 58.7, 16.5;

^{19}F NMR (376 MHz, CD_3CN) δ −73.0 (d, J = 707.2 Hz);

^{31}P NMR (202 MHz, CD_3CN) δ −143.5 (hept, J = 707.2 Hz);

IR (neat) 3142, 3083, 2996, 1643, 1569, 1559, 1510, 1455, 1357, 1223, 1200, 1180, 826 cm^{-1};

HRMS (ESI-TOF): *m/z* for $C_{32}H_{34}F_{18}N_4P_3$ calcd 909.1709, found 909.1695.

meta-xylyl bis(viologen) tetra(hexafluorophoshate) **9** (*m*-benzene dimer **9**)

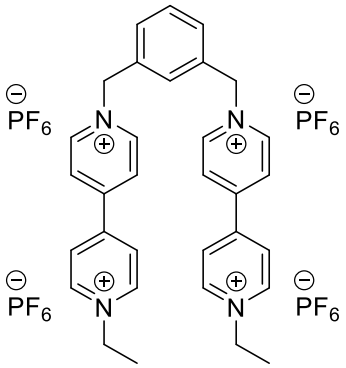

9

Following the general protocol, 1,3-Bis(bromomethyl)benzene (0.51 mL, 1.9 mmol, 1.0 equiv) was reacted with *N*-Ethyl-4,4'-bipyridinium hexafluorophosphate (1.3 g, 3.9 mmol, 2.1 equiv) in DMF (5 mL). NH_4PF_6 (2.8 g, 11 mmol, 5.8 equiv) was used for the anionic exchange to yield the expected *m*-Benzene dimer **9** (0.54 g, 27%, 2 steps) as a beige solid.

M.P. 269 °C (deg.)

^{1}H NMR (400 MHz, CD_3CN) δ 8.97 – 8.89 (m, 8H), 8.43 – 8.34 (m, 8H), 7.66 – 7.54 (m, 4H), 5.83 (s, 4H), 4.68 (q, *J* = 7.4 Hz, 4H), 1.65 (t, *J* = 7.4 Hz, 6H);

^{13}C NMR (151 MHz, CD_3CN) δ 151.5, 150.7, 146.6, 146.3 (t, *J* = 8.5 Hz), 134.7, 131.74, 131.70, 131.5, 65.0, 58.7, 16.5;

^{19}F NMR (470 MHz, CD_3CN) δ −73.1 (d, *J* = 706.9 Hz);

^{31}P NMR (202 MHz, CD_3CN) δ −143.5 (hept, *J* = 706.9 Hz);

IR (neat) 3144, 3082, 2996, 2950, 1643, 1569, 1560, 1509, 1456, 1357, 1223, 1201, 1180, 823 cm^{-1};

HRMS (ESI-TOF): *m/z* for $C_{32}H_{34}F_{18}N_4P_3$ calcd 909.1709, found 909.1690.

(4-bromo-1,2-phenylene)dimethanol **13**

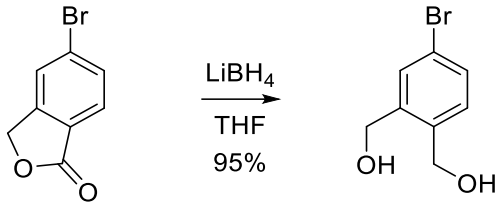

12 **13**

A solution 2M solution of $LiBH_4$ in THF (24 mL, 48 mmol, 1.0 equiv) was slowly added to a solution of 5-bromophtalide (10. g, 47 mmol, 1.0 equiv) in THF (0.15 L), at 0 °C. MeOH (0.30 mL) was added and the reaction was allowed to reach room temperature. The reaction was stirred 24 h, even if TLC showed full conversion of starting material after 30 minutes. The solution was cooled to 0 °C, and MeOH was slowly added until H_2 evolution ceased. Water was then slowly added, followed by a 10% HCl aqueous solution. Organic were removed under vacuo and aqueous was extracted with EtOAc. Aqueous layer were separated and extracted again with EtOAc. Organic were combined, dried over Na_2SO_4, and concentrated. The resulting residue was purified via flash chromatography (80 g, SiO_2, 2:3 EtOAc:Hex) to yield the known diol **13** (9.7 g, 95 %) as a white solid.[3]

3,4-di(hydroxymethyl)styrene

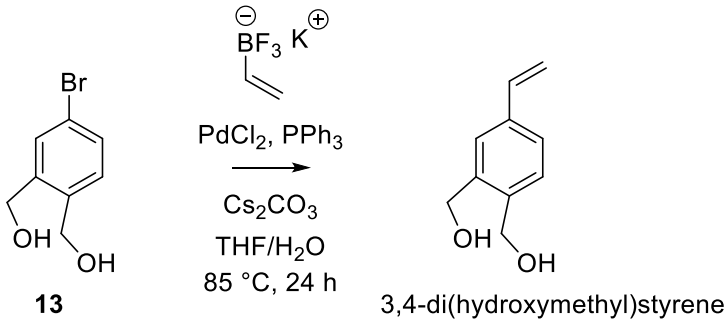

13 3,4-di(hydroxymethyl)styrene

In a Schlenk flask, a mixture of diol **13** (1.0 g, 4.6 mmol, 1.0 equiv), potassium vinyltrifluoroborate (0.6 g, 4.5 mmol, 1.0 equiv), $PdCl_2$ (16 mg, 0.090 mmol, 0.020 equiv), PPh_3, (70. mg, 0.27 mmol, 0.060 equiv), Cs_2CO_3 (bis3.9 g, 12 mmol, 2.7 equiv), and THF:H_2O solution (10 mL, 9:1) was degassed by freeze-pump thaw (3 cycles). The mixture was then stirred at 85 °C for 24 h. Reaction mixture was cooled to room temperature, added of H_2O, and extracted with EtOAc. Aqueous layer was separated and extracted again with EtOAc. Organic were combined, dried over Na_2SO_4, and concentrated. Crude NMR confirmed the formation of the desired product. The residue was The resulting residue was purified via flash chromatography (40 g, SiO_2, 1:4 to 3:7 EtOAc:Hex) to yield the corresponding unstable 3,4-di(hydroxymethyl)styrene, which was used in the next step immediately after isolation.

3,4-di(chloromethyl)styrene (monomer) **14**

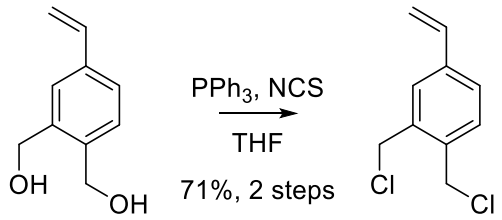

14

PPh_3 (3.1 g, 12 mmol, 2.7 equiv) was slowly added to a vigorously stirred solution of NCS (1.5 g, 11 mmol, 2.4 equiv) at 0 °C. Upon addition of PPh_3, a precipitate was formed. The mixture was allowed to reach room temperature, and stirred for 30 minutes. A solution of the aforementioned 3,4-di(hydroxymethyl)styrene (theoretically 4.5 mmol, 1.0 equiv) was added to the freshly prepared phosphonium chloride mixture and stirred overnight at room temperature (monitored by TLC). Overtime, mixture turned to solution. Water was slowly added to the mixture and THF was removed under vacuo. Aqueous was extracted with EtOAc. Aqueous was separated and extracted again with EtOAc. Organic were combined, dried over Na_2SO_4, filtered and concentrated. The residue was purified via flash chromatography (40 g SiO_2, Hex) to afford 3,4-di(chloromethyl)styrene **14** (0.65 g, 72 % over 2 steps) as a clear oil. The pure oil was immediately hidden from light and stored in the freezer.

^{1}H NMR (400 MHz, $CDCl_3$) δ 7.43 (d, *J* = 1.7 Hz, 1H), 7.38 (dd, *J* = 7.9, 1.7 Hz, 1H), 7.35 (d, *J* = 7.9 Hz, 1H), 6.70 (dd, *J* = 17.6, 10.9 Hz, 1H), 5.80 (d, *J* = 17.6 Hz, 1H), 5.33 (d, *J* = 10.9 Hz, 1H), 4.75 (s, 2H), 4.74 (s, 2H);

^{13}C NMR (101 MHz, $CDCl_3$) δ 139.0, 136.6, 135.8, 135.7, 131.3, 128.8, 127.2, 115.7, 43.5, 43.3;

IR (neat) 3090, 3007, 2974, 1445, 1262, 989, 914, 839, 758, 717, 681 cm^{-1};

HRMS (EI-TOF): *m/z* for $C_{10}H_{10}Cl_2$ calcd 200.0160, found 200.0150.

Poly 3,4-di(chloromethyl)styrene **15**

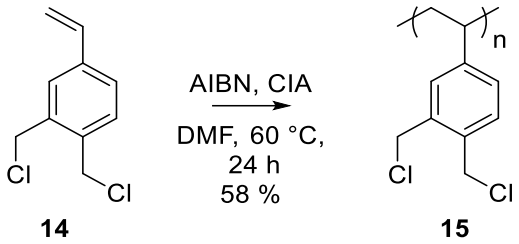

In a schlenk flask, 3,4-di(chloromethyl)styrene **14** (0.59 g, 2.9 mmol, 1.0 equiv), CIA (0.90 mg, 5.5 µmol, 0.0020 equiv), and AIBN (0.90 mg, 2.8 µmol, 0.0010 equiv) were mixed with DMF (0.1 mL) and degassed with 3 cycles of freeze-pump thaw. The reaction mixture was then stirred at 80 °C for 24 h. The reaction mixture was cooled to room temperature, precipitated out in MeOH (rinse with a minimal amount of THF). The precipitate was dissolved in THF and precipitated out again in MeOH. Repeat precipitation. The solid was rinsed with Et_2O and dried under vacuo to yield a Poly 3,4-di(chloromethyl)styrene **15** (0.34 mg, 58%).

^{1}H NMR (499 MHz, $CDCl_3$) δ 7.21 – 6.91 (m, 1H), 6.74 – 6.15 (m, 2H), 4.78 – 3.88 (m, 4H), 2.19 – 1.30 (m, 3H);

IR (neat) 3014, 2923, 2853, 1612, 1502, 1445, 1426, 1262, 1236, 1166, 1104, 896, 834;

GPC:

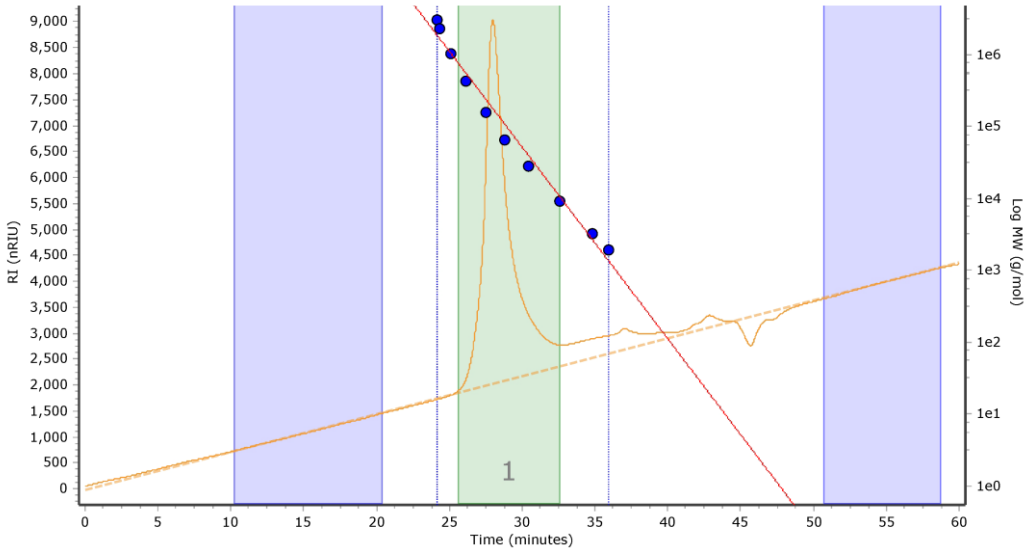

Molecular Weight Averages

	g/mol)	Mn (g/mol)	Mw (g/mol)	Mz (g/mol)	Mz+1 (g/mol)	Mv (g/mol)	PD
Peak 1	174311	80311	148724	207672	265524	199616	1.852

Image B.1. Screenshot of GPC analysis of polymer **15**.

Poly 3,4-di(methylene(1-ethylviologen)styrene tetra hexafluorophosphate **10** (*o*-Benzene polymer **10**)

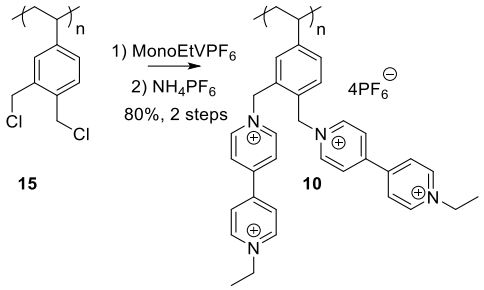

N-Ethyl 4,4'-bipyridinium hexafluorophosphate (1.7 g, 5.1 mmol, 5 .1 equiv) was added to a solution of polymer **15** (0.21 g, 1.0 mmol, 1.0 equiv) in DMF (1 mL). The solution was heated at 60 °C for 5-6 days. The reaction solution was cooled to room temperature and polymer was precipitated out in MeOH. The polymer was dissolved on a minimal amount of MeCN, and precipitated out in Et_2O. Repeat. Polymer was dissolved in a solution of MeCN:H_2O (1:1, 20 mL) and added of NH_4PF_6 (8.3 g, 51 mmol, 10 equiv). The mixture was stirred 24 h at room temperature. MeCN was removed under vacuum. Solid separated from water. The polymer was dissolved back in MeCN and stirred fresh distillated water was added. MeCN was removed under vacuo and the solid separated from water. Repeat. The solid was washed twice with MeOH, followed by 2 cycles of dissolution/precipitation from MeCN and Et_2O. The solid was dried under vacuum to afford expected polymer **10** (0.86 g, 80%, 2 steps), as an off-white solid.

^{1}H NMR (600 MHz, CD_3CN) δ 9.26 – 8.50 (m, 8H), 8.50 – 7.88 (m, 8H), 7.81 – 6.35 (m, 3H), 6.32 – 4.99 (m, 4H), 4.99 – 4.20 (m, 4H), 1.85 – 0.96 (m, 9H);

^{19}F NMR (564 MHz, CD_3CN) δ −71.6 (d, J = 710.5 Hz);

^{31}P NMR (243 MHz, CD_3CN) δ −144.9 (hept, J = 710.5 Hz);

IR (neat) 3139, 3076, 2950, 1639, 1562, 1505, 1450, 1221, 1173, 1090, 825 cm^{-1};

Anal. Calcd for $C_{34}H_{36}F_{24}N_4P_4$: C, 37.79; H, 3.36; N, 5.19. Found: C, 37.68; H, 3.61; N, 5.06.

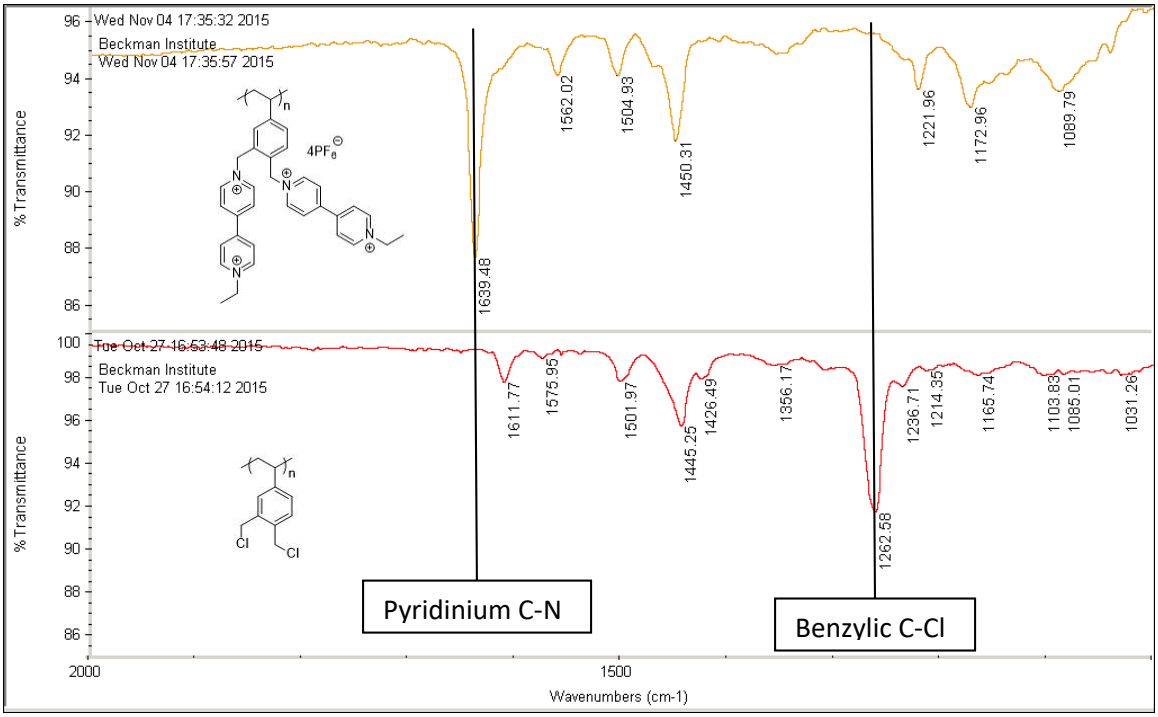

Image B.2. Screenshot of infrared spectral comparison of poly viologen **10** and polymer di(chloromethyl)styrene **15**.

4,5

3,5-di(hydroxymethyl)iodobenzene **17**

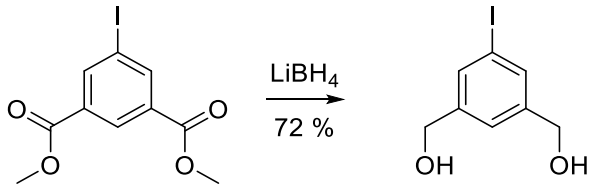

16 **17**

A solution 2M solution of $LiBH_4$ in THF (3.0 mL, 6.0 mmol, 1.0 equiv) was slowly added to a solution of dimethyl 5-iodoisophtalate **16** (1.9 g, 5.9 mmol, 1.0 equiv) in THF (20 mL), at 0 °C. MeOH (0.1 mL) was added and the reaction was allowed to reach room temperature. The reaction was stirred 24 h. The solution was cooled to 0 °C, and MeOH was slowly added until H_2 evolution ceased. Water was then slowly added, followed by a 10% HCl aqueous solution. Organic were removed under vacuo and aqueous was extracted with EtOAc. Aqueous layer were separated and extracted again with EtOAc. Organic were combined, dried over Na_2SO_4, and concentrated. The resulting residue was purified via flash chromatography (25 g, SiO_2, 1:19 MeOH:CH_2Cl_2) to yield the known diol **17** (1.2 g, 76%) as a white solid.[6]

3,5-di(hydroxymethyl)styrene

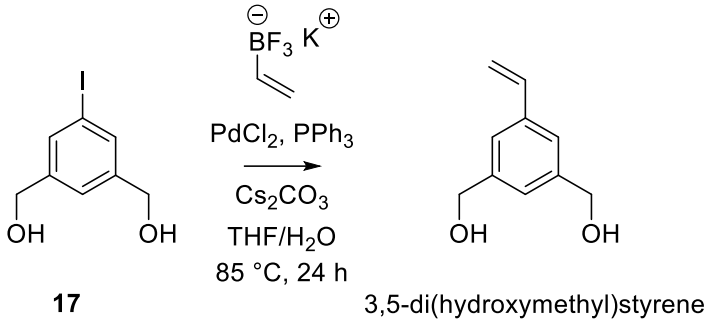

17 3,5-di(hydroxymethyl)styrene

In a Schlenk flask, a mixture of diol **17** (1.0 g, 3.8 mmol, 1.0 equiv), potassium vinyltrifluoroborate (0.51 g, 3.8 mmol, 1.0 equiv), $PdCl_2$ (13 mg, 0.073 mmol, 0.019 equiv), PPh_3, (60. mg, 0.23 mmol, 0.061 equiv), Cs_2CO_3 (3.8 g, 12 mmol, 3.2 equiv), and THF:H_2O solution (10 mL, 9:1) was degassed by freeze-pump thaw (3 cycles). The mixture was then stirred at 85 °C for 24 h. Reaction mixture was cooled to room temperature, added of H_2O, and extracted with EtOAc. Aqueous layer was separated and extracted again with EtOAc. Organic were combined, dried over Na_2SO_4, and concentrated. Crude NMR confirmed the formation of the desired product. The residue was The resulting residue was purified via flash chromatography (25 g, SiO_2, CH_2Cl_2) to yield the corresponding unstable 3,5-di(hydroxymethyl)styrene, which was used in the next step immediately after isolation.

3,5-di(chloromethyl)styrene **18** (monomer **18**)

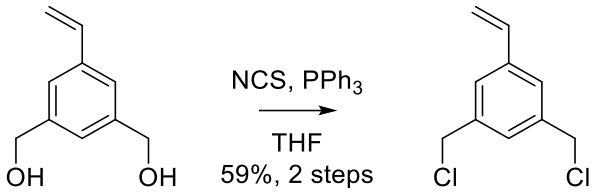

18

PPh_3 (3.0 g, 11 mmol, 2.9 equiv) was slowly added to a vigorously stirred solution of NCS (1.5 g, 11 mmol, 2.9 equiv) at 0 °C. Upon addition of PPh_3, a precipitate was formed. The mixture was allowed to reach room temperature, and stirred for 30 minutes. A solution of the aforementioned 3,5-di(hydroxymethyl)styrene (theoretically 3.8 mmol, 1.0 equiv) was added to the freshly prepared phosphonium chloride mixture and stirred overnight at room temperature (monitored by TLC). Overtime, mixture turned to solution. Water was slowly added to the mixture and THF was removed under vacuo. Aqueous was extracted with EtOAc. Aqueous was separated and extracted again with EtOAc. Organic were combined, dried over Na_2SO_4, filtered and concentrated. The residue was purified via flash chromatography (80 g, SiO_2, Hex) to afford 3,5-di(chloromethyl)styrene **18** (0.45 g, 59 % over 2 steps) as a clear oil. The pure oil was immediately hidden from light and stored in the freezer.

^{1}H NMR (499 MHz, $CDCl_3$) δ 7.39 (s, 2H), 7.32 (s, 1H), 6.71 (dd, *J* = 17.7, 10.9 Hz, 1H), 5.81 (d, *J* = 17.7 Hz, 1H), 5.34 (d, *J* = 10.9 Hz, 1H), 4.58 (s, 4H);

^{13}C NMR (126 MHz, $CDCl_3$) δ 138.8, 138.4, 135.8, 128.0, 126.5, 115.4, 45.8;

IR (neat) 3097, 2961. 2918, 2848, 1599, 1466, 1446, 1261, 989, 915, 710 cm^{-1};

HRMS (EI-TOF): *m/z* for $C_{10}H_{10}Cl_2$ calcd 200.0160, found 200.0159.

Poly 3,5-di(chloromethyl)styrene **19**

18 **19**

In a schlenk flask, 3,5-di(chloromethyl)styrene **18** (0.40 g, 2.2 mmol, 1.0 equiv), CIA (1.0 mg, 3.2 µmol, 0.0014 equiv), and AIBN (0.50 mg, 3.0 µmol, 0.0014 equiv) were mixed with DMF (0.1 mL) and degassed with 3 cycles of freeze-pump thaw. The reaction mixture was then stirred at 80 °C for 2 h. The reaction mixture was cooled to room temperature, precipitated out in MeOH (rinse with a minimal amount of THF). The precipitate was dissolved in THF and precipitated out again in MeOH. Repeat precipitation. The solid was rinsed with Et_2O and dried under vacuo to yield Poly 3,5-di(chloromethyl)styrene **19** (0.22 g, 55%).

^{1}H NMR (499 MHz, $CDCl_3$) δ 7.19 – 6.74 (m, 1H), 6.73 – 6.04 (m, 2H), 4.77 – 4.37 (m, 4H), 2.35 – 1.05 (m, 3H);

IR (neat) 3027, 2926, 2848, 1603, 1457, 1295, 1261, 1159, 1066, 972, 894, 855 cm^{-1};

GPC:

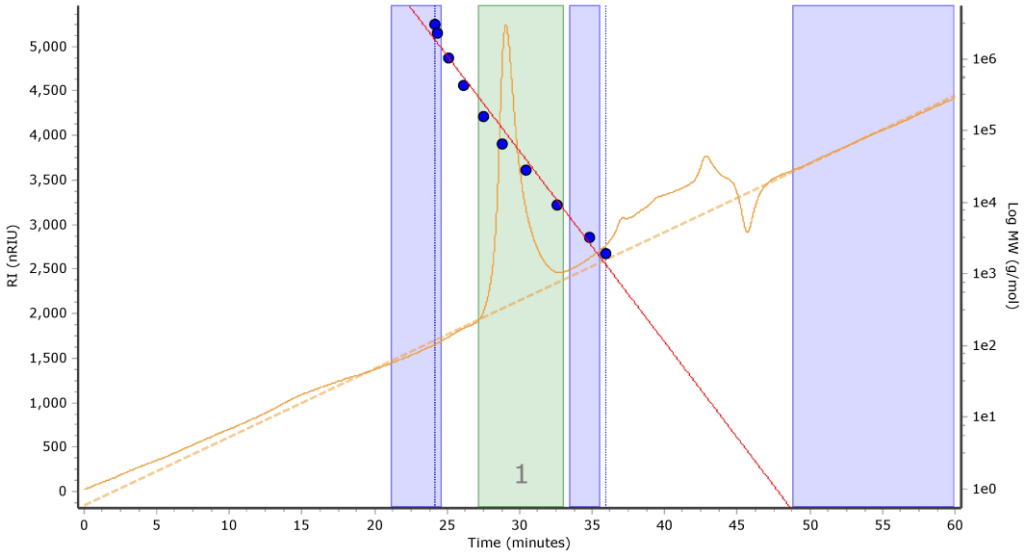

Molecular Weight Averages

Peak	Mp (g/mol)	Mn (g/mol)	Mw (g/mol)	Mz (g/mol)	Mz+1 (g/mol)	Mv (g/mol)	PD
Peak 1	91064	52959	76243	94949	111117	92503	1.44

Image B.3. Screenshot of GPC analysis of polymer **19**.

Poly 3,5-di(methylene(1-ethylviologen)styrene tetra hexafluorophosphate **11** (*m*-Benzene polymer **11**)

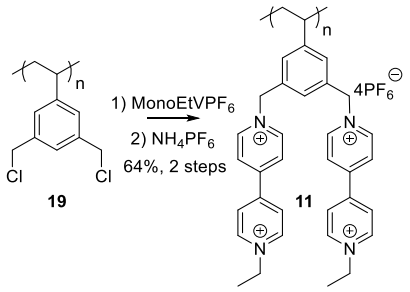

N-Ethyl 4,4'-bipyridinium hexafluorophosphate (0.79 g, 2.4 mmol, 5.0 equiv) was added to a solution of polymer **19** (96 mg, 0.48 mmol, 1.0 equiv) in DMF (1 mL). The solution was heated at 60 °C for 5 days. The reaction solution was cooled to room temperature and polymer was precipitated out in MeOH. The polymer was dissolved on a minimal amount of MeCN, and precipitated out in Et_2O. Repeat. Polymer was dissolved in a solution of MeCN:H_2O (1:1, 10 mL) and added of NH_4PF_6 (0.78 g, 4.8 mmol, 10. equiv). The mixture was stirred 24 h at room temperature. MeCN was removed under vacuum. Solid separated from water. The polymer was dissolved back in MeCN and stirred fresh distillated water was added. MeCN was removed under vacuo and the solid separated from water. Repeat. The solid was washed twice with MeOH, followed by two cycles of dissolution/precipitation from MeCN and Et_2O. The solid was dried under vacuum to afford expected polymer **11** (0.33 g, 64%, 2 steps) as a yellow solid.

^{1}H NMR (600 MHz, CD_3CN) δ 9.22 – 8.53 (m, 1H), 8.53 – 7.86 (m, 1H), 7.80 – 6.27 (m, 0H), 6.29 – 4.96 (m, 1H), 4.79 – 4.36 (m, 1H), 1.82 – 1.05 (m, 1H);

^{19}F NMR (564 MHz, CD_3CN) δ −71.5 (d, J = 710.2 Hz);

^{31}P NMR (243 MHz, CD_3CN) δ −144.8 (hept, J = 710.2 Hz);

IR (neat) 3137, 3080, 1640, 1564, 1507, 1451, 1220, 1174, 824;

Anal. Calcd for $C_{34}H_{36}F_{24}N_4P_4$: C, 37.79; H, 3.36; N, 5.19. Found: C, 38.43; H, 3.23; N, 4.89.

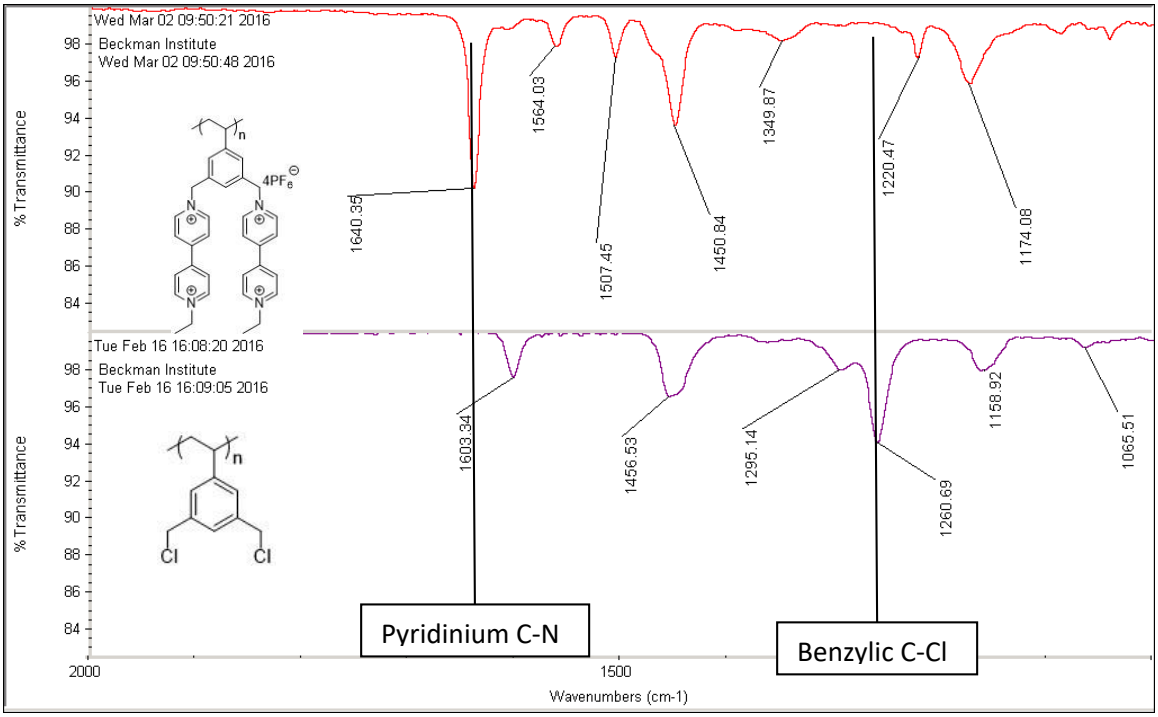

Image B.4. Screenshot of infrared spectral comparison of poly viologen **11** and poly di(chloromethyl)styrene **19**.[4,5]

Method to Estimate *Mn* of Final Polymers 10 and 11

We assumed that full conversions of polymer **15** and **19** to polymer **10** and **11**, respectively, based on NMR, IR, and elemental analysis. For polymer 11, bulk electrolysis also exhibited 92% of the theoretical charge for this RAP solution assuming 100% functionalization.

Comparison between **15** or **19** and **10** of **11** suggests that polymers bearing two viologen units has a molecular weight which is 5.4 bigger than its precursor. With this molecular weight ratio, we could estimate that the polymer 15 with a Mn of 80 kDa will convert to polymer 10 with a Mn of 432 kDa (5.4 x 80kDa). The same approach is used for polymer 11, since is an isomer of 10.

NMR Spectra

Diethyl viologen bis(hexafluorophosphate) **2** NMRs

499 MHz, CD_3CN

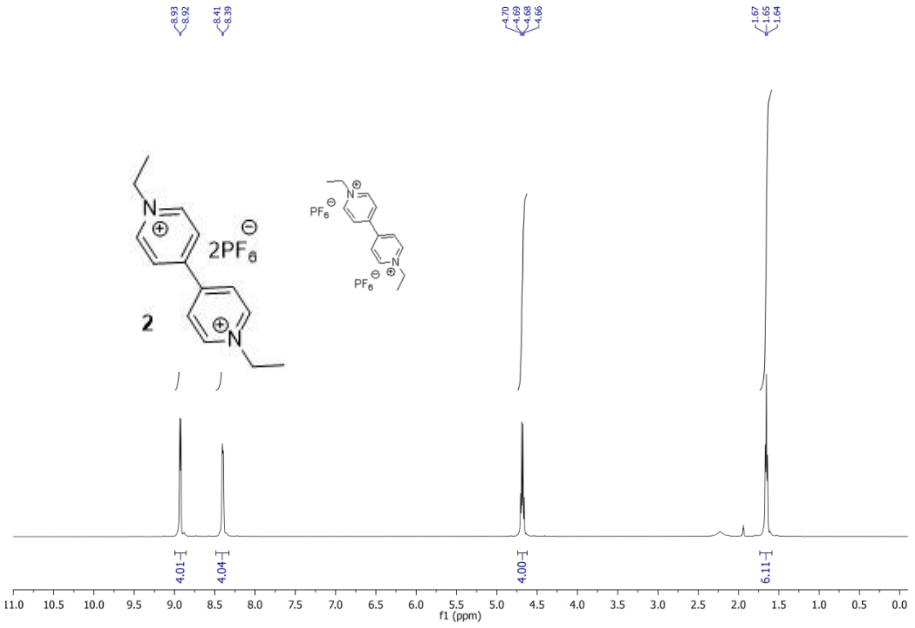

126 MHz, CD_3CN

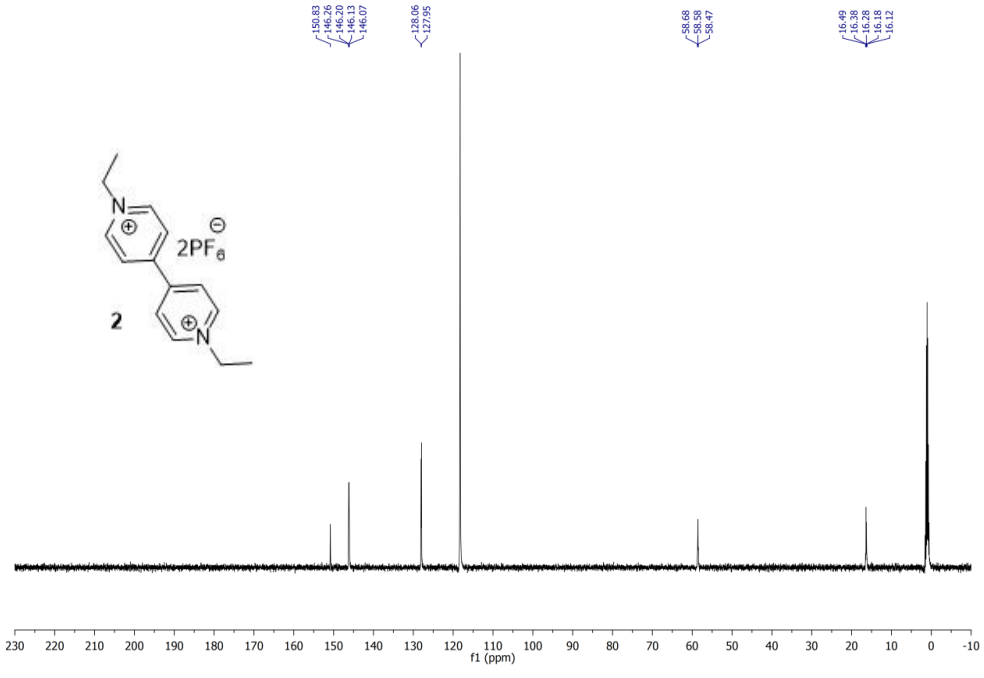

470 MHz, CD_3CN

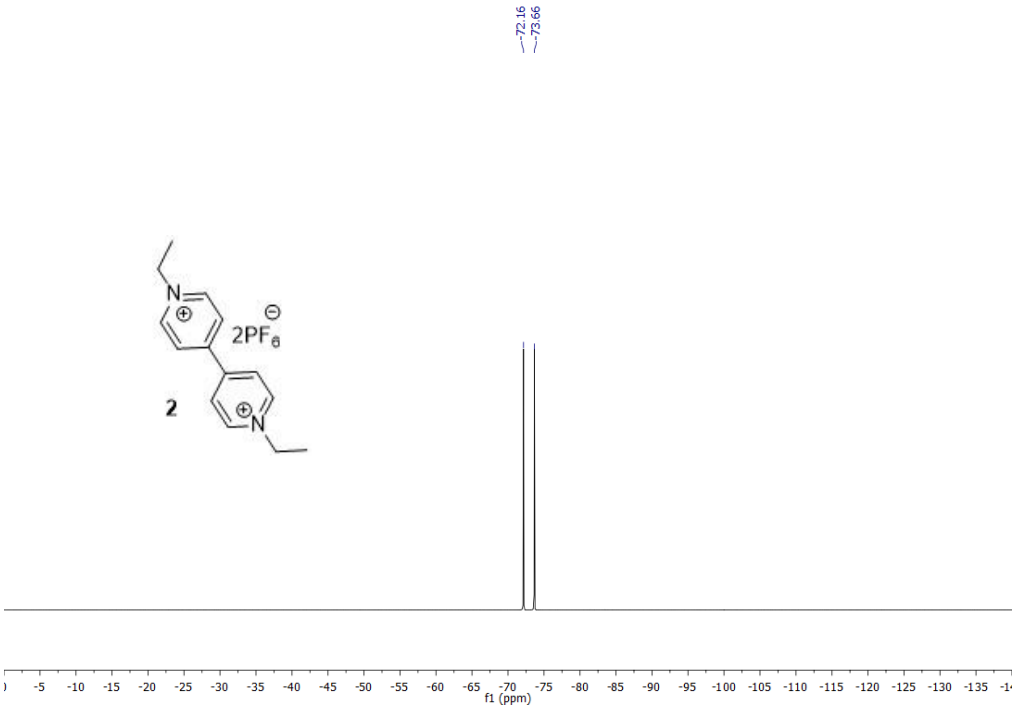

202 MHz, CD_3CN

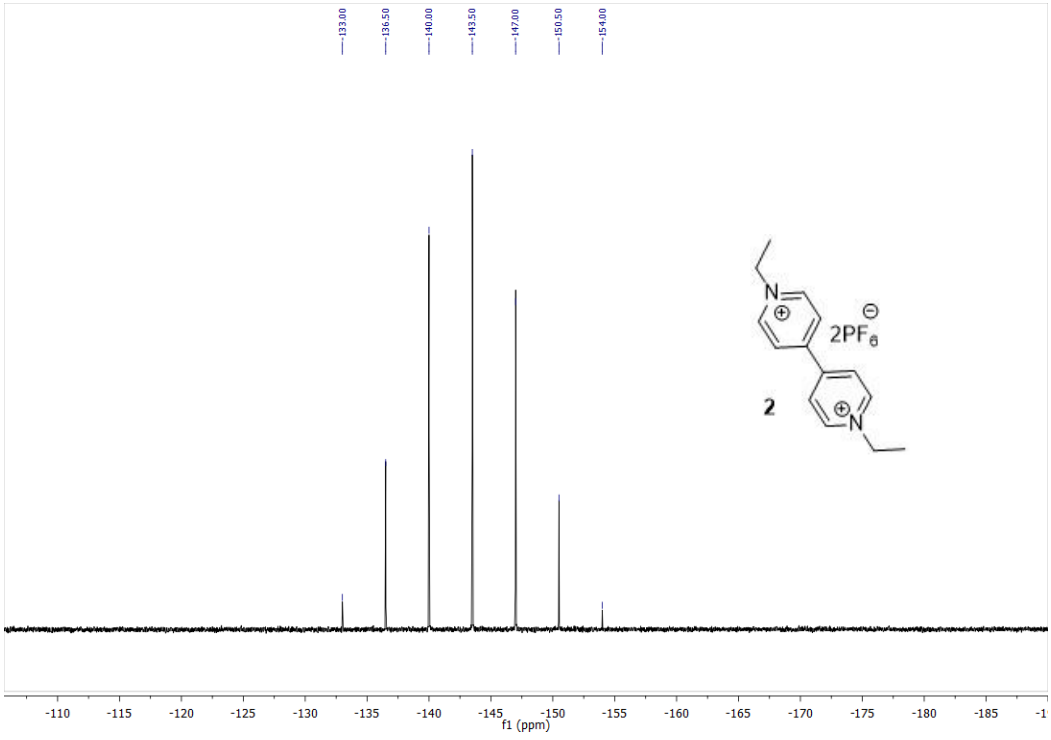

1,3-propyl bis(viologen) **3** NMRs

500 MHz, CD_3CN

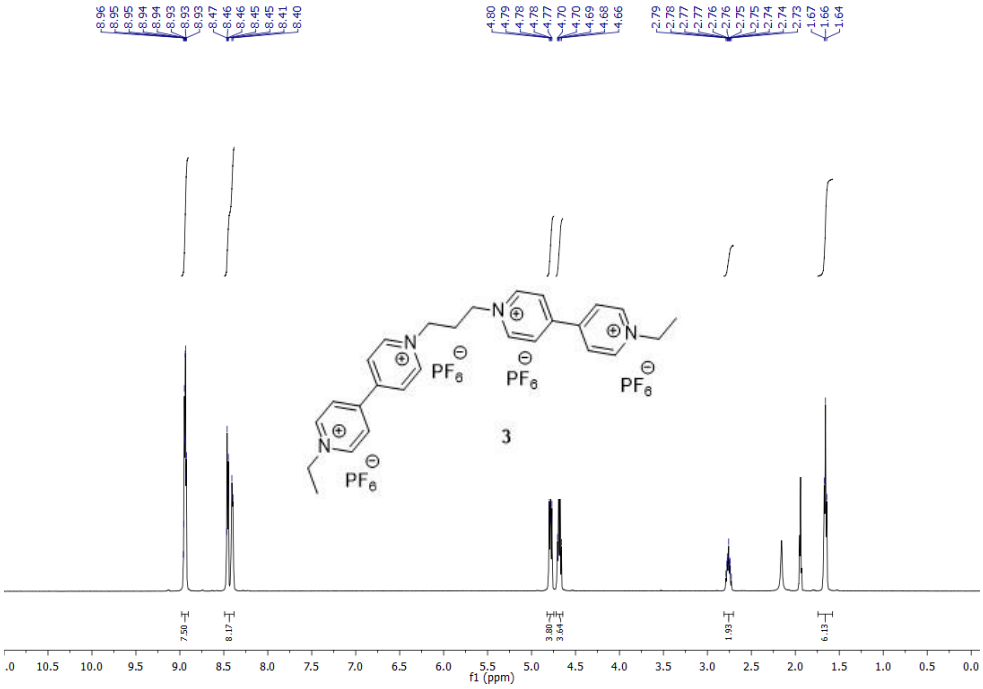

126 MHz, CD_3CN

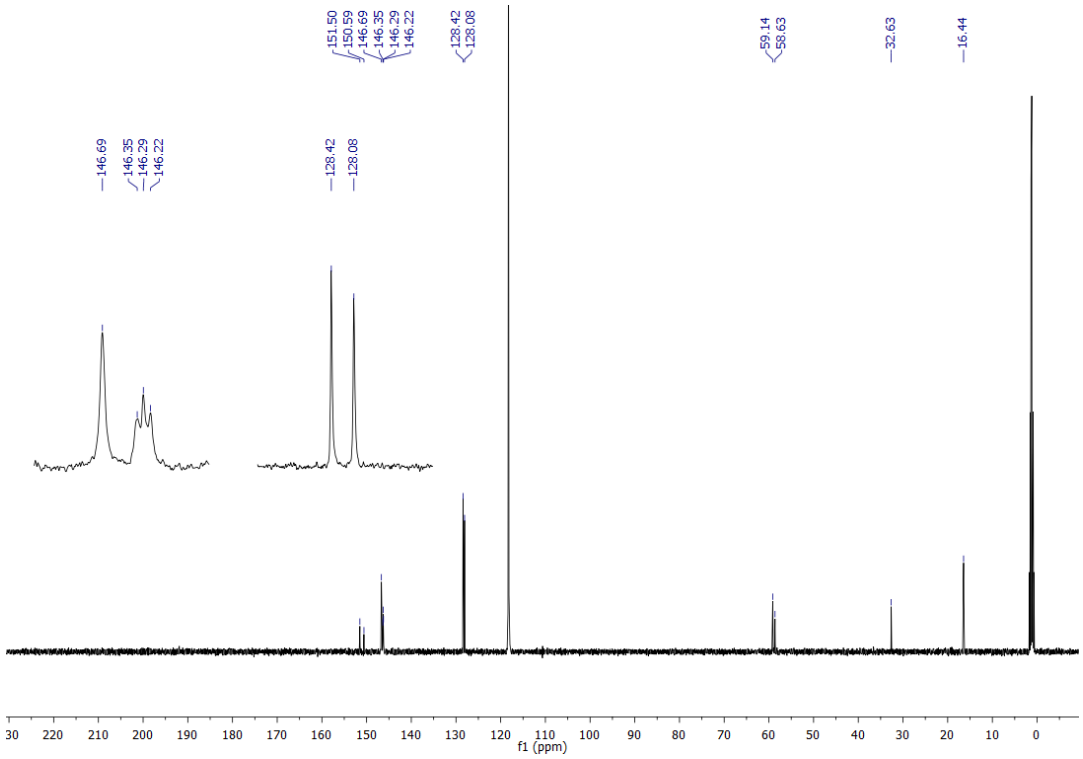

470 MHz, CD_3CN

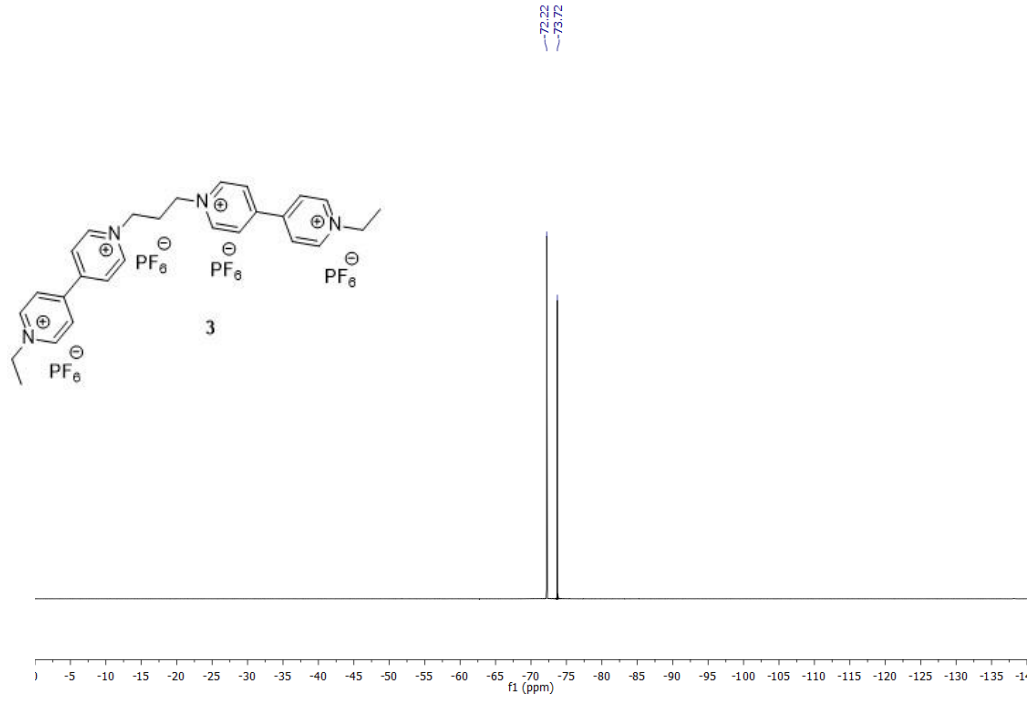

202 MHz, CD3CN

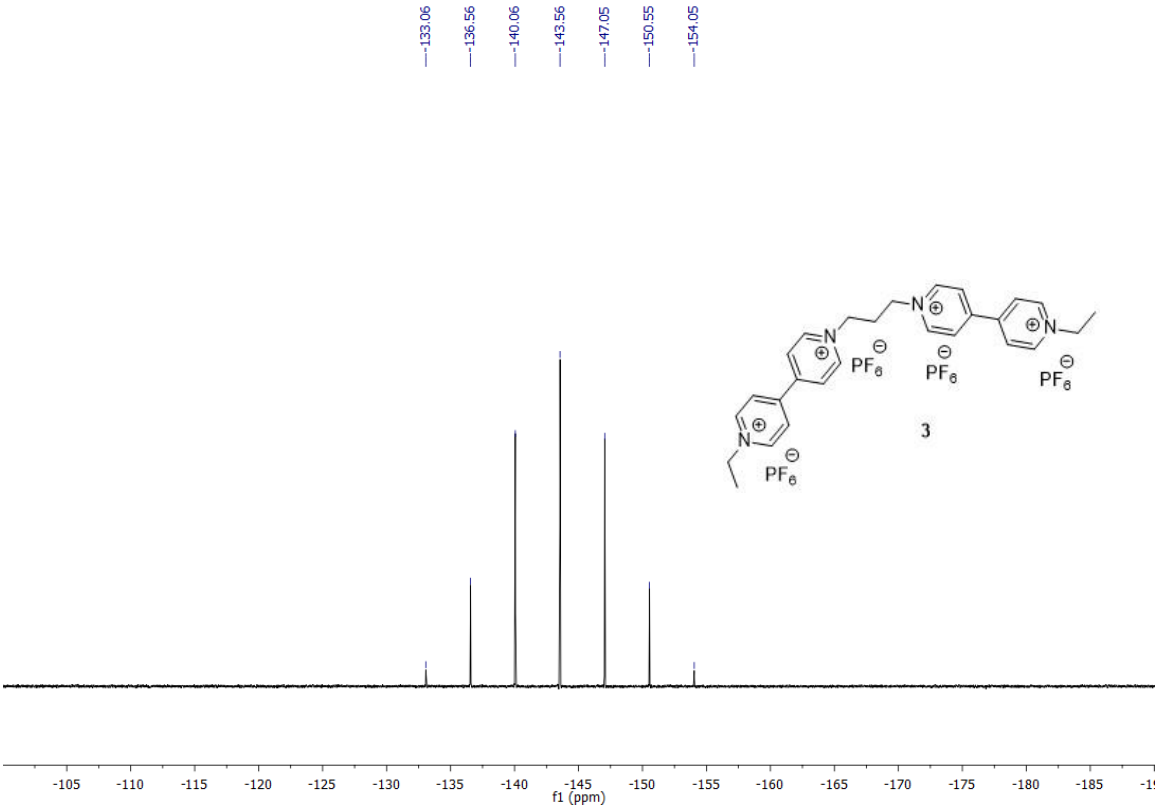

1,4-butyl bis(viologen) **4** NMRs

499 MHz, CD_3CN

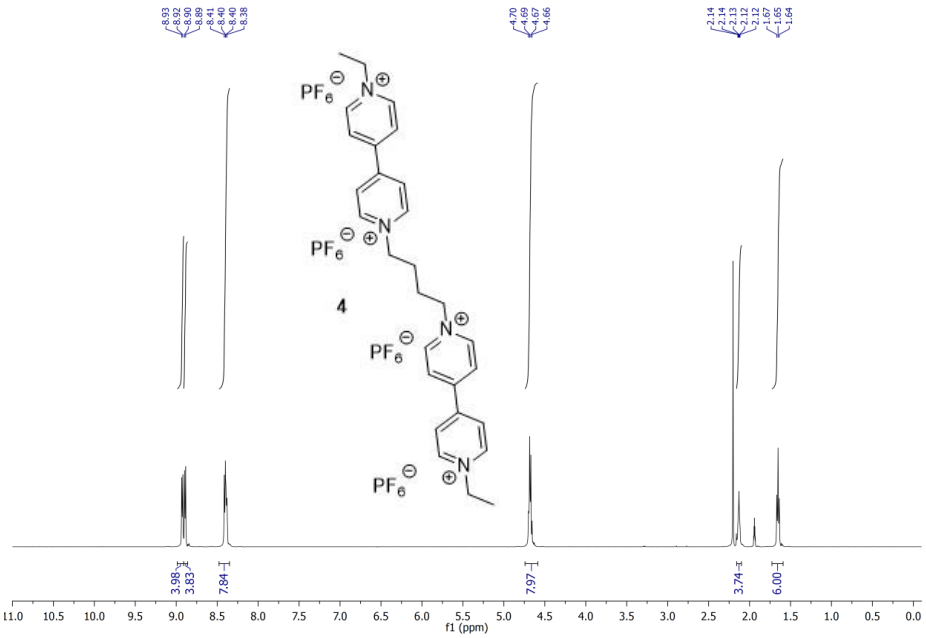

126 MHz, CD_3CN

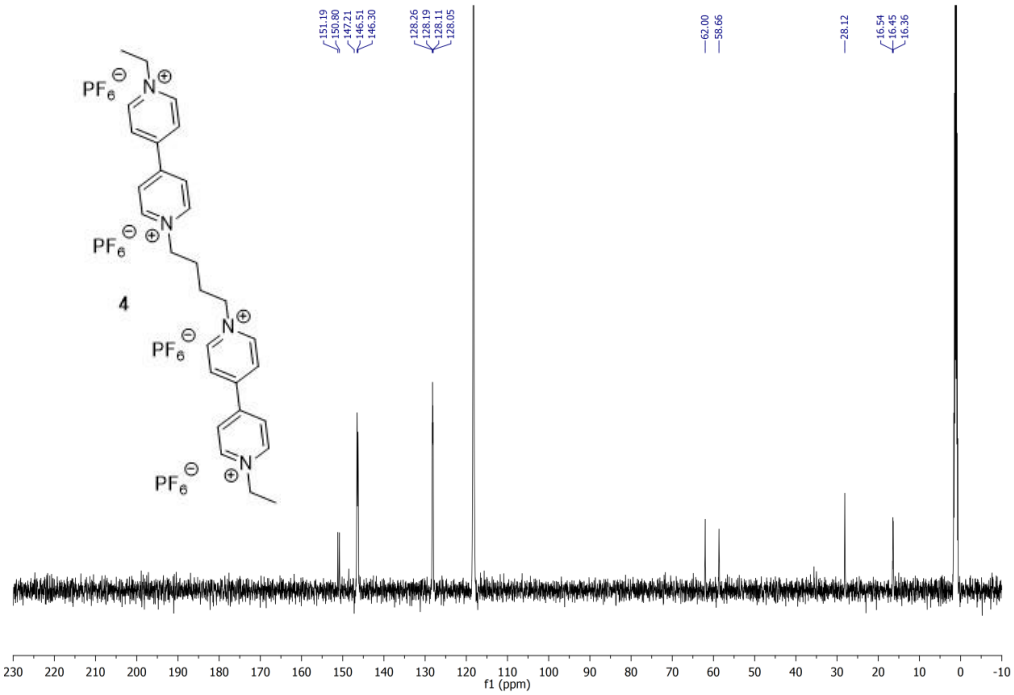

470 MHz, CD_3CN

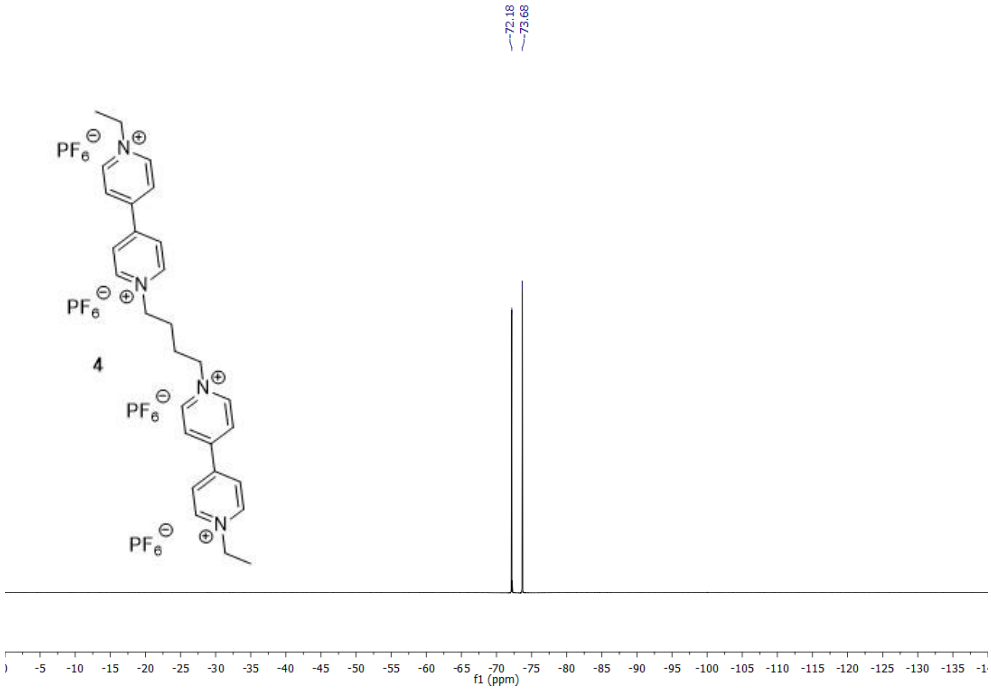

202 MHz, CD_3CN

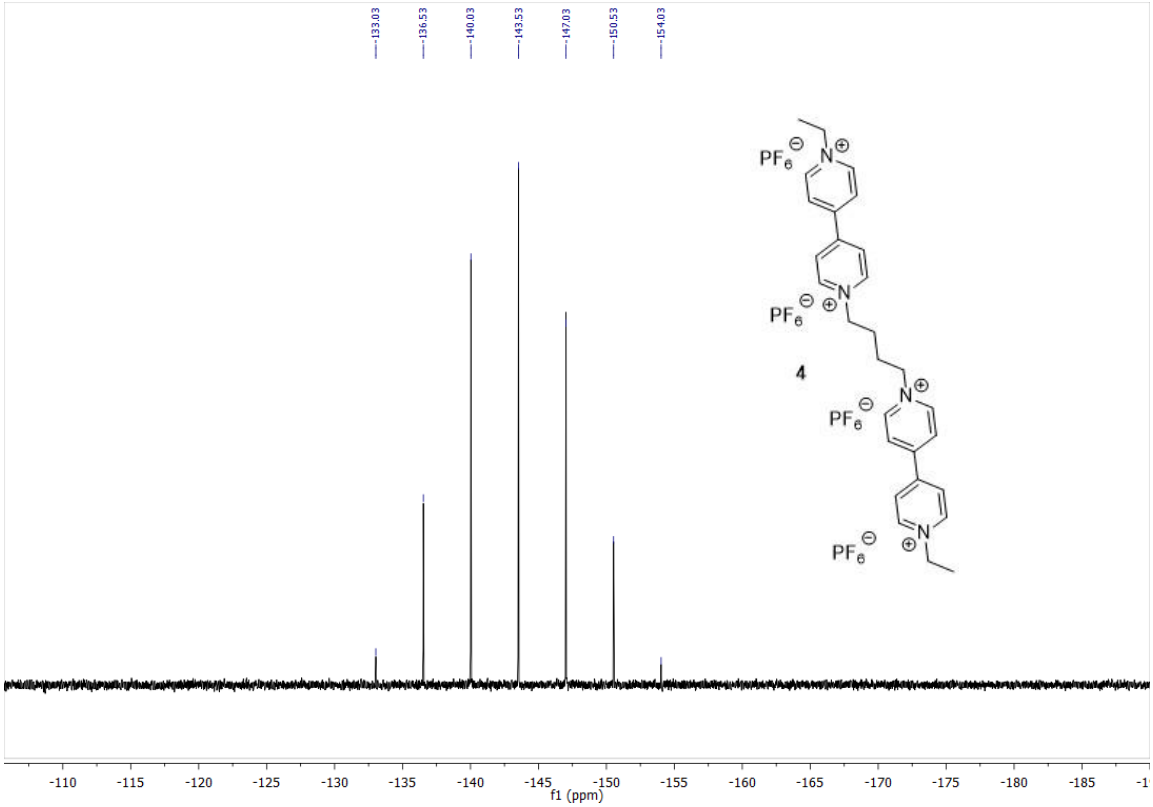

1,5-pentyl bis(viologen) **5** NMRs

499 MHz, CD_3CN

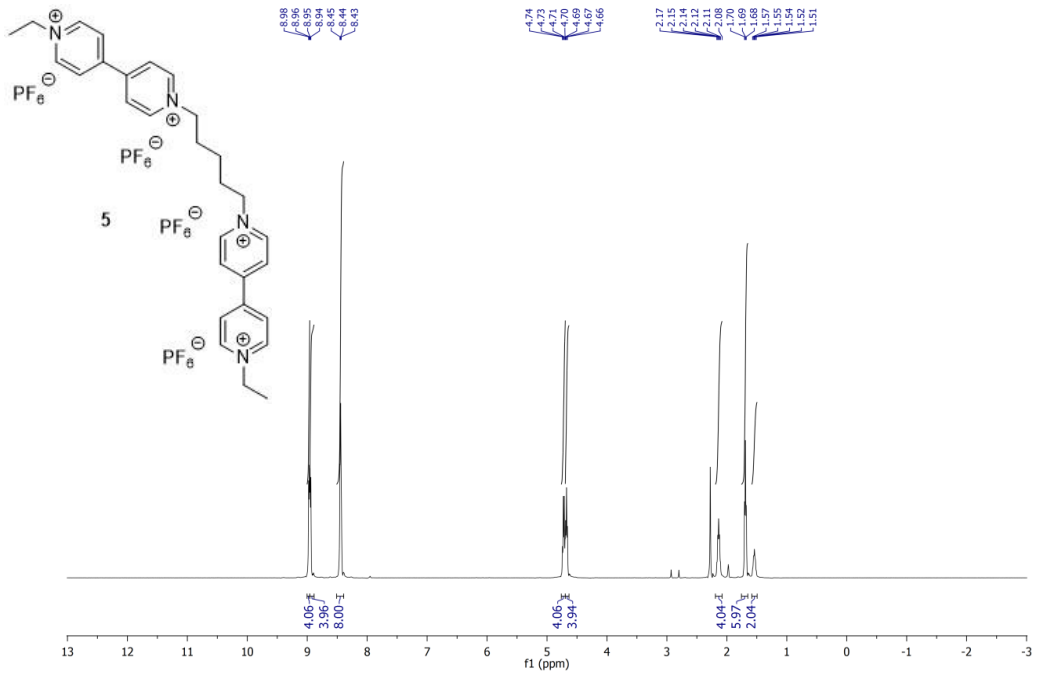

126 MHz, CD_3CN

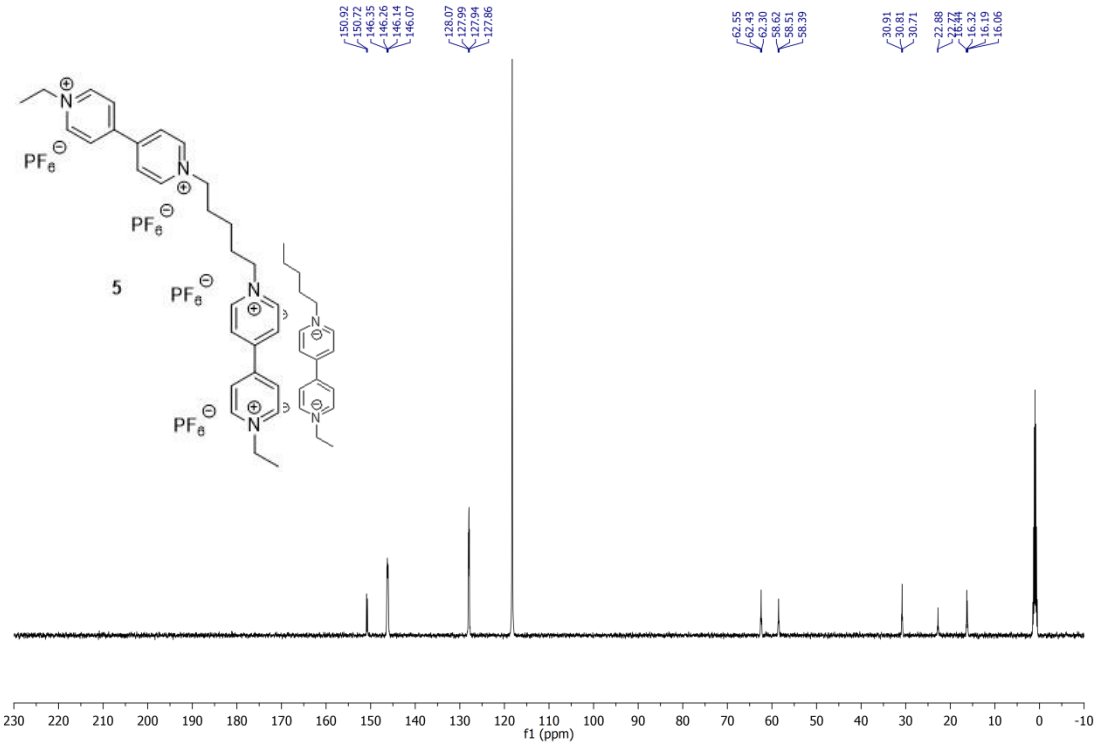

470 MHz, CD_3CN

202 MHz, CD_3CN

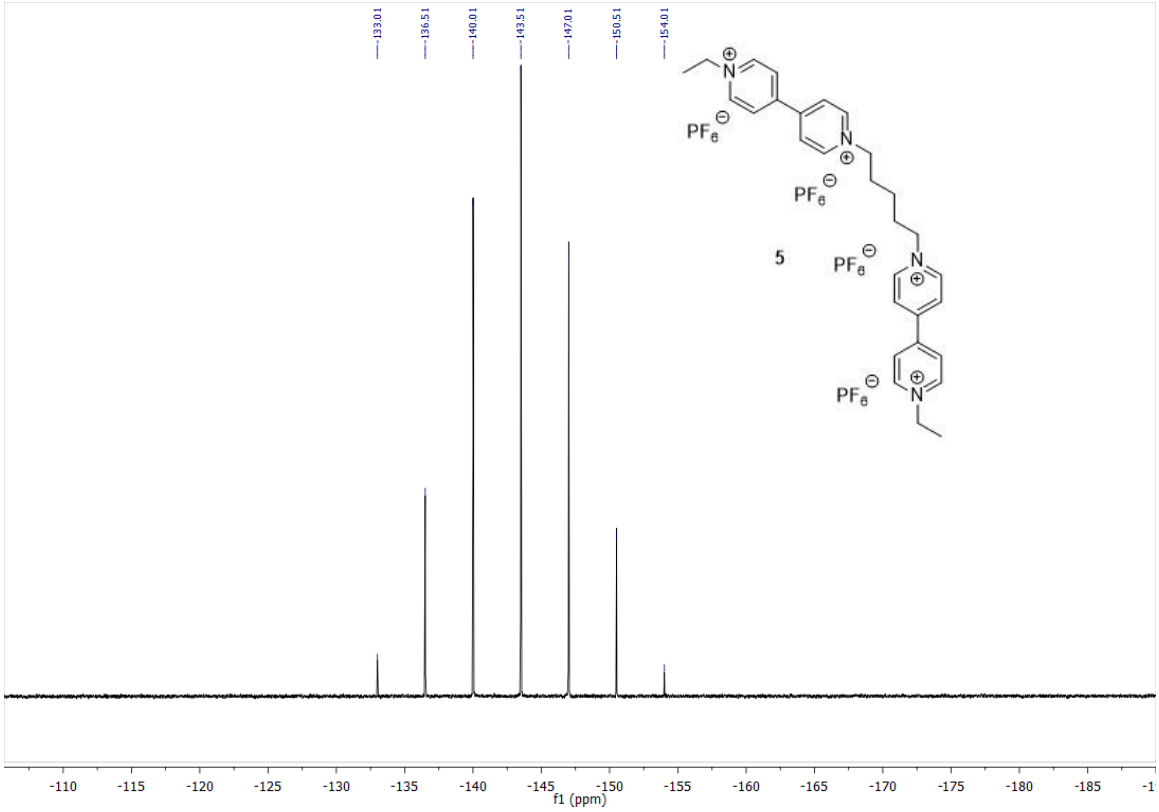

1,6-hexyl bis(viologen) **6** NMRs

499 MHz, CD_3CN

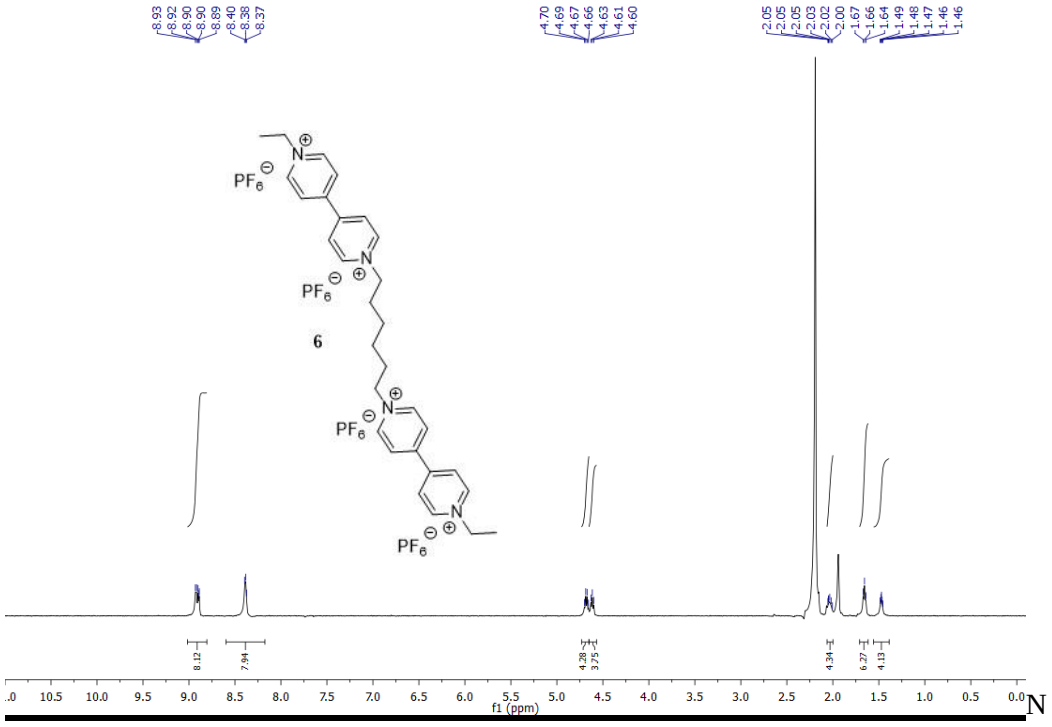

126 MHz, CD_3CN

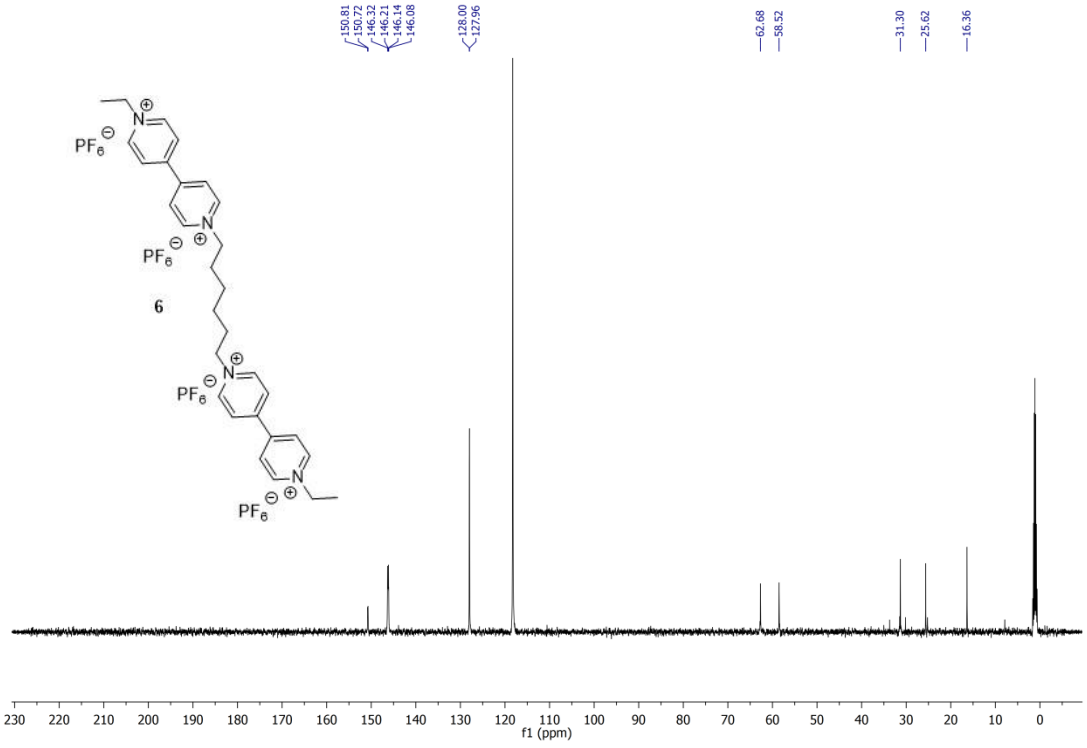

470 MHz, CD_3CN

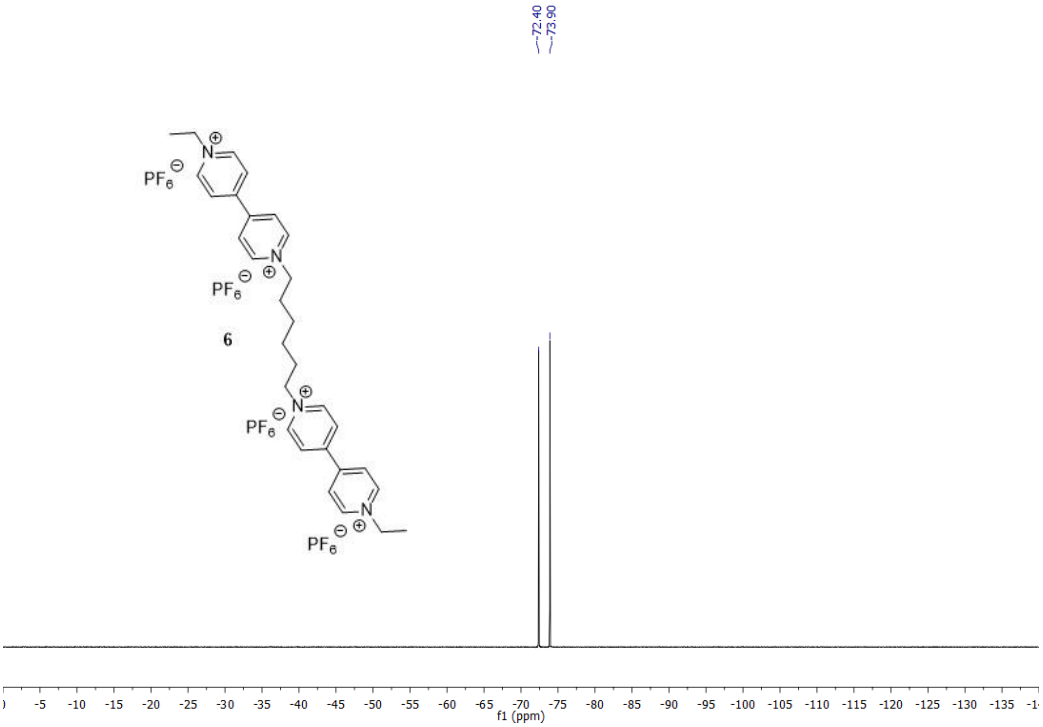

243 MHz, CD_3CN

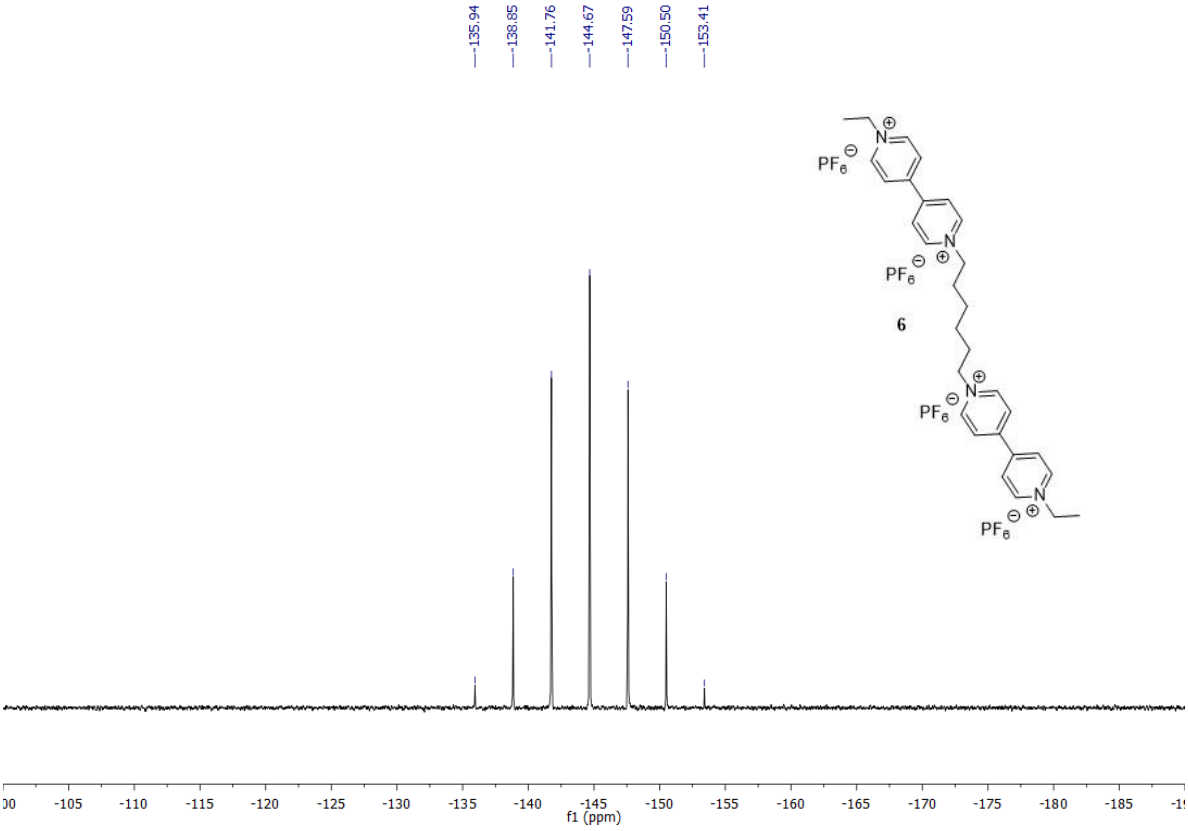

1,7-heptyl bis(viologen) **7** NMRs

500 MHz, CD_3CN

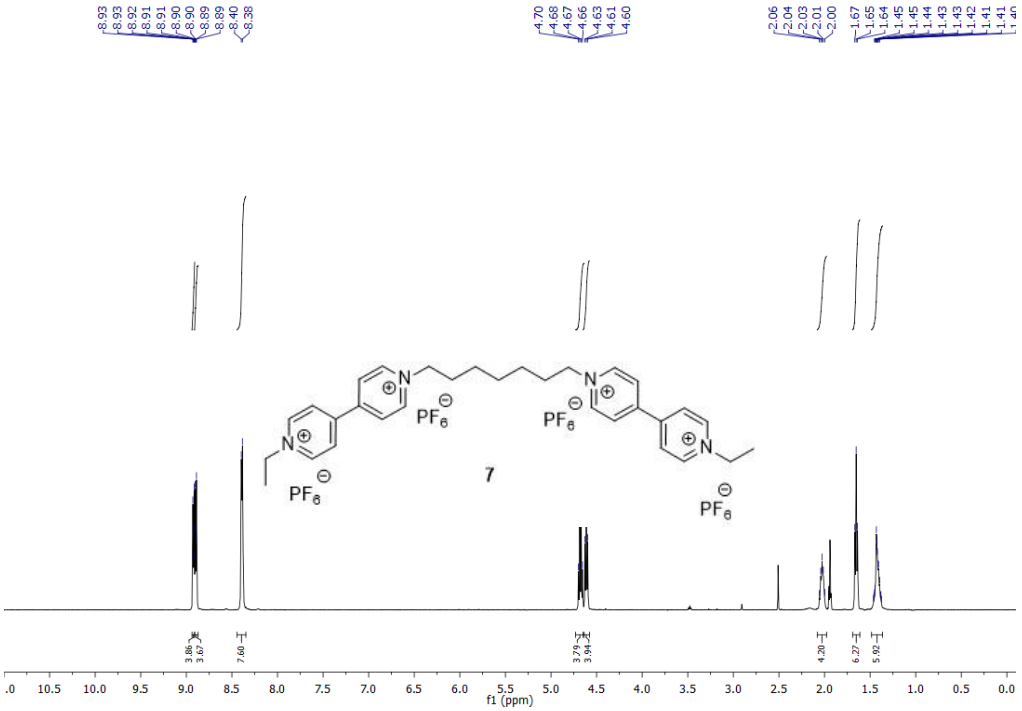

126 MHz, CD_3CN

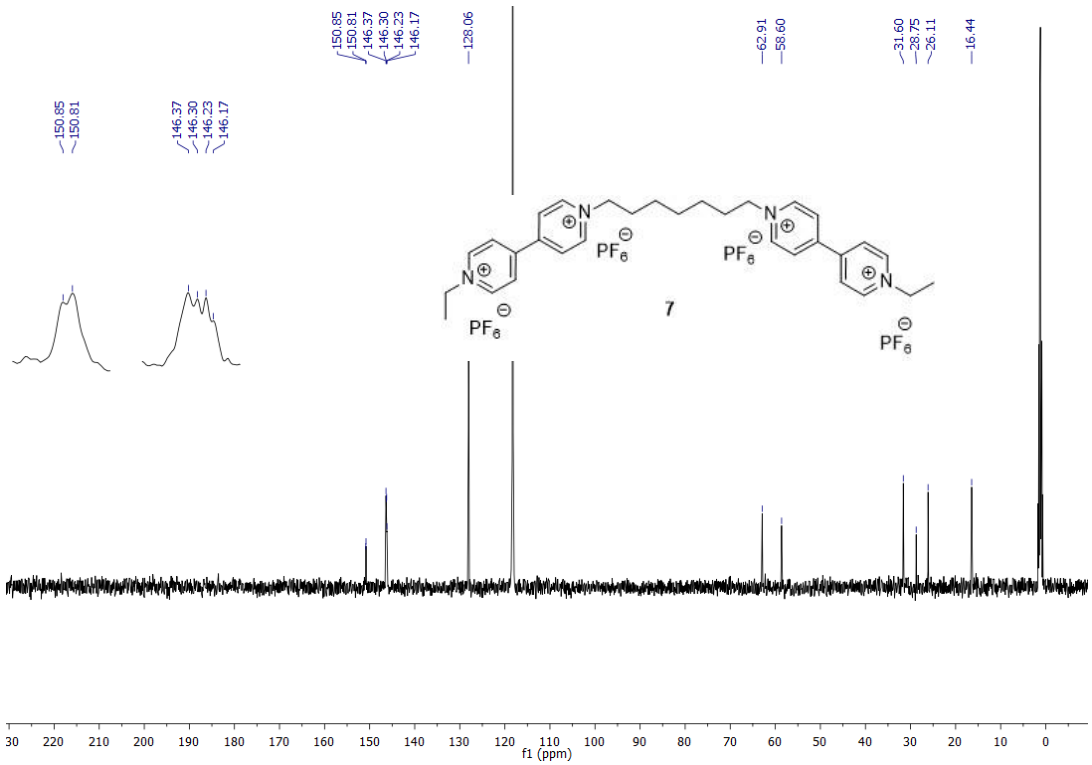

470 MHz, CD_3CN

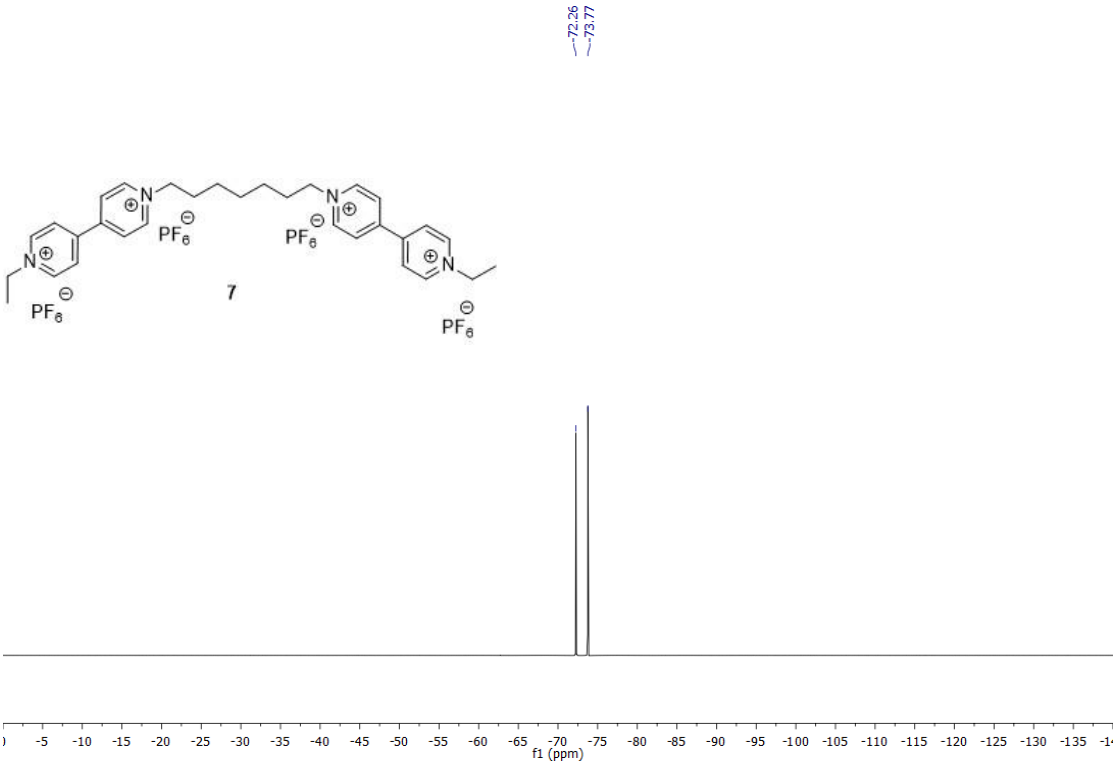

202 MHz, CD_3CN

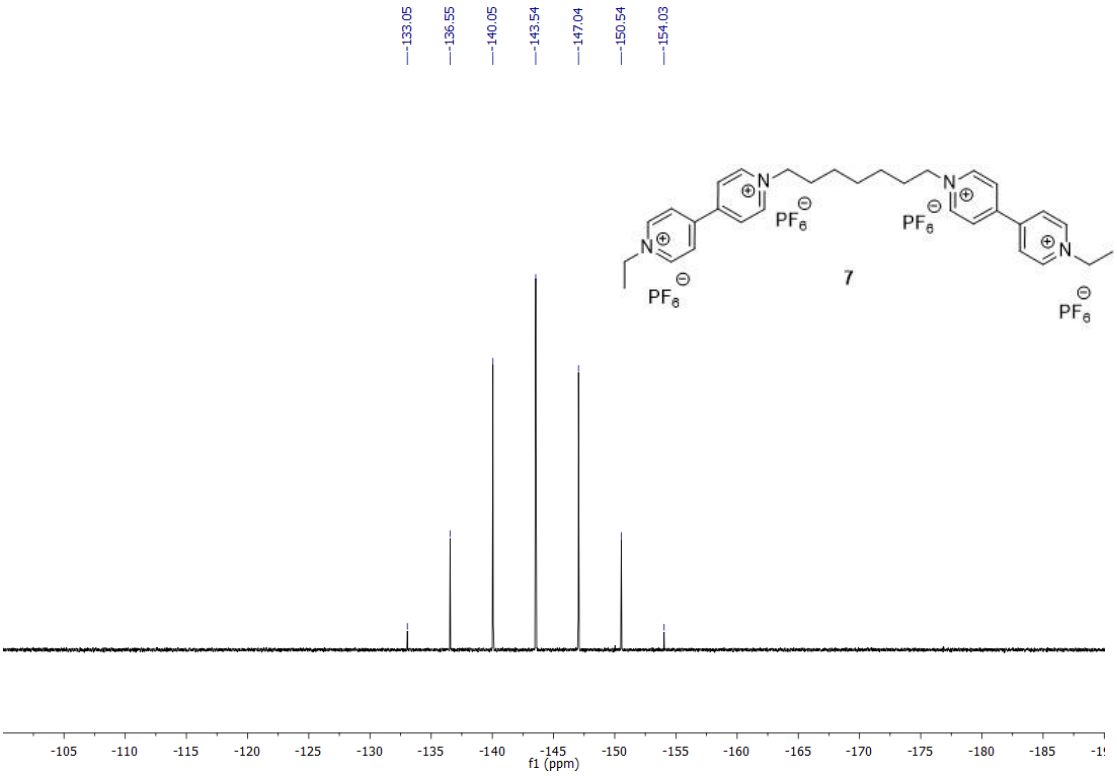

ortho-xylyl bis(viologen) tetra(hexafluorophoshate) **8** NMRs

400 MHz, CD_3CN

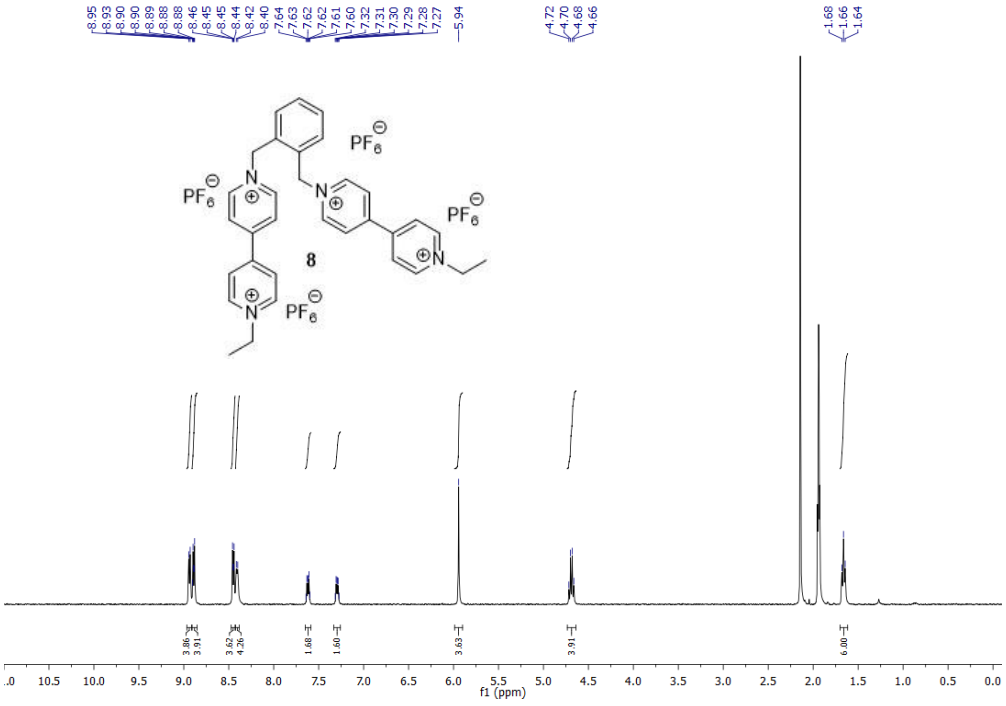

151 MHz, CD_3CN

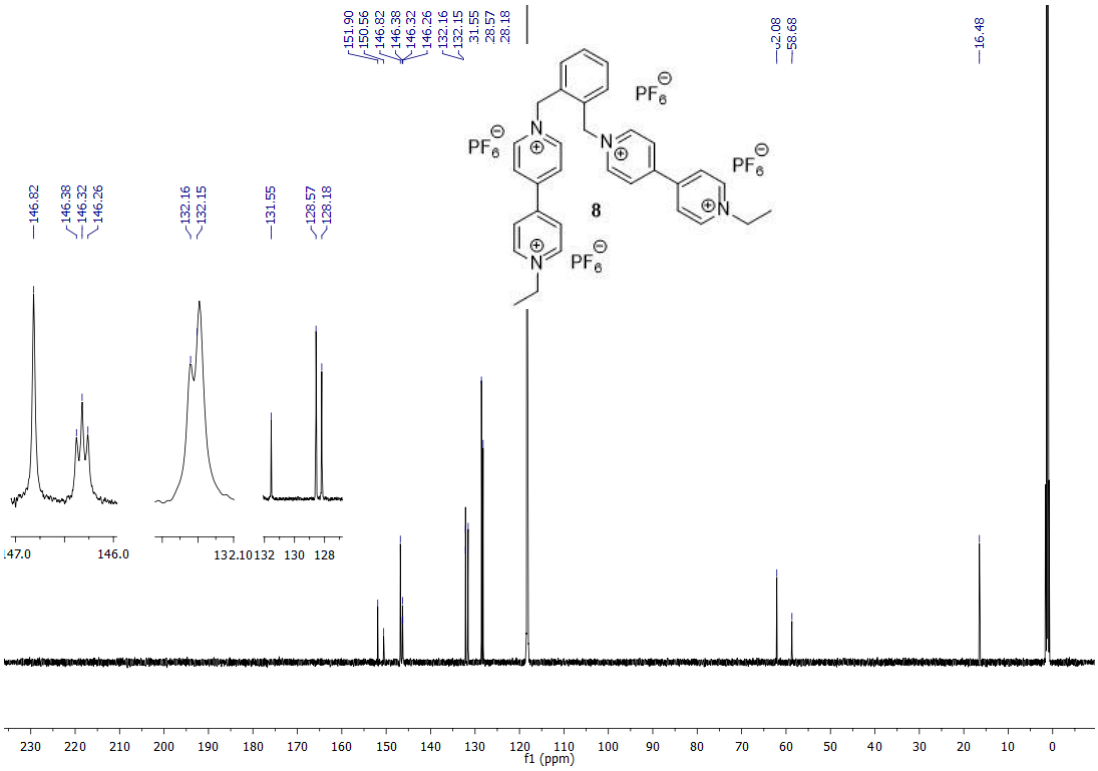

376 MHz, CD_3CN

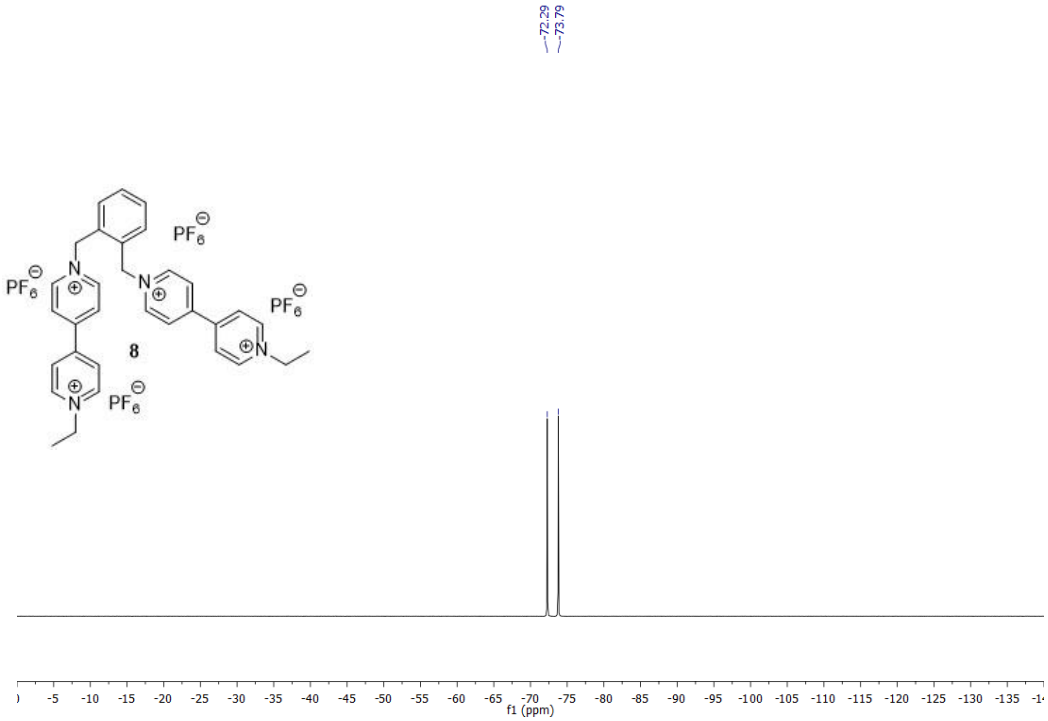

202 MHz, CD_3CN

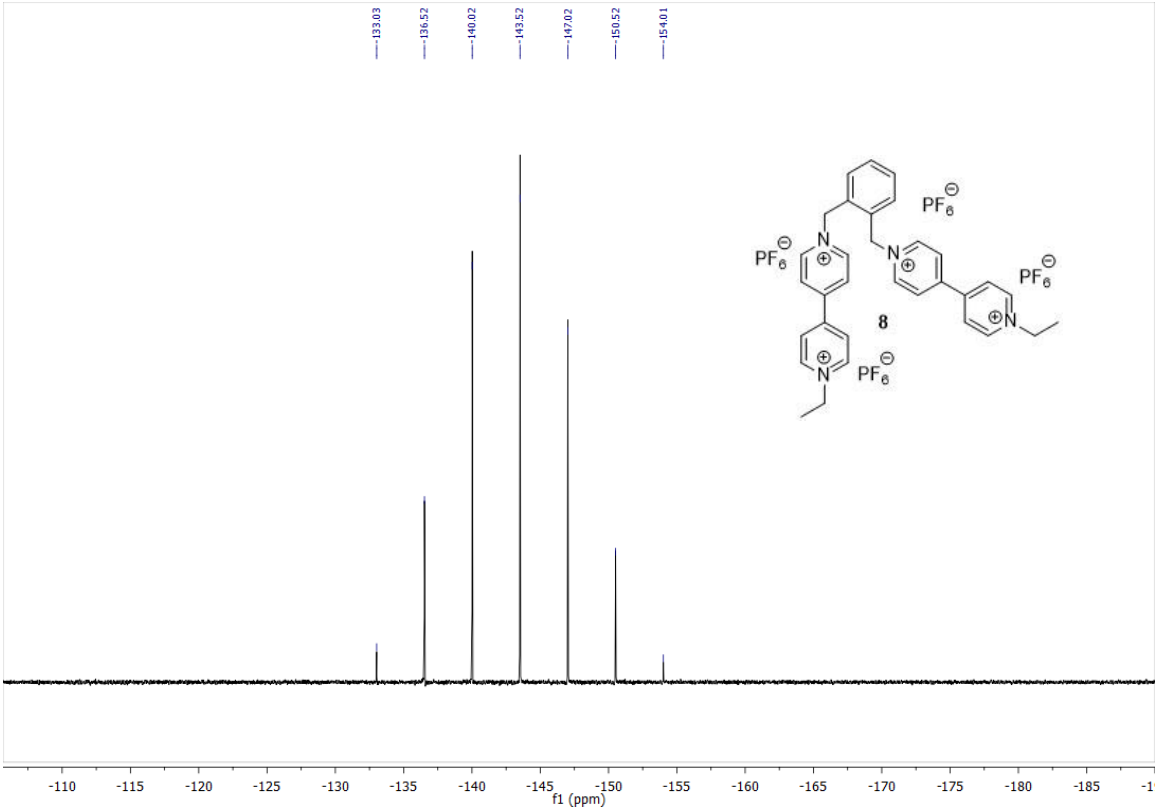

meta-xylyl bis(viologen) tetra(hexafluorophoshate)**9** NMRs

400 MHz, CD_3CN

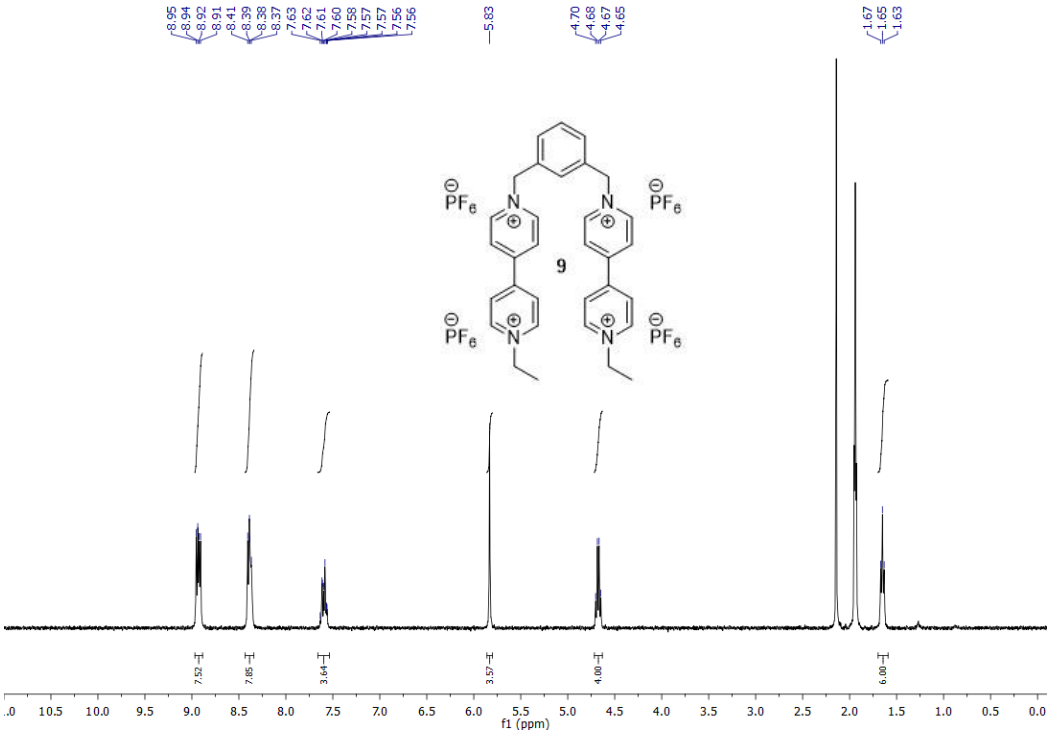

151 MHz, CD_3CN

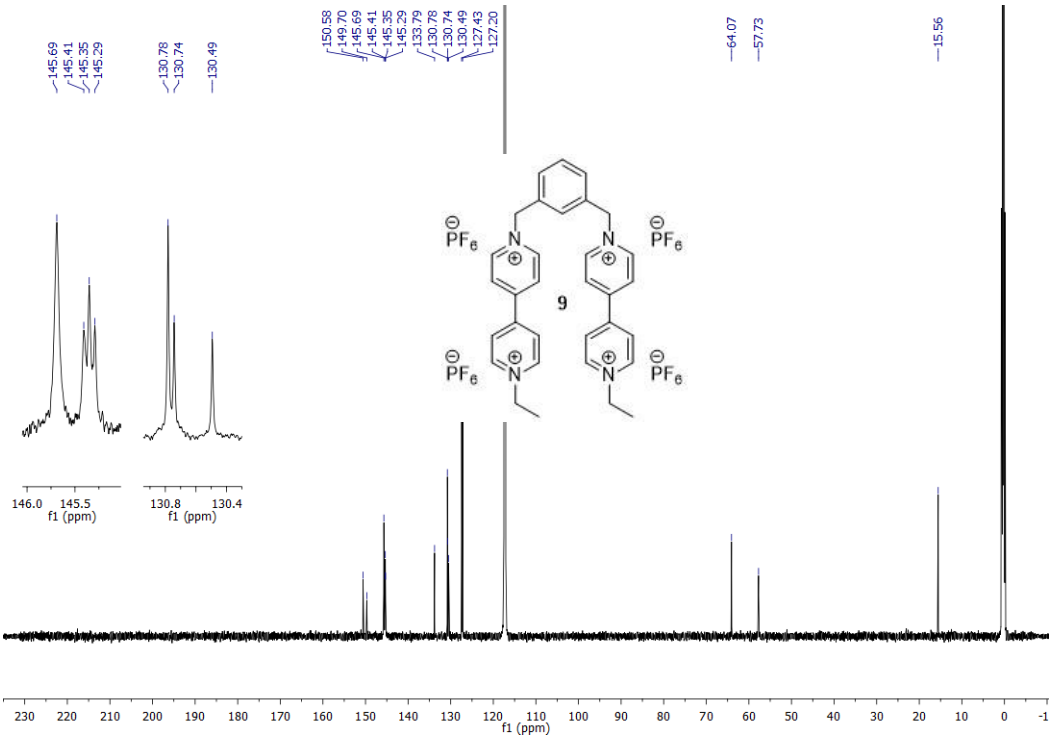

470 MHz, CD_3CN

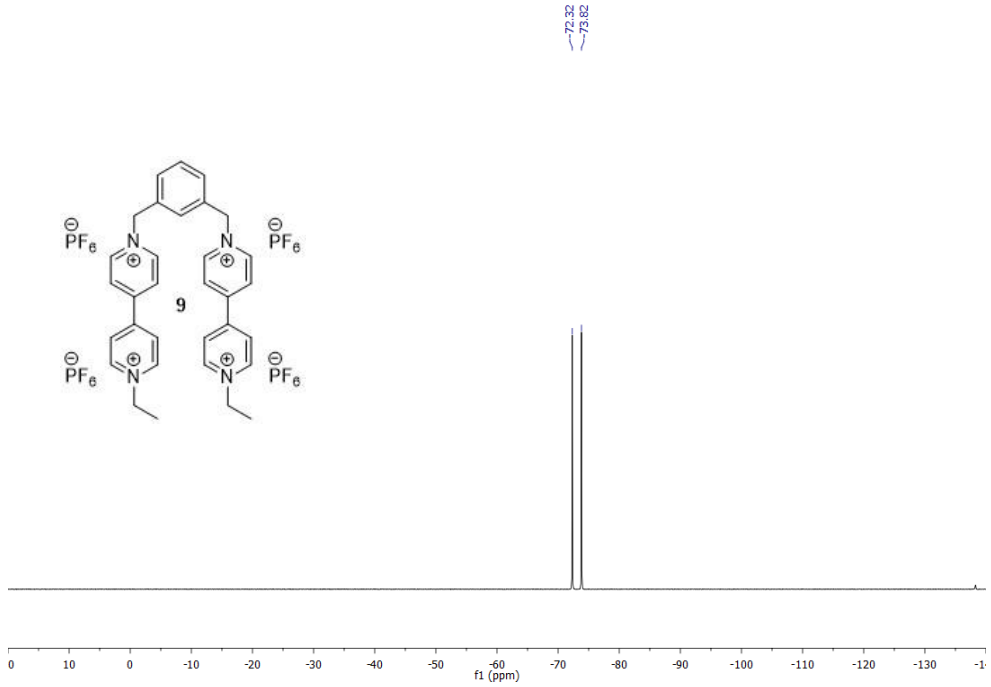

202 MHz, CD_3CN

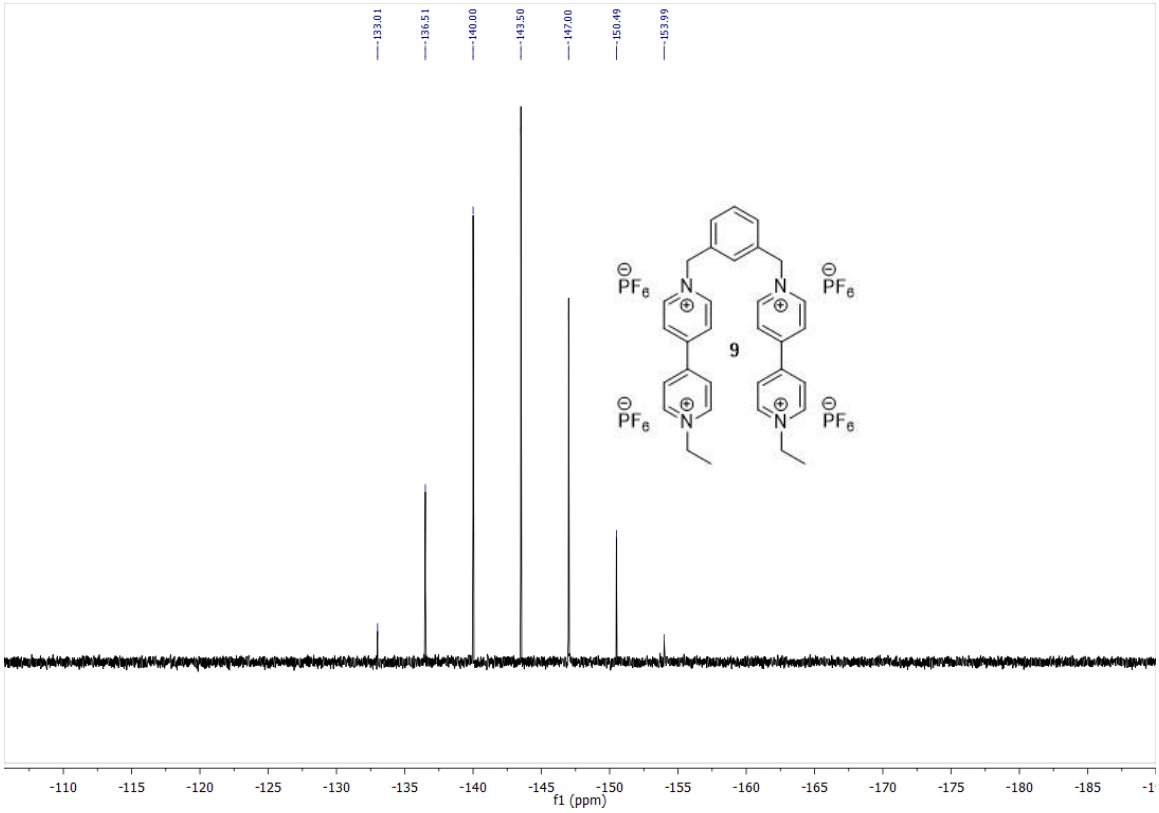

Poly 3,4-di[(1-ethylviologen)methyl]styrene tetra hexafluorophosphate **10** NMRs

600 MHz, CD_3CN

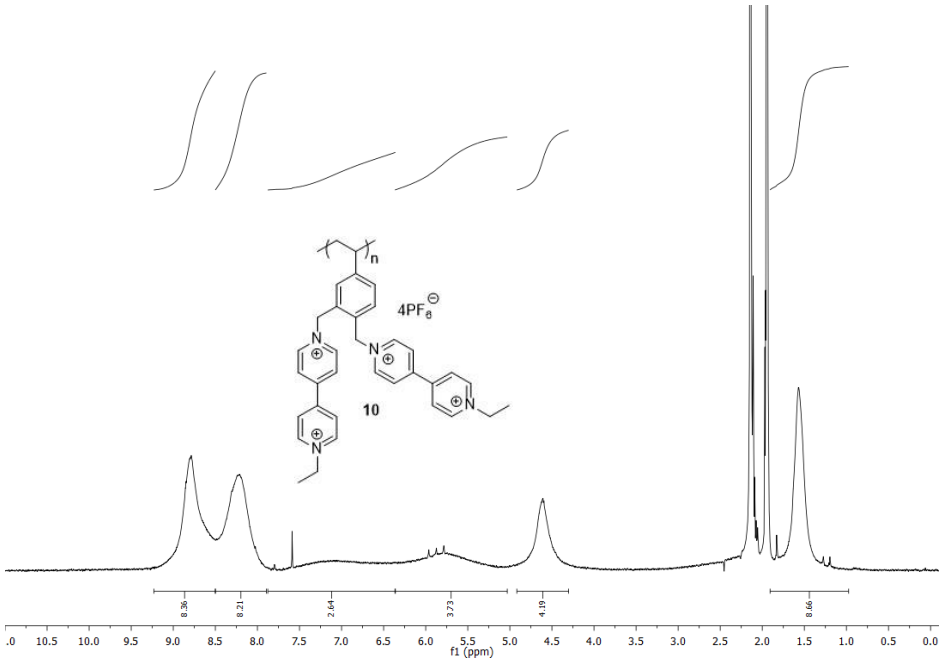

564 MHz, CD_3CN

243 MHz, CD_3CN

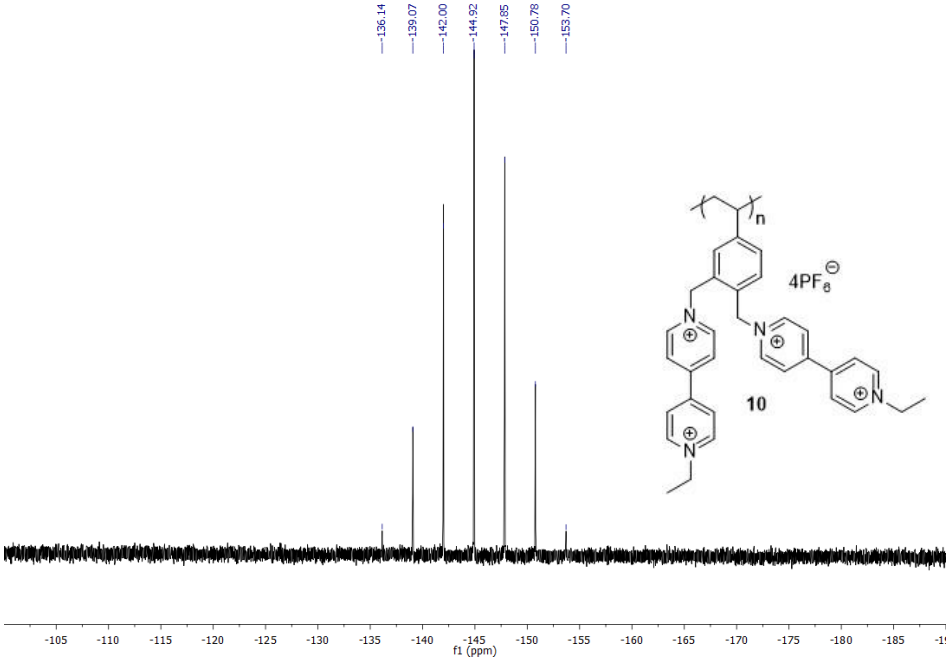

Poly 3,5-di[(1-ethylviologen)methyl]styrene tetra hexafluorophosphate **11** NMRs

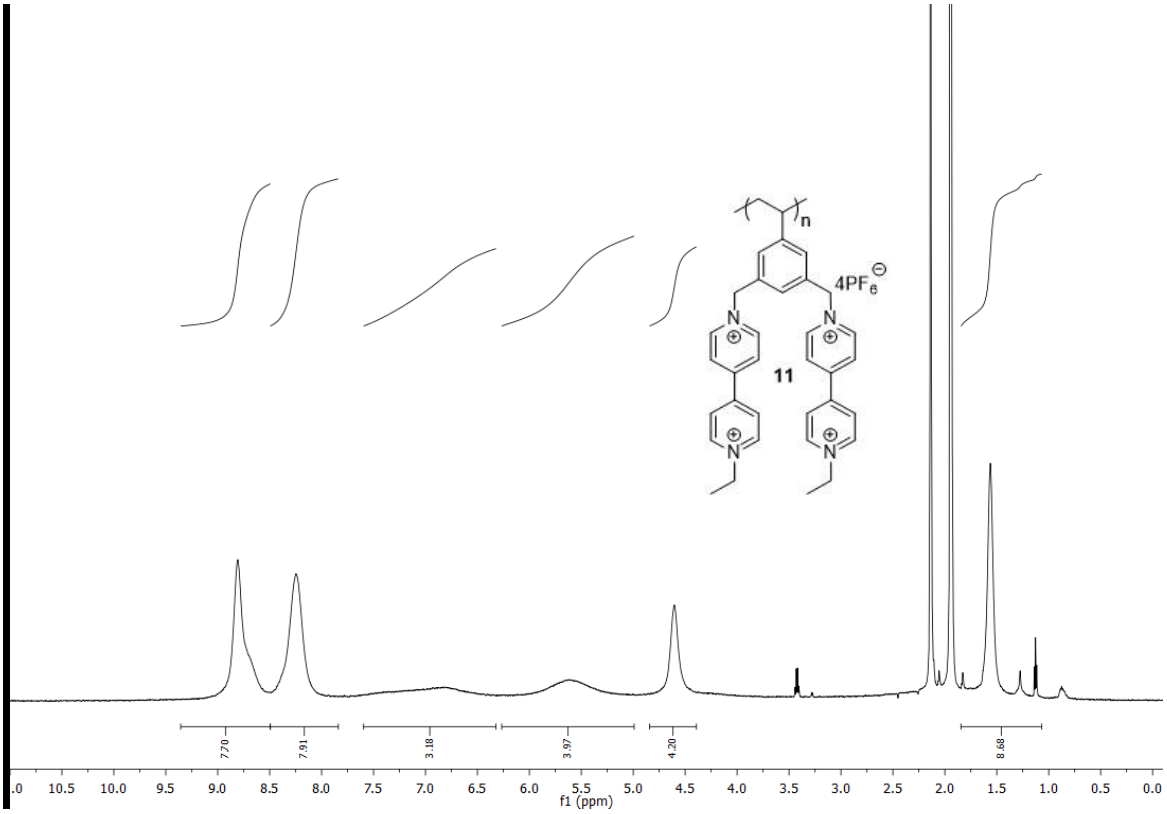

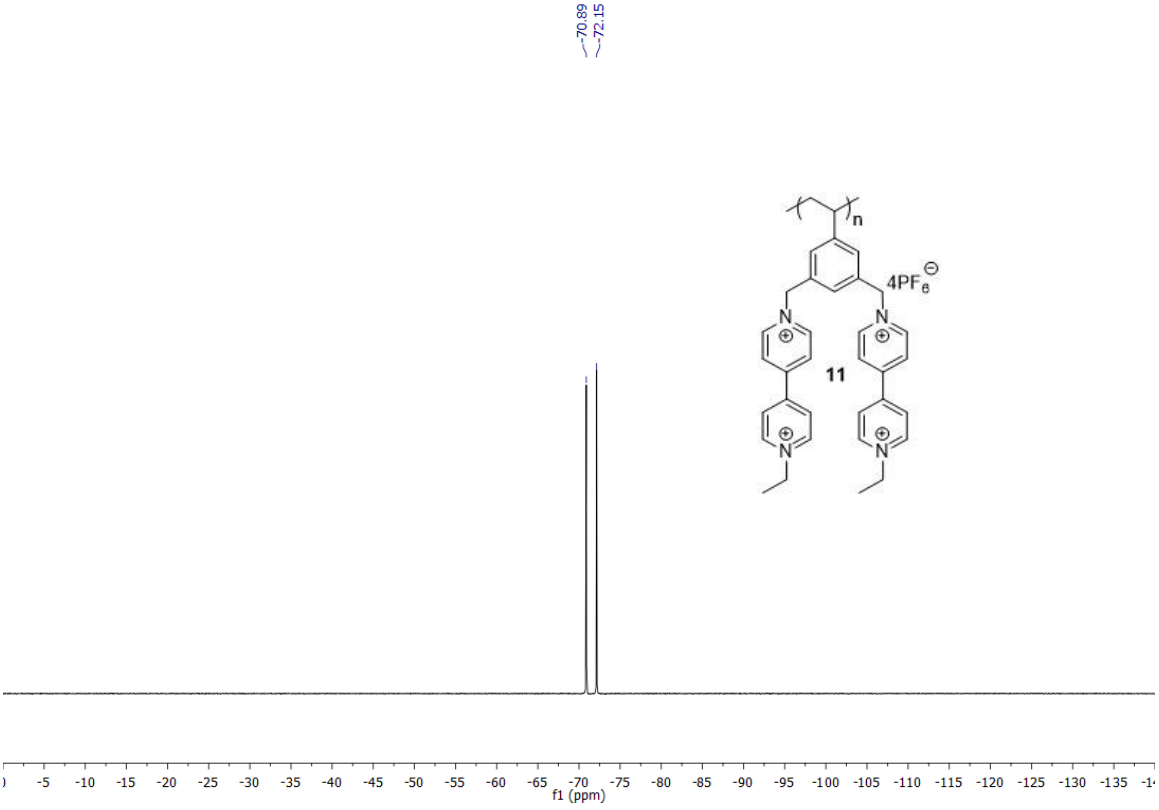

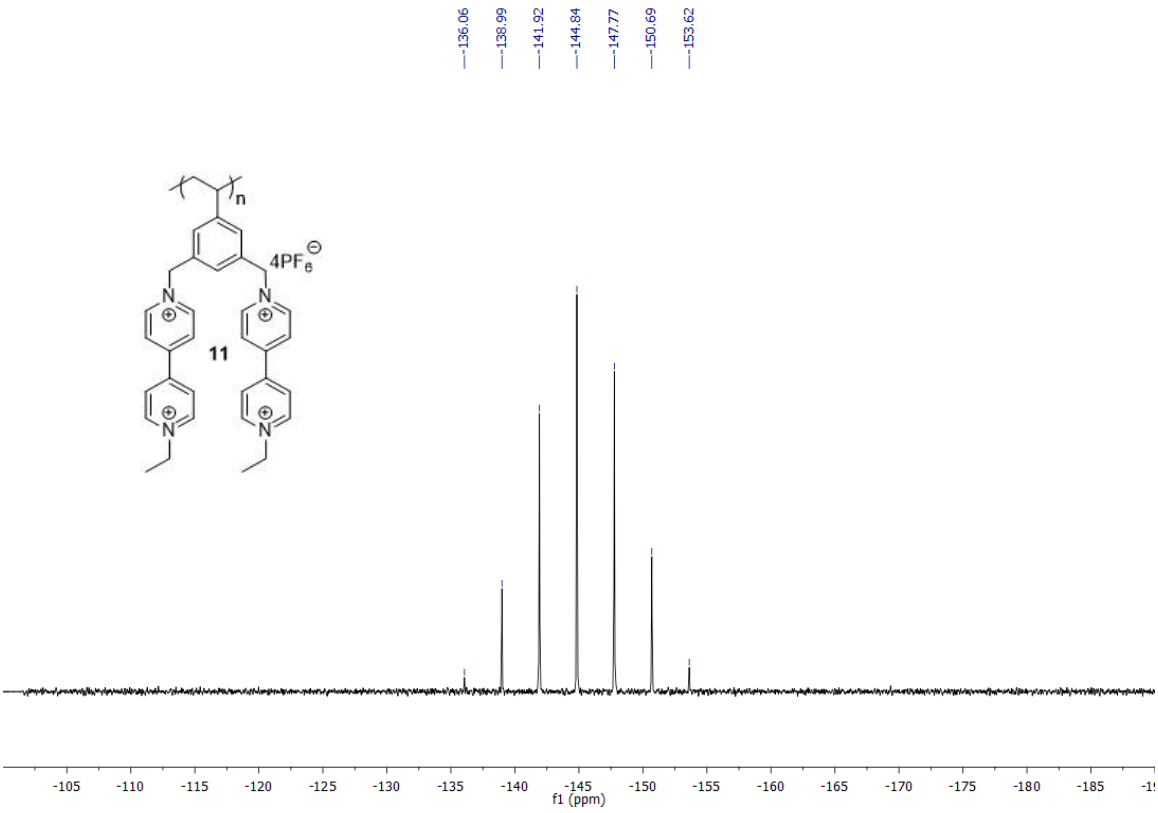
-136.06
-138.99
-141.92
-144.84
-147.77
-150.69
-153.62
n
4PF6
N
11
-105
-110
-115
-120
-125
-130
-135
-140
-145
-150
-155
-160
-165
-170
-175
-180
-185
f1 (ppm)

3,4-di(chloromethyl)styrene **14** (monomer) NMRs

400 MHz, $CDCl_3$

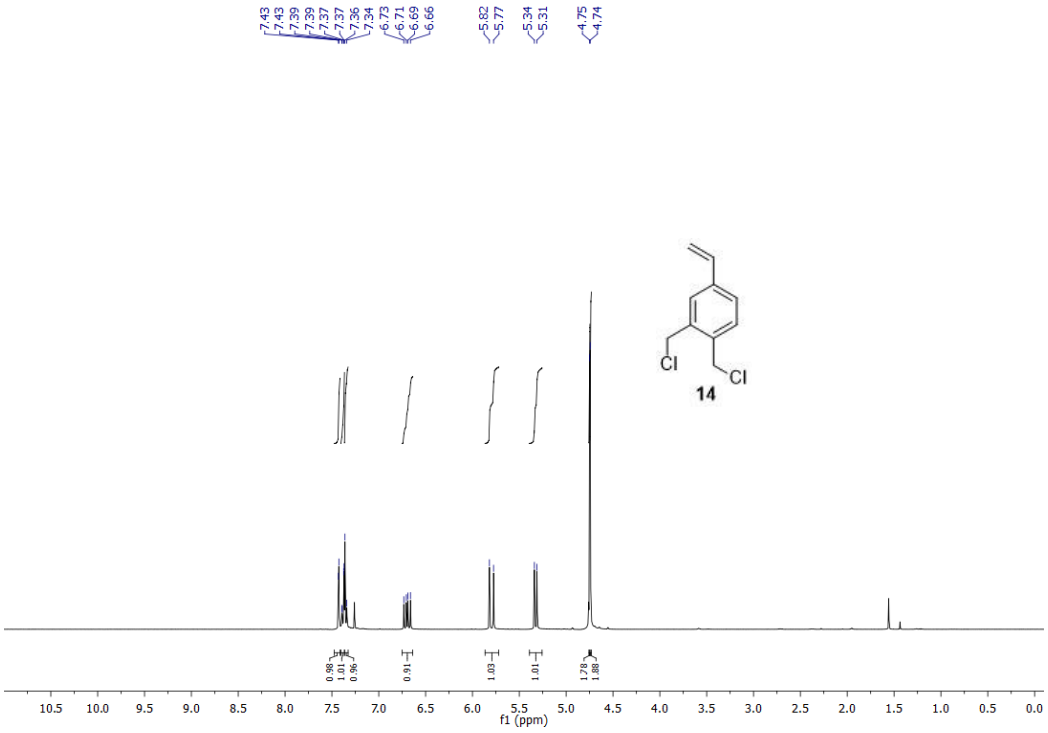

101 MHz, $CDCl_3$

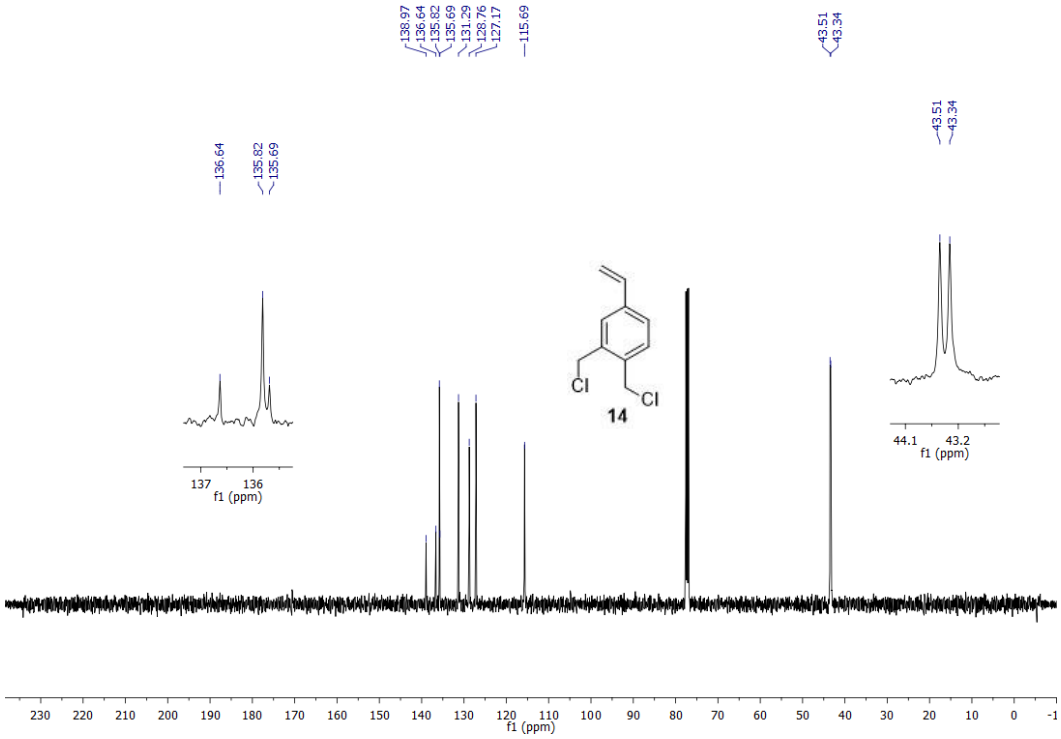

Poly 3,5-di(chloromethyl)styrene **15** NMR

499 MHz, $CDCl_3$

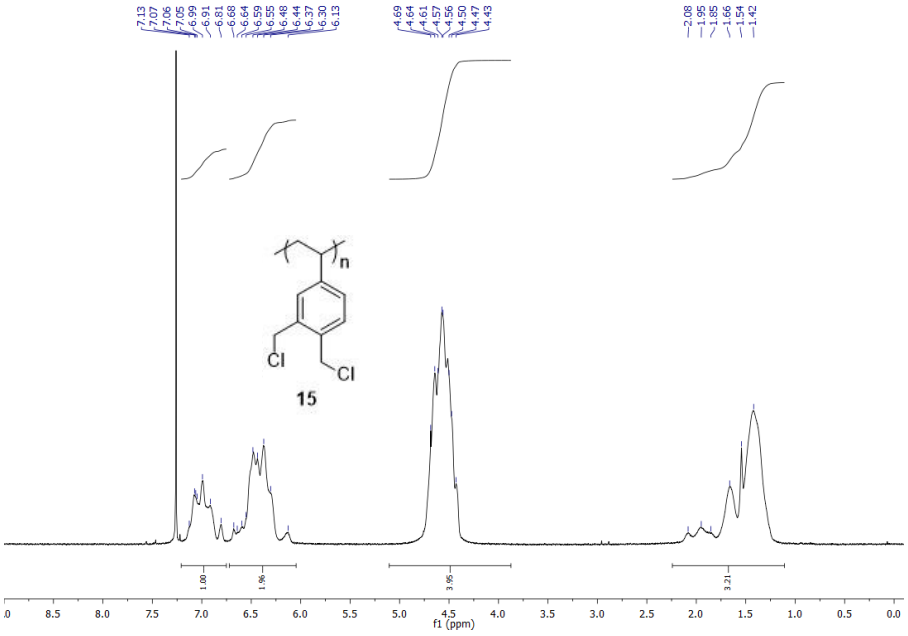

3,5-di(chloromethyl)styrene **18** (monomer) NMRs

499 MHz, $CDCl_3$

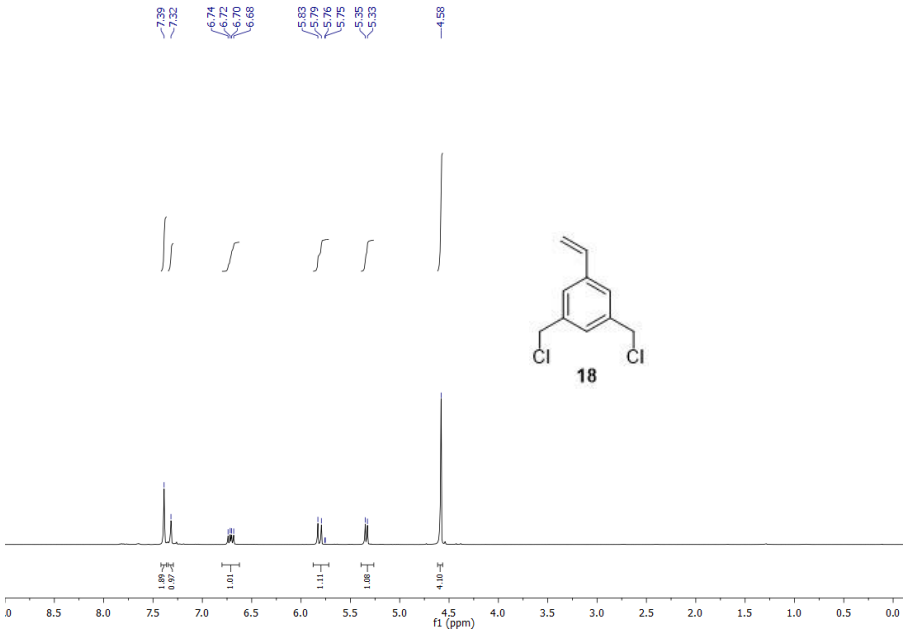

126 MHz, $CDCl_3$

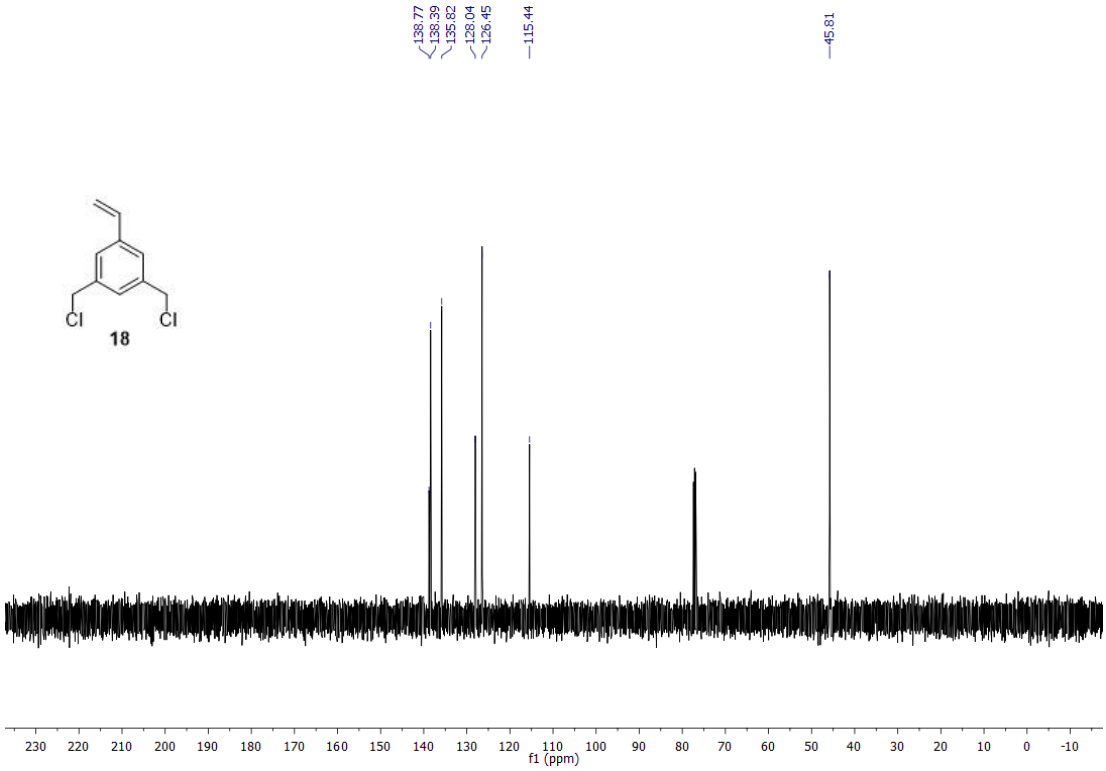

Poly 3,5-di(chloromethyl)styrene **19** NMR

499 MHz, $CDCl_3$

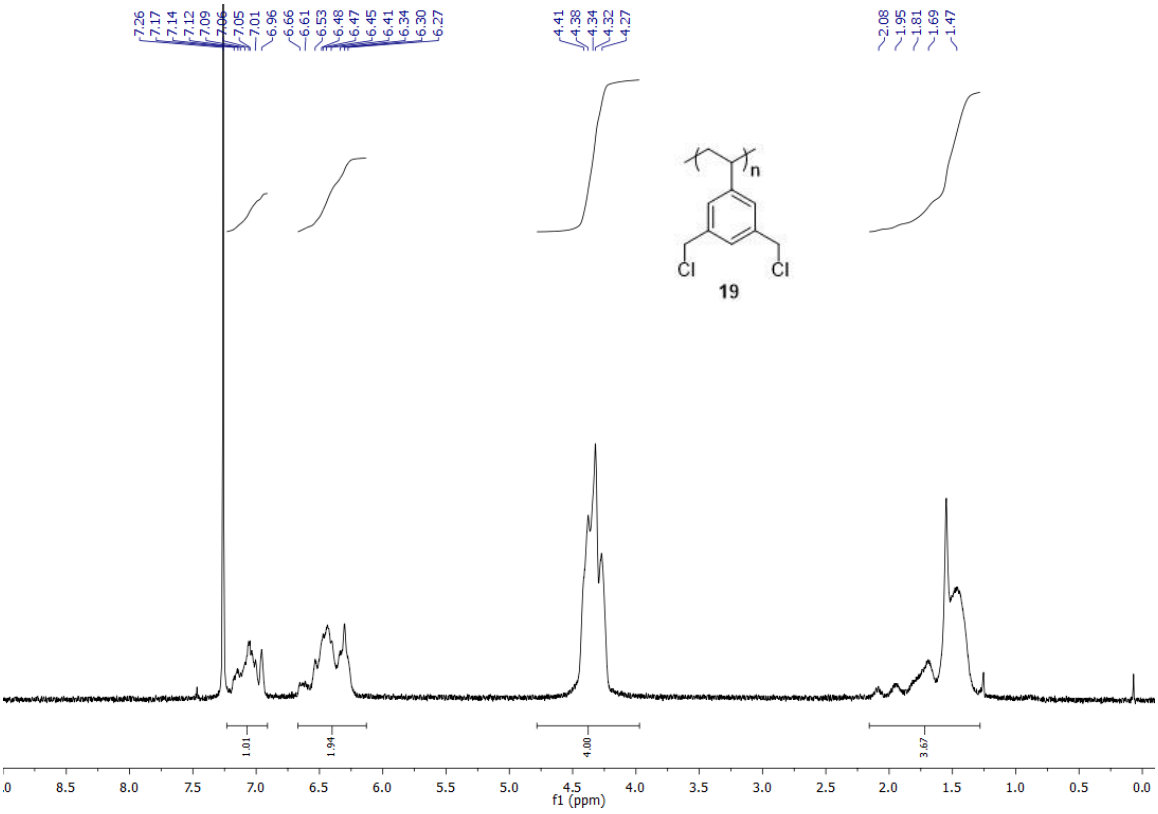

Electrochemistry

SECM UME Fabrication

A 12.5 µm radius wire was purchased from Goodfellow (Huntington, England) and sealed in a patch clamp glass capillary (World Instruments) using a Narishige pipette puller (Japan). Electrical connection to the Pt UME from the back was done with silver epoxy and copper wire. The Pt UME was then exposed using sandpaper and verified for connection by performing voltammetry.

Results

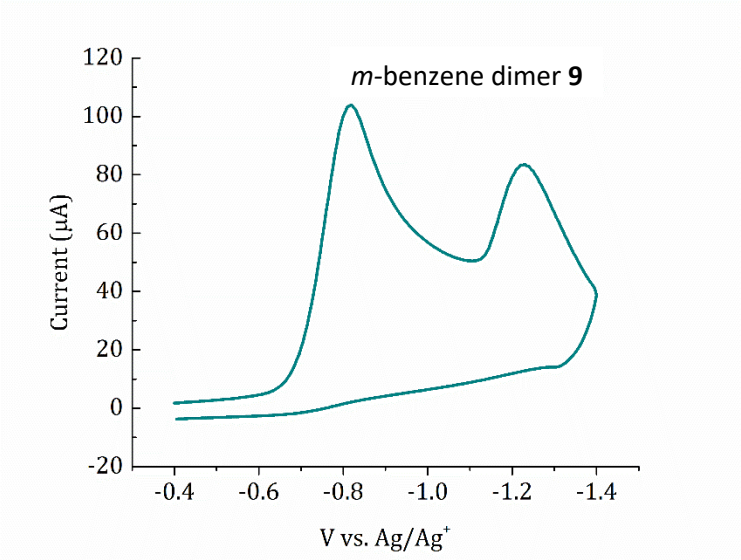

Figure B.1. Cyclic Voltammogram at 200 mV/s for the *m*-benzene dimer **9** at 5 mM accesing the second redox process. It can be observed that this process passivates the electrode surface.

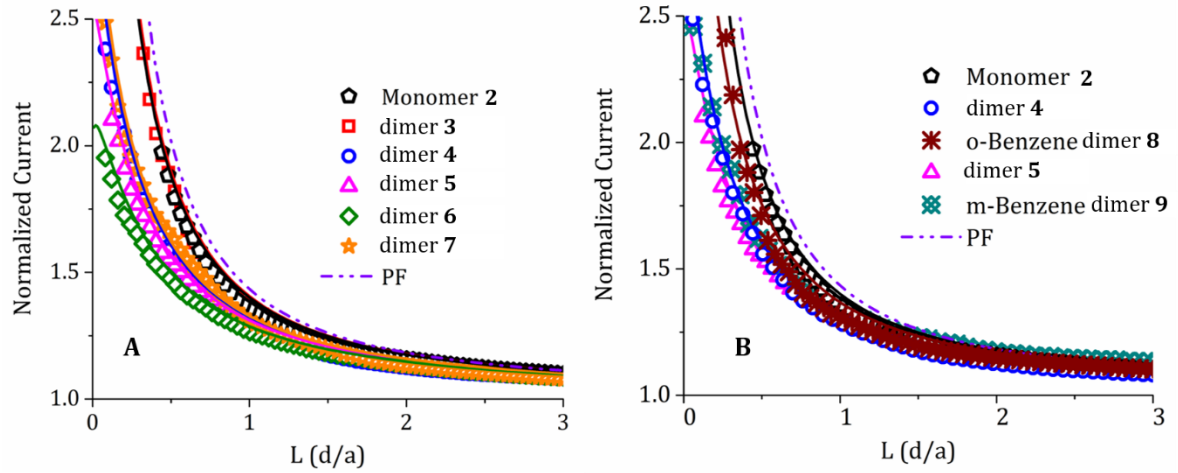

Figure B.2. Scanning electrochemical microscopy feedback approach curves. All approach curves were performed in a solution of 5 mM of the dimer (repeat unit) in 0.1 M $LiBF_4$ supporting electrolyte in acetonitrile. All approach curves were measured using a 12.5 µm radius Pt UME with an *Rg* of 2 moving at 3 µm/s. The substrate was a 1.5 mm Pt disk electrode that was biased at 120 mV positive of the E^0 for each of the dimers. Colored open symbols represent experimental data points and the solid lines indicate theoretical fits. PF indicates the theoretical curve for perfect positive feedback which corresponds to pure mass transfer limited kinetics (A) Approach curves for all of the alkyl based dimers. (B) Approach curves with the benzene based dimers and their alkyl counterparts, dimer **4** and dimer **5**.

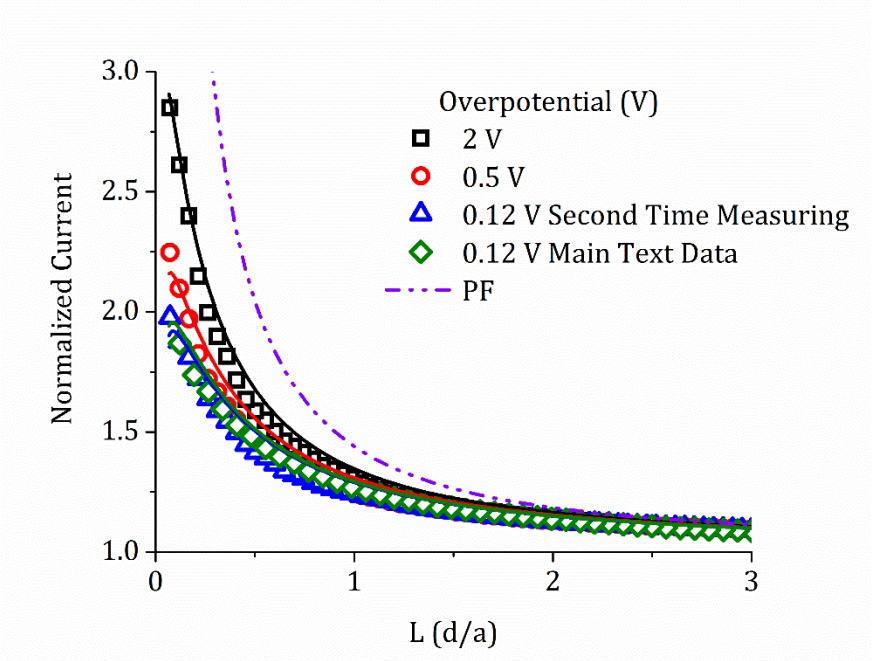

Figure B.3. SECM approach curves with 5 mM of the repeat unit of the dimer **6** in 0.1 M $LiBF_4$ in acetonitrile. SECM tip had a radius of 12.5 um and an *Rg* of 2, with a motor speed of 3 um/s. The feedback kinetics of dimer **6** respond to substrate overpotential in a manner predicted by Butler-Volmer theory, the feedback kinetics increase. The approach curves with 120 mV overpotential are shown to be reproducible over different days.

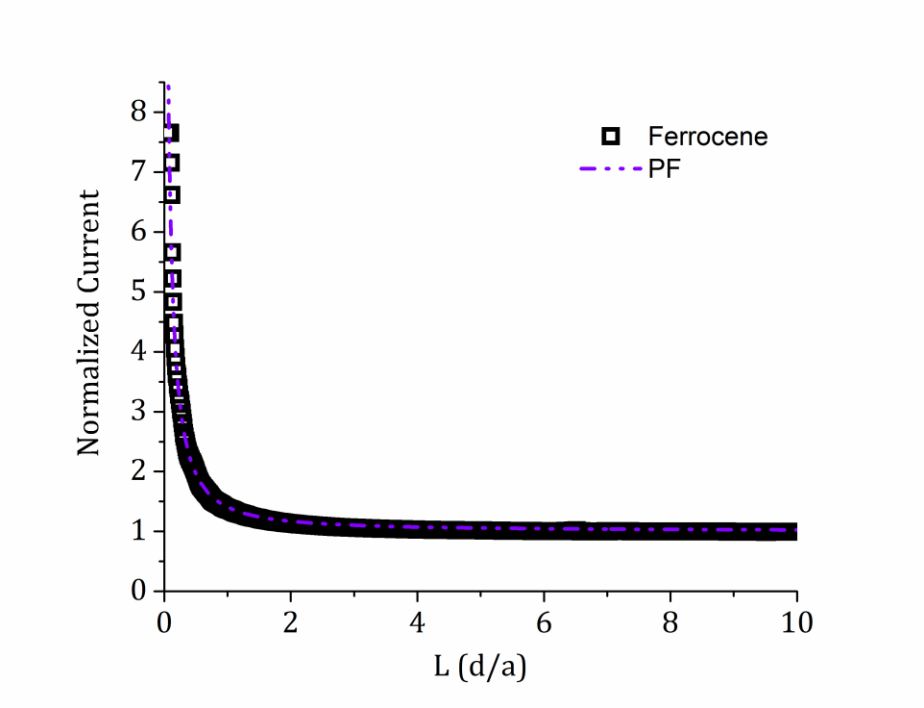

Figure B.4. Calibration of the SECM tip-substrate separation distance d_0 when at the approached position. Solution contained 10 mM ferrocene in 0.1 M $LiBF_4$ in acetonitrile. Identification of the d_0 parameter was done by approaching a 12.5 µm radius Pt UME with an *Rg* of 2 using the oxidation of ferrocene to a Pt macrodisk substrate poised at -0.1 V vs. Ag/Ag^+ in order to observe perfect positive feedback. Fitting of the experimental approach curve to positive feedback theory finds that the tip was separated off the electrode surface by 0.058 L, or 725 nm. All approach curves measured with the viologen dimers and polymers were adjusted by the d_0 value of 0.058 *L* to account for this calibrated tip separation distance.

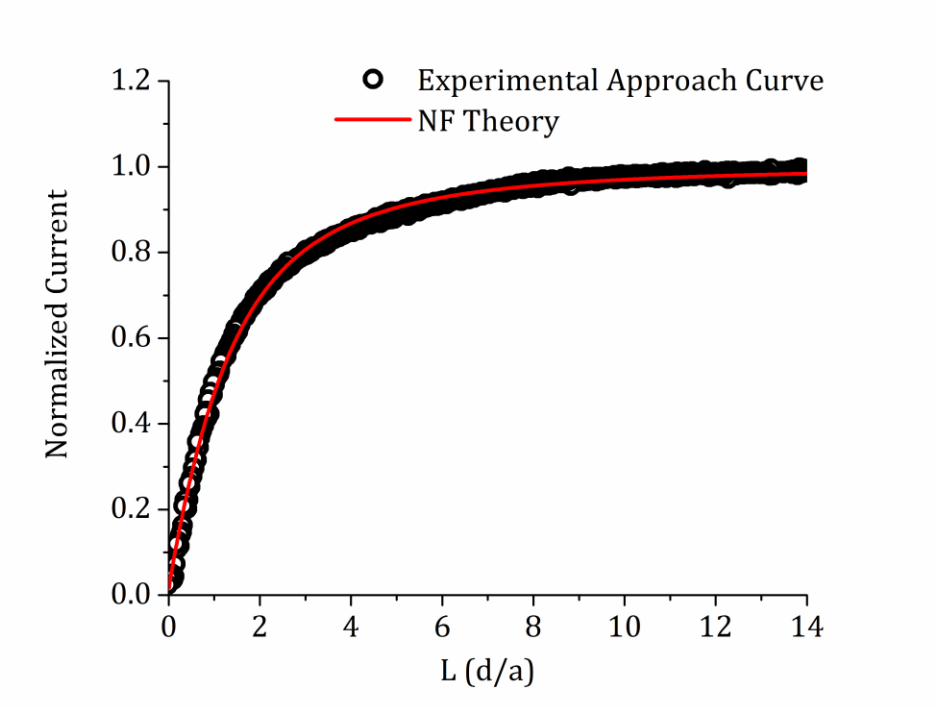

Figure B.5. Calibration of the *Rg* for the Wollaston SECM tip with an electrode radius of 300 nm using negative feedback approach curves. The solution contained 10 mM TMPD in 0.1 M $LiBF_4$ in acetonitrile. The Wollaston tip was approached to a glass substrate using the first oxidation of TMPD until complete negative feedback was observed. Fitting of the approach curve to negative feedback theory finds that the electrode had an effective *Rg* of 16. At the approached position, the electrode was 77 nm off the surface indicating that this electrode is able to be placed very near to a substrate without crashing.

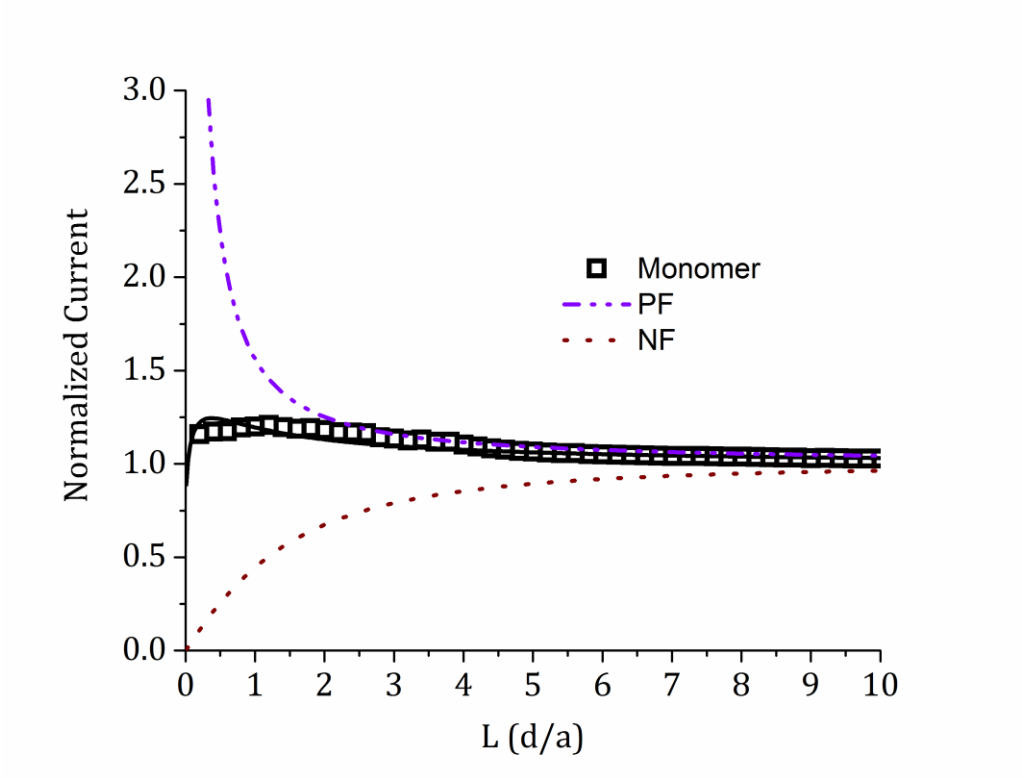

Figure B.6. SECM approach curves using the Wollaston SECM tip with 10 mM ethyl viologen monomer in a solution of 0.1 M $LiBF_4$ in acetonitrile to a Pt macrodisk electrode biased at 120 mV positive of the redox couple. Here, the approach curves find that the kinetics for the reduction of ethyl viologen are able to be distinguished from pure positive feedback and are above negative feedback. Fitted kinetics from the approach curves find that the standard rate constant is 7.57 cm/s.

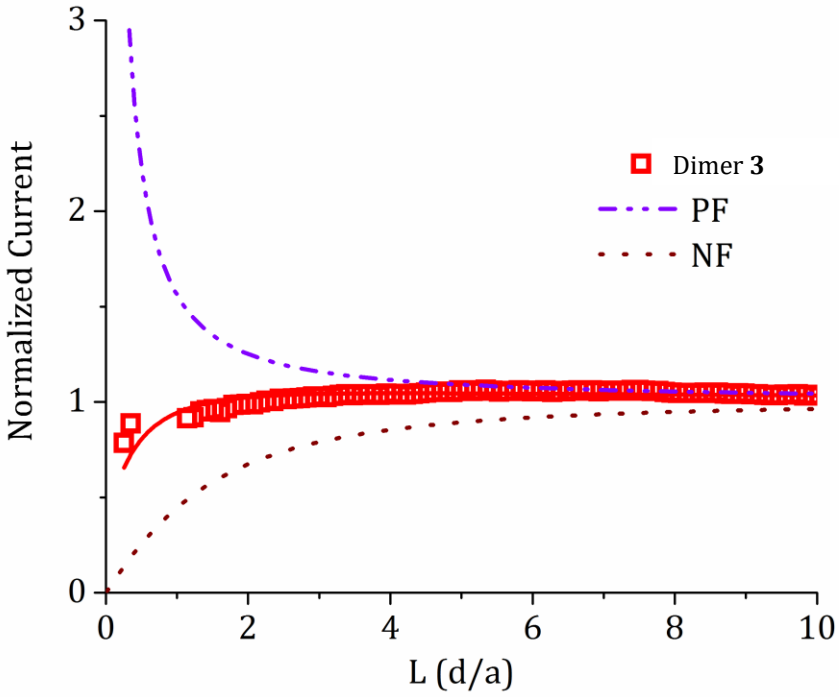

Figure B.7. SECM approach curves using the Wollaston SECM tip with 5 mM of the repeat unit of dimer **3** in a solution of 0.1 M $LiBF_4$ in acetonitrile to a Pt macrodisk electrode biased at 120 mV positive of the redox couple. Here, the approach curves find that the kinetics for the reduction of dimer **3** are able to be distinguished from pure positive feedback and are above negative feedback. Fitted kinetics from the approach curves find that the standard rate constant is 1.9 cm/s.

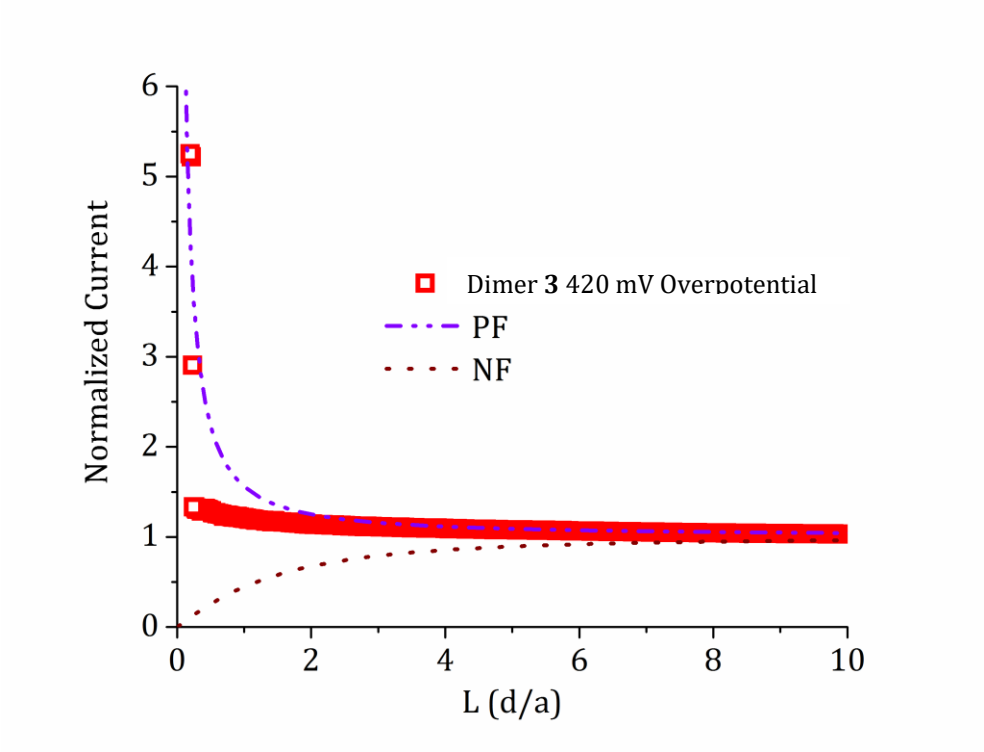

Figure B.8. SECM approach curves using the Wollaston SECM tip with 5 mM of the repeat unit of dimer **3** in a solution of 0.1 M $LiBF_4$ in acetonitrile to a Pt macrodisk electrode biased at 420 mV positive of the redox couple. Under the conditions of 420 mV substrate overpotential, the feedback kinetics fit approximately to mass transfer limited conditions indicating the redox couple is responding to substrate overpotential.

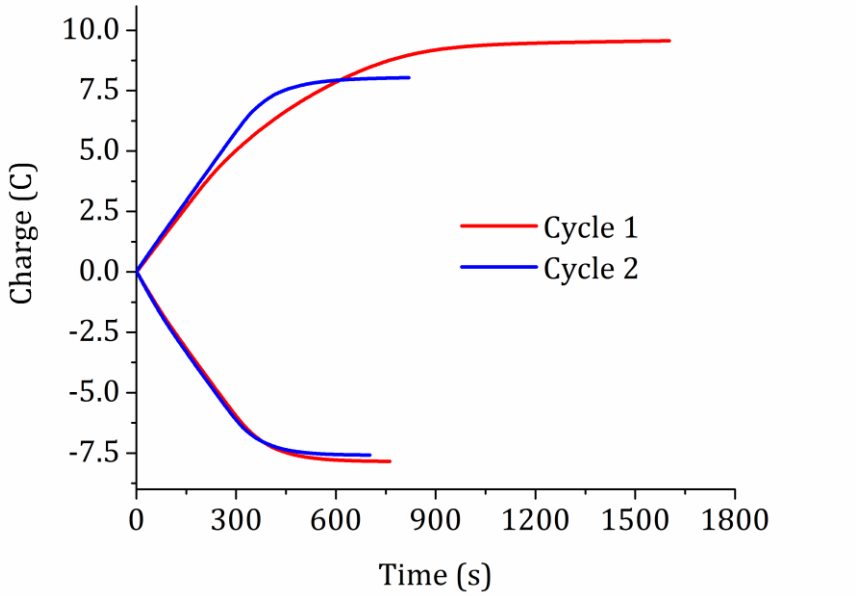

Figure B.9. Bulk electrolysis for dimer **3** at 10 mM in 0.1 M $LiBF_4$ in acetonitrile.

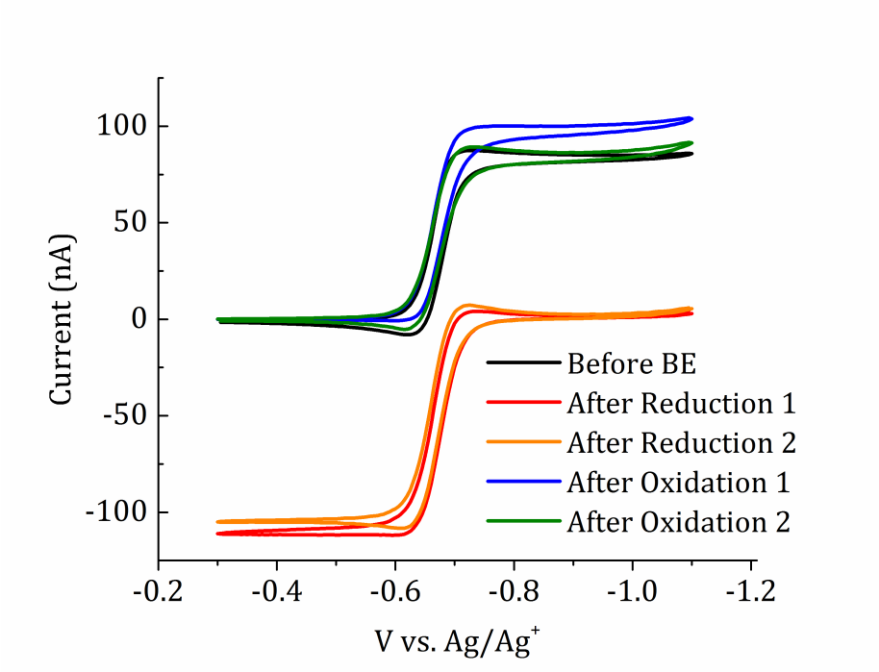

Figure B.10. Resulting cyclic voltammograms before, during and after the bulk electrolysis experiments for dimer **3** at 10 mM in 0.1 M $LiBF_4$ in acetonitrile.

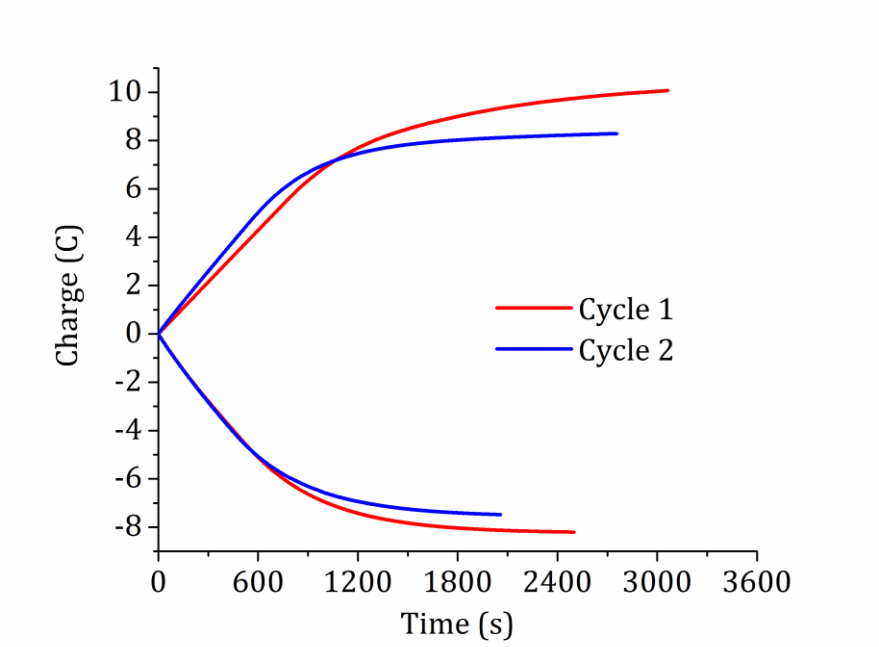

Figure B.11. Bulk electrolysis for dimer **7** at 10 mM in 0.1 M $LiBF_4$ in acetonitrile.

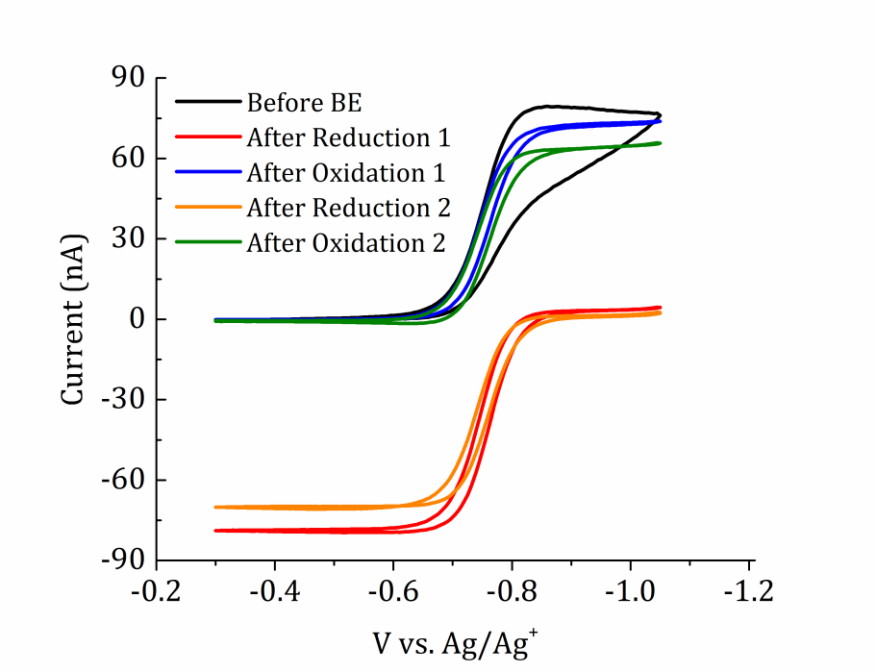

Figure B.12. Resulting cyclic voltammograms before, during and after the bulk electrolysis experiments for the dimer **7** at 10 mM in 0.1 M $LiBF_4$ in acetonitrile.

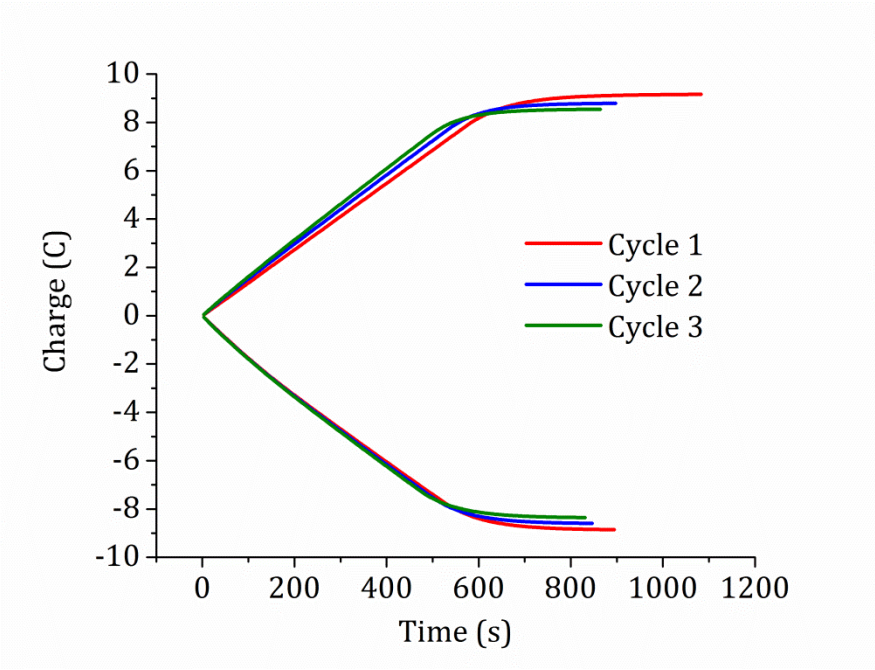

Figure B.13. Bulk electrolysis for the *o*-benzene dimer **8** at 10 mM in 0.1 M $LiBF_4$ in acetonitrile.

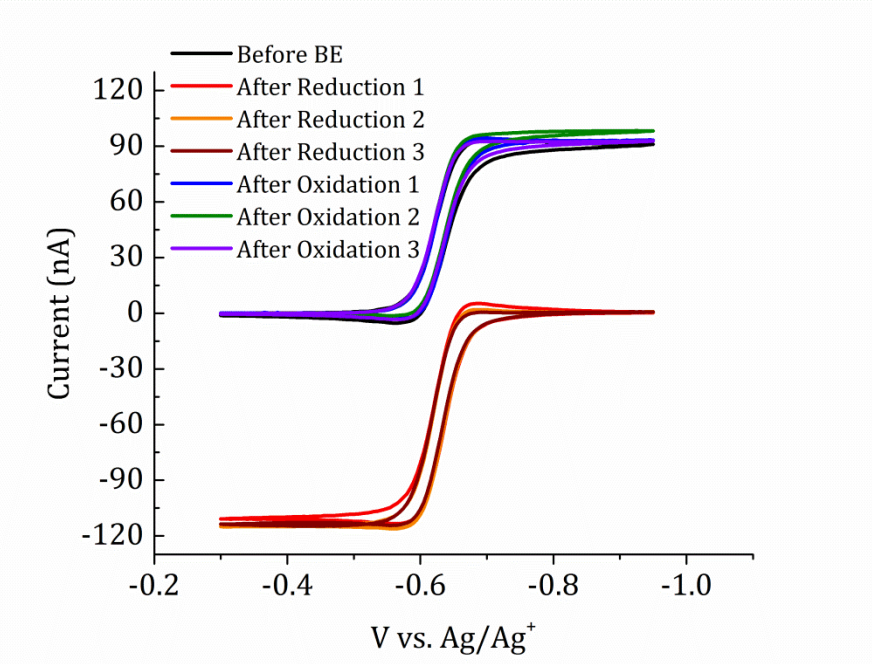

Figure B.14. Resulting cyclic voltammograms before, during and after the bulk electrolysis experiments for the *o*-benzene dimer **8** at 10 mM in 0.1 M $LiBF_4$ in acetonitrile.

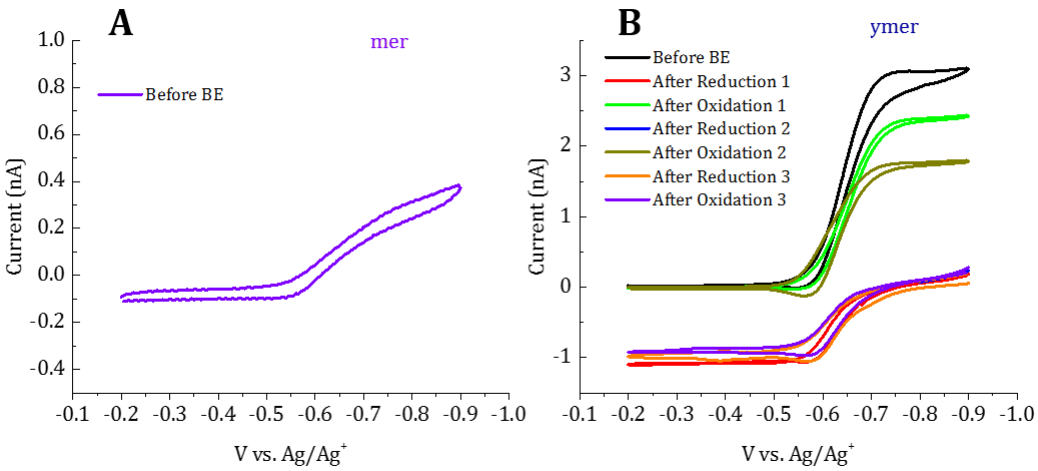

Figure B.15. Resulting cyclic voltammograms before, during and after the bulk electrolysis experiments for the (A) *o*-benzene polymer **10** and (B) *m*-benzene polymer **11** at 10 mM of monomer units in 0.1 M $LiBF_4$ in acetonitrile.

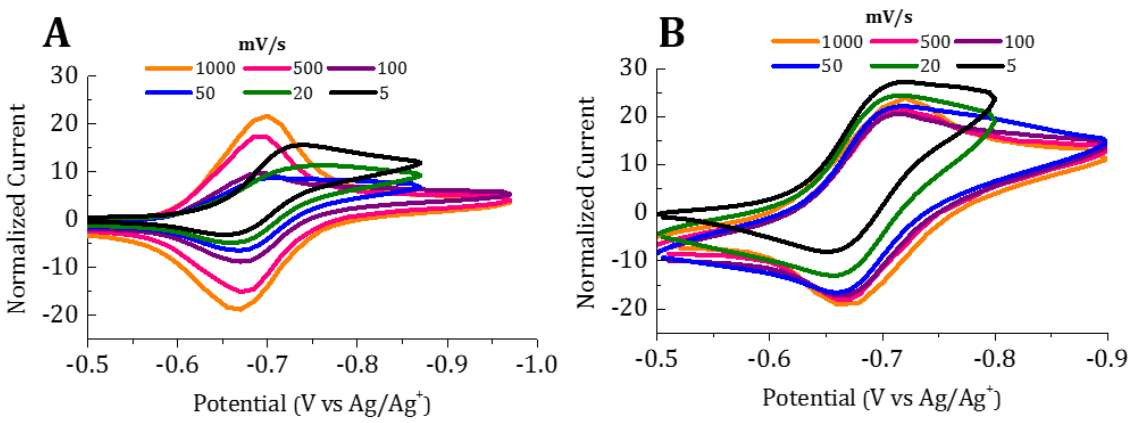

Figure B.16. (A) Normalized current by the square root of scan rate for Poly *o*-benzene dimer **10** and (B) Normalized current by the square root of scan rate for *m*-benzene polymer **11** (2 mM of monomer in 0.1 M $LiBF_4$ in acetonitrile).

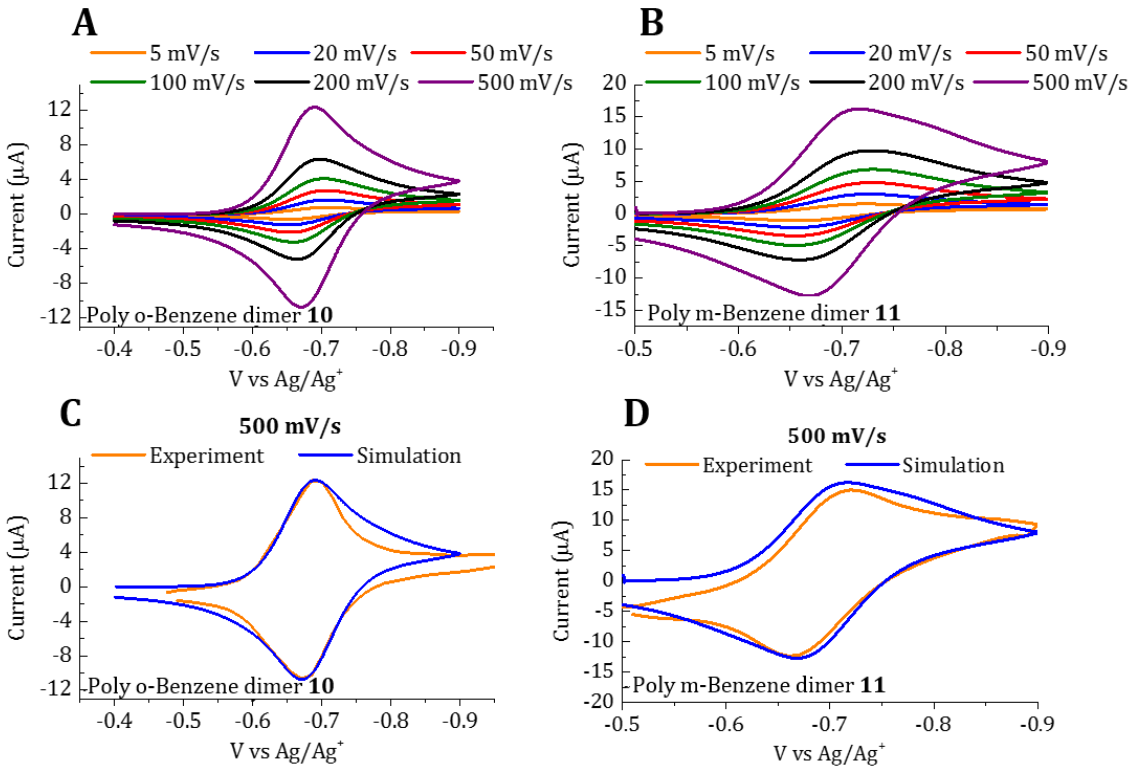

Figure B.17. Simulated cyclic voltammograms using the experimentally calculated data. In the simulation we added a pre-absorption equilibrium in which the K of absorption *o*-Benzene polymer **10** is 20 times larger than the one for *m*-benzene polymer **11**. For surface coverage we used 6 x 10^{-10} mol/cm^2 and for the Marcus constant we used the k_{EX} values from the polymers. Simulated scan rate dependence for (A) **10** (B) *m*-benzene polymer **11**. Comparison with the experimentally obtained cyclic voltammogram at 500 mV/s for (C) *o*-benzene polymer **10** (D) *m*-benzene polymer **11**.

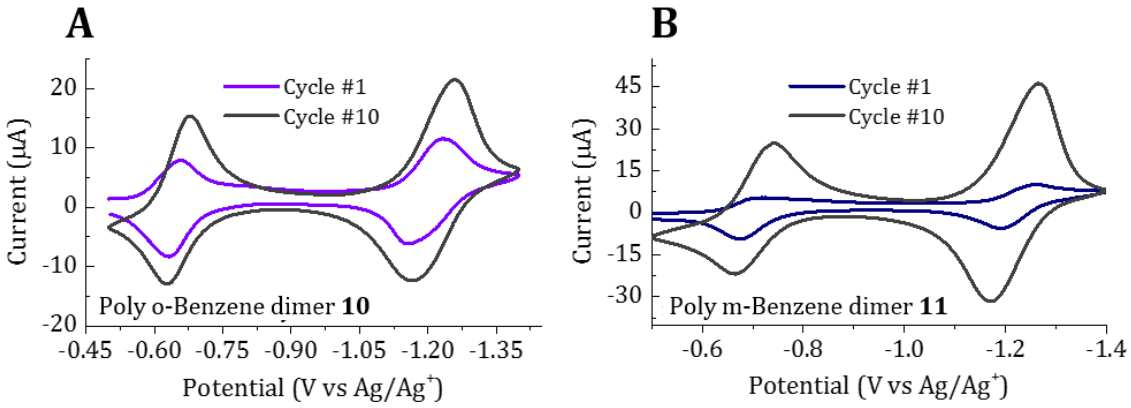

Figure B.18. Cyclic voltammograms (1mM concentration of the monomer at 50 mV/s) going to the second redox process which promote absorption. The current increase with cycle (up to 10), showing that the polymer is being deposit onto the electrode surface. (A) *o*-benzene polymer **10** (B) *m*-benzene polymer **11** (2 mM of monomer in 0.1 M $LiBF_4$ in acetonitrile).

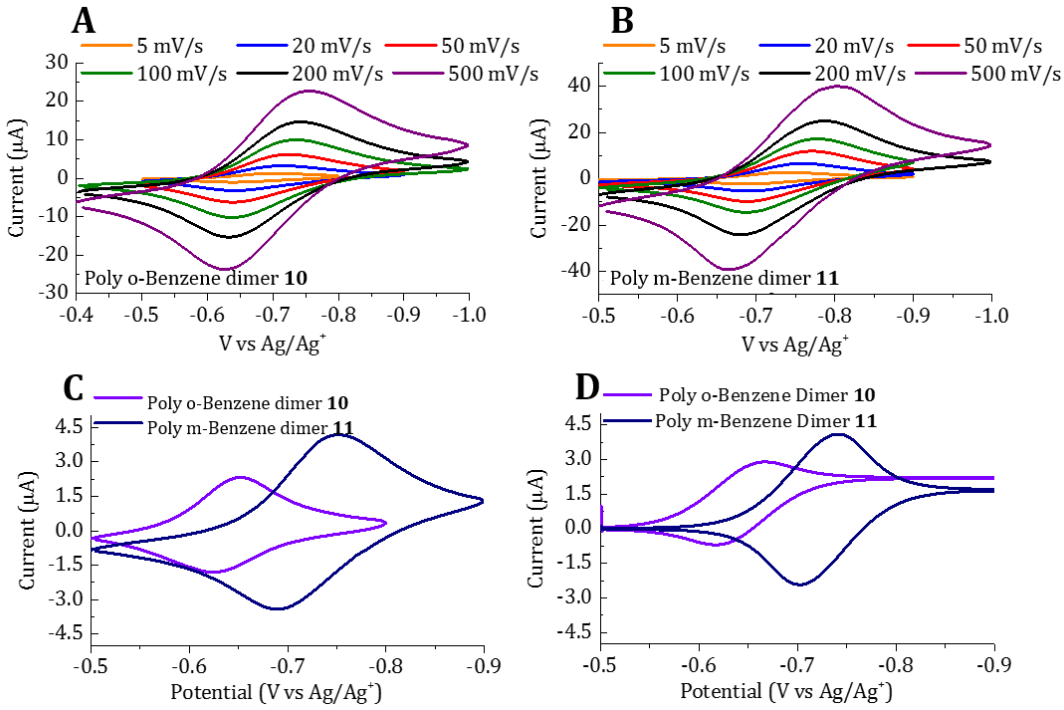

Figure B.19. Scan rate dependence voltammograms for the surface confine polymers (A) *o*-benzene polymer **10**, (B) *m*-benzene polymer **11**, (2 mM of monomer in 0.1 M $LiBF_4$ in acetonitrile) (C) Cyclic voltammograms at 10 mV/s for the resulting films after accessing the second redox process. (D) Simulated cyclic voltammograms using the experimentally calculated data.

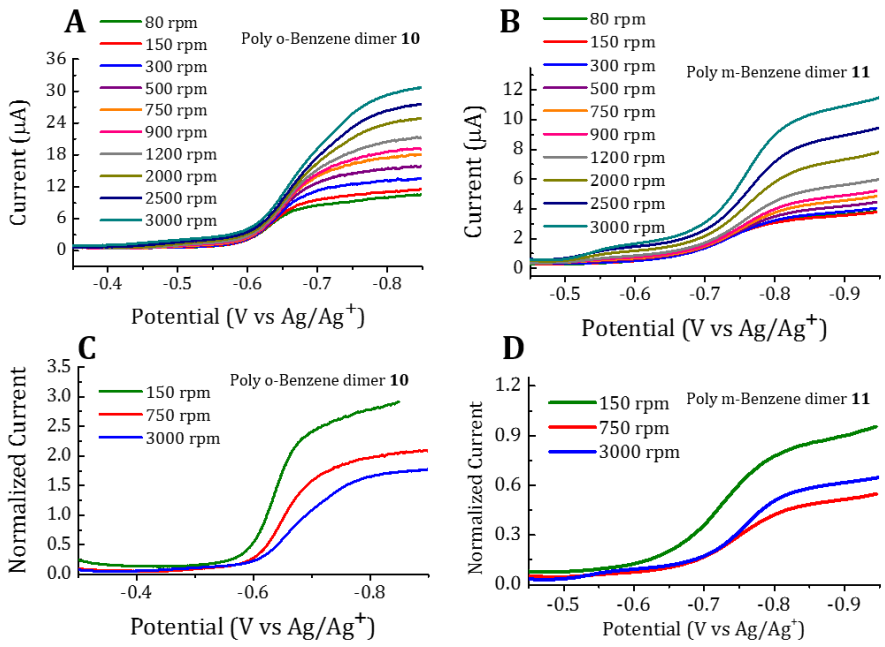

Figure B.20. Rotating disk electrode voltammograms for (A) *o*-benzene polymer **10** (1mM of monomer (0.5 mM of monomer in 0.1 M $LiBF_4$ in acetonitrile) and (B) *m*-benzene polymer **11** (0.5 mM of monomer in 0.1 M $LiBF_4$ in acetonitrile). Normalized Rotating disk electrode voltammograms for (C) *o*-benzene polymer **10** and (D) *m*-benzene polymer **11**, indicating the presence of a preceding chemical step which for this case is the adsorption of the polymer onto the electrode surface.

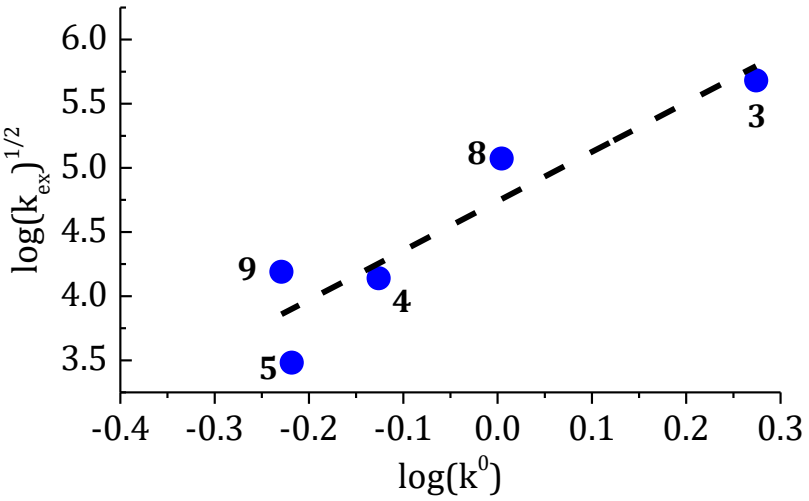

Figure B.21. Marcus relation for the Viologen Based dimer species.

Spectroelectrochemistry

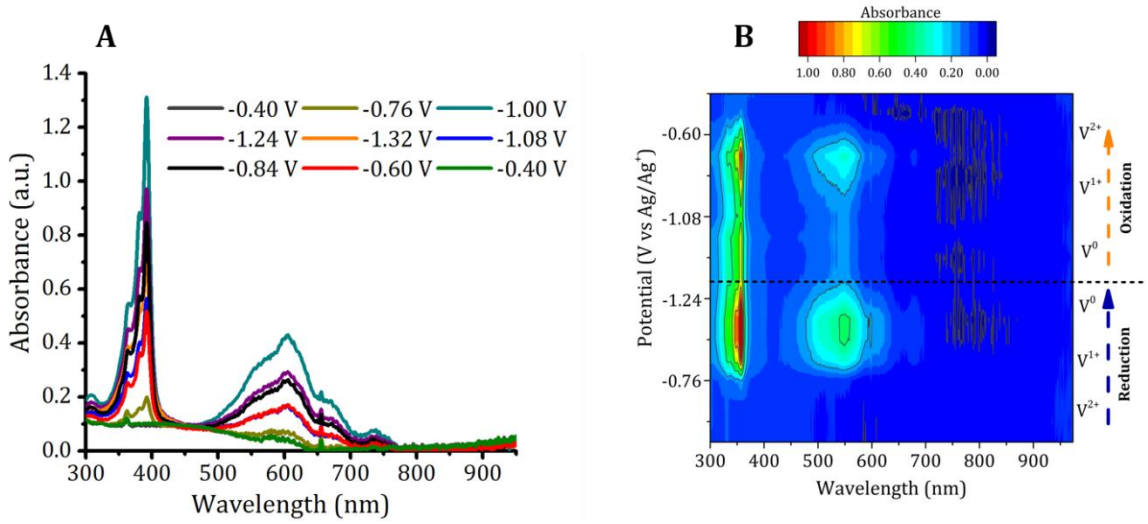

Figure B.22. (A) UV-Vis spectra for the viologen monomer **2** (0.5 mM in 0.1 M $LiBF_4$ in acetonitrile) as a function of potential and (B) Contour plot of the in situ UV-vis spectroelectrochemistry of the viologen monomer **2**.

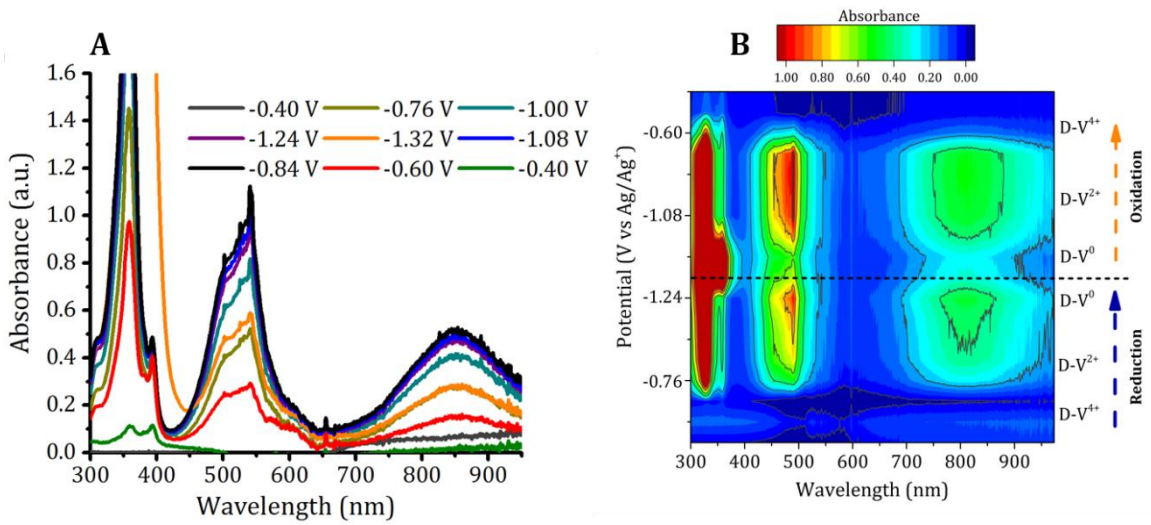

Figure B.23. (A) UV-Vis spectra for dimer **3** (0.5 mM of monomer in 0.1 M $LiBF_4$ in acetonitrile) as a function of potential and (B) Contour plot of the in situ UV-vis spectroelectrochemistry of dimer **3**.

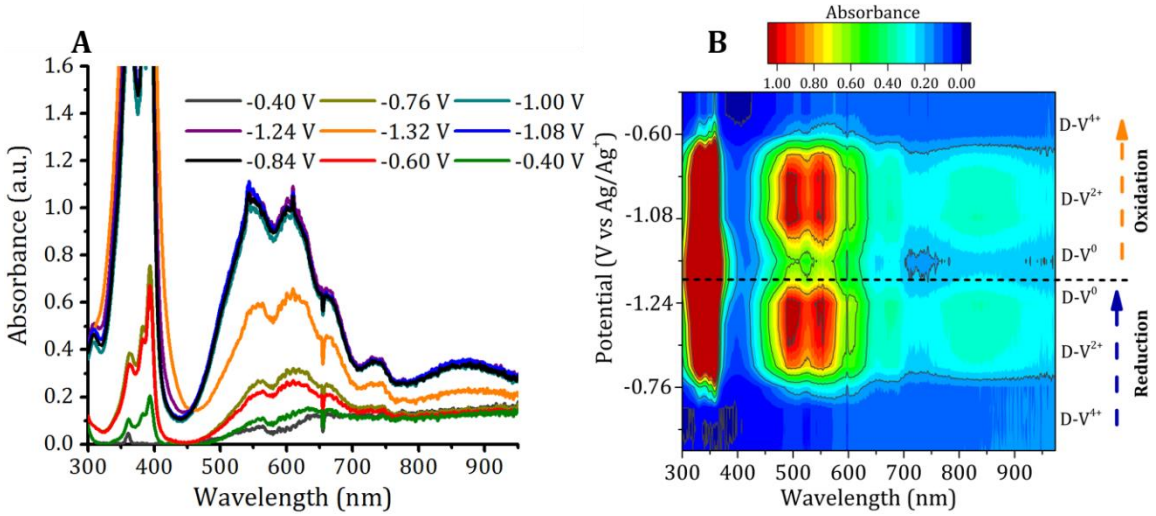

Figure B.24. (A) UV-Vis spectra for dimer **4** (0.5 mM of monomer in 0.1 M $LiBF_4$ in acetonitrile) as a function of potential and (B) Contour plot of the in situ UV-vis spectroelectrochemistry of dimer **4.**

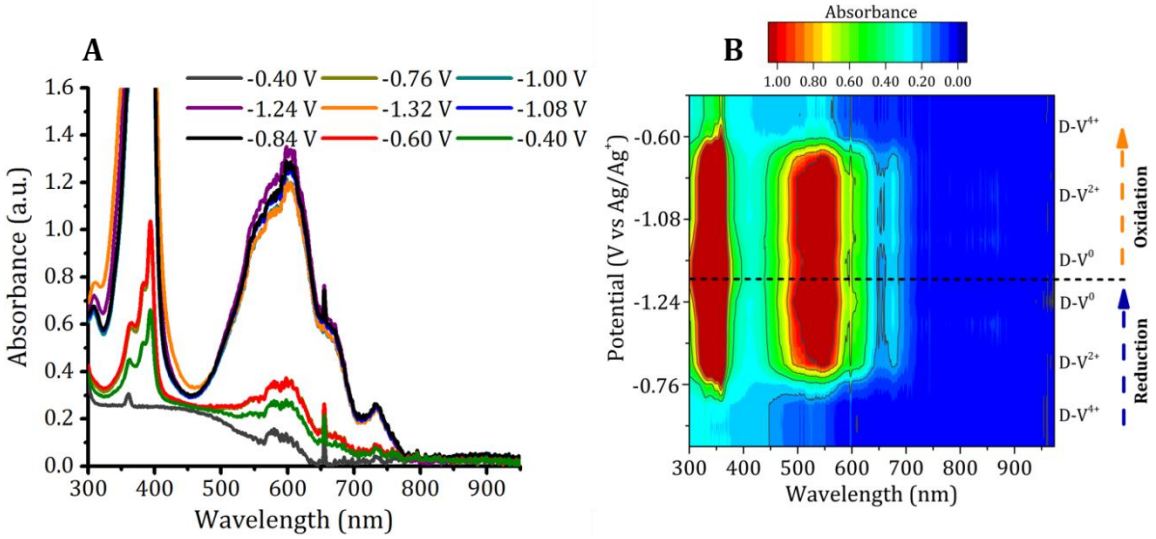

Figure B.25. (A) UV-Vis spectra for dimer **5** (0.5 mM of monomer in 0.1 M $LiBF_4$ in acetonitrile) as a function of potential and (B) Contour plot of the in situ UV-vis spectroelectrochemistry of dimer **5.**

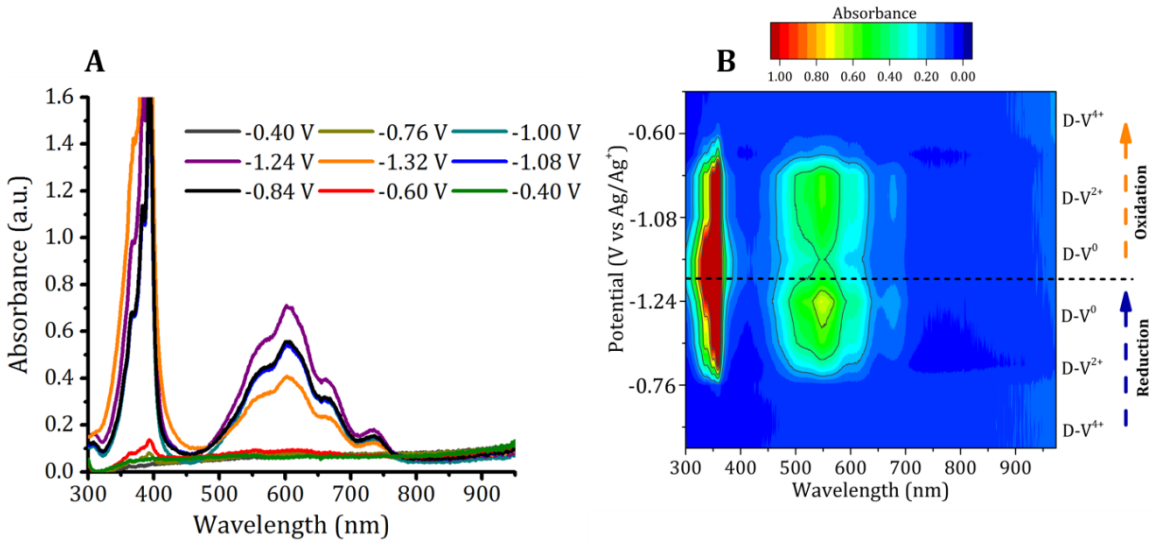

Figure B.26. (A) UV-Vis spectra for dimer **6** (0.5 mM of monomer in 0.1 M $LiBF_4$ in acetonitrile) as a function of potential and (B) Contour plot of the in situ UV-vis spectroelectrochemistry of dimer **6.**

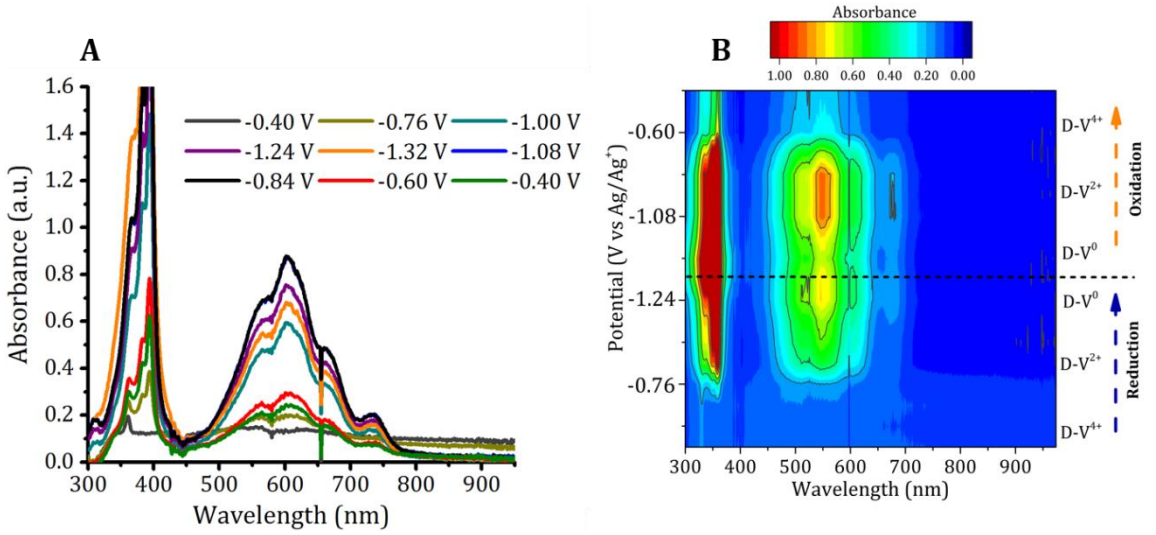

Figure B.27. (A) UV-Vis spectra for dimer **7** (0.5 mM of monomer in 0.1 M $LiBF_4$ in acetonitrile) as a function of potential and (B) Contour plot of the in situ UV-vis spectroelectrochemistry of dimer **7.**

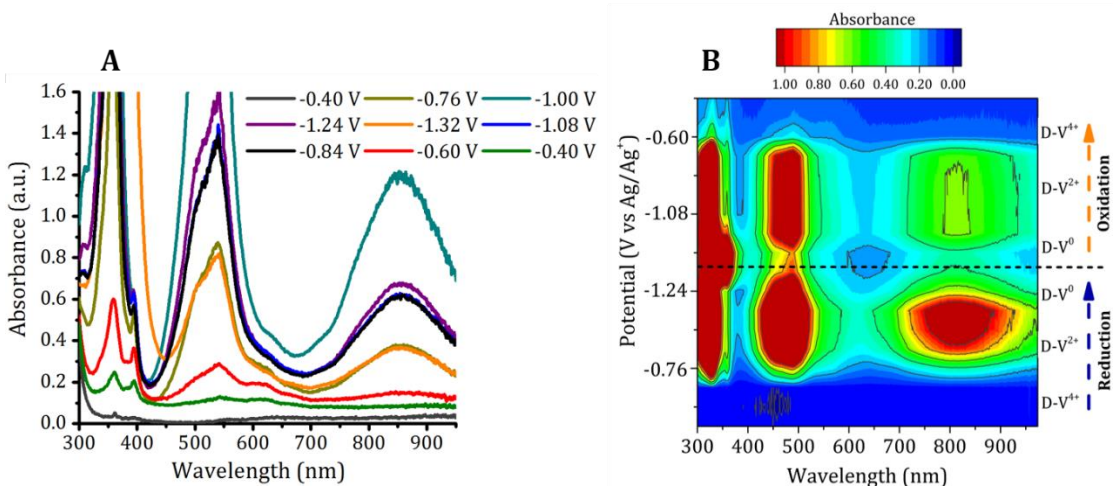

Figure B.28. (A) UV-Vis spectra for the *o*-benzene dimer **8** (1.0 mM of monomer in 0.1 M $LiBF_4$ in acetonitrile) as a function of potential and (B) Contour plot of the in situ UV-vis spectroelectrochemistry of the *o*-benzene dimer **8**.

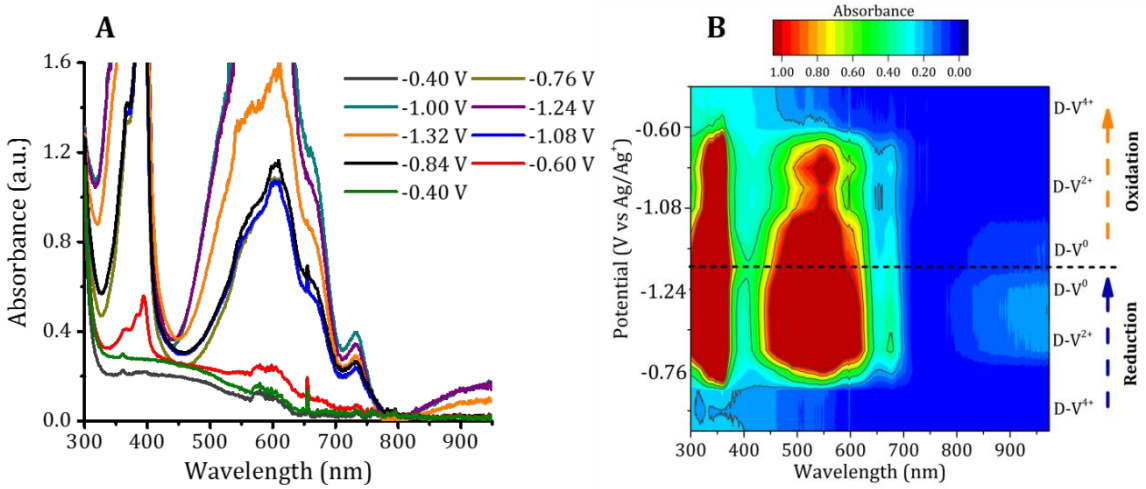

Figure B.29. (A) UV-Vis spectra for the *m*-benzene dimer **9** (1.0 mM of monomer in 0.1 M $LiBF_4$ in acetonitrile) as a function of potential and (B) Contour plot of the in situ UV-vis spectroelectrochemistry of the *m*-benzene dimer **9**.

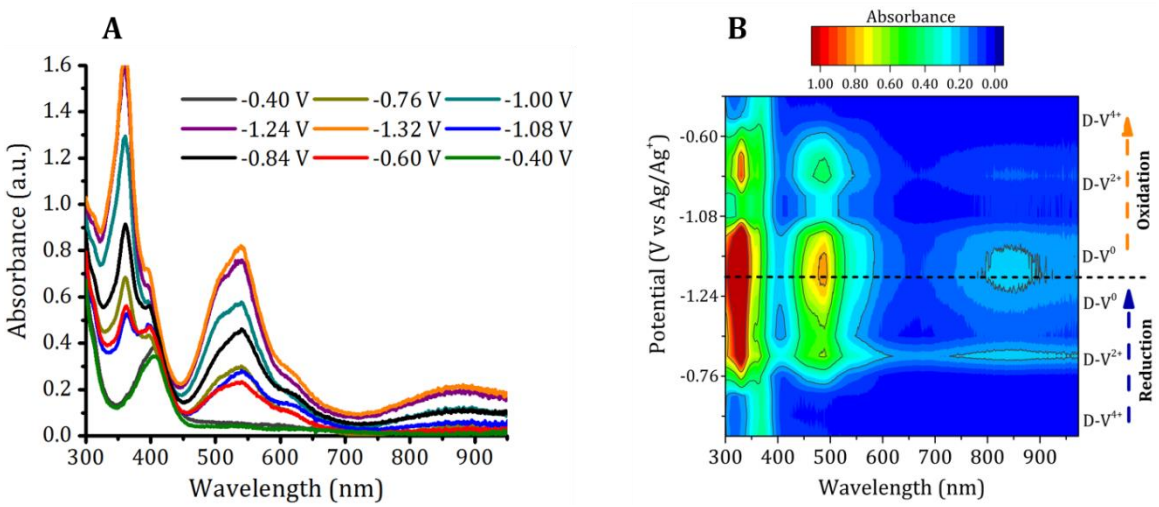

Figure B.30. (A) UV-Vis spectra for the *o*-benzene polymer **10** (2.0 mM of monomer in 0.1 M $LiBF_4$ in acetonitrile) as a function of potential and (B) Contour plot of the in situ UV-vis spectroelectrochemistry of the Poly *o*-benzene dimer **10**.

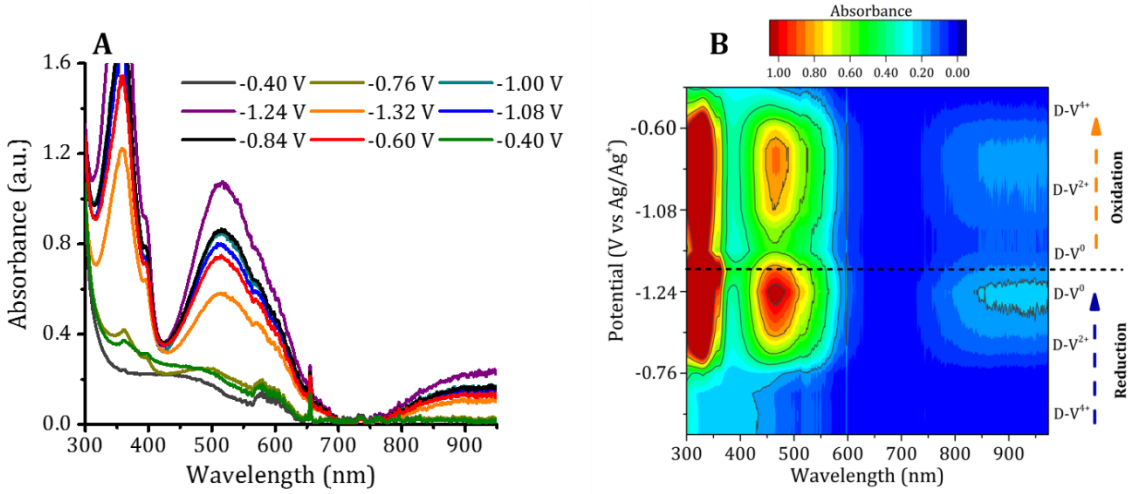

Figure B.31. (A) UV-Vis spectra for the *m*-benzene polymer **11** (2.0 mM of monomer in 0.1 M $LiBF_4$ in acetonitrile)as a function of potential and (B) Contour plot of the in situ UV-vis spectroelectrochemistry of the *m*-benzene polymer **11**.

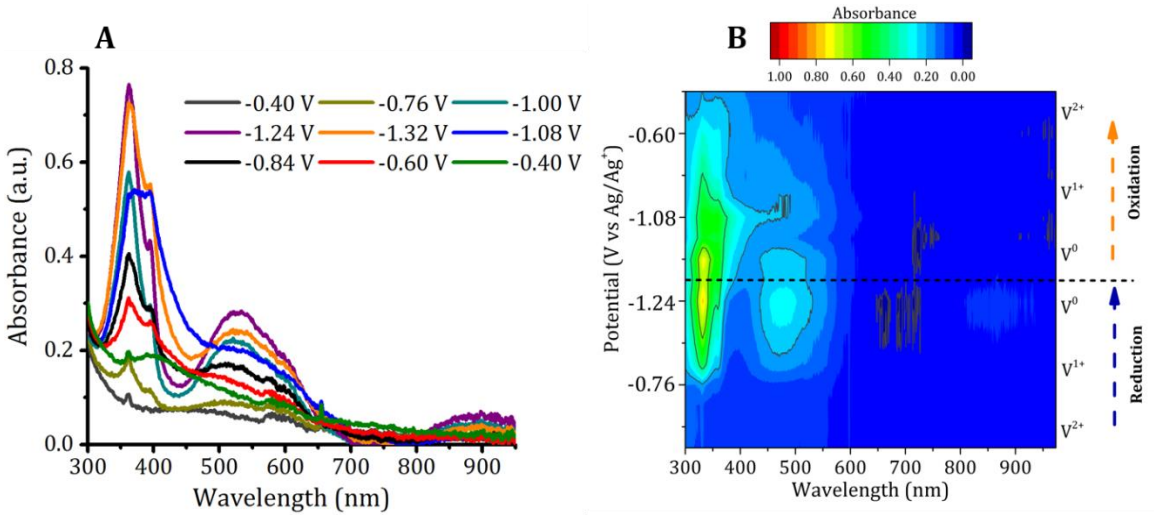

Figure B.32. (A) UV-Vis spectra for the 318 kDa benzyl Viologen Polymer **1** (2.0 mM of monomer in 0.1 M $LiBF_4$ in acetonitrile)as a function of potential and (B) Contour plot of the in situ UV-vis spectroelectrochemistry of the 318 kDa benzyl Viologen Polymer **1**.

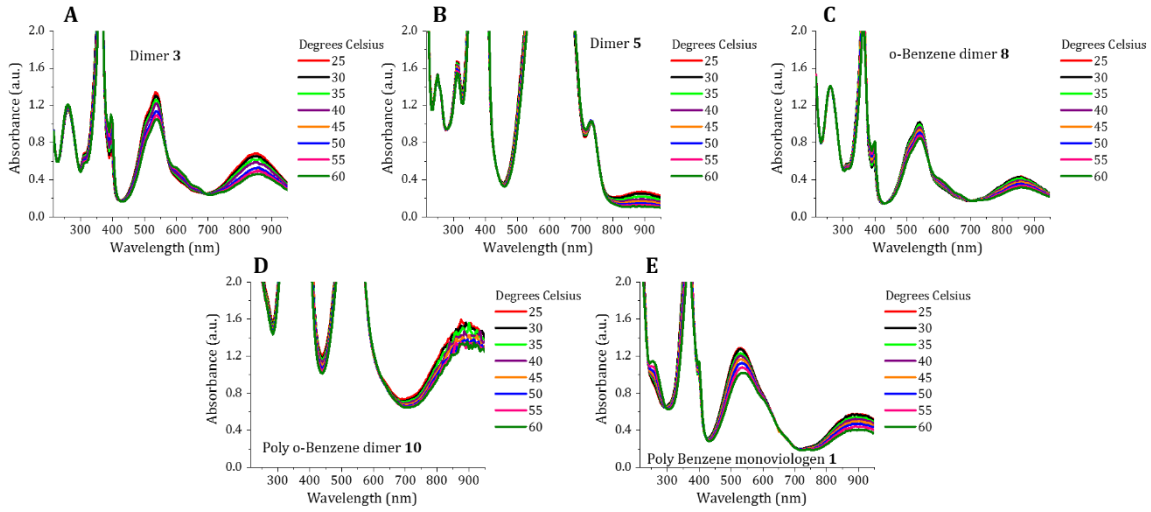

Figure B.33. Temperature dependence UV-Vis data for (A) dimer **3** (0.06 mM), (B) dimer **5** (0.15 mM), (C) *o*-benzene dimer **8** (0.06 mM), (D) *o*-benzene polymer **10** (0.15 mM)and (E) 318 kDa benzyl Viologen Polymer **1** (0.15 mM).

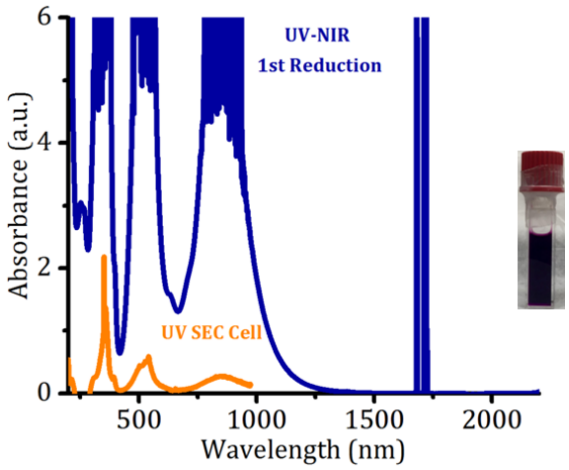

Figure B.34. UV-Vis near infrared spectra for dimer **3** (0.5 mM).

Table B.1 Comparison Between the k_{EX} for the Chemically and Electrochemically Reduced Systems

Molecule	**Electrochemistry (k_{EX}, s^{-1})**	**Zn Powder (k_{EX}, s^{-1})**
dimer **3**	2.3×10^{11}	9.3×10^{11}
dimer **4**	1.9×10^{8}	9.7×10^{11}
dimer **5**	9.2×10^{6}	6.9 x1 0^{8}
o-benzene dimer **8**	1.4×10^{10}	1.6×10^{11}
m-benzene dimer **9**	2.4×10^{8}	4.1×10^{8}
o-benzene polymer **10**	6.7×10^{8}	5.4×10^{11}
m-benzene polymer **11**	6.0×10^{7}	4.2×10^{10}
318 kDa Polymer **1**	8.1×10^{6}	5.5×10^{7}

Computational Analysis of Viologen Dimers

We have performed density functional calculations to investigate the geometric features and the relative energetics of the family of molecules presented. All calculations were performed using Gaussian09 software.[7] The M062-2X/6-31+G(d) level of theory was used to compute the structure, electronic energy, vibrational frequencies, and the free energy corrections of all species described in this manuscript.[8] All calculations were performed by including an SMD[9] solvation model using a dielectric medium of acetonitrile to include the solvation effects in the structure and energetics. The reduction potentials (E^{red} w.r.t. Li/Li^+) are computed from the computation of Gibbs free energy change ($\Delta G^{red,}$ eV) at 298 K in the solution (dielectric) for addition of an electron to the species of interest, using the following equation:

$$E^{red} = \frac{-\Delta G^{red}}{nF} - 1.24\ V\ ,$$

Where F is the Faraday constant (in eV) and n is the number of electrons involved in the reduction process. The addition of the constant '-1.24 V' is required to convert the free energy changes to reduction potential (Li/Li^+ reference electrode), a commonly used convention to compute the reduction potentials in solution.[10,11] The change in energy of electrons when going from vacuum to non-aqueous solution is treated as zero, similar to what has been used by others.[12] Details regarding the computation of redox potential can be found elsewhere.[12-16]

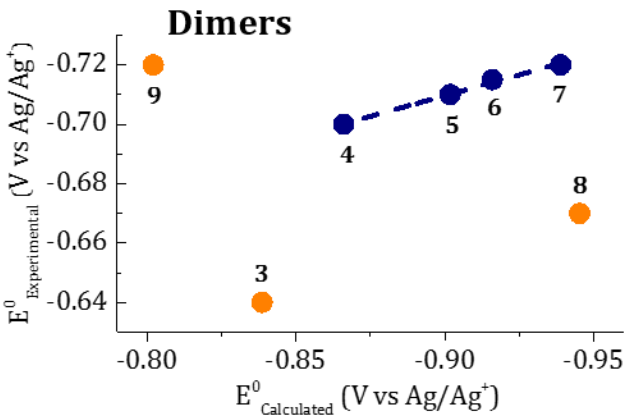

Figure B.35. Linear regression showing the fit between the Calculated and Experimental reduction potentials of dimer **3** to **9**. All the calculated data was done for the V-shaped structures.

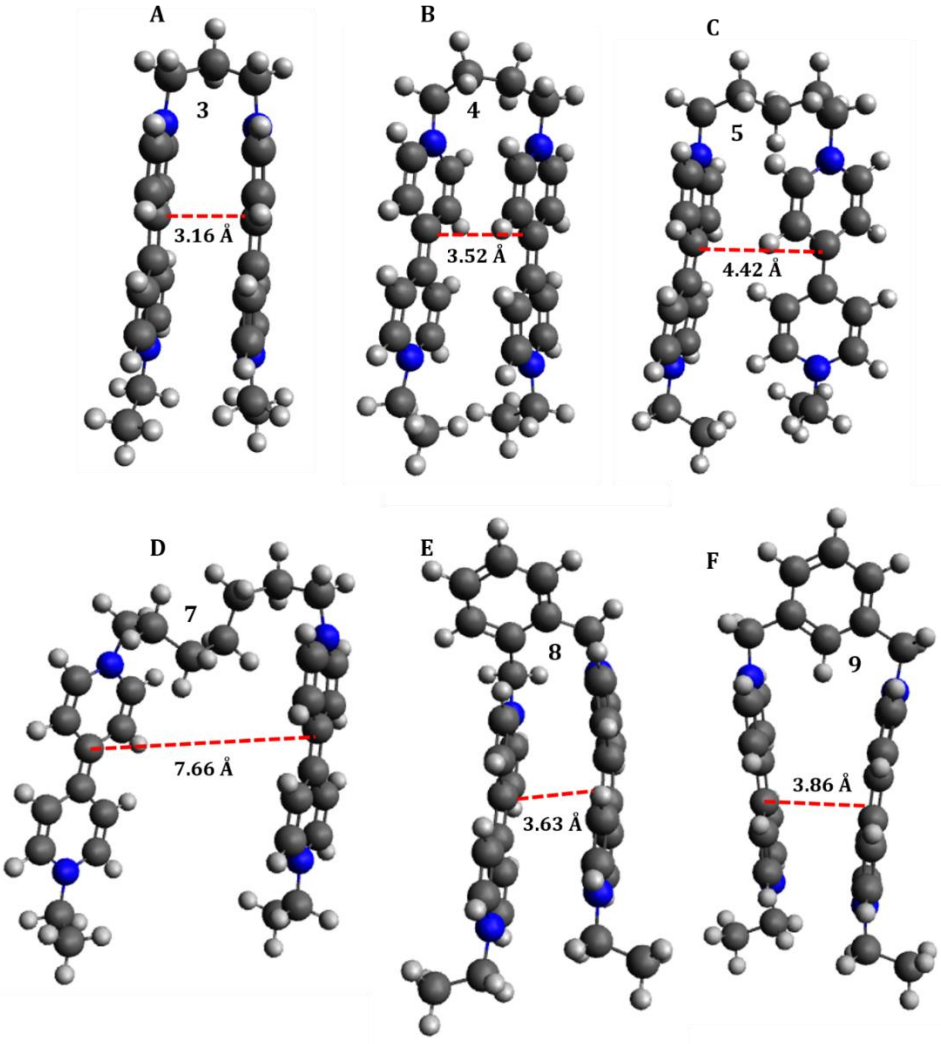

Figure B.36. Optimized structures showing distance between redox centers for the 2+ oxidation state.

Table B.2 Distance Between Redox Centers in the 4^+ and 2^+ Oxidation States

Dimer	**Distance (Å) 4^+**	**Distance (Å) 2^+**
dimer **3**	3.65	3.16
dimer **4**	3.53	3.52
dimer **5**	4.72	4.42
dimer **7**	8.29	7.66
o-benzene dimer **8**	3.89	3.63
m-benzene dimer **9**	7.34	3.86

Polymer Film Charge Transport

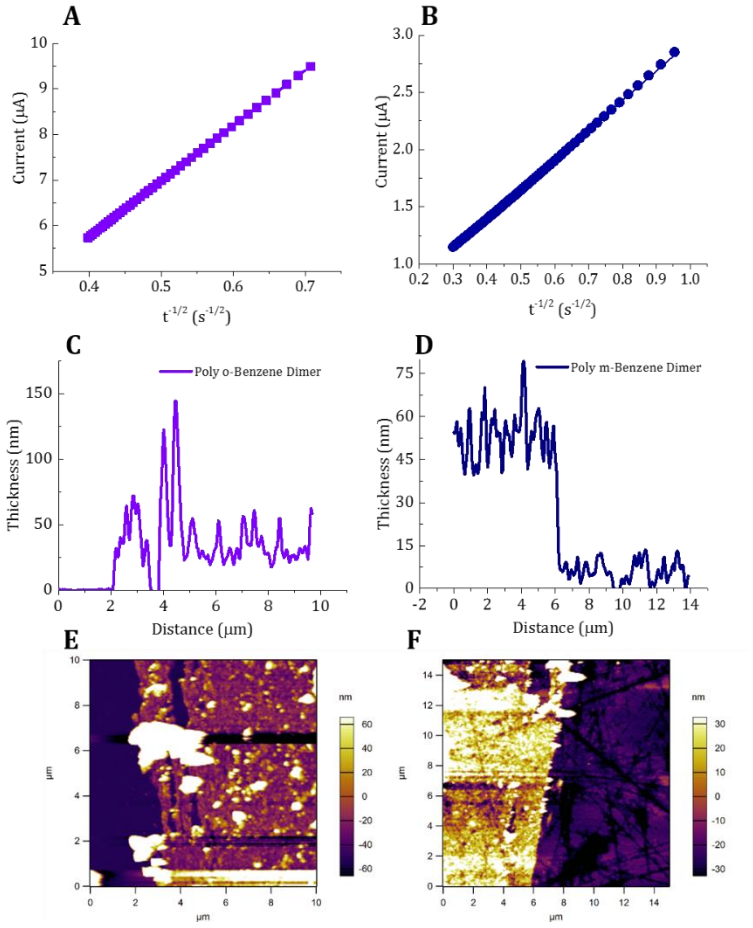

Figure B.37. Cottrell Plots for the plots used to calculate the electron diffusion coefficient for (A) *o*-benzene polymer **10** and (B) *m*-benzene polymer **11**. AFM line scans to determine the film thickness for (C) *o*-benzene polymer **10** and (D) *m*-benzene polymer **11**. AFM image showing the morphology of the electrodeposited films for (E) *o*-benzene polymer **10** and (F) *m*-benzene polymer **11**.

Table B.3 Calculated Electron Diffusion and the Charge Transport Rate Constant for the Resulting Polymer Films

Molecule	**Electron Diffusion (D_E, cm^2/s)**	**Film Charge Transport (k_{EX}, s^{-1})**
o-benzene polymer **10**	4.1 x 10^{-10}	1.9 x 10^5
m-benzene polymer **11**	2.5 x 10^{-11}	1.0 x 10^5
Polymer **1**	7.9 x 10^{-11}	5.3 x 10^4

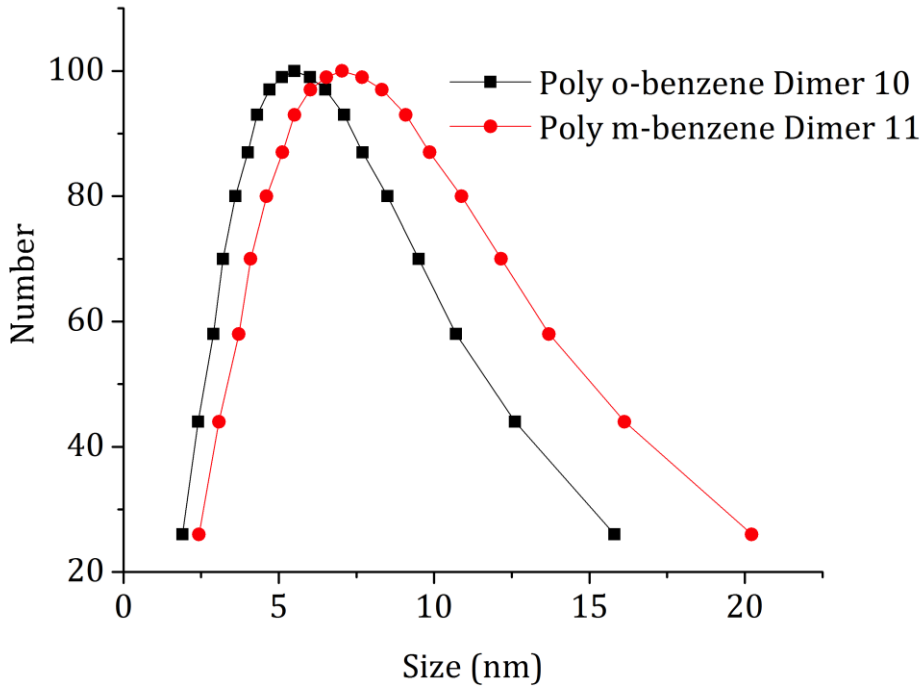

Figure B.38. Dynamic light scattering to determine the hydrodynamic radius of *o*-benzene polymer **10** and *m*-benzene polymer **11** at 5 mM concentration in acetonitrile.

Calculation of Areal Impingement Rate

To calculate the collisional frequency of species to an electrode surface, the following equation for areal impingement rate was used

$$Z_A = \frac{P}{(2 * \pi * M * k_B * T)^{1/2}}$$

Where Z_A is the collisional frequency per unit area, P is the pressure of the system (assumed to be sea level at 101,315 Pa), M is the mass of the species in kg, k_B is the Boltzmann Constant (1.38×10^{-23} J/K), and T is the temperature of the system in Kelvin.

Nanoelectrode Voltammetry for Charge Transfer Kinetics Determination

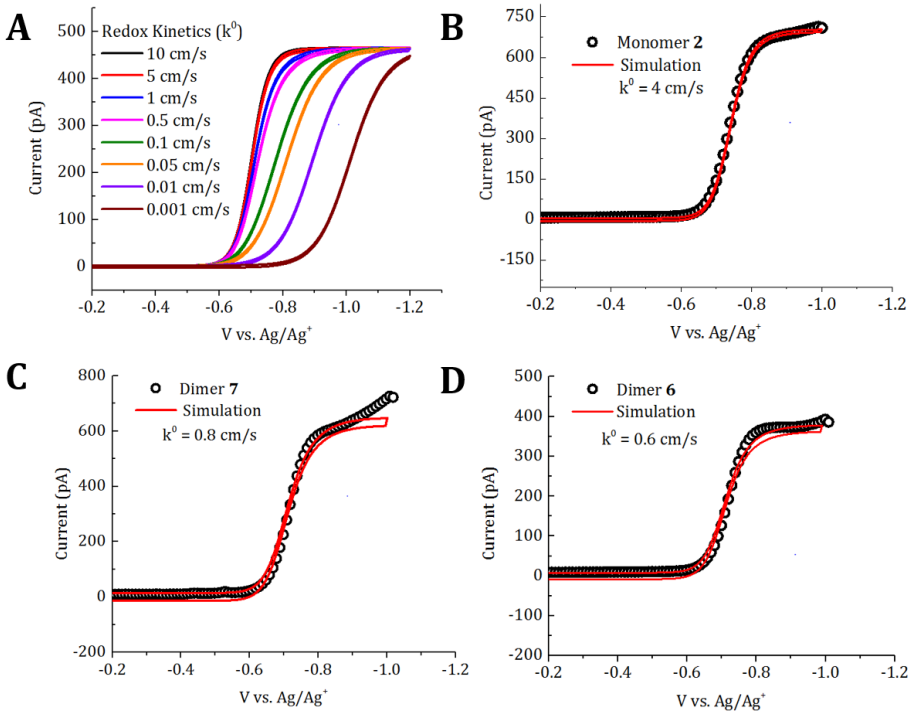

Figure B.39. (A) Cyclic voltammetry simulations in DigiElch (Gamry Instruments) of an arbitrary redox couple utilizing a 300 nm radius electrode with a concentration of active species of 5 mM and a diffusion coefficient for both the oxidized and reduced species to be equal to 1 x 10^{-5} cm2/s at a scan rate of 50 mV/s. The redox kinetics are swept to different magnitudes while everything else is held constant. (B) Simulation and experimental voltammetry of viologen monomer **2** using a 300 nm radius electrode in acetonitrile with 0.1 M $TBAPF_6$ electrolyte with 4 mM viologen at a scan rate of 20 mV/s. (C) Simulation and experimental voltammetry of viologen dimer **7** using a 300 nm radius electrode in acetonitrile with 0.1 M $TBA.PF_6$ electrolyte with 4 mM viologen at a scan rate of 20 mV/s. (D) Simulation and experimental voltammetry of viologen dimer **6** using a 300 nm radius electrode in acetonitrile with 0.1 M $TBA.PF_6$ electrolyte with 3 mM viologen at a scan rate of 20 mV/s.

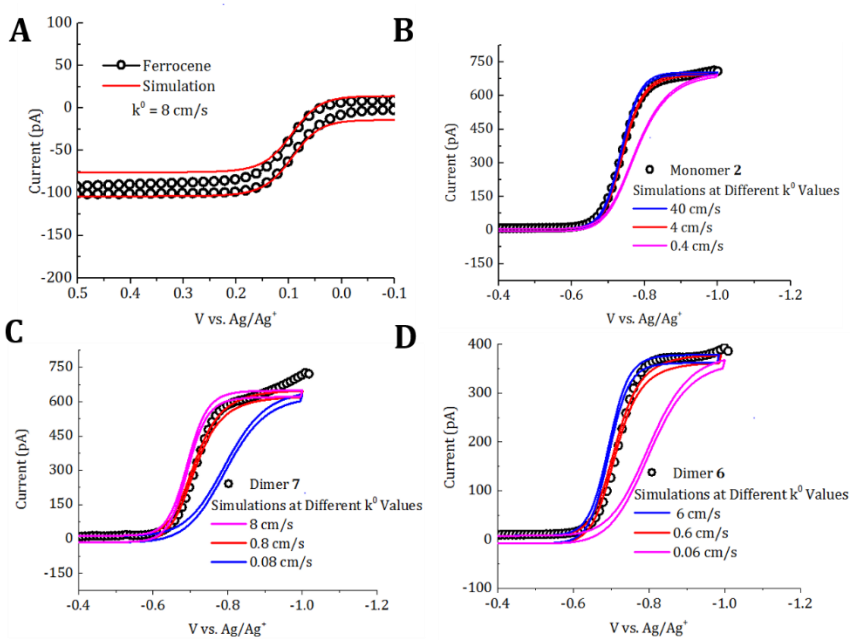

Figure B.40. (A) Simulation and experimental voltammetry of ferrocene using a 300 nm radius electrode in acetonitrile with 0.1 M $TBAPF_6$ electrolyte with 0.5 mM ferrocene at a scan rate of 20 mV/s. (B) Simulation and experimental voltammetry of viologen monomer **2** using a 300 nm radius electrode in acetonitrile with 0.1 M $TBAPF_6$ electrolyte with 4 mM viologen at a scan rate of 20 mV/s. An order of magnitude of k^0 higher and lower are shown to provide reference points. (C) Simulation and experimental voltammetry of viologen dimer **7** using a 300 nm radius electrode in acetonitrile with 0.1 M $TBAPF_6$ electrolyte with 4 mM viologen at a scan rate of 20 mV/s. An order of magnitude of k^0 higher and lower are shown to provide reference points. (D) Simulation and experimental voltammetry of viologen dimer **6** using a 300 nm radius electrode in acetonitrile with 0.1 M $TBAPF_6$ electrolyte with 3 mM viologen at a scan rate of 20 mV/s. An order of magnitude of k^0 higher and lower are shown to provide reference points.

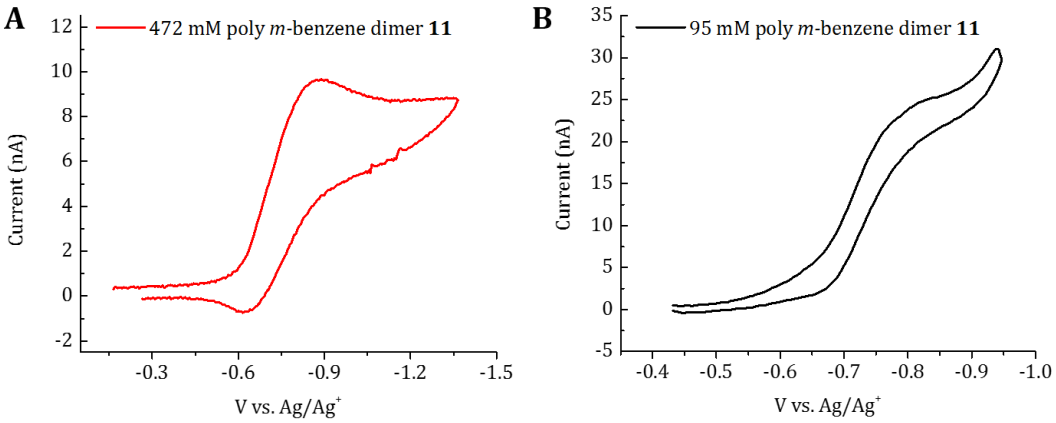

Figure B.41. Resulting cyclic voltammograms for *m*-benzene polymer **11** in $LiBF_4$ and acetonitrile for (A) 472 mM of monomer with a resulting diffusion coefficient of 3.8 x 10^{-8} cm^2/s and (B) 95 mM of monomer with a resulting diffusion coefficient of 6.5 x 10^{-7} cm^2/s. The decreased current of the higher concentration RAP solution is primarily due to viscosity. We have measured the viscosity ratio of viologen RAP between 500 mM and 100 mM in 100 mM supporting electrolyte to be ~9, which explains the order of magnitude difference in diffusion coefficients. To prevent any *i-R* drop contributions all the measurements were done using a UME with a radius of 12.5µm.

References

1. Gottlieb, H. E.; Kotlyar, V.; Nudelman, A. *J. Org. Chem.*, **1997**, *62*, 7512.

2. Nagarjuna, G.; Hui, J.; Cheng, K. J.; Lichtenstein, T.; Shen, M.; Moore, J. S.; Rodríguez-López, J. *J. Am. Chem. Soc.*, **2014**, *136*, 16309.

3. Yus, M.; Foubelo, F.; García, D. *Heterocycles*, **2009**, *77*, 991.

4. Mannion, J. J.; Wang, T. S. *Spectrochim. Acta*, **1964**, *20*, 45.

5. Katcka, M.; Urbanski, T. *B. Acad. Pol. Sci. Biol.*, **1964**, *12*, 615.

6. Ueno, Y.; Kawamura, A.; Takasu, K.; Komatsuzaki, S.; Kato, T.; Kuboe, S.; Kitamura, Y.; Kitade, Y. *Org. Biomol. Chem.*, **2009**, *7*, 2761.

7. Frisch, M. J.; Trucks, G. W.; Schlegel, H. B.; Scuseria, G. E.; Robb, M. A.; Cheeseman, J. R.; Scalmani, G.; Barone, V.; Mennucci, B.; Petersson, G. A.; Nakatsuji, H.; Caricato, M.; Li, X.; Hratchian, H. P.; Izmaylov, A. F.; Bloino, J.; Zheng, G.; Sonnenberg, J. L.; Hada, M.; Ehara, M.; Toyota, K.; Fukuda, R.; Hasegawa, J.; Ishida, M.; Nakajima, T.; Honda, Y.; Kitao, O.; Nakai, H.; Vreven, T.; Montgomery, J. A.; Peralta, J. E.; Ogliaro, F.; Bearpark, M.; Heyd, J. J.; Brothers, E.; Kudin, K. N.; Staroverov, V. N.; Kobayashi, R.; Normand, J.; Raghavachari, K.; Rendell, A.; Burant, J. C.; Iyengar, S. S.; Tomasi, J.; Cossi, M.; Rega, N.; Millam, J. M.; Klene, M.; Knox, J. E.; Cross, J. B.; Bakken, V.; Adamo, C.; Jaramillo, J.; Gomperts, R.; Stratmann, R. E.; Yazyev, O.; Austin, A. J.; Cammi, R.; Pomelli, C.; Ochterski, J. W.; Martin, R. L.; Morokuma, K.; Zakrzewski,

V. G.; Voth, G. A.; Salvador, P.; Dannenberg, J. J.; Dapprich, S.; Daniels, A. D.; Farkas; Foresman, J. B.; Ortiz, J. V.; Cioslowski, J.; Fox, D. J. Wallingford CT, **2009**.

8. Zhao, Y.; Truhlar, D. G. *Theor. Chem. Acc.*, **2008**, *120*, 215.

9. Marenich, A. V.; Cramer, C. J.; Truhlar, D. G. *J. Phys. Chem. B*, **2009**, *113*, 6378.

10. Kelly, C. P.; Cramer, C. J.; Truhlar, D. G. *J. Phys. Chem. B*, **2006**, *110*, 16066.

11. Bhattacharyya, S.; Stankovich, M. T.; Truhlar, D. G.; Gao, J. *J. Phys. Chem. A*, **2007**, *111*, 5729.

12. Guerard, J. J.; Arey, J. S. *J. Chem. Theory Comput.*, **2013**, *9*, 5046.

13. Moens, J.; Geerlings, P.; Roos, G. *Chem. Eur. J.*, **2007**, *13*, 8174.

14. Borodin, O.; Behl, W.; Jow, T. R. *J. Phys. Chem. C*, **2013**, *117*, 8661.

15. Vollmer, J. M.; Curtiss, L. A.; Vissers, D. R.; Amine, K. *J. Electrochem. Soc.*, **2004**, *151*, A178.

16. Kelly, C. P.; Cramer, C. J.; Truhlar, D. G. *J. Phys. Chem. B*, **2006**, *111*, 408.

Appendix C: Supporting Information File for Chapter 4

Notes and Acknowledgements

This appendix appeared in its entirety in the journal *The Analyst* with authors Burgess, M.; Hernández-Burgos, K.; Cheng, K..; Moore, J. S.; Rodríguez-López, J. "Impact of Electrolyte Composition on the Reactivity of a Redox Active Polymer Studied Through Surface Interrogation and Ion-Sensitive Scanning Electrochemical Microscopy". **2016,** 141, 3842-3850. This appendix is reprinted with the permission of the publisher and is available from http://www.pubs.rsc.org and using DOI: 10.1039/C6AN00203J. M.B. performed all of the SECM analysis, helped in voltammetry experiments, helped write the manuscript, and made figures. This work was supported as part of the Joint Center for Energy Storage Research, an Energy Innovation Hub funded by the U.S. Department of Energy, Office of Science, Basic Energy Sciences. M. B. acknowledges support by the National Science Foundation Graduate Research Fellowship Program under grant No. DGE-1144245.

General Information

^{1}H spectra were recorded on a UNITY INOVA™ 500 NB High-Resolution NMR. UV-Vis absorption spectra were recorded on Shimadzu instruments. Elemental analyses were performed on the following instruments: CHN analysis - Exeter Analytical CE 440 and Perkin Elmer 2440, Series II

Unless otherwise stated, all starting materials and reagents were purchased from Sigma-Aldrich or Matrix Scientific and used without further purification. Polystyrene of 190 kDa (PDI: 1.01) was purchased from Polymer Source.

Polynitrostyrene (PNS)

Synthesis based on work by Philippides *et. al.* A flask was charged with 4-nitrotoluene (100 mL) and polystyrene (5.0 g). Then nitric acid (80 mL) was added to the flask and stirred vigorously while cooled to 0 ºC in an ice bath. Sulfuric acid (20 mL) was added slowly to the flask under vigorous stirring. The mixture was allowed to return to room temperature and stirred for 16 hours. The resultant emulsion product was precipitated into isopropanol and then redissolved into dimethylformamide. The precipitation was repeated three times and placed under high vacuum for 24 hours. Functionalization was found to be 78% by UV-Vis spectroscopy.

The molecular weight of the PNS RAP was calculated using the degree of polymerization of the polystyrene multiplied by the monomer molecular weight. The degree of polymerization of the polystyrene is the molecular weight of polystyrene (M_n) /104.15. The calculated molecular weight for PNS was 270 kDa.

Scheme C.1 Synthetic pathway to PNS

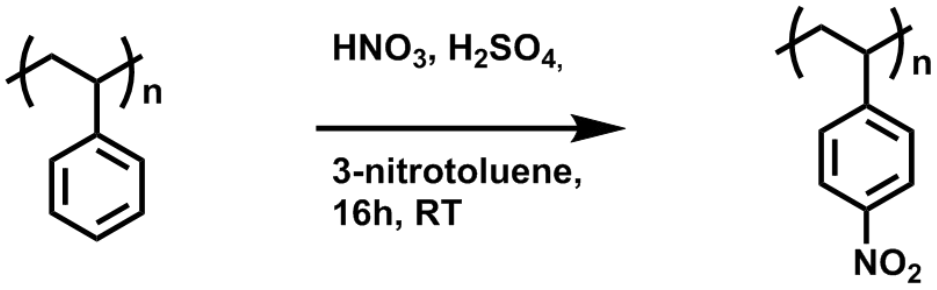

Redox Active Polymer Characterization

Table C.1 Elemental Analysis

	Element	C	H	N
PNS RAP	Theoretical (%)	64.42	4.73	9.39
	Experimental (%)	57.99	4.49	8.86
	Difference	6.43	-0.24	-0.53

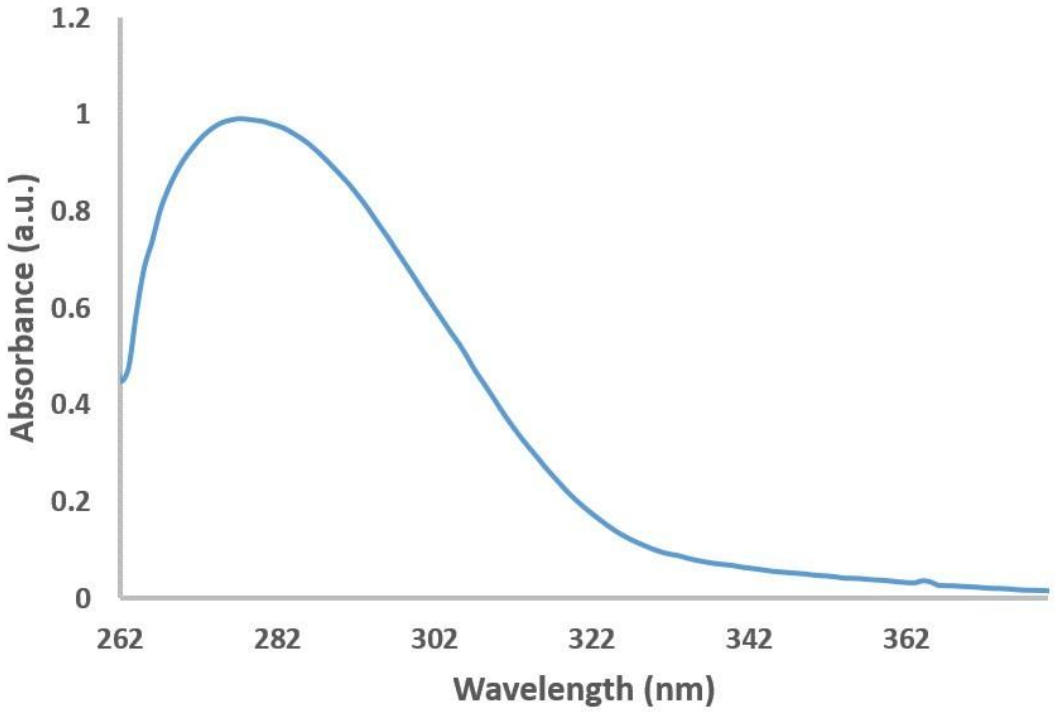

Figure C.1. UV-Vis absorption spectrum of 0.5 mM PNS in DMF using a quartz cuvette with a 1 cm path length.

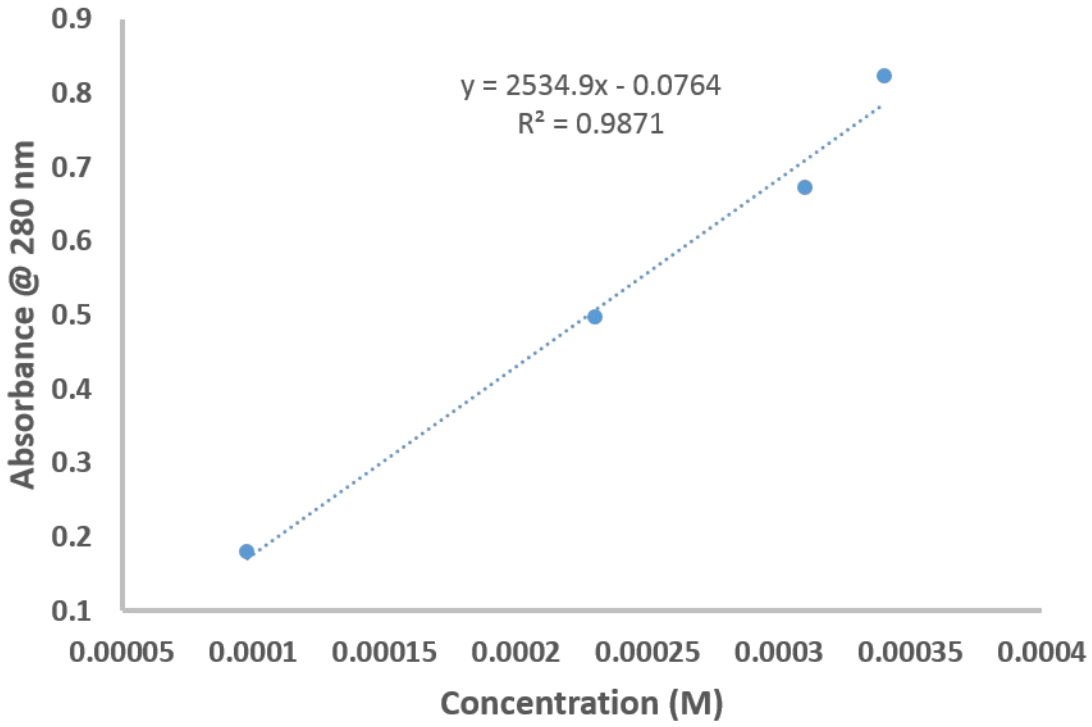

Figure C.2. UV-Vis calibration curve using 4-nitrotoluene as the PNS standard in DMF.

Table C.2 Molar Extinction Coefficients of 260 kDa PNS in DMF

Molecular Weight of PNS	**Molar Extinction Coefficient ε (M^{-1}·cm^{-1})**
270 kDa	2523.9

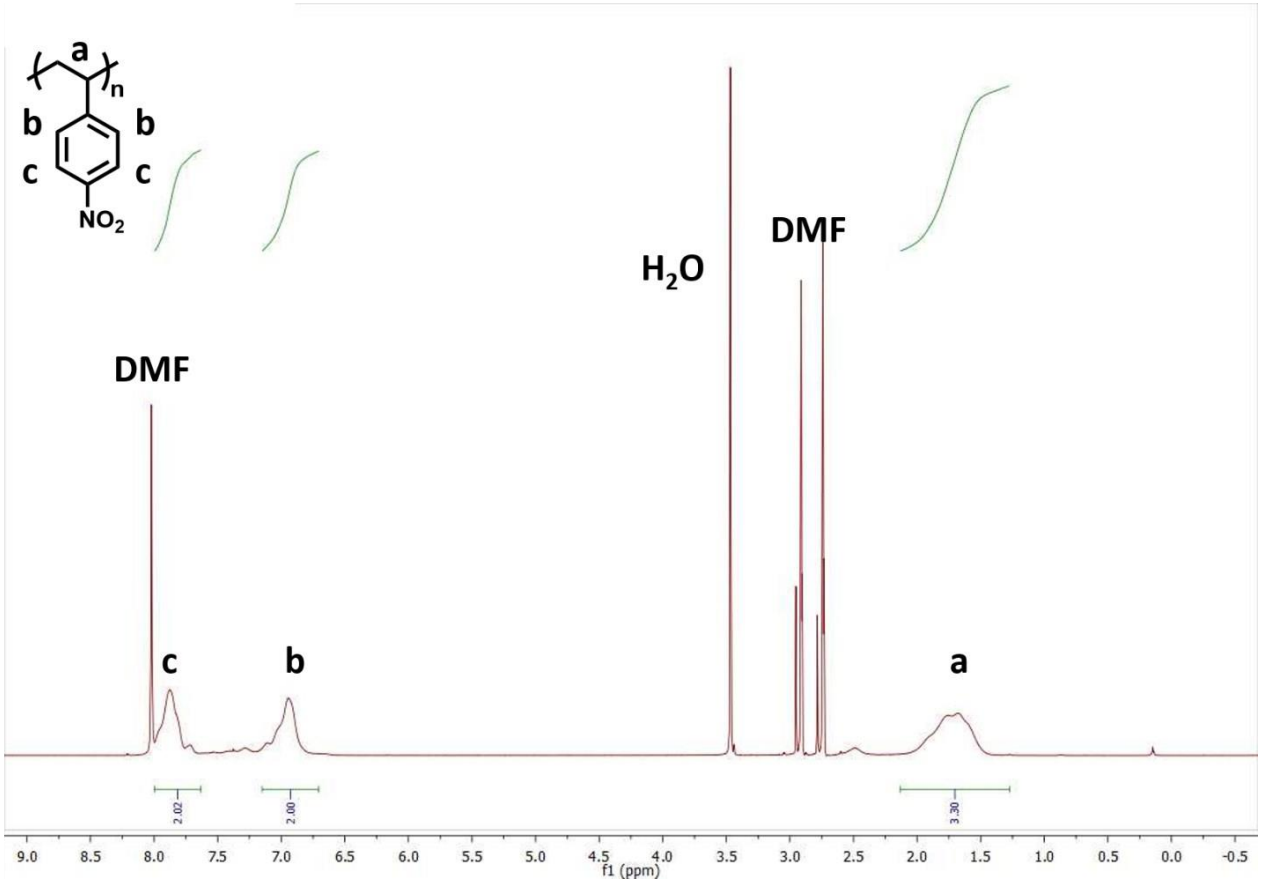

Figure C.3. ^{1}H NMR spectra of 0.5 mM PNS in d-DMF.

Electrochemistry

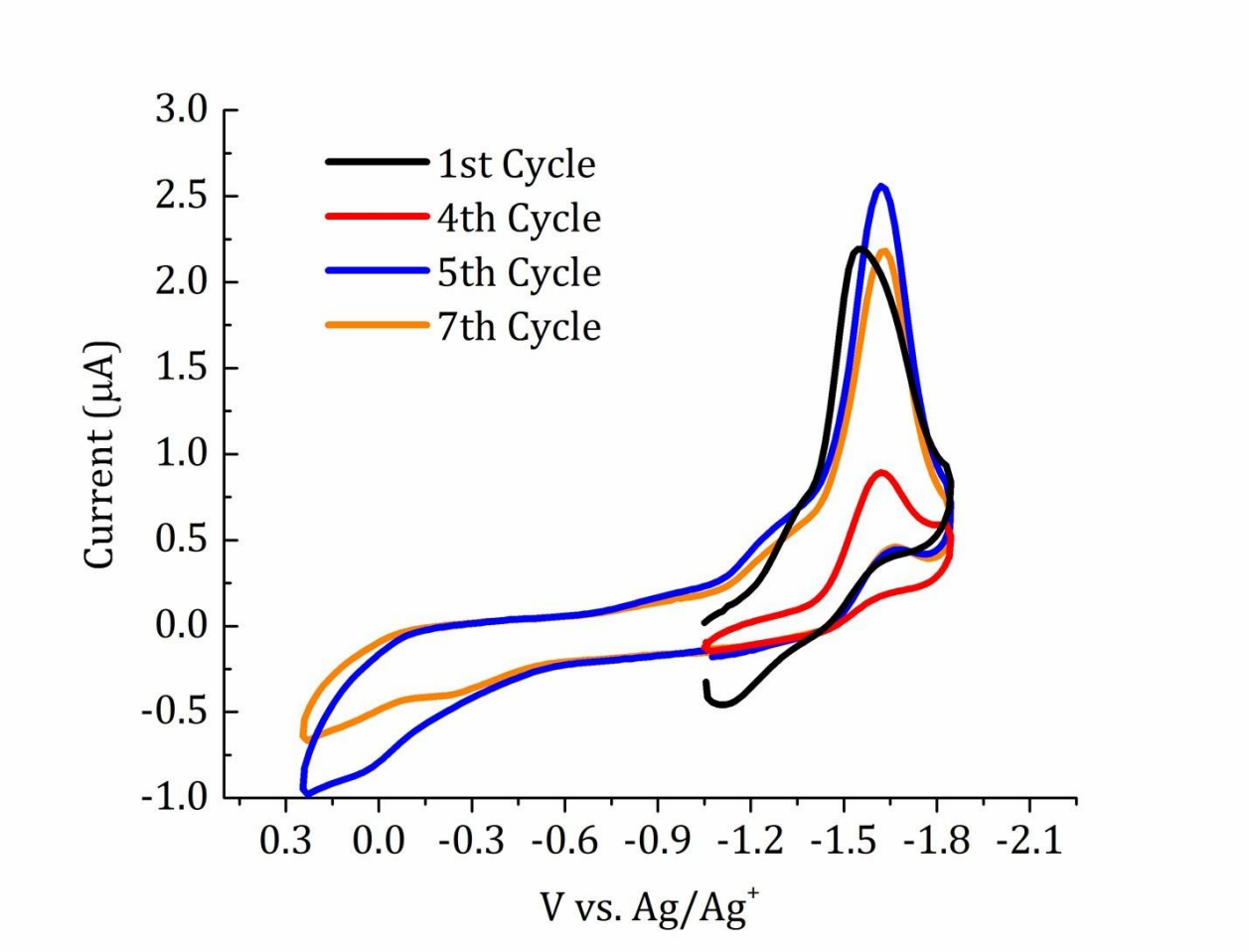

Figure C.4. Cyclic voltammetry with a 1.15 mm Pt disk electrode in the presence of 5 mM PNS in DMF with 0.1 M $TBAPF_6$ and 17 mM $LiPF_6$ electrolytes. The black voltammogram is the same voltammogram shown in Chapter 4 in Figure 4.3, scanned at 20 mV/s demonstrating the irreversibility of PNS in the presence of Li^+. The red voltammogram is the same electrode scanned between the same potentials at the fourth cycle. There is a significant decrease in current from the first cycle due to irreversibility of the PNS with Li^+. The blue voltammogram is the same electrode and same solution scanned more positively to show the potential at which the oxidation of PNS in Li^+ electrolyte can be finally be seen, ~0.2 V, after which the reduction the reduction peak is now restored to its initial current magnitude. The seventh cycle shows the reduction peak is maintaining its peak current magnitude, but the oxidation peak is decreased because there has not been a buildup of reduced PNS as was the case in cycles 1-4.

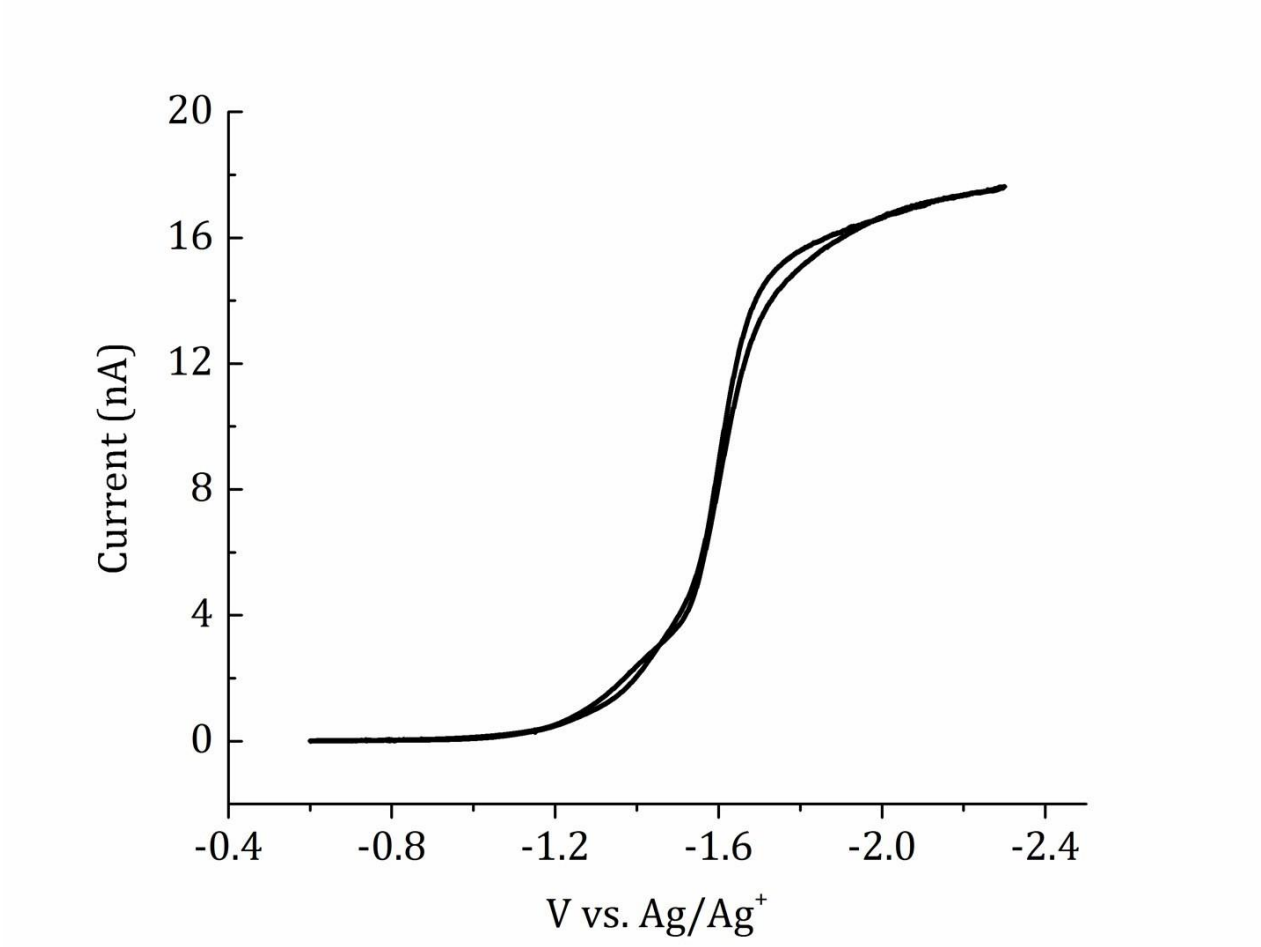

Figure C.5. Voltammetry of 33 mM PNS at 100 mV/s using a 12.5 µm radius microelectrode in 0.1 M $TBAPF_6$. The diffusion coefficient (*D*) was calculated using the steady state current at -2.3 V, ~18 nA, and using the equation $i_{steady\ state} = 4nFaDC^*$, in which *F* is Faraday's constant (96,485 C/mol), *a* is the radius of the microelectrode, and C^* is the bulk concentration (mol/cm^3). The calculated value of the diffusion coefficient for PNS in TBA^+ electrolyte was 1.1 x 10^{-6} cm^2/s.

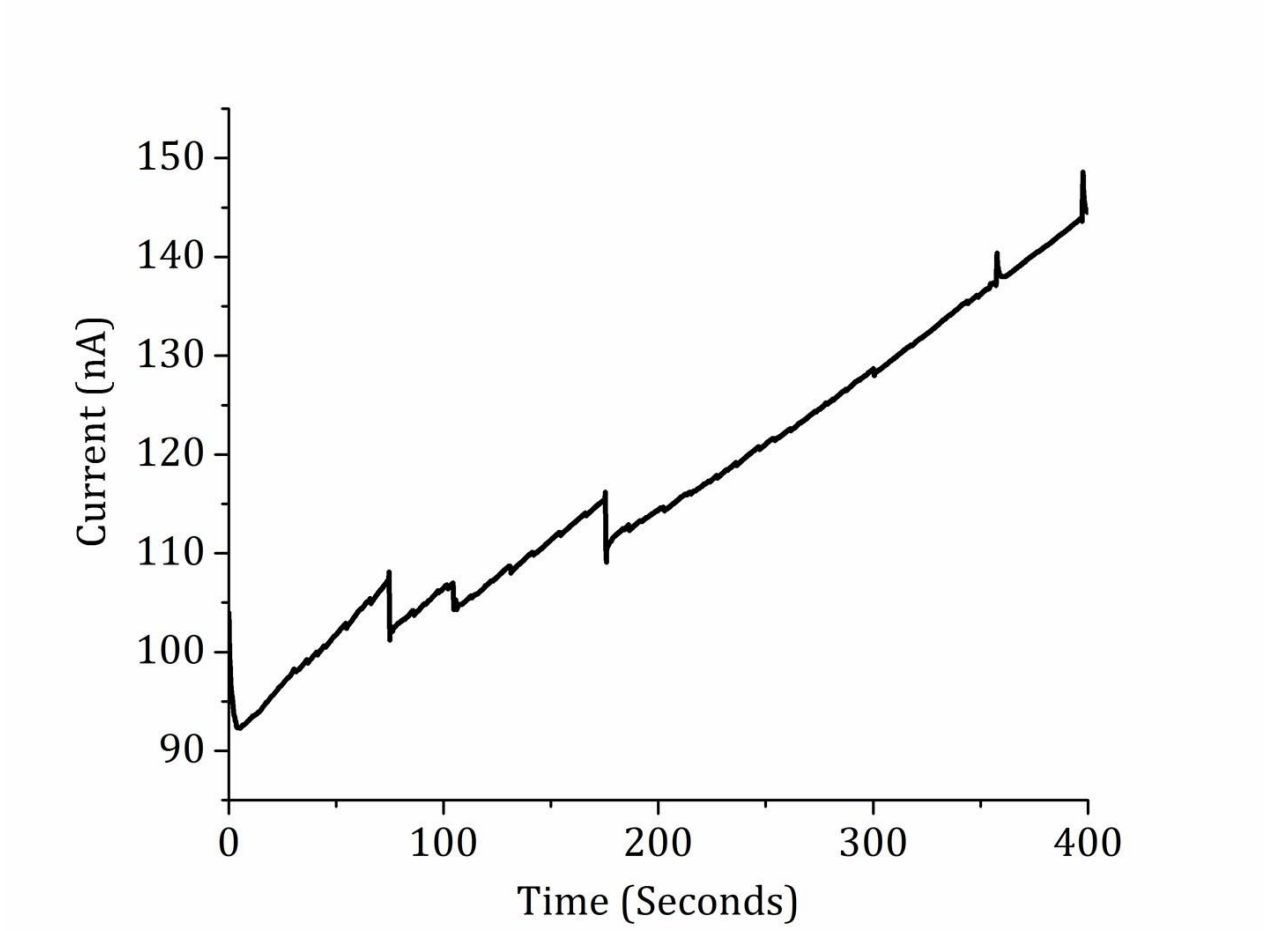

Figure C.6. Electrodeposition of Hg onto the Pt UME surface. Deposition solution was 10 mM $Hg(NO_3)_2$ with 0.1 M tetramehtylammonium nitrate electrolyte, with 0.1% HNO_3 (by volume) in distilled water. The UME was poised at -0.4 V vs. a tungsten wire quasi-reference electrode for 400 seconds. The current blips in the chronoamperometric step are indicative of the growth and subsequent combination of micro-Hg droplets. Deposited charge was 48 nC, which after accounting for 2 electrons passing per molecule to reduce Hg^{2+} to Hg metal, the Hg droplet was found to be 11.75 microns tall, which to one significant figure gives ratio of the height of the Hg droplet to the radius of the UME as 1.

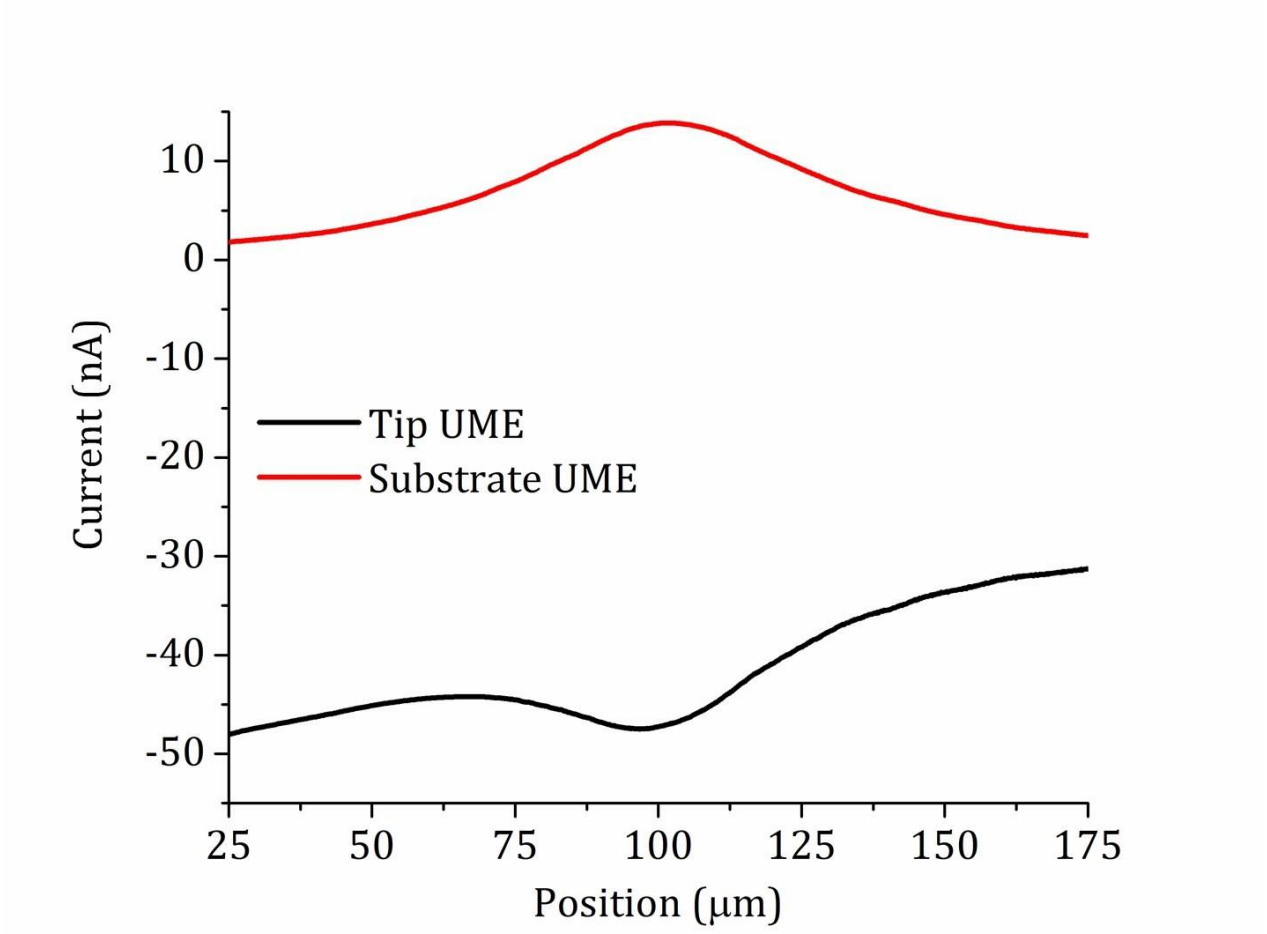

Figure C.7. Aligning of the microelectrodes via the feedback mode of SECM. The tip UME is generating $TMPD^+$ and the PNS filmed substrate is reducing it to neutral TMPD. When feedback is sensed (~100 µm position in Figure C.6) the tips are aligned in that particular dimension. Both of the UMEs had a radius of 12.5 µm. The solution contained 10 mM TMPD, 0.1 M $TBAPF_6$, 17 mM KBF_4, and 17 mM $LiPF_6$.

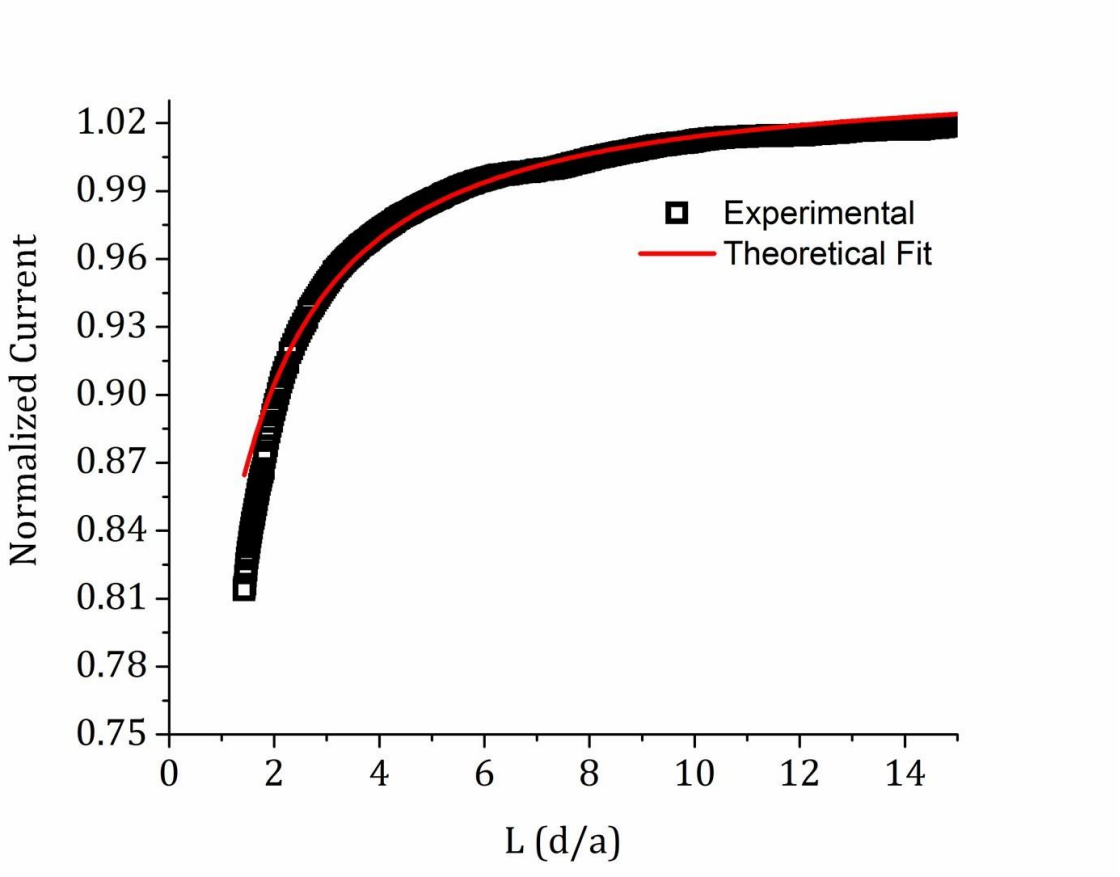

Figure C.8. Approach curve of a Hg capped UME using the first oxidation of TMPD to the PNS filmed substrate UME that was placed at open circuit. The motor speed was 36 microns per second. The theoretical fitting of the experimental data was made using an *Rg* of 2 for the Hg capped UME and used fitting protocol from Lindsey *et. al*.. After accounting for the height of the droplet, the final placement of the Hg capped UME was found to be 5 microns above the PNS filmed substrate UME, as measured from the top of the Hg droplet.

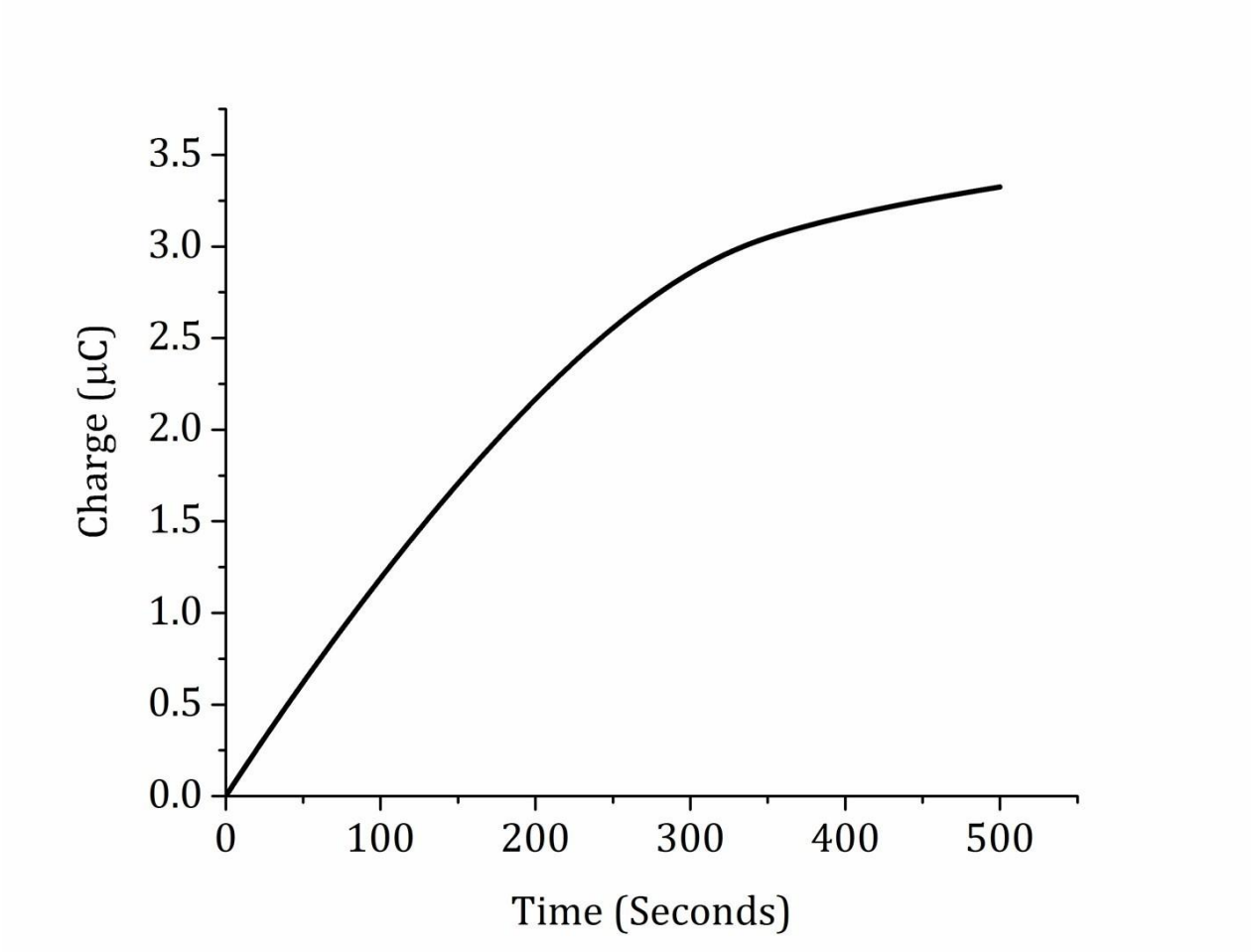

Figure C.9. Deposition of a PNS film onto the substrate UME by a chronoamperometric step at -2 V from a solution of 33 mM PNS in 0.1 M $TBAPF_6$ supporting electrolyte for 400 seconds. The total charge passed was 3.35 μC.

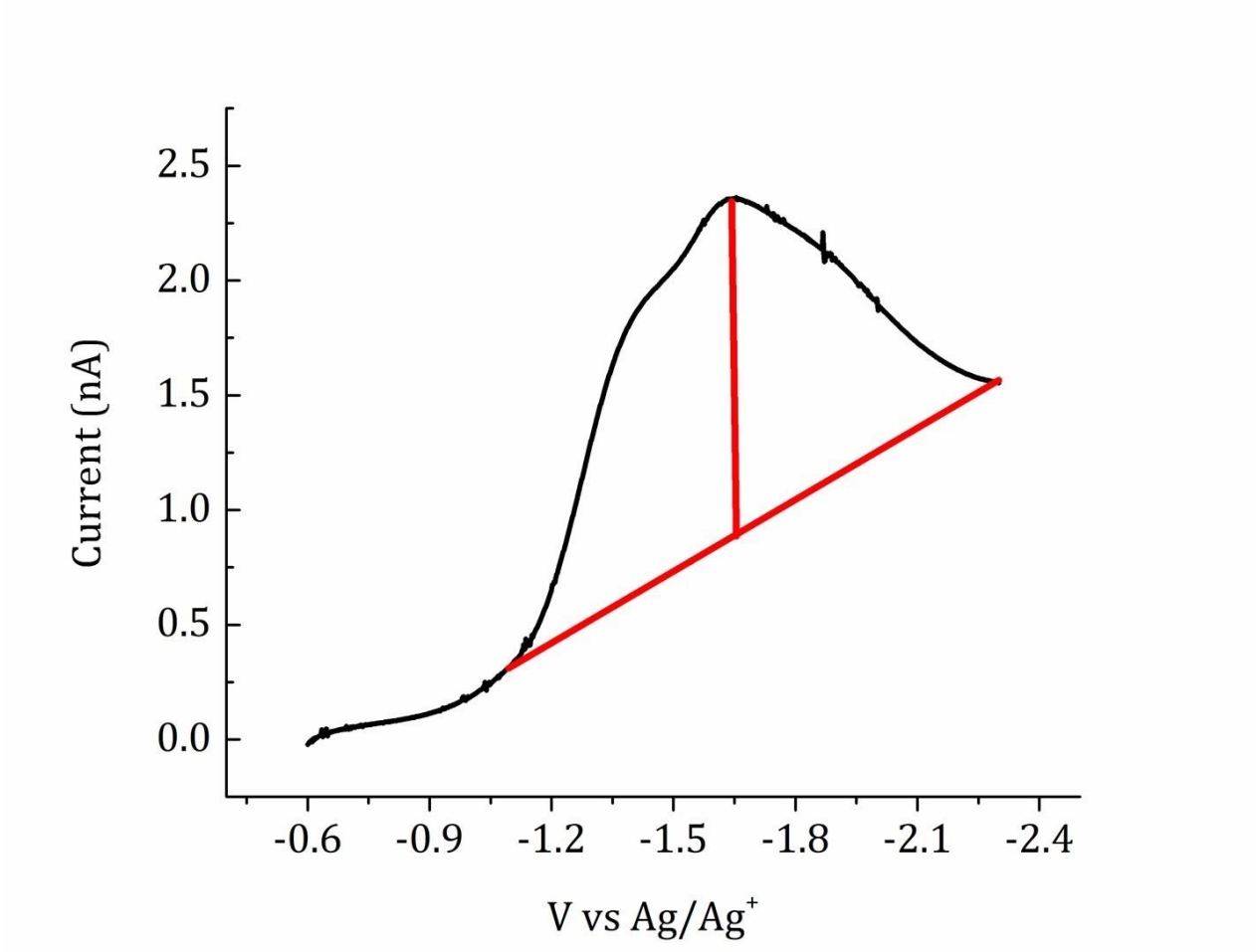

Figure C.10. Voltammetry with the PNS filmed UME in a solution only containing 0.1 M $TBAPF_6$ in DMF at 10 mV/s. The voltammogram was integrated in the region shown by the red lines to determine the amount of accessible nitro groups on the UME surface. The integrated charge was 45.7 nC, which equates to 2.85×10^{11} accessible nitro groups.

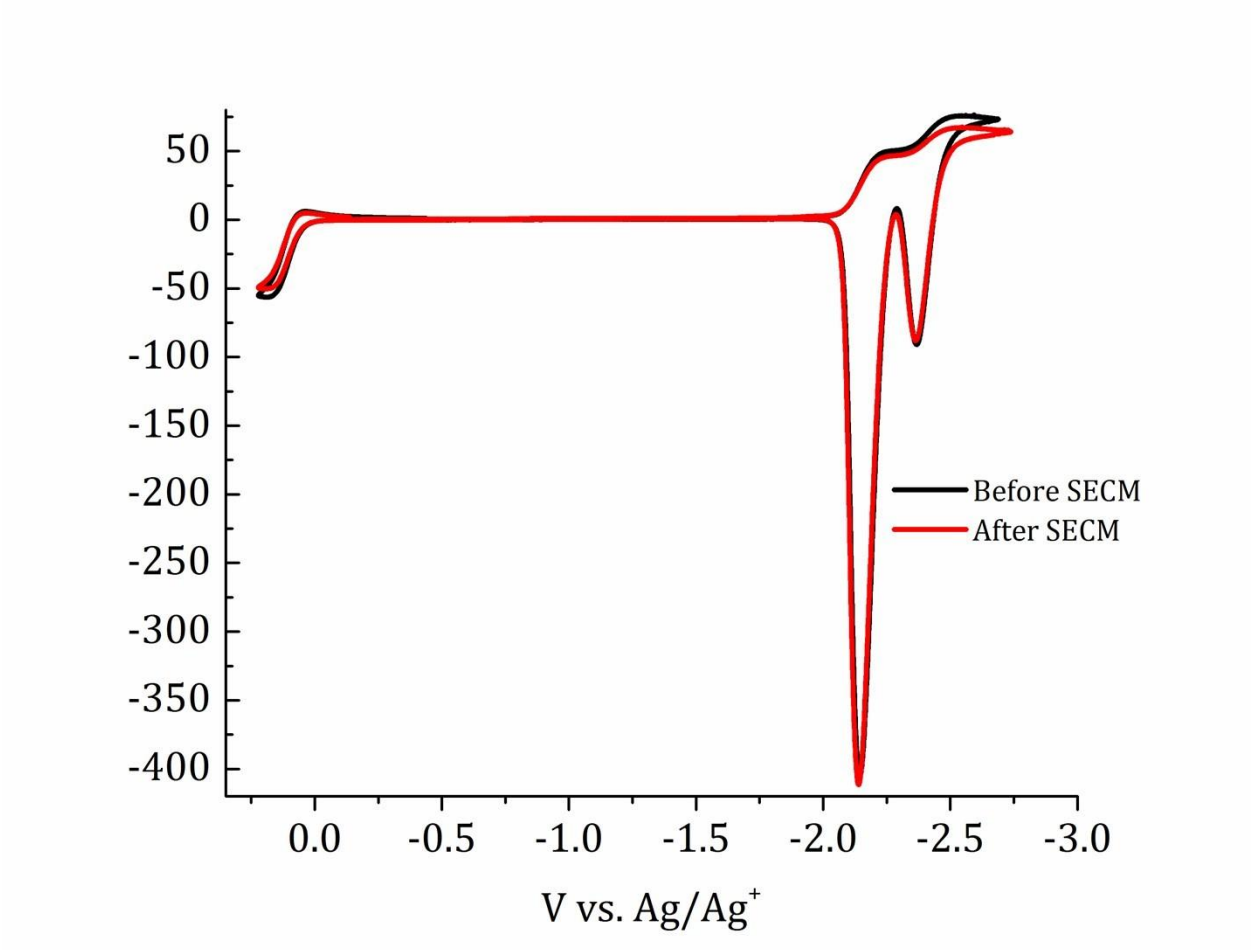

Figure C.11. Voltammetry with the Hg capped tip UME before and after the SECM experiments. The electrode was scanned at 0.5 V/s in the presence of 10 mM TMPD, 17 mM $LiPF_6$, 17 mM KBF_4, and 0.1 M $TBAPF_6$. The current levels for the oxidation of TMPD and the stripping of K^+ and Li^+ are nearly identical before and SECM experiments, demonstrating that the size of the Hg droplet electrode had not been perturbed in any significant amount.

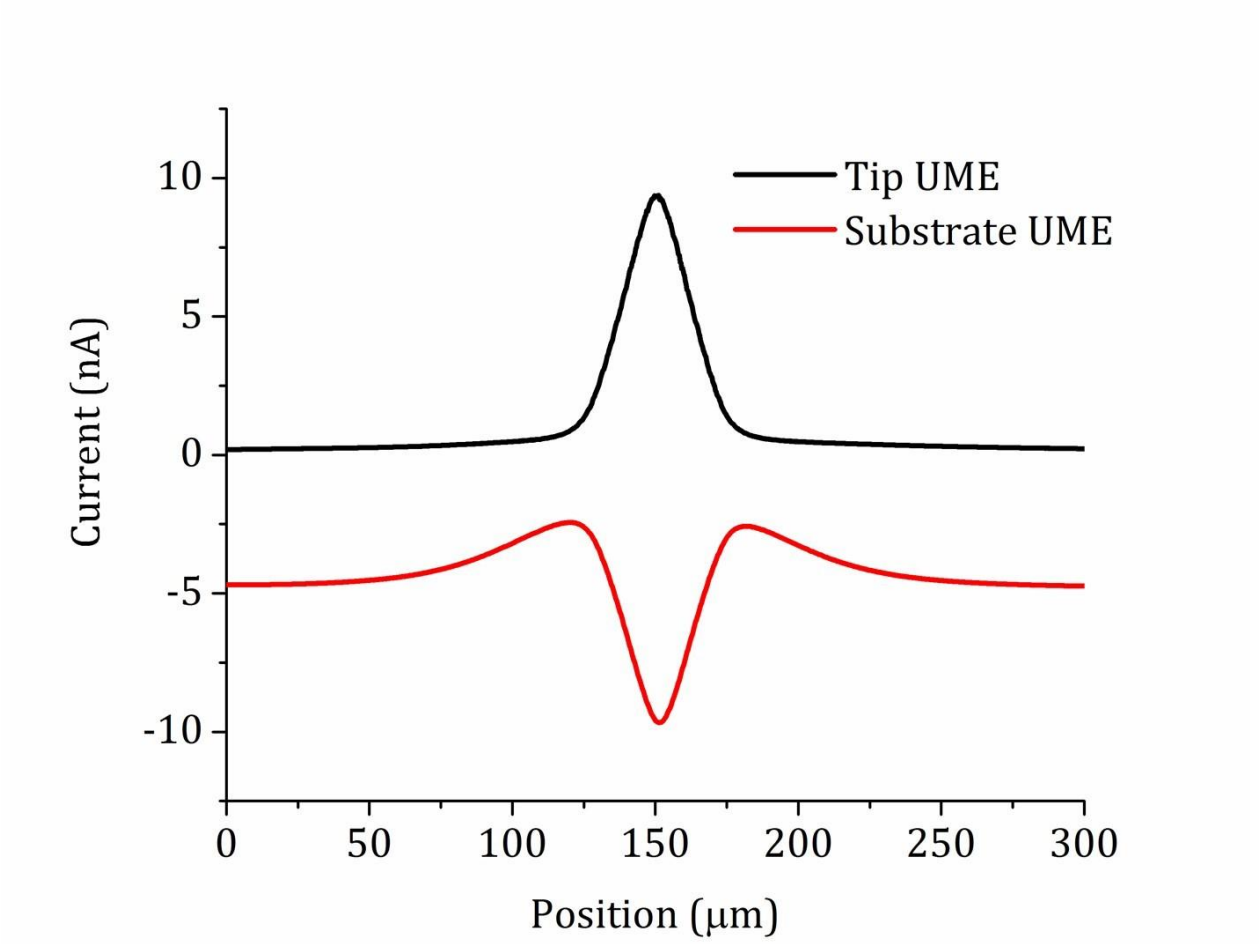

Figure C.12. The coaligning of the two UMEs used in the surface interrogation SECM experiments using the collection mode of SECM. The substrate UME was generating $TMPD^{+}$ and the tip UME was collecting it and reducing the species back to neutral TMPD. The solution contained 1 mM TMPD in 0.1 M $TBAPF_6$. The large spike in currents for both UMEs at approximately the 150 μm position is from the collection and subsequent regeneration of the redox mediator between the tips when aligned.

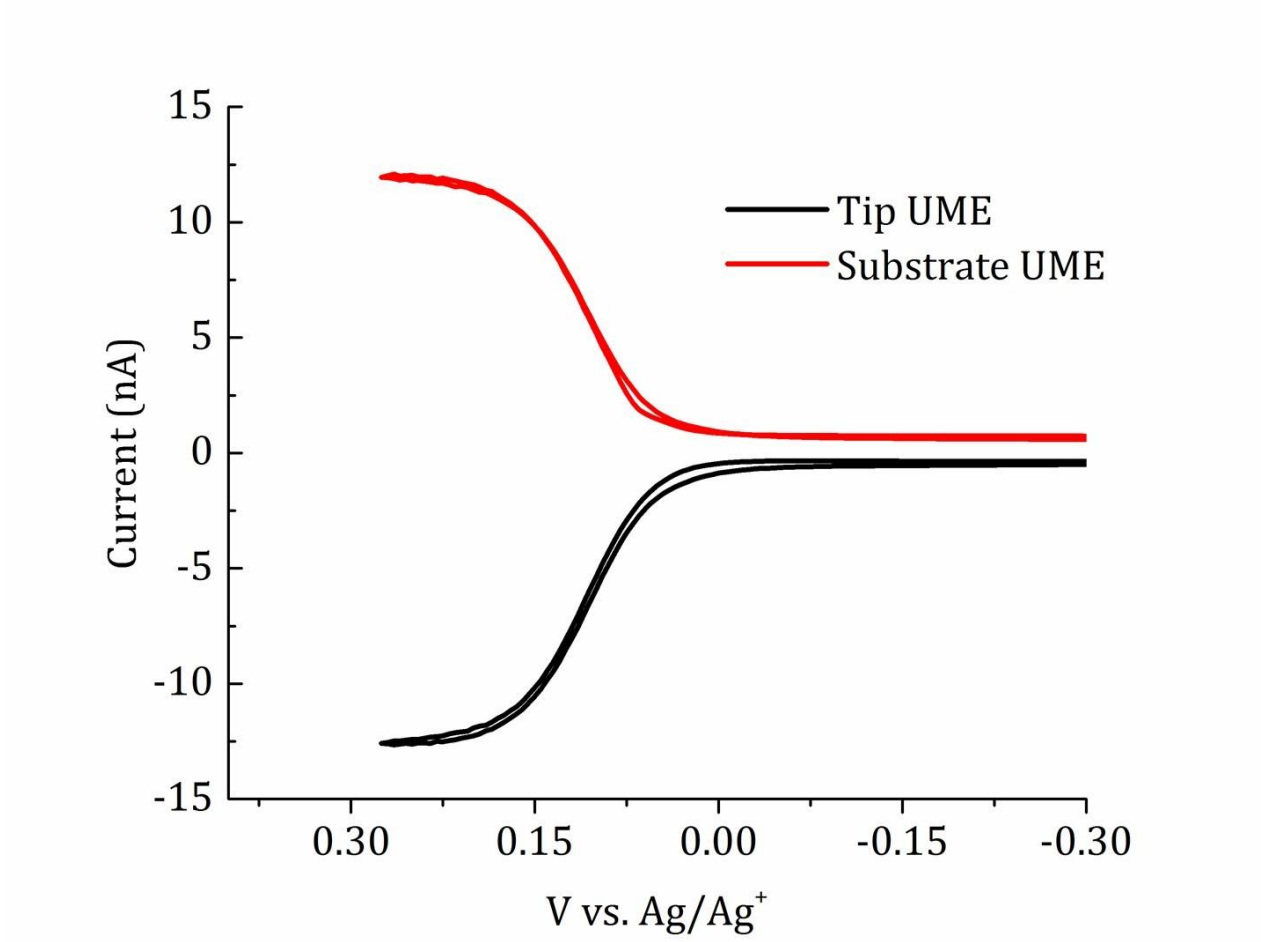

Figure C.13. Collection voltammograms between the tip UME and a Pt substrate UME. The tip UME generates $TMPD^{+}$ via voltammetry and the substrate UME is poised at -1.9 V during this process. The collection efficiency between the tips for the redox mediator is approximated as 100 %, due to the same order of magnitude of current being measured between both tips. This high collection efficiency of the species between the SECM tips is only possible when the tips are properly aligned and placed very near each other (< 6 µm for the size of the UMEs used here).

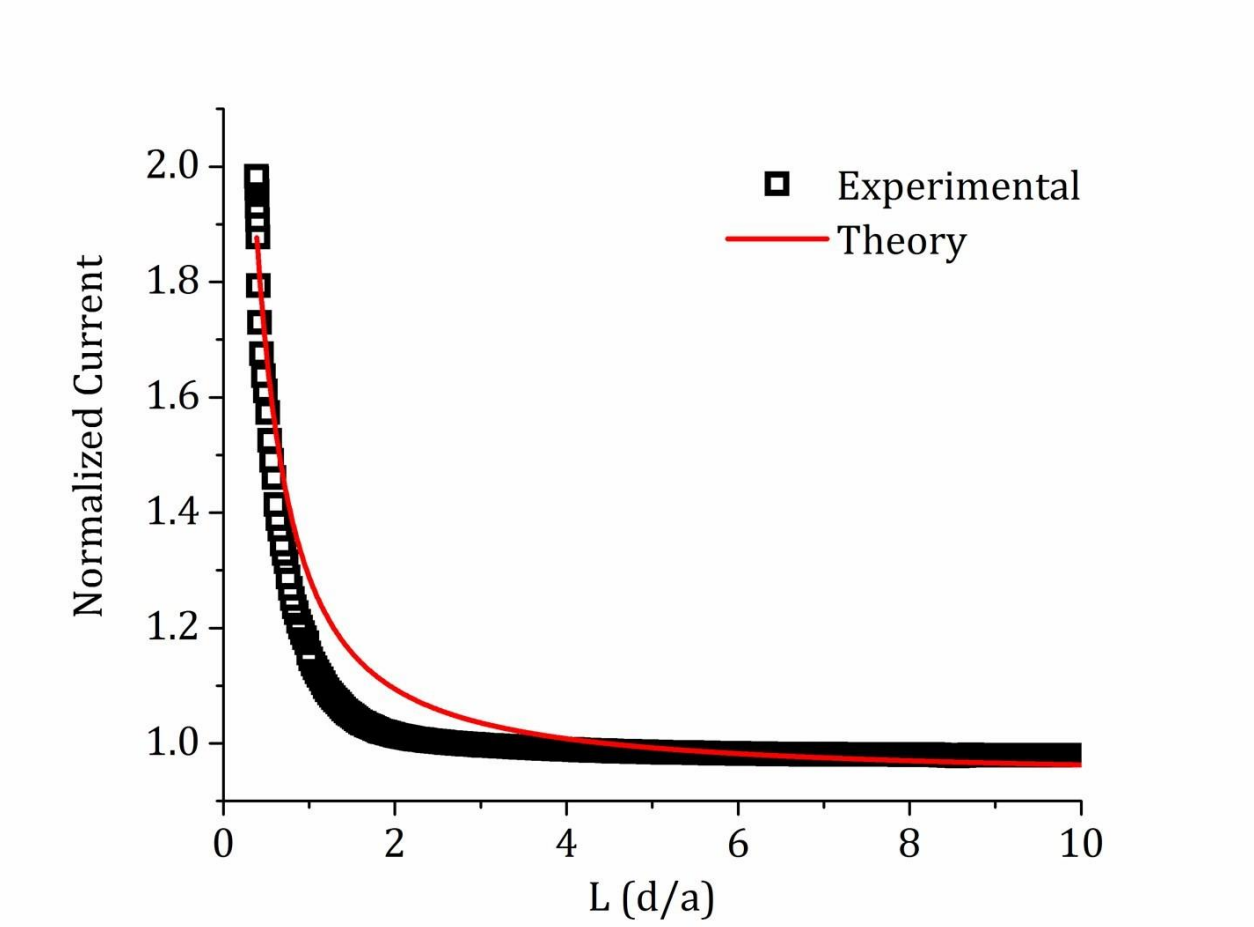

Figure C.14. Approach curve in the feedback mode of SECM of a Pt UME to a Pt UME substrate after alignment of the tips. The tip UME is generating $TMPD^{+}$ and the substrate is reducing this species back to neutral TMPD. The distance between the tips at the approached position was estimated by fitting the approach curve to theory for SECM feedback reported by Cornut and Lefrou. The fitting program used an *Rg* of 2 for the tip UME. Fitting of the approach curve finds that the tips were separated by less than 6 microns at the approached position. The solution contained 1 mM TMPD with 0.1 M $TBAPF_6$.

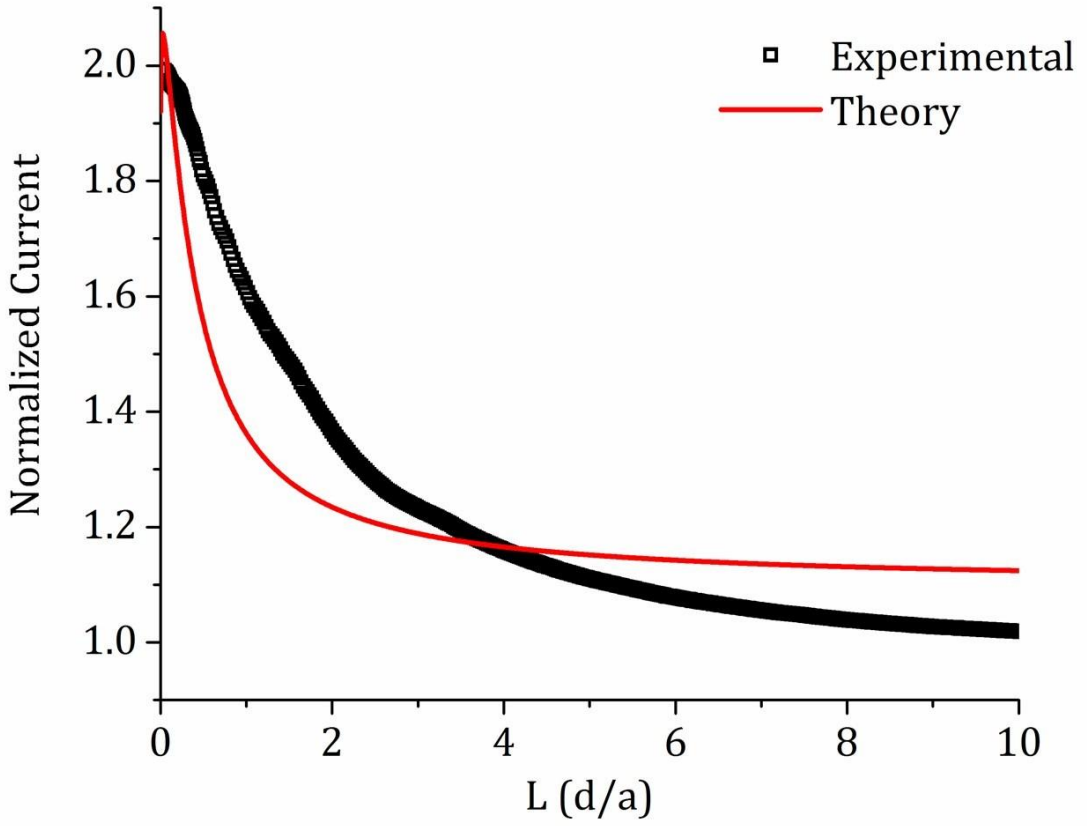

Figure C.15. Approach curve in the feedback mode of SECM of a Pt UME to a PNS filmed Pt UME substrate after alignment of the tips. The tip UME is generating $TMPD^{+}$ and the substrate is reducing this species back to neutral TMPD. The distance between the tips at the approached position was estimated by fitting the approach curve to theory for SECM feedback reported by Cornut and Lefrou. The fitting program used an *Rg* of 2 for the tip UME. Fitting of the approach curve finds that the tips were separated by less than 6 microns at the approached position. The solution contained 1 mM TMPD with 0.1 M $TBAPF_6$.

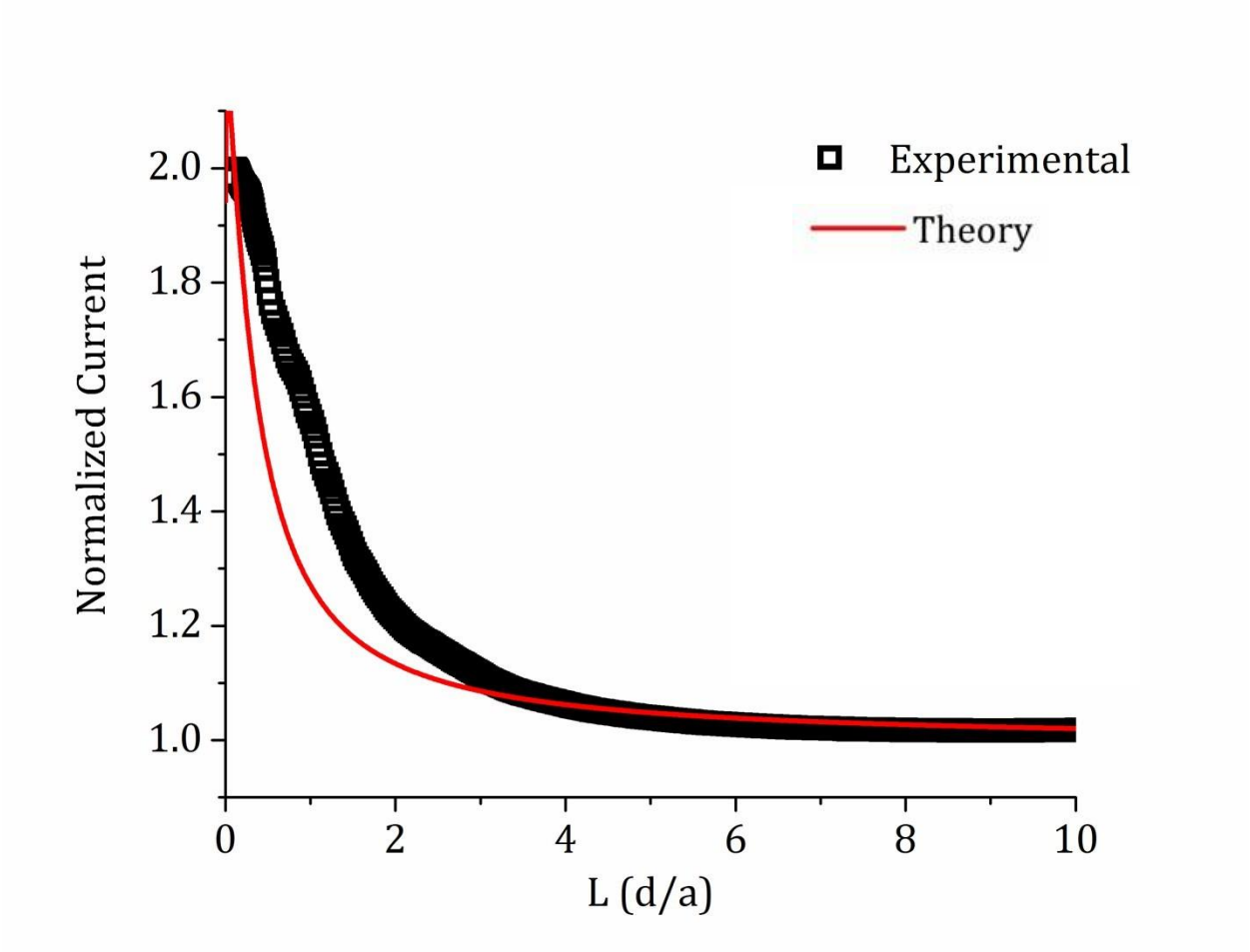

Figure C.16. Approach curve in the feedback mode of SECM of a Pt UME to a PNS filmed Pt UME substrate after alignment of the tips. The tip UME is generating $TMPD^+$ and the substrate is reducing this species back to neutral TMPD. The distance between the tips at the approached position was estimated by fitting the approach curve to theory for SECM feedback reported by Cornut and Lefrou. The fitting program used an ***Rg*** of 2 for the tip UME. Fitting of the approach curve finds that the tips were separated by less than 6 microns at the approached position. The solution contained 1 mM TMPD with 0.1 M $TBAPF_6$ and 17 mM $LiPF_6$.

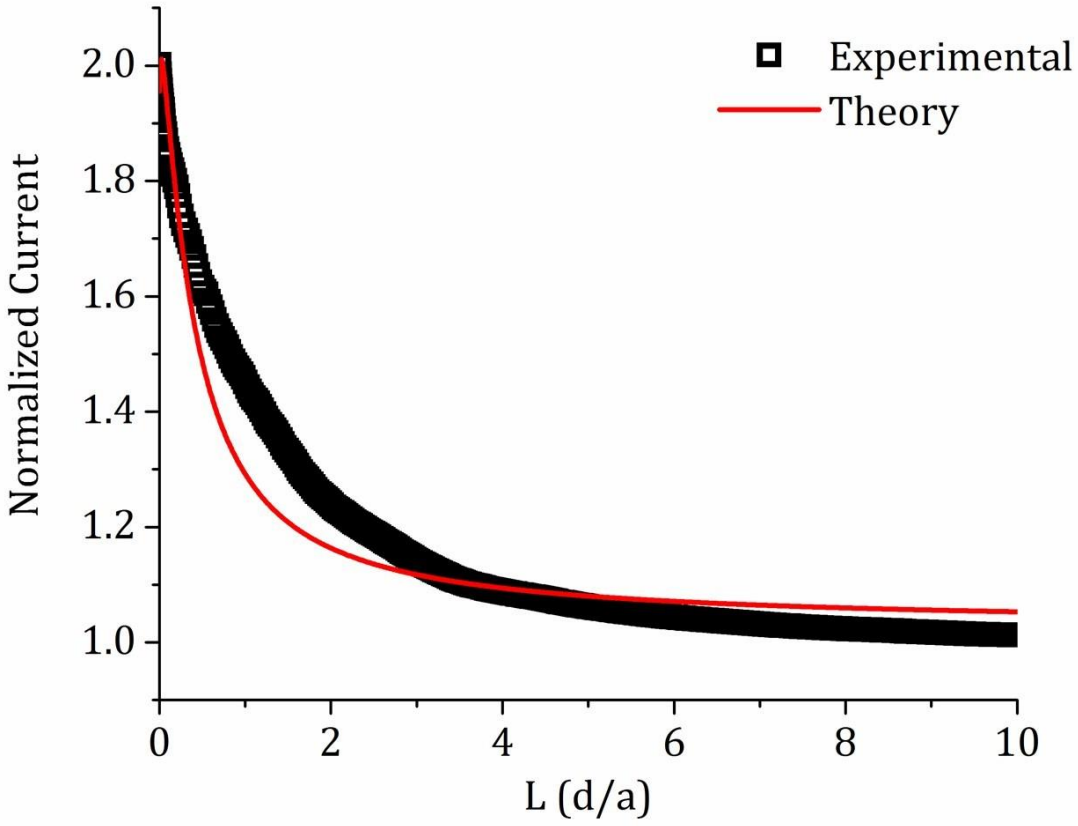

Figure C.17. Approach curve in the feedback mode of SECM of a Pt UME to a PNS filmed Pt UME substrate after alignment of the tips. The tip UME is generating $TMPD^+$ and the substrate is reducing this species back to neutral TMPD. The distance between the tips at the approached position was estimated by fitting the approach curve to theory for SECM feedback reported by Cornut and Lefrou. The fitting program used an *Rg* of 2 for the tip UME. Fitting of the approach curve finds that the tips were separated by less than 6 microns at the approached position. The solution contained 1 mM TMPD with 0.1 M $TBAPF_6$ and 17 mM KBF_4.

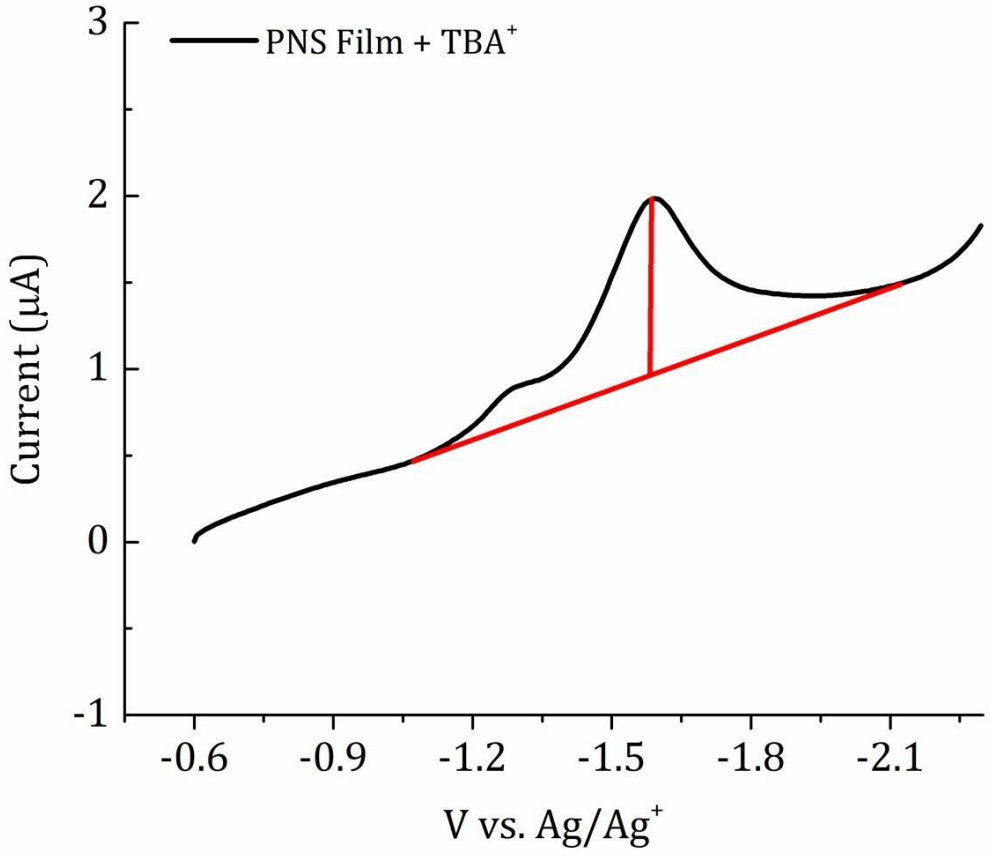

Figure C.18. The PNS film voltammogram at 100 mV/s in the presence of 0.1 M TBA^+, shown in Figure 4.3B of Chapter 4, is integrated to find the total amount of charge corresponding to the reduction of PNS. The voltammogram is integrated in the region shown by the red lines. The calculation of the film properties was as follows. The integrated charge was found to be 1.56×10^{-6} C. The surface coverage would be 37.6 μC/cm^2. Dividing the integrated charge by Faraday's constant (96,485 C/mol) finds that there were 1.62×10^{-11} mol of PNS on the electrode surface. Multiplying the amount of PNS in mol by the molecular weight of the polymer repeat unit (149 g/mol) finds that there was 2.40×10^{-9} g of PNS on the surface. Dividing the amount of PNS in grams by the density of the precursor polymer (1.05 g/mol) shows that there was a volume of PNS on the surface of 2.29×10^{-9} cm^3. Dividing the PNS volume by the macrodisk electrode area (0.0415 cm^2) finds that the polymer film was 0.6 nm thick.

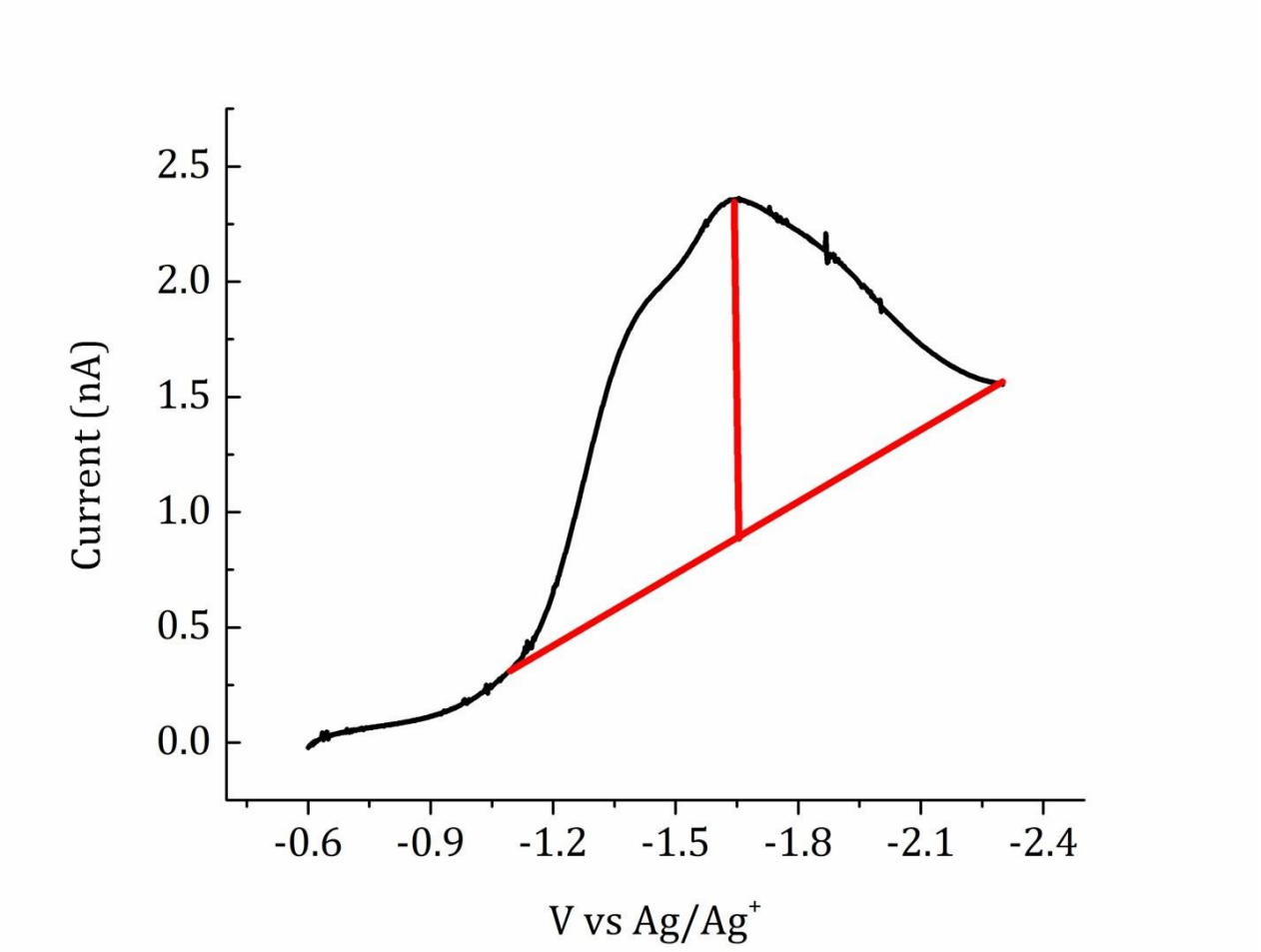

Figure C.19. Voltammetry with the PNS filmed UME in a solution only containing 0.1 M $TBAPF_6$ in DMF at 10 mV/s. The voltammogram was integrated in the region shown by the red lines to determine the amount of accessible nitro groups on the UME surface and the polymer film thickness. The integrated charge was found to be 45.7 nC. The surface coverage would be 9,300 µC/cm^2. Dividing the integrated charge by Faraday's constant (96,485 C/mol) finds that there were 4.74 x 10^{-13} mol of PNS on the electrode surface. Multiplying the amount of PNS in mol by the molecular weight of the polymer repeat unit (149 g/mol) finds that there was 7.06 x 10^{-11} g of PNS on the surface. Dividing the amount of PNS in grams by the density of the precursor polymer (1.05 g/mol) shows that there was a volume of PNS on the surface of 6.72 x 10^{-11} cm^3. Dividing the PNS volume by the UME electrode area (4.91 x 10^{-6} cm^2) finds that the polymer film was 136 nm thick.

Integrating the interrogation currents, shown in Figure 4.7A of Chapter 4, from the surface interrogation SECM experiments in the TBA^+, $TBA^+ + K^+$, and $TBA^+ + Li^+$, containing electrolytes from 0 to 100 seconds finds that there was a surface coverage of 17 ± 5 nmol/cm^2. This value in terms of charge per area would be equal to 1,700 µC/cm^2. Taking this value and multiplying by the molecular weight of the polymer repeat unit (149 g/mol), it was found there was a mass per area of the electrode ratio of 2.53 x 10^{-6} g/cm^2. Dividing this value by the density of the precursor polymer (1.05 g/cm^3) finds that the film thickness was 24 ± 7 nm.

Table C.3 Summary of Polymer Film Calculated Properties

Experiment	**Film Charge/Area (µC/cm²)**	**Approximate Film Thickness (nm)**
Macrodisk Film	37.6	0.6
UME Film Used in Hg Stripping SECM	9,300	136
UME Film Used in SI-SECM	1,700	24

Appendix D: Supporting Information File for Chapter 5

Notes and Acknowledgements

This appendix contains supplementary data for Chapter 5 for work that is in preparation for a manuscript for publication with authors Burgess, M.; Hernández-Burgos, K.; Schuh, J.K.; Davila, J.; Montoto, E.C.; Ewoldt, R.H.; Moore, J.S.; and Rodríguez-López, J. M.B. and K.H.B. contributed equally to this work. M.B. performed all DLS and ellipsometry experiments, helped do voltammetry measurements, helped do data analysis, helped write the manuscript, made figures, and helped make samples. The authors acknowledge the Joint Center for Energy Storage Research (JCESR), an Energy Innovation Hub funded by the Department of Energy, Office of Science, Basic Energy Sciences for funding. M.B. acknowledges additional support from the National Science Foundation Graduate Research Fellowship Program under Grant No. DGE-114425. Materials characterization was carried out in part in the Frederick Seitz Materials Research Laboratory Central Research Facilities at the University of Illinois at Urbana-Champaign. K.H.B. gratefully acknowledges the Beckman Institute Postdoctoral Fellowship at the University of Illinois at Urbana-Champaign, with funding provided by the Arnold and Mabel Beckman Foundation. J.R.L acknowledges additional support from a Sloan Research Fellowship.

General Information

Unless otherwise stated, all starting materials and reagents were purchased from Sigma-Aldrich, Fisher Scientific or Matrix Scientific and used without further purification. Poly(vinylbenzyl chloride) (PVBC), >90% 4-substituted, was purchased from Polymer Source, Inc. (M_n: 82kDa, PDI: 1.6). All glassware was oven-dried prior to use. Dimethyl formamide

(DMF) and tetrahedrofuran (THF) was obtained from a Solvent Delivery System (SDS) equipped with activated neutral alumina columns under argon.

Synthesis of Redox Active Polymers

Viologen redox active polymer and Ammonium ferrocenylmethyl redox active polymer (**PAF**) were synthesized using modified reported protocols.[1, 2]

Ammonium ferrocenylmethyl redox active polymer (**PAF**) Dry DMF (25 mL) was added to a flask containing PVBC (1.00 g, 6.6 mmol) and (dimethylaminomethyl)ferrocene (6.4 g, 26.2 mmol) under nitrogen. Reaction mixture was stirred at RT for 24 h. The resulting product was then precipitated into ether twice and dried under vacuum for 12 h. Product was redissolved into minimal DMF and concentrated solution of ammonium hexafluoro phosphate (5.5 g) solution prepared in water was added. Minimal acetonitrile was added to the mixture and the resultant solution was stirred at room temperature for 16 h. The collected polymer was precipitated from acetonitrile into H_2O. Then the polymer was reprecipitated once into methanol and twice into diethyl ether. Polymer was dried under high vacuum for 24 h.

Electrochemistry and Material Analysis

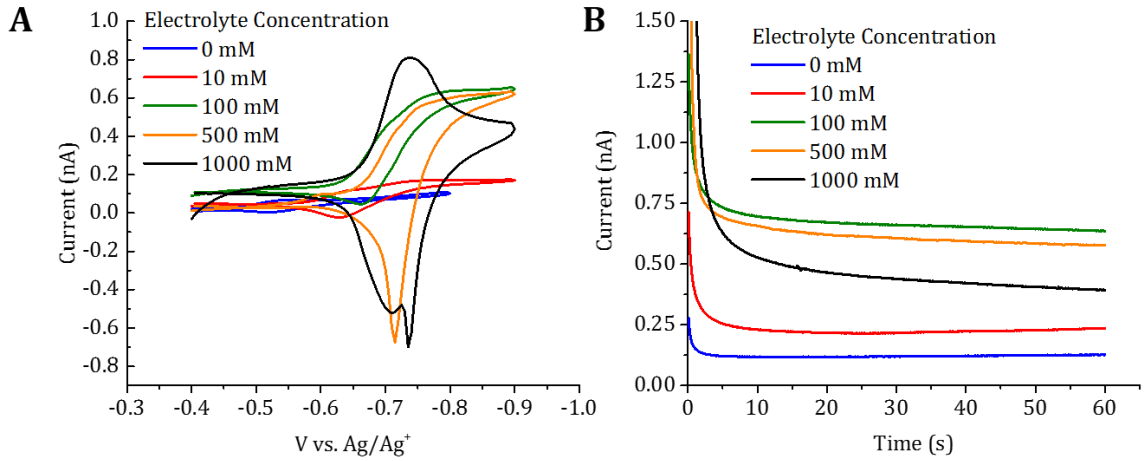

Figure D.1. (A) Cyclic voltammetry at 20 mV/s at a UME with 0.5 mM **VioRAP** in solution as a function of $TBAPF_6$ electrolyte concentration. (B) Current transients following a potential step at the UME for the first reduction of the **VioRAP** in a series of electrolyte concentrations.

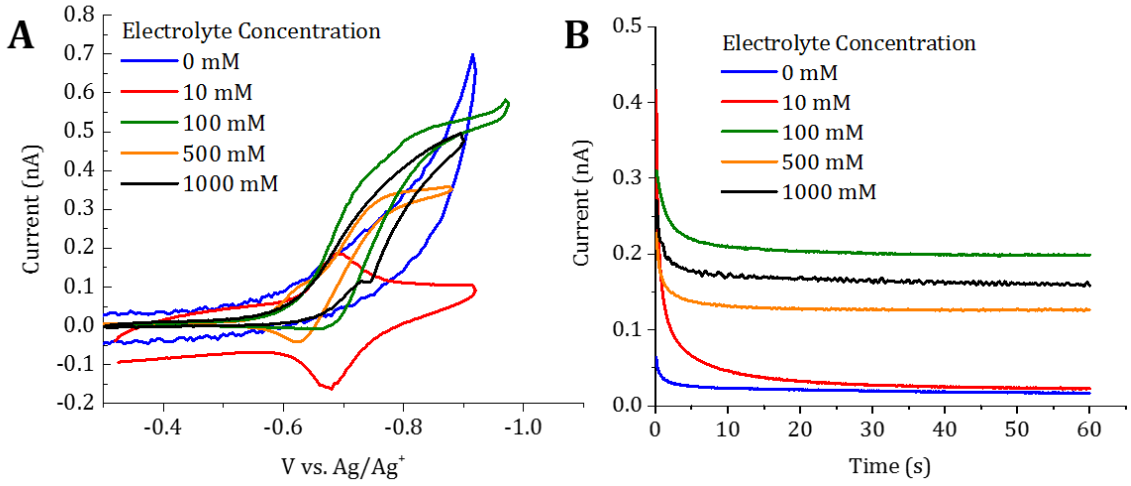

Figure D.2. (A) Cyclic voltammetry at 20 mV/s at a UME with 0.5 mM **VioRAP** in solution as a function of $LiBF_4$ electrolyte concentration. (B) Current transients following a potential step at the UME for the first reduction of the **VioRAP** in a series of electrolyte concentrations.

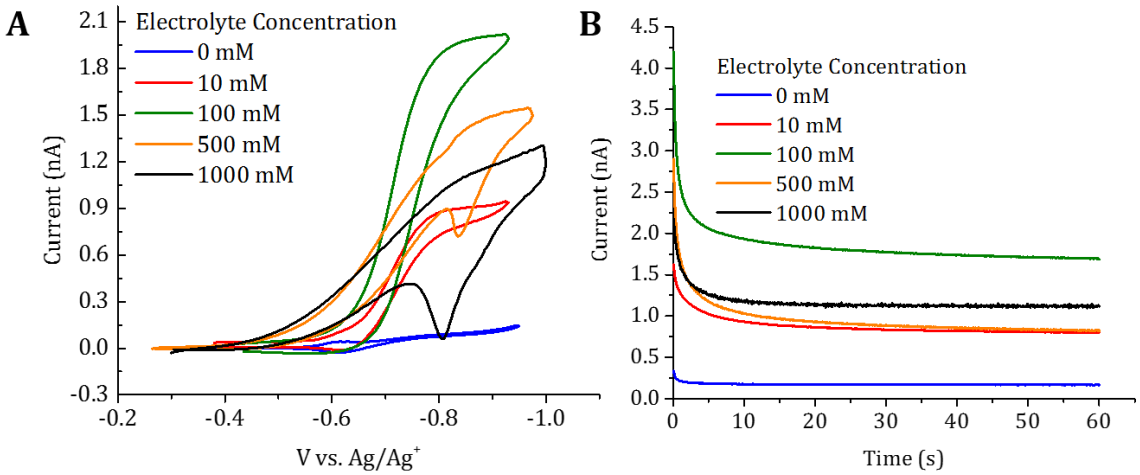

Figure D.3. (A) Cyclic voltammetry at 20 mV/s at a UME with 5 mM **VioRAP** in solution as a function of $TBAPF_6$ electrolyte concentration. (B) Current transients following a potential step at the UME for the first reduction of the **VioRAP** in a series of electrolyte concentrations.

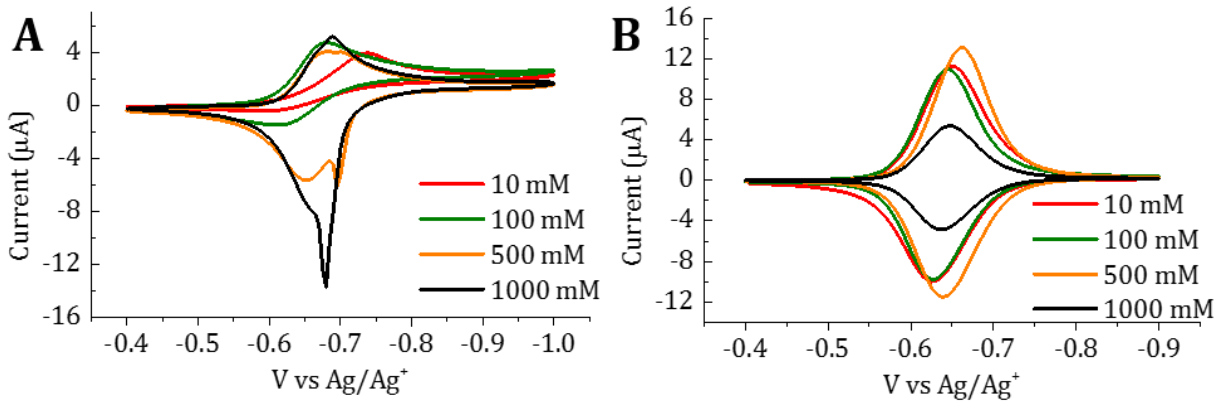

Figure D.4. (A) Cyclic Voltammograms at 10 mV/s for **VioRAP** (5 mM) as a function of electrolyte concentration ($TBAPF_6$). (B) Cyclic Voltammograms at 10 mV/s for **VioRAP** films deposited at different electrolyte concentration (as indicated in the legend), but measured at 100 mM. Film was deposited by cycling 10 times accessing the second redox process.

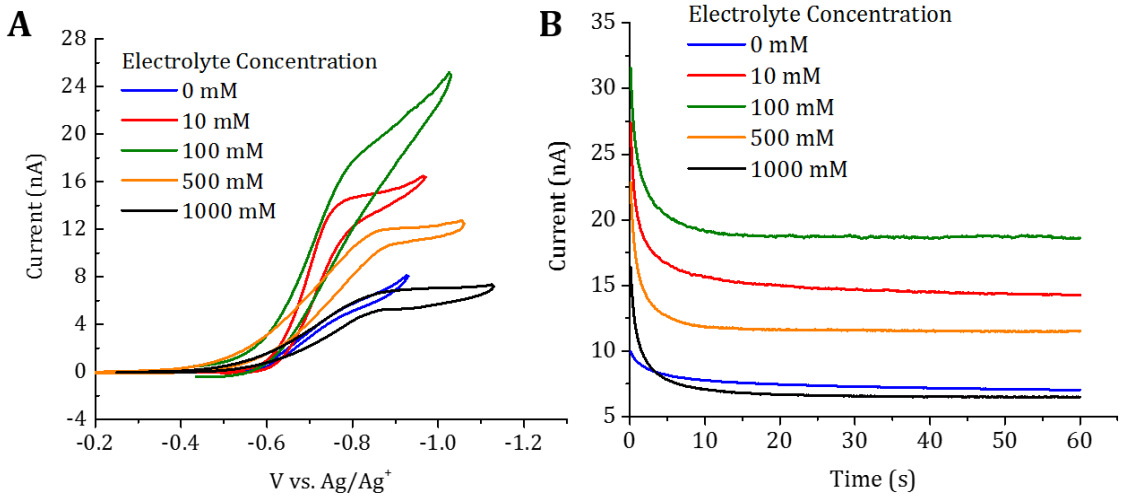

Figure D.5. (A) Cyclic voltammetry at 20 mV/s at a UME with 50 mM **VioRAP** in solution as a function of $TBAPF_6$ electrolyte concentration. (B) Current transients following a potential step at the UME for the first reduction of the **VioRAP** in a series of electrolyte concentrations.

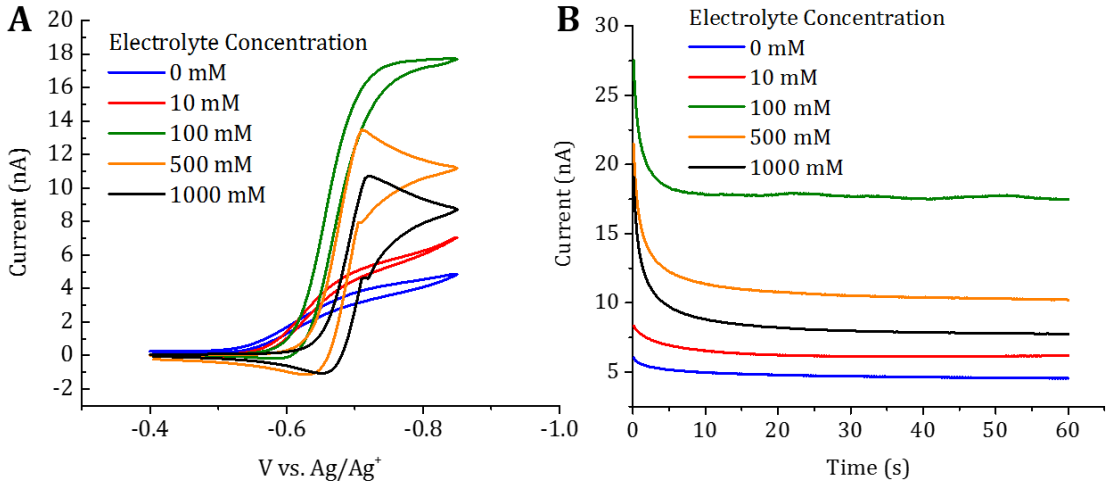

Figure D.6. (A) Cyclic voltammetry at 20 mV/s at a UME with 50 mM **VioRAP** in solution as a function of $LiBF_4$ electrolyte concentration. (B) Current transients following a potential step at the UME for the first reduction of the **VioRAP** in a series of electrolyte concentrations.

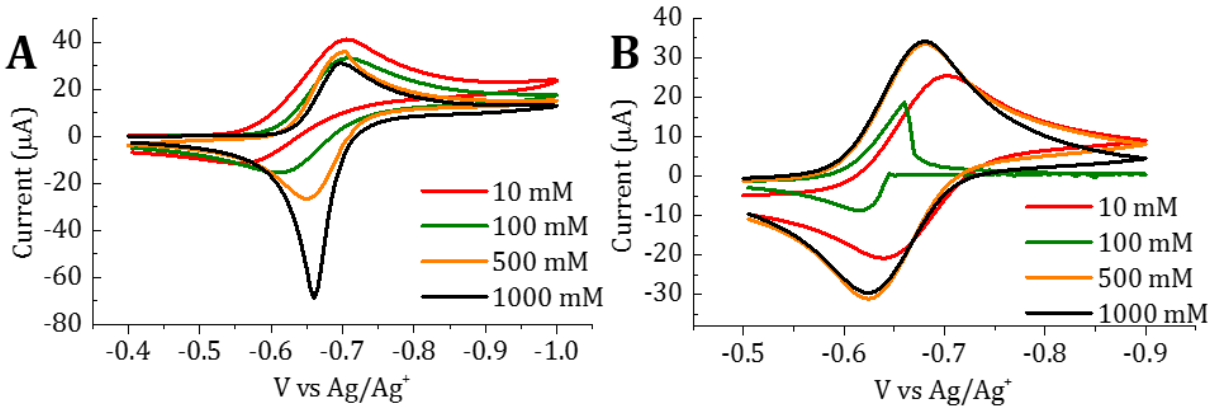

Figure D.7. (A) Cyclic Voltammograms at 10 mV/s for **VioRAP** (50 mM) as a function of electrolyte concentration ($TBAPF_6$). (B) Cyclic Voltammograms at 10 mV/s for **VioRAP** films deposited at different electrolyte concentration (as indicated in the legend), but measured at 100 mM. Film was deposited by cycling 10 times accessing the second redox process.

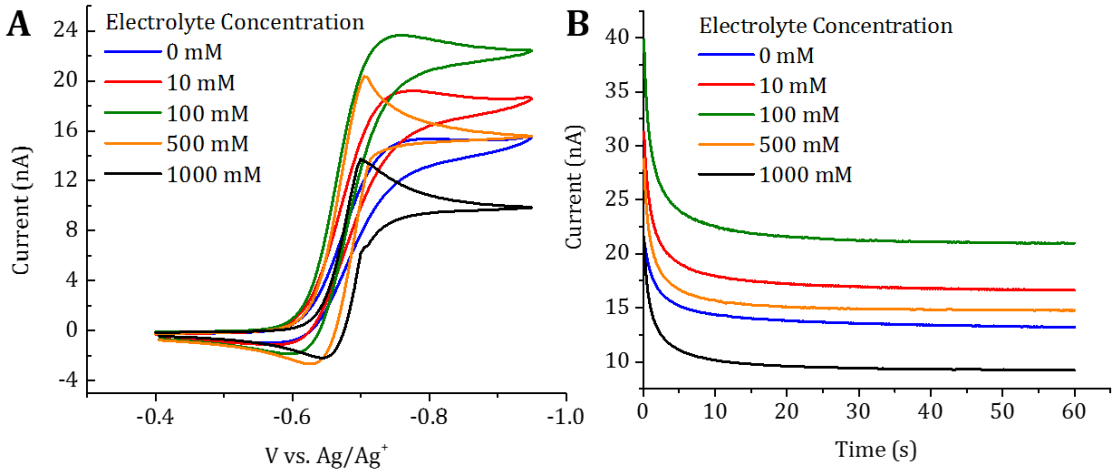

Figure D.8. (A) Cyclic voltammetry at 20 mV/s at a UME with 100 mM **VioRAP** in solution as a function of $TBAPF_6$ electrolyte concentration. (B) Current transients following a potential step at the UME for the first reduction of the **VioRAP** in a series of electrolyte concentrations.

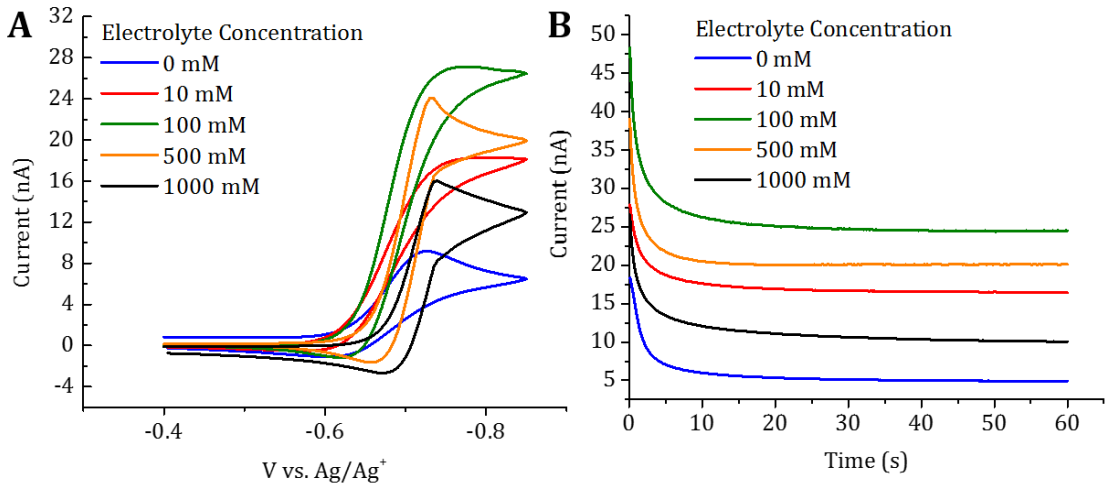

Figure D.9. (A) Cyclic voltammetry at 20 mV/s at a UME with 100 mM **VioRAP** in solution as a function of $LiBF_4$ electrolyte concentration. (B) Current transients following a potential step at the UME for the first reduction of the **VioRAP** in a series of electrolyte concentrations.

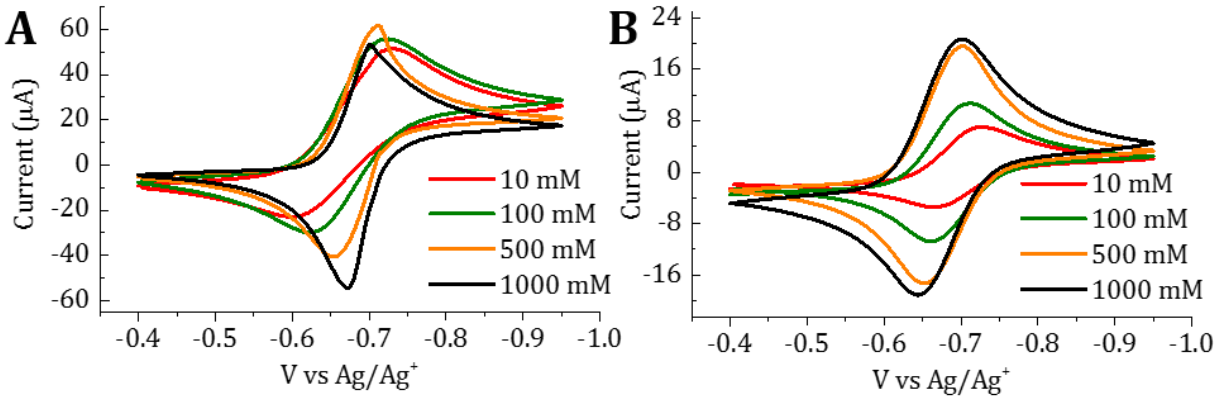

Figure D.10. (A) Cyclic Voltammograms at 10 mV/s for **VioRAP** (100 mM) as a function of electrolyte concentration ($TBAPF_6$). (B) Cyclic Voltammograms at 10 mV/s for **VioRAP** films deposited at different electrolyte concentration (as indicated in the legend), but measured at 100 mM. Film was deposited by cycling 10 times accessing the second redox process.

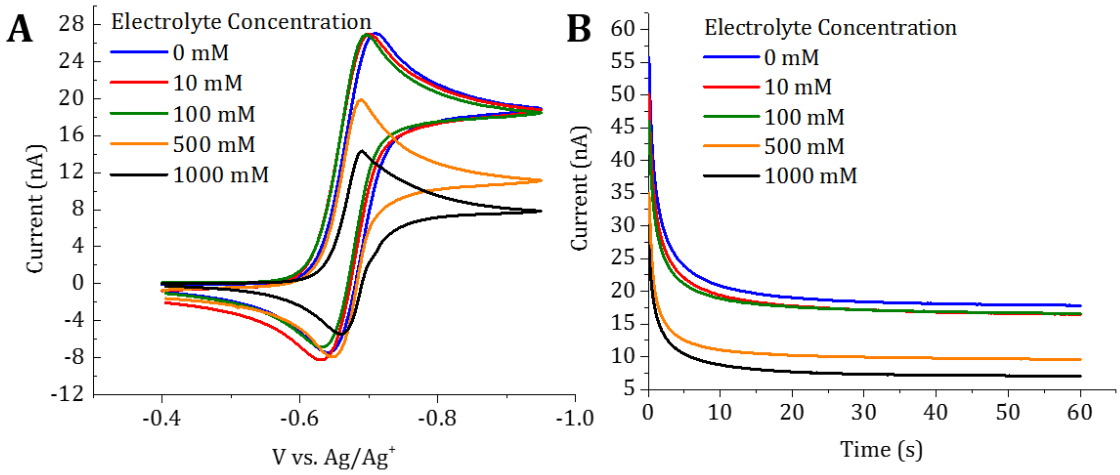

Figure D.11. (A) Cyclic voltammetry at 20 mV/s at a UME with 500 mM **VioRAP** in solution as a function of $TBAPF_6$ electrolyte concentration. (B) Current transients following a potential step at the UME for the first reduction of the **VioRAP** in a series of electrolyte concentrations.

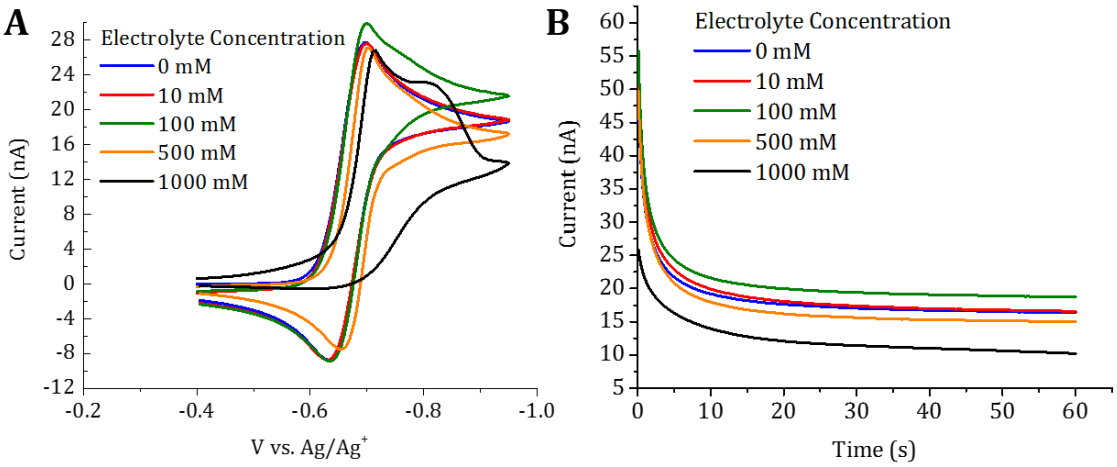

Figure D.12. (A) Cyclic voltammetry at 20 mV/s at a UME with 500 mM **VioRAP** in solution as a function of $LiBF_4$ electrolyte concentration. (B) Current transients following a potential step at the UME for the first reduction of the **VioRAP** in a series of electrolyte concentrations.

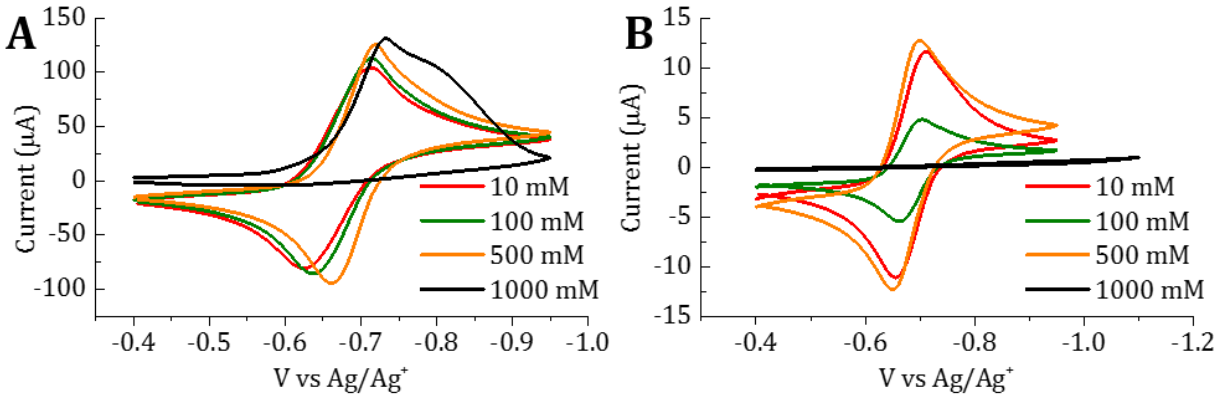

Figure D.13. (A) Cyclic Voltammograms at 10 mV/s for **VioRAP** (500 mM) as a function of electrolyte concentration ($TBAPF_6$). (B) Cyclic Voltammograms at 10 mV/s for **VioRAP** films deposited at different electrolyte concentration (as indicated in the legend), but measured at 100 mM. Film was deposited by cycling 10 times accessing the second redox process.

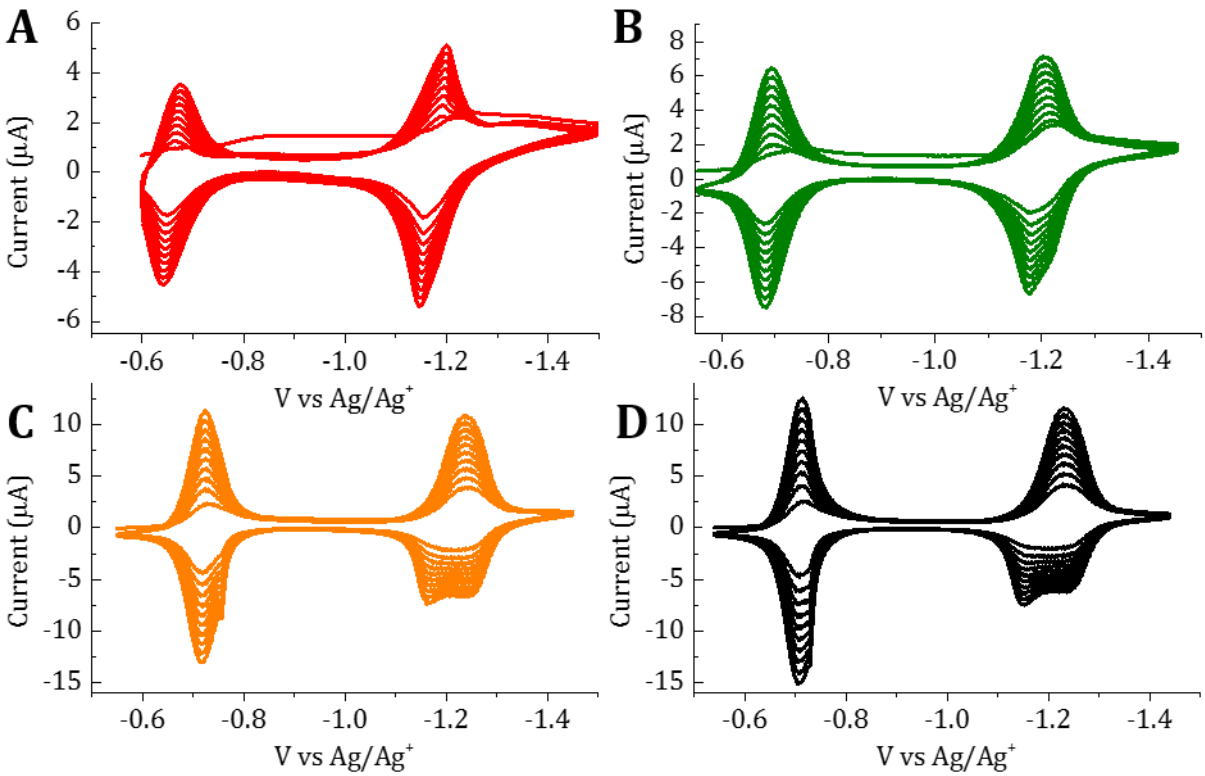

Figure D.14. Representative example for **VioRAP** (0.5 mM) deposition at low polymer concentration as a function of electrolyte concentration (A) 10 mM, (B) 100 mM, (C) 500 mM and (D) 1000 mM ($TBAPF_6$).

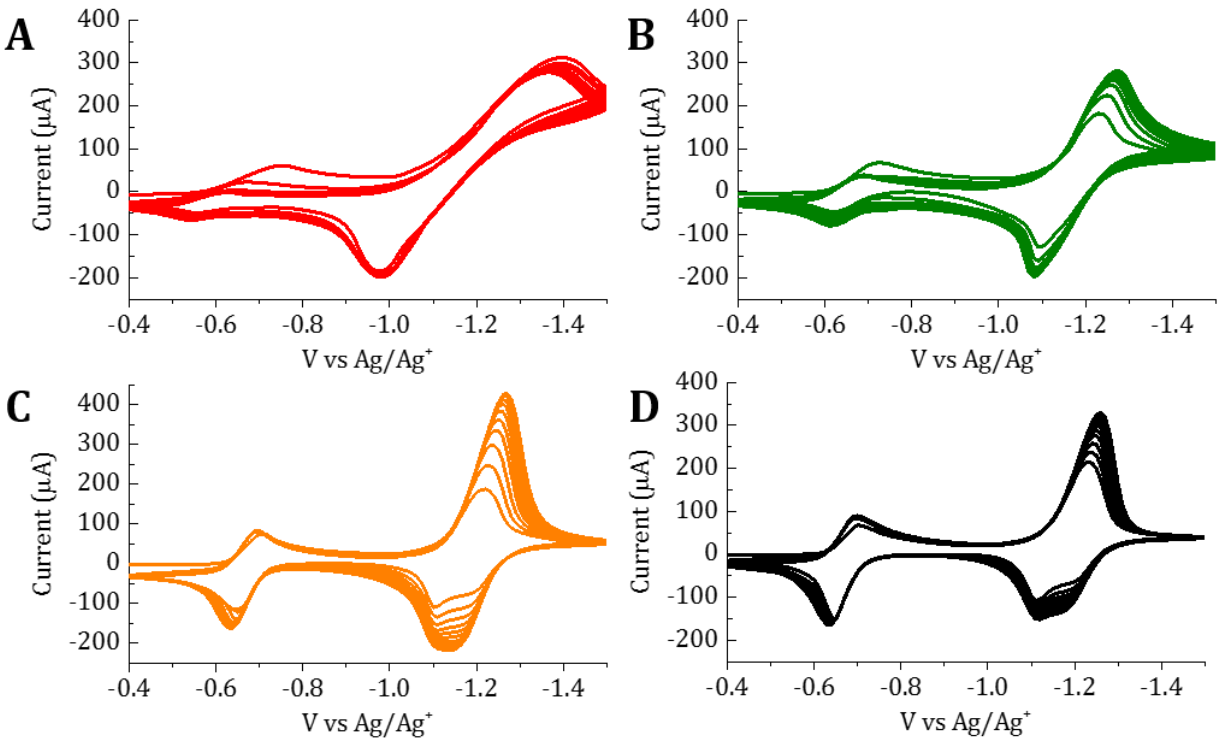

Figure D.15. Representative example for **VioRAP** (50 mM) deposition at high polymer concentration as a function of electrolyte concentration (A) 10 mM, (B) 100 mM, (C) 500 mM and (D) 1000 mM ($TBAPF_6$).

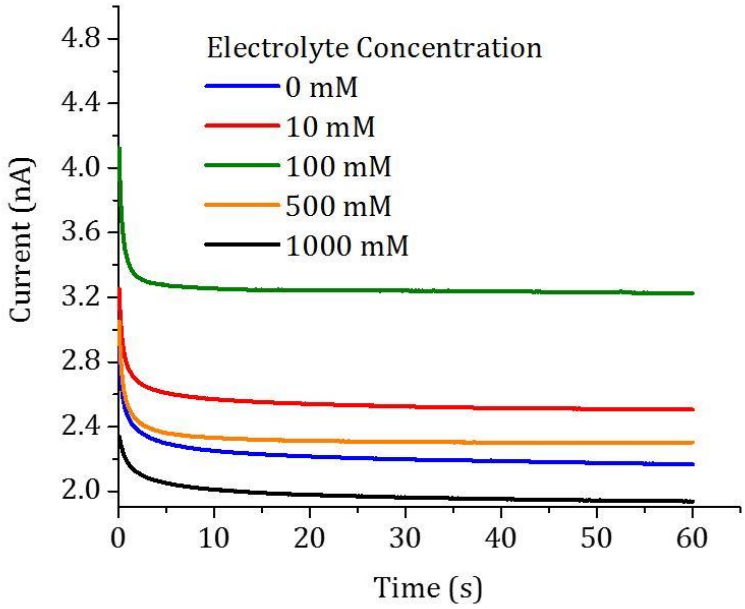

Figure D.16. Current transients following a potential step at the UME for the reduction of **Viologen** monomer at 0.5 mM concentration in a series of electrolyte concentrations.

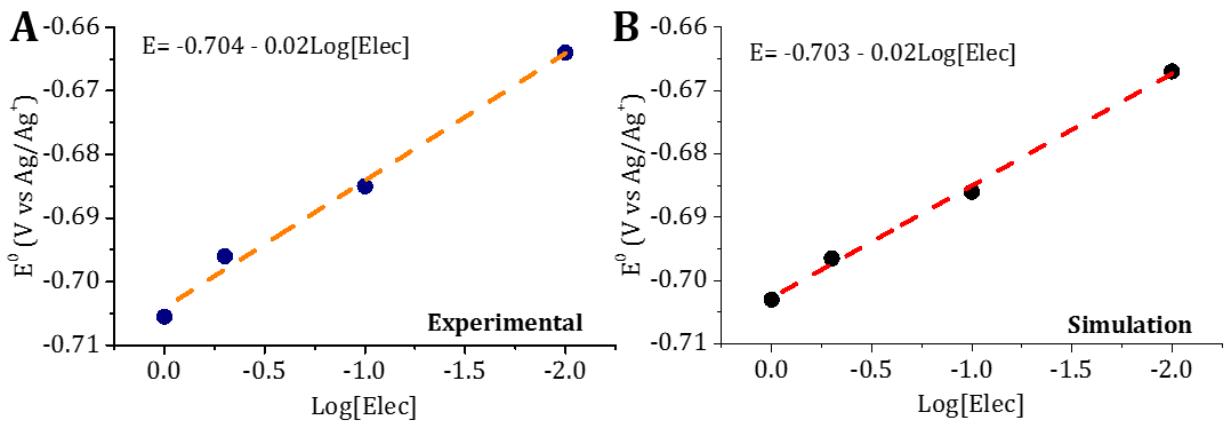

Figure D.17. (A) Observed redox potential change as a function of electrolyte concentration for the **VioRAP**. (B) Simulated redox potential change using DigiElsh Software. For these simulations the adsorption equilibrium was change to increase or decrease the pendant interactions of the polymer.

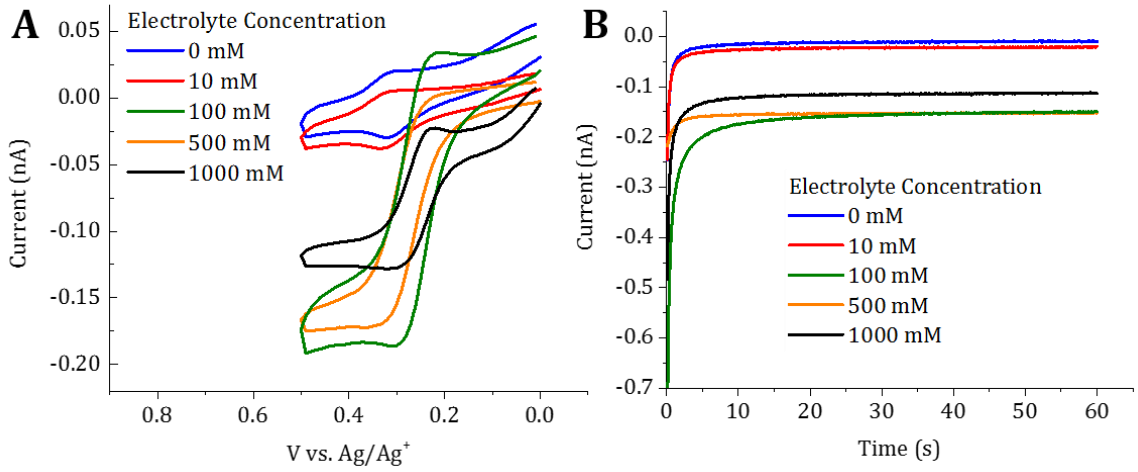

Figure D.18. (A) Cyclic voltammetry at 20 mV/s at a UME with 0.5 mM **PAF** in solution as a function of $TBAPF_6$ electrolyte concentration. (B) Current transients following a potential step at the UME for the oxidation of **PAF** in a series of electrolyte concentrations.

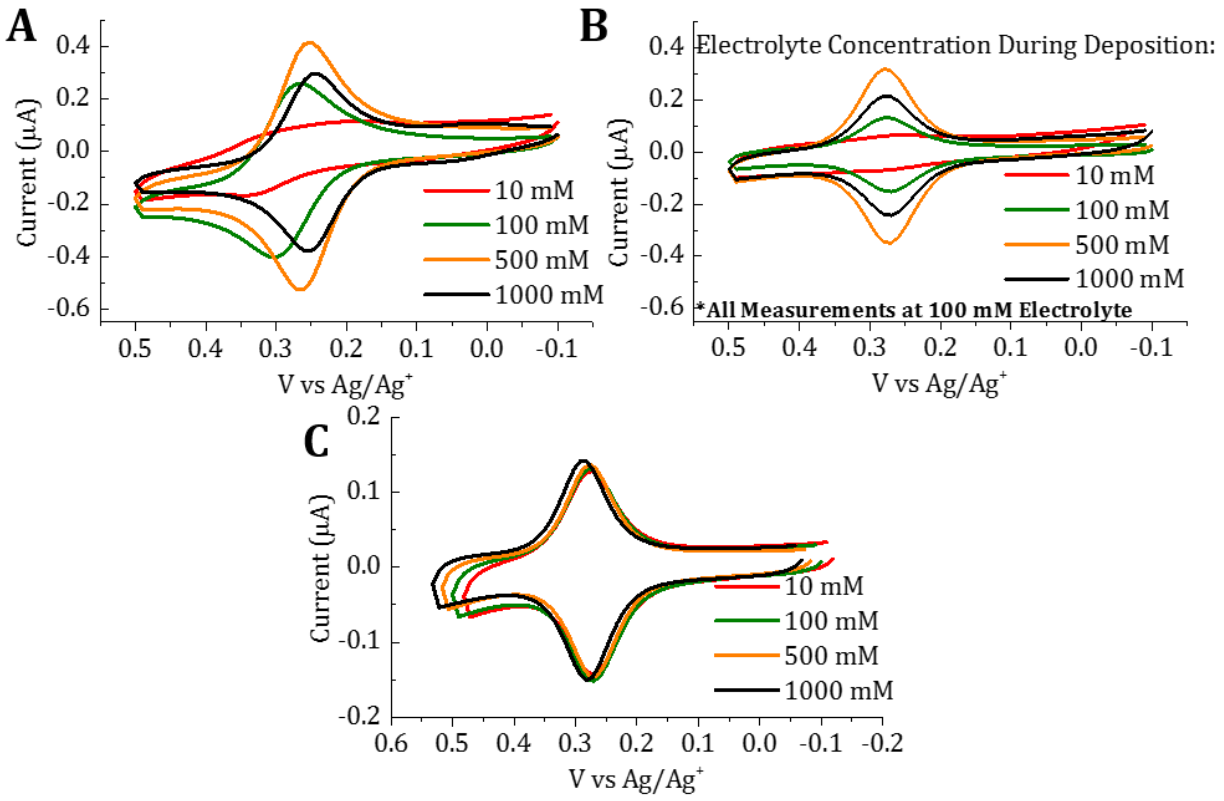

Figure D.19. (A) Cyclic Voltammograms at 10 mV/s for **PAF** (0.5 mM) as a function of electrolyte concentration ($TBAPF_6$). (B) Cyclic Voltammograms at 10 mV/s for **PAF** films deposited at different electrolyte concentration (as indicated in the legend), but measured at 100 mM. Film was deposited by cycling 10 times accessing the redox process. (C) Cyclic Voltammograms at 10 mV/s for **PAF** film deposited at a 100 mM as a function of electrolyte concentration.

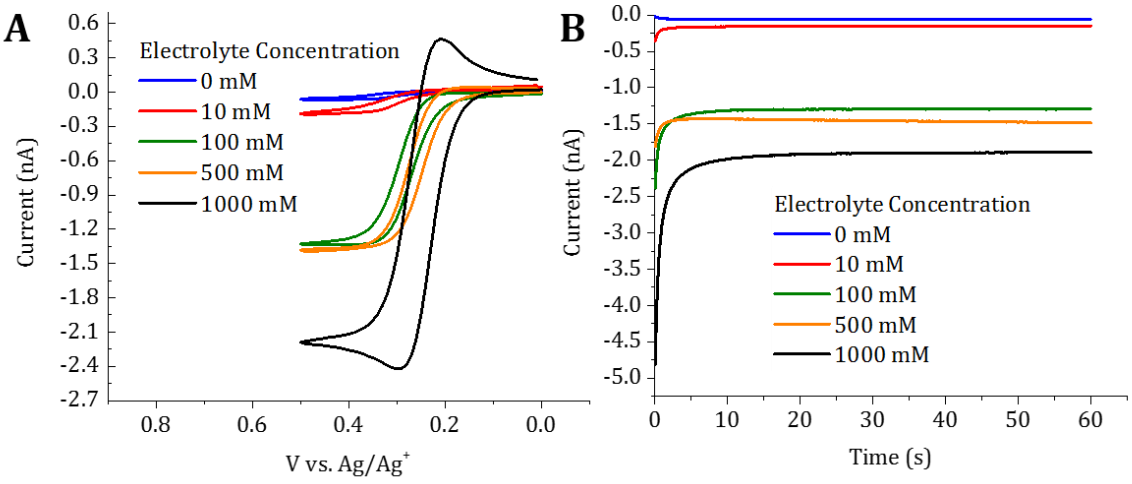

Figure D.20. (A) Cyclic voltammetry at 20 mV/s at a UME with 5 mM **PAF** in solution as a function of $TBAPF_6$ electrolyte concentration. (B) Current transients following a potential step at the UME for the oxidation of **PAF** in a series of electrolyte concentrations.

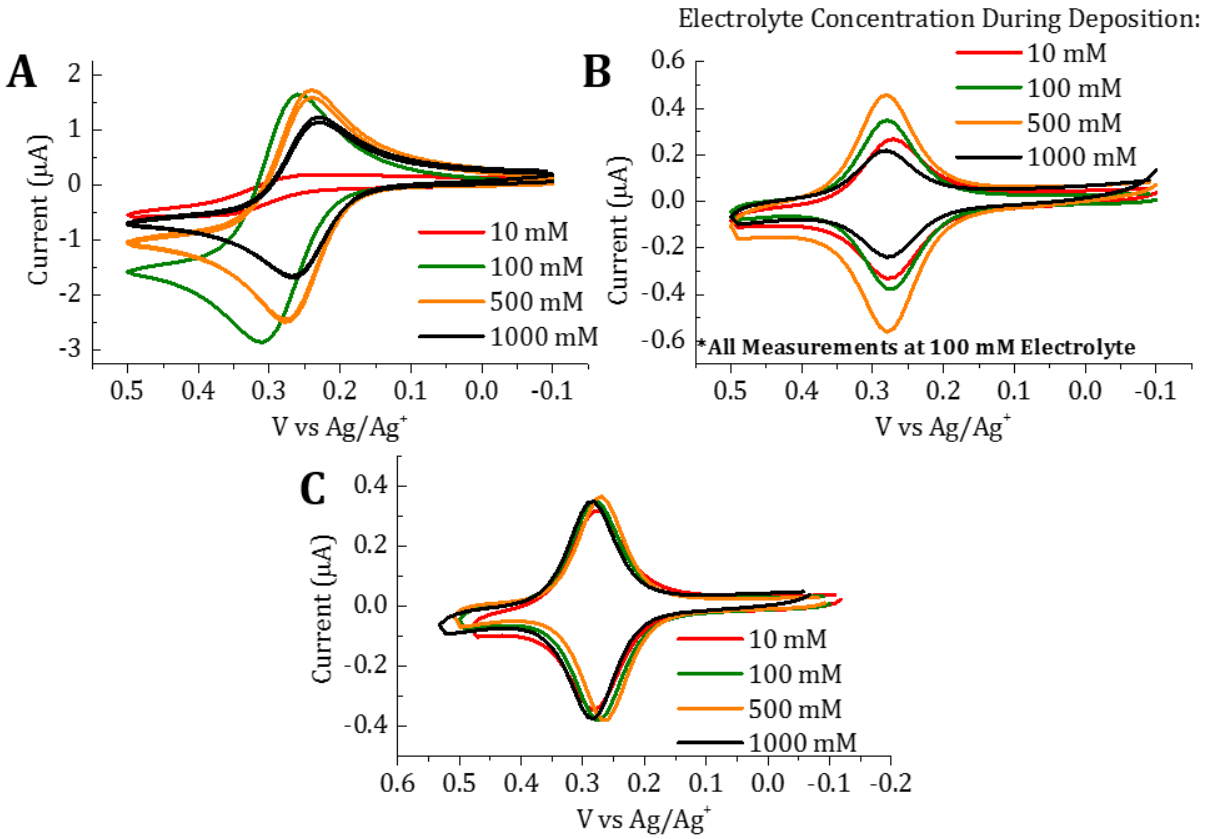

Figure D.21. (A) Cyclic Voltammograms at 10 mV/s for **PAF** (5 mM) as a function of electrolyte concentration ($TBAPF_6$). (B) Cyclic Voltammograms at 10 mV/s for **PAF** films deposited at different electrolyte concentration (as indicated in the legend), but measured at 100 mM. Film was deposited by cycling 10 times accessing the redox process. (C) Cyclic Voltammograms at 10 mV/s for **PAF** film deposited at a 100 mM as a function of electrolyte concentration.

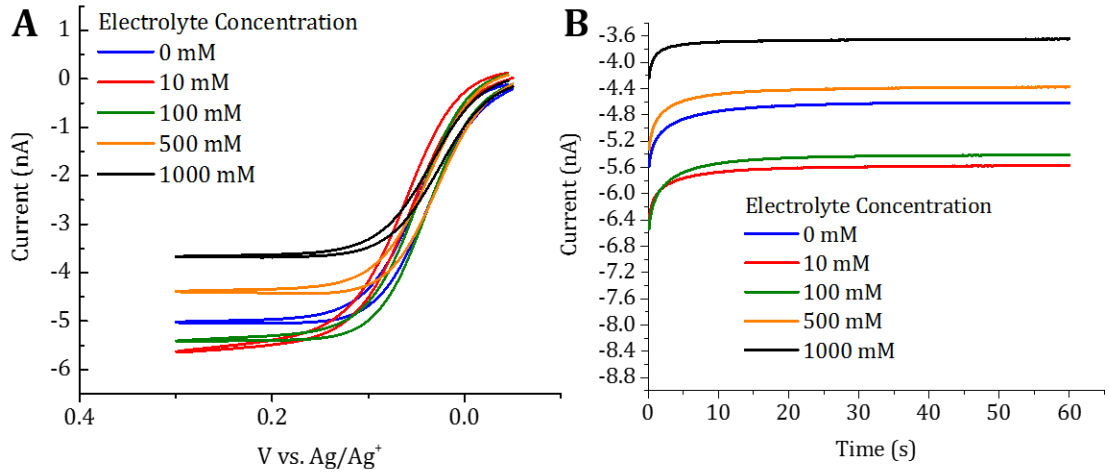

Figure D.22. (A) Cyclic voltammetry at 20 mV/s at a UME with 5 mM **Ferrocene** in solution as a function of $TBAPF_6$ electrolyte concentration. (B) Current transients following a potential step at the UME for the oxidation of **Ferrocene** in a series of electrolyte concentrations.

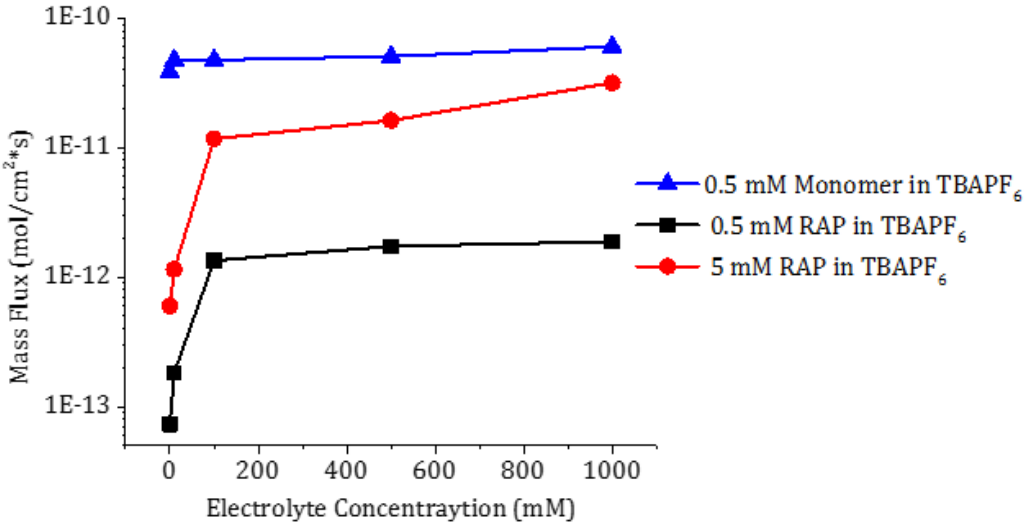

Figure D.23. Viscosity corrected mass flux plot. Points are generated by taking the steady state current at the listed conditions and dividing the experimental current by *nFa*, where *n* is the number of electrons, *F* is Faraday's constant (96,485 C/mol), and *a* is the UME radius (12.5 μm).Viscosity corrections to the steady state current are made using Walden's rule.

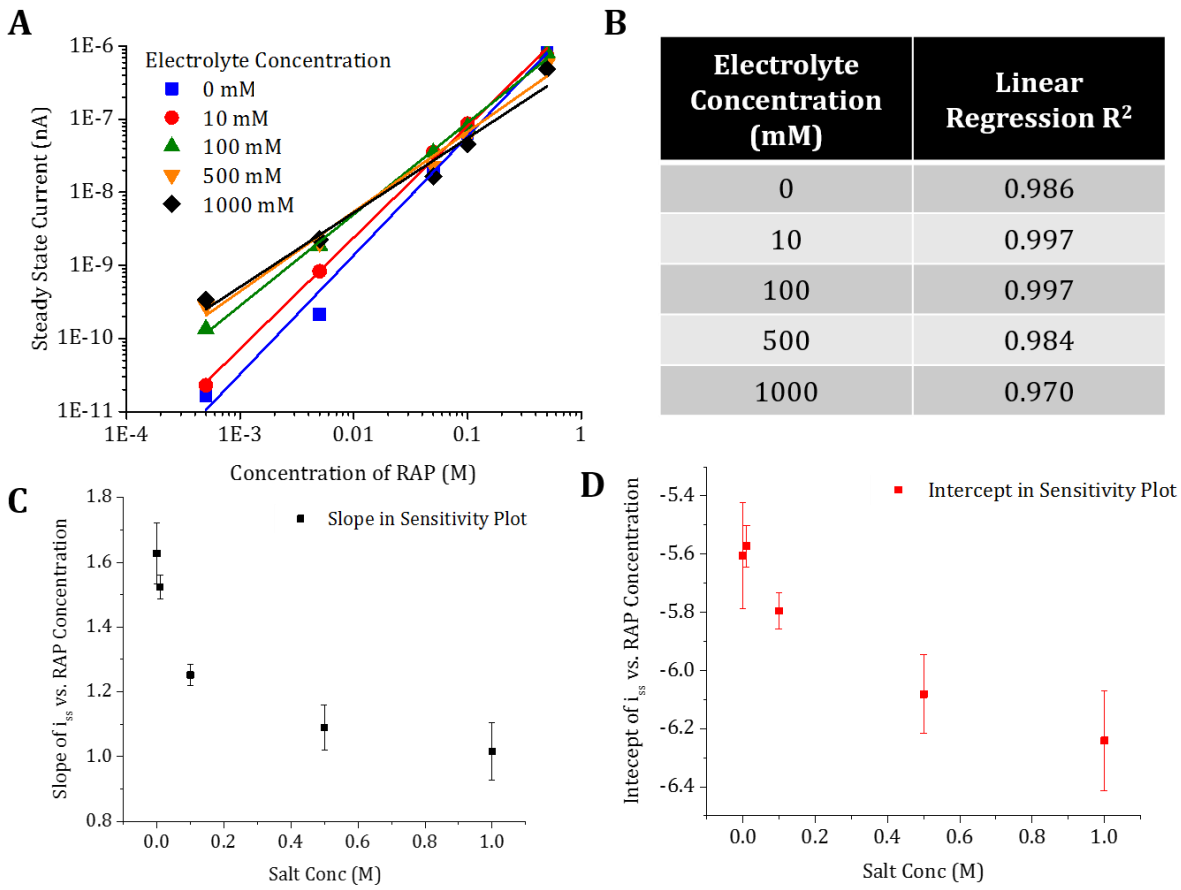

Electrolyte Concentration (mM)	Linear Regression R^2
0	0.986
10	0.997
100	0.997
500	0.984
1000	0.970

Figure D.24. (A) Linear regression analysis of the viscosity corrected **VioRAP** steady state currents for a series of VioRAP concentrations evaluated at a series of electrolyte concentrations in $TBAPF_6$. (B) Linear regression R^2 values for the fittings. (C) The extrapolated slopes from the sensitivity plot in (A) at all of the evaluated salt concentrations. The uncertainty in the fitted slope is shown as error bars at each data point. (D) The extrapolated intercepts from the sensitivity plot in (A) at all of the evaluated salt concentrations. The uncertainty in the fitted intercept is shown as error bars at each data point.

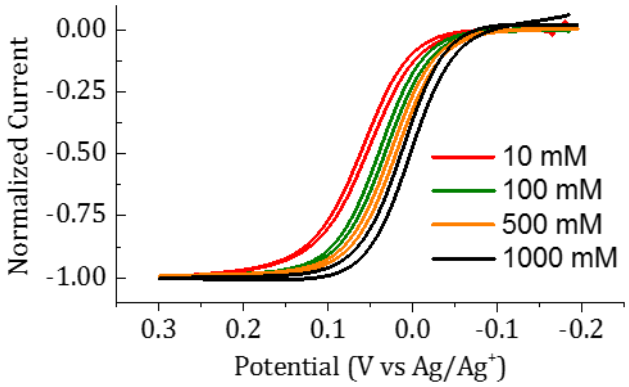

Figure D.25. (A) UME Voltammograms at 50 mV/s for **Ferrocene** as a function of electrolyte concentration ($TBAPF_6$). This data was used to correct the redox potentials of our experimental data.

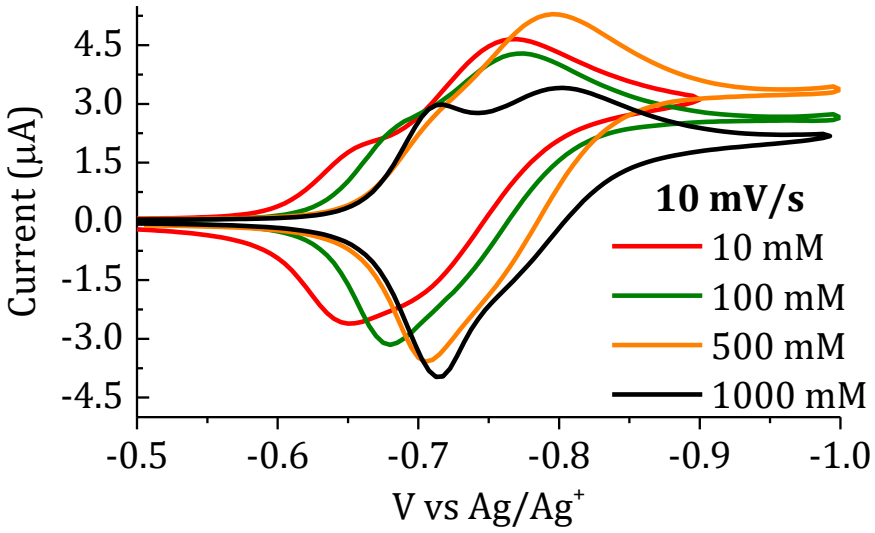

Figure D.26. Cyclic Voltammograms at 10 mV/s for a modified **VioRAP** film in a 1 mM Viologen monomer solution as a function of electrolyte concentration.

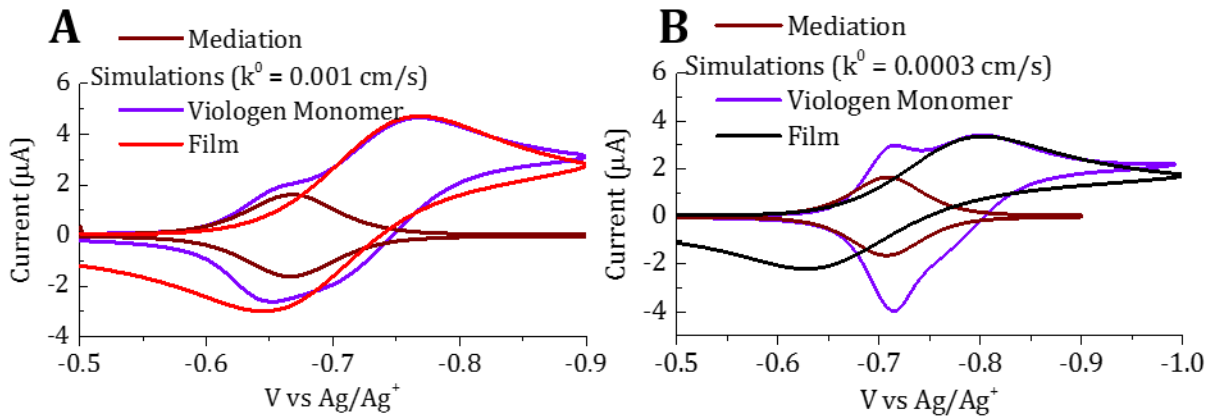

Figure D.27. Cyclic Voltammograms at 10 mV/s for a modified **VioRAP** film, a modified **VioRAP** film in a 1 mM Viologen monomer solution and simulated CV for viologen monomer at (A) 10 mM and (B) 1000 mM.

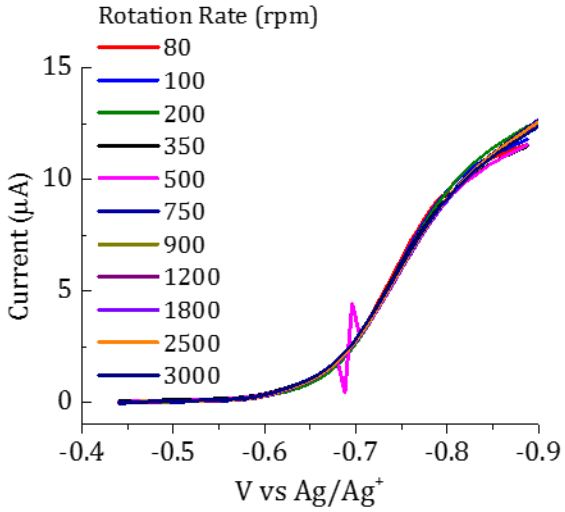

Figure D.28. Linear sweep voltammograms of **VioRAP** (5 mM) in acetonitrile as a function of rotation rate at 10 mM electrolyte concentration ($TBAPF_6$).

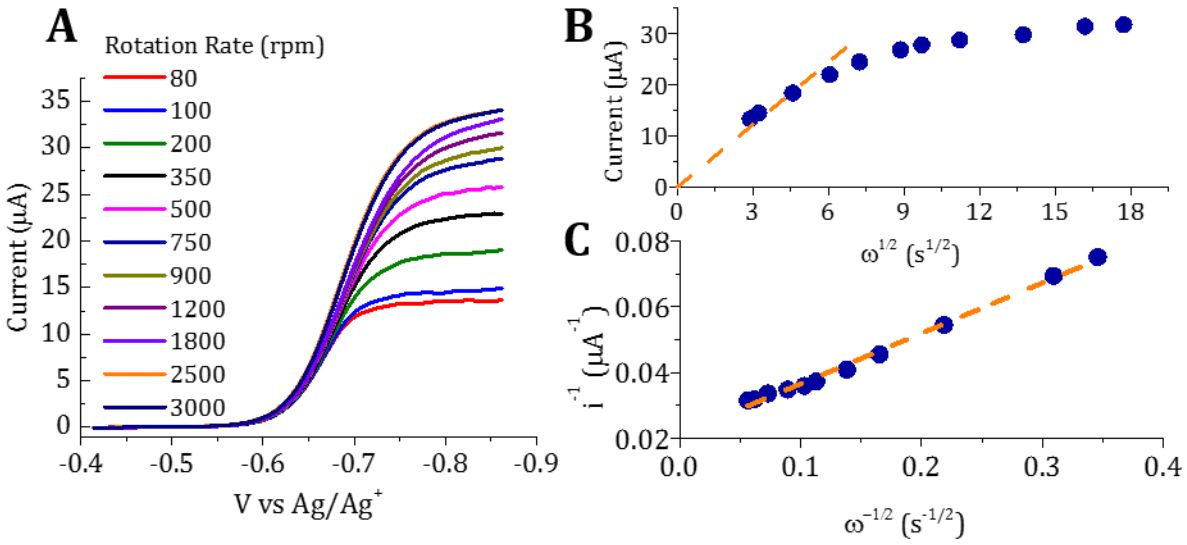

Figure D.29. (A) Linear sweep voltammograms of **VioRAP** (5 mM) in acetonitrile as a function of rotation rate at 100 mM electrolyte concentration ($TBAPF_6$). (B) Levich and (C) Koutecky-Levich plots for the RDE data shown in A.

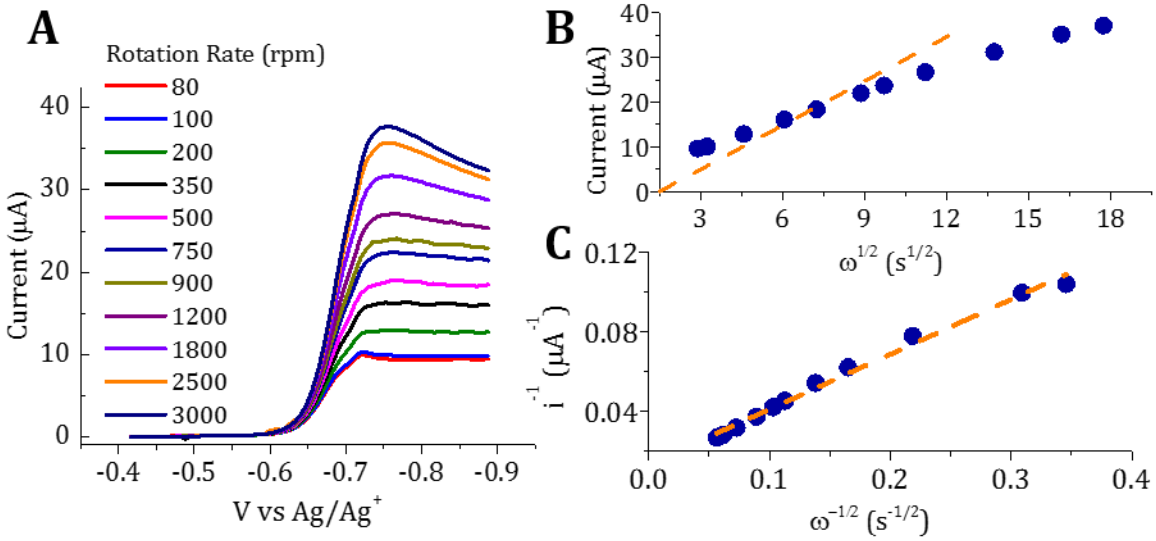

Figure D.30. (A) Linear sweep voltammograms of **VioRAP** (5 mM) in acetonitrile as a function of rotation rate at 500 mM electrolyte concentration ($TBAPF_6$). (B) Levich and (C) Koutecky-Levich plots for the RDE data shown in A.

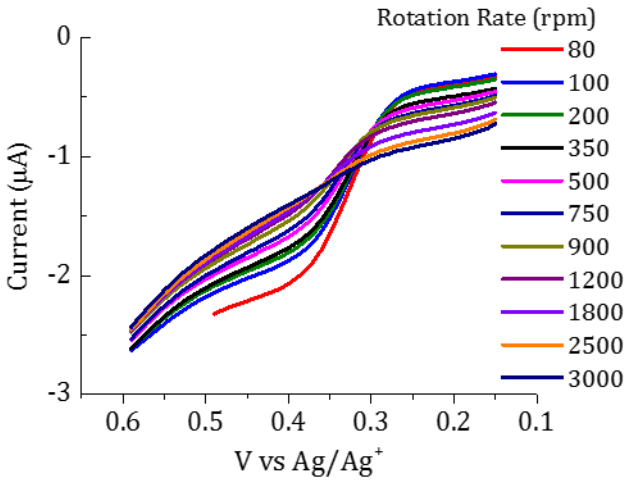

Figure D.31. Linear sweep voltammograms of **PAF** (5 mM) in acetonitrile as a function of rotation rate at 10 mM electrolyte concentration ($TBAPF_6$).

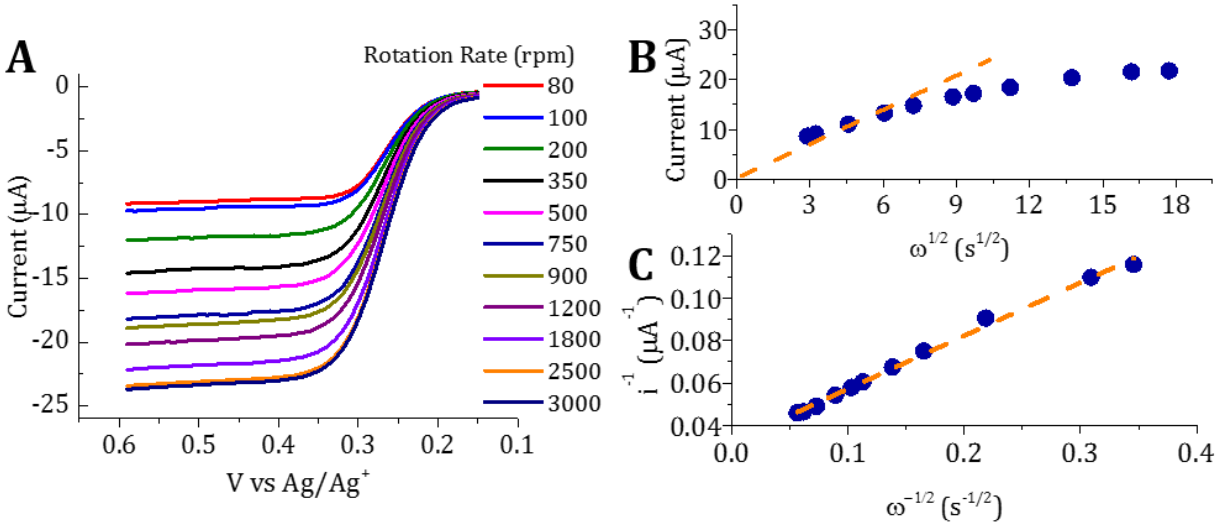

Figure D.32. (A) Linear sweep voltammograms of **PAF** (5 mM) in acetonitrile as a function of rotation rate at 100 mM electrolyte concentration ($TBAPF_6$). (B) Levich and (C) Koutecky-Levich plots for the RDE data shown in A.

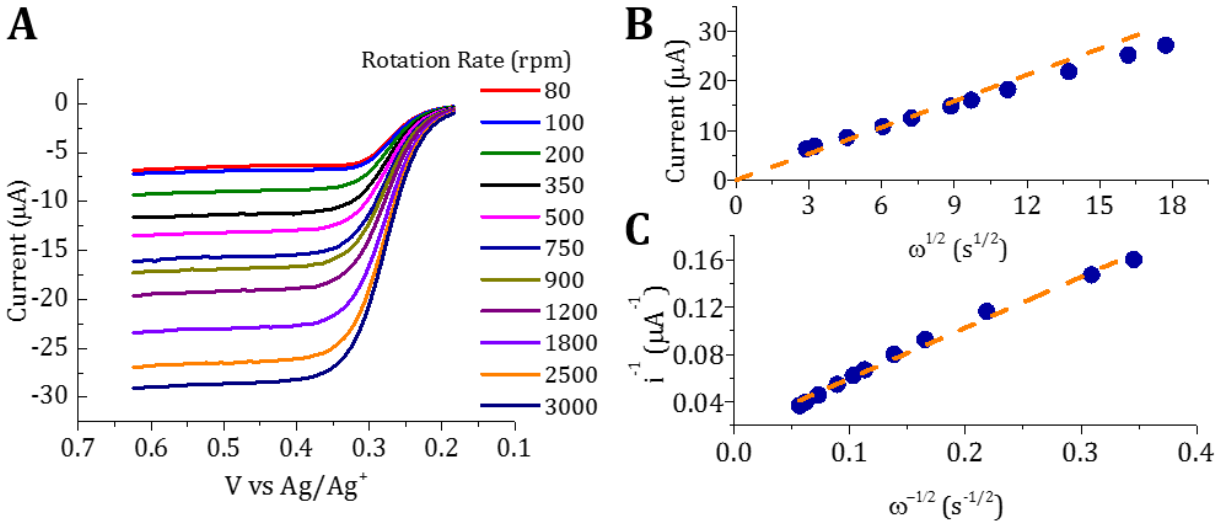

Figure D.33. (A) Linear sweep voltammograms of **PAF** (5 mM) in acetonitrile as a function of rotation rate at 500 mM electrolyte concentration ($TBAPF_6$). (B) Levich and (C) Koutecky-Levich plots for the RDE data shown in A.

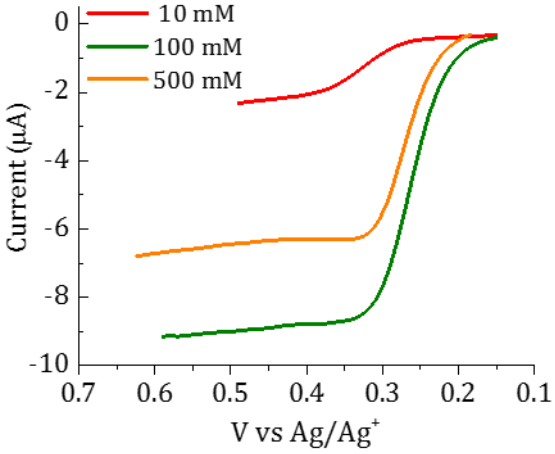

Figure D.34. Linear Sweep Voltammograms of **PAF** (5 mM) in acetonitrile at 80 rpm as a function electrolyte concentration ($TBAPF_6$).

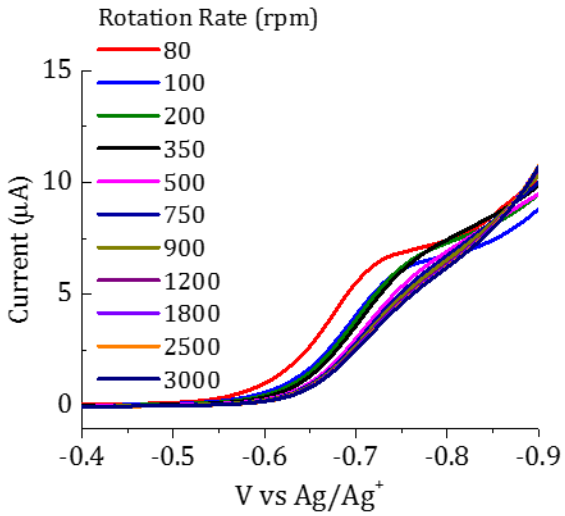

Figure D.35. Linear sweep voltammograms of **VIORAP** (5 mM) in dimethylformamide as a function of rotation rate at 10 mM electrolyte concentration ($TBAPF_6$).

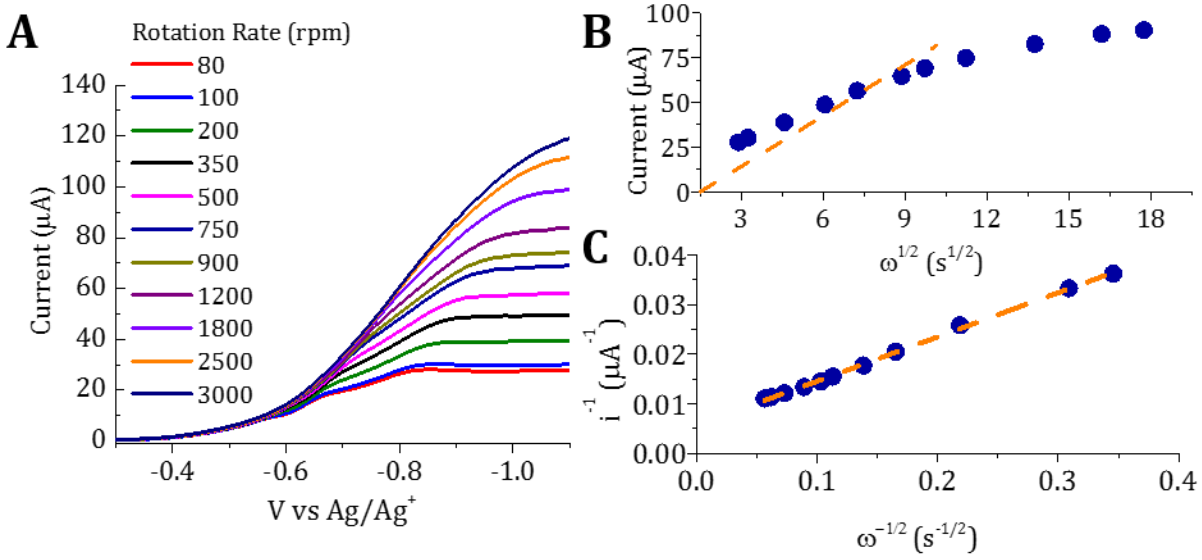

Figure D.36. (A) Linear sweep voltammograms of **VIORAP** (5 mM) in dimethylformamide as a function of rotation rate at 100 mM electrolyte concentration ($TBAPF_6$). (B) Levich and (C) Koutecky-Levich plots for the RDE data shown in A.

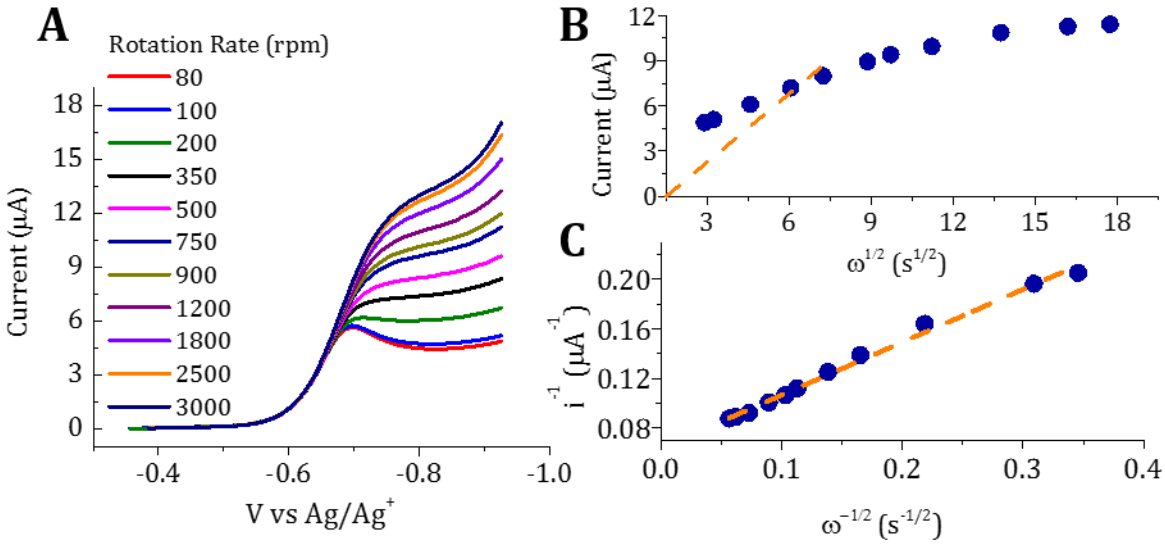

Figure D.37. (A) Linear sweep voltammograms of **VioRAP** (5 mM) in dimethylformamide as a function of rotation rate at 500 mM electrolyte concentration ($TBAPF_6$). (B) Levich and (C) Koutecky-Levich plots for the RDE data shown in A.

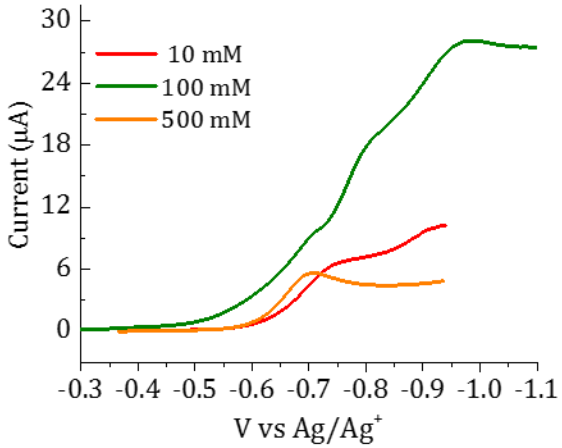

Figure D.38. Linear Sweep voltammograms of **PAF** (5 mM) in dimethylformamide at 80 rpm as a function electrolyte concentration ($TBAPF_6$).

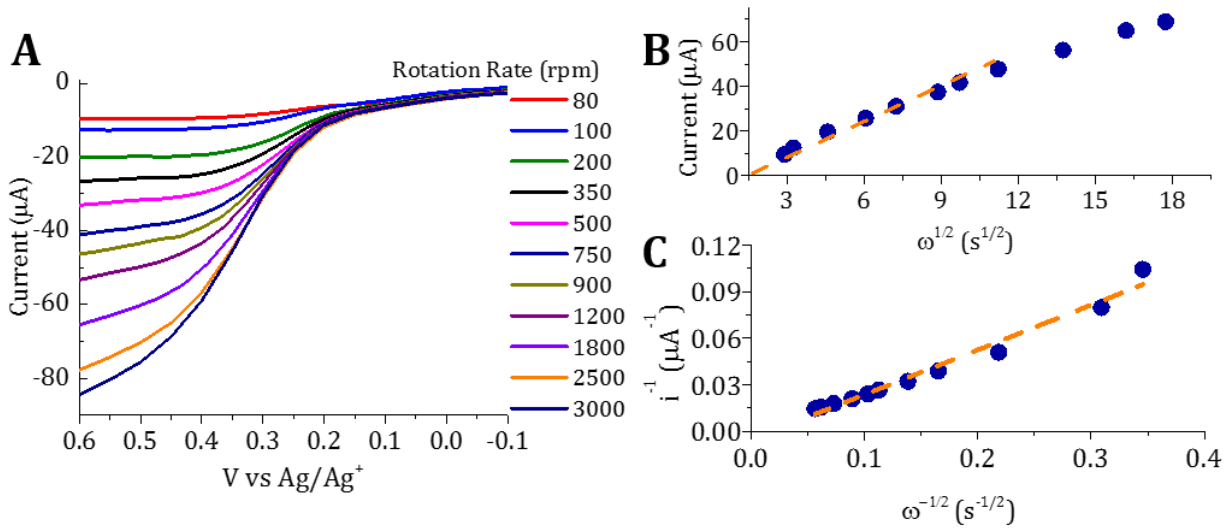

Figure D.39. (A) Linear sweep voltammograms of **PAF** (5 mM) in dimethylformamide as a function of rotation rate at 100 mM electrolyte concentration ($TBAPF_6$). (B) Levich and (C) Koutecky-Levich plots for the RDE data shown in A.

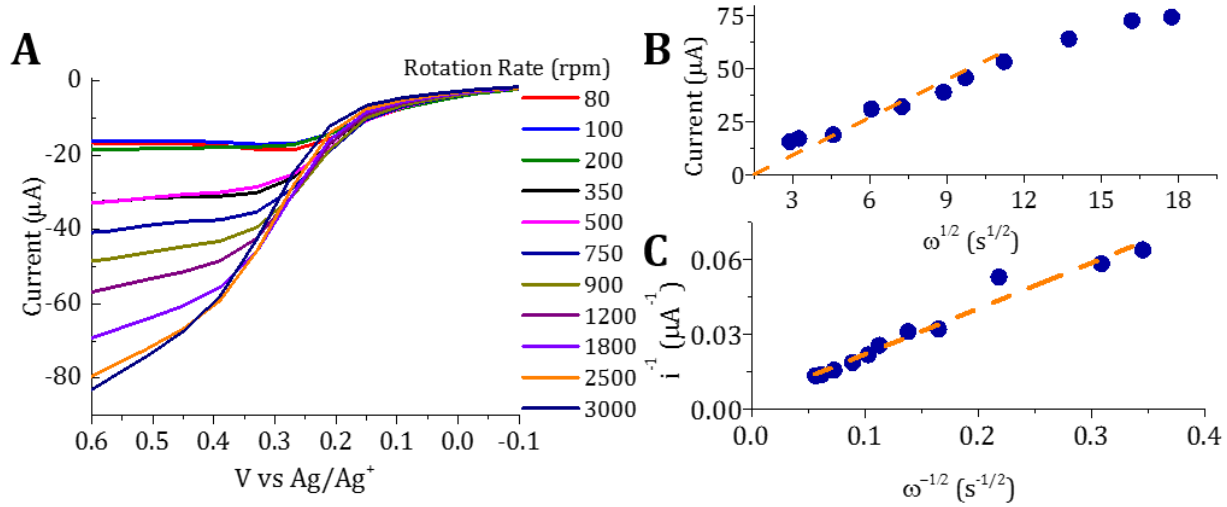

Figure D.40. (A) Linear sweep voltammograms of **PAF** (5 mM) in dimethylformamide as a function of rotation rate at 500 mM electrolyte concentration ($TBAPF_6$). (B) Levich and (C) Koutecky-Levich plots for the RDE data shown in A.

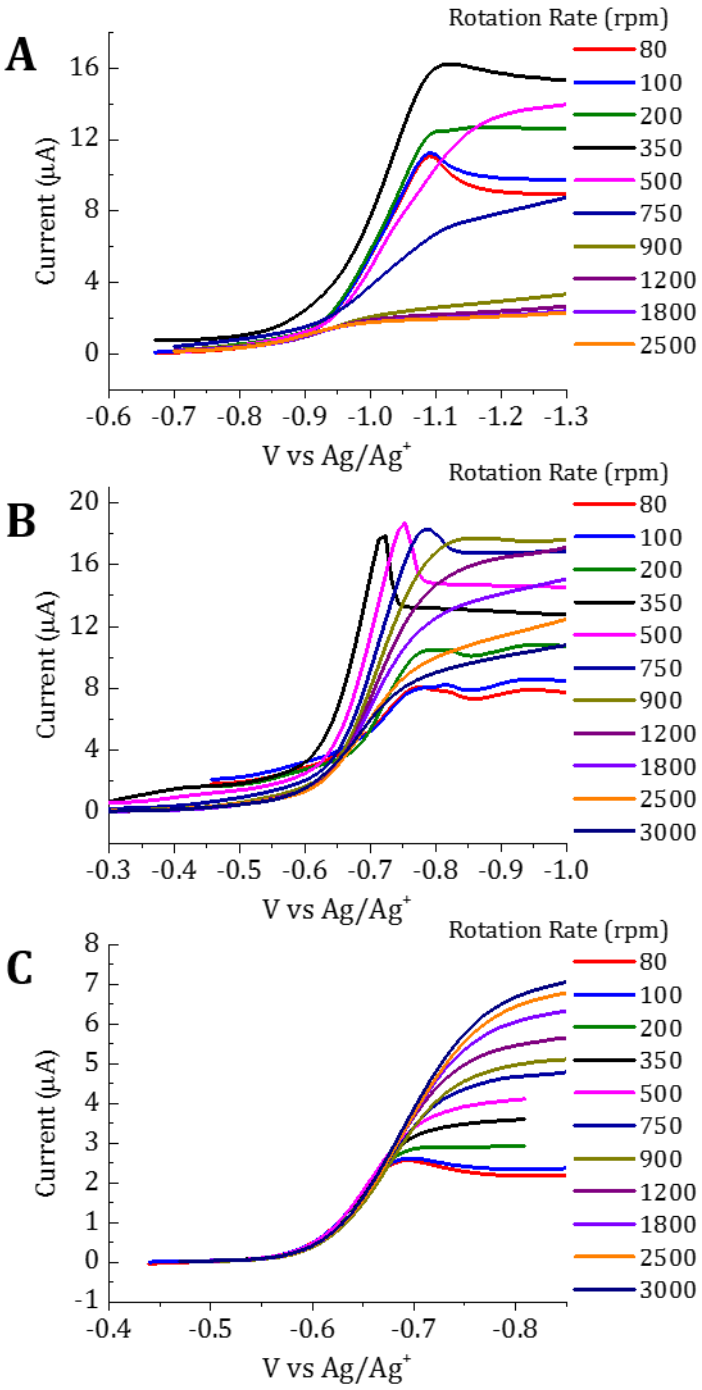

Figure D.41. (A) Linear sweep voltammograms of **VioRAP** (5 mM) in propylene carbonate as a function of rotation rate at (A) 10 mM, (B) 100 mM and (C) 500 mM electrolyte concentration ($TBAPF_6$).

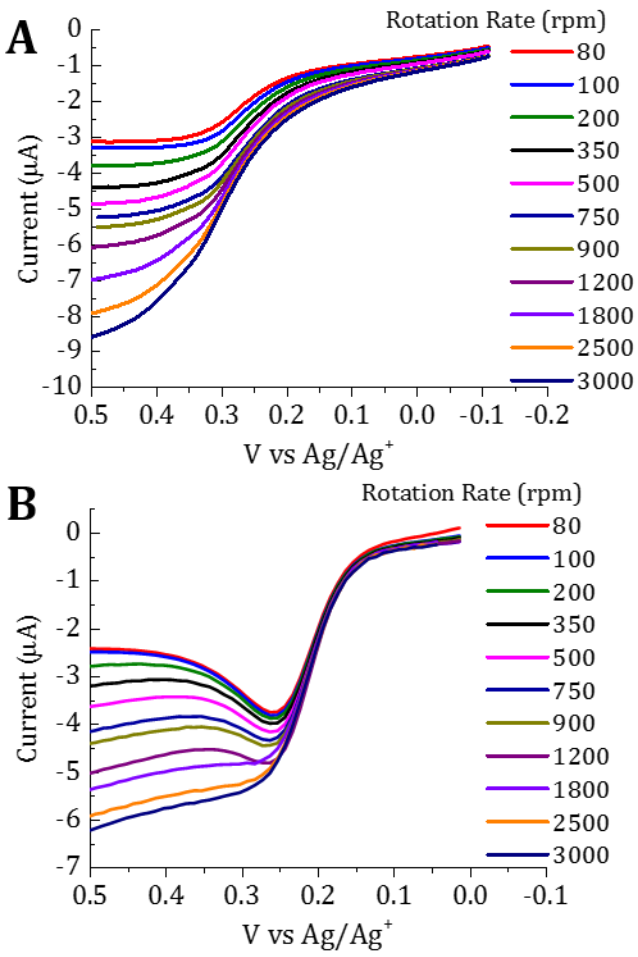

Figure D.42. (A) Linear sweep voltammograms of **VioRAP** (5 mM) in propylene carbonate as a function of rotation rate at (A) 100 mM and (C) 500 mM electrolyte concentration ($TBAPF_6$).

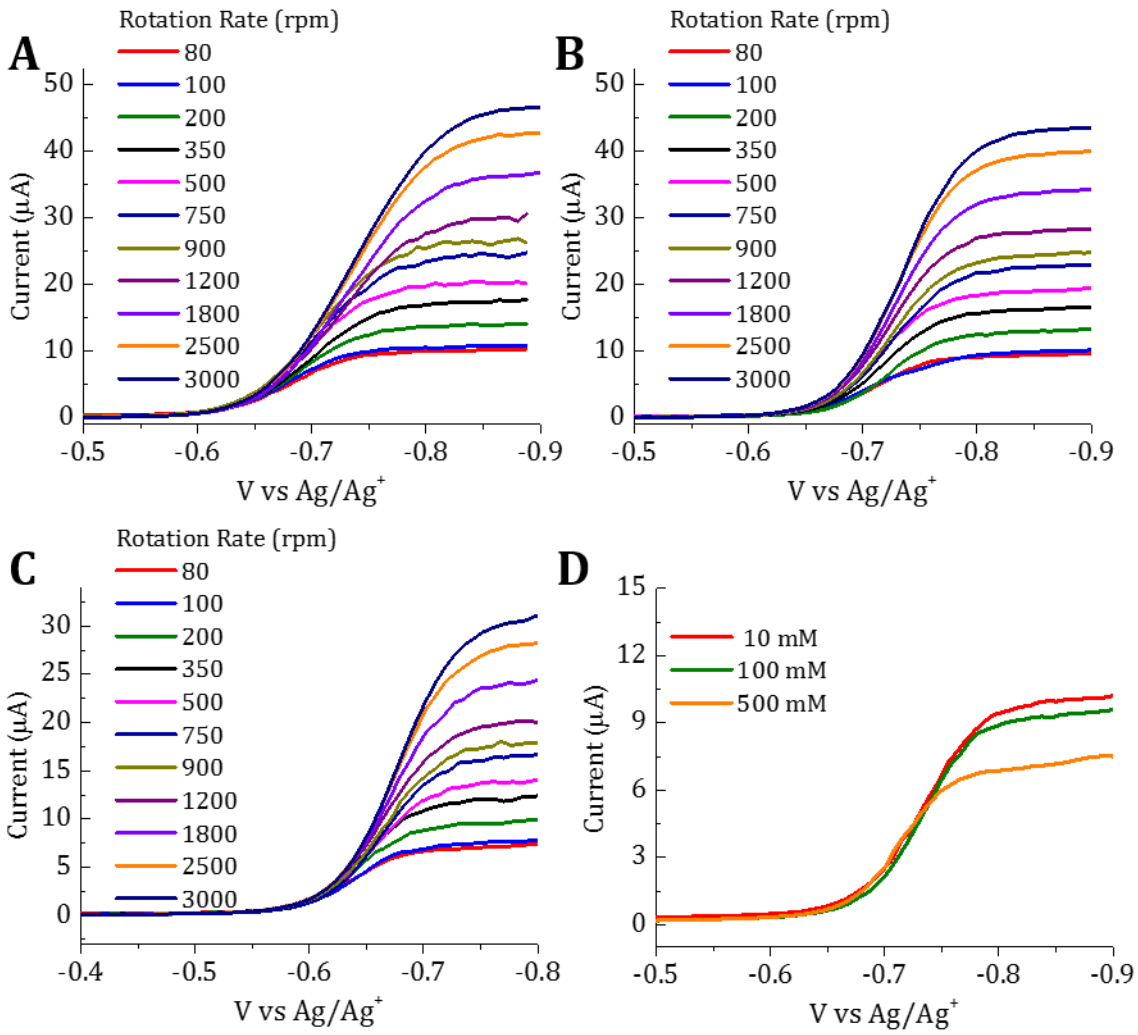

Figure D.43. Linear sweep voltammograms of **Viologen Monomer** (5 mM) in acetonitrile as a function of rotation rate at (A) 10 mM, (B) 100 mM and (C) 500 mM of electrolyte concentration ($TBAPF_6$). (D) Linear sweep voltammograms comparison at 80 rpm.

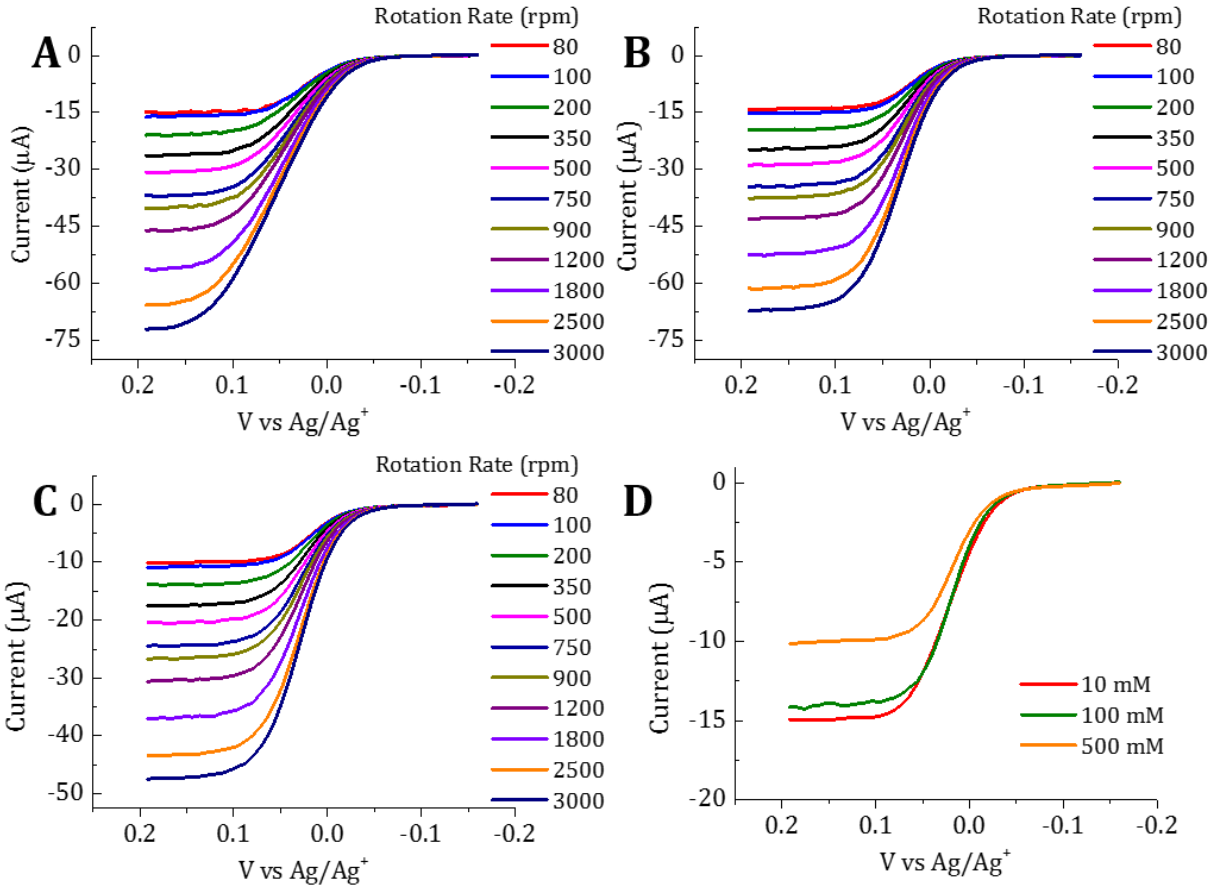

Figure D.44. Linear sweep voltammograms of **Ferrocene** (5 mM) in acetonitrile as a function of rotation rate at (A) 10 mM, (B) 100 mM and (C) 500 mM of electrolyte concentration ($TBAPF_6$). (D) Linear sweep voltammograms comparison at 80 rpm.

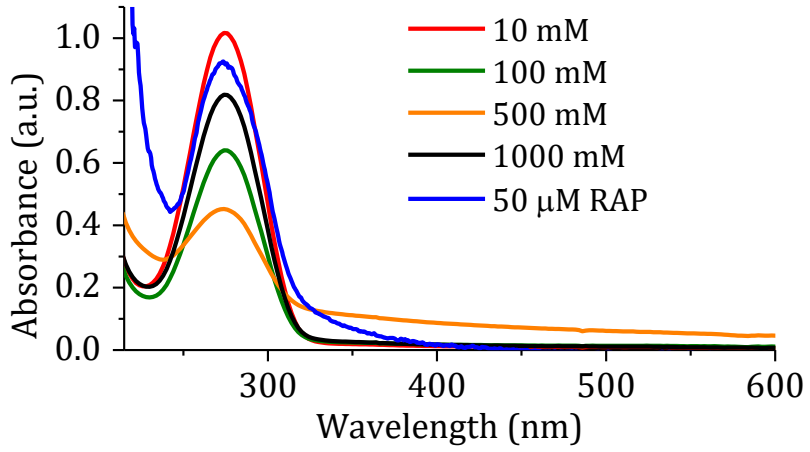

Figure D.45. UV-Visible spectra for the deposited films as function of the electrolyte concentration.

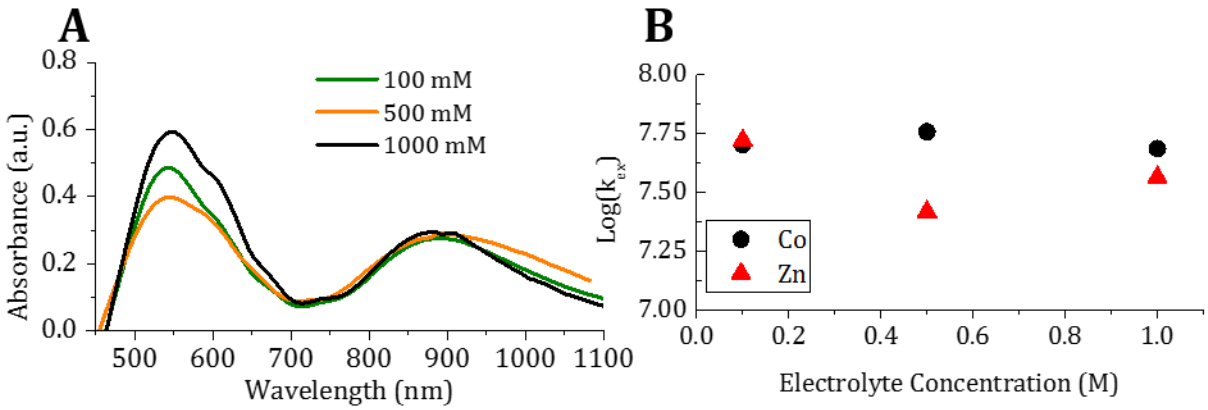

Figure D.46. (A) UV-Visible spectra for the chemically reduced (with Cobaltocene) **VioRap** in acetonitrile at different electrolyte concentrations. (B) Plot of the charge exchange kinetic as function of the electrolyte concentration.

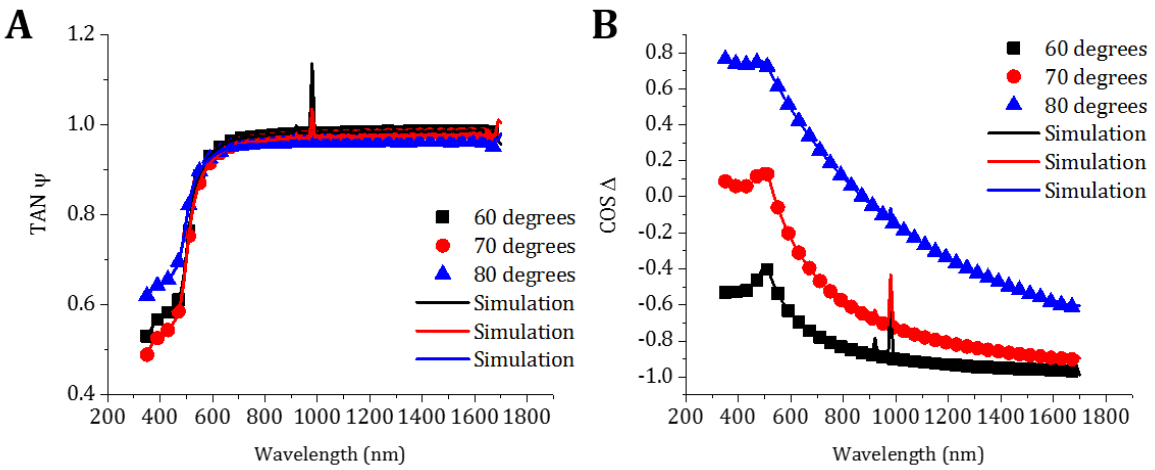

Figure D.47. (A) Tangent of the reflectance ratio, Psi, for spectroscopic ellipsometry analysis of a bare gold substrate. (B) Cosine of the phase shift, Delta, for spectroscopic ellipsometry analysis of a bare gold substrate. The symbols represent experimental data points and the solid lines are the simulated curves.

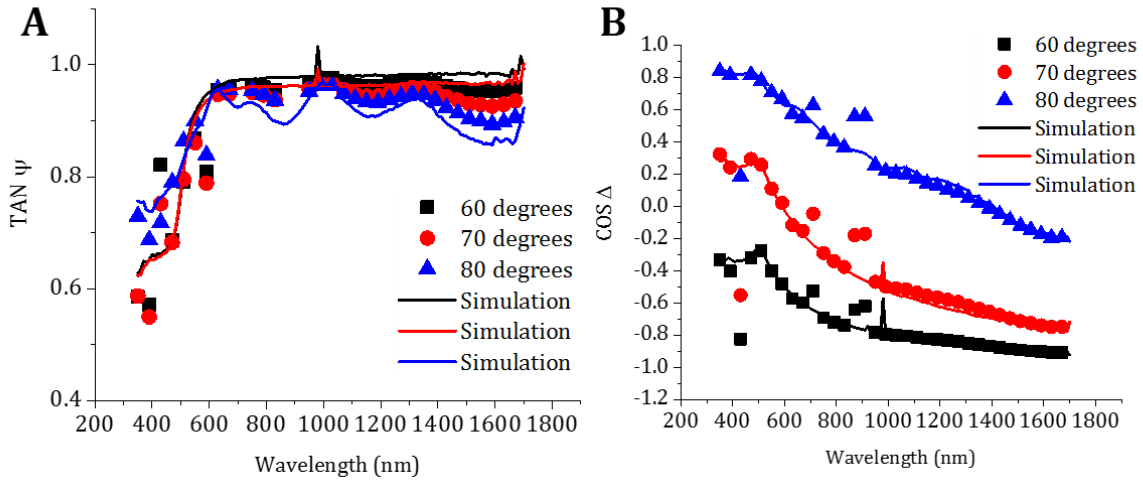

Figure D.48. (A) Tangent of the reflectance ratio, Psi, for spectroscopic ellipsometry analysis of a gold substrate filmed with **PAF** when in the presence of 10 mM supporting electrolyte. (B) Cosine of the phase shift, Delta, for spectroscopic ellipsometry analysis of a gold substrate filmed with **PAF** when in the presence of 10 mM supporting electrolyte. The symbols represent experimental data points and the solid lines are the simulated curves.

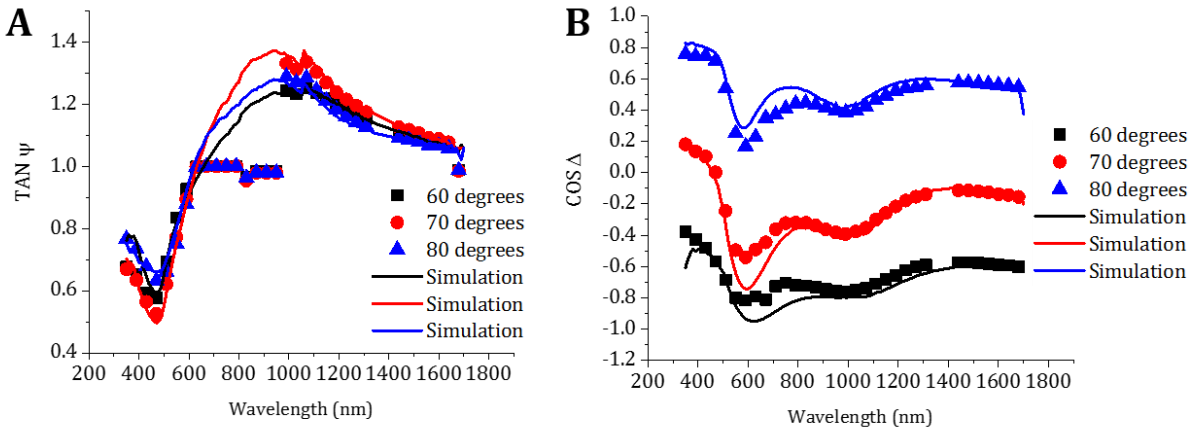

Figure D.49. (A) Tangent of the reflectance ratio, Psi, for spectroscopic ellipsometry analysis of a gold substrate filmed with **PAF** when in the presence of 100 mM supporting electrolyte. (B) Cosine of the phase shift, Delta, for spectroscopic ellipsometry analysis of a gold substrate filmed with **PAF** when in the presence of 100 mM supporting electrolyte. The symbols represent experimental data points and the solid lines are the simulated curves.

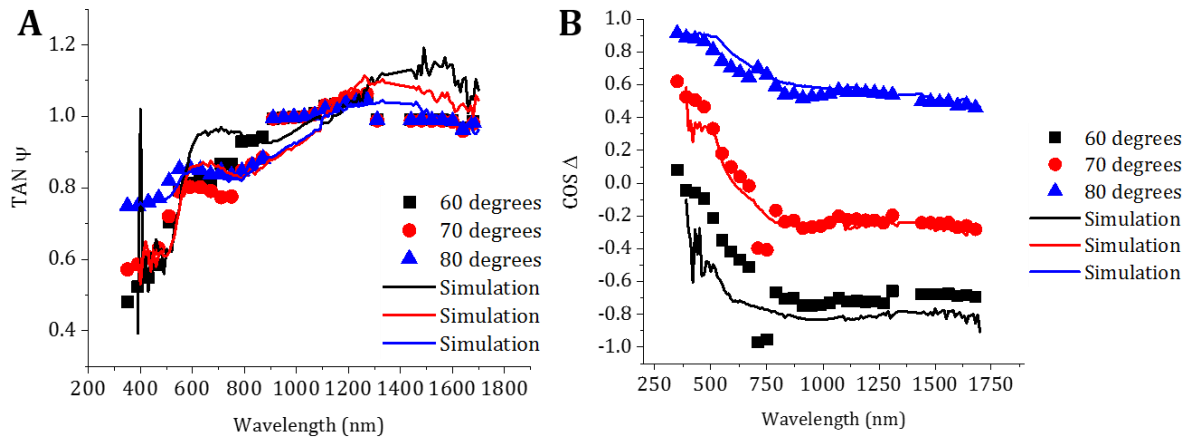

Figure D.50. (A) Tangent of the reflectance ratio, Psi, for spectroscopic ellipsometry analysis of a gold substrate filmed with **PAF** when in the presence of 500 mM supporting electrolyte. (B) Cosine of the phase shift, Delta, for spectroscopic ellipsometry analysis of a gold substrate filmed with **PAF** when in the presence of 500 mM supporting electrolyte. The symbols represent experimental data points and the solid lines are the simulated curves.

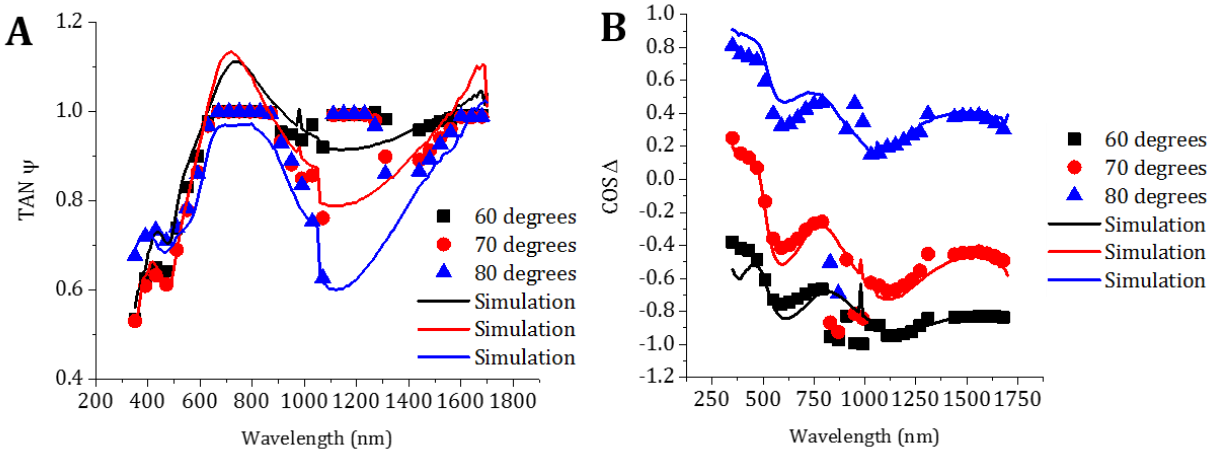

Figure D.51. (A) Tangent of the reflectance ratio, Psi, for spectroscopic ellipsometry analysis of a gold substrate filmed with **PAF** when in the presence of 1000 mM supporting electrolyte. (B) Cosine of the phase shift, Delta, for spectroscopic ellipsometry analysis of a gold substrate filmed with **PAF** when in the presence of 1000 mM supporting electrolyte. The symbols represent experimental data points and the solid lines are the simulated curves.

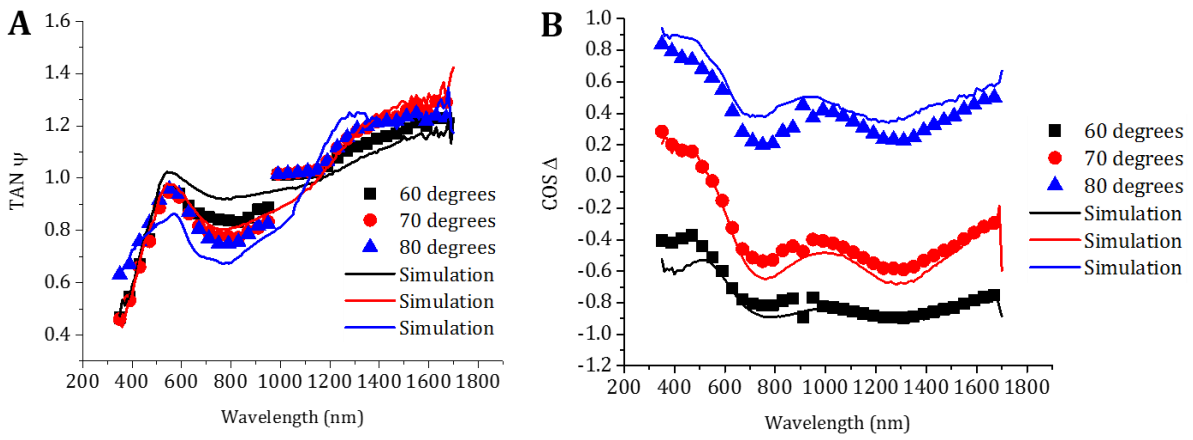

Figure D.52. (A) Tangent of the reflectance ratio, Psi, for spectroscopic ellipsometry analysis of a gold substrate filmed with **VioRAP** when in the presence of 10 mM supporting electrolyte. (B) Cosine of the phase shift, Delta, for spectroscopic ellipsometry analysis of a gold substrate filmed with **VioRAP** when in the presence of 10 mM supporting electrolyte. The symbols represent experimental data points and the solid lines are the simulated curves.

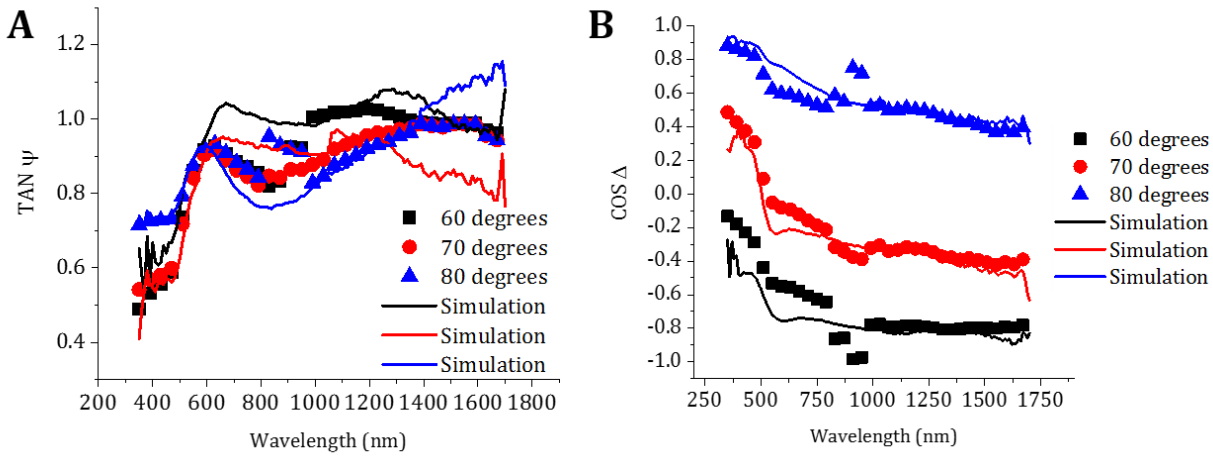

Figure D.53. (A) Tangent of the reflectance ratio, Psi, for spectroscopic ellipsometry analysis of a gold substrate filmed with **VioRAP** when in the presence of 500 mM supporting electrolyte. (B) Cosine of the phase shift, Delta, for spectroscopic ellipsometry analysis of a gold substrate filmed with **VioRAP** when in the presence of 500 mM supporting electrolyte. The symbols represent experimental data points and the solid lines are the simulated curves.

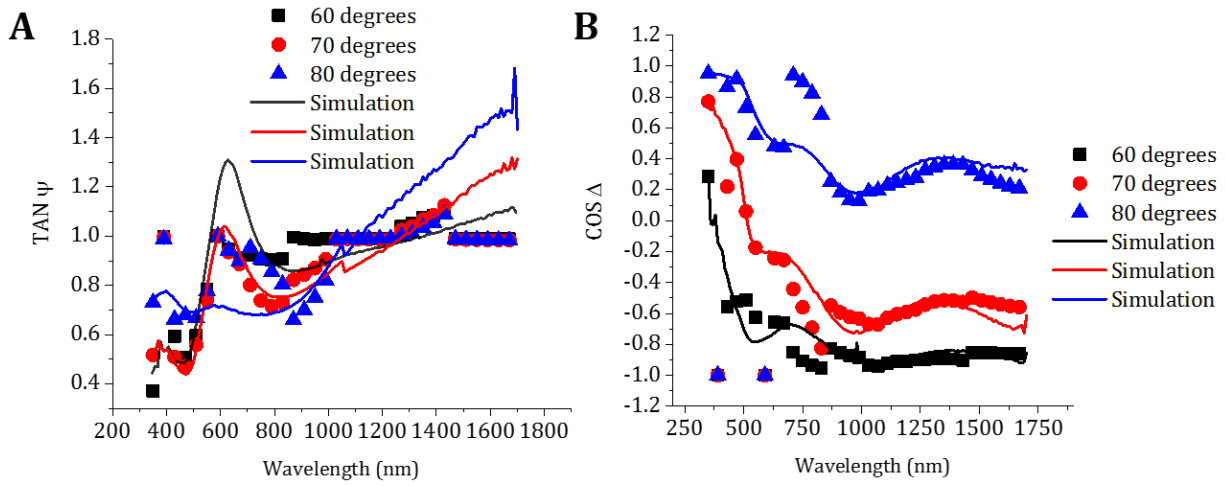

Figure D.54. (A) Tangent of the reflectance ratio, Psi, for spectroscopic ellipsometry analysis of a gold substrate filmed with **VioRAP** when in the presence of 1000 mM supporting electrolyte. (B) Cosine of the phase shift, Delta, for spectroscopic ellipsometry analysis of a gold substrate filmed with **VioRAP** when in the presence of 1000 mM supporting electrolyte. The symbols represent experimental data points and the solid lines are the simulated curves.

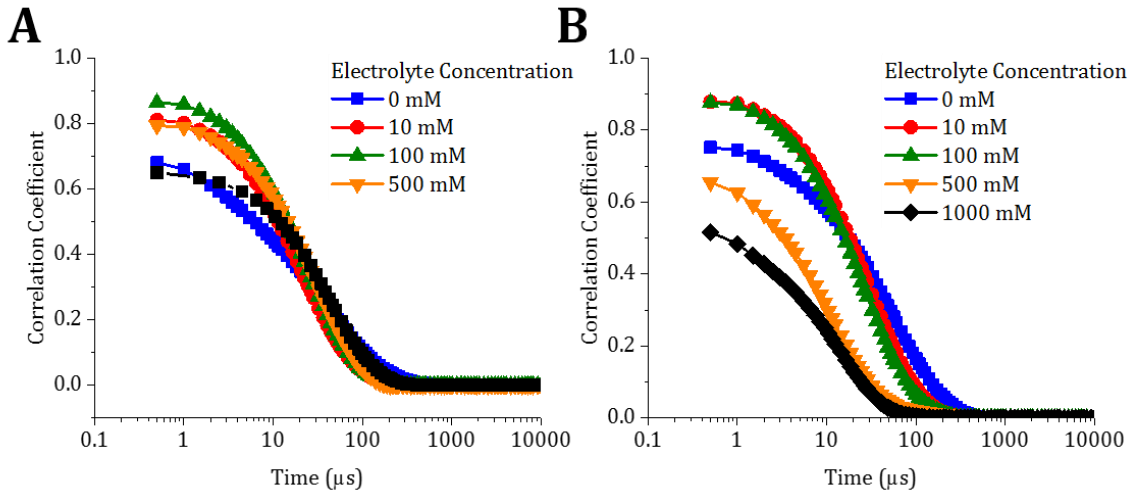

Figure D.55. (A) Auto correlation functions and fit to the cumulants from DLS measurements of solutions of **VioRAP** at 5 mM concentration in acetonitrile at different ionic strengths. (B) Auto correlation functions and fit to the cumulants from DLS measurements of solutions of **PAF** in acetonitrile at 5 mM concentration at different ionic strengths.

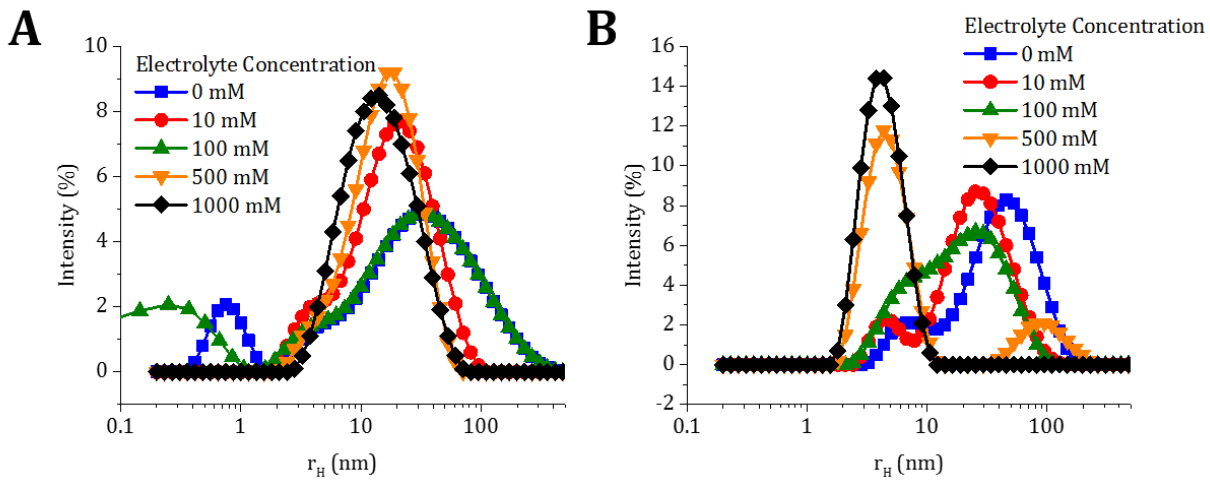

Figure D.56. (A) Intensity distribution of DLS scattering events of solutions of **VioRAP** at 5 mM concentration in acetonitrile at different ionic strengths as function of particle size in solution. (B) Intensity distribution of DLS scattering events of solutions of **PAF** at 5 mM concentration in acetonitrile at different ionic strengths as function of particle size in solution.

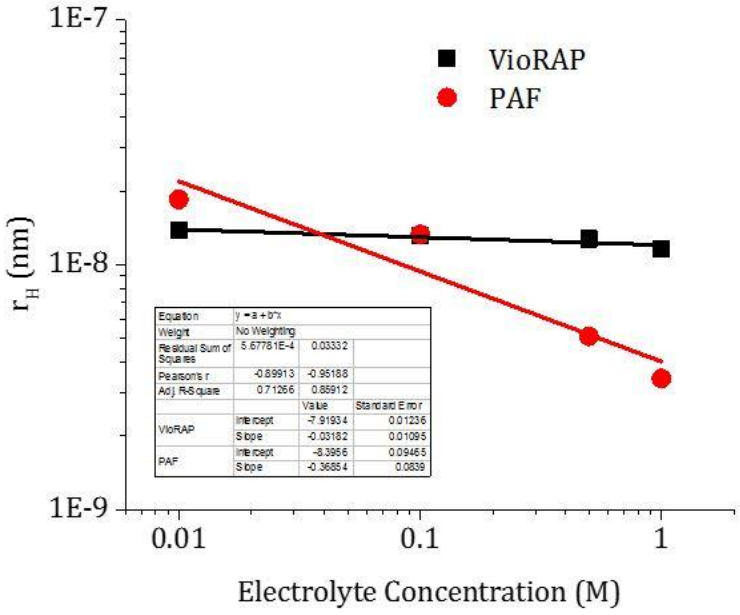

Figure D.57. Calculated Z-average sizes for **VioRAP** and **PAF** as a function of solution ionic strength.

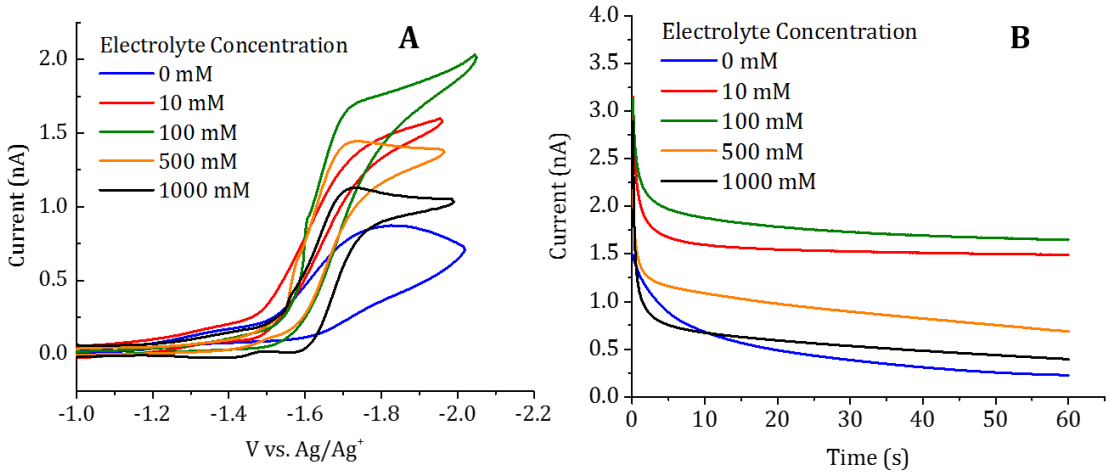

Figure D.58. (A) Cyclic voltammetry at 20 mV/s at a UME with 5 mM **PNS** in solution as a function of $TBAPF_6$ electrolyte concentration. (B) Current transients following a potential step at the UME for the first reduction of the **PNS** in a series of electrolyte concentrations.

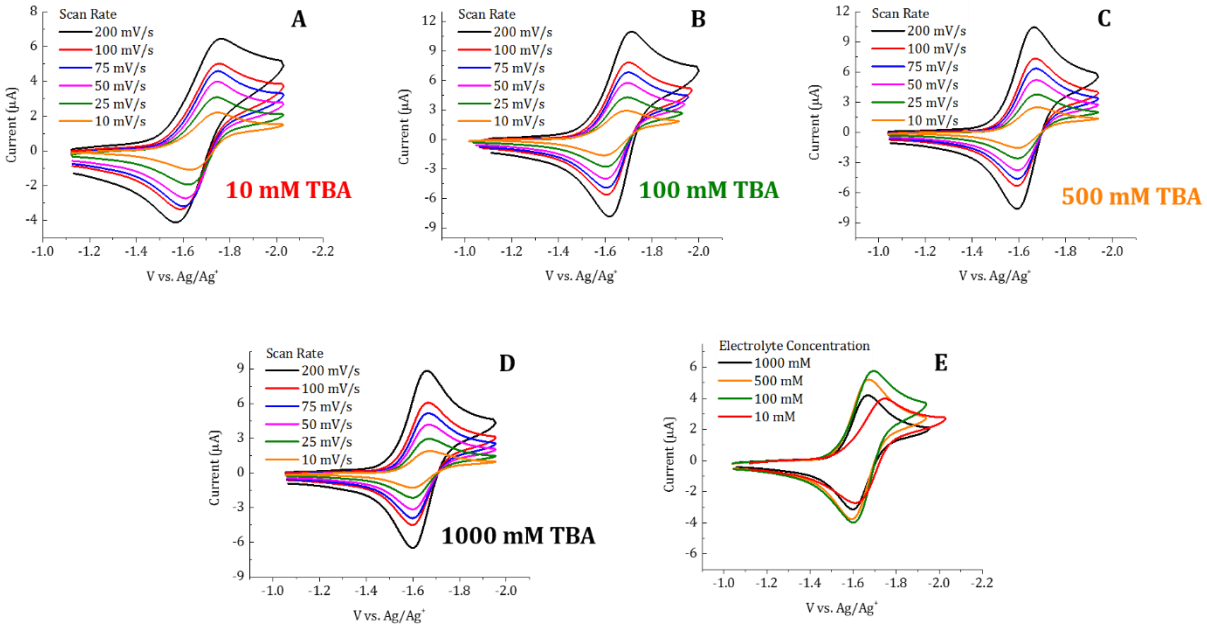

Figure D.59. (A) Cyclic voltammetry at series of scan rates with 5 mM **PNS** in solution with 10 mM $TBAPF_6$ electrolyte concentration. (B) Cyclic voltammetry at series of scan rates with 5 mM **PNS** in solution with 100 mM $TBAPF_6$ electrolyte concentration. (C) Cyclic voltammetry at series of scan rates with 5 mM **PNS** in solution with 500 mM $TBAPF_6$ electrolyte concentration. (D) Cyclic voltammetry at series of scan rates with 5 mM **PNS** in solution with 1000 mM $TBAPF_6$ electrolyte concentration. (E) Overlay of cyclic voltammograms at 50 mV/s with 5 mM **PNS** in solution as a function of $TBAPF_6$ electrolyte concentration.

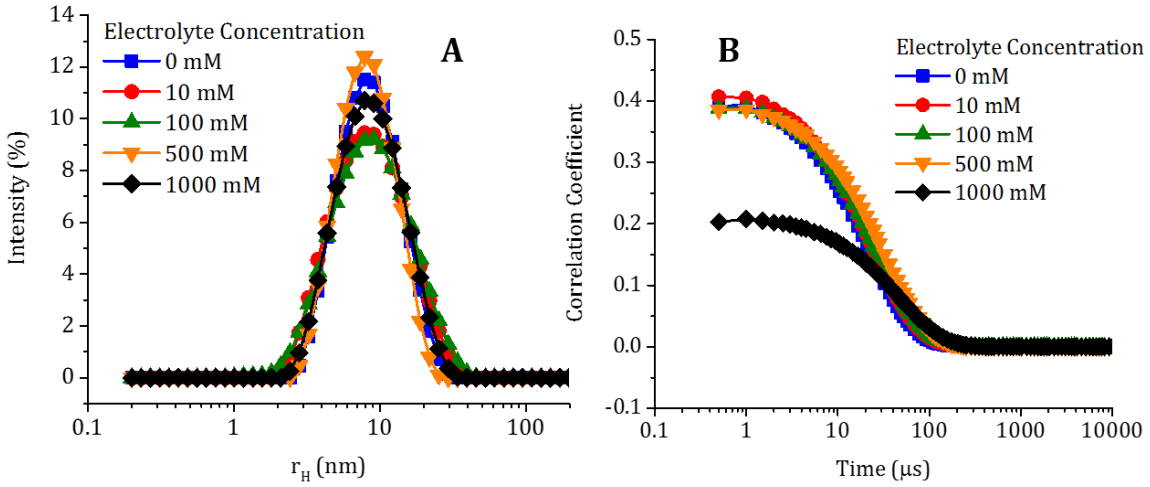

Figure D.60. (A) Intensity distribution of DLS scattering events of solutions of **PNS** at 5 mM concentration in dimethylformamide at different ionic strengths as function of particle size in solution. (B) Intensity distribution of DLS scattering events of solutions of **PNS** at 5 mM concentration in dimethylformamide at different ionic strengths as function of particle size in solution.

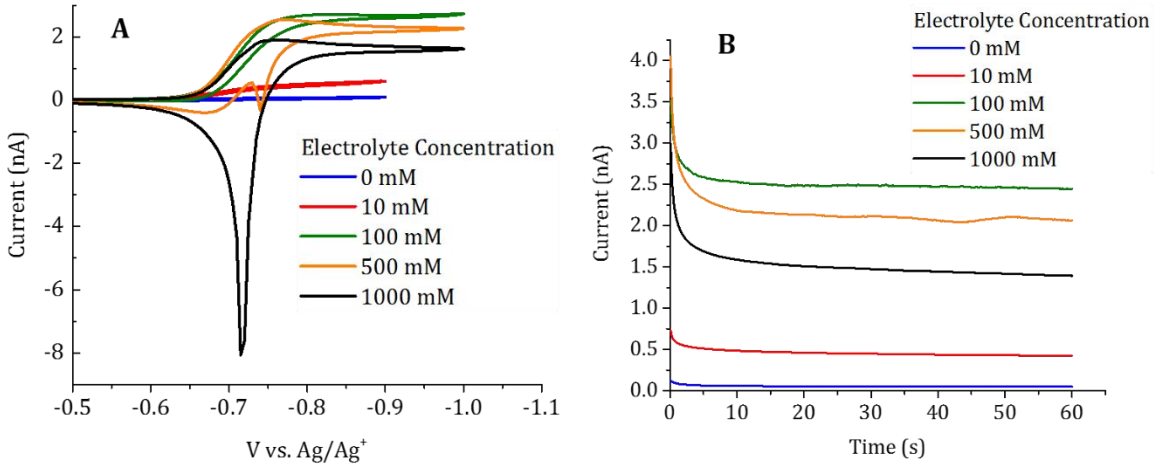

Figure D.61. (A) Cyclic Voltammograms at 10 mV/s for 22 kDa **VioRAP** (5 mM) as a function of electrolyte concentration ($TBAPF_6$). (B) Current transients following a potential step at the UME for the first reduction of the 22 kDa **VioRAP** in a series of electrolyte concentrations.

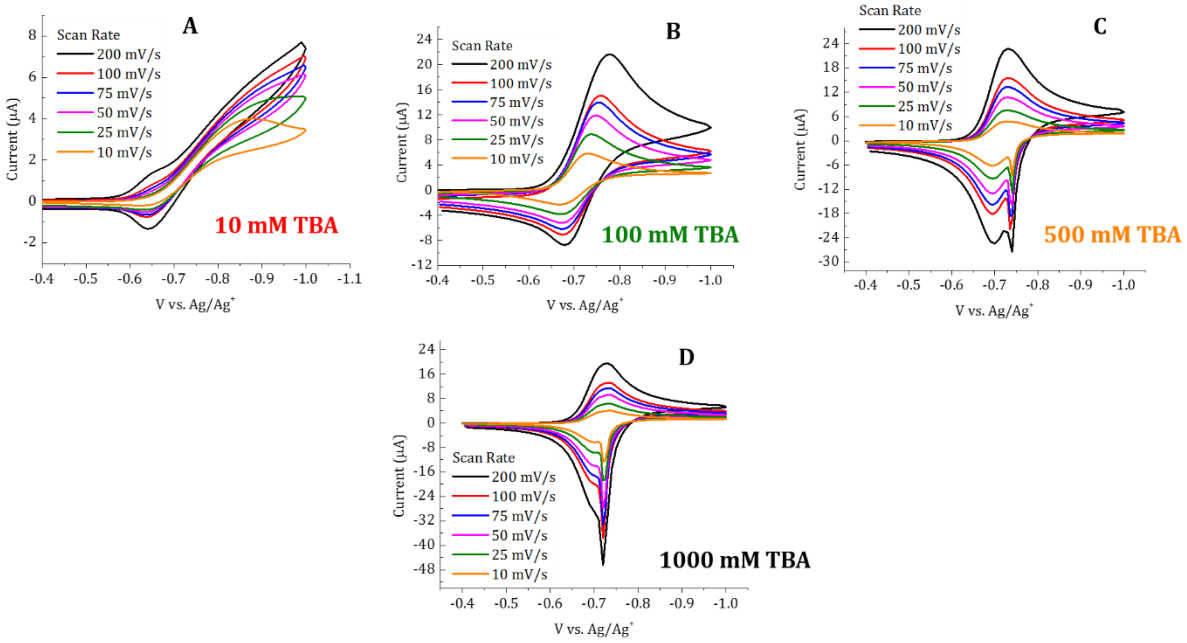

Figure D.62. (A) Cyclic voltammetry at series of scan rates with 5 mM 22 kDa **VioRAP** in solution with 10 mM $TBAPF_6$ electrolyte concentration. (B) Cyclic voltammetry at series of scan rates with 5 mM 22 kDa **VioRAP** in solution with 10 mM $TBAPF_6$ electrolyte concentration. (C) Cyclic voltammetry at series of scan rates with 5 mM 22 kDa **VioRAP** in solution with 10 mM $TBAPF_6$ electrolyte concentration (D) Cyclic voltammetry at series of scan rates with 5 mM 22 kDa **VioRAP** in solution with 10 mM $TBAPF_6$ electrolyte concentration. (E) Overlay of cyclic voltammograms at 50 mV/s with 5 mM 22 kDa **VioRAP** in solution as a function of $TBAPF_6$ electrolyte concentration.

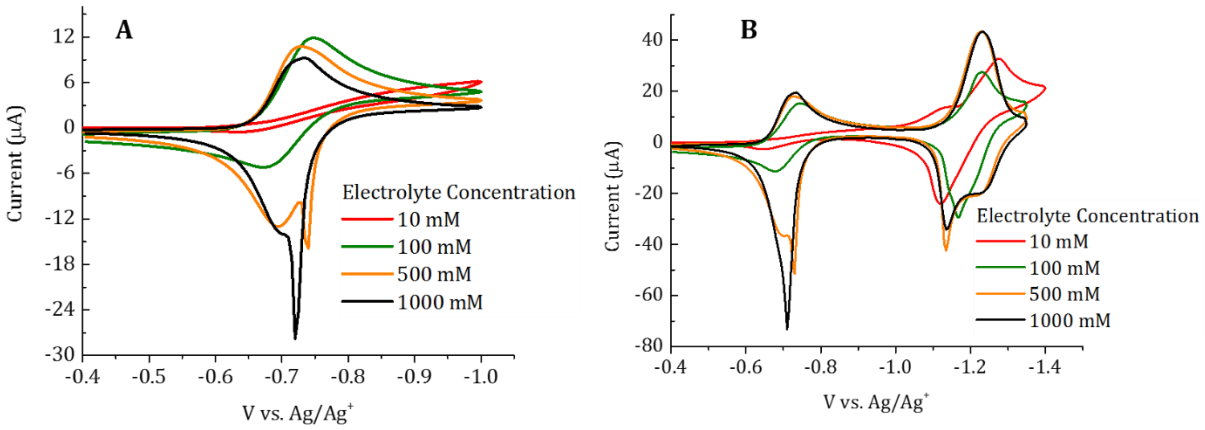

Figure D.63. (A) Cyclic voltammetry through the first reduction of 5 mM 22 kDa **VioRAP** in solution at 50 mV/s as a function of $TBAPF_6$ electrolyte concentration. (B) Cyclic voltammetry through the second reduction of 5 mM 22 kDa **VioRAP** in solution at 50 mV/s as a function of $TBAPF_6$ electrolyte concentration.

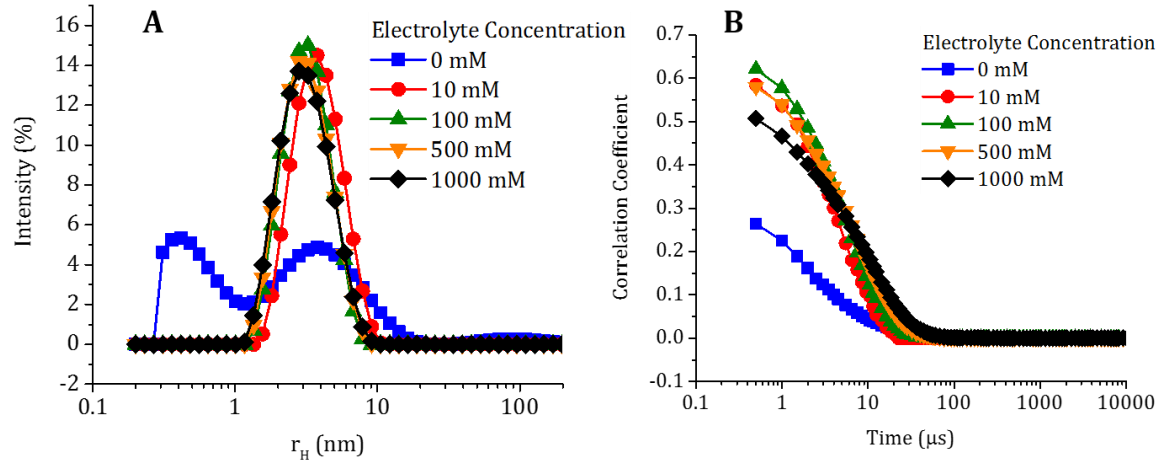

Figure D.64. (A) Intensity distribution of DLS scattering events of solutions of 22 kDa **VioRAP** at 5 mM concentration in acetonitrile at different ionic strengths as function of particle size in solution. (B) Intensity distribution of DLS scattering events of solutions of 22 kDa **VioRAP** at 5 mM concentration in acetonitrile at different ionic strengths as function of particle size in solution.

Table D.1 Measured Values of Viscosity for 318 kDa **VioRAP** at Different Concentrations of RAP and Ionic Strengths

Viscosity (mPa*s)					
	Electrolyte Concentration (mM)				
RAP Concentration (mM)	***0***	***10***	***100***	***500***	***1000***
0.5	0.472	0.423	0.443	0.552	0.781
1.8	0.437	0.380	0.414	0.564	0.756
3.2	0.477	0.451	0.450	0.582	0.823
5.6	0.640	0.488	0.499	0.645	0.885
10	0.745	0.572	0.545	0.695	0.905
17.8	0.944	0.702	0.631	0.860	1.050
31.6	1.357	0.936	0.792	0.840	1.136
56.2	1.728	1.457	1.029	1.242	1.564
100	2.517	2.294	1.767	1.801	2.227
177.8	5.191	4.380	3.659	4.085	2.456
316.2	11.384	10.351	9.127	10.901	2.010
500	18.19	16.24	15.41	13.86	N/A

Table D.2 Evaluated Parameters for **PAF** Films

Electrolyte Concentration (mM)	Thickness (nm)	Charge (mC)	Surface coverage (mol/cm^2)	Concentration (mol/L)
10	13.1 ± 4.5	0.130	4.82 x 10^{-9}	3.7
100	123.2 ± 30.1	0.144	5.33 x 10^{-9}	0.43
500	305.5 ± 6.3	0.175	6.47 x 10^{-9}	0.21
1000	366.1 ± 37.3	0.144	5.35 x 10^{-9}	0.15

References

1. Nagarjuna, G.; Hui, J.; Cheng, K.; Lichtenstein, T.; Shen, M.; Moore, J. S.; Rodriguez-Lopez, J., *J. Am. Chem. Soc.*, **2014,** 136, 16309-16316.

2. Burgess, M.; Hernandez-Burgos, K.; Simpson, B. H.; Lichtenstein, T.; Avetian, S.; Nagarjuna, G.; Cheng, K. J.; Moore, J. S.; Rodriguez-Lopez, J., *J. Electrochem. Soc.*, **2016,** *163*, H3006-H3013